Experimental and numerical studies on the micromechanical crystal plasticity behavior of an RPV steel

Qiwei Shi

université PARIS-SACLAY

NNT : 2018SACLN009

Thèse de doctorat

école normale supérieure paris–saclay

Experimental and numerical studies on the micromechanical crystal plasticity behavior of an RPV steel

Etudes expérimentales et numériques de plasticité cristalline d'un acier de cuve

Thèse de doctorat de l'Université Paris-Saclay
préparée à l'Ecole Normale Supérieure de Cachan
(Ecole Normale Supérieure Paris-Saclay)

École doctorale n°579 : Sciences mécaniques et énergétiques, matériaux et géosciences (SMEMAG)

Spécialité de doctorat: Mécanique des solides

Thèse présentée et soutenue à Cachan, le 23 Avril 2018, par

M. Qiwei SHI

Composition du Jury :

M. Jérôme CREPIN DR Mines ParisTech, CdM, Mines ParisTech/CNRS	Président
M. Alan Cocks Professeur, Oxford University	Rapporteur
M. Marc G.D. Geers Professeur, Eindhoven University of Technology	Rapporteur
Mme. Véronique AUBIN Professeure, MSSMat, CentraleSupelec/CNRS	Examinatrice
M. Stéphane ROUX DR CNRS, LMT, ENS Paris-Saclay/CNRS	Co-Directeur de thèse
M. Félix LATOURTE Ingénieur chercheur, Département MMC, EDF R&D	Encadrant industriel
M. François HILD DR CNRS, LMT, ENS Paris-Saclay/CNRS	Directeur de thèse

Acknowledgements

First of all, I would like to thank sincerely the rapporteurs Alan COCKS and Marc De GEERS, and the examinaters Véronique AUBIN and Jérôme CREPIN. Thank you for taking the time to read carefully my thesis and your encouragements. The exchanges with you at the defense are very enlightening.

Special thanks to all my directors and tutors at LMT and MMC EDF, François HILD, Stéphane ROUX and Félix LATOURTE. All three tutors work perfectly as a tutoring team and every one contributes in a unique and essential way in my works for the last three years. François has a special talent at encouragement: "do you know someone in the whole world who can do this? To my knowledge, NO!" And at the same time his eyes are shining and his face smiling broadly. I admire very much his rigorousness in doing research and his meticulous way of working. His kindness and affection towards his PhD students are heartfelt by us all. His concise and insightful remarks at the UTR meeting always point the good directions. Stéphane is always full of good ideas, very active and audacious in rewriting each and every document I sent him, to the point that I start to look forward to his reply the second after the sent of the mail. What amazes me is his efficiency during his 2-hour ranging for all doctorate students each Thursday afternoon, during which he answers all the questions and give never heard-of suggestions. His emails are a rich source of new scientific ideas, witty jokes and beautiful French phrases. All his straight-put suggestions and critics have helped me a lot for the last few years and will be revisited constantly in my future careers. Félix, my internship tutor immediately prior to the doctorate study, has enlightened and encouraged me to continue the scientific exploration in EDF. Félix has accompanied me quotidianly and removes plenty of encountered obstacles in time. He acts as an easy-going supervisor and a sincere big brother for the past few years. He is thanked for his timely suggestions and reorientation, especially when I'm refractory, which is quite not rare. What's more, the constant exchange with Félix has enlightened me concerning not only the PhD but also the life as a researcher in general. It has been a privilege for me to work with all my tutors.

During the three years I've received precious help in experiments from Dominique LOISNARD, Nicolas BRYNAERT, Julien STODOLNA and Michel MAHE. Without their dedication and exceptional skills, all the experimental test would have been impossible. If not for the large-volume data and high-resolution images that they bequeath me, all the develop-

ment of algorithms and image correlation would be a river without source or a tree without root. The shared hatred of “saloperie” on sample surface and the gallantry to offer each other the privilege to click on a RUN button for a painstakingly prepared experiment have forged our friendship. The last three years have been “colorful”, both literally and figuratively, thanks to your help.

The meetings with Ghiath Monnet, Marc Berveiller, Rémy MEUNIER, Sébastien, Edouard POUILLER and Nicolas Rupin were very helpful to the PhD project, too. Many thanks to Adrien GUERY for his presence and suggestions at each advancement meeting, and his kind help for all sorts of problems. Thanks to Lydie BLANCHARD, Valérie KERVARGANT, Cathérine GENIN and Charlène MARCHE for all the help for administrative chores. Thanks especially to Yan NEGGERS, Denis THOMASSON, Martin PONCELET and Yoan GUILHEM for their pedagogic help.

Georges-Arthur is particularly thanked for his kindness and friendship. Though we support different French president election candidate last year, I share totally your pity that our favorites are not elected. All the political, social and economical debates during the lunch are very enriching for me. Thanks to Damien, Faïza and Arina for those happy lunch hours we spent together.

I’d like to thank fellow doctorate students at EDF, Elodie, Emeric, Wen, Julien, Laurie, Abel and Ronan for their help all along the PhD work. Good luck to Ziling, Aboubakar, Shun, Maoyuan and Amina for future PhD researches. Fellows at LMT Cachan, Ante, Benoit, Clément, Adriana, Arduro, Paul, Yanjun, Xuyang, Kévin, Myriam, Ali, Morgan are also sincerely thanked for their companion. Each exchange in the Eikology UTR meeting with you is very enlightening. Finally, special thanks to all the members of the MMC department for their warm welcome and their friendship. The PhD study would not have been the same without them.

Thanks to French *Agence Nationale de la Recherche* (ANR) for financing the thesis, thanks to EDF R&D for providing a decent salary and state-of-the-art equipment for three years. And thanks to French government for allocating me the Eiffel Scholarship between 2012 and 2014. Without the generosity of France, it would be very difficult, if not impossible, for me to pursue a scientific endeavor. Francophile, I would always keep the motto of French Republic "Liberty, Equality and Fraternity" in heart.

I’d also thank my family, mother and younger brother, for their support for the last three years and preceding years of study. My son Chaoyi’s birth in 2016 brings much pleasure

to me. He is in particular thanked for waking me up once at 3 AM to submit a paper, 1 hour before the deadline, by his pressing hunger for milk. My mother-in-law Ying Li is particularly thanked for her kindness to take care of my son in France. My wife Liangjun is thanked for her endless push to the top, especially when I felt satisfied myself: "another paper in a never-heard-of journal" or "when will you publish in *Science* or *Nature*?". Special thoughts to my father, I hope that you are happy to see what I've done for the last decade and that you continue to take pride in your elder son.

Contents

Résumé français étendu

La cuve de réacteur est un composant majeur d'une centrale nucléaire et son intégrité est essentielle pour la sûreté nucléaire. Plusieurs projets ont été lancés par EDF pour caractériser le comportement mécanique de l'acier de cuve, nommé 16MND5 en France, et des approches expérimentales et numériques ont été adoptées à différentes échelles [Sekfali 2004; Vereecke 2004; Mathieu 2006]. L'acier possède une microstructure fine avec deux phases principales, qui sont la ferrite et la bainite. Cette thèse vise à étudier le comportement plastique de l'acier de cuve à l'échelle microscopique en réalisant des comparaisons entre un essai et des simulations numériques. Le gain apporté par la connaissance de la microstructure en profondeur est étudié. L'essai consiste à réaliser des tractions *in-situ* à l'intérieur d'une chambre d'un microscope électronique à balayage (MEB) et à observer l'évolution de la surface de l'éprouvette par plusieurs modalités d'imageries disponibles dans un MEB. La simulation numérique consiste à prévoir la réponse mécanique de l'éprouvette avec des lois de comportement élasto-plastique cristalline, tout en prenant en compte des conditions aux limites pertinentes. La comparaison entre l'essai et la simulation permet de valider des lois de plasticité cristalline et d'en identifier les paramètres.

Un algorithme de *corrélation des quaternions* a été proposé dans le cadre de cette thèse. L'algorithme prend en entrée deux images d'orientation crystallographique, obtenues par la technique EBSD, et mesure le champ de déplacement entre les deux images et un champ de résidu. Le quaternion (voir Figure 1) a été utilisé car il est bien adapté pour traiter l'orientation, surtout pour la symmétrie cristalline par rapport à d'autres outils tels que l'angle Euler ou le vecteur de Rodrigues. Si la corrélation de quaternions est réussie, le résidu contient le champ de rotation entre les deux images EBSD et l'erreur d'acquisition de l'orientation, voir Figure 2. L'incertitude sur le champ de déplacement a été évaluée à environ 0.3 pixel, et celle de la rotation mesurée est estimée de l'ordre de 10^{-3} degré, bien en dessous de l'indexation EBSD. L'algorithme a été exploité dans cette thèse à plusieurs reprises pour analyser les données EBSD. Un article a été publié sur le sujet [Shi et al. 2016].

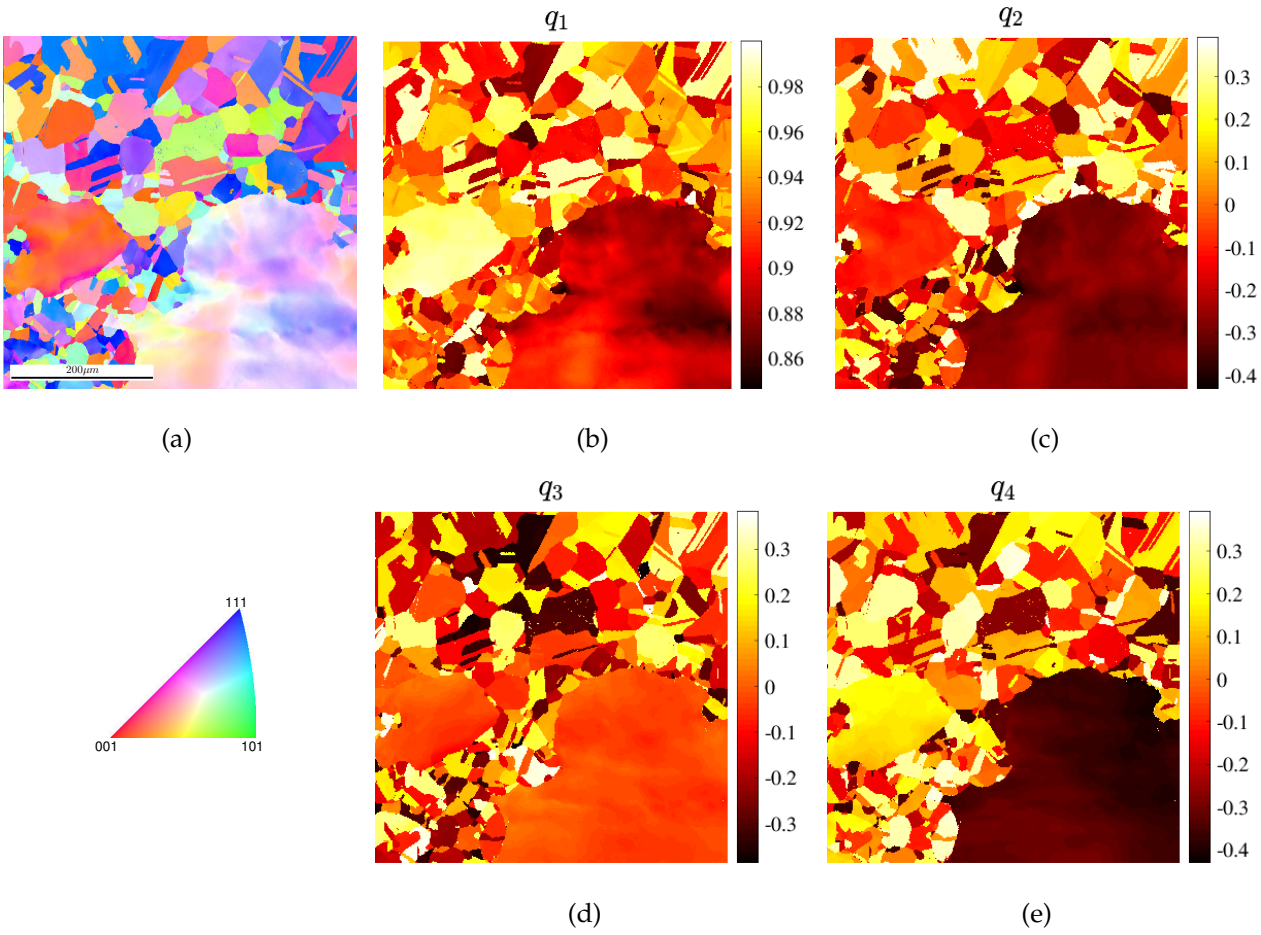

Figure 1: Une acquisition EBSD (a) et sa présentation de quaternion (b-e).

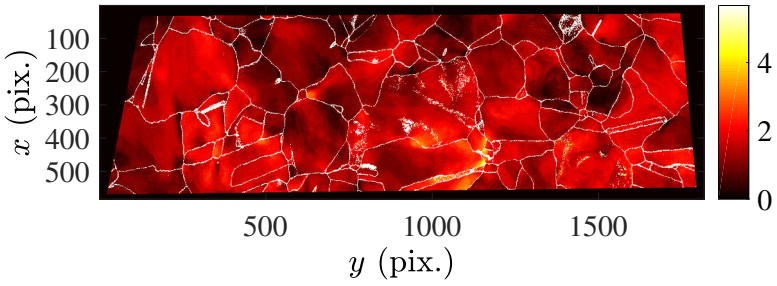

Figure 2: Le champ de rotation cristalline (en degré) mesuré par corrélation de quaternion.

Un algorithme ADDICTED a été développé pour traiter les images de diffraction électronique obtenues par la technique EBSD à haute résolution (HR-EBSD). Des pré-traitements ont été proposés pour éliminer la variation globale du niveau de gris des images de Kikuchi. Une approche de corrélation d'images numériques intégrée a été adaptée avec pour objectif de déduire directement 8 des 9 composantes du tenseur de gradient de transformation. L'algorithme a été testé sur deux cas expérimentaux et ces résultats ont été comparés avec ceux des logiciels existants basés sur l'inter-corrélation. Le premier essai est l'acquisition

HR-EBSD sur une éprouvette monocristalline en flexion quatre points, et le second est réalisé sur une éprouvette à trois gros grains sollicitée en traction à 0.5% de déformation. Une diminution de l'incertitude de mesure a été observée pour le premier essai, voir Figure 3. Une accélération du temps de calcul d'un facteur 4 a été observée pour la méthode ADDICTED, dans le cas du deuxième essai. La méthode ADDICTED a également réduit les valeurs extrêmes des contraintes élastiques estimées, voir Figure 4. La méthode ADDICTED est par nature capable de traiter les images de diffraction en cas de grande rotation (>1°) et les champs de résidus fournis sont une source riche d'informations sur la qualité de corrélation, la qualité de l'image Kikuchi et le champ de niveau de gris de fond de l'image Kikuchi. Un article a été soumis suite à un dépôt de brevet [Shi et al. 2017c].

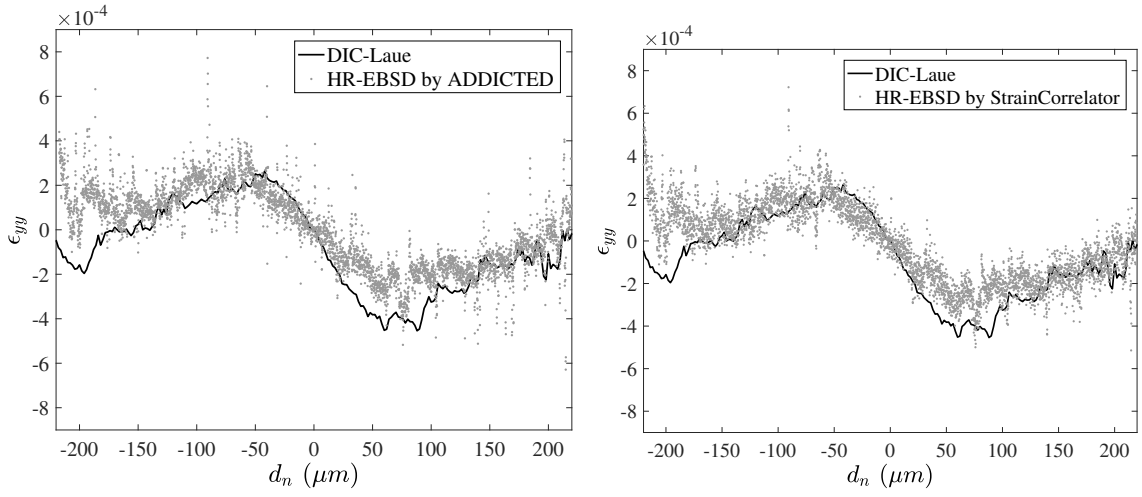

(a) (b)

Figure 3: Profils de déformation longitudinale ϵ_{yy} en fonction de la distance à l'axe neutre d'un essai de flexion à 4 point. (a) ADDICTED (b) StrainCorrelator.

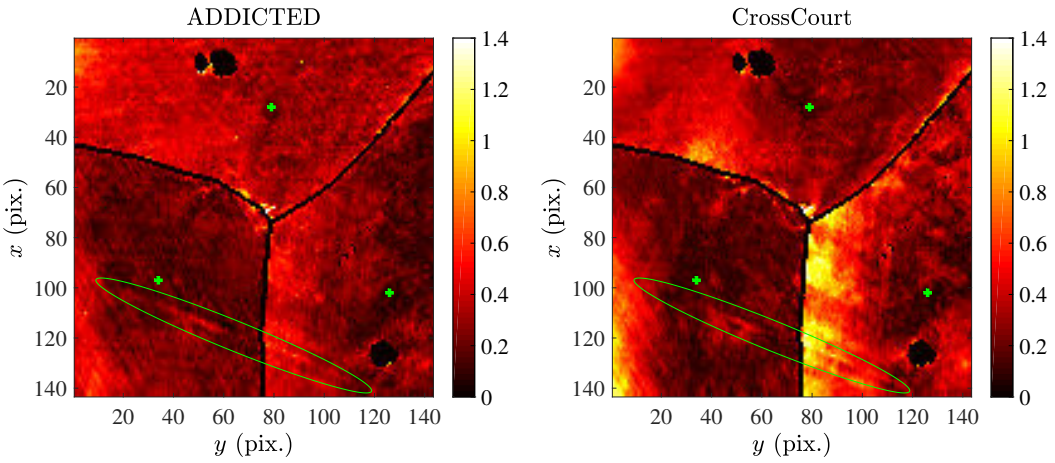

(a) (b)

Figure 4: Contrainte équivalente Von Mises (en GPa) obtenues par (a) ADDICTED et (b) CrossCourt.

Deux essais de traction pour des éprouvettes d'acier 16MND5 ont été réalisés, le premier avec l'éprouvette inclinée à 70° et l'autre à plat. Des mouchetis aléatoires de platine ont été déposés sur l'éprouvette pour faciliter les calculs de corrélation d'images numériques. Le premier a connu une erreur spécifique des coordonnées suivant direction y et donc a été rejeté. La thèse s'est focalisée sur l'exploitation du second essai. Des images d'électrons rétrodiffusés (BSE) ont été prises au cours de la déformation *in-situ*, et à chaque étape deux images sont acquises avec des directions de balayge orthogonales. Un algorithme a été adopté pour corréler les deux images BSE de chaque étape, et l'erreur de repositionnement de ligne de balayage a été quantifiée et corrigée. Avec l'hypothèse que les coordonées dans la ligne de balayage sont correctes, une série d'images BSE sans erreur de distortion de MEB a été obtenue (voir Figure 5(b)). La corrélation d'images numériques (CIN) sur cette série d'images fournit les champs de déplacement et de déformation au cours de la traction (voir Figure 5(d)). Des acquisition EBSD ont été réalisées avant et après la traction de l'éprouvette (Figure 5(a)). La rotation cristalline de l'éprouvette a été obtenue par corrélation de quaternion des images EBSD (Figure 5(c)). Les images EBSD et BSE ont été corrélées grâce au mouchetis et d'importantes distortions ont été révélées pour l'acquisition EBSD. Ainsi toutes les images (EBSD, BSE) prises sur l'éprouvette ont été corrélées précisément. La rotation cristalline et la déformation peuvent être comparées directement (Figure 5(e)). Une corrélation positive a été établie entre la rotation et la déformation pour les deux phases du matériau. Un article a été publié sur le sujet [Shi et al. 2018a].

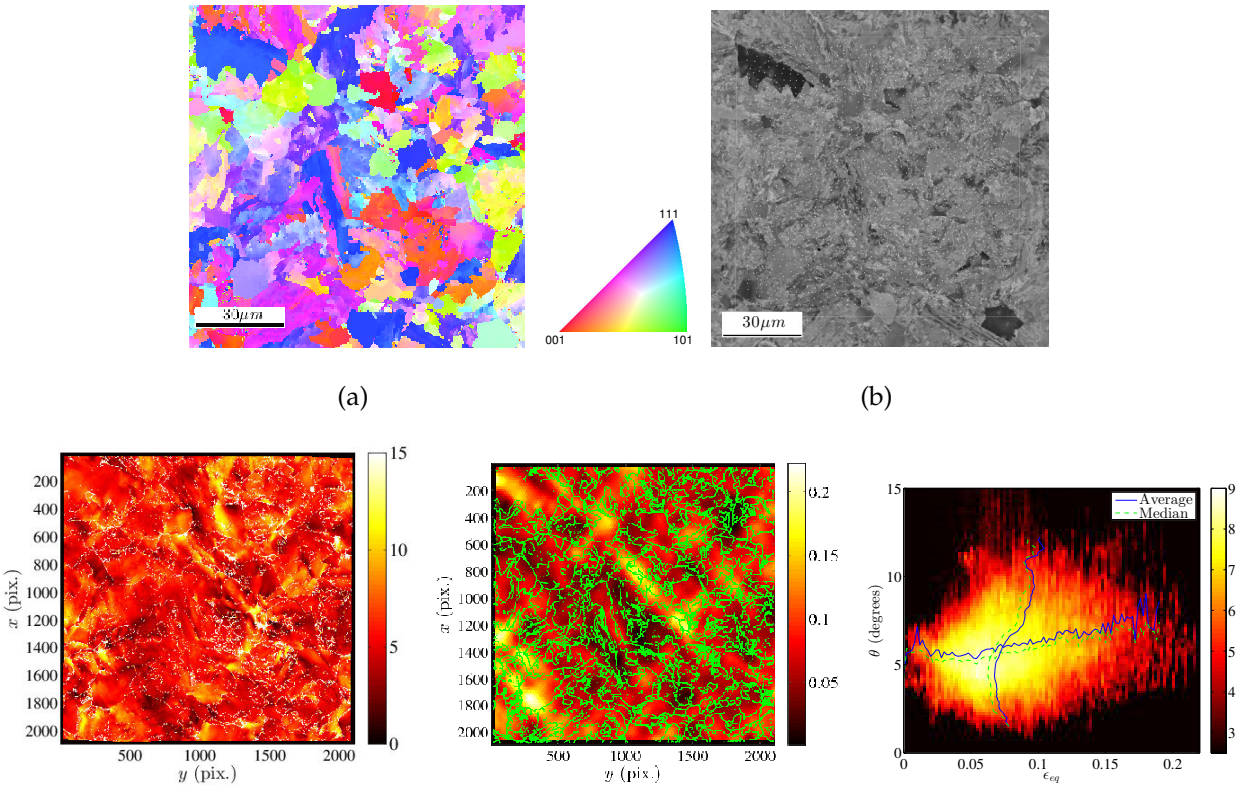

(a) (b)

(c) θ (d) ϵ_{eq} (e) $\log(\rho)$

Figure 5: Mesure de la rotation cristalline et de la déformation lors d'un essai de traction. (a) Figure de pôle inverse issue de l'acquisition EBSD de l'éprouvette. (b) Image BSE de l'éprouvette. (c) Rotation cristalline obtenue par corrélation de deux images EBSD (en degrés). (d) Déformation équivalente obtenue par corrélation de deux images BSE. Les joints de grain extraits de l'image EBSD sont superposés dans le champ de déformation. (e) Carte de corrélation entre la rotation et la déformation équivalente. L'échelle est logarithmique. Les profils moyens et médians de rotation et de déformation sont superposés.

Après l'essai de traction *in-situ*, un processus de polissage sérié automatique accompagné des acquisitions EBSD (FIB-EBSD) a été réalisé sur l'éprouvette. Quelques coupes de l'essai sont montrés en Figure 6. L'empilement de ces coupes par CIN globale avec un maillage adapté a été proposé et comparé avec l'algorithme existant. La microstructure déformée de l'éprouvette en trois dimensions est ainsi acquise.

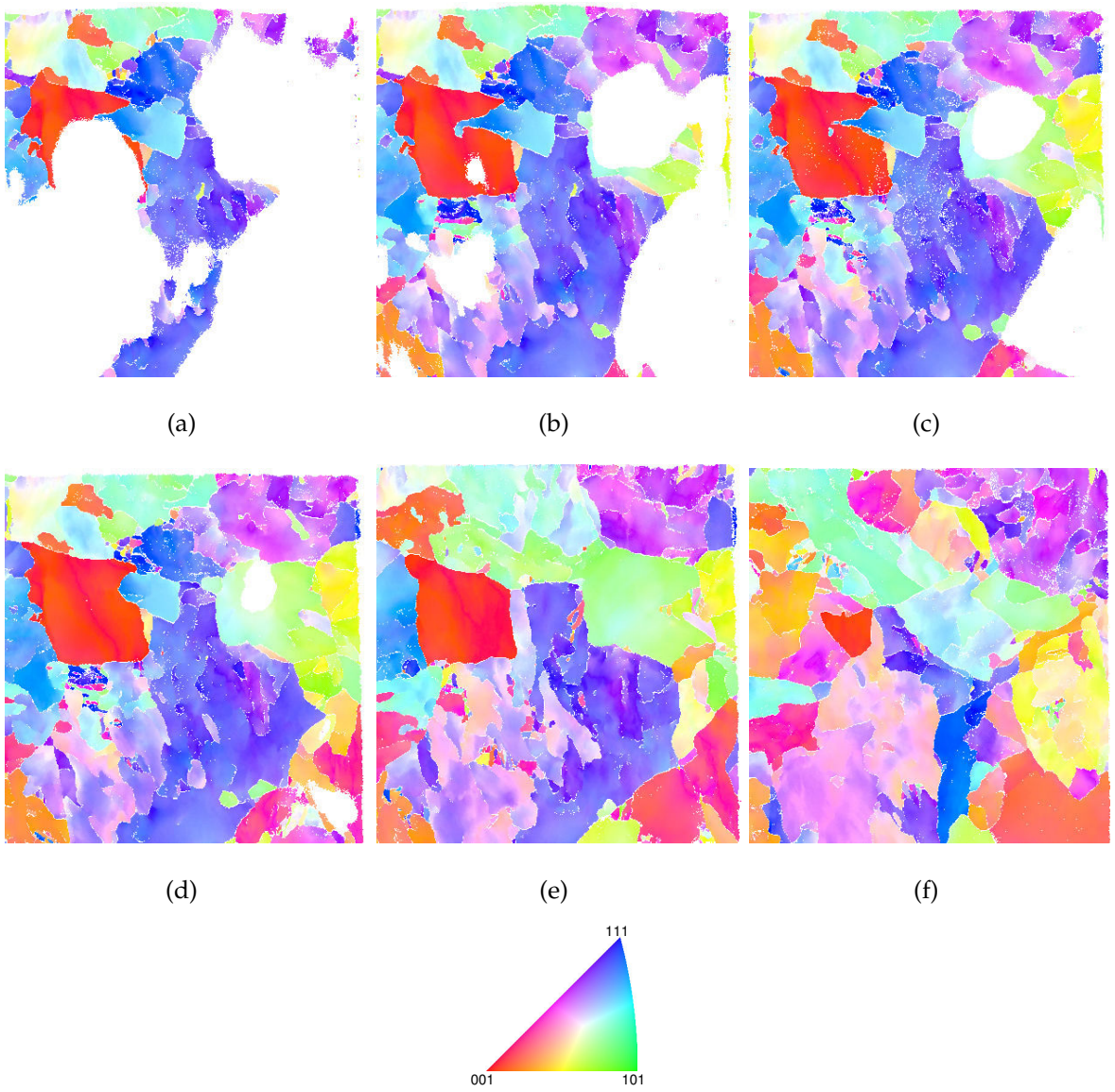

Figure 6: Champs d'orientation des première (a), troisième (b), cinquième (c), septième (d), vingt-septième (e) et quatre-vingt-septième (f) couches de l'essai FIB-EBSD.

La mesure de topographie de l'éprouvette dans MEB a également été traitée. Trois méthodes distinctes ont été proposées et testées sur l'éprouvette après traction. La méthode de stéréo-corrélation a été étendue à une image prise à plat et l'autre prise avec un angle d'inclinaison de 70°, qui est la position conventionnelle d'acquisition EBSD. Le mouchetis déposé en surface de l'éprouvette permet à la paire d'images d'être corrélée par CIN régularisée. Deux informations capitales peuvent être tirées du champ de déplacement obtenu: l'angle précis d'inclinaison et le champ de topographie (voir Figure 7(b)). Une deuxième méthode consiste à couvrir la surface de l'éprouvette par du platine amorphe et de tailler successivement l'éprouvette couche par couche (FIB), puis acquérir une image EBSD de

chaque coupe (technique FIB-EBSD). Progressivement la couche de platine est érodée et l'éprouvette est émergée et indexée, ainsi des informations de topographie de la surface sont obtenues. La topographie obtenue par cette méthode est par nature discontinue, comme les marches d'un escalier, et la distance entre les marches est l'épaisseur de chaque coupe. Des méthodes d'interpolation peuvent régulariser et lisser le résultat de topographie, par exemple l'interpolation par transformation de Fourier en imposant les valeurs de topographie aux bords de marches (voir Figure 7(a)). Ces méthodes de stéréo-corrélation et de FIB-EBSD appliquées sur l'éprouvette donnent des résultats similaires, l'écart quadratique moyen étant d'environ 50nm. Une troisième méthode traite les images EBSD avant et après déformation, et traduit la rotation cristalline entre ces deux états en déplacement hors-plan par une méthode d'intégration (voir Figure 7(c)). Cette méthode de rotation-intégration n'est sensible qu'à la topographie due à l'élasticité, étant donné que la plasticité par l'activité des systèmes de glissement ne génère pas de rotation mesurable par la technique EBSD. La comparaison des résultats entre la stéréo-corrélation et la rotation-intégration a démontré une similitude remarquable avec un coefficient de Pearson de 0.64. En plus, l'écart quadratique moyen de topographie est sous-estimée de 10% par rotation-intégration, ce qui prouve que la topographie dûe à la plasticité est faible pour cette éprouvette par rapport celle causée par l'élasticité. Un article a été accepté pour publication sur le sujet [Shi et al. 2018b].

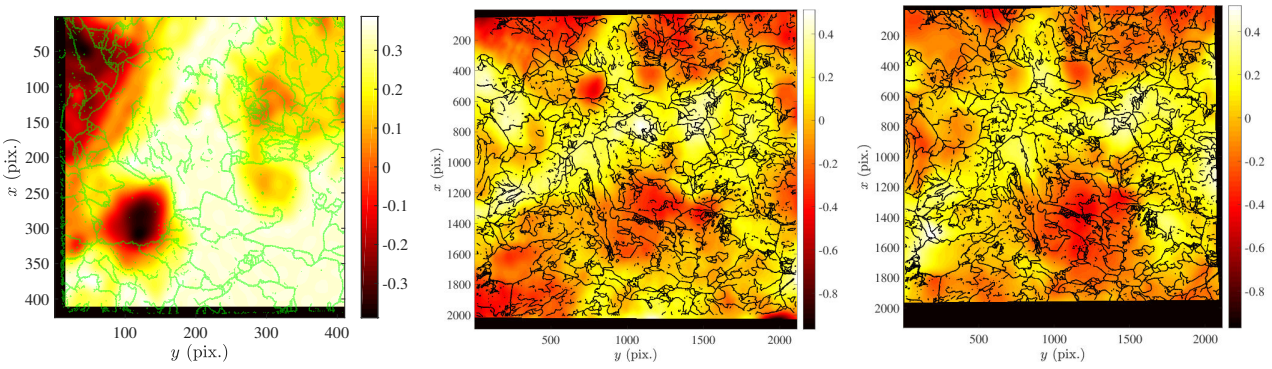

(a) (b) (c)

Figure 7: Comparaison des champs de topographie (en µm) mesurés par FIB-EBSD (a), stéréo-corrélation (b) et rotation-intégration (c).

Des études ont aussi été menées pour résoudre le problème posé par la nature destructive du FIB. Seule la microstructure *post mortem* peut être acquise par cette technique destructive, alors que les simulations directes nécessitent la connaissance de la microstructure initiale. De plus, les paramètres des lois de comportement plastique sont eux aussi inconnus. Il a

été proposé de partir de la microstructure *post mortem* mesurée par FIB-EBSD et d'utiliser les champs cinématiques de surface mesurés au long de la déformation, et de déterminer la microstructure initiale et les paramètres des lois de comportement itérativement (voir l'organigramme montré dans Figure 8). Des approches itératives sont mises en oeuvre dans la détermination de la microstructure et des paramètres respectivement. Un cas synthétique 2D a été adopté pour tester la validité de l'approche, où les données "expérimentales" ont été produites par simulation avec une loi de plasticité [Monnet et al. 2013] sur un modèle plus grand que la zone d'intérêt. Le cas test a montré que la configuration de référence a été retrouvée et les paramètres utilisés pour produire les données "expérimentales" ont été identifiés précisément. Le cas test a également montré que le chargement par une loi de plasticité virtuelle à écrouissage constant, qui est pris comme le module tangent de la courbe contrainte-déformation, permet de retrouver une part significative de la microstructure initiale. Deux articles ont été publiés sur le sujet [Shi et al. 2017a;b].

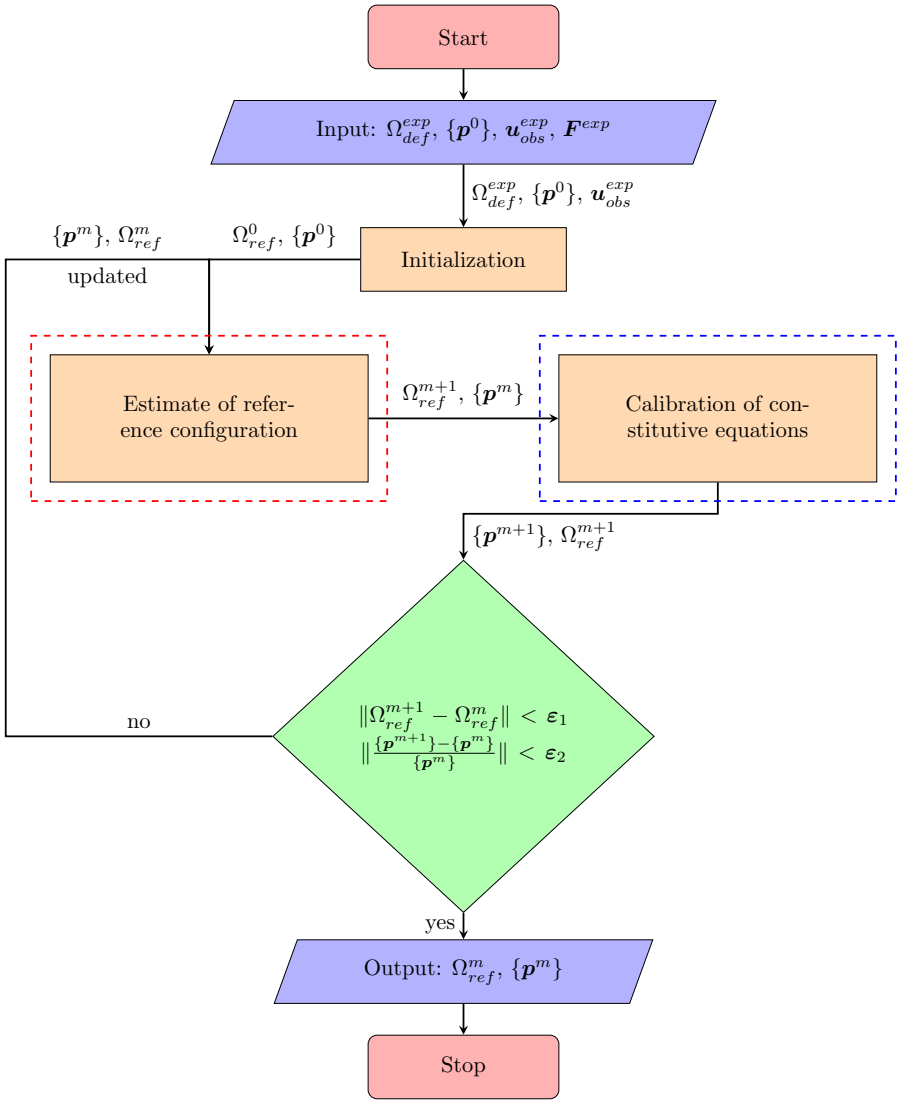

Figure 8: Organigramme de l'approche itérative pour déterminer la microstructure de référence et les paramètres de la loi de plasticité étudiée.

Un maillage d'éléments finis tetrahédriques a été généré à partir de la microstructure réelle mesurée par FIB-EBSD. Pour y parvenir, un regroupement important des voxels a été adopté pour réduire la complexité. Un maillage triangulaire 2D a été d'abord créé au long des joints de grains. Après avoir lissé ce maillage triangulaire, des noeuds ont été insérés pour créer un maillage tétrahédrique, qui est montré en Figure 9. Le maillage de la surface du modèle est montré en Figure 10.

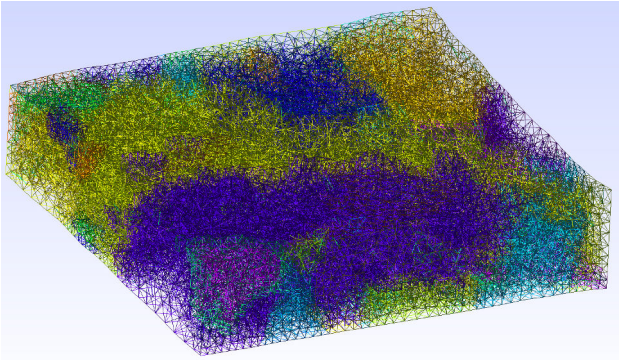

Figure 9: Maillage éléments finis généré à partir des données de FIB-EBSD. Les différentes couleurs correspondent aux différent grains.

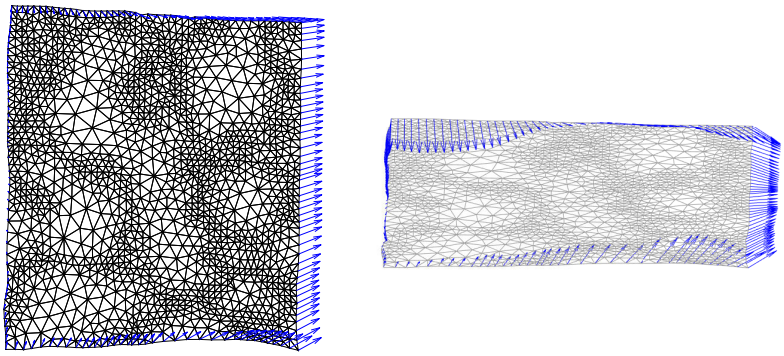

(a) (b)

Figure 10: Conditions aux limites cinématique en surface du modèle adoptées pour la simulation de l'essai de traction en 2D (a) et 3D (b). Le déplacement hors-plan est multiplié par 5 dans (b) afin de le rendre plus visible.

L'essai de traction réalisé dans cette thèse a également été simulé par des lois de comportement plastique cristalline. Deux lois ont été adoptées, l'une basée sur la dynamique des dislocations des cristaux cubiques centrés. L'autre loi est une version simplifiée du modèle de Méric-Cailletaud. Les conditions aux limites (CL) surfaciques du modèle ont été extraites des mesures de champs cinématiques issue de la corrélation d'images numériques (voir Figure 10). Les CL cinématiques suivant les directions x et y sont obtenues en profondeur par propagation des informations de surface. Les déplacements suivant z des surfaces latérales sont ceux qui annulent les contraintes de cisaillement. Les faces extérieure et profonde sont laissées libres (condition de Neumann). Une similitude remarquable a été retrouvée entre les champs cinématiques expérimentaux et numériques suivant trois directions, comme montré en Tableau 1. Pourtant, une incohérence a été observée entre la rotation expérimentale et numérique. C'est un résultat très satisfaisant étant donné plusieurs simplifications

présentes, par exemple le regroupement des voxels et les CL estimées.

Table 1: Comparaison des champs cinématiques surfaciques expérimentaux et simulés avec différentes lois.

	SMC avec éléments quadratiques	SMC avec éléments linéaires	Données expérimentales	DD_CC avec éléments linéaires
u_x	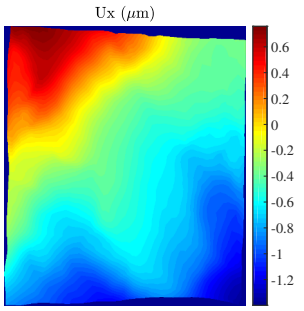	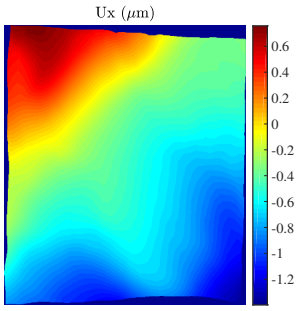	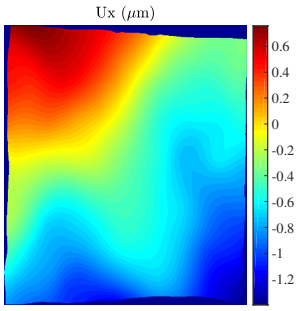	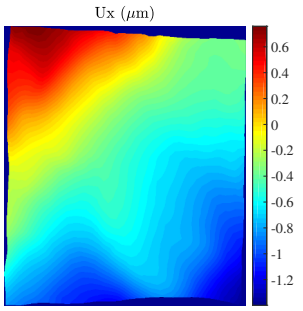
u_y	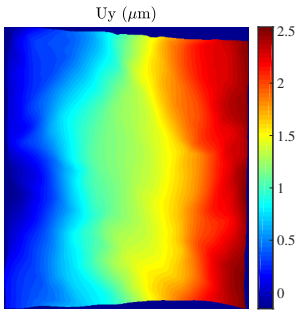	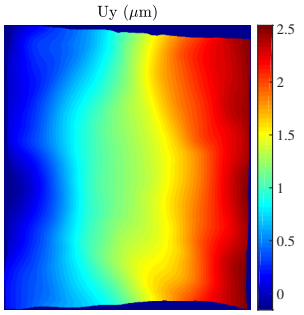	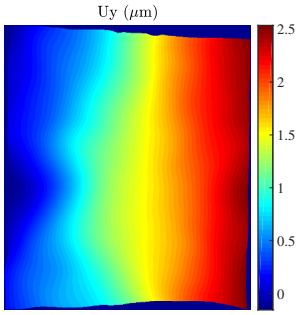	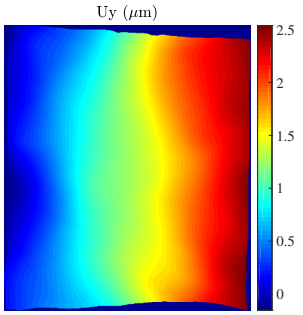
u_z	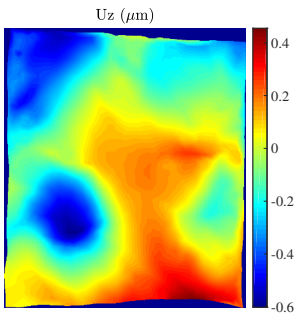	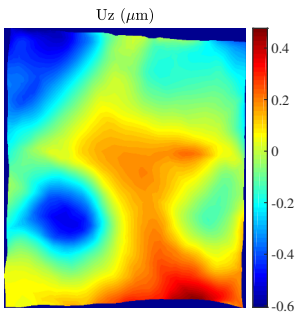	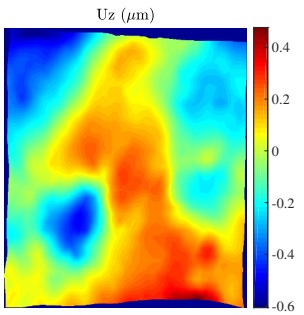	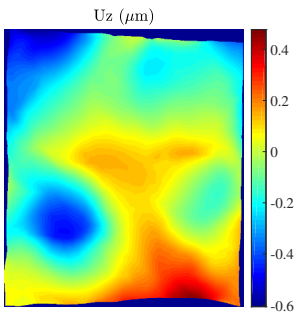
θ	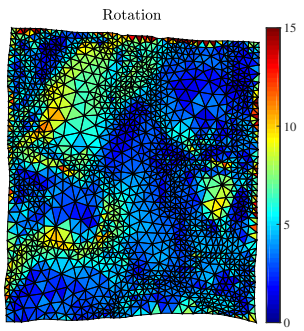	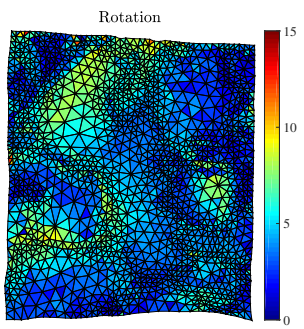	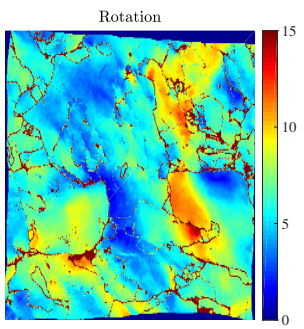	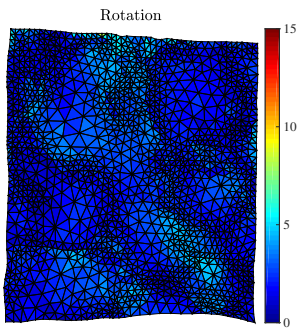

Numériquement efficace, la version simplifiée de la loi Méric-Cailletaud (SMC) a été identifiée en distinguant les deux phases du matériau. Le recalage de modèles à partir des champs cinématiques et de la force macroscopique est adopté. Après une étude

d'identifiabilité des paramètres, le paramètre qui joue sur la limite d'élasticité R_0 est cherché pour chaque phase, alors que le paramètre influençant la contrainte d'écrouissage Q est supposé identique pour les deux phases. Cette stratégie d'identification, dénommée RQR, réduit davantage la fonction coût que l'identification qui ne distingue pas les phases. De plus, le paramètre R_0 identifié pour la ferrite est plus bas que celui pour la bainite (voir Figure 11), en accord avec les valeurs physiques attendues [Mathieu 2006]. Ce jeu de paramètres pourra être utilisé pour la prévision des réponses mécaniques de l'acier, par exemple le champ de contrainte (voir Figure 12) et la probabilité de rupture (fragile).

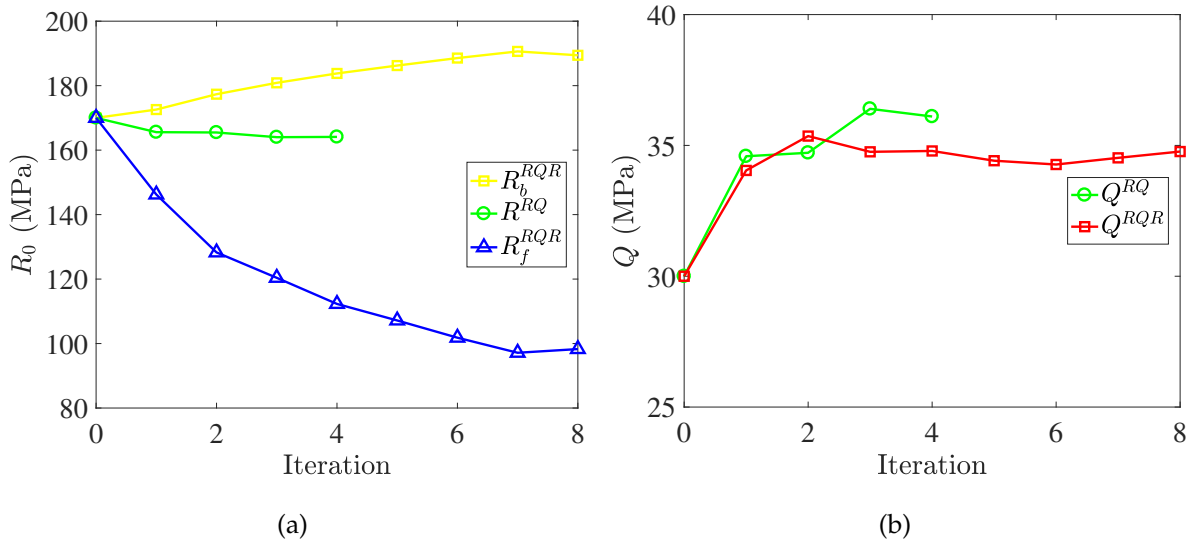

Figure 11: Evolution des paramètres R_0 (a) and Q (b) dans les identifications RQ et RQR.

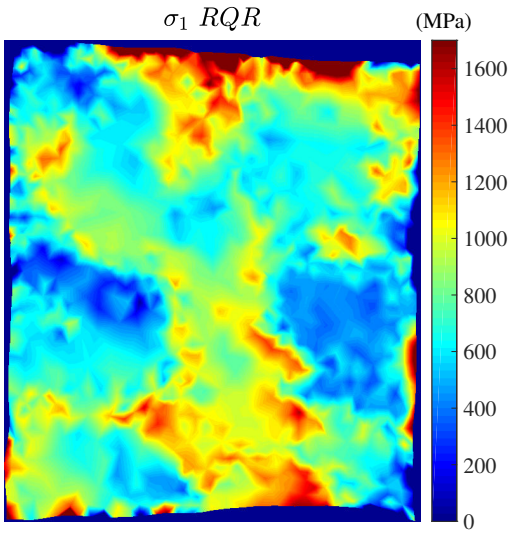

Figure 12: Le champ de la première contrainte principale à la surface du modèle prédit avec les paramètres identifiés par la méthode RQR.

Plusieurs aspects de l'étude expérimentale et numérique de la plasticité cristalline d'un métal fin ont été abordés dans cette thèse. La thèse met en évidence également quelques perspectives possibles pour les futures recherches. La technique EBSD à haute résolution n'a pas été adoptée pour l'essai de traction sur l'acier 16MND5, suite aux problèmes liés à l'absence d'une image Kikuchi de référence sans contrainte. Si cette difficulté est résolue dans le futur, l'acquisition HR-EBSD pourra être réalisée et fournira des informations très riches et précises sur la rotation et la contrainte élastique de l'éprouvette. La génération du maillage à partir de la microstructure 3D réelle pourra aussi être améliorée. Par exemple, le regroupement des voxels pourra être atténué afin de décrire la microstructure plus finement, et la génération du maillage quadratique pourra être optimisée pour réduire le nombre d'éléments final. Les conditions aux limites pourront aussi être mieux estimées, par exemple prendre en compte les concentrations de déformation mesurées en surface et les propager dans la profondeur suivant une direction pertinente. En plus, davantage d'études sont nécessaires pour expliquer l'incohérence entre les rotations cristallines expérimentales et numériques.

Chapter 1

Introduction

The present dissertation studies the crystal plasticity of a strategic steel used in the French pressurized water reactor vessels. This chapter first introduces the studied material in the PhD project, namely, a dual-phase steel with fine microstructures and heterogeneous properties. Then the commonly used *in-situ* experiments are presented for studying polycrystals at the microscale, where an introduction of digital image correlation methods will be provided. The finite strain formalism and two crystal plasticity laws used in the PhD project are detailed, followed by realistic 3D model generation for crystal plasticity simulations. The constitutive parameter calibration method based on coupling experimental and numerical simulation results is also introduced. Last, the outline of the PhD work is given.

1.1 Steel of reactor pressure vessels

1.1.1 Reactor pressure vessels

Figure 1.1 illustrates the operating principle of a Pressurized Water Reactor (PWR), or réacteur à eau pressurisée (REP) in French. The heat of the reactor core is extracted by a water circuit called primary circuit, which is maintained at high pressure to avoid boiling. Then the heat of the primary circuit is transferred to the second circuit through the vapor generator. The second circuit is also maintained at high pressure, (although not as high as the primary one), and the vaporization of water occurring there propels the turbo-alternator of the generator and electricity is produced.

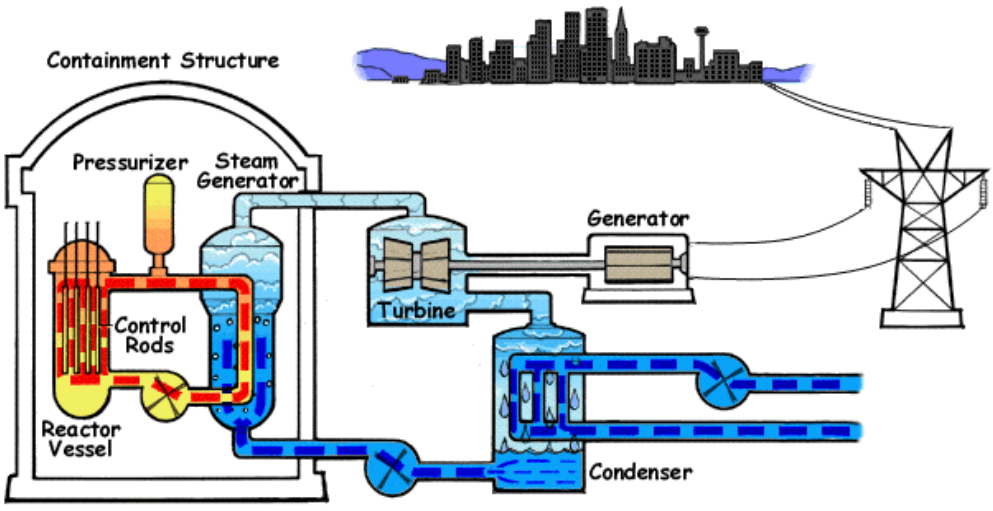

Figure 1.1: Overall principles of a pressurized water reactor. Image is issued from Wikipedia (https://en.wikipedia.org/wiki/Pressurized_water_reactor, June 2007).

Nuclear power plants produce in France around 75% of electricity. To ensure a safe operation of nuclear power plants, it is extremely important to be able to check the integrity of all the components of the nuclear reactor and in particular the pressure vessel , the only non-replaceable part of a nuclear reactor. Figure 1.2 shows the main components of the nuclear reactor, where the pressure vessel is the major component. Taking the French PWR of 1300MW capacity as an example, the pressure vessel is 22 cm thick, 4.4 m in diameter and 12.6 m high (actual dimensions could vary between different reactors). From the safety point of view, it is the second barrier between the nuclear fuel and the environment, after the fuel cell cladding and before the concrete confinement of the reactor building. It has the following functions:

- Hold the nuclear fuel assemblies, controlling rods and the other internal instruments that constitute the reactor core.
- Resist the high pressure of the primary circuit, which is 155 bar in normal service, and allow its circulation.
- Allow the replacement of depleted fuel by new one, and the rearrangement of fuel assemblies during the recharging campaign.

To sum up, the pressure vessel is considered as the principal component of a nuclear reactor.A large number of codifications and safety assessments are devoted to this component in order to prevent its failure even during severe accidents.

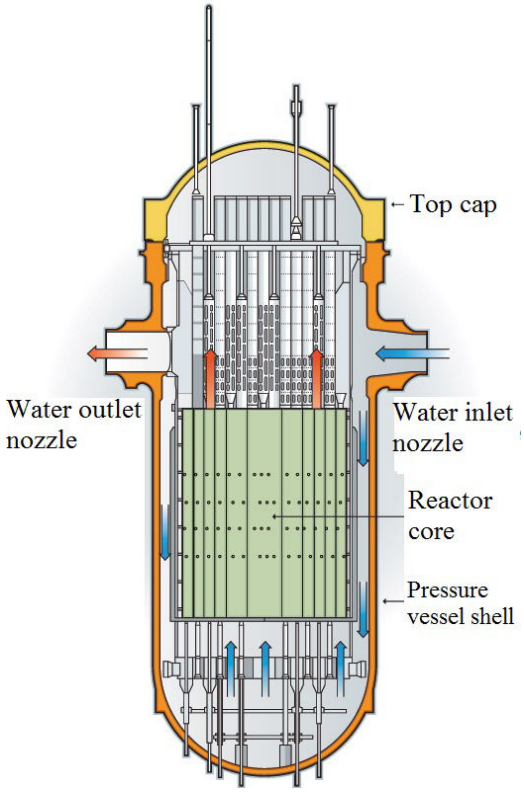

Figure 1.2: Components of nuclear reactor of capacity 900MW. Image is issued from Institut de Radioprotection et de Sûreté Nucléaire (IRSN, www.irsn.fr/FR/connaissances/Installations_nucleaires/Pages/Home.aspx).

The pressure vessel is in the form of a cylindrical reservoir, composed of 2 core flange shells (C1 and C2), a tubular flange shell (B) and two heads. Flange shells and heads are welded together. Several holes are present at the top and bottom of the pressure vessel, in order to make way for the controlling rods. The internal surface of the pressure vessel is entirely weld coated by two layers of austenitic stainless steel to reduce corrosion.

The pressure vessel has to sustain very high pressures (155 bar) and high temperature (350 °C) during at least 40 years. The utility companies have to demonstrate that the pressure vessel is able to withstand an increase of pressure and temperature that can occur during LOCA (loss of coolant accident). The under-cladding defects lead to stress concentrations and mechanical assessments are conducted on postulated defects. EDF is trying to increase the lifetime of French nuclear reactors from 40 to 60 years. It has to prove to the safety authority that the pressure vessel is safe during these extra 20 years. The PhD program goal is a (small) part of that project and more precisely of SOTERIA project (formerly Perform60 [Leclercq et al. 2010; Mazouzi et al. 2011]). SOTERIA is an international joint project between many nuclear research institutes such as EDF, CEA, Areva and EPRI. As

summarized in Figure 1.3, this project uses multiscale methods, from ab-initio and molecular dynamics simulations to finite element calculations to increase the knowledge of pressure vessel and in-core material safety. A series of PhD projects has been carried out in recent years in the framework of project Perform60, ranging from characterizing the microstructure of the RPV steel [Diawara 2011], studying the plastic behavior of the steel [Queyreau 2008; Naamane 2008], to predicting the failure curve of the RPV steel by local approach to fracture [Hausild 2002; Mathieu 2006; Libert 2007].The present PhD project is specialized to the study of the crystal plasticity of RPV steel by experimental and numerical tools at the microscale. The main industrial objective of the PhD project is to improve the understanding of crystal plasticity properties of 16MND5 steel, a prerequisite step for studying the material damage mechanisms.

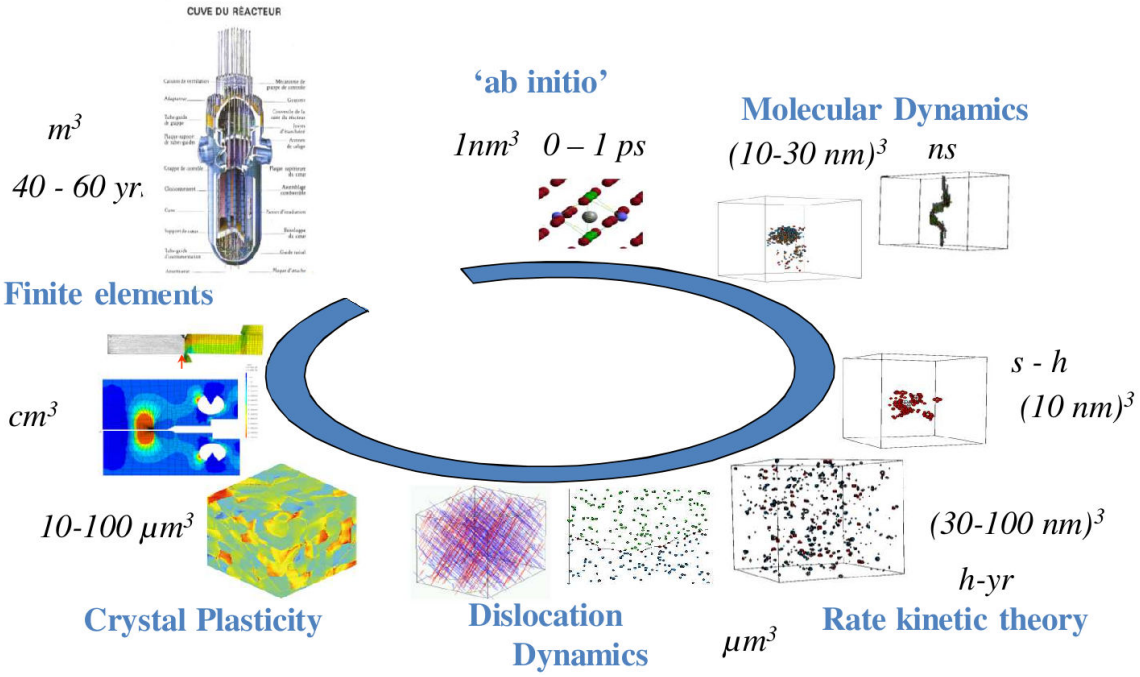

Figure 1.3: Different aspects of numerical simulations of the joint SOTERIA project (formerly Perform60) [Mazouzi et al. 2011]

1.1.2 Microstructure of 16MND5 steel

The French reactor pressure vessel is made of steel of grade AISI A508cl3 (or 16MND5 in French nomenclature) and obtained by forging. The material is a low-alloyed steel containing Mn, Ni and Mo, and its chemical composition is listed in Table 1.1. Its fabrication includes quenching and tempering, leading to a mainly bainitic microstructure [Diawara

2011]. The steel exhibits an excellent trade-off between a high toughness and good weldability, thus allows for a limited vessel thickness.

Table 1.1: Chemical composition of 16MND5 steel (weight percentage)

C	Mn	Ni	Mo	Si	Cr	Cu	V	Co	S	P	Fe
0.16	1.35	0.70	0.50	0.20	0.20	0.07	0.005	0.01	0.006	0.006	bal.

The 16MND5 samples of the present thesis have been cut from a CT50 specimen machined for a previous work [Bouchet 2007], which is located at 3/4 of the thickness of the vessel part H3BC18. Figure 1.4(a) shows the picking position and orientation of the CT50, and the tensile samples of the present PhD project are taken along the radial direction of the CT50 sample, as shown in Figure 1.4(b).

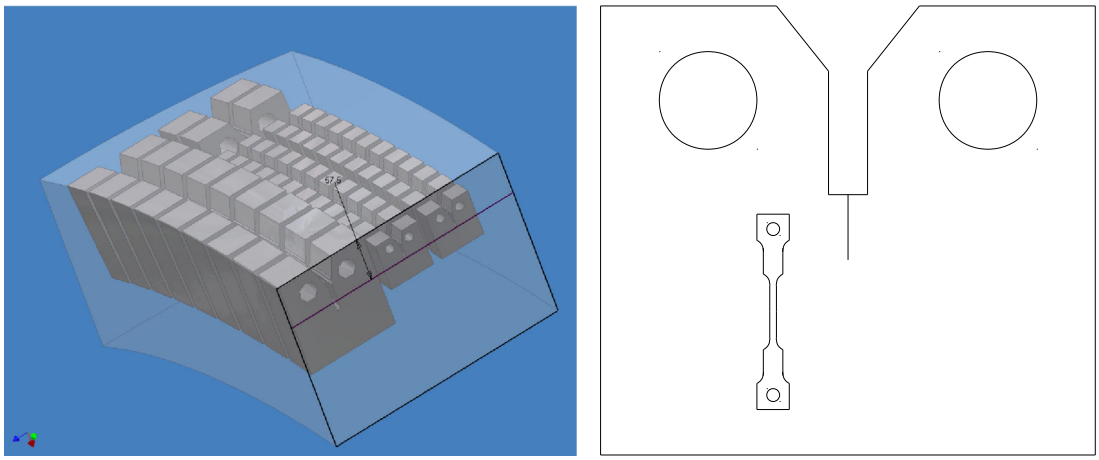

(a) (b)

Figure 1.4: (a) Location of CT fracture sample [Bouchet 2007]. (b) Location of the 16MND5 steel samples used in this work within the CT fracture sample

Due to its significant economic importance and relatively complicated microstructure, 16MND5 steel has been the subject of many past studies [Sekfali 2004; Mathieu 2006; Diawara 2011]. Its microstructure has been extensively characterized [Sekfali 2004; Diawara 2011]. The distribution of carbides, ferrite morphology, general texture of 16MND5 steel have been studied, in order to assess the failure curve [Mathieu 2006]. The same approach has been adopted to analyze the effect of microstructure heterogeneity on the fracture properties [Shi et al. 2015] in a work preceding the PhD project. It has been found that the consideration of 2 constitutive models for bainitic and ferritic grains respectively increases

the dispersion of failure probabilities. The relationship between the microstructure and the local plastic properties of the steel has been studied for tempered martensite and bainite phases [Sekfali 2004]. Damage mechanisms at high temperatures ($\approx$1000 °C) of two grades of 16MND5 and how they relate to the local microstructure have been addressed by experiments and simulations [Vereecke 2004]. Its austenite-to-ferrite transformation, diffusive phase transformations involving crystal plasticity, has been simulated by FE analyses [Barbe and Quey 2011]. Microplasticity and its related internal stresses are shown to develop during the phase transformations and to affect significantly the elastoplasticity of the resulting material. The Charpy ductile to brittle transition curve of the steel has also been investigated, especially the effect of neutron irradiation [Bouchet et al. 2005]. It is found that irradiation affects hardening and brittle failure, leading to a decrease of the Charpy upper shelf. The toughness of the steel, in the form of a Master Curve, is also studied to correctly account for specimen geometry effects and the micromechanisms of fracture [Bouchet et al. 2005]. This method has been established from statistical assessment of a large toughness database [Cogswell 2010] by Rolls-Royce Nuclear Materials and Chemistry Service Support. The general effect of neutron irradiation on the steel is of major concern, and a series of simulation packages has been proposed to simulate its effect: RPV-1 [Jumel and Van-Duysen 2005] and RPV-2 [Adjanor et al. 2010].

Figure 1.5(a) reveals the ferritic and bainitic grains, the two major phases in RPV steel, by an image quality (IQ) field of EBSD acquisition. The grain size is generally between 5 and 20 µm. It can be seen that proeutectoid ferritic grains are very 'clean' in terms of electron back-scattering pattern (EBSP) quality, while bainitic grains show internal variations. It can be concluded that the ferritic grains are homogeneous and the crystal lattice is more regularly organized, while more heterogeneous structures exist in bainitic grains. The packet (or assembly) of laths inside the bainitic grains is shown in Figure 1.5(b), and the definition of lath and packet of laths can be found in Figure 1.6. The width of the laths varies between 1 and 2 µm, and laths tend to be organized along the same longitudinal axis. Carbides exist in the bainitic grains with a significant density.

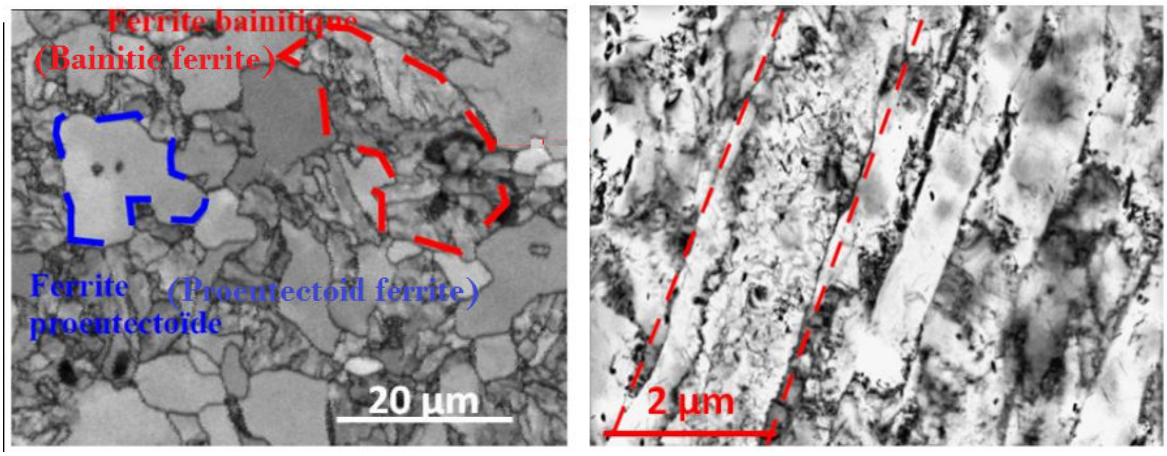

(a) (b)

Figure 1.5: Microstructure of 16MND5 steel. (a) Ferritic and bainitic grains in an IQ image of an EBSD acquisition. (b) Laths in bainitic grains revealed by TEM [Diawara 2011].

The crystallographic orientations inside and between packets of ferritic laths are shown in Figure 1.6. It is visible that inside a ferritic lath a small misorientation exists, which is roughly equal to the EBSD orientation indexation error. Between laths, the misorientation reaches several degrees. Between packets of laths the misorientation can be very high.

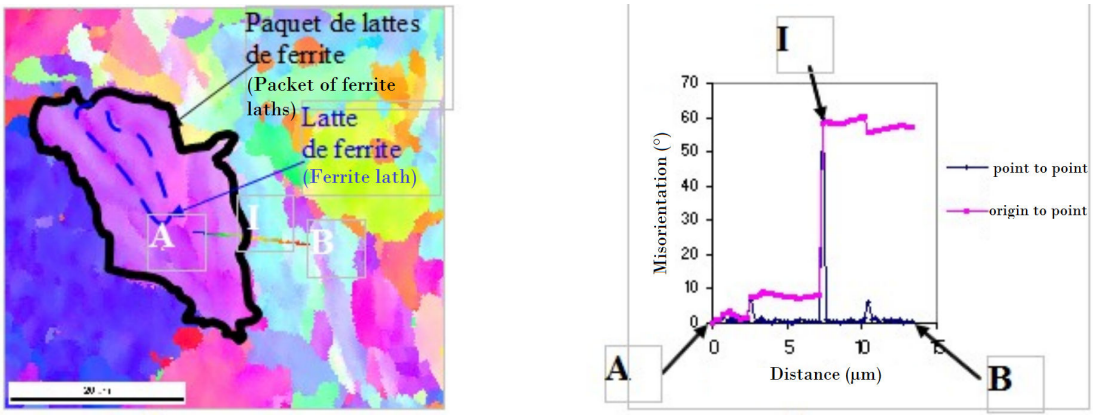

Figure 1.6: Misorientation profiles between ferritic laths. (a) Definition of lath and packet of laths in an inverse pole figure. (b) Misorientation along the trajectory between point A and B in (a) [Diawara 2011].

TEM images reveal the various distribution of carbides in bainitic laths, as shown in Figure 1.7. The density and assembly orientation of carbides vary significantly as functions of the bainitic types [Diawara 2011].

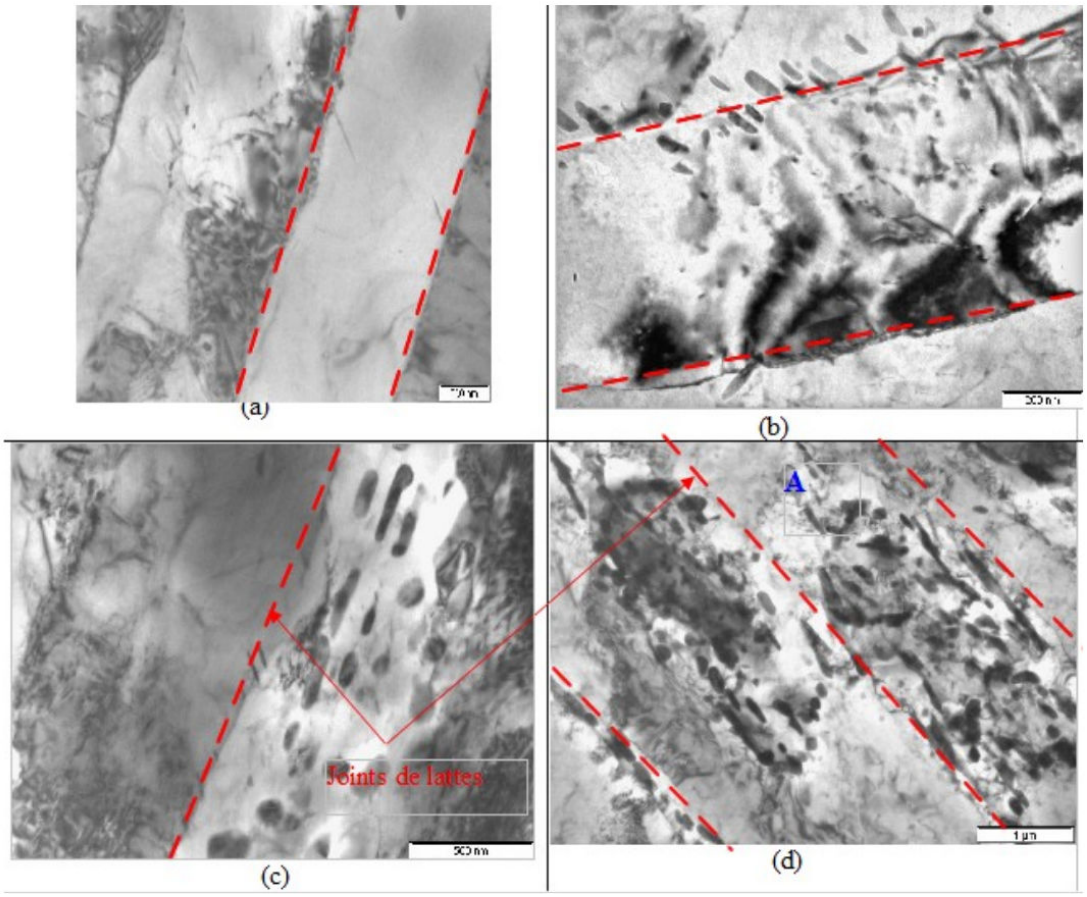

Figure 1.7: Distribution of carbides in bainitic laths. (a) Bainitic lath without carbides (type 1). (b) Bainitic lath with carbides concentrated on the lath boundaries (type 2). (c) Bainitic lath with carbides precipitated in the center, and along the longitudinal direction (type 3). (d) Bainitic lath with carbides precipitated in the center and on the lath boundaries (type 4) [Diawara 2011].

1.1.3 Heterogeneity of mechanical properties of 16MND5

Due to the dual-phase nature of 16MND5 and relatively fine grains, the steel exhibits heterogeneous mechanical properties. A series of mechanical tests has been performed on 16MND5 steel at room temperature [Sekfali 2004] and at low temperature [Mathieu 2006].

The influence of 16MND5 steel grain sizes on the strain pattern has been studied experimentally. Figure 1.8 shows the SE images of 15% strained 16MND5 with different grain sizes [Mathieu 2006]. It can be seen that strain localization is more significant in regions with larger grains.

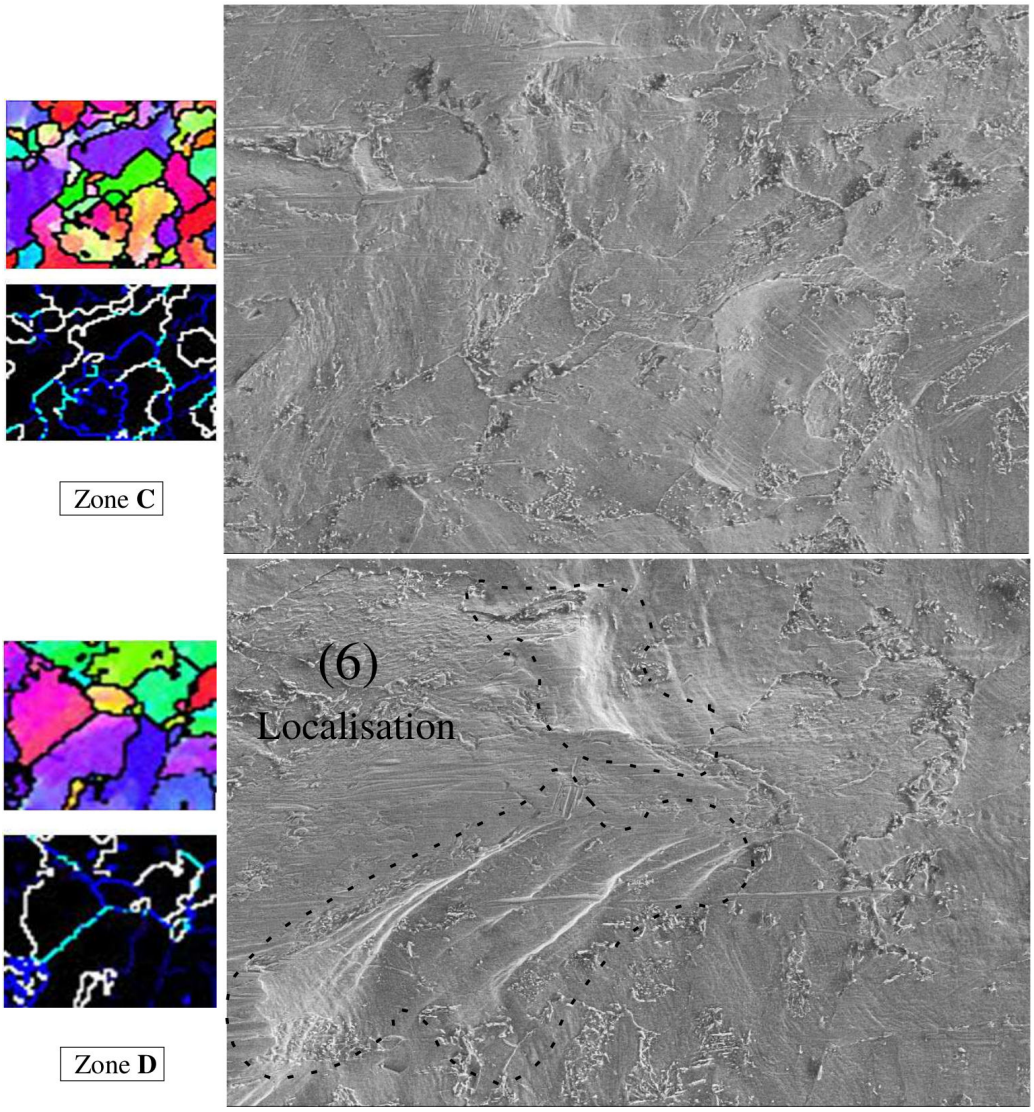

Figure 1.8: SE image of 16MND5 steel after 15% tensile loading at -150 °C for regions with different grain sizes. Strain localization is more pronounced in regions with larger grains [Mathieu 2006].

The distribution of carbides, a harder phase compared to other steel phases, influences the mechanical properties significantly. For example, the plastic deformation has largely stopped in the vicinity of cementite clusters, as shown in Figure 1.9.

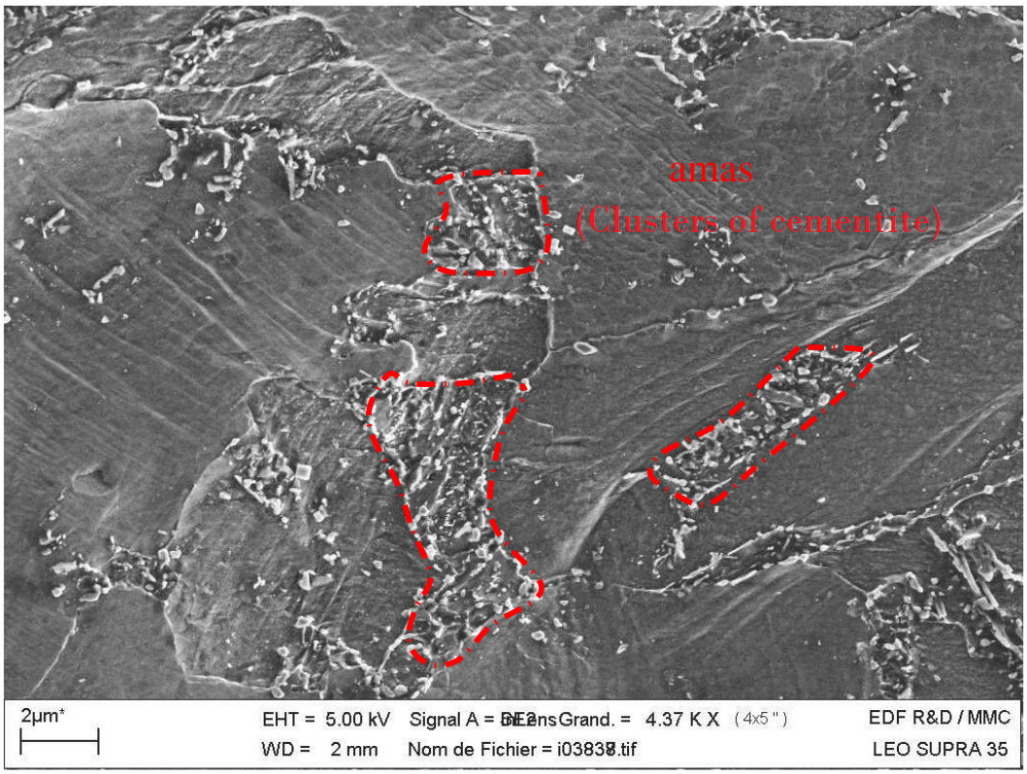

Figure 1.9: SE image of 16MND5 steel after 13% tensile loading at -150 °C. Slip traces are stopped by clusters of cementite, which are highlighted by red contours [Mathieu 2006].

Different 16MND5 steel phases also exhibit different strength levels. For example, the stress levels in ferritic and bainitic grains during loading and relaxation steps have been measured by X-ray diffraction [Mathieu 2006]. It has been found that they have a consistent difference of around 110MPa at -150 °C, as shown in Figure 1.10.

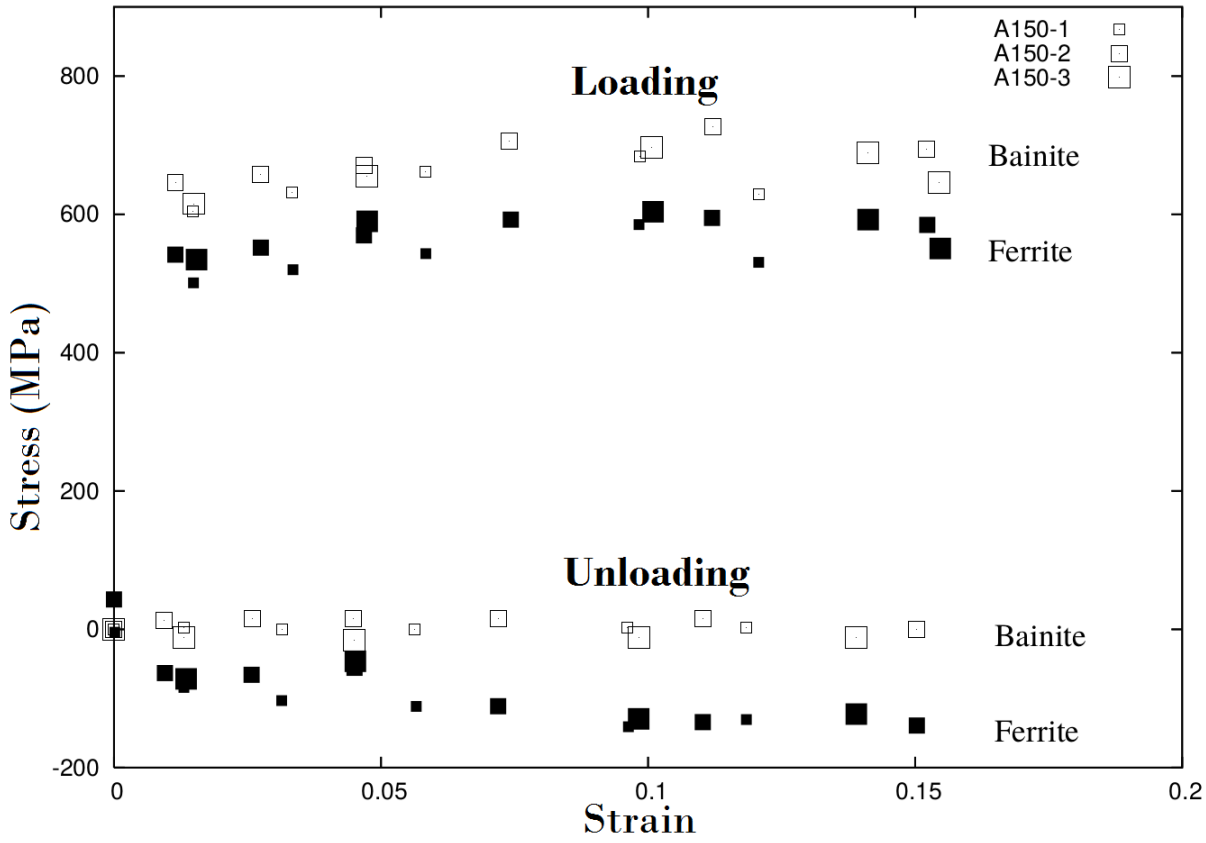

Figure 1.10: The stress levels for ferritic and bainitic grains measured by X-ray diffraction during loading and unloading [Mathieu 2006].

It is concluded that the 16MND5 steel has a binary phase microstructure and relatively fine grains, with very curvy grain boundaries. Bainitic grains have more complex microstructure. To solve the challenging problem of its microscale crystal plasticity, adapted experimental tools must be available at the corresponding scale.

1.2 *In-situ* experiments

An *in-situ* experiment means performing a mechanical test inside an equipment chamber that allows the material to be characterized. It can be as simple as a visual test, or measured by physico-chemical methods. This type of experimentation can overcome the limits of classical tests in laboratory and measure physical/chemical properties of the sample under loading in real time. In fact, the measurement is carried out all along, not before or after the loading history. This brings about many constraints: the experimental device applying the mechanical load should be miniaturized, and the device should not interfere with the measurement or be sensitive to the acquisition environment (*e.g.*, particular atmosphere,

temperature, nuclear radiation), and the acquisition time should be long enough to let the observed phenomenon happen. If all these conditions are satisfied, various types of information can be obtained along a test. For example, an *in-situ* test inside an SEM chamber allows tracking the phase transformation of a material at high temperature by EBSD images [Seward et al. 2004]. An *in-situ* test in transmission electron microscopy (TEM) can characterize the elongation of a nanometric structure when a few milli-N forces are applied [Zhu et al. 2006; Espinosa et al. 2012]. *In-situ* tests can also be carried out in atomic force microscopy (AFM) to monitor the surface corrosion initiation [Martin et al. 2008], or analyze the diffraction properties of a material in a synchrotron facility [Brauser et al. 2010; Dutta et al. 2013; Plancher 2015].

The validation of crystal plasticity models requires the acquisition of experimental data at the microstructural scale. The SEM emerges naturally as the most relevant experimental tool to study the crystal properties. The EBSD imaging mode characterizes the orientation microstructure, and different SEM imaging modalities allow the sample surface to be observed over different scales (from around 100 nm to a few milimeters). Digital image correlation is a tool for measuring kinematic fields from SEM images with a spatial resolution below the grain sizes [Allais et al. 1994; Sutton et al. 2007b;a]. The kinematic information is much richer than the average elongation of the sample, classically measured by an extensometer (or clip gage). The first full-field measurements with SEM images were performed for interrupted tests [Belgacem and Bretheau 1985], and for *in-situ* tests [Allais et al. 1994; Crépin et al. 1995; Liu and Fischer 1997; Doumalin and Bornert 2000]. The development of marking techniques is mandatory to enable pattern tracking during the test. The measurement is not confined to small deformations and local displacement field of a macroscopic strain as large as 100% has been reported [Schroeter and McDowell 2003]. Even 3D surface kinematic fields can be evaluated by stereovision in SEMs [Zhu et al. 2011; Li et al. 2013]. SEM has also been used to observe *in-situ* mechanical tests at high [Podesta 2016] and low [Mathieu 2006] temperatures.

However, not all experimental conditions can be met inside the SEM chamber. For example when imaging material subjected to high irradiations. In these cases only the residual displacement can be measured [Miller and Burke 1992]. Note that other experimental techniques can also provide microstructural kinematic fields, such as optical microscopy [Saai et al. 2010; Badulescu et al. 2011].

Numerous works have indicated the possibilities to perform full-field measurements at

the microstructural scale, in order to study the grain boundary effects [Ma et al. 2006a;b], to link strain localization and the crystallographic orientation maps [Tschopp et al. 2009], to determine the parameters of fracture mechanics [Forquin et al. 2004], or investigate the accumulated plastic strain around the crack tip [Carroll et al. 2013]. If coupled with numerical analyses, the measurement of kinematic fields offers more possibilities, such as studying inter-granular fracture [Pouillier et al. 2012], or the identification of crystal plasticity parameters [Hoc et al. 2003; Héripré et al. 2007; Gérard et al. 2009; Guery et al. 2016b]. The latter is one of the major objectives of the present work and all the manuscript will be developed along this axis. It will detail one by one the challenges and solutions of *in-situ* tests and numerical analyses.

Compared to more classical full-field measurements, with a camera at the macroscopic scale, the measurement with SEM images has some specific challenges. The electromagnetic environment of SEM imaging introduces spatial and temporal distortions, and non-negligible bias and uncertainties [Sutton et al. 2006; 2007b; Ru et al. 2011; Zhu et al. 2011; Guery et al. 2014]. If the sample surface and its changes are to be precisely captured, the SEM imaging bias and uncertainties must be characterized and, if possible, corrected. These correction procedures should be carried out on every adopted SEM imaging mode.

1.2.1 Digital image correlation

Image-based measurement methods, known as digital image correlation, have been developed and widely used both in industry and academia [Sutton 2013]. A variety of DIC techniques have been proposed to register different types of images, for example 2D-DIC [Sutton et al. 1983; Allais et al. 1994; Hoc et al. 2003; Sutton et al. 2007b;a], 3D-DIC (also known as stereo-correlation) [Khan-Jetter and Chu 1990; Zhu et al. 2011; Dufour et al. 2016], and digital volume correlation [Bay et al. 1999; Bornert et al. 2004; Verhulp et al. 2004; Roux et al. 2008].

1.2.1.1 General principle

The same principle applies to all DIC techniques. The input of DIC methods is image pairs, denoted as $f(\boldsymbol{x})$ and $g(\boldsymbol{x})$, with some features, for example marking or topography. DIC techniques search for a displacement field $\boldsymbol{u}(\boldsymbol{x})$ that relates f and g by invoking gray level

conservation

$$f(\boldsymbol{x}) \approx g(\boldsymbol{x} + \boldsymbol{u}(\boldsymbol{x})) \tag{1.1}$$

where $\boldsymbol{u}(\boldsymbol{x})$ is sought as the solution that minimizes the quadratic norm of the difference η_c between the two images on a domain Ω, generally a subset or interrogation window [Sutton et al. 2009].

$$\Phi_c^2 = \sum_{\boldsymbol{x}} \eta_c^2(\boldsymbol{x}) = \sum_{\boldsymbol{x}} [f(\boldsymbol{x}) - g(\boldsymbol{x} + \boldsymbol{u}(\boldsymbol{x}))]^2 \tag{1.2}$$

An interpolation is necessary to evaluate $g(\boldsymbol{x} + \boldsymbol{u}(\boldsymbol{x}))$ at non-integer pixel positions. The DIC outputs are i) the displacement field between the two input images plus possibly extra corrections such as gray levels ($f(\boldsymbol{x}) \approx h(g(\boldsymbol{x} + \boldsymbol{u}(\boldsymbol{x})))$) [Charbal et al. 2016]; ii) the indicator of quality of registration. For the local approach of DIC, the indicator is the correlation product [Sutton et al. 1983]. For the global approach, it is the difference between $f(\boldsymbol{x})$ and $g(\boldsymbol{x} + \boldsymbol{u}(\boldsymbol{x}))$, also called gray level residuals. Assuming good registration of the two images, the residual field only contains the physical evolution and imaging errors. For example, the DIC residual of infrared images indicates the temperature variation at the corresponding point [Maynadier et al. 2012].

1.2.1.2 Global approach of DIC

Equation (1.2) corresponds to an ill-posed problem, since for a given reference image that can be arbitrary, the number of information brought by $g(\boldsymbol{x})$ is lower than the number of degrees of freedom for describing the displacement at each pixel. To solve this problem, one has to reduce the number of unknowns by parameterizing the displacement field $\boldsymbol{u}(\boldsymbol{x})$. A global approach to DIC, which was proposed by [Broggiato 2004; Besnard et al. 2006], consists in decomposing $\boldsymbol{u}(\boldsymbol{x})$ with shape functions of finite elements. The continuity of displacement field is enforced by the method. Contrary to the local approach, the functional Φ_c is minimized over the entire region of interest, which leads to a decrease of measurement uncertainty for an identical element size or interrogation window [Hild and Roux 2012b]. The displacement field is decomposed over the shape function bases $\boldsymbol{\varphi}_i(\boldsymbol{x})$ in the following way

$$\boldsymbol{u}(\boldsymbol{x}) = \sum_i \lambda_i \boldsymbol{\varphi}_i(\boldsymbol{x}) \tag{1.3}$$

This formulation leaves λ_i as unknowns that can be determined through a Gauss-Newton algorithm [Lucas and Kanade 1981]. The majority of the DIC calculations in the thesis is

based on linear triangles forming an unstructured mesh. The solution is approached iteratively [Besnard et al. 2006], where at each iteration n the vector containing all the amplitudes λ_i is corrected by displacement amplitudes $\{\boldsymbol{\delta\lambda}^{(n)}\}$, which is the solution to the linear system

$$[\boldsymbol{M}]\{\boldsymbol{\delta\lambda}^{(n)}\} = \{\boldsymbol{\gamma}^{(n-1)}\} \tag{1.4}$$

where $[\boldsymbol{M}]$ is the Hessian matrix (calculated once for all), and $\{\boldsymbol{\gamma}^{(n-1)}\}$ the residual vector that is updated at each iteration n. The corrected vector is $\{\boldsymbol{\lambda}^{(n)}\} = \{\boldsymbol{\lambda}^{(n-1)}\} + \{\boldsymbol{\delta\lambda}^{(n)}\}$. The gradient of the functional $\{\boldsymbol{\gamma}^{(n)}\}$ reads

$$\begin{aligned} \gamma_i^{(n)} &\equiv \tfrac{\partial \Phi_c}{\partial \lambda_i} \\ &= -\textstyle\sum_{ROI}(f(\boldsymbol{x}) - \tilde{g}^{(n)}(\boldsymbol{x}))(\boldsymbol{\varphi}_i(\boldsymbol{x}) \cdot \boldsymbol{\nabla} f(\boldsymbol{x})) \end{aligned} \tag{1.5}$$

and the Hessian

$$\begin{aligned} M_{ij} &\equiv \tfrac{\partial^2 \Phi_c}{\partial \lambda_i \partial \lambda_j} \\ &= -\textstyle\sum_{ROI}(\boldsymbol{\varphi}_i(\boldsymbol{x}) \cdot \boldsymbol{\nabla} f(\boldsymbol{x}))(\boldsymbol{\varphi}_j(\boldsymbol{x}) \cdot \boldsymbol{\nabla} f(\boldsymbol{x})) \end{aligned} \tag{1.6}$$

where $\tilde{g}^{(n)}$ is the deformed image corrected by the current estimation of displacement field (*i.e.*, $\tilde{g}^{(n)}(\boldsymbol{x}) = g(\boldsymbol{x} + \boldsymbol{u}^{(n)}(\boldsymbol{x}))$). The matrix $[\boldsymbol{M}]$ contains a precious information about the uncertainty of the degrees of freedom, which will be detailed in the following chapters, since $[\boldsymbol{M}]$ is proportional to the inverse of the covariance matrix $[\boldsymbol{C}_u]$ of the measured nodal displacements [Besnard et al. 2006; Hild and Roux 2012b]

$$[\boldsymbol{C}_u] = 2\eta_f^2 [\boldsymbol{M}]^{-1} \tag{1.7}$$

where η_f^2 is the variance of image acquisition noise.

1.2.1.3 Mechanical regularization

Often the gray level conservation hypothesis is not well verified leading to correlation difficulties , for example when the image noise is very high or when there is not sufficient contrasts in parts of image. It is necessary to help the DIC calculation by regularization methods [Tikhonov and Arsenin 1977]. The main idea is to restrict the displacement field searching for mechanically admissible solutions [Réthoré et al. 2009; Leclerc et al. 2009; Roux et al. 2012; Tomičević et al. 2013]. Thus the displacement field should meet supplementary conditions issued from mechanics. These supplementary conditions are formed in the following way.

For internal points in a static object, the local balance of momentum equation reads

$$\boldsymbol{\nabla} \cdot \boldsymbol{\sigma} = \boldsymbol{0} \tag{1.8}$$

This condition satisfies the minimization of a penalty term based on the domain integral of the quadratic norm of the above divergence, which is suitable to be used in FE analyses [Claire et al. 2004]. Let $\boldsymbol{\sigma}$ be the Cauchy stress tensor and $\boldsymbol{\epsilon}$ the infinitesimal strain tensor. According to Hooke's elastic law, $\boldsymbol{\sigma} = \mathcal{C} : \boldsymbol{\epsilon}$, where $\mathcal{C}$ is the fourth order elastic tensor. In the FE discretization scheme, the unbalanced body force vectors is related to the nodal displacement vector by $\boldsymbol{KU} - \boldsymbol{F}$, where $\boldsymbol{F}$ is the nodal vector of external body forces, and $\boldsymbol{K}$ the stiffness matrix. For our application $\boldsymbol{F} = \boldsymbol{0}$, and hence the so-called equilibrium gap is the L2 quadratic norm of the unbalanced (internal and free boundary) node vector

$$\Phi_m^2 = \frac{1}{2}\{\boldsymbol{U}\}^T[\boldsymbol{K}]^T[\boldsymbol{D}][\boldsymbol{K}]\{\boldsymbol{U}\} \tag{1.9}$$

where $[\boldsymbol{D}]$ is the diagonal matrix valued 1 for internal (and free boundary) nodes, and 0 on boundary nodes where an external force can be applied.

For nodes at the boundary of the region of interest, a penalization of short wavelength displacement fluctuations along the edges is introduced

$$\Phi_b^2 = \frac{1}{2}\{\boldsymbol{U}\}^T[\boldsymbol{L}]^T[\boldsymbol{L}]\{\boldsymbol{U}\} \tag{1.10}$$

where $[\boldsymbol{L}]$ is an operator acting on the ROI boundary, and its construction is detailed in [Tomičević et al. 2013]. Note that Φ_c^2, Φ_m^2 and Φ_b^2 are not directly comparable, since they are not of the same unit. The normalization of the functional Φ_c^2, Φ_m^2 and Φ_b^2 has been proposed

$$\tilde{\Phi}_c^2 = \frac{\Phi_c^2}{\{\boldsymbol{v}_n\}^T[\boldsymbol{M}]\{\boldsymbol{v}_n\}},\ \ \tilde{\Phi}_m^2 = \frac{\Phi_m^2}{\{\boldsymbol{v}_n\}^T[\boldsymbol{K}]^T[\boldsymbol{D}][\boldsymbol{K}]\{\boldsymbol{v}_n\}},\ \ \tilde{\Phi}_b^2 = \frac{\Phi_b^2}{\{\boldsymbol{v}_n\}^T[\boldsymbol{L}]^T[\boldsymbol{L}]\{\boldsymbol{v}_n\}} \tag{1.11}$$

where $\boldsymbol{v}_n$ is the displacement field chosen for the normalization. To sum up, instead of minimizing the residual between images Φ_c, in a mechanical regularized DIC the cost function Φ_t^2 consists of $\widetilde{\Phi}_c^2$, $\widetilde{\Phi}_m^2$ and $\widetilde{\Phi}_b^2$

$$(1 + w_m + w_b)\Phi_t^2 = \tilde{\Phi}_c^2 + w_m\tilde{\Phi}_m^2 + w_b\tilde{\Phi}_b^2 \tag{1.12}$$

where w_m and w_b are weights attached to Φ_m^2 and Φ_b^2 respectively. The equilibrium gaps on the internal forces and boundary regularization kernels act as fourth-order low-pass filters, damping out deviations from mechanical admissibility and edge displacement fluctuations below a given wavelength [Tomičević et al. 2013]. Weights w_m and w_b are chosen as

$$w_m = (2\pi|\boldsymbol{k}|\ell_m)^4,\ \ w_b = (2\pi|\boldsymbol{k}|\ell_b)^4 \tag{1.13}$$

where $\boldsymbol{k}$ is the chosen wave vector and ℓ_m and ℓ_b denote the regularization lengths for $\tilde{\Phi}_m^2$ and $\tilde{\Phi}_b^2$ respectively. As a result, ℓ_m and ℓ_b are the parameters controlling the mechanical

regularization extent in the adopted DIC calculation code, namely Correli-RT3 [Tomičević et al. 2013]. It has been found that the mechanical regularization reduces the uncertainty of the displacement measurement, while it allows for DIC calculation on finer meshes thus gains in spatial resolution, as shown in Figure 1.11. It is a good practice to start regularized DIC with a large regularization length, and decrease ℓ_m gradually, to avoid being trapped in local minima, as shown in Figure 1.12.

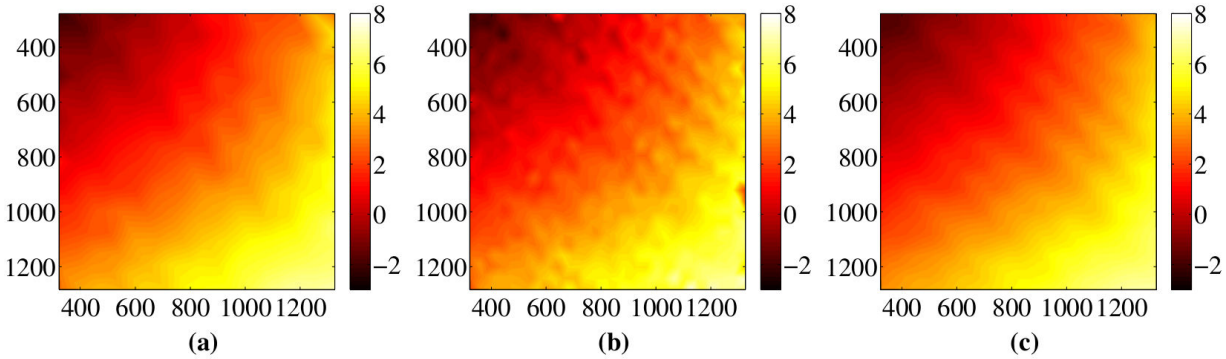

Figure 1.11: Measured displacement field in y direction by DIC (a) with a triangular mesh of length 80 pixels without regularization, (b) with a triangular mesh of length 40 pixels without regularization, and (c) with a triangular mesh of length 40 pixels with regularization ($\ell_m = \ell_b = 120$ pixels) [Guery 2014].

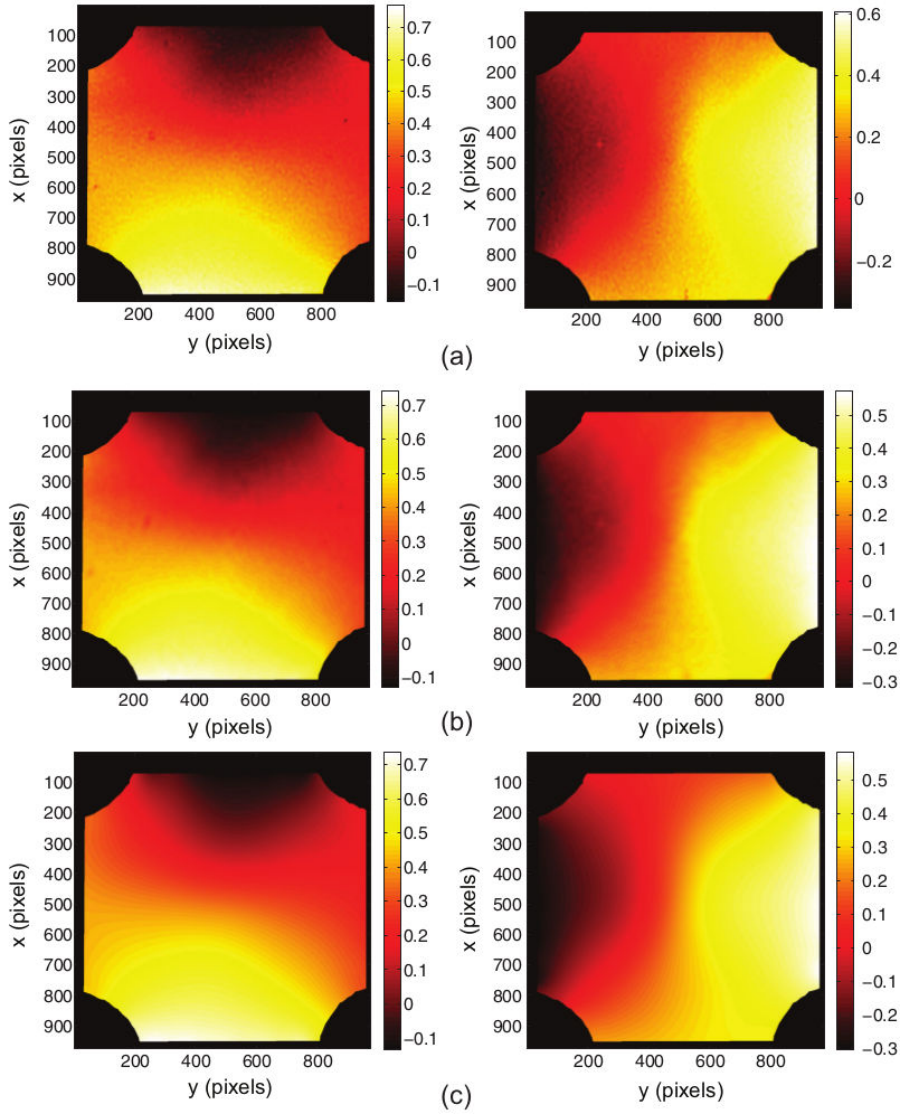

Figure 1.12: Measured displacement field in a biaxial test in x and y directions. Three initial regularization lengths ℓ_m are tested: (a) 32, (b) 128, and (c) 1024 pixels. Final regularization length is identical for the three cases [Tomičević et al. 2013].

It can also be stated that, in the absence of contrast, the minimization of $\tilde{\Phi}_m^2$ and $\tilde{\Phi}_b^2$ is the sole driving force of regularized DIC. Consequently, the mechanical regularization acts as an interpolation method for image regions without sufficient contrast. This interpolation has a better performance than the linear interpolation, as the obtained kinematic field is more mechanically reasonable.

The linear and isotropic elastic constitutive law has been adopted for mechanical regularization by previous works in DIC [Tomičević et al. 2013] and DVC [Taillandier-Thomas et al. 2014] and the present thesis. Although named 'elastic' regularization, a Poisson's-like ratio close to 0.5 may be chosen to prescribe incompressibility during plastic deformation. It

should be stated that the regularized DIC not only helps the DIC to converge, it is also used to identify elastic properties [Leclerc et al. 2009], stress intensity factors [Réthoré et al. 2009; Rannou et al. 2010] or thermal quantities (*e.g.,* local diffusivity or conduction) [Batsale et al. 2012].

1.2.1.4 Integrated DIC

DIC gives access to displacement field $\boldsymbol{u}$ and gray level residuals r between the analyzed images principally. But generally, the quantities $\boldsymbol{u}$ and r are only intermediate data in the pursuit of the main experimental goal, for example mechanical parameters of the studied sample. Integrated digital image correlation (IDIC) has been proposed to measure directly the sought physical quantity. In doing so, the measured displacement field is expressed *a priori* on the basis dictated exactly by the investigated physical phenomenon [Hild and Roux 2006]. No additional degrees of freedom are allowed in the displacement field. As a result, IDIC allows targeted physical values to be extracted directly, and reduces the measurement uncertainty than those obtained by post-processing displacement fields given by DIC [Leclerc et al. 2009; Roux and Hild 2006], if the displacement field is fully expressed in the physical model.

In IDIC, the set of parameters $\{\boldsymbol{p}\}$ is generally chosen as the space for the degrees of freedom of the correlation problem. The corrections $\{\boldsymbol{\delta p}^{(n)}\}$ are expressed as

$$[\boldsymbol{N}^{(n-1)}]\{\boldsymbol{\delta p}^{(n)}\} = \{\boldsymbol{B}^{(n-1)}\} \tag{1.14}$$

and

$$[\boldsymbol{N}^{(n-1)}] = [\boldsymbol{S}_u^{(n-1)}]^t[\boldsymbol{M}][\boldsymbol{S}_u^{(n-1)}] \tag{1.15}$$

$$\{\boldsymbol{B}^{(n-1)}\} = [\boldsymbol{S}_u^{(n-1)}]^t\{\boldsymbol{b}^{(n-1)}\} \tag{1.16}$$

with the sensitivity matrix $[\boldsymbol{S}_u^{(n-1)}]$ satisfying

$$\{\boldsymbol{\delta u}_{\boldsymbol{c}}^{(n-1)}\} = [\boldsymbol{S}_u^{(n-1)}]\{\boldsymbol{\delta p}^{(n-1)}\} \tag{1.17}$$

Therefore, $[\boldsymbol{N}^{(n-1)}]$ is the projection of the DIC matrix with the sensitivity fields, and $\{\boldsymbol{B}^{(n-1)}\}$ is the projection of the DIC vector $\{\boldsymbol{b}^{(n-1)}\}$ with the sensitivity field. It is worth noting that Equation (1.14) uses the same setting as Equation (1.4), but expressed directly

in terms of the sought parameters rather than the kinematic values of the DIC mesh. The needed additional information is the sensitivity fields, which is expressed as the *a priori* knowledge on the constitutive behavior. IDIC has been adopted, for instance, in the identification of elastic properties [Hild and Roux 2006], elasto-plastic parameters [Mathieu et al. 2015].

1.2.1.5 Codes used herein

The present thesis employs intensively 2D-DIC to perform the measurements for different types of images taken during the *in-situ* mechanical test. A regularized and global DIC algorithm is used and the DIC procedure is characterized by its spatial resolution given by the largest length scale between the displacement discretization (here an unstructured FE mesh made of 3-noded triangular elements) and a regularization length promoting small scale smoothness [Tomičević et al. 2013].

1.3 Introduction to micromechanical modeling

Mastering the mechanical property of metallic materials used in the nuclear power plant is key to ensure safe exploitation. It is necessary to understand the damage and fracture of the materials used in the reactor components. Experimentally it is for example cleavage and trans-granular fracture that are identified as failure mechanism in the low temperature regime. To explain the observed phenomena, appropriate calculation methods at the adapted scale are usually undertaken, as briefly summarized in Figure 1.3. If mean fields homogenization methods are often sufficient to predict the average property of a material [Tjahjanto et al. 2010], they are in contrast not able to provide the local mechanical fields that result in material degradation phenomena. Some advanced homogenization methods could be adopted to take into consideration the field fluctuations in different phases [Liu and Castañeda 2004; Lahellec and Suquet 2013], but they do not include the interactions between phases. In this sense, the full-filed calculations are better adapted to study localized phenomena, for example the mechanical behavior at grain boundaries that is essential in fracture mechanics. Some studies have been conducted to explore the phenomena of stress-related corrosion [Kamaya and Itakura 2009; Couvant et al. 2012], initiation and propagation of fatigue cracks [Guilhem et al. 2010; Schwartz et al. 2010], and inter-granular fracture [Diard et al. 2005; Simonovski and Cizelj 2013].

The potential of micromechanics is partly linked to the development of numerous experimental tools allowing for the observation of mechanical phenomena at the microscopic scale, as explained in Section 1.2. Besides, considerable advancements have been made in the modeling of material properties at the same scale, making the direct comparison of experimental and modeling data possible. A series of crystal plasticity laws have been brought up to describe the local mechanical fields either by a fast Fourier transformation (FFT) based method [Lebensohn et al. 2008; Kanjarla et al. 2012; Brenner and Suquet 2013], or by finite element method [Roters et al. 2010]. In the PhD project two FE based crystal plasticity laws have been adopted, namely DD_CC [Monnet et al. 2013] and the so-called Méric-Cailletaud law [Méric et al. 1991].

Once validated by experimental data, crystal plasticity laws become very useful tools for analysis and prediction [Roters et al. 2010]. For example, they can provide the strain and stress state of a polycrystal under mechanical loading, an information particularly sought after to study the degradation mechanism. However, validation of constitutive equations at this scale is difficult. The robustness of the law, the quality and credibility of the analysis and prediction by the law all depend on the validation procedure. The fundamentals of crystal plasticity simulation and two hardening laws will be presented in this section.

1.3.1 Cubic elasticity

When a steel object is subjected to a mechanical loading, it will first undergo an elastic deformation before plastic strains. The studied 16MND5 steel has a cubic elastic behavior, and the relationship between its stress $\boldsymbol{\sigma}$ and elastic strain $\boldsymbol{\epsilon}$ before yielding is described by Hooke's law

$$\boldsymbol{\sigma} = \boldsymbol{\Lambda}_{cub}\boldsymbol{\epsilon} \tag{1.18}$$

where $\boldsymbol{\Lambda}_{cub}$ is the stiffness matrix for cubic elasticity. Equation (1.18) can be expressed explicitly with the Voigt-Kelvin notation

$$\begin{bmatrix} \sigma_{xx} \\ \sigma_{yy} \\ \sigma_{zz} \\ \sqrt{2}\sigma_{yz} \\ \sqrt{2}\sigma_{xz} \\ \sqrt{2}\sigma_{xy} \end{bmatrix} = \begin{bmatrix} C_{11} & C_{12} & C_{12} & 0 & 0 & 0 \\ C_{12} & C_{11} & C_{12} & 0 & 0 & 0 \\ C_{12} & C_{12} & C_{11} & 0 & 0 & 0 \\ 0 & 0 & 0 & 2C_{44} & 0 & 0 \\ 0 & 0 & 0 & 0 & 2C_{44} & 0 \\ 0 & 0 & 0 & 0 & 0 & 2C_{44} \end{bmatrix} \begin{bmatrix} \epsilon_{xx} \\ \epsilon_{yy} \\ \epsilon_{zz} \\ \sqrt{2}\epsilon_{yz} \\ \sqrt{2}\epsilon_{xz} \\ \sqrt{2}\epsilon_{xy} \end{bmatrix} \tag{1.19}$$

where C_{11}, C_{12} and C_{44} are elastic constants of the material, and they are respectively equal to 206, 133 and 119 GPa [Ledbetter and Reed 1973]. These elastic constants will be used for all the present PhD work. The elastic behavior at each point is related to the local crystal orientation

$$\boldsymbol{\Lambda}_e = \boldsymbol{Q}_e \boldsymbol{\Lambda}_{cub} \boldsymbol{Q}_e^T \tag{1.20}$$

where $\boldsymbol{Q}_e$ is the local rotation matrix that links the coordinate system of the sample and the local crystal lattices. The behavior of the studied steel after reaching its yield strength will be presented in the following.

1.3.2 Crystal plasticity modeling

1.3.2.1 Dislocations

The plastic deformation of a metal is achieved through dislocations movement. Dislocations are linear defects in the crystal. There are two primary types of dislocations: edge dislocations and screw dislocations. In an edge dislocation, a half atomic plane is introduced in the crystal, distorting the surrounding planes as shown in Figure 1.13(a). A pure screw dislocation is shown in Figure 1.13(b). In reality, within the crystal most of the dislocations are mixed ones, meaning that they are partly screw and partly edge dislocations.

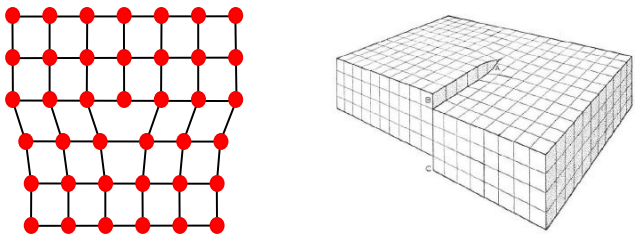

(a) Edge dislocation (b) Screw dislocation

Figure 1.13: Edge and screw dislocations [Askeland and Wright 2013].

Dislocations motion at the microscopic scale is directly linked to the macroscopic plastic deformation of the material. The principle of edge-dislocation-induced deformation is presented in Figure 1.14. Due to Franck-Read sources, dislocations tend to proliferate during the hardening of the metal. Dislocations interact elastically with each other, and an increase of dislocation density provides hardening. The dislocation density is introduced to quantify the number of dislocations. This parameter corresponds to the number of dislocations in a given volume times the average length of each dislocation and is therefore expressed in

m^{-2}. At room temperature, the dislocation density ranges between 10^{10} m^{-2} and 10^{14} m^{-2} but it can increase to 10^{16} m^{-2} if the material has undergone severe mechanical transformations [Askeland and Wright 2013].

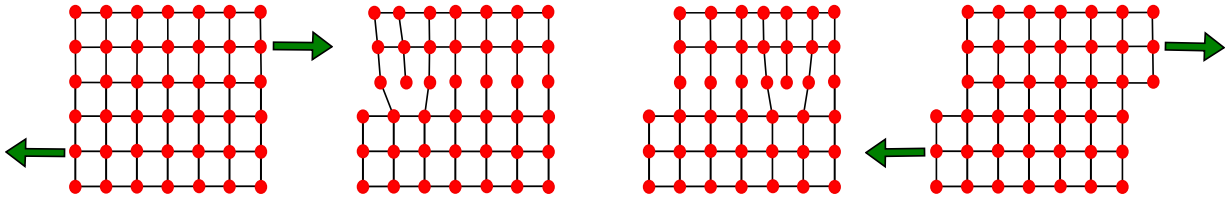

(a) (b) (c) (d)

Figure 1.14: Motion of an edge dislocation under an applied shear stress [Askeland and Wright 2013]. (a) A stress is applied on the crystal. (b) An edge dislocation starts moving. (c) The dislocation moves due to the stress on a plane. (d) The crystal has displaced by a Burgers vector length

1.3.2.2 Slip systems

The motion of a dislocation requires much less energy than the simultaneous gliding of the entire plane. Plasticity is therefore mainly due to the gliding of planes through activated dislocations, as Figure 1.14 shows the motion of atoms through an activated edge dislocation. Note that plastic deformation could also result from twinning, diffusion and phase transformation, but these mechanisms are not considered in the PhD project as they do not happen for 16MND5 steel at room temperature. However the slip directions and the slip planes are not unspecified: they are the densest planes and directions [Jaoul 1965]. Figure 1.15 shows an example of a slip plane and direction in body-centered cubic (bcc) crystal. Ferrite is a body centered cubic crystal and has therefore 48 slip systems [Askeland and Wright 2013]. The specific slip directions are written $[\cdots]$ and the normal vectors of the specific slip planes $(\cdots)$, while the family of slip directions are written $< \cdots >$ and the normal vectors of the family of slip planes $\{\cdots\}$:

- 12 systems <111>{110}. These systems are active at both low and high temperatures
- 12 systems <111>{112}. These systems are only active at high temperatures ($\geqslant$ room temperature)
- 24 systems <111>{123}. These systems are only active at very high temperatures ($\approx$ 800 °C).

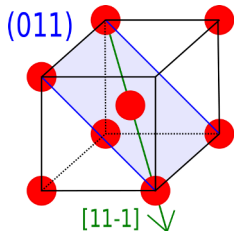

Figure 1.15: Example of slip plane and direction [Askeland and Wright 2013]

During the thesis only the 12 <111>{110} systems are considered. At low temperatures, dislocations are mainly screw dislocations and they glide very slowly. The mechanism leading to the motion of the dislocations in bcc crystals at these temperatures is a double-kink mechanism [Hirth 1960]. A more accurate description of the systems <111>{110} is presented in Table 1.2 and one of them is shown in Figure 1.15.

Plane	(110)		($\bar{1}$01)		(011)	
Direction	[1$\bar{1}$1]	[$\bar{1}$11]	[1$\bar{1}$1]	[111]	[1$\bar{1}$1]	[11$\bar{1}$]
Schmid & Boas notation	D6	A6	D4	B4	D1	C1
Order in Code_Aster	1	7	2	5	3	12

Plane	(0$\bar{1}$1)		($\bar{1}$10)		(101)	
Direction	[111]	[$\bar{1}$11]	[111]	[11$\bar{1}$]	[$\bar{1}$11]	[11$\bar{1}$]
Schmid & Boas notation	B2	A2	B5	C5	A3	C3
Order in Code_Aster	4	9	6	10	8	11

Table 1.2: bcc <111> {110} slip systems

According to Schmid's law, a given slip system will not be activated until the resolved shear stress reaches a threshold called the critical resolved shear stress (CRSS). For a given system s, whose normal is $\boldsymbol{n}_s$ and direction is $\boldsymbol{m}_s$, the resolved shear stress is given by

$$\tau_s = \boldsymbol{\mu}_s : \boldsymbol{\sigma} = \frac{1}{2}(\boldsymbol{n}_s \otimes \boldsymbol{m}_s + \boldsymbol{m}_s \otimes \boldsymbol{n}_s) : \boldsymbol{\sigma} \tag{1.21}$$

where $\boldsymbol{\sigma}$ is the stress tensor applied to the crystal and $\boldsymbol{\mu}_s$ is the orientation tensor. For a given applied stress on a crystal, it is possible to know which slip system will be activated first using Schmid's factor tensor M_s. M_s is defined, for a tensile test of scalar stress level σ

along direction $\boldsymbol{t}$ (*i.e.*, $\boldsymbol{\sigma} = \sigma \boldsymbol{t} \otimes \boldsymbol{t}$):

$$\tau_s = M_s \sigma = (\boldsymbol{n}_s \cdot \boldsymbol{t})(\boldsymbol{m}_s \cdot \boldsymbol{t})\sigma \tag{1.22}$$

Under a given stress the slip systems whose Schmid factor is the highest will be activated first.

The soft ferrite within the steel will undergo first plastic strain under a sufficient stress. This strain is the result of dislocation movements due to the activation of slip systems within the crystals.

The dislocation activities are the main local deformation mechanisms in the scale of atoms, and they will lead to micro-, meso- and macroscale deformations that are more easily observed. The passage from dislocation dynamics to strains of larger scale is detailed in the next section.

1.3.3 Finite strain formalism

Let us define the initial configuration of a continuum object as C_0, and its configuration at time t (or current configuration) as C_t. For a transformation, let us note the position of a point in the initial configuration as $\boldsymbol{X}$ and the position at time t as $\boldsymbol{x}$. Then the deformation gradient tensor is $\boldsymbol{F} = \partial \boldsymbol{x} / \partial \boldsymbol{X}$.

Let $\boldsymbol{v} = \dot{\boldsymbol{x}}$ be the velocity vector of point $\boldsymbol{x}$ in the current configuration. Then the velocity gradient tensor $\boldsymbol{L}$ writes as $\boldsymbol{L} = \text{grad}\boldsymbol{v} = \frac{\partial \dot{\boldsymbol{x}}}{\partial \boldsymbol{x}} = \dot{\boldsymbol{F}} \boldsymbol{F}^{-1}$. In the case of crystalline plasticity, the deformation gradient tensor is commonly decomposed into two tensors: a plastic one, $\boldsymbol{P}$, which corresponds to plastic flow resulting from the activities of slip systems, and an elastic transformation $\boldsymbol{E}$ that describes the pure elastic deformation and the rigid body rotation of a crystal lattice. Mandel has proposed a relaxed configuration $\overline{C_t}$, which possesses the same crystallographic orientation as the initial crystal lattice [Mandel 1973]. The relaxed configuration allows the overall deformation to be performed in two steps: the initial configuration is first transformed plastically into the relaxed configuration, then an elastic deformation is applied to transform it into the current configuration, see Figure 1.16.

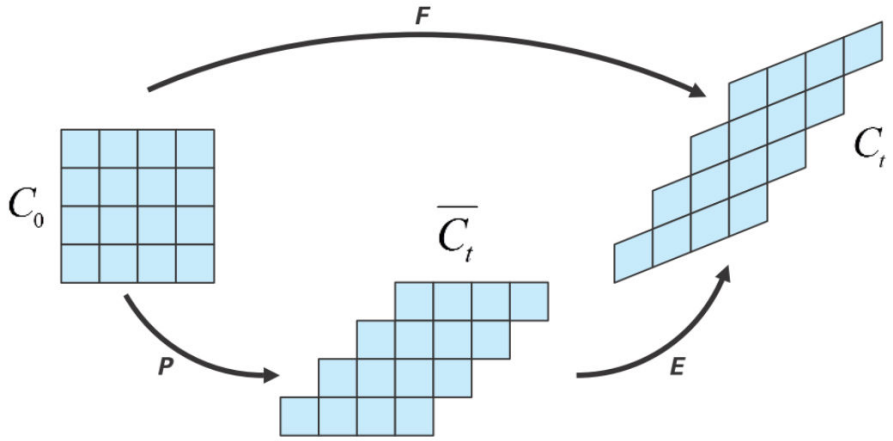

Figure 1.16: Decomposition of deformation gradient tensor: initial configuration, relaxed isocline configuration and the current configuration [Mandel 1973].

Then the velocity gradient becomes

$$\boldsymbol{L} = \dot{\boldsymbol{F}}\boldsymbol{F}^{-1} = (\dot{\boldsymbol{E}}\boldsymbol{P} + \boldsymbol{E}\dot{\boldsymbol{P}})\boldsymbol{P}^{-1}\boldsymbol{E}^{-1} = \dot{\boldsymbol{E}}\boldsymbol{E}^{-1} + \boldsymbol{E}\dot{\boldsymbol{P}}\boldsymbol{P}^{-1}\boldsymbol{E}^{-1} = \boldsymbol{L}^e + \boldsymbol{E}\boldsymbol{L}^p\boldsymbol{E}^{-1} \tag{1.23}$$

where $\boldsymbol{L}^e = \dot{\boldsymbol{E}}\boldsymbol{E}^{-1}$ and $\boldsymbol{L}^p = \dot{\boldsymbol{P}}\boldsymbol{P}^{-1}$ are the two parts of the velocity gradient tensor corresponding to the two deformation steps. Thus the tensor $\boldsymbol{L}$ is the sum of its elastic component and its plastic component, which is transported in its current configuration. The symmetric part of $\boldsymbol{L}$ is defined as the strain rate tensor $\boldsymbol{D} = \mathtt{sym}(\boldsymbol{L}) = \frac{1}{2}\left(\boldsymbol{L} + \boldsymbol{L}^T\right)$.

In the relaxed configuration, the right Cauchy-Green elastic deformation tensor is defined as $\boldsymbol{C}^e = \boldsymbol{E}^T\boldsymbol{E}$. The Green-Lagrange elastic strain tensor is thus defined as $\boldsymbol{E}^e_{GL} = \frac{1}{2}(\boldsymbol{C}^e - \boldsymbol{1}) = \frac{1}{2}\left(\boldsymbol{E}^T\boldsymbol{E} - \boldsymbol{1}\right)$

The Cauchy stress tensor $\boldsymbol{\sigma}$ is defined in the current configuration. Then the second Piola-Kirchhoff tensor, which is defined in the relaxed configuration $\boldsymbol{\Pi}^e$, reads

$$\boldsymbol{\Pi}^e = J_E\boldsymbol{E}^{-1}\boldsymbol{\sigma}\boldsymbol{E}^{-T}, \text{ with } J_E = \mathtt{det}(\boldsymbol{E}) \tag{1.24}$$

For a complete transformation, the stress-induced power is expressed as

$$\boldsymbol{P} = \frac{1}{\rho}\boldsymbol{\sigma} : \boldsymbol{D} = \frac{1}{\rho}\boldsymbol{\sigma} : \boldsymbol{L} = \frac{1}{\rho}\boldsymbol{\sigma} : (\boldsymbol{L}^e + \boldsymbol{E}\boldsymbol{L}^p\boldsymbol{E}^{-1}) = \frac{1}{\rho}\boldsymbol{\sigma} : \boldsymbol{L}^e + \frac{1}{\rho}\boldsymbol{\sigma} : (\boldsymbol{E}\boldsymbol{L}^p\boldsymbol{E}^{-1}) \tag{1.25}$$

where ρ is the mass density in the current configuration.

According to Han [2013], the power can also be expressed as the sum of two components in the relaxed configuration

$$\boldsymbol{P} = \frac{1}{\rho_i}\boldsymbol{\Pi}^e : \dot{\boldsymbol{E}}^e_{GL} + \frac{1}{\rho_i}\boldsymbol{M} : \boldsymbol{L}^p \tag{1.26}$$

where ρ_i is the mass density in the intermediary configuration, and $\boldsymbol{M}$ is the Mandel tensor that is conjugated with the plastic strain rate tensor $\boldsymbol{L}^p$

$$\boldsymbol{M} = J_E \boldsymbol{E}^T \boldsymbol{\sigma} \boldsymbol{E}^{-T} \tag{1.27}$$

The Mandel tensor will be used to describe plastic flow.

In the relaxed configuration, the plastic strain rate tensor associated with plastic slip activities is defined as

$$\boldsymbol{L}^p = \sum_s \dot{\gamma}^s \boldsymbol{N}^s, \text{ with } \boldsymbol{N}^s = \boldsymbol{m}^s \otimes \boldsymbol{n}^s \tag{1.28}$$

For crystal plasticity laws, $\boldsymbol{M} : \boldsymbol{L}^p = \sum_s \dot{\gamma}^s \tau^s$, where τ^s is the resolved shear stress projected onto the slip system s: $\tau^s = \boldsymbol{M} : \boldsymbol{N}^s$. The Simo-Miehe formulation [Simo and Miehe 1992] for finite transformation integration has been adopted in Code-Aster, which is widely applied in the present PhD work. Detailed expression of the partial derivative equations to be solved in the finite deformation regime can be found in [Han 2013; Ling 2017]. Note that after integration, the lattice rotation matrix $\boldsymbol{R}$ can be extracted by polar decomposition of the elastic deformation gradient tensor: $\boldsymbol{E} = \boldsymbol{V}_e \boldsymbol{R}$.

The above equations provide the general frameworks for crystal plasticity calculations. The relationship between the shear rate $\dot{\gamma}$ and the resolved shear stress τ is the core of constitutive equations and it varies for different crystal plasticity laws.

1.3.4 Méric-Cailletaud constitutive law

The so-called Méric-Cailletaud model [Méric et al. 1991] has been introduced for face centered cubic (fcc) nickel single crystals. It uses the shear strain rate of each slip system as internal variable, thus is a phenomenological constitutive law as opposed to physical constitutive equations based on dislocation dynamics. Both kinematic and isotropic hardenings are accounted for. The shear strain rate $\dot{\gamma}_s$ is expressed as a function of the resolved shear stress τ_s

$$\dot{\gamma}_s = \dot{p}_s \frac{\tau_s - c\alpha_s}{|\tau_s - c\alpha_s|} \tag{1.29}$$

$$\dot{p}_s = \left\langle \frac{|\tau_s - c\alpha_s| - R_s(p_s)}{K} \right\rangle_+^n \tag{1.30}$$

where $\langle x \rangle_+ = \frac{1}{2}(|x| + x)$ is the positive part of x, K the hardening modulus, $R_s(p_s)$ the hardening function on slip system s and n a dimensionless power. c is the modulus of kinematic

hardening. The isotropic hardening law is non-linear and described by two parameters Q and b

$$R_s(p_s) = R_0 + Q\left(\sum_r h_{sr}\left(1 - e^{-bp_r}\right)\right) \tag{1.31}$$

where h_{sr} is the interaction matrix between all slip systems. Figure 1.17 illustrates the interaction between a mobile dislocation with the forest dislocations, where the moving dislocation is curbed by the forest dislocations and becomes curvy. The interactions between dislocations and obstacles will lead to material hardening. Some terms h_{sr} have been identified by inverse approaches for 316L stainless steel [Guery 2014]. In crystal plasticity simulations with only 12 slip systems, h_{sr} can be constructed with 6 coefficients as listed in Figure 1.18.

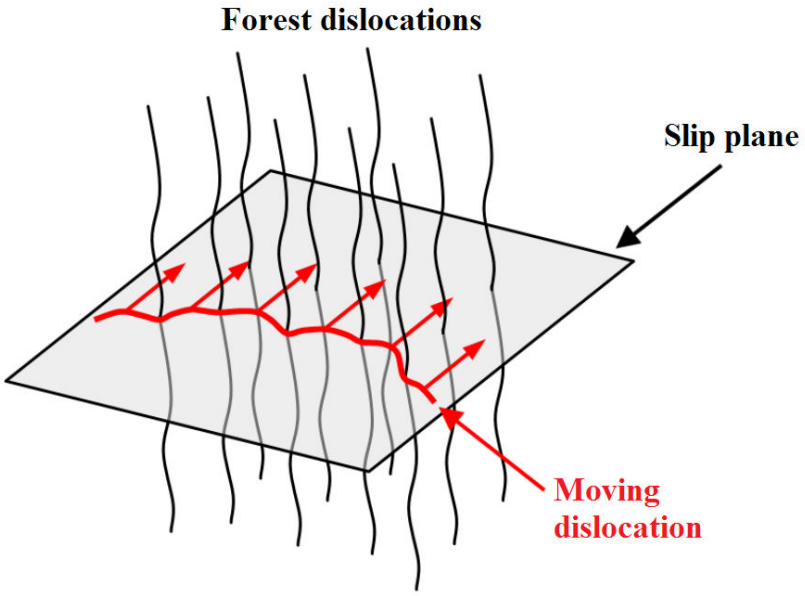

Figure 1.17: Sketch of the interaction between a mobile dislocation and the forest dislocations [Schwartz 2011].

	1	2	3	4	5	6	7	8	9	10	11	12
1	h_1	h_2	h_2	h_4	h_5	h_5	h_5	h_6	h_3	h_5	h_3	h_6
2		h_1	h_2	h_5	h_3	h_6	h_4	h_5	h_5	h_5	h_6	h_3
3			h_1	h_5	h_6	h_3	h_5	h_3	h_6	h_4	h_5	h_5
4				h_1	h_2	h_2	h_6	h_5	h_3	h_6	h_3	h_5
5					h_1	h_2	h_3	h_5	h_6	h_5	h_5	h_4
6						h_1	h_5	h_4	h_5	h_3	h_6	h_5
7							h_1	h_2	h_2	h_6	h_5	h_3
8								h_1	h_2	h_3	h_5	h_6
9									h_1	h_5	h_4	h_5
10										h_1	h_2	h_2
11											h_1	h_2
12												h_1

Figure 1.18: The symmetric interaction matrix between 12 slip systems [Franciosi 1985].

The detailed definition of the 6 coefficients can be found in [Guery 2014]. The Méric-Cailletaud model has been implemented into Code-Aster package for different crystal types, including ccc, bcc and hexagonal close-packed [EDF 2017]. Two versions exist for bcc crystals, namely bcc24 considers the 12 primary <111>{110} and 12 secondary <111>{112} slip systems, and bcc12 only considers the 12 primary slip systems. All the crystal plasticity calculations (with Méric-Cailletaud and DD_CC) in the present work use bcc12. As all the micromechanical simulations are for monotonic loading, the kinematic hardening term is not accounted for. So the tailored (or trimmed) Méric-Cailletaud hardening law reads

$$\dot{\gamma}_s = \dot{p}_s \frac{\tau_s}{|\tau_s|} \tag{1.32}$$

$$\dot{p}_s = \left\langle \frac{|\tau_s| - R_s(p_s)}{K} \right\rangle_+^n \tag{1.33}$$

$$R_s(p_s) = R_0 + Q \left(\sum_{r=1}^{12} h_{sr} \left(1 - e^{-bp_r} \right) \right) \tag{1.34}$$

The reference crystal plasticity parameters of SMC are listed in Table 1.3

Table 1.3: Reference parameters used in the modified Méric-Cailletaud for 16MND5 steel (adapted from [Guilhem et al. 2013] and [Ledbetter and Reed 1973]).

C_{11} (GPa)	C_{12} (GPa)	C_{44} (GPa)	b	n	K (MPa·s^{-n})	R_0 (MPa)
206	133	119	12	12	20	170
Q (MPa)	h_1	h_2	h_3	h_4	h_5	h_6
30	1	1	0.6	12.3	1.6	1.8

It can be found that R_0 is the factor influencing the yield stress, b and Q the main factors influencing the hardening ratio of the model. As a result, they are often the sought parameters [Guilhem et al. 2013]. They have been previously obtained by inverse identification on kinematic fields and stress-strain responses of 316L stainless steel [Guery et al. 2016b]. In the present work R_0, b and Q are again chosen as parameters to be calibrated for 16MND5 steel.

1.3.5 DD_CC constitutive law

The so-called DD_CC (Dislocation Dynamics for body Centered Cubic crystals) is based on physical properties of the crystal obtained through dislocation dynamics simulations. Therefore the dislocation density on each slip system, ρ_s is an essential internal variable of the DD_CC law. All equations in this section are issued from [Monnet and Vincent 2011; Monnet et al. 2013]. This law has been designed for bcc crystals and its formulation focuses on two cases, namely, low and high temperatures.

1.3.5.1 Low temperatures

At low temperatures, most of the dislocations are screws and the gliding velocity is determined by the effective resolved shear stress on the screw dislocation. These screw dislocations move at low temperature according to a double kink mechanism. The screw dislocation has not enough internal energy and is therefore trapped within valleys of minimum energy called Peierls valleys. Under a significant applied stress they can move from one valley to another one through the formation of a double kink as shown in Figure 1.19. Consequently the shear strain rate is controlled by the nucleation rate of double kinks, thus the plastic strain rate at low temperatures is denoted as $\dot{\gamma}_{nuc}$.

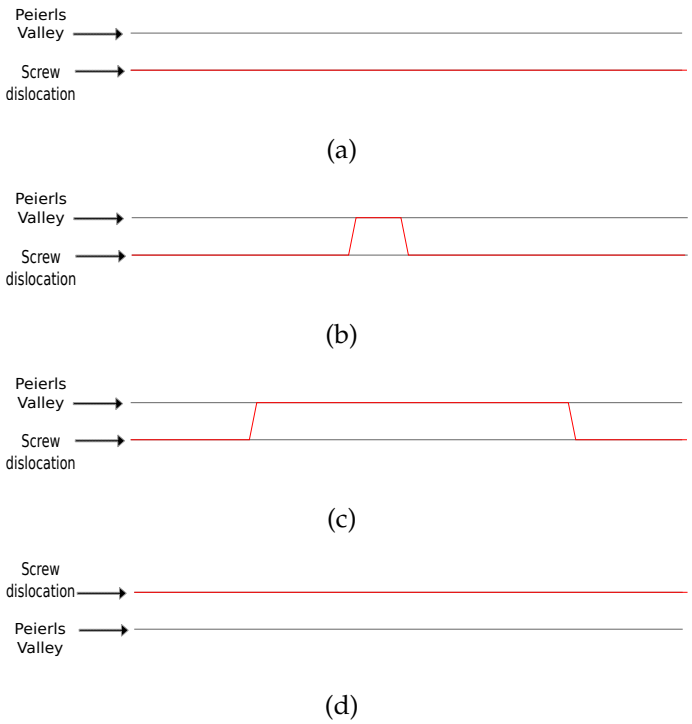

Figure 1.19: Double kink mechanism [Swinburne et al. 2013]. (a) Screw dislocation trapped within a Peierls valley. (b) Under stress a double kink is created, a jog has been thrown over a Peierls hill. (c) Expansion under stress of the double kink. (d) The screw dislocation is now in the neighboring Peierls valley.

It is possible to express $\dot{\gamma}^s_{nuc}$ as a function of the effective resolved shear stress, the average length of screw dislocations l^s, the mobile dislocation density ρ^s_m (considered as constant in this model), the absolute temperature T and the activation energy for double-kink nucleation under a given effective resolved shear stress ΔG

$$\dot{\gamma}^s_{nuc} = \rho^s_m bH \cdot l^s \left(\boldsymbol{\rho}, \tau^s_{eff}\right) \cdot \exp\left(\frac{-\Delta G\left(\tau^s_{eff}\right)}{kT}\right) \frac{\tau_s}{|\tau_s|} \tag{1.35}$$

where b is the magnitude of the dislocation Burgers vector, τ^s_{eff} the effective resolved stress on slip system s, H a frequency factor connected to the Debye frequency ν_D by $H = b\nu_D/l_{dk}$, where l_{dk} is a characteristic length of the double-kink mechanism, close to 10b [Tang et al. 1998]. H is considered as a constant parameter in the model and k is the Boltzmann constant. In the case of iron, direct analysis of experimental loading curves [Naamane et al. 2010] provided the following expression that was found to cover the entire stress range observed in the thermal regime

$$\Delta G\left(\tau^s_{eff}\right) = \Delta G_0 \left(1 - \sqrt{\frac{\left\langle \tau^s_{eff} \right\rangle_+}{\tau_0}}\right) \tag{1.36}$$

The index s corresponds to the slip system s.

1.3.5.2 High temperatures

At high temperatures Equation (1.35) is no longer valid. The flow stress at the macroscopic level exhibits a thermal dependency [Thornton et al. 1962] also responsible for the dependence of flow stress on strain rate. The origin of this thermal component can be attributed to the thermally activated jog drag or destruction of cross-states in the dislocation microstructure. For this reason, the high-temperature regime is referred as the "drag regime" [Monnet and Vincent 2011]. The Orowan relationship implies that the effective steady velocity of dislocations is thermally activated with characteristically large activation volumes [Sevillano 1993]. This observation allows for the simplification of the Arrhenius equation in the form of a power law, using for example the widely used Norton law [Monnet et al. 2013]. The shear strain rate on a slip system s in the drag regime is expressed as

$$\dot{\gamma}^s_{drag} = \dot{\gamma}_0 \left(\frac{|\tau^s_{app}|}{\tau^s_c} \right)^n \cdot \frac{\tau^s_{app}}{|\tau^s_{app}|} \tag{1.37}$$

where $\dot{\gamma}_0$ is a constant strain rate and n is a dimensionless parameter. τ^s_c is the critical resolved shear stress calculated by

$$\tau^s_c = \tau^s_f + \sqrt{\sum_{i=1}^{N} a^{si} \rho^i} \tag{1.38}$$

where τ^s_f is the alloy friction, ρ^i the dislocation density of an obstacle system i (with N the total number of obstacle systems) and a^{si} the interaction coefficients with obstacle system i. The interaction coefficients between slip systems were calculated for bcc materials with the help of DD simulations [Queyreau et al. 2009].

1.3.5.3 General case

In the general case, there is a competition between the two regimes and the total slip is expressed as a harmonic average of $\dot{\gamma}^s_{drag}$ and $\dot{\gamma}^s_{nuc}$

$$\frac{1}{\dot{\gamma}^s} = \frac{1}{\dot{\gamma}^s_{nuc}} + \frac{1}{\dot{\gamma}^s_{drag}} \tag{1.39}$$

Many variables are introduced in Equation (1.35) and are implemented in Code_Aster with the following relationships:

Average length of screw dislocation

$$l_s = \max(\lambda_s - 2\alpha^s R^s; l_c) \text{ with } l_c = 500b\,(T/T_0) \tag{1.40}$$

$$(\lambda^s + D_{obs})^{-1} = \min\left(\sqrt{\rho^s_{obs}}\,;\ (D_{obs} + 2R^s)\rho^s_{obs}\right) \text{ with } \rho^s_{obs} = \sum_{j\neq s}\rho^j, \tag{1.41}$$

$$R^s = \frac{\lambda^s}{2\alpha^s};\ \ \alpha^s = \sqrt{\sum_{j\neq s} a^{sj}\frac{\rho^j}{\rho^s_{obs}}} \tag{1.42}$$

where l_c is the critical length of a screw dislocation, λ the average distance between two obstacles, D_{obs} the average obstacle diameter, α^s the mean obstacle strength, ρ^s_{obs} the obstacle density (including forest dislocations, irradiation defects, particles) and finally T_0 a reference temperature (300 K). The interaction matrix is, considering only the 12 <111>{110} slip systems introduced in Section 1.3.2.2, composed of 144 parameters. Using the symmetries and simplifications, this number can be reduced and in fact in the DD_CC model only two independent parameters are considered, namely, a_c for the collinear systems that interact strongly and a_n for the non-collinear systems whose interaction is lower. The full expression of the interaction matrix is given in Table 1.4.

Table 1.4: Interaction matrix of the 12 primary slip systems in DD_CC [Monnet et al. 2013].

	1	2	3	4	5	6	7	8	9	10	11	12
1	a_c	a_c	a_c	a_n	a_n	a_n	a_n	a_n	a_n	a_n	a_n	a_n
2	a_c	a_c	a_c	a_n	a_n	a_n	a_n	a_n	a_n	a_n	a_n	a_n
3	a_c	a_c	a_c	a_n	a_n	a_n	a_n	a_n	a_n	a_n	a_n	a_n
4	a_n	a_n	a_n	a_c	a_c	a_c	a_n	a_n	a_n	a_n	a_n	a_n
5	a_n	a_n	a_n	a_c	a_c	a_c	a_n	a_n	a_n	a_n	a_n	a_n
6	a_n	a_n	a_n	a_c	a_c	a_c	a_n	a_n	a_n	a_n	a_n	a_n
7	a_n	a_n	a_n	a_n	a_n	a_n	a_c	a_c	a_c	a_n	a_n	a_n
8	a_n	a_n	a_n	a_n	a_n	a_n	a_c	a_c	a_c	a_n	a_n	a_n
9	a_n	a_n	a_n	a_n	a_n	a_n	a_c	a_c	a_c	a_n	a_n	a_n
10	a_n	a_n	a_n	a_n	a_n	a_n	a_n	a_n	a_n	a_c	a_c	a_c
11	a_n	a_n	a_n	a_n	a_n	a_n	a_n	a_n	a_n	a_c	a_c	a_c
12	a_n	a_n	a_n	a_n	a_n	a_n	a_n	a_n	a_n	a_c	a_c	a_c

Effective shear stress

$$\tau^s_{eff} = \left|\tau^s_{app}\right| - \tau^s_c, \quad \text{with } \tau^s_c = \sqrt{{\tau^s_{self}}^2 + {\tau^s_{LT}}^2} + \tau_F \tag{1.43}$$

$$\tau^s_{self} = \mu b\sqrt{a^{ss}\rho^s}; \quad \tau^s_{LT} = \max\left[0\ ;\ \alpha^s \mu b\left(\frac{1}{\lambda^s} - \frac{1}{2\alpha^s R^s + l_c}\right)\right] \tag{1.44}$$

where τ^s_{app} is the applied shear stress, τ^s_c the critical shear stress, τ_F accounts for the lattice friction, τ^s_{self} for self hardening and τ_{LT} is related to the line tension.

Dislocation density evolution (Derived from Discrete Dislocation Dynamics simulations) It will depend on the dislocation mean free path and requires the average diameter of the bainitic grains and two parameters called K_{self} and K_f

$$\dot{\rho}^s = \left[\frac{1}{D_{lath}} + \frac{\sqrt{a^{ss}\rho^s}}{K_{self}} + \frac{\alpha^s\lambda^s\rho^s_{obs}}{K_f} - y^s\rho^s\right]\frac{\dot{\gamma}^s}{b} \tag{1.45}$$

$$a^{sj}_{eff} = a^{sj}\left(1 - \frac{\tau^s_{eff}}{\tau_0}\right)^2; \quad \frac{1}{y^s} = \frac{1}{y_{AT}} + \frac{2\pi\tau^s_{eff}}{\mu b} \tag{1.46}$$

where a_{eff}^{sj} is the corrected interaction coefficients, which is a function of τ_{eff}^{s}. The parameters K_{self} and K_f are not independent

$$K_f = \frac{K_{self}}{\beta} \tag{1.47}$$

$$\beta = \min\left(3\ ;\ 1+\frac{2\cdot T}{T_0}\right) \tag{1.48}$$

1.3.5.4 Summary

The material parameters used by DD_CC routines are gathered in Table 1.5. Most of them can be determined using physical measurements such as the average obstacle length. Preliminary works of the PhD project have shown that ρ_{ini}, τ_f and K_{self} are the main factors influencing the yield stress and the hardening ratio of DD_CC. Normally, ρ_{ini} and τ_f are not variables, but they are not easily accessible by physical measurements. As a result, the three parameters are often the sought ones. They have been previously obtained by inverse identification on a stress-strain curve of 16MND5 steel at different temperatures [Shi 2014]. To perform this identification, the tensile response was calculated using a Berveiller-Zaoui mean field homogenization method applied to a 100 grain model. τ_f and K_{self} are sought again in this work by identification based on richer and more localized experimental data at the microscale.

Table 1.5: Material parameters used herein (adapted from [Monnet et al. 2013; Shi 2014])

C_{11} (GPa)	G (GPa)	b (nm)	ρ_m (mm^{-2})	H (s^{-1})	ΔG_0 (eV)	
206	80	0.248	$9\cdot10^7$	$1\cdot10^{11}$	0.84	
C_{12} (GPa)	D_{obs} (nm)	τ_0 (MPa)	ρ_{ini} (mm^{-2})	$\dot{\gamma}_0$ (s^{-1})	n	
133	10	363	10^6	10^{-6}	20	
C_{44} (GPa)	y_{AT} (nm)	τ_F (MPa)	D_{lath} (mm)	a_c	a_n	K_{self}
119	2	35	0.005	0.7	0.1	100

1.3.6 Homogenization of crystal plasticity laws

Crystal plasticity constitutive laws are capable of describing kinematic fields and local mechanical responses at the microscale. In order to simulate macroscopic or effective mechan-

ical responses, for example strain-stress curves, a homogenization procedure must be applied.

1.3.6.1 Berveiller-Zaoui homogenization rule

The Berveiller-Zaoui scale transition allows for the scale change between macroscopic data and microscopic quantities. Within Code_Aster, two localization rules are implemented, Berveiller-Zaoui and the so-called β-rule [Cailletaud and Sai 2008]. The former rule has been used during this work and it will be detailed hereafter.

The Berveiller-Zaoui model [Berveiller and Zaoui 1978] is based on a self-consistent scheme. This means that each phase (grain) of the polycrystal is successively regarded as an inclusion within the matrix of the homogeneous equivalent medium (HEM). Each grain interacts therefore with the equivalent medium of the whole considered volume. The Berveiller-Zaoui rule assumes that elasticity is uniform and isotropic, and that the grains are equiaxed and that the loading is monotonic.

The localization equation given by this model is

$$\boldsymbol{\sigma}_g = \boldsymbol{\Sigma} + 2\alpha\mu\left(1-\beta\right)\left(\boldsymbol{E}^p - \boldsymbol{\varepsilon}_g^p\right) \tag{1.49}$$

where g is a given phase, $\boldsymbol{\sigma}_g$ the microscopic stress tensor on grain g, $\boldsymbol{\Sigma}$ the macroscopic stress tensor, μ the elastic shear modulus, α a parameter that can be approximated by Equation (1.50), β is described in Kröner's model [Kröner 1961] and given by Equation (1.52), $\boldsymbol{E}^p$ the macroscopic plastic strain and $\boldsymbol{\varepsilon}_g^p$ the microscopic plastic strain in grain g. It is important to notice that since the plasticity of a metal comes from dislocation motion, the plastic deformation occurs at constant volume and therefore the trace of the plastic strain is equal to zero.

$$\alpha \approx \frac{1}{1+\frac{3}{2}\mu\frac{E^p}{\Sigma}} \tag{1.50}$$

$$E^p = \sqrt{\frac{3}{2}\boldsymbol{E}^p : \boldsymbol{E}^p} \qquad \text{and} \qquad \Sigma = \sqrt{\frac{3}{2}\text{dev}\left(\boldsymbol{\Sigma}\right) : \text{dev}\left(\boldsymbol{\Sigma}\right)} \tag{1.51}$$

$$\beta = \frac{2\cdot\left(4-5\cdot\nu\right)}{15\cdot\left(1-\nu\right)} \tag{1.52}$$

where ν is Poisson's ratio which is typically equal to 0.3 for most steels. Therefore, $\beta = 0.476 \approx 0.5$ and Equation (1.49) is rewritten as

$$\boldsymbol{\sigma}_g = \boldsymbol{\Sigma} + \alpha\mu \left(\boldsymbol{E}^p - \boldsymbol{\varepsilon}_g^p \right) \tag{1.53}$$

and via homogenization

$$\dot{\boldsymbol{E}}^p = \sum_g x_g \dot{\boldsymbol{\varepsilon}}_g^p \tag{1.54}$$

where x_g is the volume fraction of the phase g, each phase being composed of a single grain with the same orientation.

1.3.6.2 Numerical homogenization

Homogenization also can be carried out in FE frameworks, which involves an explicit representation of the representative volume element model (RVE). An RVE is a volume representative of the entire microstructure, not only in the crystallographic or morphological sense, but also in a mechanical sense. This means that the simulated model should have the same crystallographic texture and mean grain size as well as the same mean stress and strain as the global sample. In practice, an RVE model could be extracted from experimental observations (see *e.g.,* [Héripré et al. 2007; Wang et al. 2017]), or generated synthetically from tessellation (see Section 1.4.1). Figure 1.20 illustrates the procedure of RVE extraction from EBSD acquisitions, and the resulting simulation of the stress-strain response of the RVE.

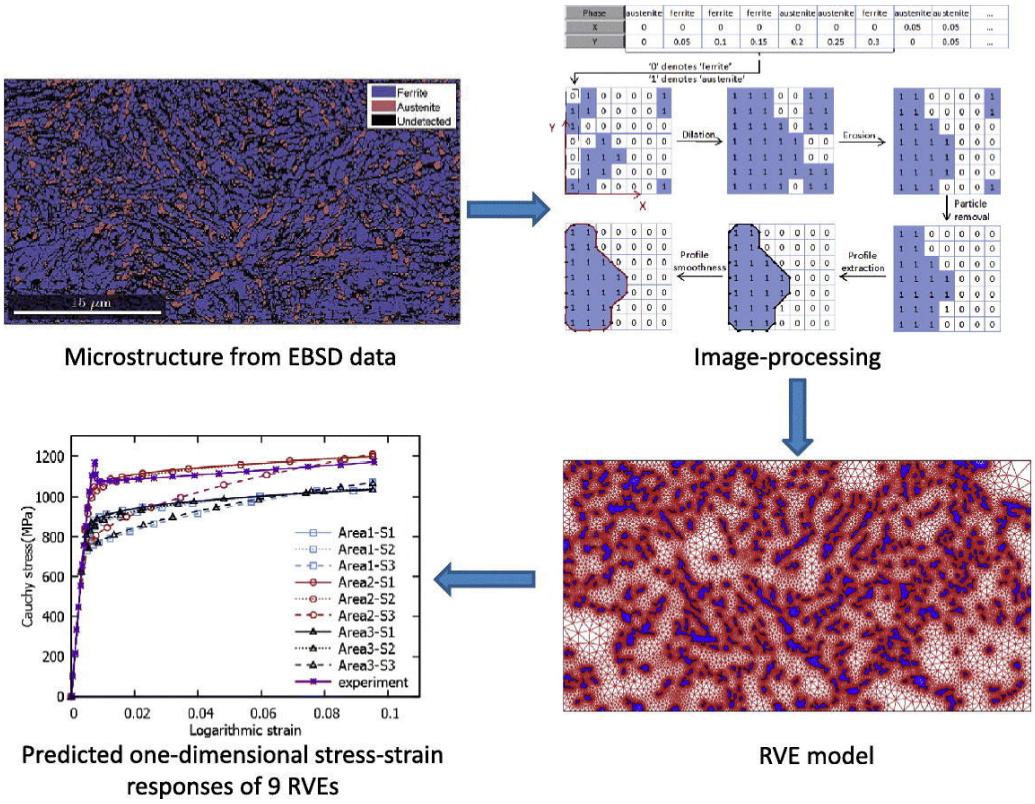

Figure 1.20: Flowchart of the extraction of an RVE model, and an example of its application [Wang et al. 2017]

1.4 Model generation for 3D crystal plasticity simulations

Only surface measurements are accessible in SEMs. For the purpose of validating the identification procedure and its upscaling to macroscopic laws, samples with columnar and coarse grains have been prepared so that mere extrusion of the surface microstructure is a valid description [Grennerat et al. 2012; Lim et al. 2015]. Such an approach has the merit of addressing the methodology with a good control of the microstructure. Yet, it is limited to materials that are not representative of most industrial applications. If a similar procedure, *e.g.*, extrusion of the surface microstructure as shown in Figure 1.21, is applied to materials with unknown grain geometry in the depth direction, numerical modeling is expected to lead to poor agreement with *in-situ* observations, as documented from numerous numerical simulations (see *e.g.*, [Zeghadi et al. 2007b]).

Another option is to generate synthetically in-depth microstructure based on surface grain structures, which introduces uncertainties (or errors) into models.

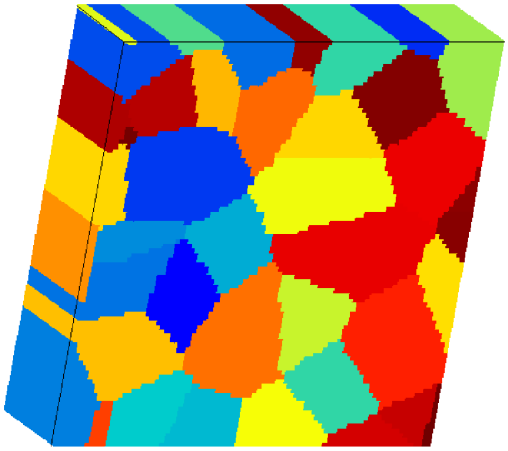

Figure 1.21: Conventionally used 3D simulation model based on surface microstructure. Extrusion of surface grains into the volume [Zeghadi et al. 2007b].

1.4.1 Microstructure tessellation

For the first polycrystal plasticity simulations, the geometrical approximation of grain shape is based on a regular honeycomb structure [Dève et al. 1988; McHugh et al. 1993]. An example model of 27 grains is shown in Figure 1.22. This idealized model does not capture the actual nature of the microstructure associated with the random distribution of shape and size of the grains. This shortcoming can be partly overcome by using tessellation methods to generate more accurate representations of the geometrical nature of the polycrystal.

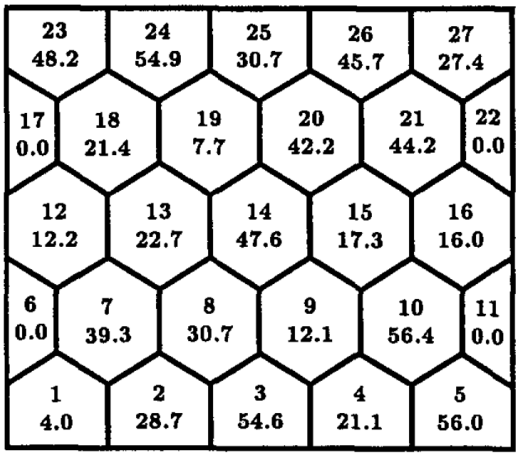

Figure 1.22: Polycrystal model used in the composite simulations. For each of the 27 grains, the grain number and the grain initial lattice orientation in degrees are shown [McHugh et al. 1993].

Tessellation is a commonly used method to generate synthetic polycrystal microstructure, either stemming from surface grain structures or not [Zeghadi et al. 2007a; Falco et al.

2017]. There exist several tessellation algorithms, such as Voronoi and Laguerre tessellations [Falco et al. 2017]. High-quality meshing of polycrystals with large number of grains (up to 10^5) can be generated [Quey et al. 2011]. A 2D Voronoi model is shown in Figure 1.23(a), and a 3D Laguerre tessellation is shown in Figure 1.23(b).

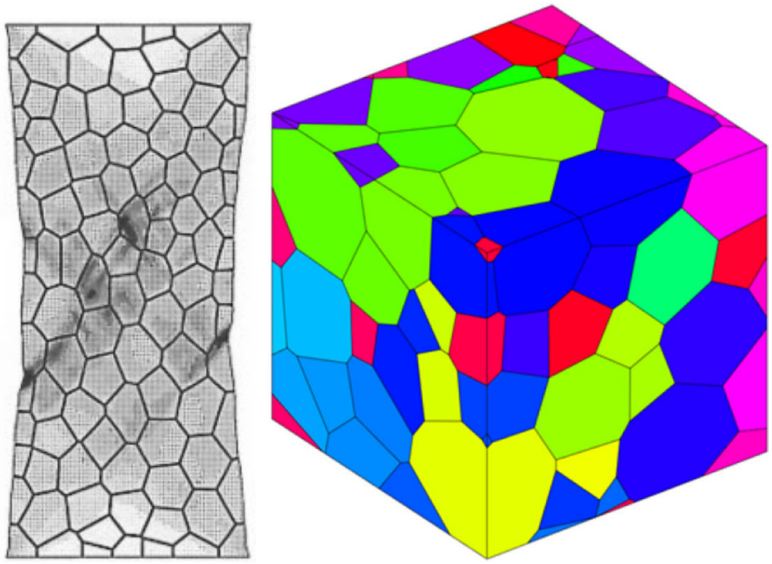

(a) (b)

Figure 1.23: Examples of FEM models generated by tessellation. (a) A 2D Voronoi model used in micromechanical simulation, where supra-granular strain is visible [Watanabe et al. 1998]. (b) A 3D Laguerre tessellation model [Falco et al. 2017].

Statistically-equivalent virtual microstructure has also been proposed for crystal plasticity finite elements (CPFE) simulations. The first step in virtual microstructure synthesis is the real microstructure characterization [Groeber et al. 2008a], where 3D polycrystalline microstructure data are first compiled from 2D focused ion beam (FIB) image slices. After reconstruction, statistics of microstructure descriptors such as distribution functions of morphological parameters like grain volume, number of contiguous neighbors, aspect ratio and surface-to-volume ratio, as well as crystallographic parameters such as orientation, misorientation and microtexture are generated. The correlation between each parameter and grain size is also investigated [Groeber et al. 2008a]. The second step involves using the distribution and correlation functions for generating statistically-equivalent synthetic 3D grain structures. A sequence of modules, namely (i) equivalent ellipsoidal grain generator, (ii) constrained grain packer, (iii) seed point generator, (iv) constrained tessellation tool and (v) crystallographic orientation assignment is utilized for reconstructing virtual microstructures [Groeber et al. 2008b]. The collection of these modules and the experimental

characterization processes constitute an automated methodology for simulating representative polycrystalline microstructures [Cheng and Ghosh 2015].

Simulations on models generated by microstructure tessellation generally cannot be compared to experimental observations at the microscale, due to the arbitrary nature of the tessellation. The effect of the synthetically generated in-volume data on the mechanical responses at the microscale has been studied. Figure 1.24 shows two artificially generated 3D simulation models based on the same surface grains, and the corresponding Von Mises stress field on the surface. It can be seen that the Von Mises field is very different between the two models, thereby indicating the vital importance of knowing the in-depth grain morphologies to study the mechanical properties of polycrystals at the microscale [Zeghadi et al. 2007b].

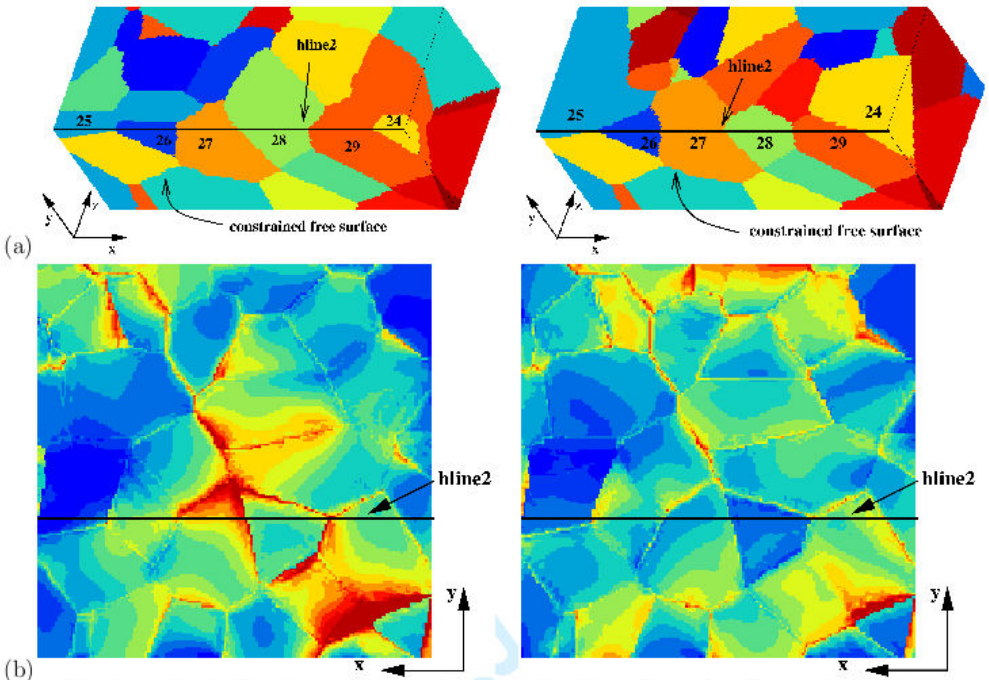

Figure 1.24: Two sets of synthetically generated in-depth grains from surface grains, and the corresponding calculated mechanical responses [Zeghadi et al. 2007b].

Nonetheless, numerous works have adopted extruded models from the surface [Guery et al. 2016b] or synthetic in-depth microstructure [Lebensohn et al. 2008] in 3D simulations, due to the lack of knowledge of real 3D microstructures. It is believed that any progress achieving a better determination of the microstructure will lead to much more constrained, and hence reliable, identification.

1.4.2 Non-destructive 3D microstructure measurement

On the experimental side, a major breakthrough has been achieved in the past few years with techniques such as 3D-XRD and Diffraction Contrast Tomography (DCT) [Herbig et al. 2011; Ludwig et al. 2009]. These techniques allow the full 3D grain geometry (though only average orientation per grain) to be retrieved with its associated crystallography. Such a complete characterization will certainly lead to a major step forward in the context of identification and validation of crystal plasticity in the future. Yet, using such methods, is still exceptional as they require monochromatic and coherent X-ray beams as produced by synchrotron facilities. They also suffer (today) from some limitations, such as a small (few thousand at most) number of large grains with simple shapes and very uniform orientations found in, for example, annealed fcc alloys.

1.4.3 FIB-EBSD

During the last decades one approach to access 3D microstructure, which is compatible with a broad class of materials, has been proposed and adopted. It is 3D-FIB SEM tomography also known as 3D-EBSD [Groeber et al. 2006; Calcagnotto et al. 2010]. This technique consists of EBSD characterization of surfaces obtained after successive FIB milling, which progressively reveals the material in depth [Zaefferer and Wright 2009].

The principle of FIB-EBSD is shown in Figure 1.25. Figure 1.25(a) illustrates the cross section along the SEM chamber, showing the sample positions for milling and EBSD analysis in the corresponding tilted set-up [Konrad et al. 2006]. During the milling process the EBSD camera is retracted and a beam of Ga^+ ions is projected towards the sample surface. When the surface layer removal is complete, the sample rotates to the EBSD position to allow EBSD acquisition. Then the sample is rotated back to the milling position for another FIB-EBSD loop. After numerous iterations a parallelepipedic section of the sample will be machined, as shown in Figure 1.25(b). To avoid specimen contamination by Ga^+ and milled material debris, usually the part behind the target area is eroded beforehand. A series of EBSD images and corresponding SEM images are the main experimental data of the process. Depending on the incident Ga^+ beam current and the milled and indexed area, the whole process takes days and even weeks to accomplish. 3D microstructure of the milled zone is obtained by compiling the EBSD data layer by layer. Usually some readjustments are necessary during the compilation. An example is shown in Figure 1.25(c), where the pearlite lamella can be

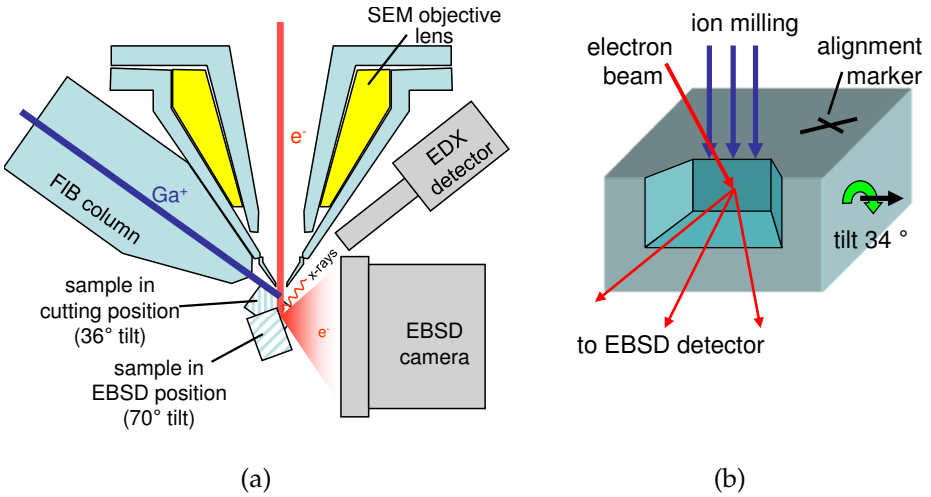

Figure 1.25: (a) Mechanism of FIB-EBSD [Konrad et al. 2006]. (b) Sample and the milled part in FIB-EBSD process. (c) An example of reconstructed 3D pearlite microstructure by FIB-EBSD, where the pearlite lamella can be observed [Zaefferer and Wright 2009].

observed in full 3D [Zaefferer and Wright 2009]. This example illustrates the high stability and satisfactory resolution of FIB-EBSD.

Such technique allows for very fine spatial resolutions down to 50 nm [Konrad et al. 2006], and very accurate crystallographic orientations (about 0.5°). Contrary to the DCT technique, the orientation is determined for each voxel instead of average for each grain. 3D-EBSD has been widely used to study the mechanical properties with the real microstructure at the microscale [Zaafarani et al. 2006; Bhandari et al. 2007]. The 3D texture and microstructure below a nanoindent in a Cu single crystal has been analyzed using 3D-EBSD and crystal plasticity FE calculations [Zaafarani et al. 2006]. A 'cradle to grave' methodology has been proposed to create an FE mesh of 3D polycrystalline material microstructures, based on experimentally acquired 3D-EBSD data [Bhandari et al. 2007]. The effect of alignment of all 3D-EBSD data slices is illustrated in Figure 1.26, with a view from the direction normal to the sectioning direction. Before alignment, continuous and spurious protrusions exist on many grain boundaries in the vertical direction. After rigid alignment, the protruding features are reduced significantly, resulting in a more realistic microstructure.

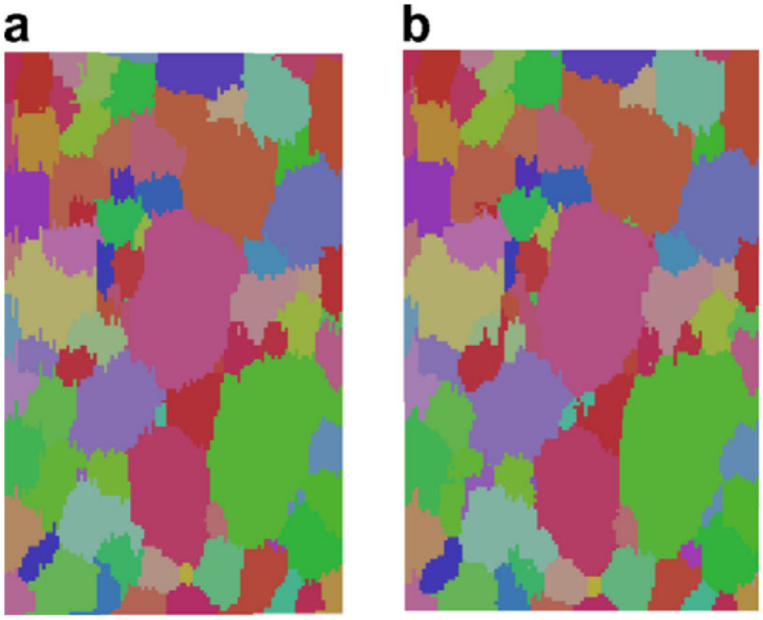

Figure 1.26: Effect of alignment of 3D-EBSD data between slices. (a) Before alignment, continuous protrusions exist on many grain boundaries in the vertical direction. (b) After alignment the protruding features reduce significantly. Both figures are viewed normal to the sectioning direction [Bhandari et al. 2007].

Figure 1.27 shows the treatment of 3D-EBSD data prior to mesh generation. All grains are labelled, and the grain boundaries are simplified, which facilitates the following mesh generation. A set of tetrahedral mesh has been generated and optimized, as shown in Figure 1.28, ready for running FE simulations. An open-source software has since been developed to reconstruct of 3D microstructure, namely, Dream3D [Groeber and Jackson 2014].

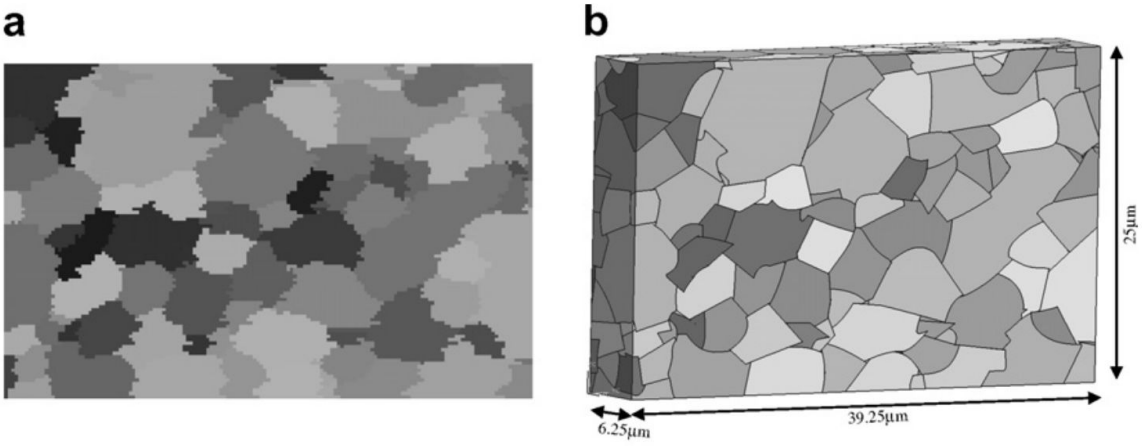

Figure 1.27: Treatment of 3D-EBSD data. (a) Surface slice. (b) Grains are labelled and grain boundaries simplified [Bhandari et al. 2007].

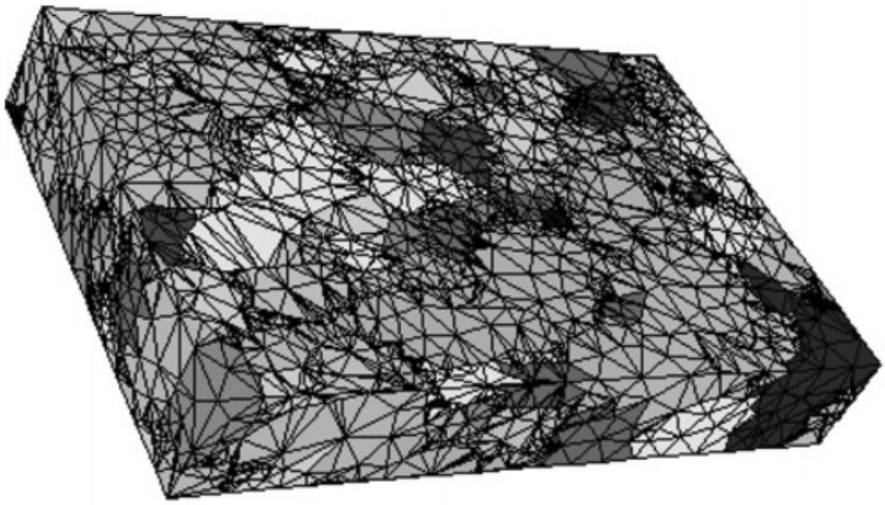

Figure 1.28: Tetrahedral element mesh generated according to experimental data [Bhandari et al. 2007].

The limitation of 3D-EBSD is its *destructive* character, which poses a specific problem to an *in-situ* mechanical test. In fact, 3D-EBSD could be performed but only at the end of the mechanical test, and hence after potentially large deformations, whereas a standard mechanical model requires the knowledge of the undeformed state. Besides, the preparation of 3D-EBSD demands careful operations and calibrations, and the running time is quite long.

For all its pros and cons, FIB-EBSD has been adopted in the PhD project to acquire a 3D microstructure data of 16MND5 steel. The present study aims at addressing the feasibility of backtracking the 3D depth-resolved microstructure from its final state to its initial one, in order to increase the reliability of interpretations of surface characterizations of mechanical tests performed *in-situ* (*i.e.*, in an SEM). The dissertation will also evaluate the added value of the backtracked 3D grain geometry and crystallography on the identification of the crystal plasticity constitutive law from the kinematic characterization of the free surface during the test. The essential steps of crystal plasticity parameters identification will be presented in the next section.

1.5 Identification of crystal plasticity parameters

1.5.1 Coupling experiment and simulation

Prior to identification, a unitary comparison of experimental and simulation results has to be performed to prove the feasibility of validating the constitutive law. For larger grains and

samples, optical imaging field measurements provide sufficient resolution for simulation needs [Zhao et al. 2008; Grennerat et al. 2012; Lim et al. 2014]. For example, the displacement field and activated slip systems are revealed by optical images for an annealed aluminum sample with average grain size 3.5 mm [Zhao et al. 2008]. Experimental characterization of the intragranular strain field in columnar ice during transient creep, and identification of the parameters by an FFT approach have been performed [Grennerat et al. 2012]. The setup of the test is shown in Figure 1.29, where the ice grains of average radius ≈ 6 mm can be seen directly. It has been found that the adopted periodic boundary conditions, though different from reality, has a minor influence compared to the mechanical interaction between grains. The 3D surface topography of strained specimens was measured using a white-light confocal microscope, then compared to simulated values, where both similarities and discrepancies have been found, as shown in Figures 1.30 and 1.31.

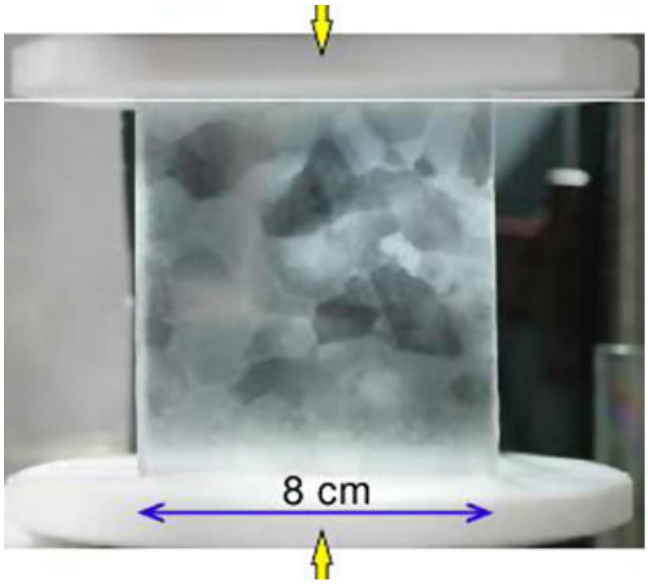

Figure 1.29: Compression test on columnar-grained ice [Grennerat et al. 2012].

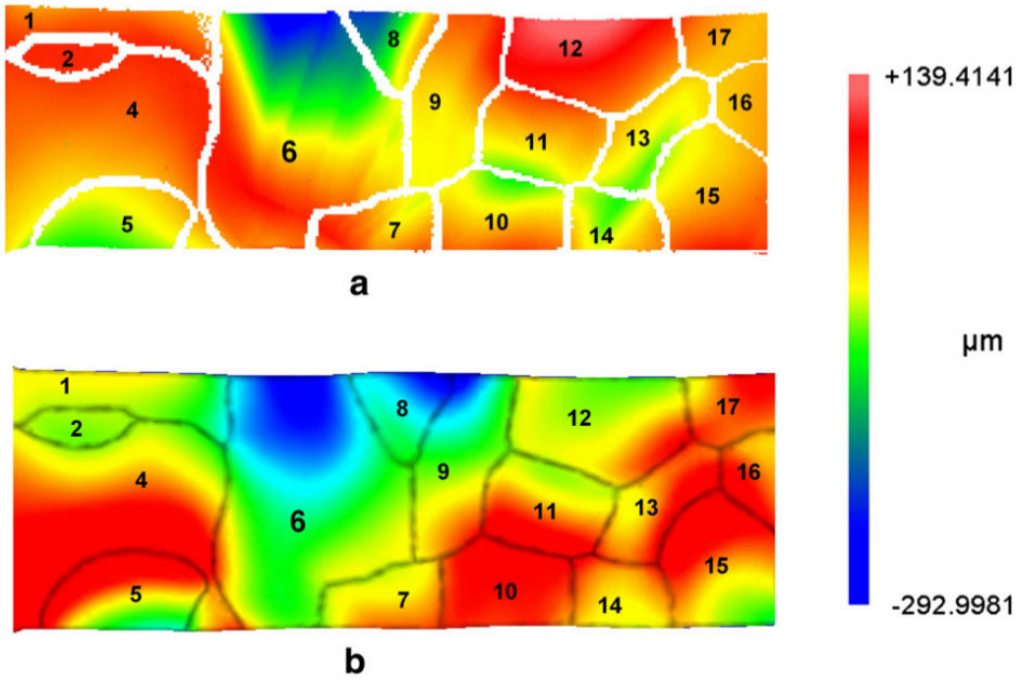

Figure 1.30: Comparison of the topography of a coarse-grain quasi-2D Al sample after 10.5% plastic strains. (a) Experimental observation. (b) CPFE predictions [Zhao et al. 2008].

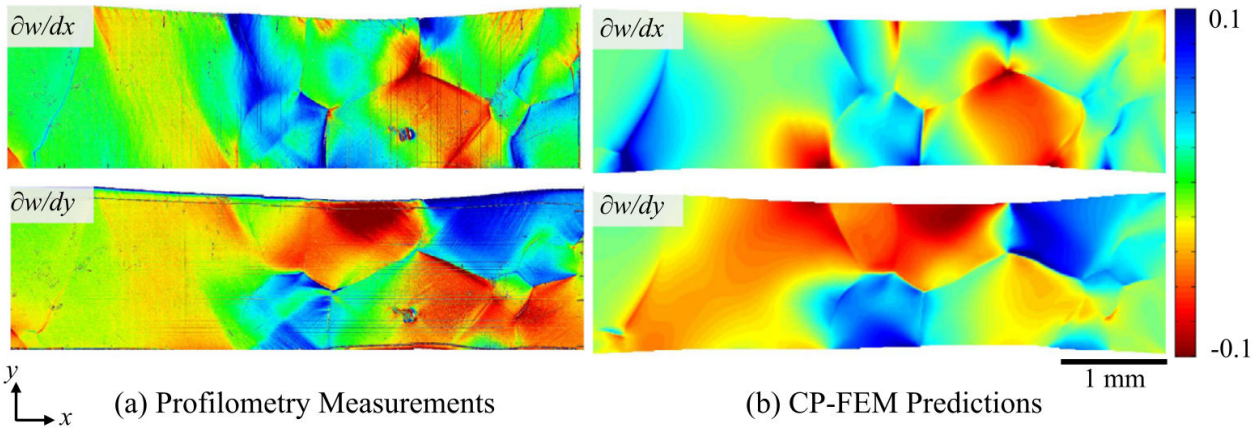

Figure 1.31: Comparison of the topography gradients in x and y directions of a coarse-grain quasi-2D Ta sample after 6.8% plastic strains. (a) Experimental observation. (b) CPFE predictions [Lim et al. 2014].

SEM imaging techniques have been widely used for samples with finer microstructure, and the main steps of the coupling between experimental tests and FE simulations are summarized in Figure 1.32. Plastic heterogeneity of a copper polycrystal deformed in uniaxial tension has been studied in experiments and finite element simulations [Delaire et al. 2000], and a satisfactory agreement has been found regarding plastic strain, crystallographic slip,

and crystal rotations. Using DIC, Raabe et al. [2001] provided a detailed surface strain mapping of oligo-crystal samples under plane strain compression and a simulation arguing that this heterogeneity arises from the combination of the macroscopic boundary condition and the grain interaction. Similar analyses have been carried out for zirconium alloys and near-gamma titanium aluminides. It has been found that the boundary conditions measured by DIC improve the simulation accuracy, especially near the model boundaries [Héripré et al. 2007]. CRSS values have been identified for the two materials.

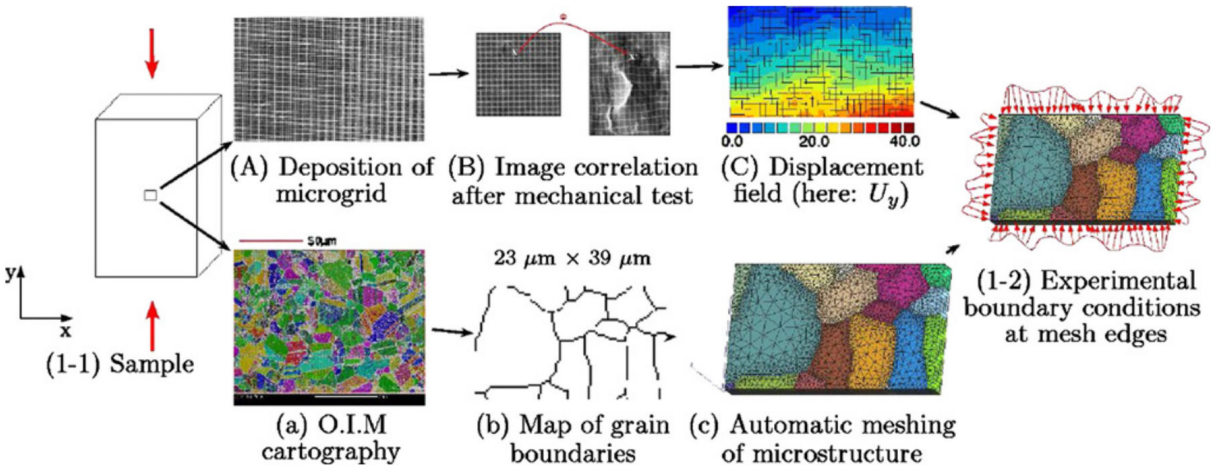

Figure 1.32: Coupling between experimental tests and FE simulations [Héripré et al. 2007].

1.5.2 Identification of constitutive equation parameters

Beyond the validation of the numerical simulations, the abundant experimental information provided by full-field measurements is ideal for identifying crystal plasticity parameters by inverse methods. Lots of previous studies have exploited full-field measurement in the identification at macroscopic scale. Elasto-plastic properties of aluminum have been identified based on the displacements of a limited number of markers attached to the sample to determine its yield stresses [Meuwissen et al. 1998; Kajberg et al. 2004] and based on a full displacement field by weighted finite element model updating (FEMU) and Integrated-DIC [Mathieu et al. 2015], orthotropic elastic parameters of a composite material have been calibrated by using kinematic fields of biaxial tensile tests [Lecompte et al. 2007].

Fewer authors have performed the identification at the microscopic scale [Hoc et al. 2003; Dexet 2006; Héripré 2006; Guery et al. 2016b]. They consist in comparing numerical simulation of crystal plasticity and full-field measurements by optical imaging [Montagnat et al. 2011] or electron microscopy [Hoc et al. 2003]. The critical local grain boundary tensile

stress of crack initiation for hydrogen charged aluminum has been identified by analyzing surface kinematic fields [Pouillier et al. 2012]. The coupling between experiment and numerical simulation often necessitates a methodology simplifying the real experimental situation. The associated hypotheses and their effects have been analyzed previously [Héripré 2006], indicating a significant uncertainty of the identified parameter values. Efforts have been dedicated in the present PhD work to limit these sources of errors.

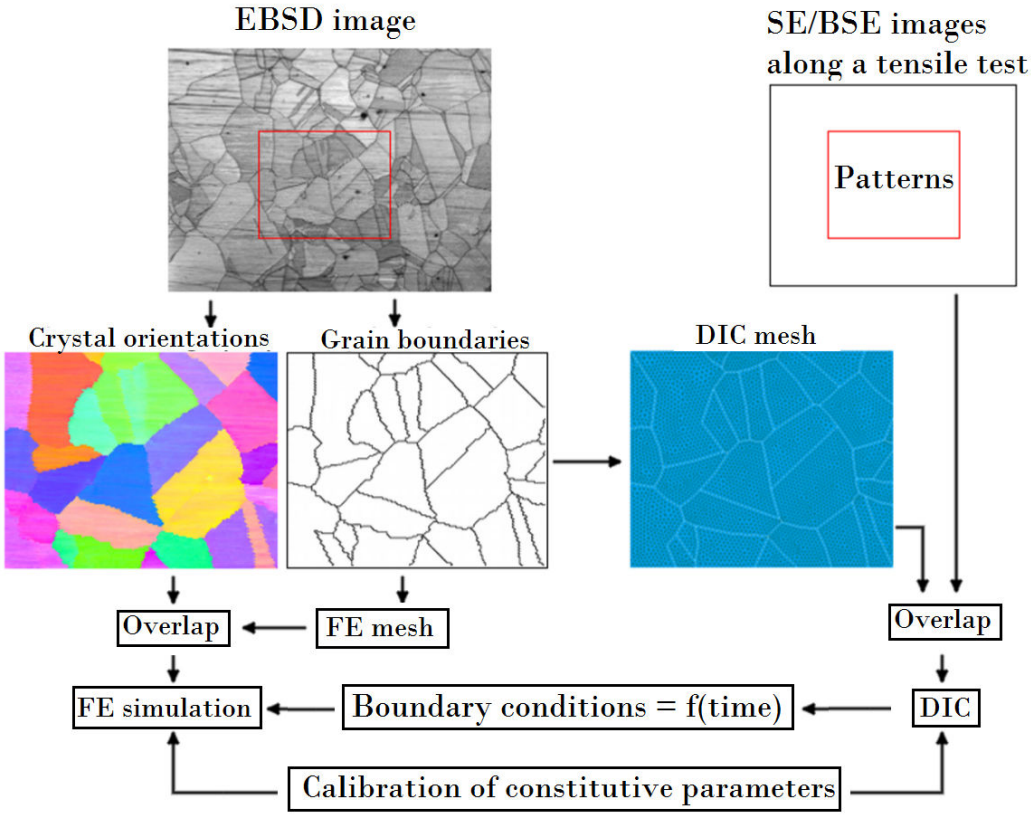

Figure 1.33: Flowchart of procedures of crystal plasticity parameter identification [Guery 2014]

Figure 1.33 illustrates the procedure of parameter identification based on 2D surface observations. By the EBSD analysis, the microstructure of a region of interest of the sample will be determined. The sample is then mechanically loaded by a tensile machine and a series of images are taken along the tensile test. Proper patterns are necessary for the success of DIC calculations, which help to measure the displacement field from the image series. Grain boundaries can be singled out from the EBSD images and a corresponding mesh could be generated, given that the grain boundaries are not exceedingly complex in the studied region. The mesh is then used in the FE simulation of the test with a crystal plasticity law. The boundary conditions prescribed on the mesh are extracted from the displacement field

measured from the experiment, as proposed by [Héripré 2006]. Then the kinematic field obtained from the numerical simulation and the experiment will be compared to validate the model in the first place, and to calibrate the constitutive parameters afterward. Note that the out-of-plane motion of the sample can also be measured by different methods, for example AFM [Kahloun et al. 2010] and stereo-correlation on SEM images [Koenig et al. 1987]. Thus not only two-dimensional but also three-dimensional kinematic fields can be used for identification purposes. The active slip systems can also be revealed experimentally since they induce surface roughness detected in SEM pictures [Abuzaid et al. 2012; Carter et al. 2014]. The active slip systems in numerical simulation have been compared to experimental observations [Guery et al. 2016a; Du et al. 2018].

In the present work Finite Element Model Updating (FEMU) will be adopted to study 16MND5 steel. In contrast to several other materials such as stainless A316 steel, the fine grains, complex texture and phases of 16MND5 lead to additional challenges in both experiments and simulations. Simplification to some extent is often necessary to make the identification procedure easier.

In the identification framework from kinematic field measurement at the microscopic scale, numerous questions arise and few answers have been proposed in the literature. How to correlate the EBSD image series and measure the crystal rotations accordingly? How to register precisely an EBSD image, a time-consuming image revealing the microstructure, and an SE/BSE image, faster imaging methods registering more loyally the coordinates of the sample, to fully benefit from the multi-modality of *in-situ* SEM tests? How to characterize and correlate the BSE raster errors? How to measure the elastic strains along the tensile test more precisely and efficiently than the commonly used cross-correlation on image subsets? How to create a 3D mesh from FIB-EBSD data? How to estimate the initial texture of the region of interest from the deformed one? How to provide reasonable in-depth boundary conditions, which are not accessible experimentally? All these questions will be discussed in the following chapters.

1.6 Outline of the thesis

The objective of the PhD project is to study crystal plasticity of the pressure vessel steel 16MND5, by both FE simulations and *in-situ* experiment on a micro-sample. Special efforts are devoted to get numerous data sets out of the experiment, and to perform an extensive

and sensitive comparison between simulation and experiment. The dissertation is organized as follows.

Chapter 2 introduces an algorithm, referred to as quaternion correlation, capable of registering crystal orientation maps (EBSD). The main result of the algorithm is the measurement of the displacement field *and* the crystal rotation field at sample surfaces. Both synthetic and experimental validations of the algorithm are provided. This work has been published [Shi et al. 2016].

Chapter 3 presents an alternative correlative method to analyze high-resolution EBSD pattern images and measure elastic strains. The new method accelerates the analysis and improves the measurement uncertainty in comparison with conventional approaches [Wilkinson et al. 2006a]. The technique has been submitted as a French patent [Shi et al. 2017c].

Chapter 4 describes an *in-situ* tensile test on the steel sample. Different imaging modalities have been adopted to characterize comprehensively the sample along the test. The measurement uncertainties of each mode have been analyzed and several correction methods have been introduced. Special efforts were dedicated to correlate images of different modalities in order to capture the most information from extensive set of images. This work has been published [Shi et al. 2018a].

Chapter 5 focuses on measuring the topography of the sample after the *in-situ* tensile test. Three different methods based on distinct approaches are explained and tested on the sample. The advantages and disadvantages of each method are summarized. Topography measurement paves the way for 3D simulation of the test by providing the out-of-plane component of the kinematic field. This work has been accepted for publication [Shi et al. 2018b].

Chapter 6 introduces a procedure that on the one hand estimates reference microstructures from deformed ones. On the other hand crystal plasticity parameters are calibrated by comparison with experimental data. A virtual test on a synthetic 'toy model' has been carried out to check the feasibility of the procedure. Two joint papers presenting the procedure have been published [Shi et al. 2017a;b].

Chapter 7 details the FIB-EBSD experimental procedure on the post-tensile sample and the corresponding analysis of data. The 3D microstructure of the sample is obtained and a corresponding 3D mesh has been generated. The procedure explained in Chapter 6 and the surface experimental data presented in Chapters 4 and 5 have been combined to calibrate the crystal plasticity model of the material. Two sets of parameters (for ferrite and bainite)

have been calibrated.

Chapter 2

Quaternion correlation for tracking crystal motions

Reproduced from: Qiwei SHI, Félix LATOURTE, François HILD and Stéphane ROUX. Quaternion correlation for tracking crystal motions. Measurement Science and Technology, September 2016, 27(9):095006.

During *in-situ* mechanical tests performed on polycrystalline materials in a scanning electron microscope, crystal orientation maps may be recorded at different stages of deformation from electron backscattered diffraction (EBSD). The present chapter introduces a novel correlation technique that exploits the crystallographic orientation field as a surface pattern to measure crystal motions. Introducing a quaternion-based formalism reveals very convenient to handle crystal symmetry and orientation extraction. Spatial regularization is provided by a penalty to deviation of displacement fields from being the solution to a homogeneous linear elastic problem. This procedure allows the large scale features of the displacement field to be captured, mostly from grain boundaries, and a fair interpolation of the displacement to be obtained within the grains. From these data, crystal rotations can be estimated very accurately. Both synthetic and real experimental cases are considered to illustrate the method.

2.1 Introduction

During the last decades, many developments of multiscale plasticity models have been proposed. The motivation is often a better prediction of the macroscopic behavior by

enriching the constitutive description with applications in metal forming or fatigue failure [Horstemeyer 2012], or to estimate the long-term behavior of materials subjected to irradiation [Leclercq et al. 2010]. For industrial applications with these multiscale models, experimental validations are needed for each model and each scale transition.

The experimental analysis proposed in this chapter is related to the scale transition from single crystal to macroscopic plasticity, which constitutes a homogenization problem. Mean-field homogenization is often analytical and for instance based on Eshelby's inclusion principle [Berveiller and Zaoui 1978], while finite element calculations on polycristalline aggregates allow numerical homogenization to be performed together with the computation of local mechanical fields [Barbe et al. 2001]. The main challenge of the scale transition between single crystal and polycrystals is to account for strain gradient contributions. Experimental assessments of strain gradient contributions have been proposed by comparing experiments involving grain boundaries with strain gradient crystal plasticity models [Ma et al. 2006a] or by measuring the lattice curvature developing near grain boundaries using high angular resolution electron backscattered diffraction (HR-EBSD) [Wilkinson et al. 2006b]. On the other hand, strain gradients have a known influence on the material macroscopic response in plasticity and on the stresses developing at grain boundaries [Cordero et al. 2012; Gurtin et al. 2007]. In this context, several validations of crystal plasticity models exploiting kinematic fields have been conducted, and more specifically the displacement and strain fields obtained from images acquired with a scanning electron microscope (SEM) [Héripré et al. 2007; Lim et al. 2015].

Digital Image Correlation (DIC) techniques [Sutton 2013] have been used to compute kinematic fields from images registered at the microscale, for instance using SEM pictures [Allais et al. 1994; Doumalin and Bornert 2000; Tatschl and Kolednik 2003; Sutton et al. 2006; Latourte et al. 2014]. It is worth noting that artifacts associated with the image capture in an SEM had to be accounted for [Sutton et al. 2007b; Ru et al. 2011; Guery et al. 2014]. DIC has also been utilized to characterize crystal deformations in processes such as fatigue and crack growth [Carroll et al. 2009; Jin et al. 2011]. In particular, EBSD images have been superimposed onto DIC strain maps to study the relationship between the texture and the plastic deformation at the crack tip [Jin et al. 2011]. Displacement fields only partly represent the kinematics of a polycrystal subjected to a mechanical loading. An important and complementary kinematics, when considering finite strain transformation, is *lattice rotation*. Measuring rotation fields can be achieved by using for instance orientation imaging microscopy

based on HR-EBSD [Han et al. 2003], or using synchrotron X-ray microdiffraction [Joo et al. 2004] providing average rotations per grain. Texture evolutions, measured using EBSD and grain averages, have already been used to validate crystal plasticity models [Hoc et al. 2003] together with strain distributions in polycrystals.

In the following, it is proposed to simultaneously measure displacement *and* rotation fields by registering EBSD maps. Because of their sharp contrasts, grain boundaries allow for a good registration as will be shown below. However, one of the challenges is that intragranular deformation cannot be followed accurately as the orientation field shows very small gradients within the grains. Elastic regularization [Réthoré et al. 2009] is an efficient way to compensate for poorly contrasted images [Tomičević et al. 2013]. Spatial regularization is provided by a penalty to deviation of displacement fields from being the solution to a homogeneous linearly elastic problem, either isotropic, cubic or orthotropic. This procedure allows the displacements to be interpolated within the grains.

The chapter is organized as follows. Section 2.2 is dedicated to the preparation of EBSD images for DIC analyses. It is proposed to use quaternions to encode orientation maps provided by EBSD analyses. The correlation algorithm based on orientation maps is developed in Section 2.3 to evaluate displacement fields. As a key result, the residual field indicates the disorientation, *i.e.*, crystal rotations between images. Hence it is possible to measure displacement *and* crystal rotation fields. A numerical validation based on a synthetic example is first presented in Section 2.4 and an experimental application of the algorithm is detailed in Section 2.5.

2.2 Quaternion-encoded orientation maps

2.2.1 General properties of quaternions

Quaternions are hyper-complex numbers generalizing to four dimensions complex numbers in two dimensions [Hamilton 1853; 1866]. Quaternion algebra is a useful tool for the description of rotations and orientations in 3D spaces (akin to complex numbers for rotations and orientations in 2D). Quaternions are devoid of the singularity at the origin of Euler angle space, which is due to the progressive degeneracy of the first and third Euler angles as the second angle approaches zero (*i.e.*, "gimbal lock"). Quaternions also provide a convenient frame to handle crystal symmetries [Cho et al. 2005].

Appendix A recalls important features of quaternions. Let us simply define here our notations. Quaternions consist of a real and three imaginary numbers $(1, \boldsymbol{i}, \boldsymbol{j}, \boldsymbol{k})$ so that any quaternion is described as $\boldsymbol{q} = q_1 + q_2\boldsymbol{i} + q_3\boldsymbol{j} + q_4\boldsymbol{k}$, which is equivalent to the 4D vector representation $\boldsymbol{q} = (q_1, q_2, q_3, q_4)$. In the following, only unit quaternions $|\boldsymbol{q}|^2 = \sum_n q_n^2 = 1$ will be considered. A rotation of angle θ about an axis defined by a unit vector $\boldsymbol{d} = (d_1, d_2, d_3)$ is represented by the unit quaternion

$$\begin{aligned} \boldsymbol{q} &= e^{\frac{\theta}{2}(d_1\boldsymbol{i}+d_2\boldsymbol{j}+d_3\boldsymbol{k})} \\ &= \cos(\theta/2) + (d_1\boldsymbol{i} + d_2\boldsymbol{j} + d_3\boldsymbol{k})\sin(\theta/2) \end{aligned} \tag{2.1}$$

Equation (2.1) can be seen as an extension of Euler's formula.

Since a crystal orientation can be identified by the 3D rotation needed to bring a reference crystal orientation onto it, it can be described by a quaternion. As a consequence, the reference orientation is the unit real number $\boldsymbol{q}_0 = (1, 0, 0, 0)$. Successive applications of rotations $\boldsymbol{q}_1$ and $\boldsymbol{q}_2$ are obtained by a (non commutative) quaternion product $\boldsymbol{q}_2 \times \boldsymbol{q}_1$ where the elementary multiplication rules are recalled in Appendix A. In the sequel the multiplicative sign $\times$ will be omitted to simplify notations. Thus the rotation that brings $\boldsymbol{q}_1$ onto $\boldsymbol{q}_2$ is $\boldsymbol{q}_2\boldsymbol{q}_1^{-1}$. A fundamental property that will be used in the sequel is that a "distance" between two orientations can be computed from the minimum magnitude of the disorientation angle θ. The real part $\Re[\boldsymbol{q}_2^{-1}\boldsymbol{q}_1] = \cos(\theta/2)$ gives the cosine of half the disorientation angle.

2.2.2 Crystal symmetry and quaternions

One practical difficulty associated with crystal symmetry is that several orientations having distinct quaternion representations are equivalent. For the cubic symmetry class, 48 quaternions $\boldsymbol{p}_i^{cub}$ $(1 \leq i \leq 48)$ are to be considered as identical to the reference orientation (Appendix B). When reading an orientation "`.ang`" file from an EBSD analysis re-encoding it as a field of quaternion requires a convention to be chosen in order to minimize spurious discontinuities due to arbitrary choices of quaternions within the symmetry class.

At a particular point of the EBSD map, where one determination of the orientation is converted into quaternion $\boldsymbol{q}(\boldsymbol{x})$, any other $\boldsymbol{p}_n^{cub}\boldsymbol{q}(\boldsymbol{x})$ (for all n) is a valid choice. One possible convention is to select the one having the largest real part,

$$\boldsymbol{q}^{(1)}(\boldsymbol{x}) = \underset{n}{\mathrm{Argmax}}\ (\Re(\boldsymbol{p}_n^{cub}\boldsymbol{q}(\boldsymbol{x}))) \tag{2.2}$$

This choice can be understood as the one that requires the smallest rotation angle to be mapped onto the reference configuration *i.e.*, $\boldsymbol{q}_0 = 1$. Figure 2.1 shows the quaternion field

$\boldsymbol{q}^{(1)}(\boldsymbol{x})$ extracted from an OIM™ file. Some discontinuities observed in those maps do not correspond to a real grain boundary but simply to a slight rotation of the physical frame that produces a change in the symmetric representative.

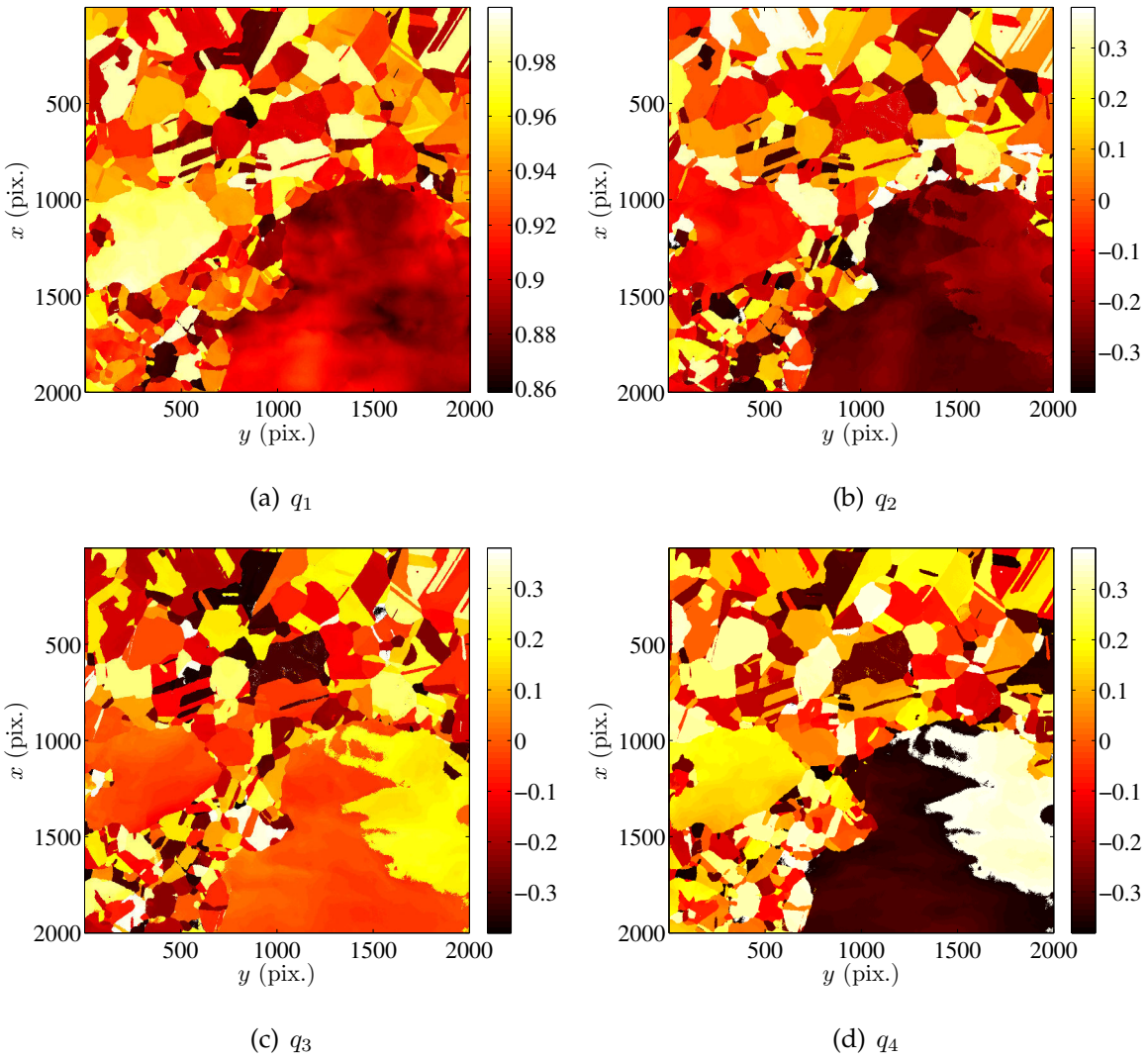

(a) q_1 (b) q_2

(c) q_3 (d) q_4

Figure 2.1: Maps of the four components of the quaternion field after selecting the closest representative with respect to the reference orientation $\boldsymbol{q}_0 = 1$. The inverse pole figure corresponding to these maps is shown in Figure 2.15(b)

In order to reduce spurious discontinuities, a second procedure is proposed herein. After the first determination of orientation has been performed a local reference is defined per grain. It is chosen as the orientation at the center of mass of each grain. The labeling of grains is performed thanks to the OIM™ software, which provides the grain boundary image according to a given disorientation threshold, set to be 1 degree in practice. From this image, a label ℓ is assigned to each grain, and shared by all pixels $\boldsymbol{x}$ of the grain, so that one may refer to its label $\ell(\boldsymbol{x})$. The center of mass of the grain is also computed, $\boldsymbol{x}_c^\ell$. The local

grain reference is then set to $\boldsymbol{q}^{ref}(\boldsymbol{x}) = \boldsymbol{q}^{(1)}(\boldsymbol{x}_c^{\ell(\boldsymbol{x})})$. A new determination of the symmetric representative $\boldsymbol{q}^{(2)}(\boldsymbol{x})$ is performed by selecting the symmetric representative n^* that maximizes the real part of $\boldsymbol{p}_n^{cub}\boldsymbol{q}^{ref}(\boldsymbol{x})^{-1}\boldsymbol{q}(\boldsymbol{x})$, *i.e.*, choosing the orientation that is the nearest to that of the center of mass of the grain. Figure 2.2 shows the resulting quaternion map. This second convention will reveal very convenient for filtering quaternion fields, which will be detailed in Section 2.3.2. Its justification is that within one grain, the change in orientation is small, and hence, no spurious apparent discontinuities will appear.

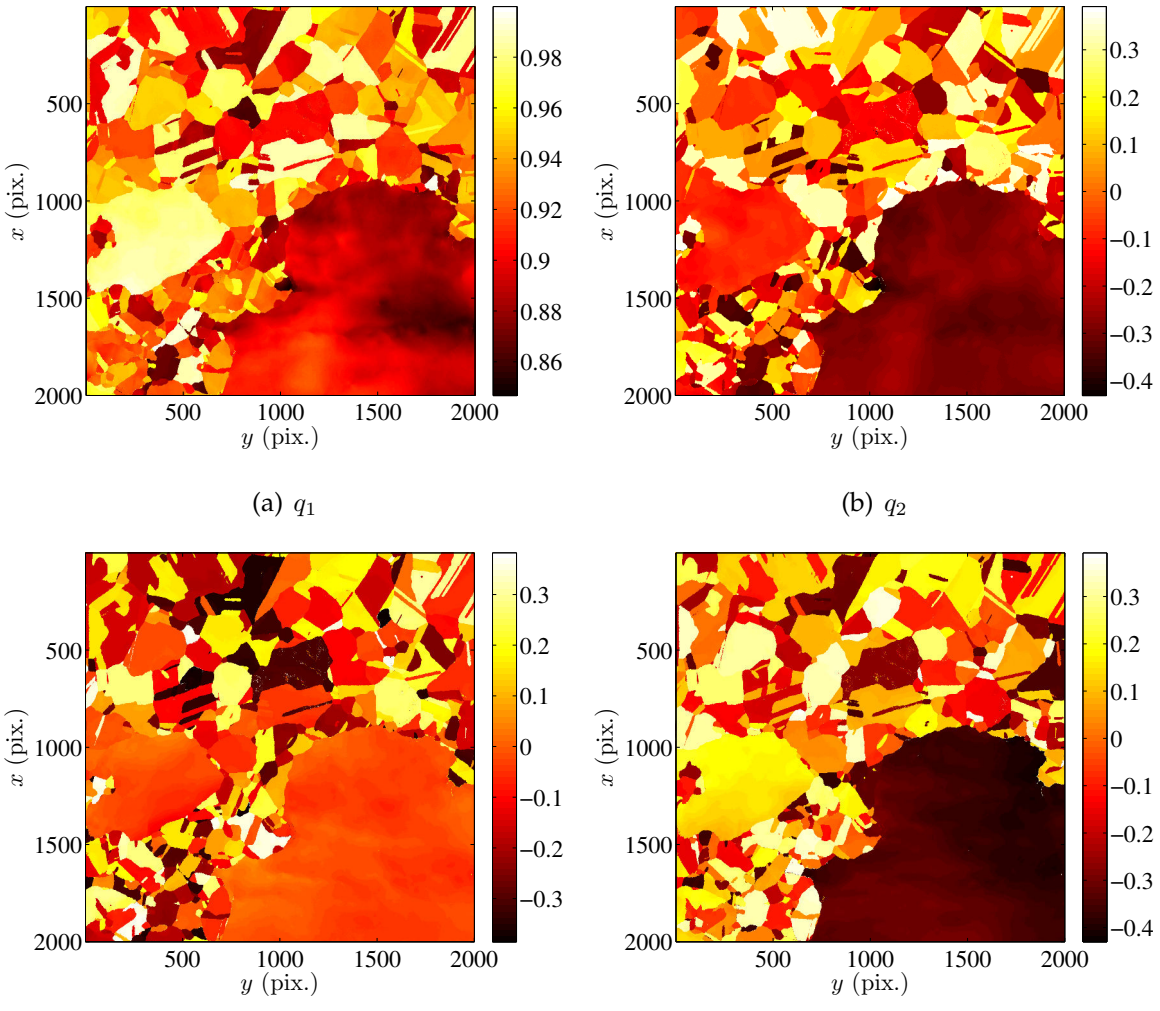

(a) q_1 (b) q_2

(c) q_3 (d) q_4

Figure 2.2: Maps of the four components of the quaternion field after selection of the closest representative to the local grain reference $\boldsymbol{q}^{ref}(\boldsymbol{x})$. The inverse pole figure corresponding to these maps is shown in Figure 2.15(b)

2.3 Proposed correlation algorithm

Conventional DIC consists in registering two gray-level images, one in the reference state $f(\boldsymbol{x})$ and a second one in the deformed state $g(\boldsymbol{x})$. It is based on the determination of the displacement field $\boldsymbol{u}(\boldsymbol{x})$ such that the corrected deformed image $\widetilde{g}_{\boldsymbol{u}}(\boldsymbol{x}) = g(\boldsymbol{x} + \boldsymbol{u}(\boldsymbol{x}))$ coincides as best as possible with the reference image $\widetilde{g}_{\boldsymbol{u}}(\boldsymbol{x}) = f(\boldsymbol{x})$, and hence minimizes the quadratic norm of the so-called residual $(\widetilde{g}_{\boldsymbol{u}}(\boldsymbol{x}) - f(\boldsymbol{x}))$ summed over the entire region of interest.

The proposed extension consists in matching quaternion-valued images $\boldsymbol{f}(\boldsymbol{x})$ and $\boldsymbol{g}(\boldsymbol{x})$. Hence, the crystallographic orientation is treated as equivalent to a speckle pattern, as the orientation is not expected to undergo large changes during deformation. Following the above schematic formulation, a corrected deformed image is introduced $\widetilde{\boldsymbol{g}}_{\boldsymbol{u}}(\boldsymbol{x}) = \boldsymbol{g}(\boldsymbol{x} + \boldsymbol{u}(\boldsymbol{x}))$, and the registration is achieved via the minimization of the "discrepancy" defined here as

$$\Phi[\boldsymbol{u}] = \sum_{ROI} \psi^2(\widetilde{\boldsymbol{g}}_{\boldsymbol{u}}(\boldsymbol{x}), \boldsymbol{f}(\boldsymbol{x})) \tag{2.3}$$

so that the sought displacement field is the minimizer of Φ

$$\boldsymbol{u}(\boldsymbol{x}) = \underset{\boldsymbol{u}}{\operatorname{Argmin}}\ \Phi[\boldsymbol{u}] \tag{2.4}$$

In order to follow a strict parallel with classical DIC, ψ should measure a distance in unit quaternion space between its two arguments. As above discussed, a good definition for this "distance" is based on the minimum magnitude of the angle of the rotation θ relating the two orientations. In addition, all possible symmetry replicas of one of the two arguments should be considered and the minimum value should be selected. This operation is numerically expensive as it has to be performed pixelwise. Considering that the discrepancy between orientations will be small at convergence, it is proposed to substitute to the above quadratic distance a function that behaves similarly close to the origin, namely $1 - \cos(\theta/2) \sim_{\theta \to 0} \theta^2/8$. Thus, assuming crystal symmetry degeneracies are accounted for, the following choice of ψ^2 is made

$$\begin{aligned} \psi^2(\boldsymbol{f}, \boldsymbol{g}) &\equiv \Re\left[1 - \boldsymbol{f}\boldsymbol{g}^{-1}\right] \\ &= 1 - f_i g_i \\ &= 1 - \cos(\theta/2) \end{aligned} \tag{2.5}$$

where $\Re$ denotes the real part (or first component) of the quaternion. Last, without further restriction, the problem is generally ill-posed. Thus following the usual practices of DIC, the

displacement field is sought as the minimizer of $\Phi[\boldsymbol{u}]$ where $\boldsymbol{u}$ is confined to a vector space generated by a suited basis of vector fields $\boldsymbol{\varphi}_i$, so that

$$\boldsymbol{u}(\boldsymbol{x}) = \sum_{i=1}^{m} \lambda_i \boldsymbol{\varphi}_i(\boldsymbol{x}) \tag{2.6}$$

This formulation leaves λ_i as unknowns that can be determined through a Gauss-Newton algorithm [Lucas and Kanade 1981].

2.3.1 Gauss-Newton scheme

A Gauss-Newton procedure iteratively computes corrections $\{\boldsymbol{\delta\lambda}^{(n)}\}$ to the column vector $\{\boldsymbol{\lambda}^{(n-1)}\}$, based on the solution to a linearized system

$$[\boldsymbol{M}^{(n-1)}]\{\boldsymbol{\delta\lambda}^{(n)}\} = \{\boldsymbol{\gamma}^{(n-1)}\} \tag{2.7}$$

where $[\boldsymbol{M}^{(n-1)}]$ and $\{\boldsymbol{\Gamma}^{(n-1)}\}$ are respectively the approximate Hessian matrix and residual vector that are to be updated at each iteration n. The correction vector is $\boldsymbol{\lambda}^{(n)} = \boldsymbol{\lambda}^{(n-1)} + \boldsymbol{\delta\lambda}^{(n)}$.

A reformulation based on quaternion algebra is given in this subsection. If the reader is interested in the final results, intuitive and familiar expressions of both Jacobian $\{\boldsymbol{\gamma}^{(n-1)}\}$ and Hessian $[\boldsymbol{M}]$ are retrieved in Equations (2.14) and (2.15) respectively. The Jacobian reads

$$\begin{aligned} \gamma_i^{(n)} &\equiv \tfrac{\partial \Phi}{\partial \lambda_i} \\ &= -\textstyle\sum_{ROI} \Re\left[\boldsymbol{f}(\boldsymbol{x})\boldsymbol{\nabla}(\widetilde{\boldsymbol{g}}^{(n)}(\boldsymbol{x}))^{-1}\right]\boldsymbol{\varphi}_i(\boldsymbol{x}) \\ &= -\textstyle\sum_{ROI}\left(\sum_\alpha f_\alpha(\boldsymbol{x})\boldsymbol{\nabla}\tilde{g}_\alpha^{(n)}(\boldsymbol{x})\right)\boldsymbol{\varphi}_i(\boldsymbol{x}) \end{aligned} \tag{2.8}$$

and the Hessian

$$\begin{aligned} M_{ij}^{(n-1)} &\equiv \tfrac{\partial^2 \Phi}{\partial \lambda_i \partial \lambda_j} \\ &= -\textstyle\sum_{ROI} \Re\left[\boldsymbol{f}(\boldsymbol{x})(\boldsymbol{\nabla}\otimes\boldsymbol{\nabla})(\widetilde{\boldsymbol{g}}^{(n-1)}(\boldsymbol{x}))^{-1}\right] : (\boldsymbol{\varphi}_i(\boldsymbol{x})\otimes\boldsymbol{\varphi}_j(\boldsymbol{x})) \\ &= -\textstyle\sum_{ROI}\left(\sum_\alpha f_\alpha(\boldsymbol{x})(\boldsymbol{\nabla}\otimes\boldsymbol{\nabla})\tilde{g}_\alpha^{(n-1)}(\boldsymbol{x})\right) : (\boldsymbol{\varphi}_i(\boldsymbol{x})\otimes\boldsymbol{\varphi}_j(\boldsymbol{x})) \end{aligned} \tag{2.9}$$

Since quaternions can be seen as unit vectors in a 4D space, they obey $\boldsymbol{q}\boldsymbol{q}^{-1} = q_\alpha q_\alpha = 1$ with $\alpha = 1, ..., 4$. Therefore they are always orthogonal to their gradient

$$\boldsymbol{\nabla}(\boldsymbol{q}\boldsymbol{q}^{-1}) = \boldsymbol{0} \tag{2.10}$$

and in particular for the real part of this identity, $q_\alpha \boldsymbol{\nabla} q_\alpha = 0$

$$(\boldsymbol{\nabla}\otimes\boldsymbol{\nabla})(\boldsymbol{q}\boldsymbol{q}^{-1}) = \boldsymbol{0} \tag{2.11}$$

and thus in particular, $q_\alpha(\boldsymbol{\nabla}\otimes\boldsymbol{\nabla})q_\alpha + \boldsymbol{\nabla}q_\alpha\otimes\boldsymbol{\nabla}q_\alpha = \mathbf{0}$. The last identity is used to rewrite second order derivatives as

$$q_\alpha(\boldsymbol{\nabla}\otimes\boldsymbol{\nabla})q_\alpha = -\boldsymbol{\nabla}q_\alpha\otimes\boldsymbol{\nabla}q_\alpha \tag{2.12}$$

or $f_\alpha f_{\alpha,ij} = -f_{\alpha,i}f_{\alpha,j}$.

Using the above properties leads to equivalent expressions of the residual vector $\{\boldsymbol{\gamma}^{(n-1)}\}$ and Hessian $[\boldsymbol{M}^{(n-1)}]$. The former is rewritten using Equation (2.10)

$$\gamma_i^{(n-1)} = -\sum_{ROI}(f_\alpha(\boldsymbol{x}) - \tilde{g}_\alpha^{(n-1)})\boldsymbol{\nabla}\tilde{g}_\alpha^{(n-1)}(\boldsymbol{x})\cdot\boldsymbol{\varphi}_i(\boldsymbol{x}) \tag{2.13}$$

Moreover since $\widetilde{\boldsymbol{g}}^{(n-1)}$ is expected to converge to $\boldsymbol{f}$, one may substitute one to the other at dominant order and finally express γ as

$$\gamma_i^{(n-1)} = \sum_{ROI}(\boldsymbol{\nabla}f_\alpha(\boldsymbol{x})\cdot\boldsymbol{\varphi}_i(\boldsymbol{x}))(\tilde{g}_\alpha^{(n-1)} - f_\alpha(\boldsymbol{x})) \tag{2.14}$$

The same simplification can be extended to the Hessian. Equation (2.12) is used to transform the second order derivatives into first order ones, and again $\boldsymbol{f}$ is substituted to $\widetilde{\boldsymbol{g}}^{(n-1)}$

$$M_{ij} = \sum_{ROI}(\boldsymbol{\nabla}f_\alpha(\boldsymbol{x})\cdot\boldsymbol{\varphi}_i(\boldsymbol{x}))(\boldsymbol{\nabla}f_\alpha(\boldsymbol{x})\cdot\boldsymbol{\varphi}_j(\boldsymbol{x})) \tag{2.15}$$

Let us emphasize that the final expression of $[\boldsymbol{M}]$ does not depend any longer on the iteration number n, and hence it can be computed once for all. Although the above detailed justification appears to be somewhat involved, the final expressions of $[\boldsymbol{M}]$ and $\boldsymbol{\gamma}^{(n-1)}$ could have been guessed by extending global DIC to quaternions componentwise. For a single α, the expression of $[\boldsymbol{M}]$ and $\boldsymbol{\gamma}^{(n-1)}$ are exactly those of global DIC [Hild and Roux 2012b], where the quaternion component f_α is analogous to the gray level of a speckle pattern. Thus the summation over the four components is equivalent to having four different speckles (*i.e.*, four imaging modalities) of the same surface, which would all obey the *same* kinematics. A parallel could be drawn with DIC based on color images, wherein each channel R, G or B would be treated as an independent information.

2.3.2 Filtering quaternion fields

One difficulty is related to the discontinuities of $\boldsymbol{f}$ (and $\boldsymbol{g}$). The orientation is uniform in each grain but each grain boundary appears as a large discontinuity. This specific texture (*i.e.*, piecewise constant texture) is not very well suited to a Gauss-Newton scheme as gradients

do not give a fair picture of how $\boldsymbol{f}$ varies with the displacement over large distances. In order to be able to correct for large displacements, a solution consists of smoothing out the grain boundaries. A simple way to achieve such filtering is to apply to the quaternion field a convolution, component-wise, with a Gaussian kernel of width ξ, followed by a reprojection on the unit sphere in 4D (to preserve the unitary property of quaternions that has been lost in the convolution). Such filtered quaternion field is denoted as $\widehat{\boldsymbol{f}}_\xi$.

For given length ξ the correlation procedure is straightforward as above discussed. The only care to be taken is that $\boldsymbol{g}$ should be first corrected by the displacement field, using the raw signal, and then filtered at the scale ξ, in order to compute differences with the filtered reference image. This determination tolerates displacement amplitudes of order ξ. Hence a large ξ is to be used to initialize the procedure. However, the accuracy of the evaluation of the displacement is based on the sharpness of the grain boundary. A smooth grain boundary may only provide a gross determination. Hence it is proposed to progressively reduce the length ξ using the previously measured displacement field at a large ξ value to initialize a computation with a smaller ξ.

2.3.3 Elastic regularization

EBSD images generally show high contrast only between grains (see *e.g.,* Figures 2.1 and 2.2) thus the correlation procedure determines the displacement field at grain boundaries. Seeking the displacement field inside grains by DIC is not a well-posed question, even if the displacement field is considered in a weak formulation as shown in Equation (2.6). An elastic regularization provides a very convenient interpolation scheme for the displacement field inside the grains where the image contrast is insufficient for registration purposes.

Mechanics-aided DIC has been proposed to solve such issues [Réthoré et al. 2009; Tomičević et al. 2013], and the regularization technique has also been applied to digital volume correlation [Taillandier-Thomas et al. 2014]. Readers are referred to these works for detailed justification. The spirit of the approach, which was pioneered by Tikhonov and Arsenin [Tikhonov and Arsenin 1977], is to introduce a regularization term, *i.e.,* an additional functional of the displacement field that incorporates a prior information (or assumption) on the displacement field. However, one would like the regularization to interfere in a minimal way with the field to be measured, minimal meaning that it should matter only when no other data can be exploited. The chosen reference is to favor locally solutions to ho-

mogeneous elasticity, without specifying boundary conditions. The "equilibrium gap" is precisely one such functional, based on a second order differential operator acting on the displacement, and which is quadratic in the displacement [Réthoré et al. 2009; Amiot et al. 2012]. It can be supplemented by a similar edge regularization (otherwise absent from the bulk equilibrium gap) [Tomičević et al. 2013].

Two parameters are used to characterize the weight of mechanical regularization, *i.e.*, ℓ_b and ℓ_m, representing the regularization lengths at the edge of the ROI and in the bulk of the ROI respectively. According to previous works [Tomičević et al. 2013], the optimized ratio $\ell_b/\ell_m = 0.5$ is chosen for all the calculations reported hereafter. It should be noted that due to the contrast being concentrated at grain boundaries, the minimal mechanical regularization length ℓ_m should at least be of the same order of magnitude as the grain size to provide a mechanical regularization in the core of the grains without constraining too much the displacement determined at grain boundaries.

2.3.4 Correlation residuals

When registering EBSD images, it is expected that the motions of grain boundaries are mainly captured. Within each grain, elastic regularization will provide a smooth interpolation that is unbiased by the superposition of arbitrary rigid body motion, or even any displacement field that would be the solution to a homogeneous linear elastic problem. While displacement accuracy is reduced far from grain boundaries, disorientations are expected to be small in these areas, and therefore the residual will allow the crystal rotations to be quantified very accurately.

Further, at the grain boundaries the confidence index and image quality of EBSD acquisition tend to be low. If the electron beam hits two grains at the same time an unreliable orientation will be recorded. Besides, at grain boundaries the interpolation procedure of $\boldsymbol{g}$ results in an orientation that is close to neither grain. Therefore grain boundaries will always appear distinctively in the residual fields.

2.4 Application of the algorithm on a synthetic test case

A synthetic test case is numerically generated in order to validate the determination of the displacement field with known values. The displacement field is computed from a finite

element simulation with Code_Aster [EDF 2017]. A two-dimensional microstructure shown in Figure 2.3 with isotropic texture is modeled from an experimental orientation map.

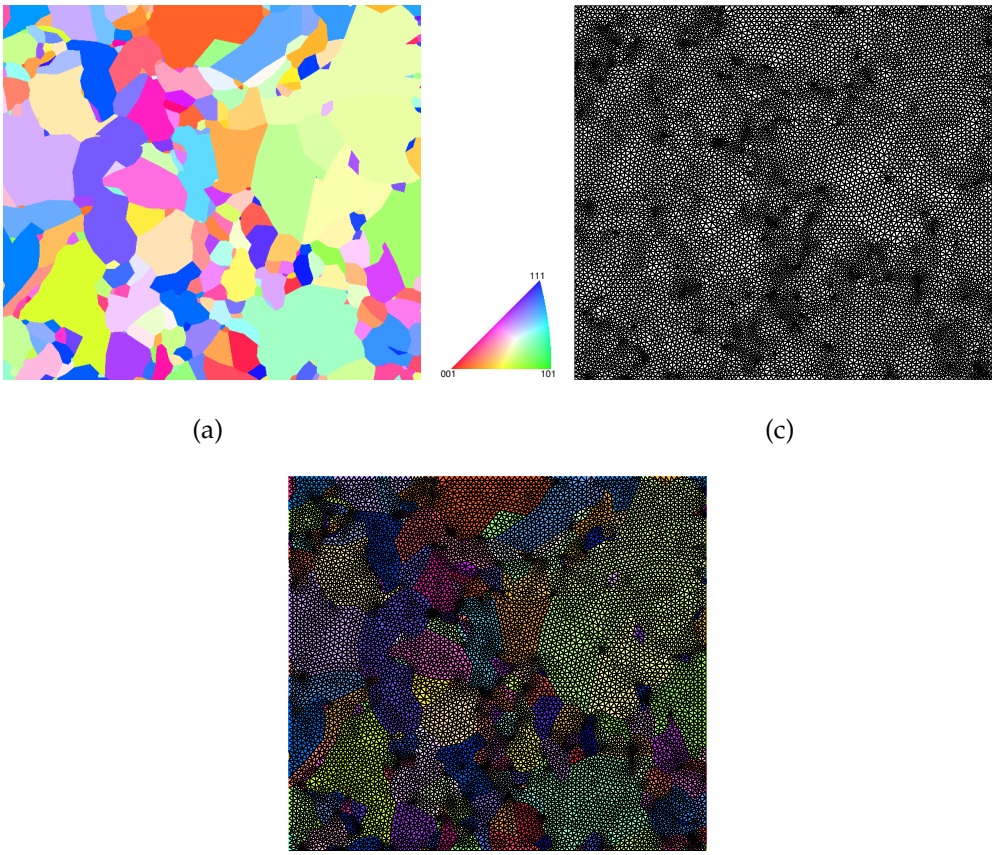

(a) (c)

(d)

Figure 2.3: (a) Inverse pole figure of the 2D polycrystalline model for FE simulations. (b) FE mesh utilized in tensile simulation. (c) FE mesh superimposed onto the polycrystalline model

It allows a mesh to be created in such a way that it very closely follows the grain boundaries, (GB), as performed in Refs. [Guery et al. 2016a;b; Bertin et al. 2016]. The ability for the mesh to conform with GBs opens the way to detect and measure strain discontinuities across GBs. This property holds for FE-based (global) DIC when a speckle pattern marking is deposited on the observed surface. It also holds herein since the GBs carry the information exploited by quaternion correlation, namely, the component of velocity normal to GBs. This property is valuable as any other approach would either betray the grain geometry or determine displacements only away from GBs.

The finite element calculation is performed under a plane strain assumption. Crystallographic orientations are uniform inside each grain. The numerical model is subjected to a monotonic uniaxial tensile simulation up to 6% of macroscopic strain. A constitutive

law based on dislocation dynamics for body centered cubic crystals (DD_CC [Monnet et al. 2013]) has been chosen in the FE simulation. A finite strain framework is used to implement the constitutive equations in order to properly account for the rotation of crystals during the tensile loading. The displacement field and crystal rotation in the ROI obtained by the FE simulation are shown in Figure 2.4.

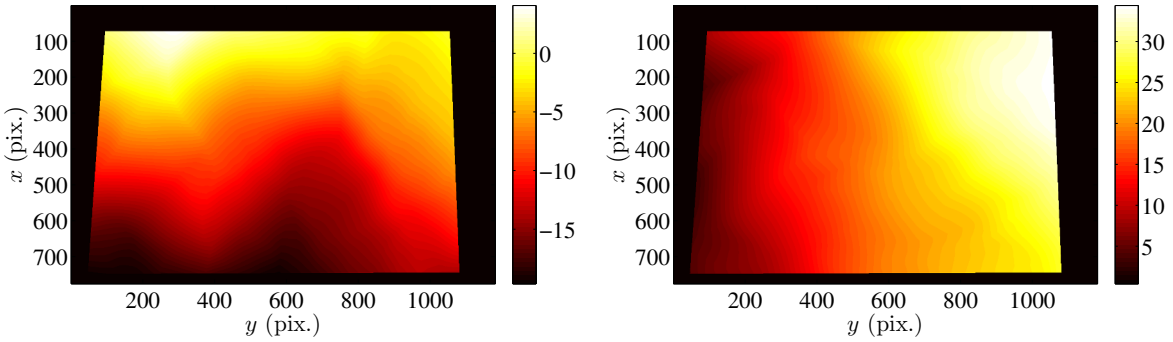

(a) u_x (pixels) (b) u_y (pixels)

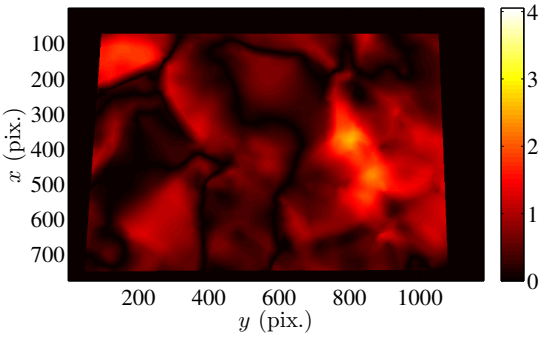

(c) θ (degrees)

Figure 2.4: Displacement (a-b) and crystal rotation θ (c) fields given by FE simulation

Virtual EBSD images are processed for different macroscopic strain levels as shown in Figure 2.5. The displacement and crystal orientation at the nodes of the model are updated by FE simulation, and the orientation at virtual acquisition points inside each element are obtained by linear interpolation (see Appendix A) from the data of the three vertices (*i.e.*, corner nodes). Therefore, the orientation at each acquisition point is always affected by the crystal orientation of only one grain, resulting in distinct grain boundaries. It should be noted that this is an ideal scenario that does not exist in realistic EBSD acquisition. A correlation analysis is performed with the orientation maps (Figure 2.3(a) and 2.5(a-c)). The calculation is run with a Matlab™ implementation on a computer with an i7 CPU.

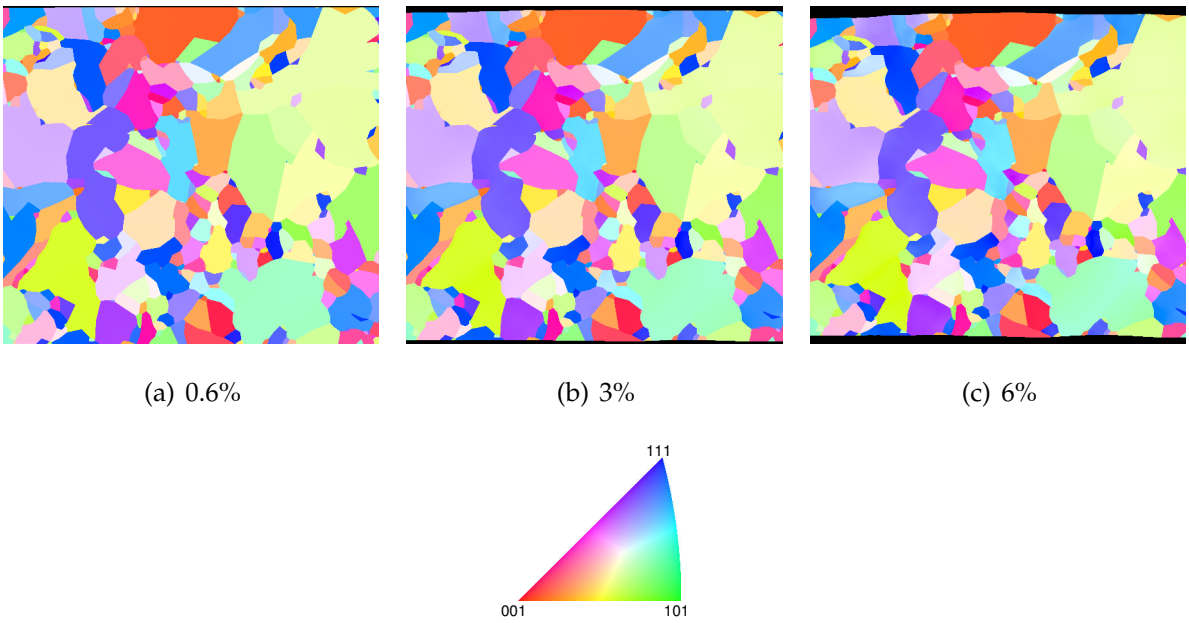

(a) 0.6% (b) 3% (c) 6%

Figure 2.5: Inverse pole figures corresponding to macroscopic strain equal to 0.6% (a), 3% (b) and 6% (c) respectively

The analyzed ROI has a size of 775×1181 pixels (Figure 2.6(a)). The registration procedure is performed twice, namely, on two different meshes consisting of triangular elements with a characteristic length of 50 pixels and 10 pixels respectively (Figure 2.6(b-c)). It should be noted that the meshes are not conforming to the grain geometry.

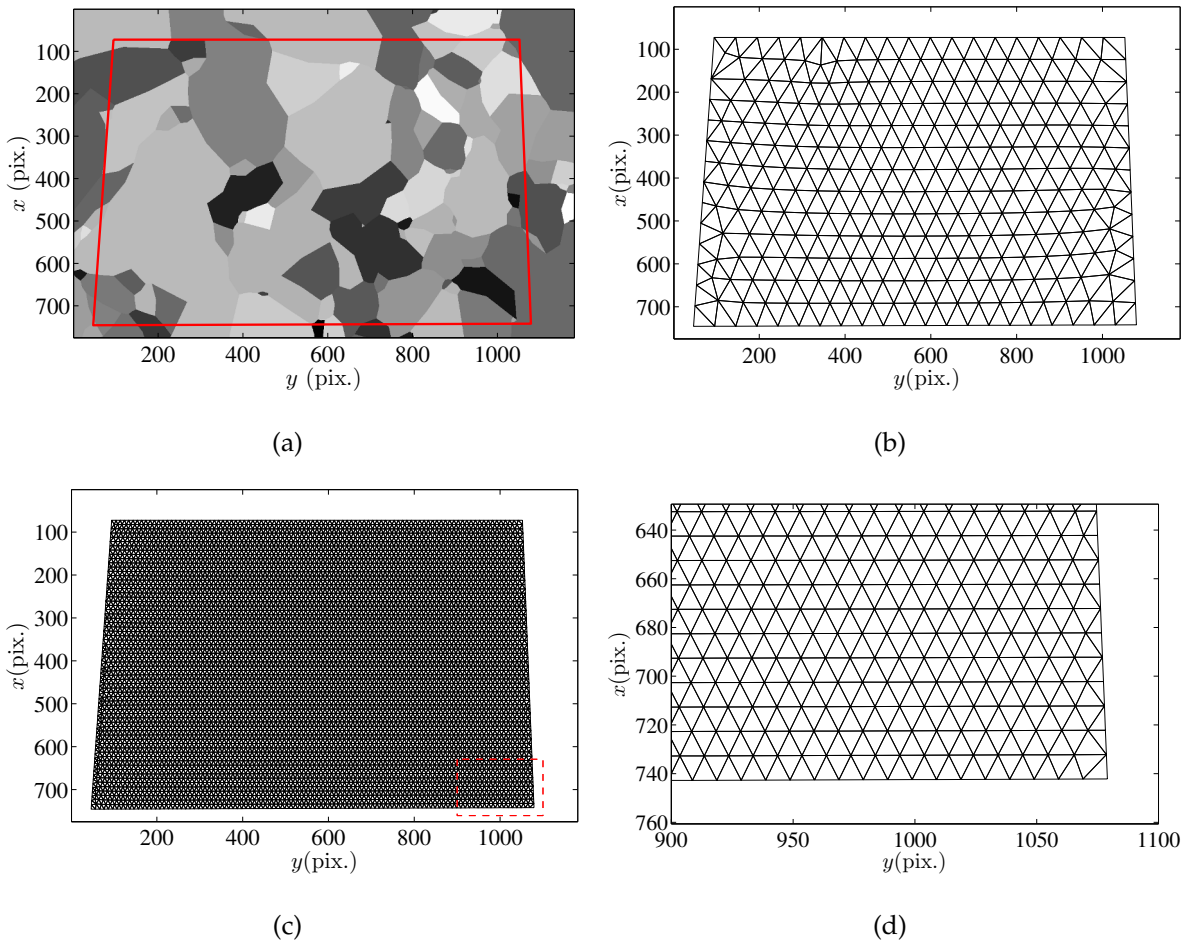

Figure 2.6: Parameters used in quaternion correlation of the validation test case. (a) ROI of the artificial reference EBSD image. (b) FE mesh with characteristic length of 50 pixels. (c) FE mesh with characteristic length of 10 pixels. The boxed zone is zoomed in (d)

When one Gauss-Newton iteration results in an average incremental displacement less than 5×10^{-5} pixel, convergence is obtained. To avoid local minimum trapping, the elastic regularization length ℓ_m and the length of the Gaussian kernel ξ are both initialized with high values. Once convergence is reached, the resulting displacement field is used to initialize the next correlation step in which the values of ℓ_m and ξ gradually decrease. Table 2.1 gives an example of the settings of quaternion correlation for the final state of $\ell_m = 100$ pixels and $\xi = 0$. It should be noted that $\xi = 0$ means that the quaternion field is not subjected to any filtering. In total, about 700 iterations are needed to reach convergence.

Table 2.1: Evolution of ℓ_m and ξ during quaternion correlation

Step	1	2	3	4	5	6	7
ℓ_m (pixel)	400	400	400	200	100	100	100
ξ (pixel)	16	3	2	2	2	1.2	0
Number of iterations	484	68	22	41	61	43	10

The displacement error is computed from the root mean square (RMS) difference between computed and measured vector displacement fields. In order to optimize the parameterization of mechanical regularization ℓ_m, the displacement error obtained with the mesh with characteristic length of 50 pixels is shown in Figure 2.7(a) for different values of ℓ_m and three different macroscopic strains, 0.6%, 3% and 6%. The error tends to be high for large ℓ_m values (200 pixels) as for such sizes, the regularization influences the registration of grain boundaries. The error displays small variations at different macroscopic strain levels in case of small ℓ_m levels (50 pixels) as the displacement field around the center of grains is not regularized by the orientation contrast at grain boundaries. Therefore the displacement error is higher inside grains. The best compromise is obtained when $\ell_m = 100$ pixels. This is in agreement with the fact that the equivalent grain size in the ROI is 85 pixels as shown in Figure 2.7(b), and hence this size is a target value for ℓ_m. It is to be noted however that the grain size is heterogeneous, and hence selecting a single value for the entire ROI results from a compromise. Let us finally note that the error tends to increase with the macroscopic strain, presumably because the effect of regularization on the displacement increases with the latter, and the elastic regularization becomes poorer and poorer adapted as the mean strain increases.

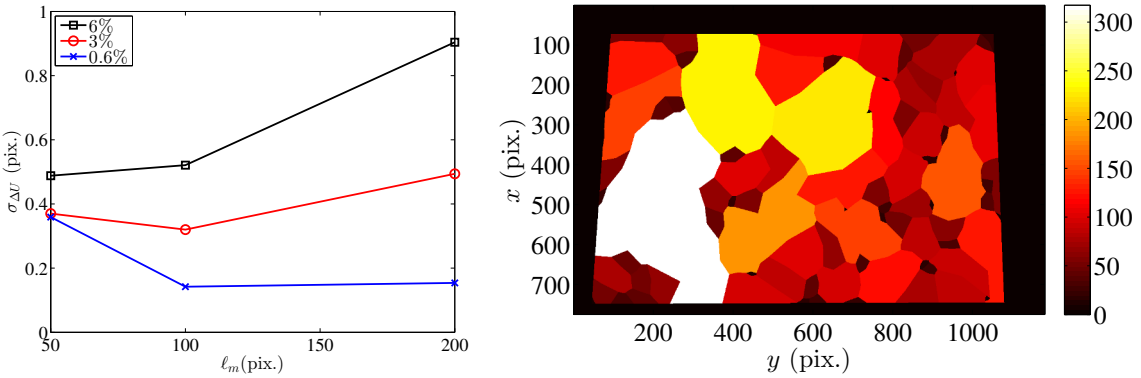

(a) (b)

Figure 2.7: (a) RMS displacement error as a function of ℓ_m for different macroscopic strain levels: 0.6%, 3% and 6%. Results with 50-pixel characteristic length mesh. (b) Equivalent grain size in ROI. The mean equivalent grain size is 85 pixels in the ROI

The performances of calculations on meshes of different sizes are listed in Table 2.2. It is seen that the error of displacement and rotation measurements is slightly lower with finer mesh elements, whereas the computation time is significantly longer.

Table 2.2: Performance of quaternion correlation for meshes of different sizes for a macroscopic strain of 3% and ℓ_m=100 pixels

Characteristic length	iteration time	RMS of ΔU	RMS of intra-grain $\Delta\theta$
50 pixels	17 s	0.320 pixel	0.0026 degree
10 pixels	135 s	0.305 pixel	0.0024 degree

The quaternion correlation results between the initial state and 3% strain with ℓ_m=100 pixels and 10-pixel elements are illustrated in Figure 2.8. At convergence, the residual, $[\boldsymbol{f}\tilde{\boldsymbol{g}}^{-1}]$, is the disorientation between the reference and the deformed orientation transported with the measured displacement field. This quaternion field can be decomposed into a disorientation angle θ, $2 \times \cos^{-1}(\Re[\boldsymbol{f}\tilde{\boldsymbol{g}}^{-1}])$, shown in Figure 2.8(a), and the orientation of the rotation direction (v_x, v_y, v_z) (*i.e.*, imaginary components of $[\boldsymbol{f}\tilde{\boldsymbol{g}}^{-1}]$ rescaled to a unit norm), shown in Figure 2.8(b-d). The disorientation angle remains quite small (typically from 1 to 2 degrees) and is markedly affected by the crystallographic orientation. Some grains are prone to displaying lattice rotations whereas others are not. It is observed from Figure 2.8(b-d) that the rotation axis, roughly uniform within grains, tends to be close to the z-axis. This

is consistent with the plane-strain setting used in the FE simulation.

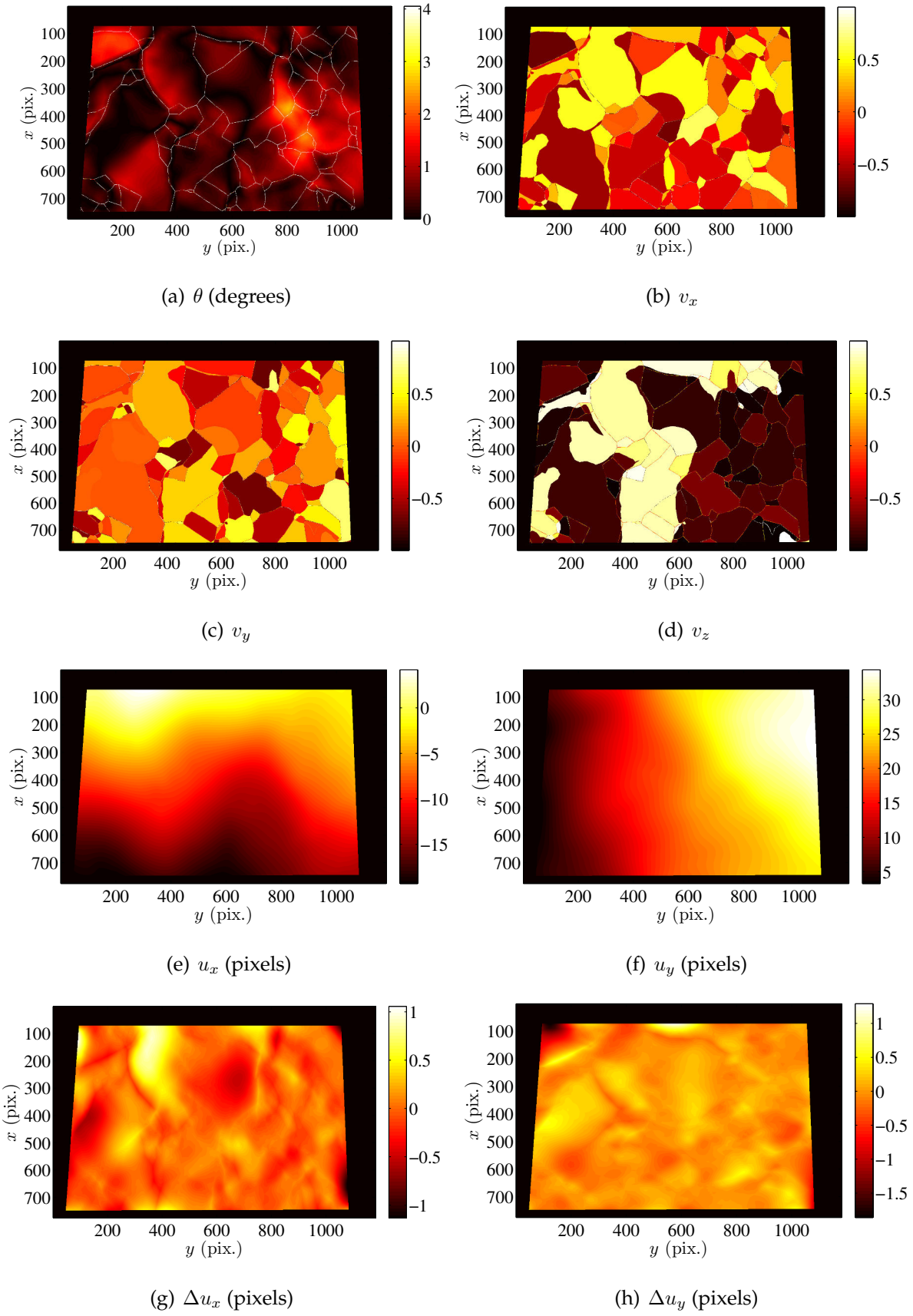

(a) θ (degrees)

(b) v_x

(c) v_y

(d) v_z

(e) u_x (pixels)

(f) u_y (pixels)

(g) Δu_x (pixels)

(h) Δu_y (pixels)

Figure 2.8: Quaternion correlation residual disorientation decomposed into a disorientation angle (a), and the three components of the rotation director (b-d). Measured displacement field along the x (e) and y (f) directions, and the displacement difference along the x (g) and y (h) directions. Results obtained with ℓ_m=100 pixels, 10-pixel elements

The measured displacement field is shown in Figure 2.8(e-f) and the differences between the measured and computed displacement fields are shown in Figure 2.8(g-h). The texture is no longer visible on the two images, which means that there is no noticeable difference for displacements at grain boundary and within grains. The RMS of displacement error reaches 0.3 pixel, which is high compared with the error of standard DIC (usually of the order of 0.01 pixel). This difference is attributed to the complete absence of contrast inside the grains, and the difficulty to set a fair interpolation of the orientation very close to grain boundaries. Figure 2.6(a) shows the used texture that is not the best suited to DIC, and even dealing with a scalar gray level would not allow such low uncertainty values to be reached. On the contrary, it is noteworthy that in spite of such poor texture, the resulting displacement difference is still well below 1 pixel.

The disorientation angle is shown in Figure 2.8(a). It should however not be considered as an error. In the simulation grains do rotate during their plastic deformation, and hence this phenomenon violates the assumption that the crystallographic orientation remains invariant. Because this rotation is small, it does not prevent the correlation procedure to extract the displacement field. This disorientation angle can be compared with the computed one. The difference using the same scale as Figure 2.8(a) is shown in Figure 2.9(a). It is observed that the difference is mostly localized at grain boundaries (for reasons discussed in Section 2.3.4). Figure 2.9(b) shows the error of rotation measurement inside the grains, with rotation error for pixels located on grain boundaries (as obtained from the EBSD file) being set to 0. The error is of the order of 10^{-3} to 10^{-2} degree, with an observable concentration of measurement error. In the calculation with 3% macroscopic strain, the average rotation of intra-grain pixels is 0.75 degree and the average rotation error is 2.6×10^{-3} degree. As a result, the present procedure can measure disorientations due to plastic deformation extremely precisely, with an error less than 0.5%.

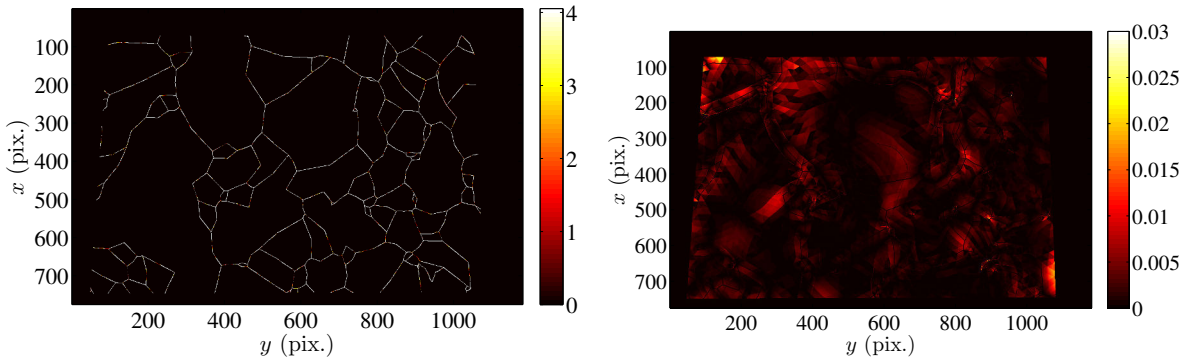

(a) $\Delta\theta$ (b) Intra-grain $\Delta\theta$

Figure 2.9: (a) Rotation difference $\Delta\theta$ (degrees) between quaternion correlation results and FE computed values. (b) $\Delta\theta$ after canceling out the grain boundary values, thus intra-grain values become visible

It should be noted that the isotropic elastic regularization does not correspond to the simulation based on crystal plasticity. However, as the previous results have shown, isotropic elastic regularization gives a fair interpolation. This result is very convenient for the registration of experimental EBSD pictures. It is concluded that the displacements measured by the correlation procedure proposed herein are very close to those calculated by FE simulation. Besides, the residual field corresponds to the simulated rotation field except along grain boundaries. The measurement error is quite low (*i.e.*, 0.3 pixel for the displacement and about 3×10^{-3} degree for crystal rotation) although image contrast essentially exists at grain boundaries. Therefore, the algorithm is deemed validated.

2.5 Application to experimental maps

The red boxes contain extra information that was not published. Quaternion correlation has been applied to EBSD acquisitions of two SEMs to assess their orientation indexing uncertainties.

2.5.1 Assessment of orientation indexing uncertainty

Like many other physical measurements, the uncertainty level of EBSD orientation indexing can be assessed by taking successive acquisitions and analyzing their differences. Two microscopes have been used on a copper sample and 16MND5 steel respectively, and quaternion correlation has been adopted to analyze the crystal orientation uncertainty.

A copper sample (purity 99.95%) was rolled at room temperature to a thickness reduction of 90%. A tensile specimen was cut from the rolled plate and annealed at 230 °C for 30 min, after which the sample was 45% recrystallized. After conventional polishing, two EBSD acquisitions on the sample were carried out in a TESCAN MIRA 3 XM SEM (denoted as SEM1) [Lin et al. 2015]. Very heterogeneous texture has been obtained, as shown in Figure 2.10, with amorphous and crystallized regions. Figure 2.10 illustrates the uncertainty analysis for SEM1. Two IPF images of successive acquisitions are shown in Figures 2.10(a) and 2.10(b), and the kernel average misorientation (KAM) and confidence index image of the first acquisition are shown in Figures 2.10(d) and 2.10(e). The pixels in Figure 2.10 can be grouped into three regions: crystallized region (denoted as A), non-crystallized region with low misorientation (denoted as B) and non-crystallized region with high misorientation (denoted as C). Regions A and C are more intertwined than regions A and B, as recrystallization tends to nucleate in regions containing predominantly large misorientations [Mishin et al. 2012]. It can be seen in Figure 2.10(e) that the confidence index is highest in region A, followed by region B, and lowest in region C.

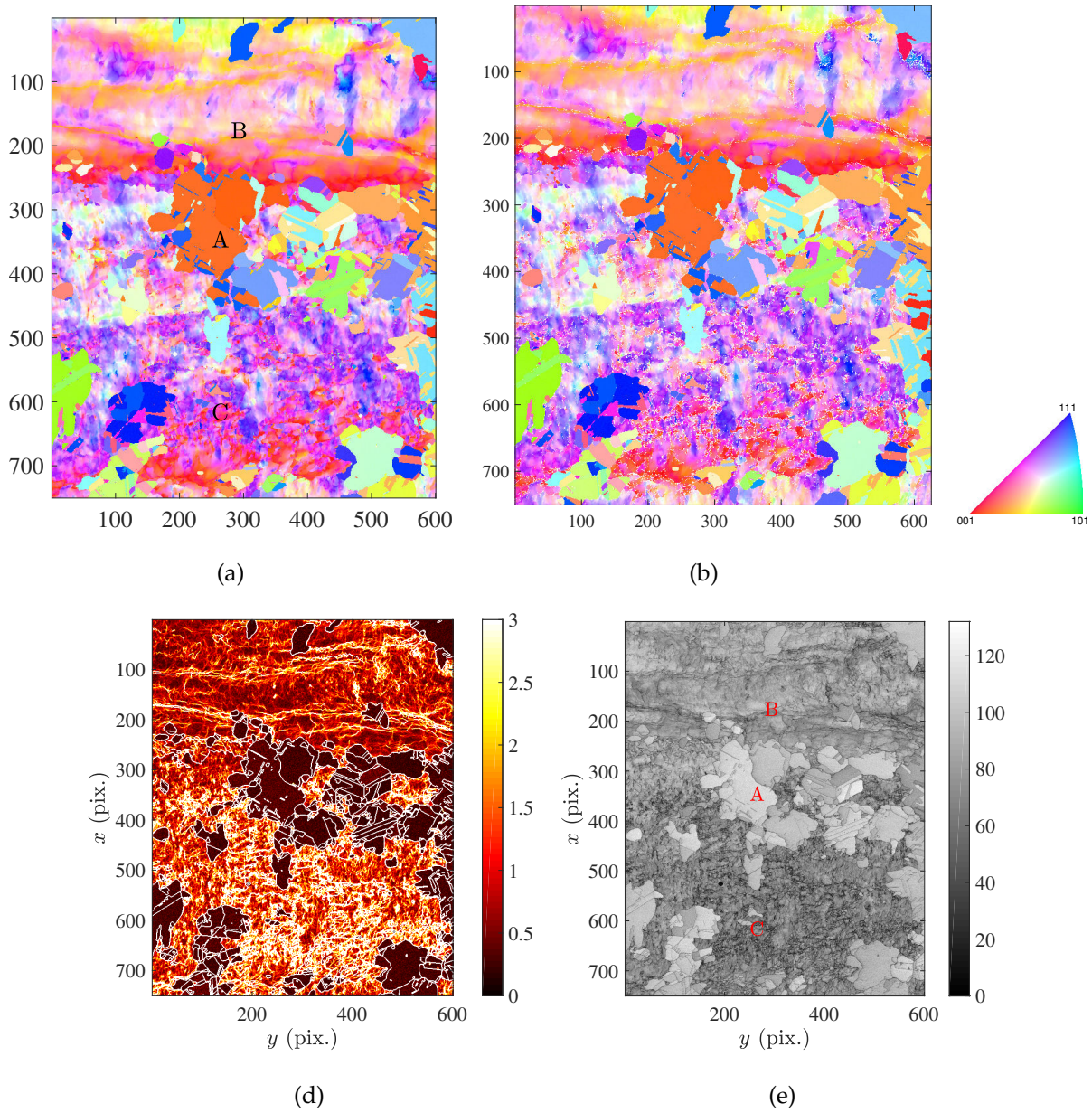

Figure 2.10: EBSD acquisition by SEM1 on copper sample (courtesy of Dr. Fengxiang LIN). Inverse pole figures of the first (a) and second (b) acquisitions. Kernel average misorientation (c) and confident index (d) of the first acquisition. The pixel size is 200 nm.

The results of quaternion correlation between Figures 2.10(a) and 2.10(b) are reported in Figure 2.11. It can be seen in figure 2.11(a) that the orientation indexing uncertainty, calculated here as 'crystal rotation', is smallest (≈0.3°) in the crystallized region A, followed by the bulk amorphous (≈0.6°) region B, and highest (≈1.0°) in the clustered amorphous region C. The Pearson correlation coefficient between the orientation uncertainty and inverse of the confidence index is 0.8. This example is a good illustration of the 'confidence' index. Future quantitative analyses on crystal orientation maps could use the confidence

index as a measure of the orientation uncertainty, similar to the gray level uncertainties in conventional images. The components of the 'rotation' axis shown in Figures 2.11(b-d) are very noisy, indicating that there exists no regularity in the orientation indexing uncertainty 'direction' for SEM1.

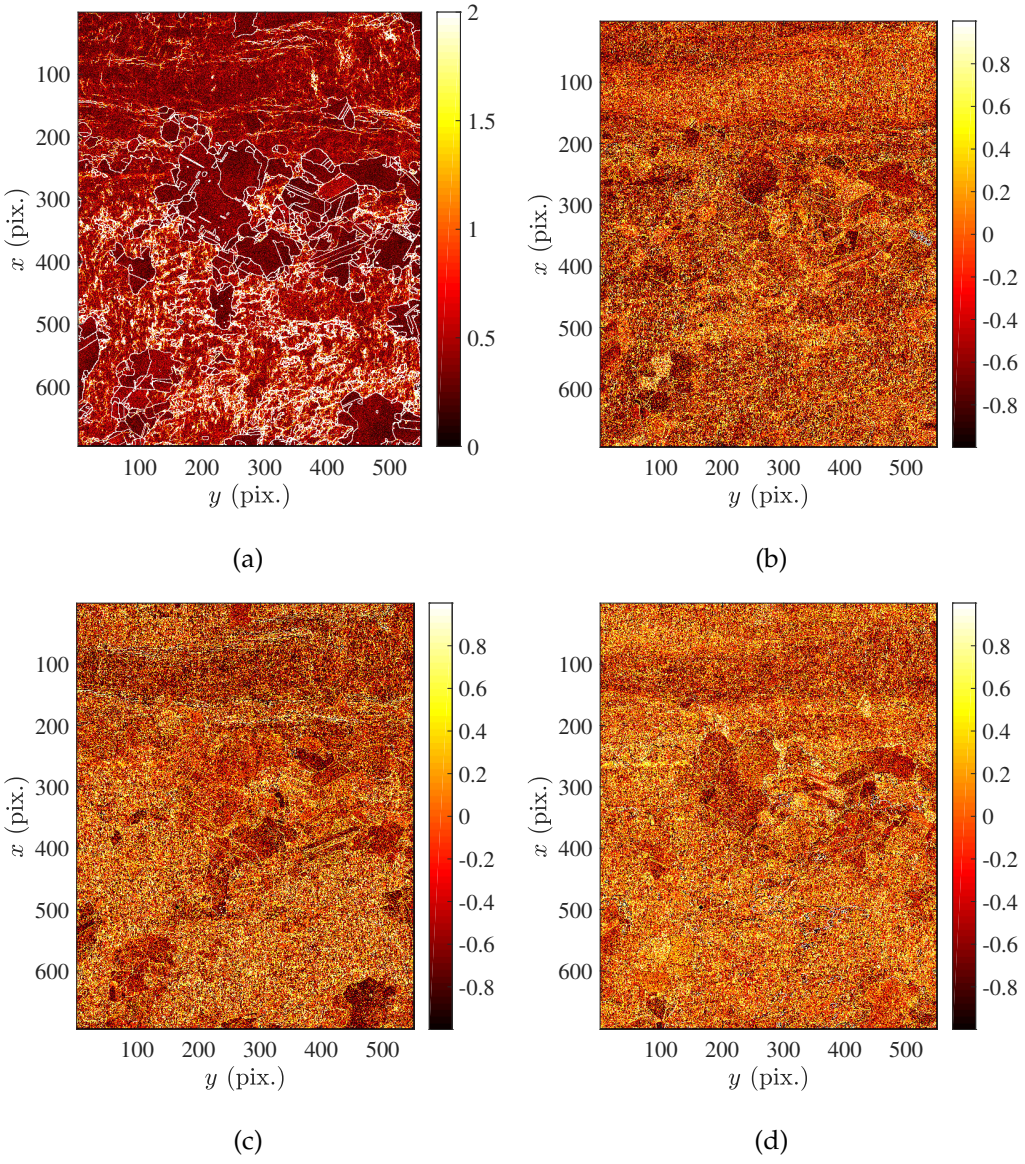

Figure 2.11: EBSD orientation indexing uncertainty of SEM1. (a) Crystal orientation difference, expressed in 'rotation', between the two successive acquisitions. Components of the crystal 'rotation' axis in x (b) y (c) and z (d) directions. The pixel size is 200 nm.

Figure 2.12 shows the correlation results between the EBSD orientation indexing uncertainty and the band contrast on the copper sample. Band contrast is a scalar indicator of the average intensity of the Kikuchi bands with respect to the overall intensity within the electron back-scattering pattern [HKL 2007]. The 90th, 50th and 10th percentile pro-

files are drawn in the figure. It can be seen that the uncertainty of EBSD orientation indexing reduces drastically and steadily as the band contrast increases. In the crystallized copper region the average misorientation is around 0.3^o, in line with values from the literature [Ram et al. 2015]. These profiles provide empirical functions to estimate the EBSD indexing uncertainty from band contrast values.

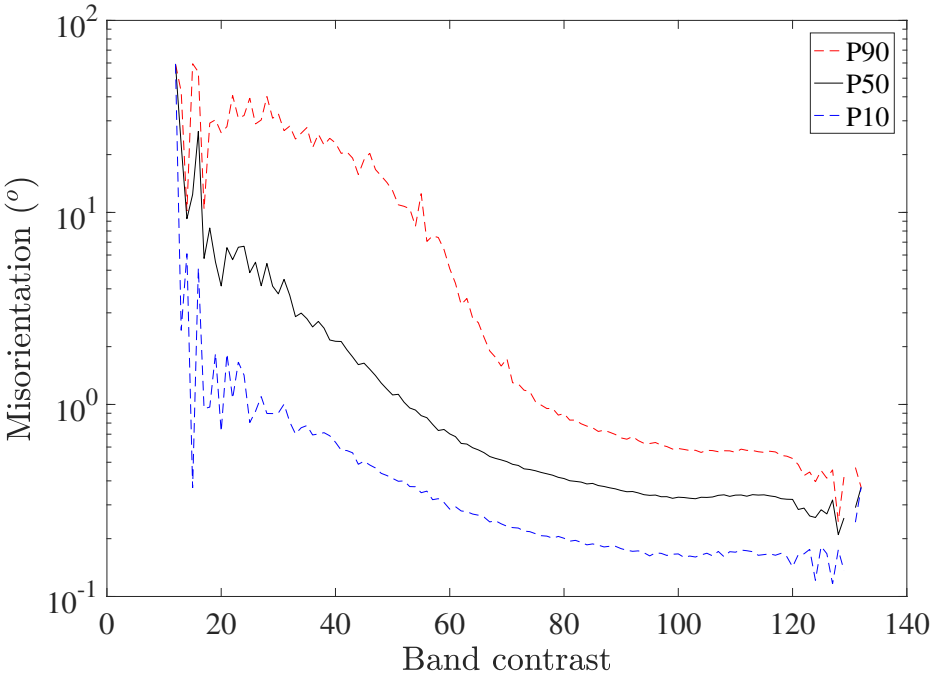

Figure 2.12: Correlation between EBSD orientation indexing uncertainty and band contrast in the copper sample. The 90th, 50th and 10th percentile profiles are drawn.

The TESCAN Mira3 600 (denoted as SEM2) SEM, which is installed at the Materials Aging Institute (MAI) of EDF R&D and available during the PhD project, has been utilized in the uncertainty measurement on 16MND5 steel. Two successive EBSD acquisitions are shown in Figures 2.13(a-b) and the quaternion correlation results are shown in Figure 2.14. It can be seen that the orientation uncertainty is very high and varies smoothly from 0.5 to ≈2 degrees. A clear tendency is also visible in the components of the rotation axis. This phenomenon suggests that the indexing procedure of SEM2 has some issues, presumably the imprecise positioning of the pattern center.

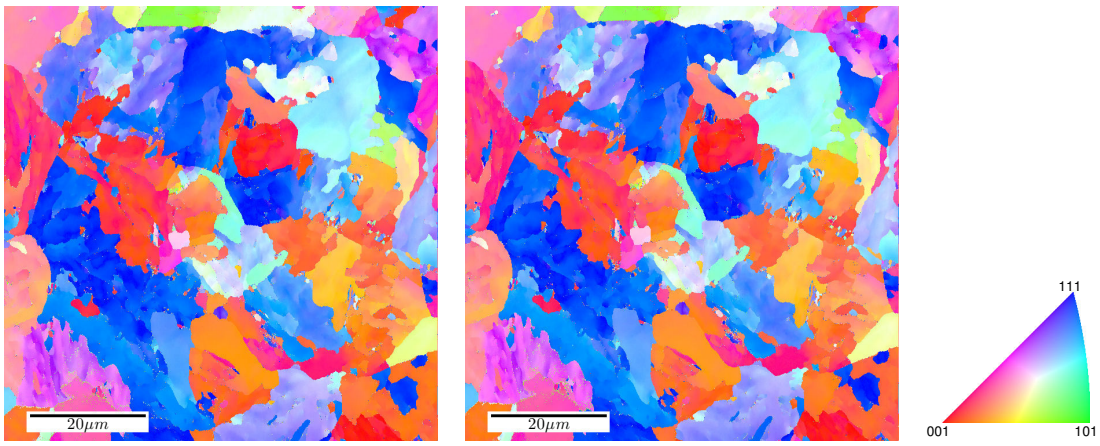

(a) (b)

Figure 2.13: EBSD acquisition by SEM2 for the 16MND5 steel sample. Inverse pole figures of the first (a) and second (b) acquisitions. The pixel size is 100 nm.

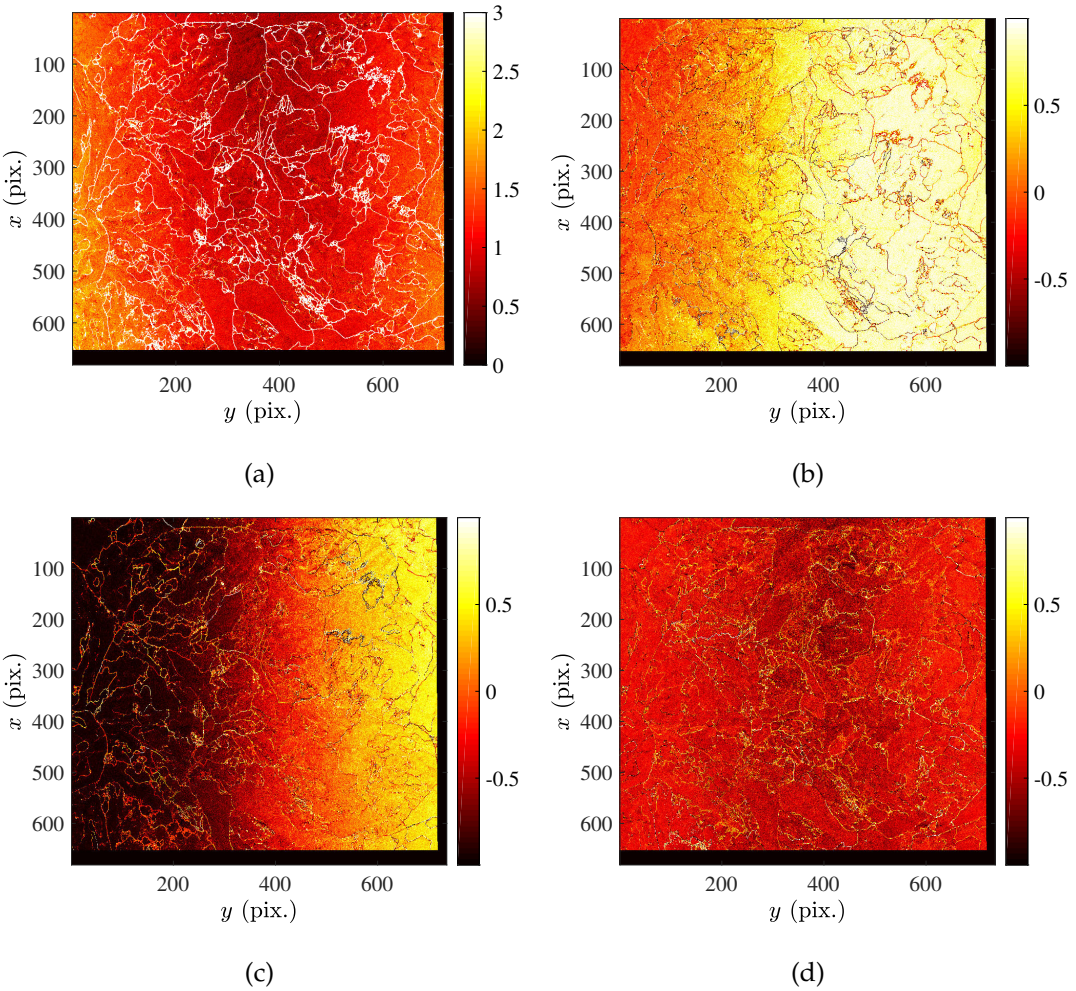

Figure 2.14: EBSD orientation indexing uncertainty of SEM2. (a) Crystal orientation difference, expressed in 'rotation', between the two successive acquisitions. Components of the crystal 'rotation' axis in x (b) y (c) and z (d) directions.

To summarize, in normal EBSD acquisition conditions on several materials, the crystallographic orientation detection has an uncertainty of ≈0.5 degree, an observation in good agreement with many previous works [Harland et al. 1981; Ram et al. 2015]. The overall orientation drift in SEM2 can be detected by quaternion correlation and corrected case by case. The effect of the orientation drift in SEM2 will be further discussed in Chapter 5. Being the only SEM equipped with a miniaturized tensile testing device, SEM2 will be used for all further two-dimensional observations in the sequel.

2.5.2 Measurement of crystal rotation

Inconel 600, which is a nickel-based alloy, is used to carry out an *in-situ* tensile experiment. A $10 \times 2 \times 1$ mm^3 tensile sample is machined. Mechanical polishing of the sample surface

is performed with cloths and diamond suspension down to 0.25 µm followed by a finishing with 40-nm colloidal silica suspension for 45 minutes. The sample is subjected to an *in-situ* tensile test at a strain rate of 4×10^{-4} s^{-1} up to 20 % longitudinal strain.

The SEM used in this study is a TESCAN Mira3 600. Backscattered electron detector in Z-contrast has been used, with an acceleration voltage of 9 kV and a working distance of 17 mm. The physical size of one pixel is 250 nm. This resolution is chosen to ensure that a sufficient number of grains could be observed and each of them with a significant number of pixels. The scanned area is 500×500 µm^2 with a definition of 2000×2000 pixels. The data obtained by EBSD acquisitions, and processed with OIM™ software are used as a starting point of the analysis. The `.ang` file contains the measurement coordinates, three Euler angles, image quality index and confidence index of each pixel.

A series of EBSD analyses performed in the course of an *in-situ* tensile experiment on the specimen has been used to test the quaternion-based registration algorithm. Figure 2.15 shows two inverse pole figures in the reference and deformed states as obtained from OIM™. Figure 2.15(b) corresponds to the raw data used to extract the quaternion fields shown in Figures 2.1 and 2.2.

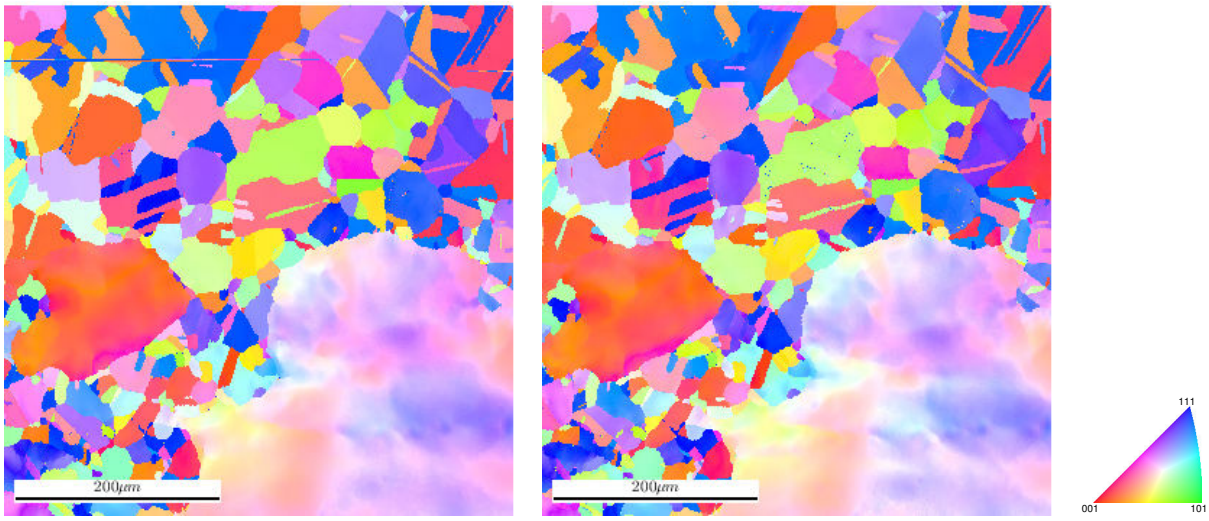

(a) Reference image (b) Deformed image

Figure 2.15: Inverse pole figures of the reference (a) and deformed (b) configurations

From these maps, a region of interest is selected (Figure 2.16(a)) in which variable grain sizes are observed. Figure 2.16(b) shows the disorientation between the reference and deformed images (as obtained by a raw discrepancy $1 - \Re[\boldsymbol{f}\boldsymbol{g}^{-1}]$), which exhibits a "ribbon" shape where the ribbon width reveals the displacement magnitude and orientation, the color

indicates the disorientation value. The mesh used for quaternion correlation consists of triangular elements with a rather uniform size (here about 30 pixels) spanning the chosen ROI but not conforming with the grain shapes (Figure 2.16(c)).

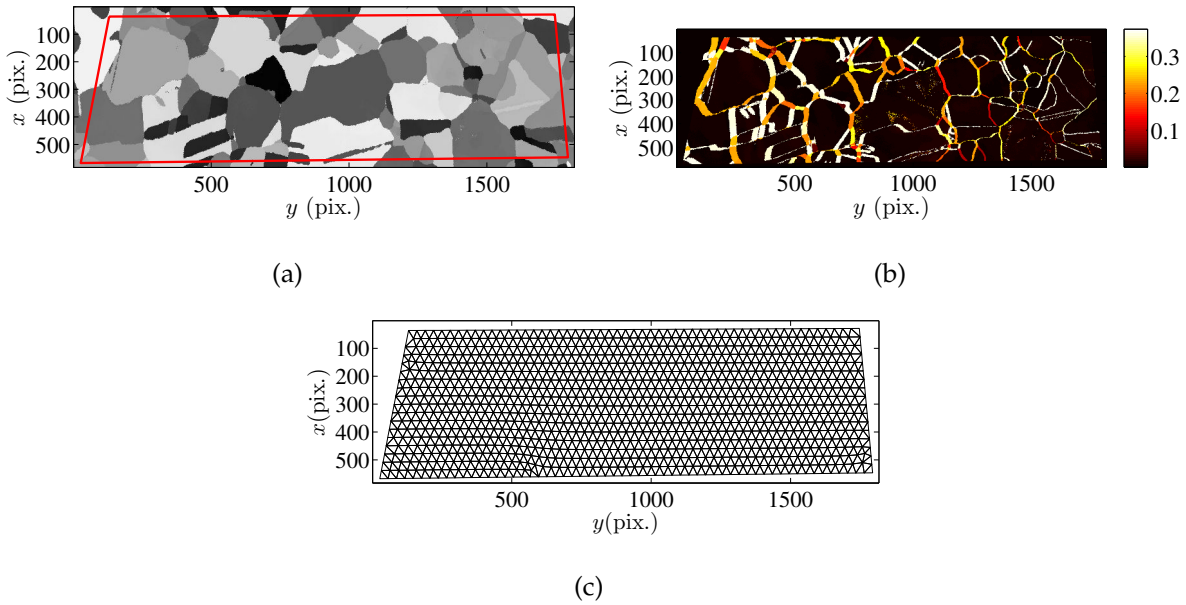

Figure 2.16: (a) ROI of the reference EBSD image. (b) Initial residual between the reference and deformed images. (c) FE mesh of the quaternion correlation calculation

The convergence criterion is still set to 5×10^{-5} pixel, which is a very low value given the fact that only grain boundaries are highly contrasted. The elastic regularization length ℓ_m is initially chosen to be 400 pixels, and decreased to 200 pixels once convergence is obtained. The value of ξ decreases from 16 to 1 pixel, and is followed by no filtering at all (*i.e.*, $\xi = 0$). The final value of ℓ_m is greater than the 100-pixel level adopted in the previous case study because the largest grain size is somewhat larger. A total of 800 iterations is needed to reach convergence. With the same implementation as for Section 2.4, each iteration requires about 30 s.

The measured displacement field in x and y directions is shown in Figure 2.17(a-b). Figure 2.17(c) displays the corresponding crystal rotation field between the two image acquisitions. It is observed that in this experimental case the rotations are specific to grains, with discontinuities across grain boundaries just as in the FE simulation (Figure 2.8(a)).

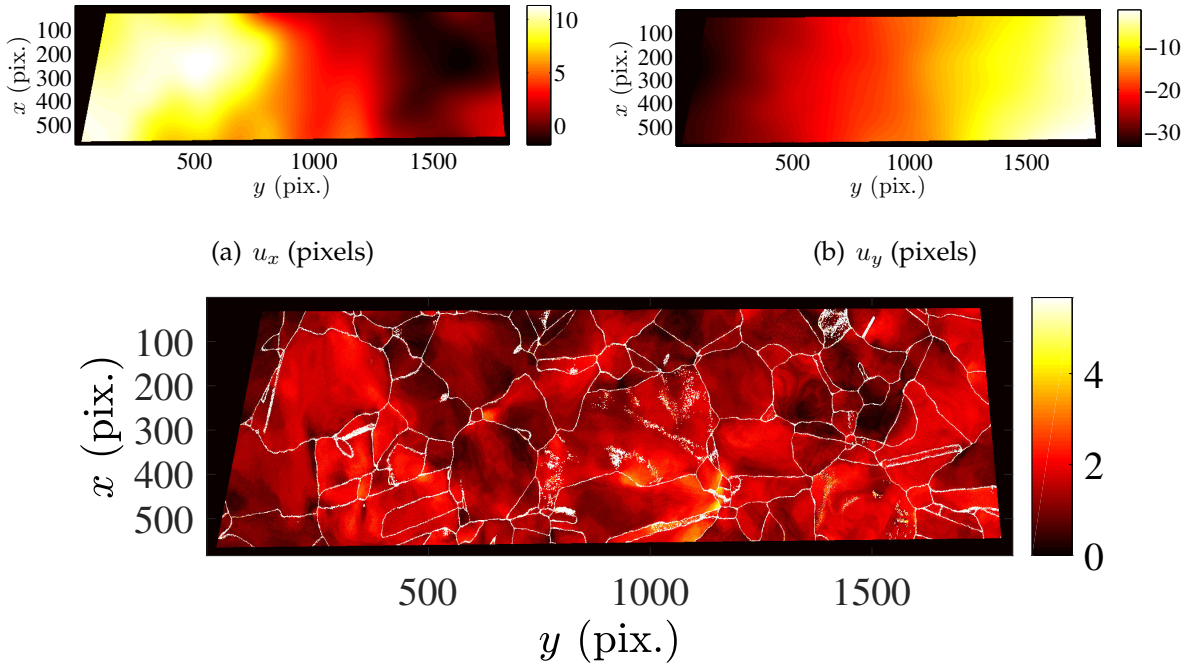

(a) u_x (pixels)

(b) u_y (pixels)

(c) θ (degrees)

Figure 2.17: Quaternion correlation results. (a-b) Measured displacement field in x and y directions (in pixels). (c) Corresponding rotation angle θ field (in degrees)

The residual of quaternion correlation is shown in Figure 2.18(a). Grain boundaries are still visible, though very thin. Isolated intra-grain points can also be noticed. They are due to EBSD acquisition noise. Most of the grain boundaries are not wider than 3 pixels (see Figure 2.18(b)) and the emergence of several bright zones indicates substantial crystal rotations during tension, which is presumably due to crystal twinning. Figures 2.18(c) and 2.18(d) show the confidence index of the reference image and the displacement-corrected deformed image of the corresponding region. It is concluded that at triple points the confidence index is lower than for regular grain boundaries, *i.e.*, the crystal orientation is not well determined and leads to high residuals. The quaternion correlation procedure cannot produce results that are more reliable than the exploited starting EBSD information.

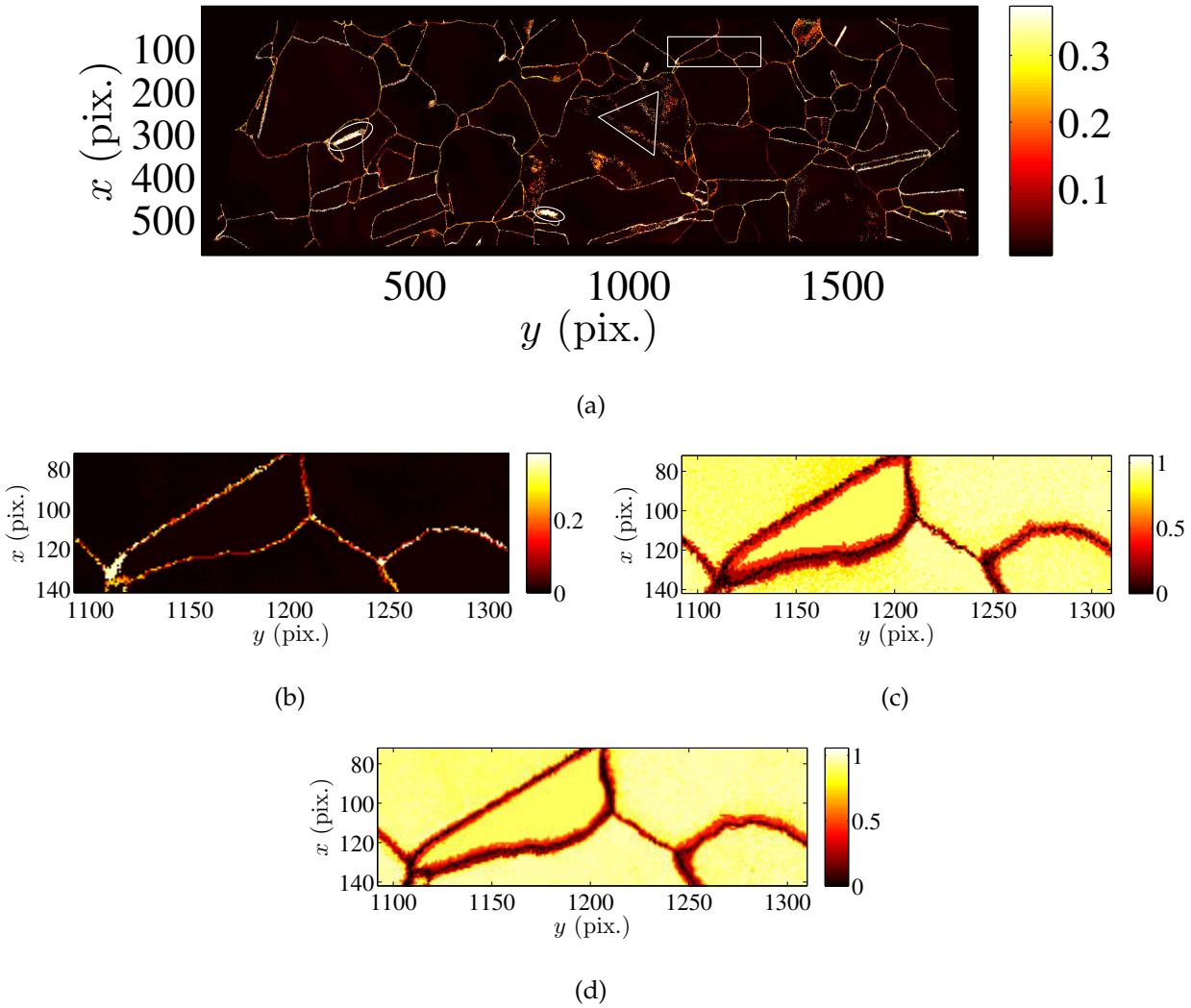

Figure 2.18: (a) Residual map in analyzed ROI. The isolated intra-grain high residuals in the triangle indicate EBSD acquisition noise. The bright zones shown in the ellipses indicate substantial crystal rotations during tension, presumably crystal twinning. The rectangle indicates the enlarged area shown in (b-d). (b) Zoomed residual map. Confidence index in the corresponding area in reference and deformed images are shown respectively in (c) and (d)

In order to validate the result, it is natural to consider the final residual, *i.e.*, disorientation angle after registration. However, as discussed above, within grains this quantity is not exactly an error, namely, it corresponds to the actual lattice rotation that takes place in the plastic flow. The other part of the residual is the one that is supported by the grain boundaries. It is the latter that validates the convergence of the procedure. As shown in the magnified region (Figure 2.18(b)) the final residuals are essentially localized on grain boundaries. It is noteworthy that they are even more concentrated than what the confidence index would suggest.

2.6 Conclusion and perspectives

The algorithm introduced herein evaluates displacements based on crystallographic orientations re-encoded as quaternions instead of gray levels. Its main application deals with EBSD acquisitions. Displacement fields are measured and correlation residuals quantify the crystallographic rotation between images. Two cases have been studied. First, a synthetic case for which the displacement and rotation fields were known thanks to a crystal plasticity computation. The algorithm was deemed validated and the error levels of the algorithm were quantified. Second, EBSD maps acquired during an *in-situ* tensile test on a nickel-based alloy show that such a technique can also be applied to experimental cases. Consequently, acquisition noise does not hinder such technique. However, drift and other artifacts related to EBSD imaging need to be quantified.

The global lack of image contrast, except at grain boundaries, makes the correlation very challenging. Consequently, convergence is slow in comparison with registrations of speckle patterns. Pixel-wise crystal symmetry application at each step leads to additional computation steps. Besides, the discontinuity of crystal orientations at grain boundaries makes the convergence very difficult near the minimum point.

Contents in the box are extra perspectives that were not published. Two possible accelerating methods of quaternion correlation are discussed hereafter.

Quaternion correlation of EBSD images with cubic symmetries are 50-100 times slower for each iteration step than standard DIC on gray-level images of the same size. To solve this time-consuming limitation, two possible solutions exist:

1. Create a disorientation function $\phi(\boldsymbol{q})$ that replicates the cubic symmetry $\boldsymbol{p}^{cub}$, i.e. that results in the same value for the different quaternion representations for a certain crystal orientation:

$$\begin{aligned} &\phi(\boldsymbol{q}) = \phi(\boldsymbol{p}^{cub}\boldsymbol{q}) \\ &\phi([1,0,0,0]) = 0 \\ &\phi(\boldsymbol{q}) \geqslant 0 \end{aligned} \tag{2.16}$$

   and ideally, for a quaternion $\boldsymbol{q}_\varepsilon$ in the vicinity of [1,0,0,0], ϕ should be parabolic:

$$\phi(\boldsymbol{q}_\varepsilon) = \varepsilon^2 + O(\varepsilon^3) \tag{2.17}$$

This function would thus replace Equation (2.5), and preliminary application of crystal symmetry would no longer be needed.

2. Standard DIC results based on the EBSD quality map treated as speckles can be used to initialize quaternion correlation, which speeds-up significantly the calculation in practice. Based on good initializations quaternion correlation needs only a few iterations to reach convergence. Most of the quaternion correlation results presented in this thesis have benefited from this method.

The measurement of kinematic and rotation fields at microstructure scale opens many possibilities in materials science. For example, the quaternion correlation algorithm can be used in the detection of crack tip, as the propagation of crack induces crystallographic rotations. Both displacement and rotation fields can be used for the study of plasticity and for the identification of constitutive laws. The algorithm can also be adapted to filter a series of consecutive EBSD results. As shown in Figure 2.18(a), isolated intra-grain high residuals indicate the noise of EBSD acquisitions either in the reference or deformed images. The algorithm provides a way of locating these spurious pixels and filter them out. Apart from detecting 'bad' pixels inside grains, the algorithm can also be used to adjust grain boundaries. Due to the discrete sampling effect, EBSD gives more rigged grain boundaries than the actual ones. Correspondence of pixels at grain boundaries has an 'averaging' effect, which helps to straighten grain boundaries. This mechanism can also be understood as several EBSD acquisitions actually improve the spatial resolution on the grain boundary, under the assumption that the grain boundary does not change much between acquisitions.

As stated earlier in this chapter, quaternion correlation takes two indexed crystallographic orientation field as input data and measure their orientation differences. The automated indexing is often based on 120×120 pixels Kikuchi images and adopts Hough transformation to get the location of Kikuchi bands. The orientation indexing uncertainty by this method is around 0.3-0.5^o, making the measurement of minor crystal rotations impossible, for example the atom lattice rotation due to elastic deformation. HR-EBSD, a technique developed in the last decade, is capable to measure elastic deformation. Chapter 3 will revisit this approach.

Chapter 3

ADDICTED: application of IDIC in HR-EBSD

Reproduced from technical memo: Qiwei SHI, Félix LATOURTE, François HILD and Stéphane ROUX. Procédé de mesure de contraintes par corrélation intégrée sur images EBSD-HR, French patent filed in December 2017, number: 1761926

High-angular-resolution electron backscattered diffraction has been developed to study local elastic strains by cross-correlations of image subsets. Precise for low disorientation, the technique fails to measure strains with adequate accuracy for misorientations greater than 1°. Besides, the strain measurement is sensitive to the size and position of image subsets, thereby showing that image noise is not optimally contained by cross-correlation. A new method is presented to estimate crystal elastic strains via integrated correlation of high resolution EBSD images. The proposed algorithm reduces 12% of measurement uncertainty and 75% of calculation time, when compared to the conventional technique. Better results are obtained at relatively high misorientation than methods based on cross-correlation. The advantages of the new method are presented through two applications on experimental data.

3.1 Introduction

When a crystalline material is subjected to mechanical loading, several modifications could take place, and this chapter focuses on two of them, namely, the crystal rotates and deforms elastically. Other possible transformations are not studied herein, for example the motion of

defects such as dislocations and interstitial atoms.

The characterization with electron microscopes has led to significant progress in crystalline materials research [Williams and Carter 1996; Reichelt 2007]. For example, the polycrystalline microstructure is characterized thanks to electron back-scattered diffraction (EBSD). The technique gives access to local orientation data at each pixel of an image and thus to the morphology of a polycrystal and the intra-granular misorientations. The orientation is obtained by analyzing diffraction images acquired by detectors positioned in such a way that maximum intensities of diffraction cones are achieved. Finer analyses of diffraction images track the rotation of a crystal and also its elastic strains, which are revealed as a deformation of diffraction patterns. The measurement of elastic strains is important in solid mechanics, since Hooke's law allows stress tensors to be calculated from elastic strain tensors.

3.2 State of the art and existing problems

Several experimental techniques allow elastic strains of crystals to be measured such as Laue diffraction [Petit et al. 2015; Zhang et al. 2015] or far field 3DXRD diffraction [Ludwig et al. 2010; Abdolvand et al. 2015]. The drawback of these techniques is that they require high energy X rays, for example obtained in synchrotron facilities.

Electron diffraction is more accessible in regular laboratories, which requires an electron beam of more moderate energy. Electron diffraction is commonly used to obtain crystallographic orientation figures in scanning electron microscopes (EBSD technique). This technique, designated herein as standard EBSD, aims principally at obtaining orientation maps with an angular resolution of the order of 1 degree. This type of uncertainty, which is related to the diffraction image resolution (*i.e.*, number of pixels of the detector for diffracted electrons), is sufficient to evaluate local orientations but not for elastic strain measurements, which are associated with low deformations of diffraction images. The accuracy of crystal rotation measurement by *quaternion correlation* on a series of EBSD images is also limited by crystallographic indexing (see Chapter 2). The number of pixels of the detector for diffracted electrons should be increased substantially, to obtain crystallographic orientations with higher accuracy [Wilkinson et al. 2006a; Wilkinson and Britton 2012]. The proposed technique is known by the acronym HR-EBSD (for High Resolution EBSD) or HAR-EBSD (for High Angular Resolution EBSD). It has been shown that, by registering diffraction im-

ages with good accuracy, HR-EBSD enables the elastic strains to be measured with satisfactory precision and excellent spatial resolution [Plancher 2015].

3.2.1 Diffraction image

3.2.1.1 Formation of diffraction image

The phenomenon of wave diffraction by a crystal is universal. For example, the Laue diagram is formed by diffraction of the X-ray by a crystal, and a Kikuchi image is formed by diffraction of an electron beam. According to Bragg's law, a monochromatic wave of length λ will diffract on crystalline plane (hkl) if

$$n\lambda = 2d_{hkl}\sin\theta \tag{3.1}$$

where n is the diffraction order, d_{hkl} the inter-reticular distance of plane (hkl), θ the half-angle between incident and diffracted beams. A crystal whose elementary lattice is described by the coordinates $(\boldsymbol{a}, \boldsymbol{b}, \boldsymbol{c})$ has a reciprocal lattice $(\boldsymbol{a}^*, \boldsymbol{b}^*, \boldsymbol{c}^*)$. By definition, $\boldsymbol{a}^*$ satisfies $\boldsymbol{a}\cdot\boldsymbol{a}^* = 1$, and $\boldsymbol{b}\cdot\boldsymbol{a}^* = \boldsymbol{c}\cdot\boldsymbol{a}^* = 0$. This reciprocal space is a convenient frame to describe Bragg's condition.

Let $\boldsymbol{k}_i$ be the wave vector of the incident beam and $\boldsymbol{k}_f$ that of the diffracted beam. Since diffraction results from an elastic process (without energy loss), the norm of vectors is identical, $|\boldsymbol{k}_f| = |\boldsymbol{k}_i| = \lambda^{-1}$, thus $\boldsymbol{k}_f$ describes a circle of radius equal to the norm of $\boldsymbol{k}_i$. The diffraction vector $\boldsymbol{q}$, defined as

$$\boldsymbol{q} = \boldsymbol{k}_f - \boldsymbol{k}_i \tag{3.2}$$

is thus a vector that, if its origin is positioned at the end of the vector $\boldsymbol{k}_i$, then its end forms a circle of the same radius $1/\lambda$ centered at the vector origin $\boldsymbol{k}_i$, as indicated in Figure 3.1.

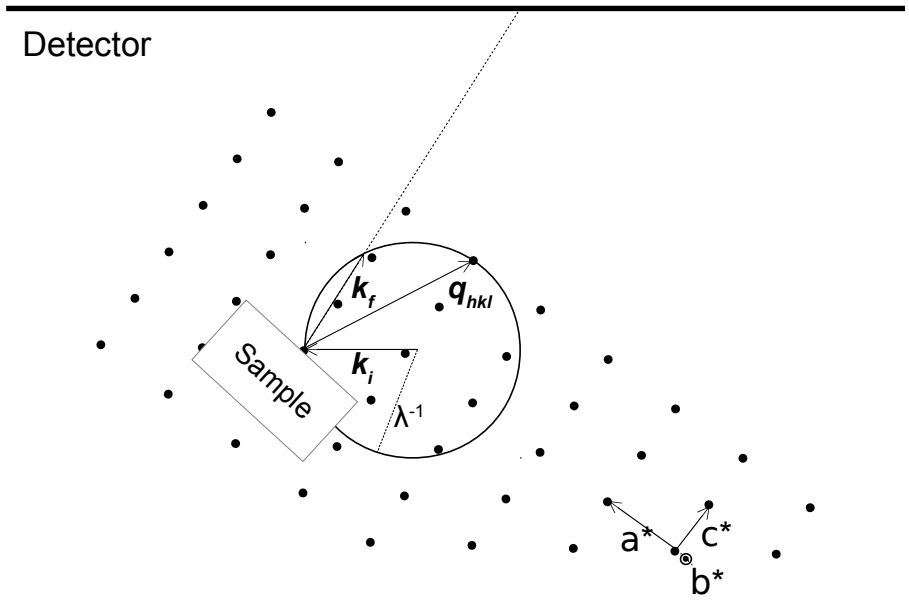

Figure 3.1: Sketch of Bragg diffraction in reciprocal space.

In the same reciprocal space, Bragg's condition is expressed as the coincidence between vector $\boldsymbol{q}^{(hkl)}$ of the crystalline (hkl) plane family, and the diffraction vector $\boldsymbol{q}$. Only a few favorable directions lead to coherent diffraction.

The electron beam adopted in EBSD analyses has a very short wave length and θ is generally less than 2°. The electrons at diffraction conditions thus remain close to the trace of the diffracting crystalline plane. Since the source is divergent, the electrons are redistributed on two Kossel cones in a symmetrical way with respect to the plane. The Kossel cones intersected by the detector have the shape of two hyperbolas whose curvature is very small and appear almost as parallel bands, see Figure 3.2. An example of the formed Kikuchi image can be found in Figure 3.3(a).

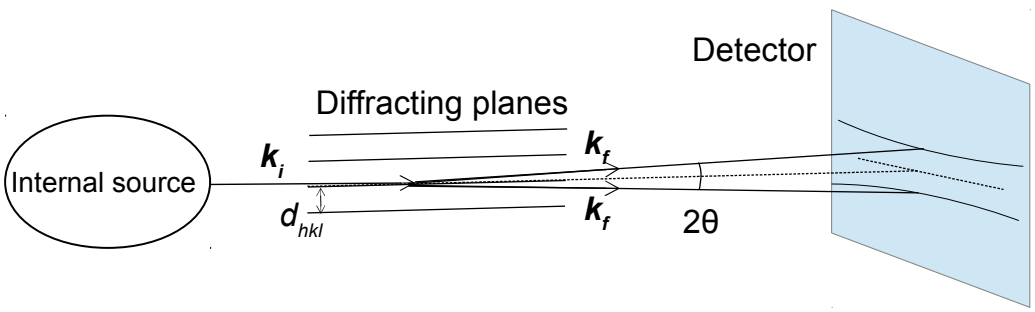

Figure 3.2: Sketch of the formation of diffraction bands.

As a result, the diffraction image is related to the studied point of the electron beam. The diffraction images are used to index crystallographic orientations, often via Hough (or

Radon) transforms [Duda and Hart 1972].

3.2.1.2 Subtraction of gray level background

The acquired images include a gray level background mainly due to the uneven energy distribution of the diffracted electrons. For example, the raw diffraction image shown in Figure 3.3(a) indicates that the intensity is higher at the image center than its periphery. It is common to correct the images by subtracting the background [Wright 2000; Dingley et al. 2005]. This correction deletes the low-frequency intensity variations in the diffraction image, which increases its contrast and makes the Kikuchi bands clearer. In doing so, an EBSD acquisition is performed at low magnification for a polycrystal to scan a big number of grains of different orientations. The corresponding diffraction images are averaged to estimate the gray level background of the EBSD setup. In principle, the background image is unique for all the studied zones of an HR-EBSD acquisition. The diffraction images with subtracted background are referred to as "corrected images," as shown in Figure 3.3(b). Kikuchi bands are clearer in Figure 3.3(b) than Figure 3.3(a). However another low-frequency gray level variation is visible. A further gray level subtraction will be proposed in Section 3.3.1. These corrected images are the starting point of all the following analyses.

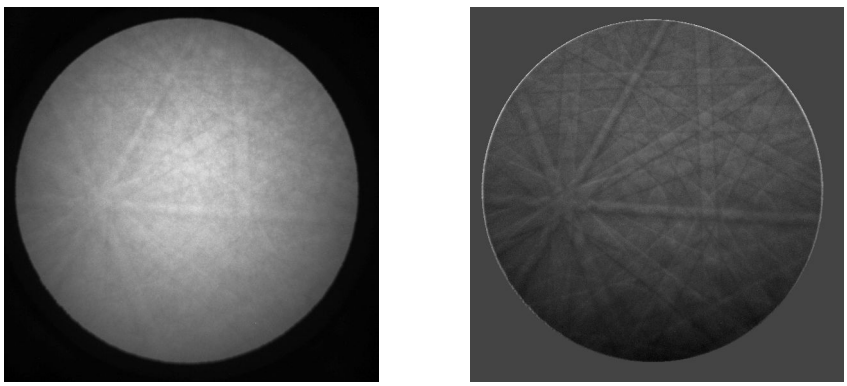

(a) (b)

Figure 3.3: Example of background correction. (a) Raw diffraction image. (b) Corrected image (provided by CrossCourt [CrossCourt3 2012]). The chosen image shows that the correction is not always completely satisfactory.

3.2.2 Principle of HR-EBSD

The HR-EBSD technique aims at extracting the deformation gradient tensor by comparing a reference Kikuchi image and another one corresponding to a deformed state. The technique processes diffraction images of good resolution and quality, often of definition 1024×1024 pixels or higher. If a zone of size $n \times n$ pixels of a specimen is studied, and each diffraction image is of definition $N \times N$, the entire data set is n^2N^2. Note that in most cases, the diffraction images of the reference and deformed states are obtained in a unique acquisition by scanning the specimen surface. A major challenge for strain mapping by HR-EBSD is the so-called "reference pattern problem" [Wilkinson and Britton 2012]. In some cases, there exist strain free points on the sample and trustworthy reference diffraction patterns can be acquired at these locations. Absolute elastic strains will be obtained by registering Kikuchi images with these reference patterns. However in the majority of cases, there is not a location on the sample from which a strain free reference pattern can be obtained with the crystal in the required orientation, so the measured strains represent relative variations to an unknown strain state at the position at which the reference pattern is obtained. The two application cases in Section 3.4 correspond to the two cases respectively.

3.2.2.1 Deformation of diffracting crystal

Let us note $\boldsymbol{F}$ the deformation gradient tensor that, when applied to a current point $\boldsymbol{X}$ in the initial configuration of the reference crystal, allows its position $\boldsymbol{x}$ in the deformed configuration to be obtained

$$\boldsymbol{F} = \frac{d\boldsymbol{x}}{d\boldsymbol{X}} = \begin{bmatrix} \frac{\partial x}{\partial X} & \frac{\partial x}{\partial Y} & \frac{\partial x}{\partial Z} \\ \frac{\partial y}{\partial X} & \frac{\partial y}{\partial Y} & \frac{\partial y}{\partial Z} \\ \frac{\partial z}{\partial X} & \frac{\partial z}{\partial Y} & \frac{\partial z}{\partial Z} \end{bmatrix} \tag{3.3}$$

$\boldsymbol{F}$ can be decomposed into two parts, namely, the elastic $\boldsymbol{F^e}$ and plastic $\boldsymbol{F^p}$ parts

$$\boldsymbol{F} = \boldsymbol{F^e}\boldsymbol{F^p} \tag{3.4}$$

The effects of plastic strains and volumetric elastic strains are summarized by [Plancher 2015]. Plastic strains make the Kikuchi bands less clear, an effect that is difficult to quantify. Thus HR-EBSD does not allow the plastic strains to be measured. In case of volumetric elastic strains, a variation of Kikuchi band width is observed. This width variation is not well resolved in HR-EBSD techniques and this hydrostatic (or spherical) elastic strain component

will not be considered as measurable and thus not exploited in the sequel [Wilkinson et al. 2006a]. Conversely, the deviatoric elastic strain tensor modifies the shape of the crystalline lattice, *i.e.*, the relative orientation of the crystalline planes, thus the diffracted electron patterns. A projection on a screen far from the diffraction source amplifies the angular distances between the two beams, thus generates a measurable variation between diffraction images.

Since only eight components of $\boldsymbol{F}^e$ are measurable, a convention should be made to set the lacking degree of freedom. Here the tensor $\widehat{\boldsymbol{F}^e}$ is chosen such that its ninth component is set to 1

$$\widehat{\boldsymbol{F}^e} = \begin{bmatrix} \hat{F}_1^e & \hat{F}_2^e & \hat{F}_3^e \\ \hat{F}_4^e & \hat{F}_5^e & \hat{F}_6^e \\ \hat{F}_7^e & \hat{F}_8^e & 1 \end{bmatrix} \tag{3.5}$$

The real elastic deformation gradient $\boldsymbol{F}^e$ reads

$$\boldsymbol{F}^e = \left(\frac{\partial z}{\partial Z}\right) \widehat{\boldsymbol{F}^e} \tag{3.6}$$

The factor $\partial z/\partial Z$ is not measurable, but can be determined by additional hypotheses such as the commonly adopted plane stress hypothesis of the studied zone [Maurice et al. 2012; Plancher et al. 2016].

3.2.2.2 Geometry of EBSD setup and axis

The fundamental equation of HR-EBSD describes the projection of the diffraction cones onto the detector plane. This projection is illustrated in Figure 3.4. The detector is chosen as coordinate system in the following, with its lower left corner as the origin. An electron beam hits the sample with an inclination of typically 70° with respect to the normal direction. A "central" point of the interaction zone is considered as the "effective" source of the diffracted electrons (different from the incident beam), which is represented by S. The "projection center" O is the normal projection of S onto the detector plane. Its coordinates are denoted as $(x^*, y^*, 0)$. Let z^* be the distance between S and O. Thus S has coordinates $(x^*, y^*, -z^*)$.

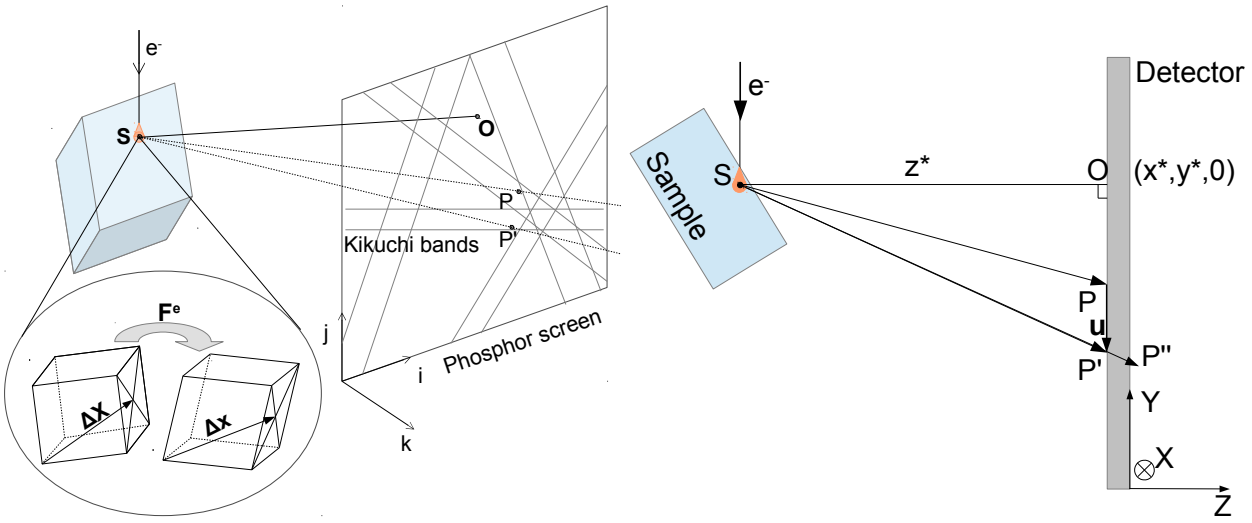

Figure 3.4: Sketch illustrating the geometry of HR-EBSD in 3D (a) adapted from [Maurice et al. 2012] and in 2D (b)

Let us consider an element $\boldsymbol{\Delta X}$ in the reference crystal lattice, and assume this particular direction generates a diffracted beam that intersects the detector plane at point P, of coordinates $(x, y, 0)$. In the following, the vector SP is denoted as $\boldsymbol{p}$. Then $\{\boldsymbol{p}\} = \{\Delta x, \Delta y, \Delta z\}^\top = \{x - x^*, y - y^*, z^*\}^\top = \alpha \boldsymbol{\Delta X}$, where α is the projection scale.

If the interaction volume around the source point S is subjected to an elastic deformation described by the deformation gradient tensor $\boldsymbol{F}^e$, *i.e.,* then the reference element $\boldsymbol{\Delta X}$ is transformed into $\boldsymbol{\Delta x} = \boldsymbol{F}^e \boldsymbol{\Delta X}$. The diffracted beam, which was initially along direction $\boldsymbol{p}$, has now moved to point P'', so that

$$\boldsymbol{p''} = \alpha \boldsymbol{F}^e \boldsymbol{\Delta X} \tag{3.7}$$

where vector SP'' is denoted as $\boldsymbol{p''}$. The straight line SP'' intersects the detector plane at point P' [Maurice et al. 2013]. The apparent motion on the detector plane is $\boldsymbol{u} = \boldsymbol{p'} - \boldsymbol{p}$ (*i.e.,* vector PP')

$$\begin{aligned} \boldsymbol{u} &= \boldsymbol{p'} - \boldsymbol{p} \\ &= \frac{p_z}{p''_z}\boldsymbol{p''} - \boldsymbol{p} \\ &= \frac{z^*}{\alpha(\boldsymbol{F}^e \boldsymbol{\Delta X})_z}\alpha \boldsymbol{F}^e \boldsymbol{\Delta X} - \boldsymbol{p} \\ &= \frac{z^*}{(\boldsymbol{F}^e \cdot \boldsymbol{p})_z}\boldsymbol{F}^e \cdot \boldsymbol{p} - \boldsymbol{p} \\ &= \frac{z^*}{(\widehat{\boldsymbol{F}^e} \cdot \boldsymbol{p})_z}\widehat{\boldsymbol{F}^e} \cdot \boldsymbol{p} - \boldsymbol{p}, \end{aligned} \tag{3.8}$$

or in an explicit form, for pixel (x, y) of the detector,

$$\begin{aligned} u_x(x,y) &= \frac{z^*(\hat{F}^e_1(x-x^*)+\hat{F}^e_2(y-y^*)+\hat{F}^e_3 z^*)}{\hat{F}^e_7(x-x^*)+\hat{F}^e_8(y-y^*)+z^*} - (x - x^*) \\ u_y(x,y) &= \frac{z^*(\hat{F}^e_4(x-x^*)+\hat{F}^e_5(y-y^*)+\hat{F}^e_6 z^*)}{\hat{F}^e_7(x-x^*)+\hat{F}^e_8(y-y^*)+z^*} - (y - y^*) \end{aligned} \tag{3.9}$$

The HR-EBSD technique is mainly based on Equation (3.9), and all the following analyses discuss its exploitation.

To summarize, the displacement field (u_x, u_y) between a reference diffraction image and a diffraction image of a deformed configuration reflects the elastic strains of the crystal lattice at the studied point with respect to the chosen reference crystal. The determination of tensor $\widehat{\boldsymbol{F}^e}$ is the major objective of HR-EBSD. Before explaining the newly developed technique, existing HR-EBSD techniques that are based on cross-correlation are introduced.

3.2.3 Principle of cross-correlation analyses

In practice, the registration of diffraction images of two different states is performed with an algorithm based on cross-correlation [Sutton et al. 1983; 2009]. It has been used to measure displacement fields and evaluate strain fields on surfaces and volumes [Sutton et al. 1983; 2009; Hild and Roux 2012b]. The correlation technique is widely employed by numerous free or commercial softwares dedicated to various objectives, thanks to its speed and satisfactory resolution. According to different groups working on metrological performances [Bornert et al. 2009; Britton et al. 2013], the standard error of measured displacements by correlation techniques is of the order of one centipixel.

Cross-correlation analyses start with dividing the *region of interest* (ROI) into subsets, whose central point motion will be tracked to get a discrete displacement field for the ROI. It is common to call these image subsets as *zones of interest* (ZOIs). Figure 3.5 shows an example of dividing the ROI into image subsets.

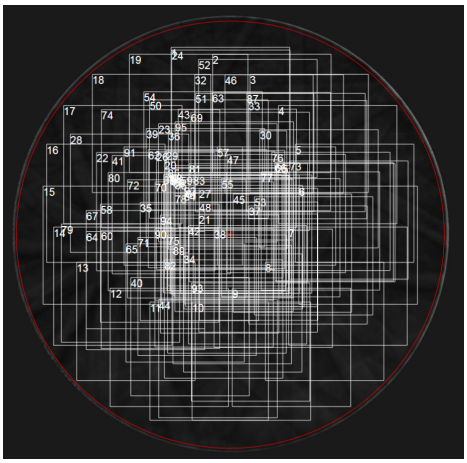

Figure 3.5: Example of image subset distributions used by CrossCourt [CrossCourt3 2012] for performing cross-correlation calculations. A significant overlap of the subsets is observed, especially at the image center.

An example of cross-correlation is shown in Figure 3.6. Figure 3.6(a) shows the ZOI in the reference diffraction image, and Figure 3.6(b) the studied diffraction image. Figure 3.6(c) reports the cross-correlation values of the ZOI with the deformed image shown in Figure 3.6(b), and an arrow depicts the mean displacement of the ZOI, which is calculated as the location of the maximum cross-correlation. A 3×3 pixel neighborhood about the maximum is extracted (Figure 3.6(d)) and an adjustment by a quadratic function [Sutton et al. 2009] allows the maximum position (marked by a star in Figure 3.6(d)) to be retrieved with a sub-pixel resolution. After treatment of all the ZOIs of Figure 3.5, a cloud of displacements (of the ZOI centers) is obtained (Figure 3.6(e)). Equation (3.9), which links measured shifts, (u_x, u_y), at particular locations, (x, y), to the elastic deformation gradient tensor is to be exploited to estimate $\widehat{\boldsymbol{F}^e}$. When more than four ZOIs are calculated, the problem becomes over determined and $\widehat{\boldsymbol{F}^e}$ is evaluated by the minimization of the mean squared error between measured and predicted shifts from $\widehat{\boldsymbol{F}^e}$ [Maurice et al. 2012]. Weighted least squares calculation has also been proposed to decrease the impact of incorrectly measured ZOIs [Britton and Wilkinson 2011].

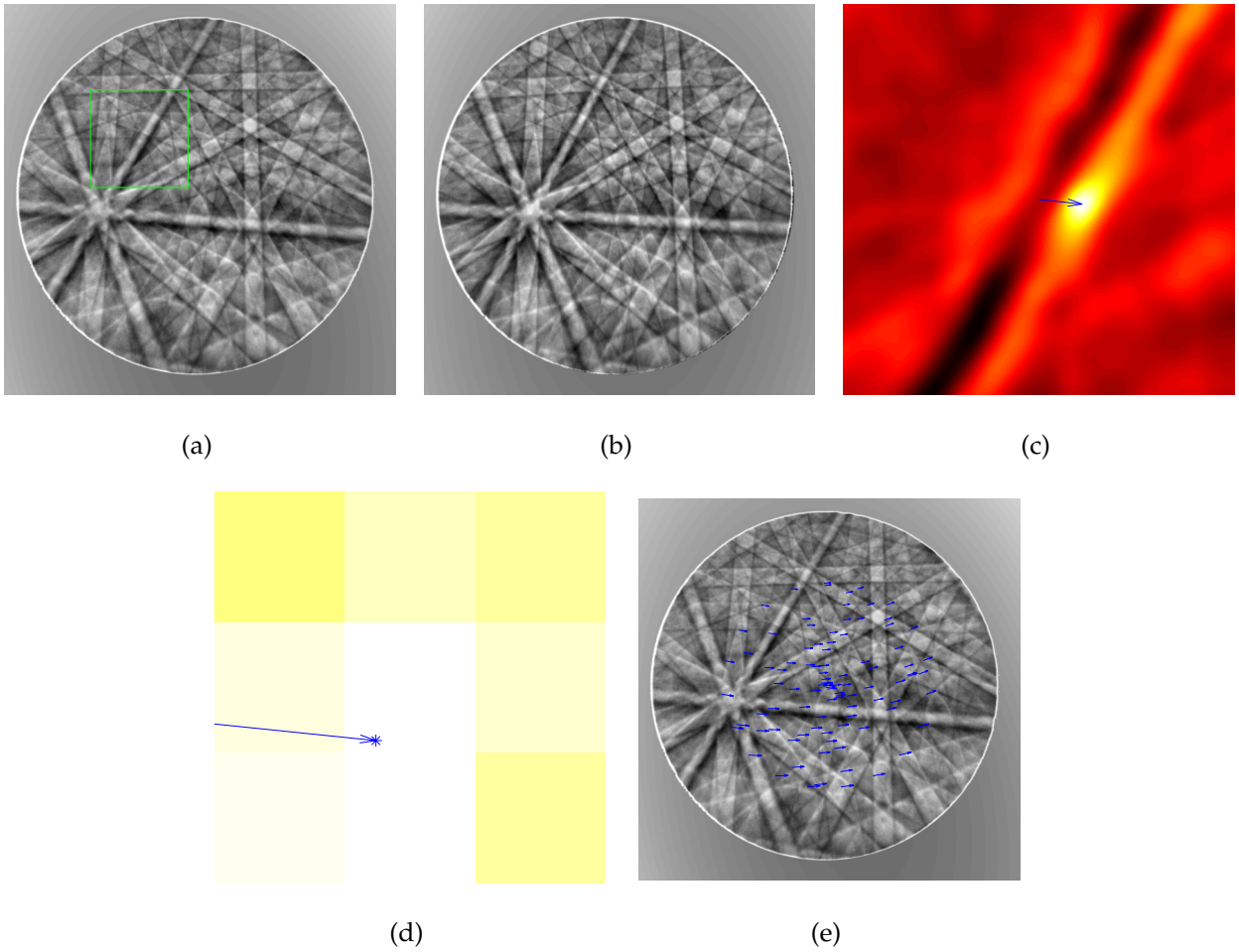

Figure 3.6: Example of DIC analysis by cross-correlation of image subsets. (a) ZOI in the reference diffraction image. (b) Studied diffraction image. (c) Field of cross-correlation results with the studied diffraction image. The arrow that links the image center and the maximum correlation indicates the ZOI motion between the reference and deformed images. (d) Enlargement of a portion of sub-figure (c), focusing on the maximum point and its immediate neighborhood. The star illustrates the maximum position obtained by bi-quadratic interpolation. (e) Measured mean displacements of ZOIs shown in Figure 3.5

Today commercial softwares exist such as "BLG CrossCourt" [CrossCourt3 2012]. Several laboratories have developed their own software for HR-EBSD analyses (*e.g.*, "Strain-Correlator" [Villert 2008] or "Phase-Only-Correlation" (POC) [Miyamoto et al. 2009]. They all are based on the same DIC algorithm as CrossCourt. In theory, four image subsets are sufficient to derive the 8 components of $\boldsymbol{F}^e$. In practice, more subsets are used (Figure 3.5) in order to make the estimation of deformation gradients more accurate and robust [Wilkinson et al. 2006a; Villert 2008; Villert et al. 2009]. However, this data processing method is not optimal (as discussed below). The motivation of this chapter is to propose a new approach

that minimizes the measurement uncertainties and the systematic errors.

3.2.4 Challenges of cross-correlation of HR-EBSD images

The difficulties linked to data treatment by cross-correlation are identified as follows:

1. Every image subset provides a mean displacement. For a good accuracy of cross-correlations, the size of the subset should be large enough to contain a sufficient number of Kikuchi bands. In order to get a rich displacement field, it is mandatory to take a large number of ZOIs (in practice varying between 25 and 100 [Villert 2008; CrossCourt3 2012; Plancher 2015]). Due to the large number and size of ZOIs, a significant overlap is present in image subsets (Figure 3.5). This property slows down the correlation process since the pixels of the diffraction image are calculated many times in different image subsets.

2. The choice of image subsets positioning could impact the obtained results [Maurice et al. 2012], which is a manifestation of non optimal cross-correlation-based HR-EBSD analyses.

3. In cases of relatively large deformations, significant rotations (*e.g.*, several degrees) between diffraction images can be observed. Then for displacement fields composed of pure translations of image subsets, the kinematic basis is no longer adapted to reproduce the observed image transformations. Consequently, cross-correlation may yield errors such as abnormally high stress levels at zones with high rotations compared to the reference image.

4. The overlap of different ZOIs produces correlations in the different estimates that should ideally be accounted for to evaluate $\boldsymbol{F}^e$.

3.2.5 Optimized cross-correlation by remapping

To solve the problem of high rotations in diffraction figures, [Maurice et al. 2012] proposed to perform image rotation as a pre-processing step, which is illustrated in Figure 3.7. A first fast calculation is performed to determine the average rotation in an image. The finer deformation calculation is then based on the rotated reference image.

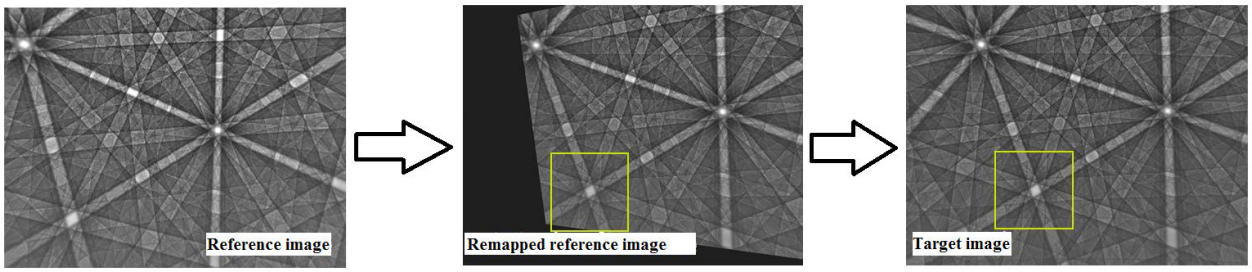

Figure 3.7: Principle of "remapping" [Maurice et al. 2012]. The reference image is corrected by the rotation measured beforehand, thus becomes more similar to the deformed image. The displacement field between the corrected reference image and the deformed picture can be measured more precisely by cross-correlation.

This procedure could also lead to bias because remapping requires the knowledge of the position of the projection center [Plancher et al. 2016], denoted O in Figure 3.4, whose precise measurement is challenging.

Existing publications deal with the issues listed in Section 3.2.4, for example [Maurice et al. 2012; Britton and Wilkinson 2011; 2012]. However no satisfactory solutions exist yet. Though cross-correlation-based HR-EBSD make the estimation of elastic strains and the corresponding stresses possible, the process remains slow, exposed to randomness in cases of relatively high strains.

3.2.6 Alternative methods

Other algorithms exist for measuring displacement fields via DIC [Hild and Roux 2012b; Sutton 2013]. An alternative to cross-correlation of image subsets (also known as local DIC) has been proposed as global DIC [Wagne et al. 2002; Besnard et al. 2006] or integrated DIC [Hild and Roux 2006; Roux and Hild 2006; Leclerc et al. 2009]. The global approach uses the entire image (and only once) instead of many image subsets. The repetitive calculations of the same pixels and the empirical choice of image subsets disappear naturally, together with the issue of dealing appropriately with correlations of measurement due to overlapping ZOIs [Hild and Roux 2012a]. Besides, global DIC provides a residual field, which is calculated at each pixel and constitutes by nature a good criterion to characterize the error of registration.

Integrated Digital Image Correlation (IDIC) has been proposed to measure directly the physical quantities (parameters) of interest from image registrations. Thus the measured

displacement fields are expressed in a "kinematic basis" that is tailored *a priori* to the studied physical phenomena (and potentially the artifacts of image formation and acquisition). No additional degrees of freedom are allowed in the displacement field. This technique can be adapted to HR-EBSD analyses, since it is based on an interpretative framework adjusted to the expected kinematics, and exploits the pixels of each image with an equal weight. This chapter proposes to substitute the current (cross-correlation) data treatments of HR-EBSD images to evaluate elastic deformation gradient tensors with an IDIC procedure.

3.3 Integrated DIC for HR-EBSD: ADDICTED

A new algorithm has been developed to measure elastic strains from HR-EBSD images. The algorithm is based on the principles of IDIC and applied to two sets of experimental images. This algorithm and the necessary pre-processing of diffraction images are summarized in Figure 3.8 and detailed in this section. It has been proposed to call the new method ADDICTED, an acronym for "Alternative Dedicated Digital Image Correlation Tailored to Electronic Diffraction."

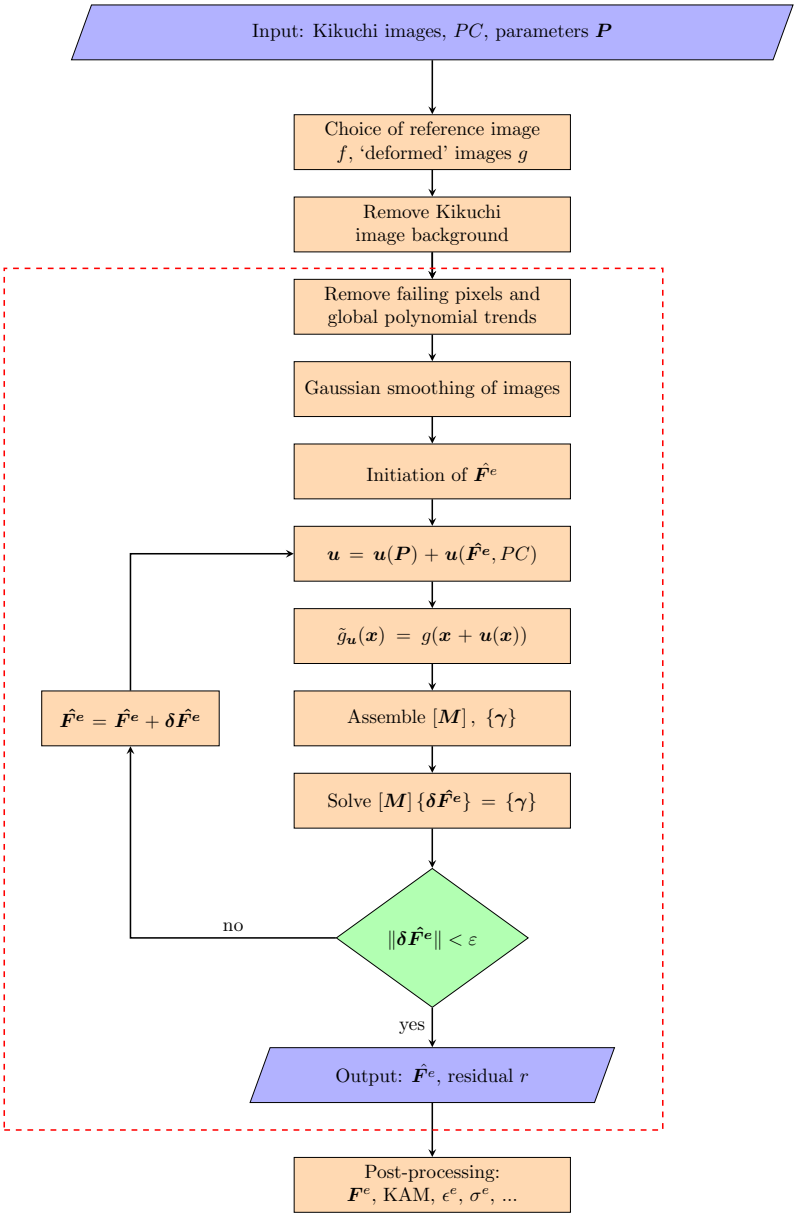

Figure 3.8: Flowchart of ADDICTED algorithm. The steps included in the box are exclusive to ADDICTED.

3.3.1 Picture preparation

3.3.1.1 Filtering of bad pixels

Because of the non-uniformity of the phosphorescent screen utilized for electron capture, the acquired images often contain, at fixed locations, over-exposed pixels. These very bright pixels are detrimental to DIC calculations and it is proposed to replace the gray level of these "bad pixels" by the mean values of neighboring pixels.

3.3.1.2 Extraction of global variation of gray levels

After the extraction of diffraction image background, explained in Section 3.2.1.2, the Kikuchi bands may possess global variations of gray levels, which are related to the fluctuations of the average energy of diffracted electrons. For example, Figure 3.9(a) shows a diffraction image brighter in the upper part and darker in the lower part. This global tendency does not impact very much the quality of cross-correlation, which studies local subsets of the image. However, for global image registration, it is preferable to extract the global changes of gray levels, which are assumed to be represented by a polynomial of order 2 or 3 (obtained by a classic regression procedure). After the extraction of the global variation of the gray levels, Figure 3.9(a) is transformed into Figure 3.9(b), which is more uniform and the contrast related to Kikuchi bands is more visible.

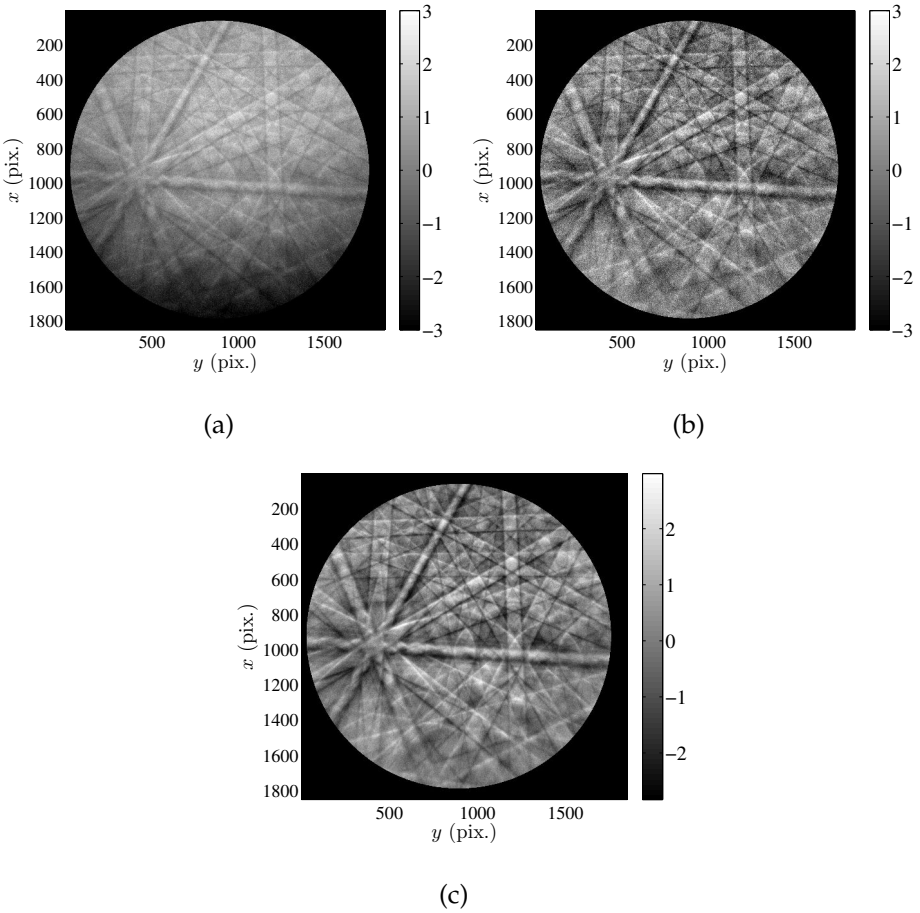

Figure 3.9: Effect of gray level correction and Gaussian filtering. (a) Diffraction Image truncated between -3 and 3. (b) Previous image corrected by subtraction of global tendency of gray levels. (c) Previous image filtered by Gaussian kernel of $\xi = 1$ pixel. The convolution with Gaussian filter eliminates efficiently the high frequency noise from the diffraction image.

3.3.1.3 Filtering of high frequency noise

Gaussian filtering at very small scale of the Kikuchi image makes the subsequent calculations easier, because the raw image is corrupted by very high white noise. The effect of Gaussian filtering $\tilde{f}$ is illustrated in Figures 3.9(b) and 3.9(c). The smoothing involves the convolution of the initial image f by a Gaussian kernel G

$$\tilde{f} = f * G \tag{3.10}$$

where $G(x, y)$ is chosen as Gaussian depending on an internal length ξ

$$G(x, y) = \frac{1}{2\pi\xi^2} e^{-\frac{x^2+y^2}{2\xi^2}} \tag{3.11}$$

In practice, the chosen length ξ lies between 1 and 2 pixels. This choice depends on the noise level of the image, which is in turn dependent on the acquisition time, the pixel number, the electron beam parameters and the imaged material.

3.3.2 Algorithm

3.3.2.1 Global digital image correlation

Conventional DIC consists of correlating two images of gray levels, one of the reference state $f(\boldsymbol{x})$ and the other one of the deformed state $g(\boldsymbol{x})$. The displacement field $\boldsymbol{u}(\boldsymbol{x})$ between the two images can be found by correcting the deformed image $\tilde{g}_{\boldsymbol{u}}(\boldsymbol{x}) = g(\boldsymbol{x}+\boldsymbol{u}(\boldsymbol{x}))$ to match as best as possible the reference image $f(\boldsymbol{x})$, which involves the minimization of the quadratic norm of the residual $r = (f(\boldsymbol{x}) - \tilde{g}_{\boldsymbol{u}}(\boldsymbol{x}))$ summed over the entire ROI.

The cost function to minimize writes

$$\Phi = \sum_{ROI} (f(\boldsymbol{x}) - \tilde{g}_{\boldsymbol{u}}(\boldsymbol{x}))^2 \tag{3.12}$$

where $\tilde{g}_{\boldsymbol{u}}(\boldsymbol{x}) = g(\boldsymbol{x} + \boldsymbol{u}(\boldsymbol{x}))$ is the deformed image corrected by the measured displacement field (for the iterative algorithm, it is the current estimation). The minimization of the cost function leads to successive corrections of the displacement estimation until convergence. The displacement field (or its corrections) is constructed by linear (or affine) combinations of fields constituting the kinematic basis. For ADDICTED, IDIC is the chosen tool to analyze diffraction images, namely, f and g are respectively the diffraction images of the reference crystal (*e.g.*, assumed to be stress-free), and of the deformed crystal. The displacement field $\boldsymbol{u}$ observed in the diffraction images has to be related to the elastic deformation gradient of the

diffracting crystal, $\widehat{\boldsymbol{F}^e}$. Besides, other parameters may influence the measured displacement field (*e.g.*, sample inclination with respect to the detector, physical size of the pixel, and the scanning step of the SEM). The column vector $\{\boldsymbol{P}\}$ gathers all parameters related to *beam-induced shift* [Wilkinson et al. 2006a]. Therefore, it is necessary to express (or make explicit) the dependence of the displacement field on $\widehat{\boldsymbol{F}^e}$ and $\boldsymbol{P}$

$$\boldsymbol{u} = \boldsymbol{u}(\boldsymbol{x}; \widehat{\boldsymbol{F}^e}, \{\boldsymbol{P}\}) \tag{3.13}$$

The displacement field usually has nonlinear dependencies with $\widehat{\boldsymbol{F}^e}$ and $\{\boldsymbol{P}\}$. First order Taylor expansions are performed

$$\boldsymbol{u}(\boldsymbol{x}; \widehat{\boldsymbol{F}^e} + \delta\widehat{\boldsymbol{F}^e}, \{\boldsymbol{P} + \delta\boldsymbol{P}\}) = \boldsymbol{u}(\boldsymbol{x}; \widehat{\boldsymbol{F}^e}, \{\boldsymbol{P}\}) + \boldsymbol{\Phi}_i(\boldsymbol{x}; \widehat{\boldsymbol{F}^e}, \{\boldsymbol{P}\})\delta\hat{F}_i^e + \boldsymbol{\Psi}_j(\boldsymbol{x}; \widehat{\boldsymbol{F}^e}, \{\boldsymbol{P}\})\delta P_j \tag{3.14}$$

with

$$\begin{aligned} \boldsymbol{\Phi}_i &= \frac{\partial \boldsymbol{u}}{\partial \hat{F}_i^e} \\ \boldsymbol{\Psi}_i &= \frac{\partial \boldsymbol{u}}{\partial P_i} \end{aligned} \tag{3.15}$$

where $\boldsymbol{\Phi}_i$ is the sensitivity field with respect to the component $\hat{F}_i^e$ ($i = 1, 8$) of the elastic deformation gradient tensor, and $\boldsymbol{\Psi}_i$ the sensitivity field of parameter P_i. As a result, for example, $\boldsymbol{\Phi}$ is a matrix of size $(2N_{pixel}) \times 8$. To be explicit, by combining Equations (3.8) and (3.9), the sensitivity fields read

$$\begin{aligned}
\Phi_{x1} &= \frac{z^*(x-x^*)}{\hat{F}_7^e(x-x^*)+\hat{F}_8^e(y-y^*)+z^*} & \Phi_{y1} &= 0 \\
\Phi_{x2} &= \frac{z^*(y-y^*)}{\hat{F}_7^e(x-x^*)+\hat{F}_8^e(y-y^*)+z^*} & \Phi_{y2} &= 0 \\
\Phi_{x3} &= \frac{(z^*)^2}{\hat{F}_7^e(x-x^*)+\hat{F}_8^e(y-y^*)+z^*} & \Phi_{y3} &= 0 \\
\Phi_{x4} &= 0 & \Phi_{y4} &= \frac{z^*(x-x^*)}{\hat{F}_7^e(x-x^*)+\hat{F}_8^e(y-y^*)+z^*} \\
\Phi_{x5} &= 0 & \Phi_{y5} &= \frac{z^*(y-y^*)}{\hat{F}_7^e(x-x^*)+\hat{F}_8^e(y-y^*)+z^*} \\
\Phi_{x6} &= 0 & \Phi_{y6} &= \frac{(z^*)^2}{\hat{F}_7^e(x-x^*)+\hat{F}_8^e(y-y^*)+z^*} \\
\Phi_{x7} &= -\frac{z^*(x-x^*)\left(\hat{F}_1^e(x-x^*)+\hat{F}_2^e(y-y^*)+\hat{F}_3^e z^*\right)}{\left(\hat{F}_7^e(x-x^*)+\hat{F}_8^e(y-y^*)+z^*\right)^2} & \Phi_{y7} &= -\frac{z^*(x-x^*)\left(\hat{F}_4^e(x-x^*)+\hat{F}_5^e(y-y^*)+\hat{F}_6^e z^*\right)}{\left(\hat{F}_7^e(x-x^*)+\hat{F}_8^e(y-y^*)+z^*\right)^2} \\
\Phi_{x8} &= -\frac{z^*(y-y^*)\left(\hat{F}_1^e(x-x^*)+\hat{F}_2^e(y-y^*)+\hat{F}_3^e z^*\right)}{\left(\hat{F}_7^e(x-x^*)+\hat{F}_8^e(y-y^*)+z^*\right)^2} & \Phi_{y8} &= -\frac{z^*(y-y^*)\left(\hat{F}_4^e(x-x^*)+\hat{F}_5^e(y-y^*)+\hat{F}_6^e z^*\right)}{\left(\hat{F}_7^e(x-x^*)+\hat{F}_8^e(y-y^*)+z^*\right)^2}
\end{aligned} \tag{3.16}$$

3.3.2.2 Correction of projection parameters

The projection parameters such as the coordinate of projection center (x^*, y^*) and the relative inclination angle between the sample and the screen are very important in HR-EBSD analyses.

• *Projection center*

The projection center (PC) positioning is crucial for elastic strain measurement and its effect has been quantified [Villert et al. 2009; Kacher et al. 2009]. "Remapping" is also limited by PC positioning. Various methods have been proposed to precisely pinpoint PC (*e.g.*, shadow-casting [LTD 2012], moving screen [Carpenter et al. 2007; Maurice et al. 2011], shadow grid [Mingard et al. 2011]). The Kikuchi figure projected onto a sphere centered on PC contains parallel Kikuchi bands on the "large circles." This phenomenon enables the PC to be positioned very accurately [Kacher et al. 2010]. The ADDICTED algorithm per se cannot determine the PC position [Alkorta 2013].

• *Beam-induced shift*

Before launching ADDICTED calculations, the shift of the Kikuchi images due to motions of the emission point (in other words the scanning motion of the electron beam) should be corrected. This shift, $\boldsymbol{w}$, can be obtained precisely by the SEM calibration with a standard sample, knowing the scanning direction on the screen and the physical size of the screen pixel. This correction of a global translation of the image by $\boldsymbol{w}$ reads

$$\hat{g}(\boldsymbol{x}) = g(\boldsymbol{x} + \boldsymbol{w}) \tag{3.17}$$

where $\hat{g}$ is the corrected image, and can be performed via cross-correlation over the whole ROI. Note that $\boldsymbol{w}$ only depends on the position of the incident electron beam, and for each diffraction image Equation (3.17) describes a pure translation.

•*Correction of relative inclination of the sample*

The sample is tilted to about 70° for HR-EBSD acquisitions and the screen is tilted by several degrees too. If the acquisition is carried out on a large zone (say greater than 100×100 µm^2), the distance between the emission point and the screen, z^*, varies in a non negligible manner. It is worth noting that varying z^* induces magnification changes. Therefore, the size of the diffraction image should be adjusted, centered about PC, $\boldsymbol{x}^* = (x^*, y^*)^\top$, before launching ADDICTED

$$\check{g}(\boldsymbol{x} - \boldsymbol{x}^*) \equiv \hat{g}\left[(z_g^*/z_f^*)(\boldsymbol{x} - \boldsymbol{x}^*)\right] \tag{3.18}$$

where z_g^* is the distance between the emission point and the screen for the deformed image, and z_f^* is that for the reference configuration. Consequently, the effects of the projection parameters on the displacement field, $\boldsymbol{\Psi}_i$, are treated and corrected before and the final solution to the minimization problem is conducted for $\widehat{\boldsymbol{F}^e}$.

3.3.2.3 Solution

The minimization algorithm follows the standard IDIC steps without particular modification [Hild and Roux 2012b]. The cost function (3.12) is iteratively minimized with Gauss-Newton algorithm. The column vector $\{\boldsymbol{\delta}\widehat{\boldsymbol{F}^e}\}$ gathering all corrections to $\widehat{\boldsymbol{F}^e}$ is obtained

$$[\boldsymbol{M}]\,\{\boldsymbol{\delta}\widehat{\boldsymbol{F}^e}\} = \{\boldsymbol{\gamma}\} \tag{3.19}$$

where $[\boldsymbol{M}]$ is the Hessian matrix of size 8×8 at iteration $n-1$

$$M_{ij}^{(n-1)} = \sum_{ROI} (\boldsymbol{\nabla} f(\boldsymbol{x}) \cdot \boldsymbol{\Phi}_i(\boldsymbol{x}, \widehat{\boldsymbol{F}^e}))(\boldsymbol{\nabla} f(\boldsymbol{x}) \cdot \boldsymbol{\Phi}_j(\boldsymbol{x}, \widehat{\boldsymbol{F}^e})) \tag{3.20}$$

and the second member $\{\boldsymbol{\gamma}_i\}$ includes the residual field

$$\gamma_i^{(n)} = \sum_{ROI} \left(f(\boldsymbol{x}) - \tilde{g}^{(n)}(\boldsymbol{x}, \widehat{\boldsymbol{F}^e}) \right) \boldsymbol{\nabla} f(\boldsymbol{x}) \cdot \boldsymbol{\Phi}_i(\boldsymbol{x}, \widehat{\boldsymbol{F}^e}) \tag{3.21}$$

When $\|\{\delta \boldsymbol{F}\}\| < \epsilon$, ϵ being chosen equal to 10^{-7} for all the calculations of this chapter, the minimization stops and $\widehat{\boldsymbol{F}^e}$ is stored. Otherwise, $\widehat{\boldsymbol{F}^e}$ is updated

$$\widehat{\boldsymbol{F}^e}^{(n)} = \widehat{\boldsymbol{F}^e}^{(n-1)} + \boldsymbol{\delta}\widehat{\boldsymbol{F}^e}^{(n)} \tag{3.22}$$

Once $\widehat{\boldsymbol{F}^e}$ is obtained, the displacement field $\boldsymbol{u}$ is derived from Equation (3.8), and the deformed image can be corrected with these new estimates.

3.3.2.4 Analysis of noise

Besides $\widehat{\boldsymbol{F}^e}$, ADDICTED gives another important result, namely, the correlation residuals evaluated at any pixel location in the ROI

$$r(\boldsymbol{x}) = f(\boldsymbol{x}) - \tilde{g}(\boldsymbol{x}) \tag{3.23}$$

The registration residual r collects all artifacts of the formation and acquisition of Kikuchi figures, and thus potentially contains very rich indications of the analyzed images. Signals in the residual that are not (white) noise often indicate an incomplete exploitation of the information, or an unadapted kinematic transformation between images. The residual may thus contain signal and noise. Let us assume that the reference image f is formed from a noiseless signal, f_p, with the superposition of a supposedly normal distributed noise b_f, which is known by the designation “Gaussian white noise"

$$f(\boldsymbol{x}) = f_p(\boldsymbol{x}) + b_f(\boldsymbol{x}) \tag{3.24}$$

The superposition is supposed to contain no spatial correlation. The same formation for a series of deformed diffraction images g^i reads

$$g^i(\boldsymbol{x}) = g_p^i(\boldsymbol{x}) + b_g^i(\boldsymbol{x}) \tag{3.25}$$

where b_g is white noise. After the application of ADDICTED, the corrected image reads

$$\tilde{g}^i(\boldsymbol{x}) = \tilde{g}_p^i(\boldsymbol{x}) + \tilde{b}_g^i(\boldsymbol{x}) \tag{3.26}$$

thus the residual reads

$$\begin{aligned} r^i(\boldsymbol{x}) &= f(\boldsymbol{x}) - \tilde{g}^i(\boldsymbol{x}) \\ &= f_p(\boldsymbol{x}) - \tilde{g}_p^i(\boldsymbol{x}) + b_f(\boldsymbol{x}) - \tilde{b}_g^i(\boldsymbol{x}) \\ &= b_f(\boldsymbol{x}) - \tilde{b}_g^i(\boldsymbol{x}) \end{aligned} \tag{3.27}$$

Equation (3.27) can be established if the ideal reference f_p and deformed $\tilde{g}_p^i$ images perfectly match after the registration.

The same reference image is utilized for a given grain, which means a unique image f is registered to a series of deformed images g. The residuals at convergence for all images g can be averaged and, by noting $\langle ... \rangle$ their average over the different points inside one grain,

$$\begin{aligned} \langle r^i \rangle &= b_f - \langle \tilde{b}_g^i \rangle \\ &= b_f \end{aligned} \tag{3.28}$$

The average of the residual field provides an estimation of b_f, which allows noise to be removed from the reference image, f_p. The "cleaned" reference image allows the measurement uncertainty to be decreased (*i.e.*, variance divided by 2).

3.4 Examples of application

The ADDICTED algorithm has been coded in Matlab. The code enables all the reported results earmarked ADDICTED or integrated image correlation to be obtained. The proposed algorithm has been tested on two sets of experimental data. The first test quantifies the uncertainty of the algorithm on a specific single crystal sample. The second test probes the feasibility of the algorithm in a more realistic case. The performance of ADDICTED has been evaluated by comparison with two existing softwares, *i.e.*, StrainCorrelator and CrossCourt.

3.4.1 Single crystal sample in 4-point flexural test

A 4-point flexural test has been performed by [Plancher 2015; Plancher et al. 2016] on a Zeiss Supra 55VP FEG-SEM operating at 20 kV with a probe current of 2.4 nA. A sample made of A316 stainless steel has been obtained by electric arc erosion from a single crystal ingot fabricated with the Bridgman-Stockbarger technique [Stockbarger 1936]. The sample is oriented along the $\langle 100 \rangle$ axis with an uncertainty of 3°. Then the sample has been mechanically and electrochemically polished to minimize the surface residual stress. The final sample is of dimensions $30 \times 4.8 \times 0.5$ mm^3. It was tested by a 4-point flexural setup, which is illustrated in Figure 3.10. During the test the maximum force reached 5.4 N. A transverse profile has been studied to get its strain state, which is representative of the loading of the central part of the sample. Along this 500 µm long profile, HR-EBSD acquisitions have been performed over 5000 points, with a step of 100 nm. The diffraction images have been recorded by a Nordlys II camera with a definition of 1344×1024 pixels. The sample has also been studied by synchrotron X-ray diffraction, in order to apply the DIC-Laue technique [Petit et al. 2015]. The Laue diffraction technique provides a comparison of coarser resolution, because the focused synchrotron beam has a diameter larger than the electron beam of SEMs. However, the Laue diffraction combined with DIC leads to a lower uncertainty on the (elastic) strain measurements (of the order of 10^{-5}) due to an averaging effect as it is less local than HR-EBSD [Plancher et al. 2016].

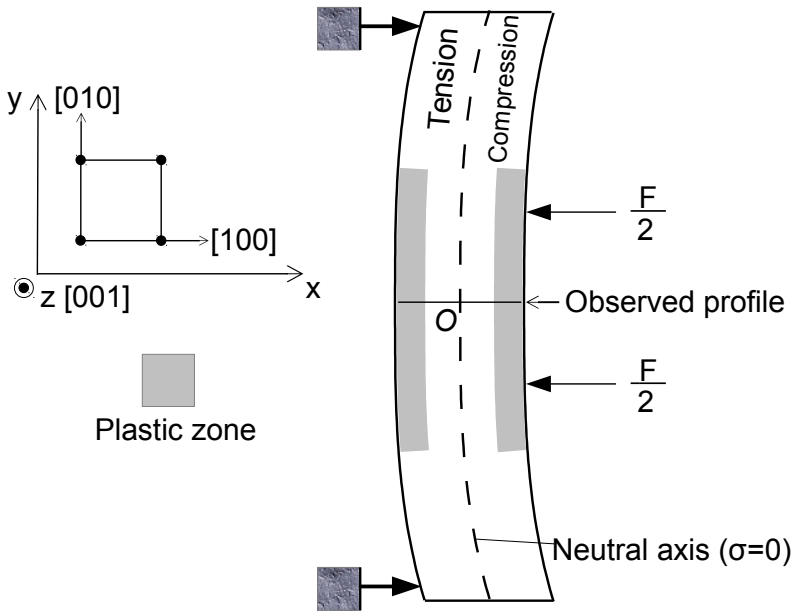

Figure 3.10: Sketch of 4-point flexural test [Plancher et al. 2016].

According to beam theory, a neutral axis where there is neither compression nor tension exists at the sample mid-height along the longitudinal direction. Therefore, the test provides a reference diffraction image, which corresponds to an unloaded state, at the intersection of the studied profile and the neutral axis, denoted by point $\boldsymbol{O}$ in Figure 3.10. The synchrotron diffraction images were treated by DIC-Laue [Plancher et al. 2016]. The HR-EBSD images along the profile were treated with the StrainCorrelator software and ADDICTED.

Figure 3.11 shows the regions utilized in the calculations on the reference image. StrainCorrelator utilizes 25 256-pixel subsets distributed close to the image center, see Figure 3.11(a). A unique (yet large) region is treated with integrated DIC (ADDICTED).

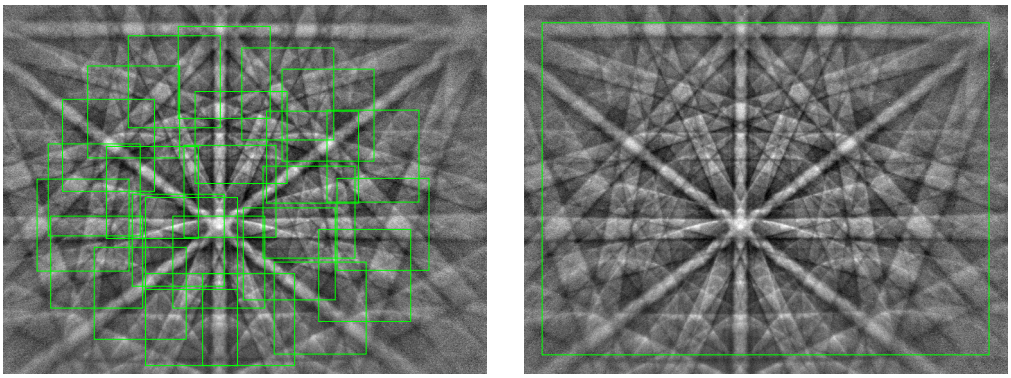

(a) (b)

Figure 3.11: Reference diffraction image and the ROIs (a) of StrainCorrelator, and (b) of ADDICTED.

The strain component ϵ_{yy} corresponds to the direction where the strain level is the highest. Its profile is shown in Figure 3.12. 5000 acquisition points are reported as a function of the distance to the beam neutral axis. Between -50 µm and 50 µm, a linear trend is observed, corresponding to the elastic deformation regime. The broadness of the band of points indicates the scatter of data. Since the sample stems from a single crystal of good quality, in theory there should be no high-frequency signal for $\boldsymbol{F}^e$. Therefore, the scatter of the resulting strains along the profile allows the performance of HR-EBSD algorithms to be compared. ADDICTED gives ϵ_{yy} results very close to those of StrainCorrelator, both for the average value and for the amplitude. Consequently it is interesting to compare the corresponding scatter. The standard deviation of the measured strains is a good indicator. To calculate it, an average strain profile has been calculated by moving average of 200 consecutive data, then the standard deviation of distances between the data points and the average profile is considered as the scatter. The standard deviation is 5.6×10^{-5} for StrainCorrelator, and 4.9×10^{-5}

for ADDICTED, *i.e.*, a 12% reduction for the latter. If the stray points at activated slip locations are excluded in calculation, the value is 4.3×10^{-5} for StrainCorrelator and 3.5×10^{-5} for ADDICTED. This uncertainty gain can be explained as ADDICTED considers a large and unique ROI, *i.e.*, only one sampling on a large number of data. The sampling bias, which affects the cross-correlation by image subsets, has been avoided. This phenomenon shows the robustness of ADDICTED against image noise. Besides, it is worth noting that this test leads to very small strains (less than 10^{-3}), and the rotation of diffraction images is limited. Therefore it is a favorable case to apply cross-correlation of image subsets (for StrainCorrelator). In cases with larger strains, ADDICTED is expected to be even more advantageous.

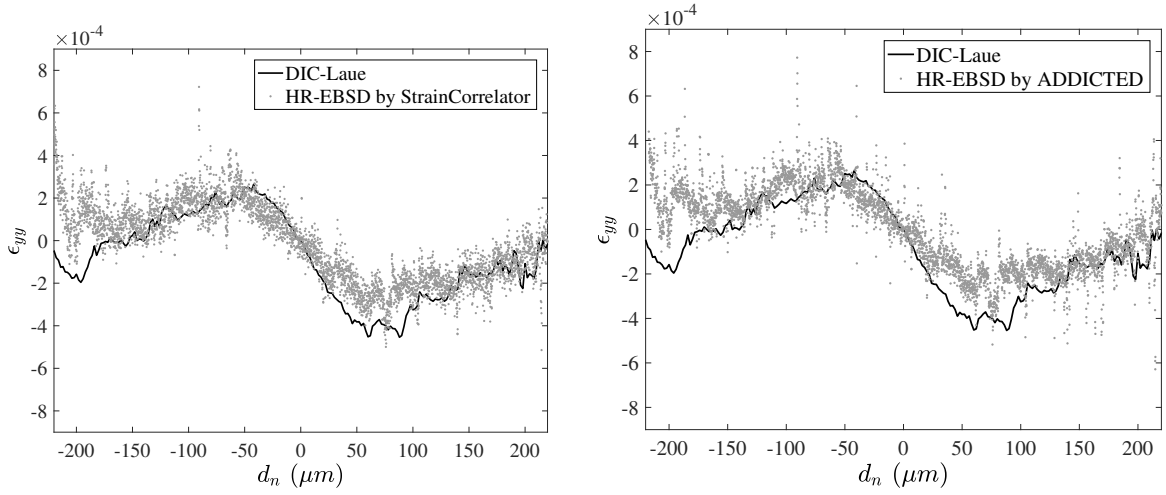

Figure 3.12: ϵ_{yy} profiles as functions of the distance to the neutral axis d_n, provided by (a) StrainCorrelator, (b) ADDICTED. For comparison purposes, ϵ_{yy} profiles calculated by DIC-Laue [Plancher et al. 2016] are drawn in both figures.

The ε_{yy} profile of Figure 3.12 is characterized by local discontinuities. It was found that discontinuities of $\boldsymbol{F}^e$ components correspond to the presence of activated slip traces [Plancher 2015]. At each discontinuity several outliers exist. The residual fields associated with outliers are shown in Figure 3.13. Apart from these outliers, the residual contains only white noise (Figures 3.13(a) and 3.13(d)). For the outliers, an unaccounted for signal remains in the residual, which is visible on the lower left part of Figure 3.13(b), and on the lower right part of Figure 3.13(c). This phenomenon shows that the diffraction images acquired in the direct vicinity of slip traces are more complex than regular diffraction images. A possible explanation is that plastic slip could cause crystal rotations, and on the two sides of a slip trace two lattices of slightly different orientations may interact simultaneously with the electron

beam. This observation proves on the one hand the high sensitivity of ADDICTED to such cases. On the other hand this example shows that the residual image calculated for each correlation between diffraction images contains a very rich information, which reveals the failure of the transformation model in this particular situation. Signals in the residual field point at the way for potential interpretation in the future.

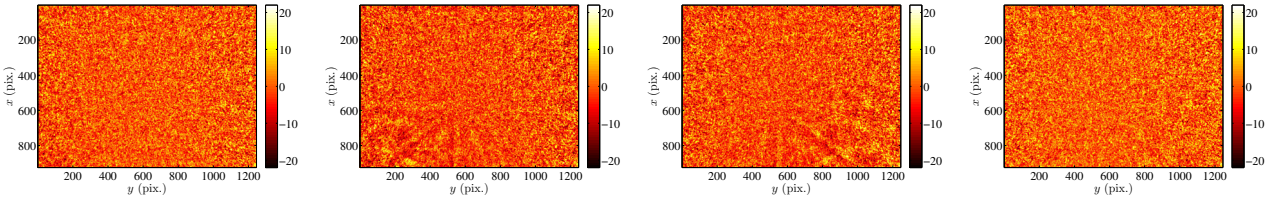

(a) (b) (c) (d)

Figure 3.13: Residual field calculated by ADDICTED. (a) and (d) correspond to images outside the zone of localized slip trace. (b) and (c) residuals of diffraction images captured on the slip trace.

Figure 3.14 shows an example of denoising with the method explained in Section 3.3.2.4. The raw diffraction image is shown in Figure 3.14(a), where noise is clearly visible. Figure 3.14(b) shows the filtered diffraction image with a Gaussian kernel of 2 pixels, leading to an attenuation of noise but also to loss of image contrast. Figure 3.14(c) shows the denoised reference image based on ADDICTED results on 400 diffraction images located between -40 µm and 0 µm. Figure 3.14(c) reports a drastic reduction of noise, while keeping the contrast of the original image. These trends are more manifest on the zoomed areas (Figures 3.14(d), 3.14(e), 3.14(f)). Figure 3.14(f) reveals very rich details that are otherwise invisible in Figures 3.14(d) and 3.14(e).

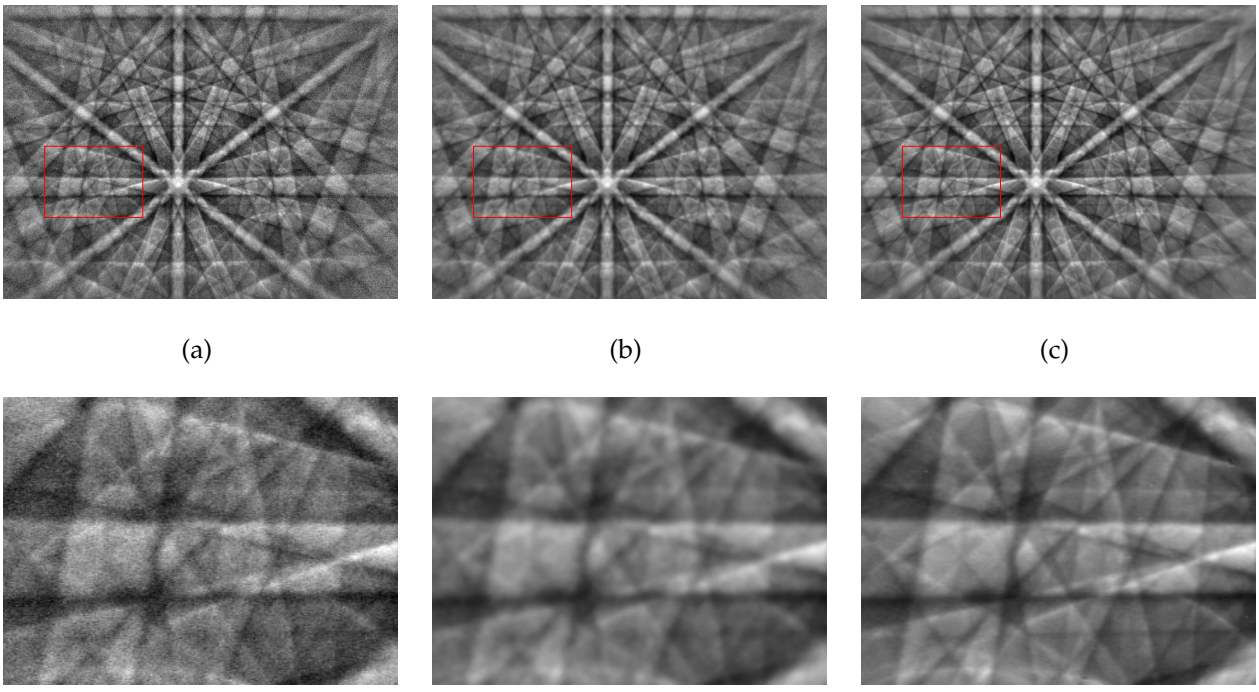

(a) (b) (c)

(d) (e) (f)

Figure 3.14: Example of noise reduction on a diffraction image. (a) Raw image. (b) Image filtered by convolution with a Gaussian kernel of length 2 pixels. (c) Denoised image with the method explained in Section 3.3.2.4. (d-f) Zooms of zones indicated by the red boxes in (a-c). It is seen that (c) and (f) show a significant decrease of noise while preserving the contrast of the Kikuchi bands.

For the flexural test on a single crystal sample, the present algorithm gives results with an uncertainty 12% lower than StrainCorrelator. The registration residual *field* shows a high sensitivity to localized phenomena.

3.4.2 Tensile test on polycrystalline sample

A more complex experiment has been performed to test the robustness of ADDICTED on an industrial material. An A316 stainless steel sample, having large grains, has been polished and subjected to an *in-situ* tensile loading inside the chamber of a Tescan Mirra SEM (Figure 3.15). The loading direction is horizontal in Figure 3.15. At first plastic straining, HR-EBSD acquisitions have been performed on a ROI focused on a triple point of the microstructure. ADDICTED has been used again to process the data. For comparison purposes, CrossCourt is also run on the same data set. The parameters are chosen to be identical for the two calculations (*i.e.*, reference image for each grain, and coordinates of projection

centers).

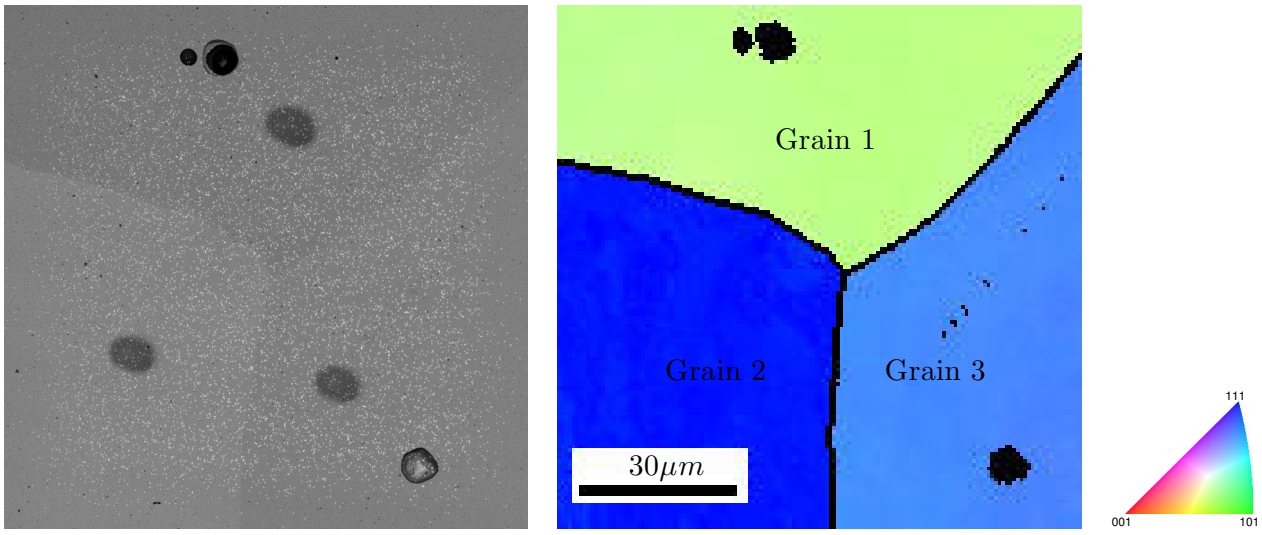

(a) (b)

Figure 3.15: Region of interest of the sample. (a) Secondary electron image. (b) Inverse pole figure obtained by standard EBSD analysis.

Figure 3.16 shows an example of integrated correlation result on two diffraction images (a-b). The same images are studied via cross-correlation (Figure 3.6). A rotation, which is not easily perceptible by naked eyes, exists between Figures 3.16(a) and 3.16(b). Yet it becomes notable when the difference between the two diffraction images is computed (Figure 3.16(c)). The 8 components of $\widehat{\boldsymbol{F}^e}$ are obtained by integrated correlation and the corresponding displacement fields are shown in Figures 3.16(e) and 3.16(f). Compared to Figure 3.6(e), the advantage of integrated correlation is noteworthy, namely, the displacement field is much richer. The rotation is intrinsically recovered by the algorithm, and does not need a "remapping" step, which is computationally costly.

Figure 3.16(g) shows the deformed image corrected by the measured displacement field, and Figure 3.16(h) the residual between Figure 3.16(a) and Figure 3.16(g). It is concluded that the dominant initial difference (Figure 3.16(c)) disappears and "phantom" bands become visible in the residual. Compared to the residuals obtained in the first example (Figure 3.13), the present residual contains more information (Figure 3.16(h)) because the sample microstructure is more complex than the single crystal studied previously. Thus the diffraction images are less sharp. For instance, single slip traces create signals in the residual field (Figures 3.13(b) and 3.13(c)). A complex industrial polycrystalline sample with more slip traces and lattice distortions will inevitably lead to more unaccounted for motions. Further,

as opposed to the previous case, it is not easy to select a stress-free point as reference and there might well be no strictly stress-free point at all.

By observing the diffraction image in Figure 3.16(i), similarities between the Kikuchi bands and the "phantom" pattern in the residual is revealed (Figure 3.16(h)). This phenomenon indicates that the "background" of diffraction images has not been acquired satisfactorily. Consequently, the diffraction signal of grain 3 is contained in the corrected diffraction images of grain 1. By analyzing the residual field provided by ADDICTED, it is possible to reveal some information that would be hidden otherwise, which is useful to construct a better "background" image.

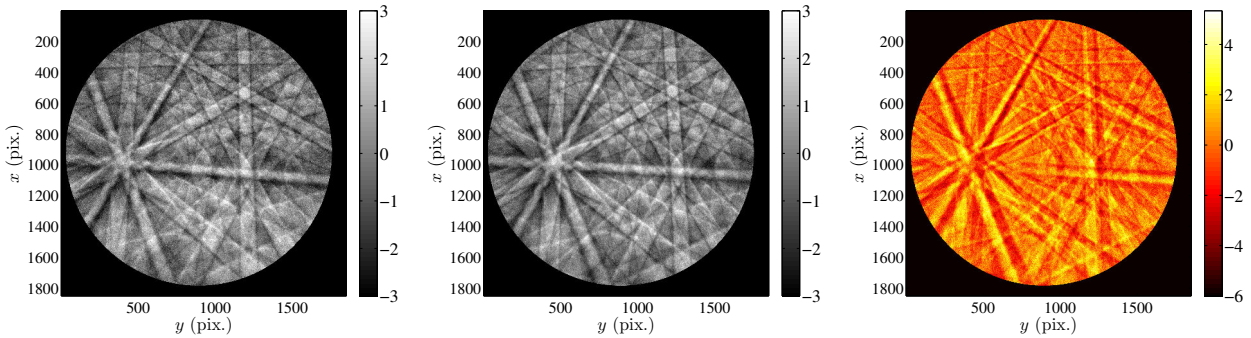

(a) Reference (b) Deformed (c) Initial difference

$\widehat{\boldsymbol{F}^e}$:

$$\begin{bmatrix} 0.9985 & -0.0342 & 0.0207 \\ 0.0355 & 1.0040 & 0.0050 \\ -0.0181 & -0.0065 & 1.0000 \end{bmatrix}$$

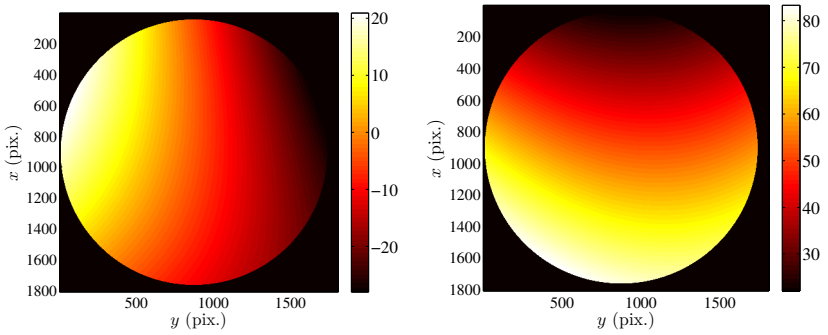

(d) Measured $\widehat{\boldsymbol{F}^e}$ (e) u_x (f) u_y

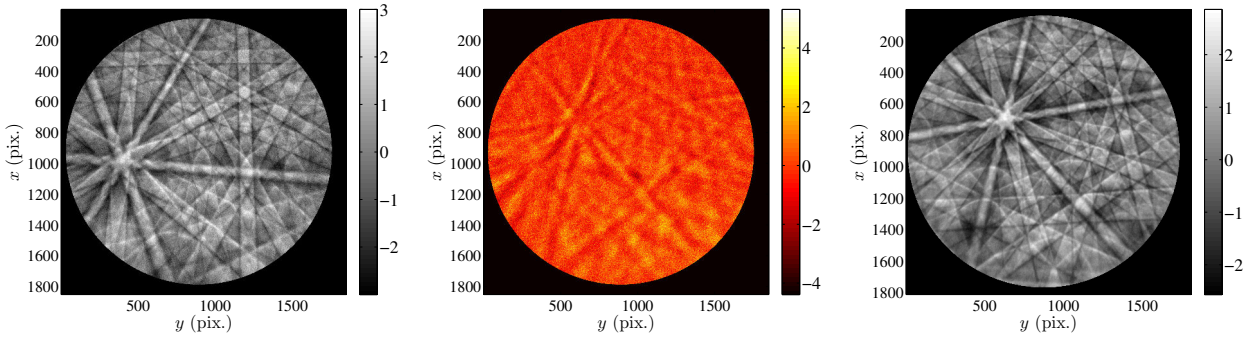

(g) Corrected deformed image (h) Residual (i)

Figure 3.16: Example of integrated correlation result. (a) Reference and (b) deformed images of grain 1. (c) Initial difference between the two images. (d) Tensor $\boldsymbol{F}^e$ obtained by integrated correlation. Displacement field component along x (e) and y (f) directions (expressed in pixels). The displacement field is to be compared with that shown in Figure 3.6(e). (g) Deformed image (b) corrected by the measured displacement field. (h) Corresponding residual (*i.e.*, difference between images (a) and (g)) (i) Diffraction image of grain 3, where the signals contained in (h) are visible.

When using ADDICTED, it is preferable to start the calculation with images near the reference point. To initialize the first integrated calculation (*i.e.*, the first "deformed" diffraction image), the identity matrix $\boldsymbol{I}$ is a good choice for $\widehat{\boldsymbol{F}^e}$, due to the assumed small strains

between those images. To initialize the calculations over other pixels, it is generally recommended to take the value of $\widehat{\boldsymbol{F}^e}$ calculated for its immediate neighbors since the strains are assumed to be close for nearby material points.

The convergence speed as a function of the calculation conditions is summarized in Table 3.1. It is concluded that Gaussian filtering of diffraction images drastically reduces the number of iterations before convergence. The smoothing with a larger kernel (2 pixels) is more efficient than a smaller one (1 pixel). The initialization with $\widehat{\boldsymbol{F}^e}$ of neighboring pixels accelerated the convergence too, especially for the calculations on unfiltered diffraction images. In terms of values of $\widehat{\boldsymbol{F}^e}$, different computation conditions do not lead to identical values, but sufficiently close, namely the standard deviation of $\widehat{\boldsymbol{F}^e}$ values is less than 10^{-4}. For the sake of computation speed, the following discussions are based on the results with diffraction images filtered with a 2-pixel Gaussian kernel and with an initialization of neighboring $\widehat{\boldsymbol{F}^e}$.

Gaussian filter	kernel of 2 pixels	kernel of 1 pixels	none
Initialized by $\boldsymbol{I}$	17	65	700
Initialized by neighboring $\widehat{\boldsymbol{F}^e}$	14	50	300

Table 3.1: Number of iterations before convergence as a function of the computation parameters

The plane stress hypothesis has been used and $\widehat{\boldsymbol{F}^e}$ is transformed into $\boldsymbol{F}^e$. The emission zone (*i.e.,* interacting with the electron beam) is about 25 nm deep, which legitimizes the plane stress hypothesis. It should be noted that this hypothesis assumes the surface normal is well known, which is generally not the case after deformation. A rough surface degrades the accuracy of HR-EBSD measurements. HR-EBSD acquisitions have been performed at the entry of plasticity thus it is legitimate to neglect the changes of topography. It is assumed that the rotation levels could be significant, yet the deformation contributions remain limited (elastic regime). Therefore it is advised to keep a finite strain formalism for $\boldsymbol{F}^e$, and calculate the rotation $\boldsymbol{R}^e$ tensor by polar decomposition

$$\boldsymbol{F}^e = \boldsymbol{V}^e \boldsymbol{R}^e \tag{3.29}$$

It has been found that the left side decomposition of $\boldsymbol{F}^e$ is more convenient to implement for HR-EBSD, since when measuring the strains of the "deformed" region, one is interested in

the strain of the crystal in the "deformed" configuration, that is the finite rotation between the reference and the current pattern is applied first, followed by an elastic distortion of the rotated crystal [Maurice et al. 2012]. Then the elastic right Cauchy Green and Green-Lagrange tensors can be computed. If the strains remain small, the left Cauchy-Green tensor reduces to

$$(\boldsymbol{V}^e)^T\boldsymbol{V}^e \simeq \boldsymbol{I} + 2\boldsymbol{\epsilon} \tag{3.30}$$

where $\boldsymbol{\epsilon}$ denotes the infinitesimal strain tensor [Maurice et al. 2012].

The Kernel Average Misorientation (KAM), or local misorientation, is a property that characterizes the local deformation level of a crystal [Wilkinson and Britton 2012]. In the present case, the KAM is defined as

$$\mathtt{KAM}_{ij} = \langle \varphi \left(\boldsymbol{R}_{ij} (\boldsymbol{R}_{neigh})^{-1} \right) \rangle \tag{3.31}$$

where $\boldsymbol{R}_{ij}$ is the rotation matrix calculated at pixel (i, j), $\boldsymbol{R}_{neigh}$ are the rotation matrices at the 4 neighboring pixels, *i.e.*, $\boldsymbol{R}_{(i-1)j}$, $\boldsymbol{R}_{(i+1)j}$, $\boldsymbol{R}_{i(j-1)}$, $\boldsymbol{R}_{i(j+1)}$, and

$$\varphi(\boldsymbol{Q}) = \mathrm{Arccos}\left(\frac{\mathrm{tr}(\boldsymbol{Q}) - 1}{2} \right) \tag{3.32}$$

is the function that links a rotation matrix $\boldsymbol{Q}$ to the misorientation angle. As illustrated in Figure 3.17(a), the KAM provided by standard EBSD analyses is too noisy to characterize a misorientation of the order of $10^{-4} - 10^{-3}$ rad. The indexing of crystallographic orientations by standard EBSD comes with an error of 0.5°. ADDICTED gives results (Figure 3.17(b)) very close to those obtained by CrossCourt (Figure 3.17(c)). The inter-granular straight traces are due to polishing artifacts/scratches, and appear in a distinct way in the two images, as highlighted by ellipses in Figures 3.17(b) and 3.17(c). Further, the kernel average misorientation is higher at grain boundaries, especially at triple points, which is consistent with predictions of dislocation pile-up [Nye 1953] and experimental observations [Caillard 1996].

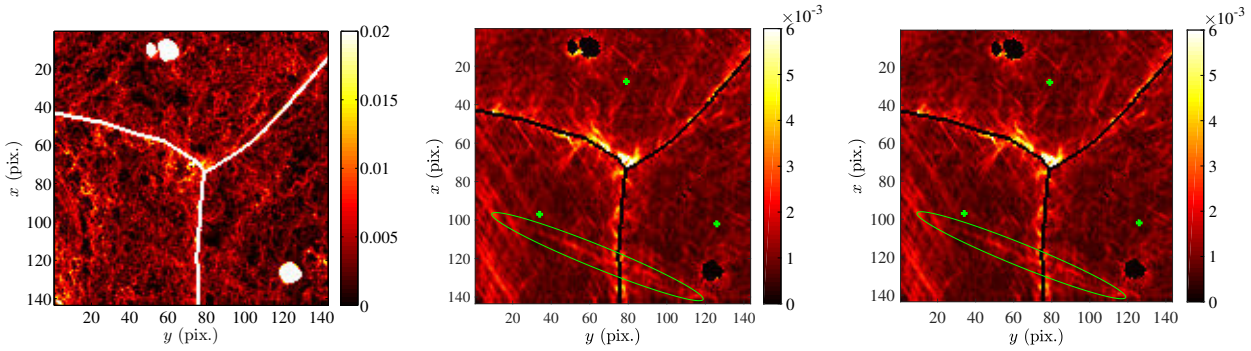

(a) (b) (c)

Figure 3.17: Kernel average misorientation obtained by (a) standard EBSD analyses, (b) ADDICTED (HR-EBSD), and (c) CrossCourt. The green crosses indicate the position of the reference diffraction images for each grain.

In the elastic regime, the complete stress tensor is calculated by Hooke's law [Plancher 2015]

$$\boldsymbol{\sigma} = J^{-1}\boldsymbol{F}^{e}\mathcal{C} : \boldsymbol{\epsilon}(\boldsymbol{F}^{e})^{\top} \tag{3.33}$$

where J is the determinant of $\boldsymbol{F}^{e}$. The elastic constants $C_{11} = 206$ GPa, $C_{12} = 133$ GPa, $C_{44} = 119$ GPa are chosen for the two algorithms [Ledbetter 1981].

The stress components obtained by CrossCourt are presented in Figure 3.18 and those obtained by ADDICTED in Figure 3.19. The component σ_{zz} is by construction vanishing and thus not presented. It is found that ADDICTED results in stress fields more homogeneous than CrossCourt. Stress discontinuities when crossing grain boundaries are also lower with ADDICTED. Besides, in order to obey the plane-stress hypothesis, the shear stress at the free surface σ_{iz} should cancel out. These shear stresses are closer to zero with ADDICTED.

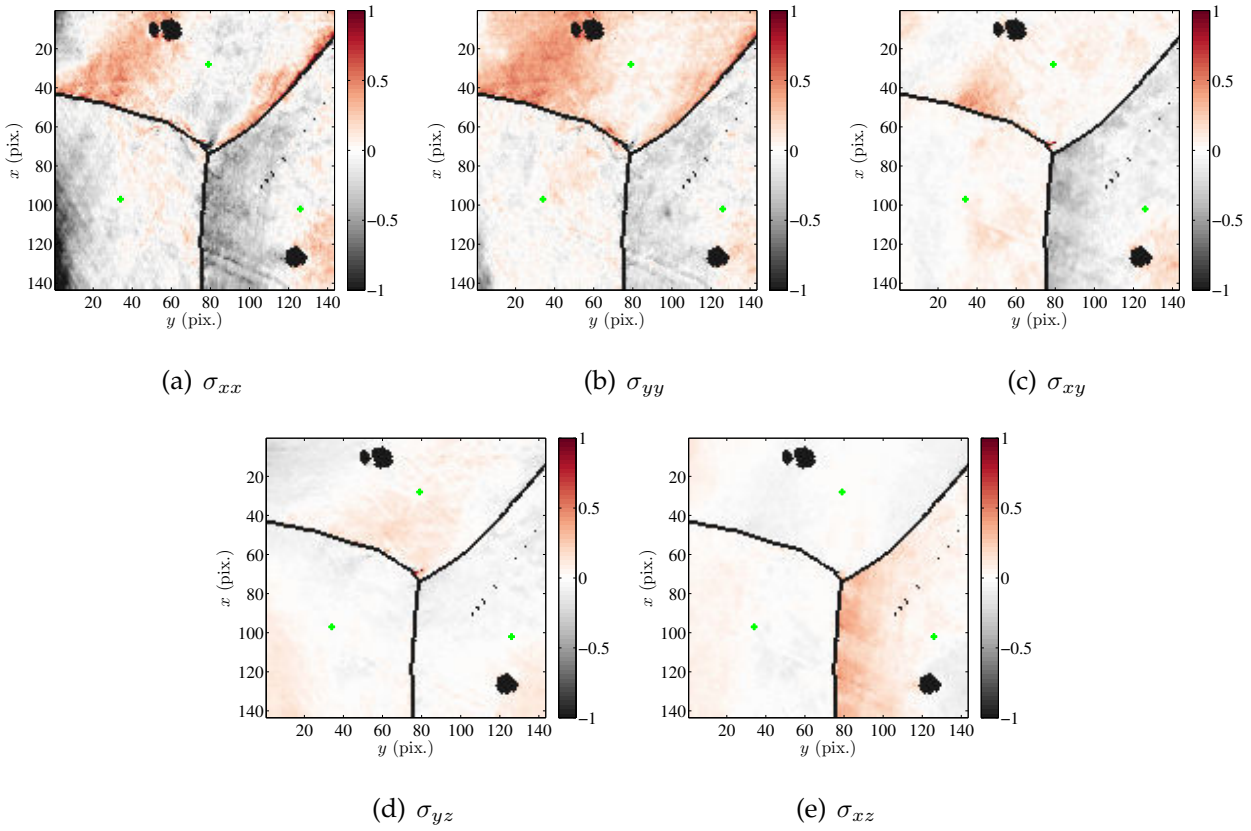

(a) σ_{xx} (b) σ_{yy} (c) σ_{xy}

(d) σ_{yz} (e) σ_{xz}

Figure 3.18: Stress tensor components (expressed in GPa) obtained by CrossCourt. (a) σ_{xx}, (b) σ_{yy}, (c) σ_{xy}, (d) σ_{yz}, (e) σ_{xz}. The component σ_{zz} is set to 0 (plane stress hypothesis), thus not shown. The green crosses indicate the position of the reference diffraction images for each grain.

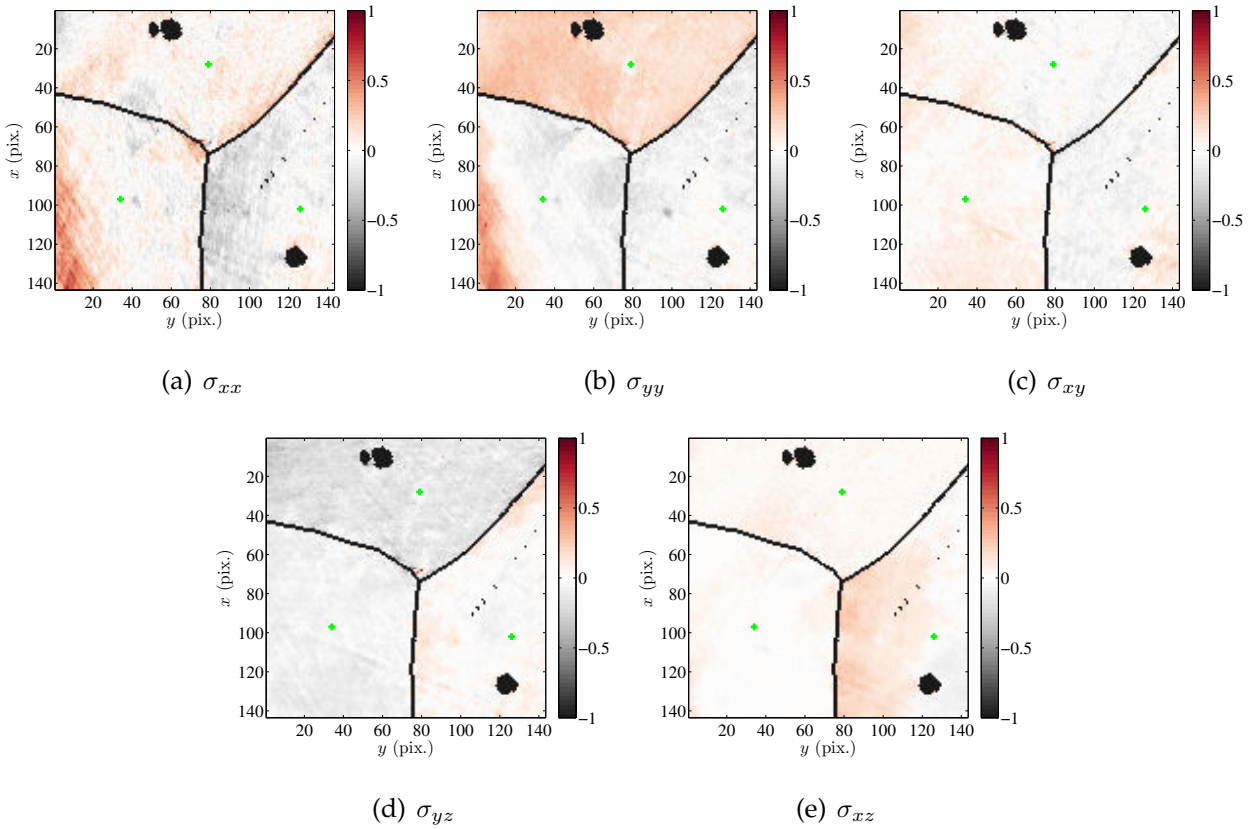

(a) σ_{xx} (b) σ_{yy} (c) σ_{xy}

(d) σ_{yz} (e) σ_{xz}

Figure 3.19: Stress tensor components (expressed in GPa) obtained by ADDICTED. (a) σ_{xx}, (b) σ_{yy}, (c) σ_{xy}, (d) σ_{yz}, (e) σ_{xz}. The component σ_{zz} is set to 0 (plane stress hypothesis), thus not shown. The green crosses indicate the position of the reference diffraction images for each grain.

Von Mises equivalent stresses are compared for ADDICTED and CrossCourt in Figure 3.20. It is concluded that the Von Mises stress field is more homogeneous and its level is lower with ADDICTED. The straight inter-granular line is always visible in the results provided by ADDICTED, contrary to those with cross-correlation, as highlighted by ellipses in Figures 3.20(a) and 3.20(b). Note that this straight inter-granular line corresponds to a scratch that goes together with a residual stress signature, so that the mark is physical and not an artifact, thus ADDICTED captures the stress level more precisely than CrossCourt. The comparison of histograms of Figure 3.20(c) and 3.20(d) indicate that the high equivalent stresses obtained by CrossCourt (*i.e.*, greater than 0.6 GPa) disappear with the present approach. These unrealistic stress levels are significantly reduced.

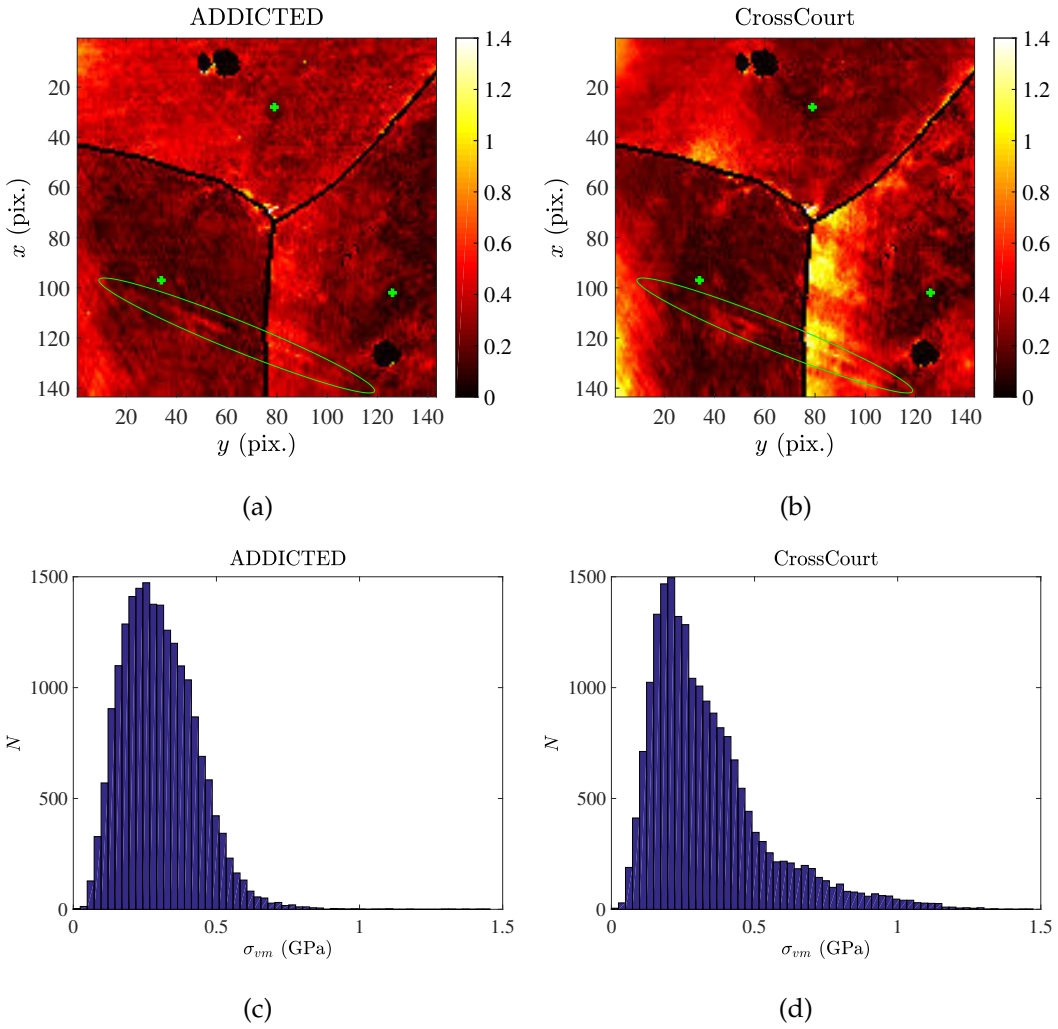

Figure 3.20: Von Mises equivalent stress (expressed in GPa) obtained by (a) ADDICTED and (b) CrossCourt softwares. The green crosses indicate the position of the reference diffraction images for each grain. (c) and (d) are the histograms of (a) and (b), respectively.

Another key point concerns the extreme value of Von Mises stress, which is 6.5 GPa for CrossCourt, and 2.7 GPa for ADDICTED. It has been checked that for the two calculations, the maximum values are reached for the same diffraction image. A lower equivalent stress also proves the better treatment of this degraded image by ADDICTED.

In terms of computation time, ADDICTED takes 40 h on an HP laptop using *two* i7 cores. On a desktop machine running *eight* i7 cores, CrossCourt takes about 40 h for the first rough cross-correlation, and 100 hours with the second cross-correlation after "*remapping*". The fact that the present algorithm reduces drastically (by about 75% compared to cross-correlation without "*remapping*", or about 90% compared to cross-correlation with "*remapping*") the computation time with an interpreted language is very encouraging to generalize and extend the technique to industrial applications.

3.5 Conclusion

This chapter has revisited the main ideas exploited in HR-EBSD and developed in the last decade in order to measure elastic strains and estimate stresses. To process diffraction images, instead of cross-correlating image subsets, integrated DIC was employed over the quasi-totality of the image, constructed directly with the most appropriate formulation of the problem, which is the geometrical projection equations of diffraction patterns onto the detector plane.

The so-called ADDICTED algorithm has the following advantages:

1. Simple implementation. The pre-rotation step (*i.e.*, "remapping") is intrinsically incorporated in ADDICTED.

2. Robustness of calculation, since the 8 components of the deformation gradient tensor are directly computed by analyzing only once the quasi-totality of the diffraction image. This property has been checked on degraded Kikuchi images. The exploitation of the studied images is complete and does not introduce spatial correlations between neighboring calculation points.

3. The strategy of global correlation also allows redundant calculations to be avoided, which is largely present with the cross-correlation method due to overlapping subsets. As a result, ADDICTED is considerably less costly in computation time (from 75% to 90% according to the test case).

4. The strategy of global correlation reduces the measurement uncertainty. For example, a reduction of 12% was obtained in the test case on a slightly deformed single crystal sample. The algorithm takes a large and unique ROI, *i.e.*, it samples once and for all large quantities of data. By drastically reducing the sampling bias of cross-correlation, ADDICTED is optimal in terms of least sensitivity to white Gaussian noise corrupting diffraction images.

5. Some optimizations of the ADDICTED calculation have been proposed, for example the application of Gaussian smoothing on the diffraction figure to attenuate the high frequency noise, and initialization of ADDICTED calculations by the results of neighboring pixels.

6. In cases of larger deformations, the transformation of Kikuchi images is not well captured by the standard image correlation method, but in theory perfectly described by the formulation based on the projection equation. A gain in accuracy is expected, resulting in a reduction of extreme stress values for the second test case.

7. The residual field of the correlation technique is intrinsically obtained by integrated DIC, while it is not naturally calculated by cross-correlation approaches. Its calculation would be very expensive because many gray level interpolations are necessary. The residual field is a good indicator of the calculation performance. The information contained in the residual can be exploited in different ways. For example, by analyzing the residuals of numerous calculations, Kikuchi images can be denoised, possible errors in the image background corresponding to Kikuchi patterns can be detected.

Last, ADDICTED, which is adapted to HR-EBSD images, could be extended to several other types of diffraction images (*e.g.*, Kossel diffraction, Laue diffraction, or TEM diffraction). These techniques derive from the same principles of projection of diffracted beams and after a simple modification, ADDICTED can be applied to those images as well. Integrated algorithms for Laue and TEM diffraction, with all the advantages cited above, will bring significant gains to their exploitations.

As illustrated by the two application cases of ADDICTED, HR-EBSD works well for samples with low residual stresses, such as a monocrystal. The results of a sample of only 3 coarse grains present already an elastic deformation field which is not fully realistic. If HR-EBSD is applied on ferritic-bainitic steel with fine grains, the results will be even more complex, possibly nonphysical. In this sense, the HR-EBSD technique is presumably not adopted for studying 16MND5 steel.

While ADDICTED provides an optimal processing algorithms for high-resolution Kikuchi images, two major challenges remain for HR-EBSD:

- the precise measurement of the projection center for every diffraction image. A specific sample holder has been designed by [Plancher 2015] that allows precise alignment of sample in SEM coordinates thus facilitates the evaluation of projection center locations. It would help if this kind of devices become commercially available;

- the simulated stress free Kikuchi figure should have a significant similarity to be registered with experimental Kikuchi figures, in order to overcome the absence of stress-free experimental diffraction images.

Should these problems be solved, HR-EBSD technique would become more robust, and capable to measure the elastic deformation of industrial fine grained metals and thus facilitate the identification of their plasticity parameters. Chapter 4 will come back to the standard EBSD technique and SE/BSE images to characterize the surface of 16MND5 sample, all along the *in-situ* tensile test.

Chapter 4

On the use of SEM correlative tools for *in-situ* mechanical tests

Reproduced from: Qiwei SHI, Stéphane ROUX, Félix LATOURTE, François HILD, Dominique LOISNARD and Nicolas BRYNAERT. On the use of SEM correlative tools for *in-situ* mechanical tests. Ultramicroscopy, January 2018, 184(Part A):71 – 87.

In-situ SEM mechanical tests are key to study crystal plasticity. In particular, imaging and diffraction (EBSD) allow microstructure and surface kinematics to be monitored all along the test. However, to get a full benefit from different modalities, it is necessary to register all images and crystallographic orientation maps from EBSD into the same frame. Different correlative approaches tracking either Pt surface markings, crystal orientations or grain boundaries, allow such registrations to be performed and displacement as well as rotation fields to be measured, a primary information for crystal plasticity identification. However, the different contrasts that are captured in different modalities and unavoidable stage motions also give rise to artifacts that are to be corrected to register the different information onto the same material points. The same image correlation tools reveal very powerful to correct such artifacts. Illustrated by an *in-situ* uniaxial tensile test performed on a bainitic-ferritic steel sample, recent advances in image correlation techniques are reviewed and shown to provide a comprehensive picture of local strain and rotation maps.

4.1 Introduction

Scanning Electron Microscopy allows contrasted images to be acquired with sub-micrometer spatial resolution at the surface of metals, using Secondary Electron (SE) imaging mode, mostly sensitive to topography. Back-Scattered Electron (BSE) imaging is sensitive to topography or chemical contrast depending on the detector configuration. The latter case is the most favorable for kinematic measurements since brightness changes due to out-of plane displacements are essentially prevented. New generations of Scanning Electron Microscopes (SEM) with field emission guns exhibit far less imaging distortions than their predecessors based on Tungsten probe technology [Sutton et al. 2007a], and are therefore very well adapted to performing digital image correlation (DIC) measurements [Sutton et al. 2007b; Guery et al. 2014; Lim et al. 2015].

Another imaging mode providing key information when studying crystal deformation is Electron Back-Scattered Diffraction (EBSD). Sensitive to crystal orientation, EBSD allows rotation fields to be tracked at the surface of a polycrystalline specimen subjected to straining (see Chapter 2). Measuring rotation and more specifically its gradients is important to address plasticity problems at the grain scale, since rotation gradients are induced by geometrically necessary dislocations involved in strain gradient plasticity models [Acharya et al. 2003; Wulfinghoff et al. 2015].

In-situ mechanical tests often rely on the combined use of BSE and EBSD images, but these two images are acquired with two different specimen configurations. The surface is normal to the electron beam for BSE images and is subsequently tilted for EBSD imaging. Matching the coordinates system of the two images is an issue seldom reported in the literature. A commonly adopted procedure is to use indent marks, which are visible in the two images, to find the transformation between the images using simple shape functions (*e.g.*, rotations, magnification changes/dilations [Héripré et al. 2007]).

Kinematic measurement by DIC requires gray level images ideally with high local contrast. Apart from natural contrast of the sample surface (*e.g.*, surface roughness), different marking techniques are available to produce a fitting artificial contrast for SEM studies, such as the deposition of microgrids by microlithography [Allais et al. 1994], random patterns generated by nanoparticle deposition techniques [Berfield et al. 2007] or UV-photolithography [Scrivens et al. 2007]. To the best knowledge of the authors, all the artificial patterns serve as contrasts in SE/BSE images, and no report exists concerning the exploita-

tion of its contrast in EBSD images. Besides, the mechanism of trace generation in EBSD images has not been investigated.

An alternative solution is to deposit *in-situ* computer-generated patterns onto the specimen surface by microlithography with a precise knowledge of the reference pattern [Guery et al. 2014]. Another advantage of the *in-situ* deposition is that the size, shape and thickness of the speckles are easily and precisely controlled by the SEM. As information depth is bigger in EBSD than SE/BSE images, and the spatial resolution of EBSD is not as good as SE/BSE images, larger and thicker speckles are necessary to create sufficient contrast in EBSD images for DIC purposes. This chapter presents a work to generate a visible random pattern in both SE/BSE and EBSD images and employs multiple correlative tools to track the pattern in these imaging modes during the *in-situ* test, thereby generating very rich experimental information about the sample.

The characterization of SEM errors is critical when images are quantitatively analyzed. Imaging distortion of SEM has been characterized by DIC [Guery et al. 2014] on samples with *in-situ* deposited speckles. Slow scan direction error in atomic force microscpy (AFM) has been quantified and corrected [Xu et al. 2008; Teyssedre et al. 2011] by capturing two images with orthogonal scan directions. A hypothesis has been made that the information acquired for each scanned line is reliable. EBSD acquisition uncertainty, both spatial distortion and orientation resolution, should be analyzed too. A detailed orientation uncertainty analysis [Venables and Bin-jaya 1977] estimates the angular resolution at $0.5°$, which has been confirmed by experimental measurements [Ram et al. 2015].

For tilted samples, distortion of EBSD images has been pointed out [Kapur and Casasent 2000; Wu et al. 2002], and a geometric transformation has been proposed to correct the distortion based on SEM images on non tilted samples. The tilt correction has since been incorporated as a basic function in standard SEMs. Trapezoidal distortion has been analyzed theoretically [Nolze 2006; 2007]. However, the uncertainty in tilt correction has not been studied.

The present study aims at coupling crystal deformation and rotation measurements of a tensile test performed *in-situ* (*i.e.*, in an SEM). Surface deformations are measured thanks to DIC [Allais et al. 1994; Hoc et al. 2003; Héripré et al. 2007] with a specific implementation already proven well adapted to polycrystals [Guery et al. 2016a]. More recently, it was shown that crystal rotation fields can also be measured on surfaces by registering EBSD images via so-called quaternion correlation (see Chapter 2). EBSD images have been overlaid manu-

ally on DIC strain map to study the relation between the texture and fatigue properties [Jin et al. 2011]. Accurate matching of the two kinds of images is necessary to describe the microstructure of polycrystals and more importantly, its changes during mechanical loadings. Rotations measured by EBSD and strains evaluated by DIC were compared [Gioacchino and da Fonseca 2015] for an austenitic steel with large grain size. Matching EBSD and BSE images was thus not mandatory in that work since only few grains were studied.

Since comparisons will be performed herein for a bainitic steel with a much finer microstructure, rotation and strain fields have to be expressed very precisely with respect to each other. The matching of BSE and EBSD images will rely on the presence of the same speckle pattern produced by lithography in the images captured with different specimen positions and detectors. Efforts will be devoted to the understanding of electronic processes leading to image capture, thereby allowing for good correlation between images acquired with different modalities, and in turn sound comparisons between plastic slip and lattice rotation. The chapter is organized as follows. Section 4.2 details the experimental procedure. Section 4.3 is dedicated to the treatment of BSE images, and Section 4.4 to that of EBSD images. Matching EBSD and BSE images and its benefit will be discussed in Section 4.5.

4.2 Experimental settings

The studied material, A508cl3 (*i.e.*, 16MND5 in French nomenclature), which is a bainitic-ferritic low-alloyed steel used in the nuclear industry, is subjected to *in-situ* uniaxial tension. Two flat tensile specimens with a gage zone of volume $10 \times 1.5 \times 1$ mm^3 are machined. For imaging and ulterior simulation purposes, sample surfaces are ground to be as plane as possible, at the same time without a hardening layer under surface. Three steps of polishing have been carried out: mechanical polishing with silk cloths and diamond suspension down to 0.25 µm to obtain a plane surface, polishing with a soft cloth and diamond suspension down to 0.1 µm to remove the hardening layer, followed by finishing with 40 nm colloidal silica suspension for 10 minutes.

A random platinum speckle has been generated and deposited *in-situ* onto the sample surface. The theoretical position of the speckles is shown in Figure 4.1(a). Note that the x direction is vertical and y direction horizontal, and the coordination origin is at the top left of the image. This convention is used in all the images of the dissertation. A platinum square of 110×110 µm^2 encompassing the speckles has also been deposited, to facilitate the sample

repositioning during the tensile test. The shape of the square also indicates intuitively the deformation, or the distortion of captured images. The diameter of the speckles is set to 300 nm and their thickness is 75 nm, as shown in Figure 4.1(b).

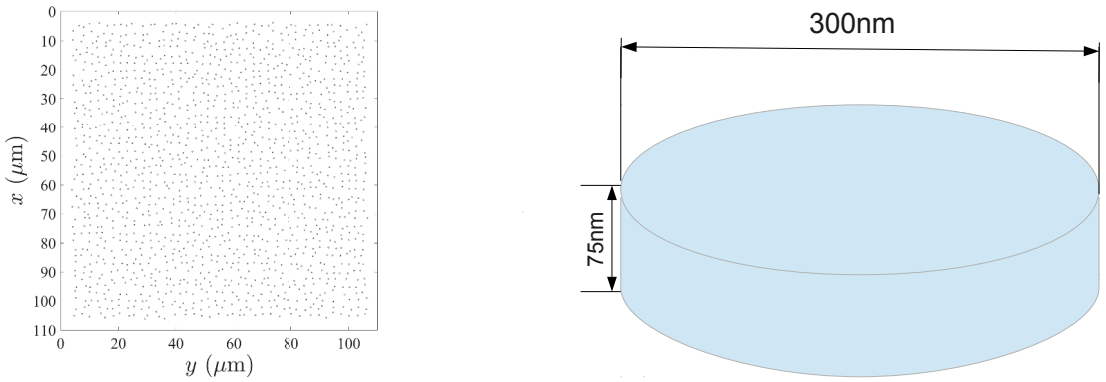

(a) (b)

Figure 4.1: (a) Theoretical positions of randomly generated speckles. (b) Size and shape of an individual speckle.

The red boxes contain extra information that was not published. The properties of several trials of speckle sizes are reported.

The speckle size is optimized prior to the test, by trial and error, to make them visible in image quality (IQ) maps and invisible in orientation maps associated with EBSD analyses. Some EBSD acquisition tests on the speckle size are shown in Figure 4.2. For tall Pt speckles, orientation indexing of underlying material is jeopardized, as shown in Figure 4.2(a). For thin Pt speckles, say 40 nm, traces in IQ image are not distinguishable enough, as shown in the lower left part of Figure 4.2(d). The speckles cover a Region of Interest of area 105×105 µm^2.

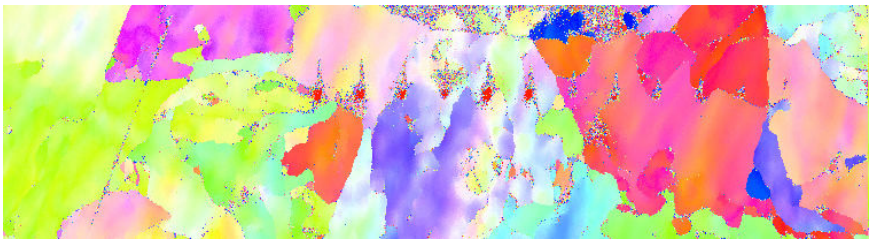

(a)

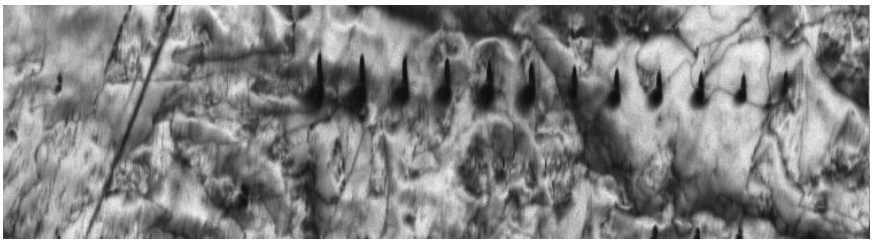

(b)

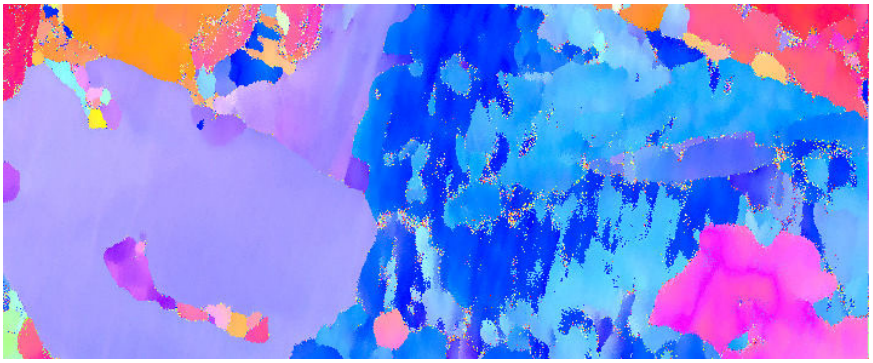

(c)

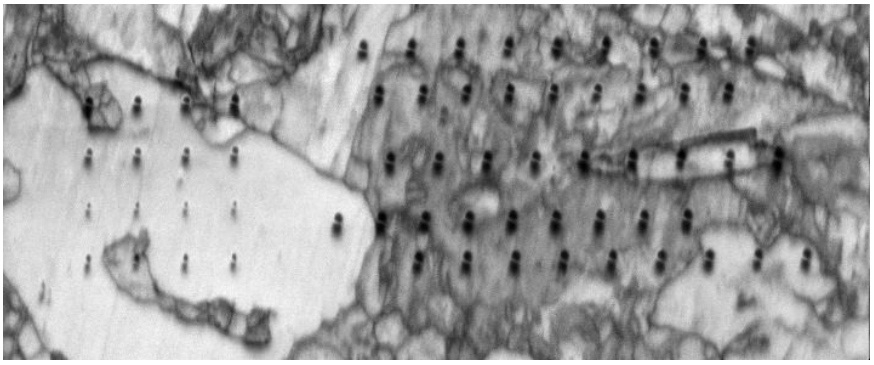

(d)

Figure 4.2: EBSD acquisitions on samples with Pt speckles of different sizes. (a) IPF image and (b) IQ image of tall Pt speckles (>500 nm). (c) IPF image and (d) IQ image of shorter Pt speckles, whose heights vary between 40 nm and 200 nm.

The SEM used in this study is of type TESCAN Mira3 600. BSE detector in Z-contrast has been used with an acceleration voltage of 30 kV and a working distance of 17 mm. The physical size of one pixel is 50 nm, which is close to the spatial resolution limit of EBSD ac-

quisitions. This very fine resolution is chosen because 16MND5 has a very fine microstructure, with 1-2 µm thick bainitic laths. The scanned area (110×110 µm^2) has a definition of 2200×2200 pixels. Two successive EBSD acquisitions have been performed for the undeformed sample and another two acquisitions for the deformed sample. Backscatter Kikuchi Pattern (BKP) size is 120×120 pixels. The diffraction pattern is imaged on a phosphor screen and the image is captured using the CCD camera (Nordif CD camera). The camera is positioned 20° from the plane formed by the normal direction of the sample and the incident beam. Each acquisition duration is about 21 h, allowing enough electrons to be collected by the EBSD detector for each scanned point. This long duration may come together with thermal drift due to temperature changes between day and night. The data obtained by EBSD acquisitions and processed with EDAX OIM™ software are used as a starting point of EBSD analyses.

An *in-situ* tensile test has been performed on the sample in the horizontal position. The macroscopic strain rate is set to 4×10^{-4} s^{-1} up to 6% longitudinal strain. Series of SE and BSE images have been acquired during the whole test. Scan rotation has been set successively to $0°$ and $90°$ for each step. The image definition is 3072×3072 pixels for a surface area of 130×130 µm^2. The images are acquired with an acceleration voltage of 30 kV and a working distance of 13 mm. It is worth noting that EBSD acquisitions necessitate a tilted configuration (surface normal inclined with respect to the SEM column by about $70°$), and are not accessible during the *in-situ* tensile test.

Let us mention that another strategy was tested to facilitate the registration of EBSD and surface imaging. The mechanical stage was positioned so that the sample surface remained inclined at about $70°$ (as required for EBSD acquisition) during the entire test. The tilt correction of the SEM was used to revert to in-plane coordinates. In this way a series of EBSD acquisitions and SE images were taken along the test.

4.3 Analysis of SEM images

The red boxes contain extra information that was not published. The results of in-situ tensile test on tilted sample are discussed.

The two series of SEM images (SE, BSE) acquired during two *in-situ* tensile tests are first analyzed. A rich kinematic information is revealed by DIC on SEM images. However, DIC can also be used to reveal artifacts.

4.3.1 SEM tilt correction error on inclined sample

In this tensile test the sample is tilted at 70° with the y-axis being the tilt axis and the tensile direction. Secondary electron images were acquired at different stages of loading, and the tilt correction of the SEM was used to correct the inclination. The initially flat surface develops a significant roughness due to plastic flow. This roughness is the prominent features used to register images. Although DIC from single-point-of-view images does not account for roughness changes, it can be used to capture incremental displacements as shown in Figure 4.3 and 4.4.

Figure 4.3(a) shows the image obtained after 0.5% macroscopic strain, chosen as the reference image, and Figure 4.3(b), after 2.0% macroscopic strain, as the deformed image. Figure 4.4(a) shows the image obtained after 5.4% macroscopic strain and arbitrarily chosen as the reference image and Figure 4.4(b), after 6% macroscopic strain, as the deformed image. DIC was performed with an unstructured mesh composed of elements of size 20 pixels and the elastic regularization length was reduced gradually from 200 to 50 pixels [Tomičević et al. 2013]. The gray level residual fields after registration are shown in Figure 4.3(c) and 4.4(c) respectively. This residual shows that most features of the initial image have been erased. However as no gray level corrections are included, the residual shows gray level differences that can be interpreted as surface slope changes (i.e. roughness evolution). Some localized scars can be attributed to shadowing effects due to the grazing incidence of the electron beam. In the center of Figure 4.4(c), two concentric squares correspond to pollution of a region scanned for refocusing the electron beam after tensile loading. Thus from those residuals, DIC is deemed trustworthy.

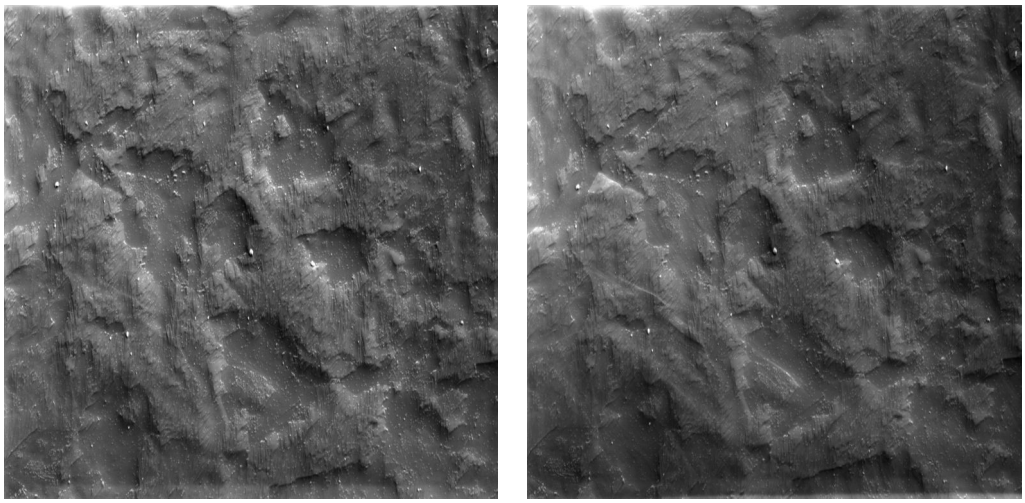

(a) Reference image (b) Deformed image

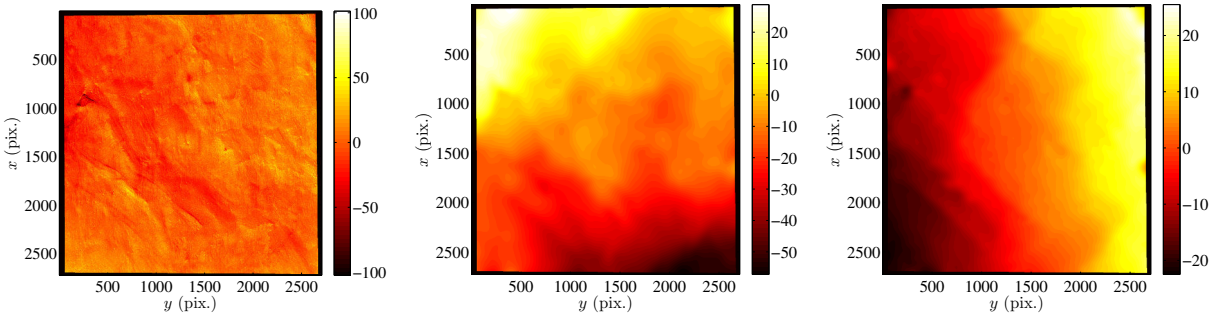

(c) (d) U_x (pixels) (e) U_y (pixels)

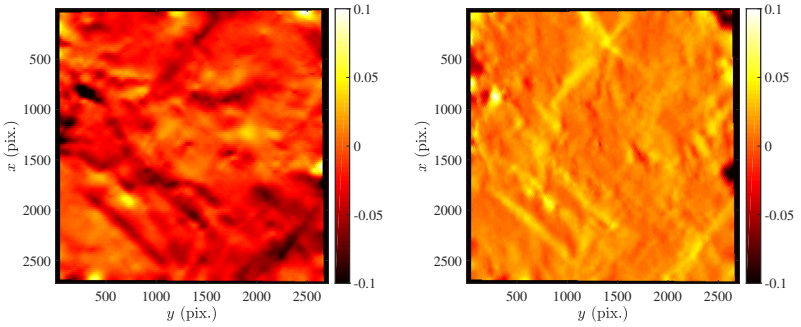

(f) ϵ_{xx} (g) ϵ_{yy}

Figure 4.3: DIC result on 2 SEM images of tilted sample. (a) SEM image of 0.6% macroscopic strain, used as reference image. (b) SEM image of 1.8% macroscopic strain, used as deformed image. (c) Gray level residual. Displacement fields between the two images in x and y directions are shown in (d) and (e) respectively. Strain field ϵ_{xx} and ϵ_{yy} between the two images are shown in (f) and (g) respectively. 1 pixel = 26 nm.

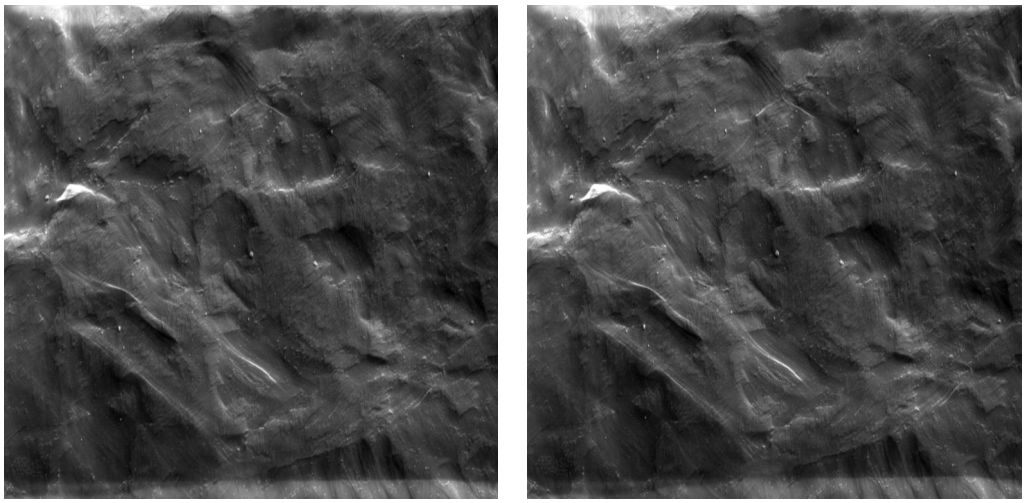

(a) Reference image (b) Deformed image

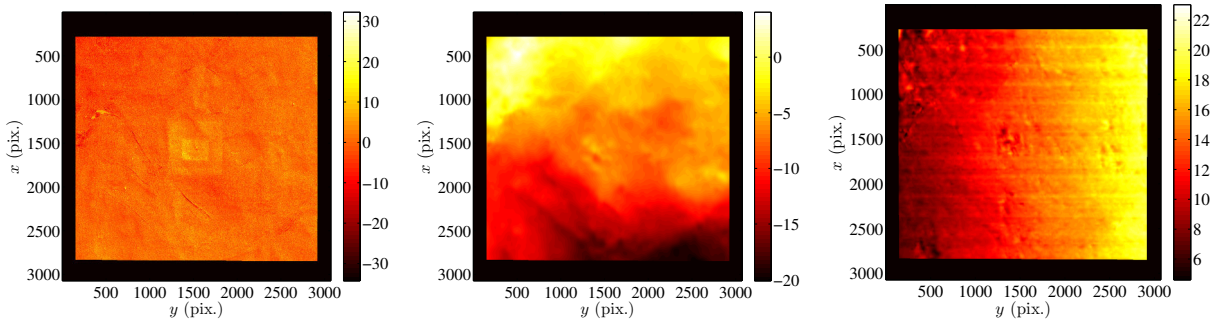

(c) (d) U_x (pixels) (e) U_y (pixels)

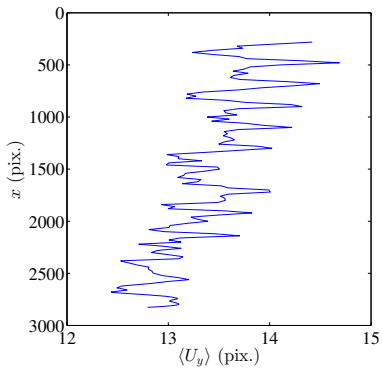

(f)

Figure 4.4: DIC result for another pair of SEM images of tilted sample. (a) SEM image of 5.4% macroscopic strain, used as reference image. (b) SEM image of 6.0% macroscopic strain, used as deformed image. (c) Gray level residual. Displacement field between the two images in x and y directions are shown in (d) and (e) respectively. (f) Average U_y value row by row. 1 pixel = 26 nm.

Figures 4.3(d), 4.3(e), 4.4(d) and 4.4(e) show the two components of the estimated dis-

placement field for the two incremental calculations. The U_x field looks trustworthy in both calculations, so does U_y in Figure 4.3(e). However, the displacement field U_y in Figure 4.4(e) displays many horizontal stripes that cannot be due to the plastic deformation. To further investigate this point, the profile of $\langle U_y(x) \rangle$ averaged row by row (along y) is shown in Figure 4.4(f). This profile exhibits an almost periodic pattern (period of about 200 pixels) of amplitude close to 1 pixel. The amplitude decreases to around 0.5 pixel in the lower half of the region. This may be due to degraded focus of the incident beam for the lower part of image, as the sample is tilted and the working distance varies during the scan. These observations are consistent with the assumption that the tilt correction is rounded at integer values. Our interpretation is that the tilt correction of the SEM is satisfactory for producing images for easy reading, but do not achieve subpixel fidelity. This is unfortunate as the U_x map shows that the instrument by itself has the capability of producing quantitative images that can be exploited at sub-pixel resolution (because the y direction is not affected by tilt corrections).

Another difficulty is related to the measured strain in x and y directions. In both calculations ϵ_{yy} are positive and ϵ_{xx} negative, in line with the fact that tension was aligned with the y direction. However, the absolute value of ϵ_{xx} is larger than that of ϵ_{yy}, as shown in Figure 4.3(f) and 4.3(g), indicating that the Poisson's ratio of the material is surprisingly larger than 1. A possible explanation to this presumably spurious observation is that the tilt correction functionality over-corrects tilt, perhaps due to the real tilt angle being less than 70°, which will be demonstrated in Section 5.2. Another possible explanation is that the specimen becomes more tilted as the tensile test goes on, and the constant tilt correction based on 70° fails to correct all the tilt effect. A simple test will validate this hypothesis (or not): take an additional SEM image with the sample in horizontal position and see if the image is consistent with the tilt correction.

Today a full DIC analysis cannot be carried out successfully because of unnecessary acquisition simplification (rounding errors). For these reasons, in the sequel, the tensile test on the tilted sample was discarded, and all further discussion deals with the test where the specimen was not tilted.

4.3.2 SEM scan orientation artifacts

According to previous studies, images acquired by scanning microscopy, *e.g.*, electron microscopy [Sutton et al. 2007b;a] and atomic force microscopy (AFM) may suffer from distor-

tions/scan drift, especially in the slow scan direction [Garnaes et al. 1998]. To assess such distortions it has been proposed to capture images in different scan directions [Sun and Pang 2006], and to combine them, relying on fast scan lines, to get an image corrected from such line to line artifacts [Teyssedre et al. 2011]. In this last reference, artificial strains due to such slow scan drift was observed to reach 16% for AFM images.

In the present experiment, all SEM images are taken with a scan rotation of $0°$ and $90°$ to correct for potential direction-related distortions. For all images with a scan rotation of $0°$, the 'fast' scan direction is y and lines at increasing x positions are progressively accumulated (x is said to be the 'slow' scan direction). Conversely, for the scan rotation of $90°$, the fast scan direction is x and line data are collected at increasing y coordinates. As a result, images taken with scan rotations $0°$ and $90°$ are comparable only after rotating an image by $90°$. Figures 4.5(a) and 4.5(b) show the BSE images of the reference state of the sample. Figure 4.5(c) shows the $90°$ acquisition (Figure 4.5(b)) exactly rotated by an angle of $90°$ anti-clock wise. The difference between Figures 4.5(a) and 4.5(c) is hardly detectable with bare eyes.

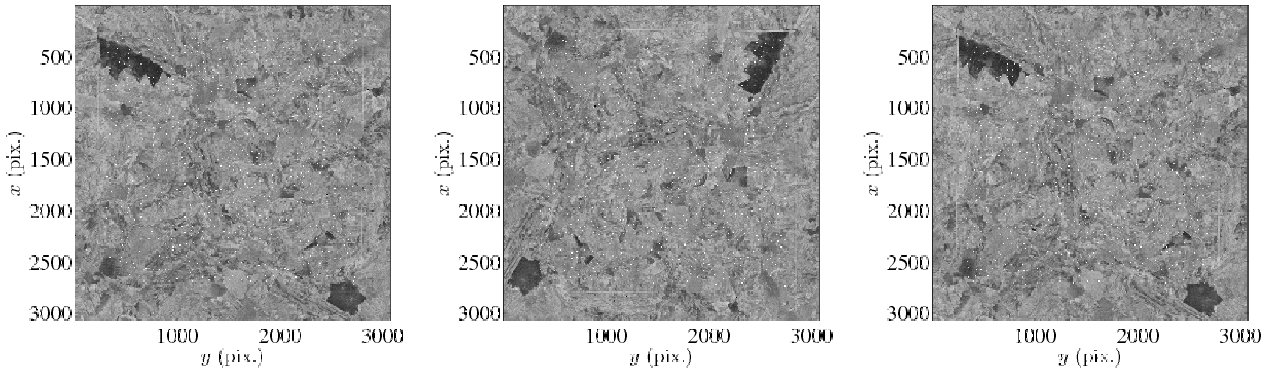

(a) $0°$-scan image (b) $90°$-scan image (c) Rotated $90°$-scan image

Figure 4.5: BSE images of the sample in the reference configuration acquired with a scan direction of (a) $0°$ and (b) $90°$. (c) Numerically rotated image (b) by $90°$ anti-clockwise. The pixel size is 42 nm for all images

DIC has been run to register images acquired with different scan directions (Figures 4.5(a) and 4.5(c)). Triangular elements with characteristic length of 25 pixels are adopted, and the regularization length is set to 200 pixels to reduce the measurement uncertainty as the spatial resolution is not an issue herein.

An example of DIC result with the BSE images of the reference state is shown in Figure 4.6. Figure 4.6(a) shows the raw difference between Figures 4.5(a) and 4.5(c), for which a clear difference is observed. A small region in Figure 4.6(a) is free of speckles, while in its

neighborhood speckles gradually appear. This phenomenon implies a slight yet persistent distortion between the two studied images. Figure 4.6(b) shows the gray level residual field at convergence of the DIC routine. Although some patterns can still be seen, the level of residuals has been greatly decreased from the initial difference. The histogram is shown in Figure 4.6(c).

This registration is achieved for a very large amplitude of apparent displacement field in both x and y directions, as shown in Figures 4.6(d) and 4.6(e). The most salient property of the displacement field is the fact that the x axis is more or less uniformly stretched by 1% whereas the y axis shows a similar uniform contraction of about -1%. This observation suggests that pixels are in fact elongated to rectangles along the slow scan direction, whatever the scan direction (0° or 90°). To get a more precise appreciation of these distortions, it is interesting to compute the strains from the apparent displacement field, as shown in Figures 4.6(f), 4.6(g) and 4.6(h). ϵ_{xx} and ϵ_{yy} show marked horizontal and vertical stripes respectively, while a 'tartan' fabric pattern is visible in ϵ_{xy} field. In agreement with the previous observation, the dominant strain is a stretch (respectively contraction) of about 1% along the x (resp. the y) direction, as can be seen from the average values of the corresponding strain components.

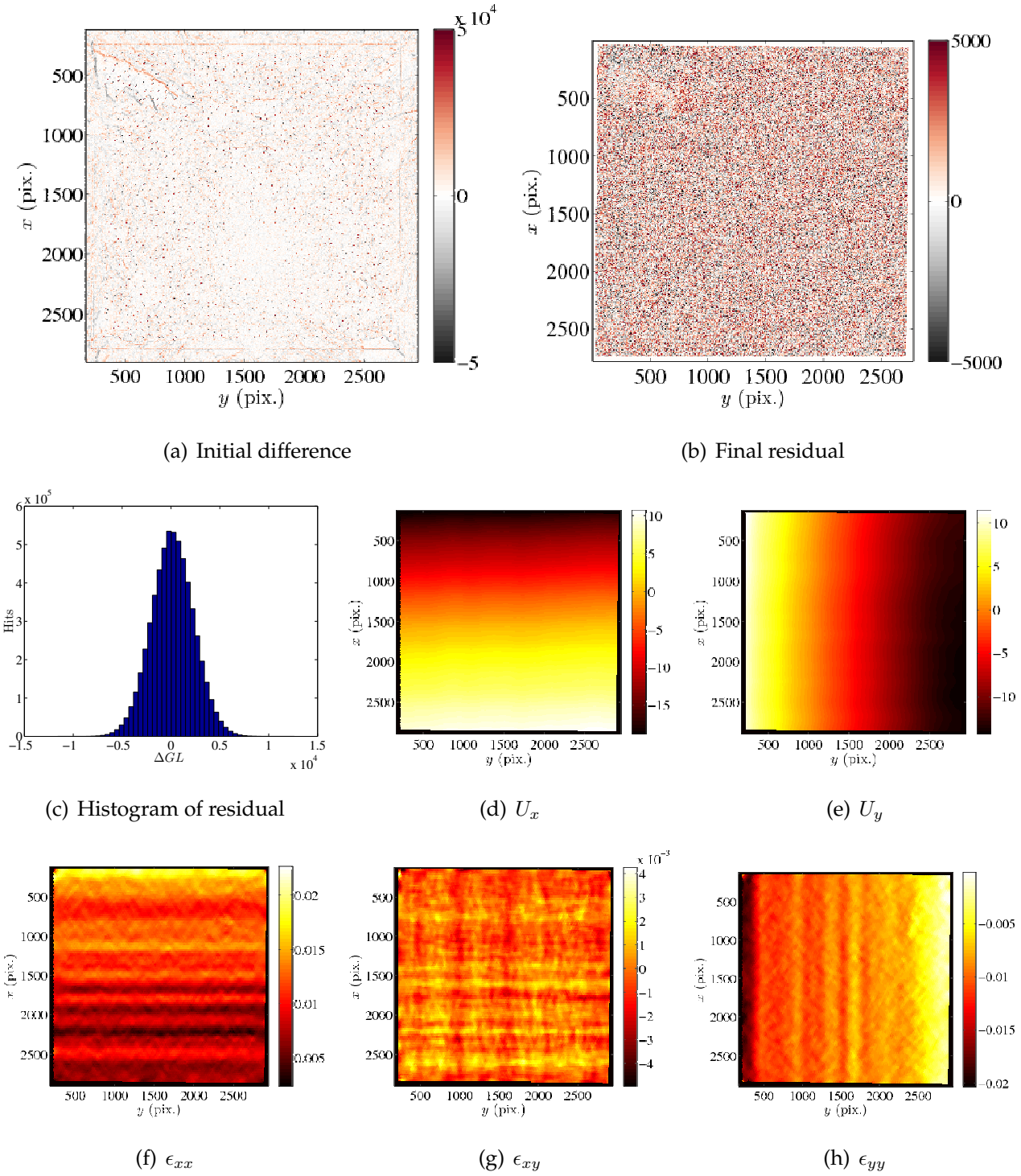

(a) Initial difference

(b) Final residual

(c) Histogram of residual

(d) U_x

(e) U_y

(f) ϵ_{xx}

(g) ϵ_{xy}

(h) ϵ_{yy}

Figure 4.6: DIC results for BSE images of the reference state acquired with rotated $0°$-scan and $90°$-scan (Figure 4.5). (a) Initial difference between the two images. (b) Corresponding residual field at convergence. A 'grid' like pattern is visible. (c) Histogram of the gray level residual. (d,e) Displacement field in x and y directions (expressed in pixels). (f-h) Strain fields. The pixel size is 42 nm for all images

The remarkable and specific patterns exhibited by the strain field can be explained by

the fact that SEMs control the electron beam more precisely in the fast scan direction, while the position of the starting point of the next scanned line is less accurate. Consequently, the spacing error between scanned lines induces bands in ϵ_{xx} and ϵ_{yy} fields and the incorrect alignment leads to the grid in ϵ_{xy} field. Following Ref. [Teyssedre et al. 2011], it is proposed to combine images acquired with different scan directions so that each fast-scan line is preserved untouched but may be repositioned at a slightly corrected starting point. This procedure, which revealed successful for AFM images, is here applied to register the above different scan orientation images.

4.3.3 SEM slow scan error correction

The correction procedure is based on the hypothesis that the fast-scan direction is correct in SEM images [Teyssedre et al. 2011]. Let $\phi(\boldsymbol{x})$ be the undistorted image, which is unknown. Image f_1 is captured with a fast-scan direction along the x-axis, and image f_2 captured along the y-axis. Thus each line $f_1(.,y)$ and $f_2(x,.)$ is considered exact. For the first image, when the incident beam moves to the start position of the next line, it is assumed that a repositioning error exists with components u_x and u_y in the sample surface plane. The two components u_i of the displacement are assumed to only depend on the slow scan direction y. Similarly for image 2, each line is repositioned with a displacement $\boldsymbol{v}(x)$. This is expressed as

$$\begin{aligned} f_1[\boldsymbol{x} + \boldsymbol{u}(y)] &= \phi(\boldsymbol{x}) \\ f_2[\boldsymbol{x} + \boldsymbol{v}(x)] &= \phi(\boldsymbol{x}) \end{aligned} \tag{4.1}$$

where $\boldsymbol{u} = (u_x, u_y)$ and $\boldsymbol{v} = (v_x, v_y)$ are two unknown vector profiles. The correct fast-scan hypothesis and the applied slow scan error correction $\boldsymbol{u}$ are illustrated in Figure 4.7.

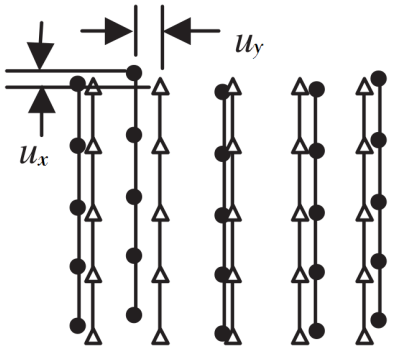

Figure 4.7: Illustration of slow scan error of SEM. The columns of triangles indicate the theoretical scanning points of SEM (for figure $\phi(\boldsymbol{x})$), while the columns of black dots show the experimental SEM scanning points (for figure $f_1(\boldsymbol{x})$). A spacing distance of (u_x, u_y) exists between those scanning points.

The objective of the procedure is to estimate ϕ from f_1 and f_2 as well as the displacements $\boldsymbol{u}$ and $\boldsymbol{v}$. Equation (4.1) belongs to the global DIC techniques, with the specific difficulty of unknown reference ϕ.

The red boxes contain extra information that was not published. The detailed process of SEM slow scan error correction is reported.

A similar strategy has been proposed to solve the problem and the unknown one-dimensional displacement fields $\boldsymbol{u}$ and $\boldsymbol{v}$ are represented by a functional basis

$$\begin{aligned} u_i(x) &= a_i^j \Phi_j(x) \\ v_i(x) &= b_i^j \Phi_j(x) \end{aligned} \tag{4.2}$$

$$\begin{aligned} \tilde{f}_1(\boldsymbol{x}) &= f_1[\boldsymbol{x} + \boldsymbol{u}(x_2)] \approx \phi(\boldsymbol{x}) \\ \tilde{f}_2(\boldsymbol{x}) &= f_2[\boldsymbol{x} + \boldsymbol{v}(x_1)] \approx \phi(\boldsymbol{x}) \end{aligned} \tag{4.3}$$

The function Φ_j is chosen as continuous piecewise linear

$$\Phi_j(x) = \frac{max(0, 1 - |x - x_j|)}{\ell} \tag{4.4}$$

for a uniform distribution of nodes x_j separated by distance ℓ. Another choice for Φ_j is using Fourier series

$$\begin{aligned} \Phi_0(x) &= x \\ \Phi_{2k-1}(x) &= \cos(2k\pi x) \\ \Phi_{2k}(x) &= \sin(2k\pi x) \end{aligned} \tag{4.5}$$

When the Fourier series is truncated, i.e., a limited number of modes is used, a linear basis $\Phi_0(x) = x$ helps to complete the basis functions. The element size ℓ and maximum Fourier wavenumber $2k$ are free parameters that control the regularization of the problem. Then the nodal values $(\{\boldsymbol{a}\}, \{\boldsymbol{b}\})$ are sought, and further used to construct the reference image $\phi(\boldsymbol{x})$.

In total, for an image of $n \times n$ pixels, the total degree of freedom using linear basis functions is $4(n/\ell + 1)$, which is much fewer than the data (n^2). A weak form has to be introduced as the minimization of the quadratic differences

$$\Im[\boldsymbol{u}, \boldsymbol{v}] = \sum \{f_1[\boldsymbol{x} + \boldsymbol{u}(x_2)] - f_2[\boldsymbol{x} + \boldsymbol{v}(x_1)]\}^2 \tag{4.6}$$

Additionally, a multi-scale procedure helps accounting for large displacements. Images are first coarsened (and reduced in size) to perform the registration, and the obtained displacement is used as an initialization of the same analysis performed on a finer resolution, and this procedure is repeated down to the original scale [Zhang et al. 2006]. Image coarsening consists of a pyramidal construction where each level is a coarse image with super-pixel obtained by averaging 4 pixels of the finer image. This procedure allows for an artificial broadening of the "well" of cost function at the corresponding solution, and diminishes the possibility of being trapped in a local minimum. In the end the original images are used to get the final results.

At each level of the pyramid, the minimization problem is linearized through a Taylor expansion of the images f_1 and f_2 over the present position value. So the cost function at step n is approximated as

$$\Im^{(n)}[\boldsymbol{du}, \boldsymbol{dv}] = \sum [f_1(\boldsymbol{x}) + \boldsymbol{du}(x_2).\boldsymbol{\nabla} f_1^{(n)}(\boldsymbol{x}) - f_2(\boldsymbol{x}) - \boldsymbol{dv}(x_1).\boldsymbol{\nabla} f_2^{(n)}(\boldsymbol{x})]^2 \tag{4.7}$$

writing $\boldsymbol{G}_1 = \boldsymbol{\nabla} f_1$, $\boldsymbol{G}_2 = \boldsymbol{\nabla} f_2$, $\boldsymbol{du} = \sum_i \boldsymbol{da}_i \Phi_i(x_2)$, $\boldsymbol{dv} = \sum_i \boldsymbol{db}_i \Phi_i(x_1)$, optimality with respect to $\boldsymbol{a}_i$ reads

$$\begin{aligned} \tfrac{\partial \Im[\boldsymbol{du}, \boldsymbol{dv}]}{\partial a_i} &= 2 \sum \left(f_1^{(n)}(\boldsymbol{x}) - f_2^{(n)}(\boldsymbol{x}) + \boldsymbol{a}_j \Phi_j(x_2).\boldsymbol{G}_1(\boldsymbol{x}) - \boldsymbol{b}_k \Phi_k(x_1).\boldsymbol{G}_2(\boldsymbol{x}) \right) \Phi_i(x_2).\boldsymbol{G}_1(\boldsymbol{x}) \\ &= 0 \end{aligned} \tag{4.8}$$

where Einstein summation notation is adopted. Hence

$$\begin{aligned}&\boldsymbol{a}_j \sum \Phi_j(x_2).\boldsymbol{G}_1(\boldsymbol{x}) \otimes \boldsymbol{G}_1(\boldsymbol{x})\Phi_i(x_2) - \boldsymbol{b}_k \sum \Phi_k(x_1).\boldsymbol{G}_2(\boldsymbol{x}) \otimes \boldsymbol{G}_1(\boldsymbol{x})\Phi_i(x_2)\\&= \sum \left(f_2^{(n)}(\boldsymbol{x}) - f_1^{(n)}(\boldsymbol{x})\right) \Phi_i(x_2).\boldsymbol{G}_1(\boldsymbol{x})\end{aligned} \tag{4.9}$$

where the notation $\boldsymbol{a}_i$ stands for the two components vector of u_1 and u_2 at the nodal point x_i. Similarly with respect to $\boldsymbol{b}_i$

$$\begin{aligned}&\boldsymbol{a}_j \sum \Phi_j(x_2).\boldsymbol{G}_1(\boldsymbol{x}) \otimes \boldsymbol{G}_2(\boldsymbol{x})\Phi_i(x_1) - \boldsymbol{b}_k \sum \Phi_k(x_1).\boldsymbol{G}_2(\boldsymbol{x}) \otimes \boldsymbol{G}_2(\boldsymbol{x})\Phi_i(x_1)\\&= \sum \left(f_1^{(n)}(\boldsymbol{x}) - f_2^{(n)}(\boldsymbol{x})\right) \Phi_i(x_1).\boldsymbol{G}_2(\boldsymbol{x})\end{aligned} \tag{4.10}$$

It has been proposed to solve iteratively $\boldsymbol{a}_j$ by Equation (4.9), neglecting the $\boldsymbol{b}$ term and solve $\boldsymbol{b}_j$ by Equation (4.10), neglecting the $\boldsymbol{a}$ term [Teyssedre et al. 2011]. Even if not optimal, it is a convenient resolution strategy. At each level of the coarsening pyramid the convergence is reached when the incremental variation of the parameters $(\boldsymbol{a}, \boldsymbol{b})$ is less than a small parameter ε.

Once completed, the displacement field $\boldsymbol{u}$ and $\boldsymbol{v}$ for f_1 and f_2 are obtained, thus corrected images $\tilde{f}_1$ and $\tilde{f}_2$ are available. The estimate of the exact image is given by

$$\phi(\boldsymbol{x}) \approx \frac{1}{2}\left[\tilde{f}_1(\boldsymbol{x}) + \tilde{f}_2(\boldsymbol{x})\right] \tag{4.11}$$

Figure 4.8 shows the correction results for the undeformed state. The displacement was decomposed over 50 Fourier modes (this is an arbitrary choice but other discretizations provide very similar results). The analysis requires less than 2 hours for 3072×3072-pixel images on a PC with i7 CPU and 32 Gb of memory.

Figure 4.8(g) shows the residual field of the slow-scan error correction procedure. No original image features are clearly apparent and hence the registration procedure is deemed trustworthy. It is worth noting that residuals are very significantly decreased as compared to the previous approach, because the effect of artifacts is more precisely formulated. Figures 4.8(a) and 4.8(b) show the x and y components of the displacement fields $\boldsymbol{u}$ between image $f_1(\boldsymbol{x})$ and the best achieved compromise $\phi(\boldsymbol{x})$.

Figure 4.8(c) shows $\partial_x u_x$, which is comparable to ϵ_{xx} shown in Figure 4.6(f). Similarly, Figures 4.8(d) and 4.8(e) show the x and y components of the displacement field $\boldsymbol{v}$ between image $f_2(\boldsymbol{x})$ and $\phi(\boldsymbol{x})$. Figure 4.8(f) shows $-\partial_y v_y$, which is comparable to ϵ_{yy} shown in Figure 4.6(f). Under a small strain assumption, the difference between these two fields, $\boldsymbol{u} - \boldsymbol{v}$, should be comparable to the previous standard DIC displacement field shown in Figure 4.6. It is observed that the agreement is quite satisfactory. All the bands in the strain field are

well captured by the slow-scan error correction procedure. This result validates the previous DIC approach, but also indicates that the present approach is more reliable (*i.e.,* showing smaller residual levels). The mean gradients of $\boldsymbol{u}$ and $\boldsymbol{v}$ are respectively 1.12%, and 1.07%, in very good agreement with the previous determination of about 1% mismatch between fast and slow scan directions.

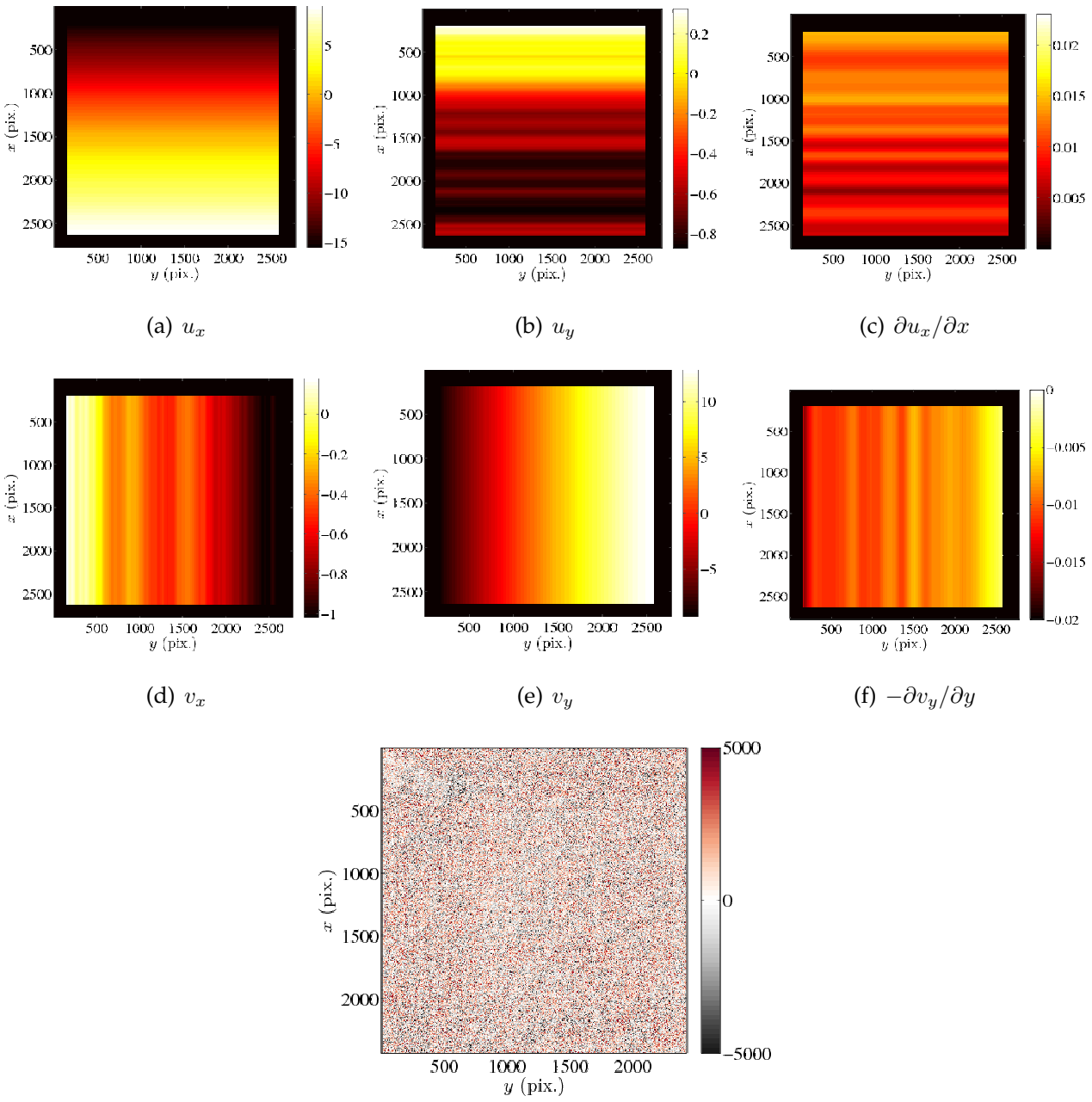

(a) u_x (b) u_y (c) $\partial u_x/\partial x$

(d) v_x (e) v_y (f) $-\partial v_y/\partial y$

(g)

Figure 4.8: DIC results for the correction of BSE images f_1 and f_2 for the initial state. (a-b) Displacement field in x and y directions between image f_1 and the corrected image. (c) Gradient of figure (a) in x direction. (d-e) Displacement field in x and y directions between image f_2 and the corrected image. (f) Gradient of figure (e) in y direction. (g) Residual field $f_1(\boldsymbol{x}+\boldsymbol{u}) - f_2(\boldsymbol{x}+\boldsymbol{v})$. The pixel size is 42 nm for all images

The above procedure confirms the existence of scan drift in SEM images, although less marked than for AFM acquisitions [Teyssedre et al. 2011]. This effect should be taken into consideration if accurate strain and displacement measurements are sought, but at the extra

cost of a double acquisition along two perpendicular scan directions. However, it should be noted that the resulting error in measuring strains is the product of the true strain and the spurious one due to scanning. In the present case, accepting a relative 1% inaccuracy in the local strain, *i.e.*, of order 6×10^{-4} uncertainty, one can consider that the BSE images can be trusted.

4.3.4 Registration of SEM images

DIC has been run on all BSE images acquired during the *in-situ* tensile test and the change of displacement fields u_x and u_y, strain fields ϵ_{xx} and ϵ_{yy} are shown in Figure 4.9, Figure 4.10, Figure 4.11 and Figure 4.12 respectively. Finite deformation theory has been adopted and the strain tensor is computed as the Green-Lagrange tensor where y is the tensile direction. From ϵ_{xx} and ϵ_{yy} changes it is concluded that the strain concentration/localization patterns revealed at the onset of plasticity do not change subsequently. This trend is confirmed by previous work on 304L stainless steel [Gioacchino and da Fonseca 2015]. The strain patterns are also consistent with slip traces at the specimen surface, inclined at $45°$ with respect to the loading direction.

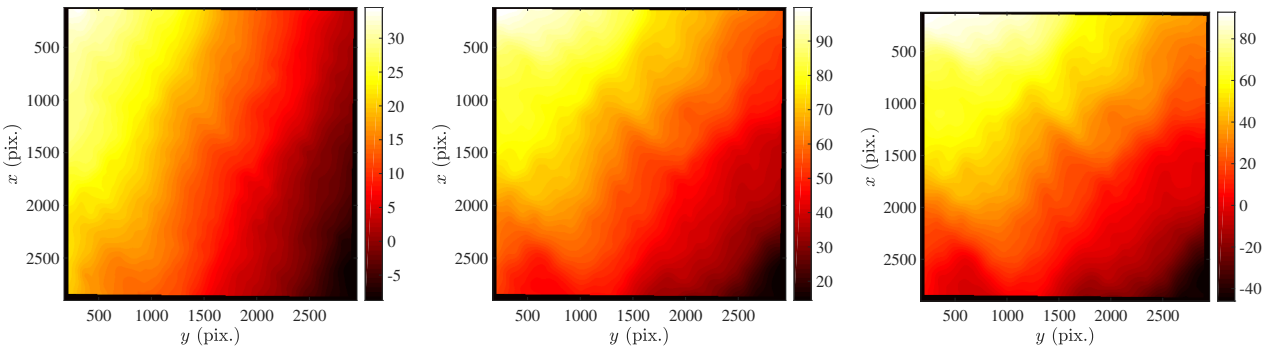

(a) $\langle \epsilon_{yy} \rangle = 0.9\%$ (b) $\langle \epsilon_{yy} \rangle = 2.4\%$ (c) $\langle \epsilon_{yy} \rangle = 5.5\%$

Figure 4.9: u_x fields calculated by DIC on the BSE images acquired during the tensile test for different macroscopic strain levels $\langle \epsilon_{yy} \rangle$. The pixel size is 42 nm for all images

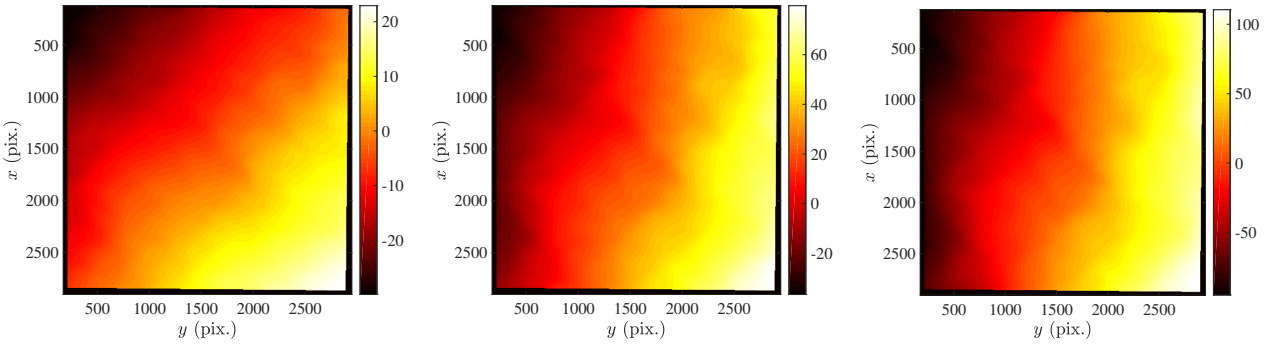

(a) $\langle \epsilon_{yy} \rangle = 0.9\%$ (b) $\langle \epsilon_{yy} \rangle = 2.4\%$ (c) $\langle \epsilon_{yy} \rangle = 5.5\%$

Figure 4.10: u_y fields calculated by DIC on the BSE images acquired during the tensile test for different macroscopic strain levels $\langle \epsilon_{yy} \rangle$. The pixel size is 42 nm for all images

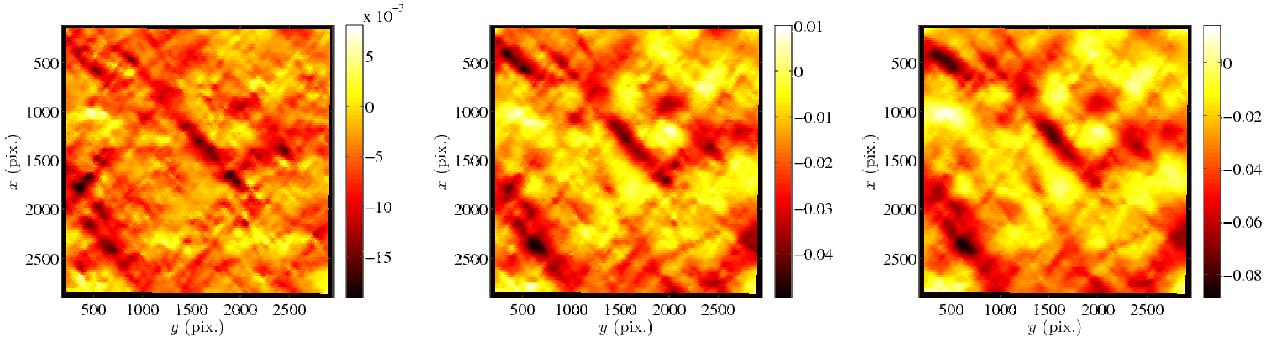

(a) $\langle \epsilon_{yy} \rangle = 0.9\%$ (b) $\langle \epsilon_{yy} \rangle = 2.4\%$ (c) $\langle \epsilon_{yy} \rangle = 5.5\%$

Figure 4.11: ϵ_{xx} fields calculated by DIC on the BSE images acquired during the tensile test for different macroscopic strain levels $\langle \epsilon_{yy} \rangle$. The pixel size is 42 nm for all images

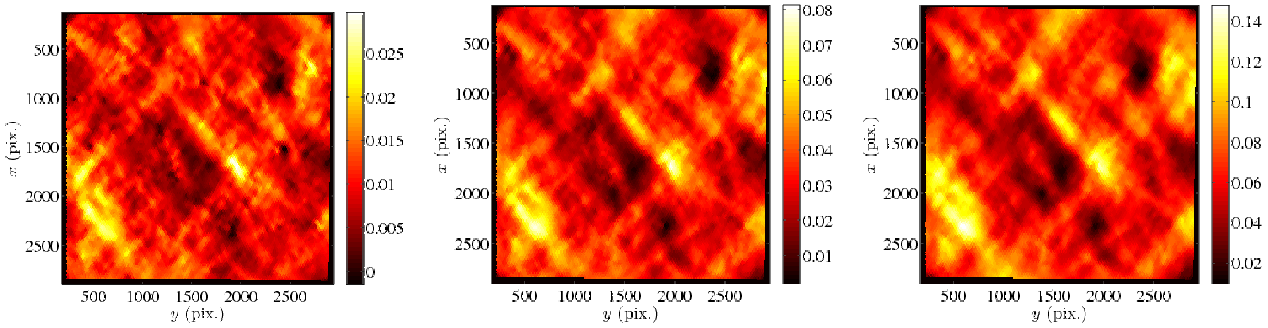

(a) $\langle \epsilon_{yy} \rangle = 0.9\%$ (b) $\langle \epsilon_{yy} \rangle = 2.4\%$ (c) $\langle \epsilon_{yy} \rangle = 5.5\%$

Figure 4.12: ϵ_{yy} fields calculated by DIC on the BSE images acquired during the tensile test for different macroscopic strain levels $\langle \epsilon_{yy} \rangle$. The pixel size is 42 nm for all images

4.4 Treatment of EBSD images

Recently, quaternion correlation has been proposed to measure crystal rotation and displacement fields (see Chapter 2). The algorithm uses the crystallographic orientation maps provided by EBSD images as registration support and the residual field indicates the rotation field. The algorithm leads to displacement fields with sub-pixel uncertainty and the rotation field with an uncertainty on the order of 10^{-3} degree, well below the orientation indexation error/resolution of EBSD.

The orientation maps of 4 EBSD acquisitions are shown in Figure 4.13. Figure 4.13(c) shows the IQ field corresponding to Figure 4.13(a). The square encompassing speckles is distorted, thereby indicating a systematic drift of EBSD acquisition, a phenomenon that will be addressed in Section 4.5. It is worth noting that two EBSD acquisitions might use different reference orientations, which will result in non-sensical disorientation through quaternion correlation even after the application of crystal symmetry. To correct this, one can choose arbitrarily a set of Euler angles from the same region in the two acquisitions, say those at the barycenter of the largest grain in the area, and transform them into a fixed interval, say $(\varphi_1 \in [0, \pi], \varphi \in [0, \pi/2], \varphi_2 \in [0, \pi/2])$, through crystal symmetry. Then the difference of their reference becomes clear and easily cancelled. The reference difference calculated from the two selected pixels can be applied for the entire region, because during an acquisition procedure the reference orientation does not change and the reference difference is universal for two given EBSD acquisitions.

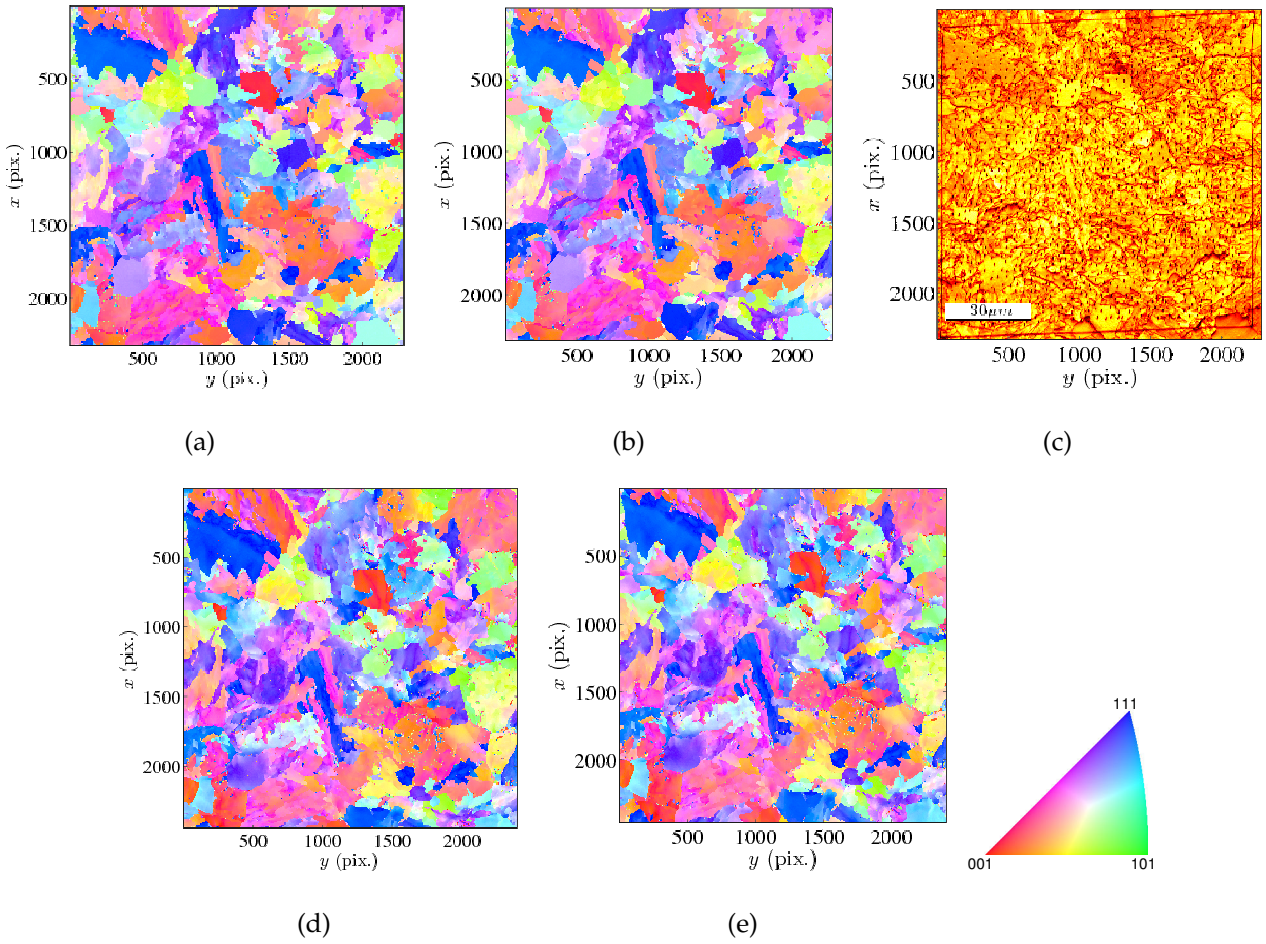

Figure 4.13: Orientation maps of successive EBSD acquisitions of the virgin sample (a,b), corresponding IQ map (c). Orientation maps of the deformed sample (d,e). The pixel size is 50 nm for all images

Figure 4.14 shows the kernel average misorientation field for the reference EBSD acquisition shown in Figure 4.13(b). The boundary of laths packages inside bainitic grains become very visible, and the grains without lath packages are noted as proeutectoid ferrites, which are encircled by green lines. Further phase-based analyses will be based on this grain classification.

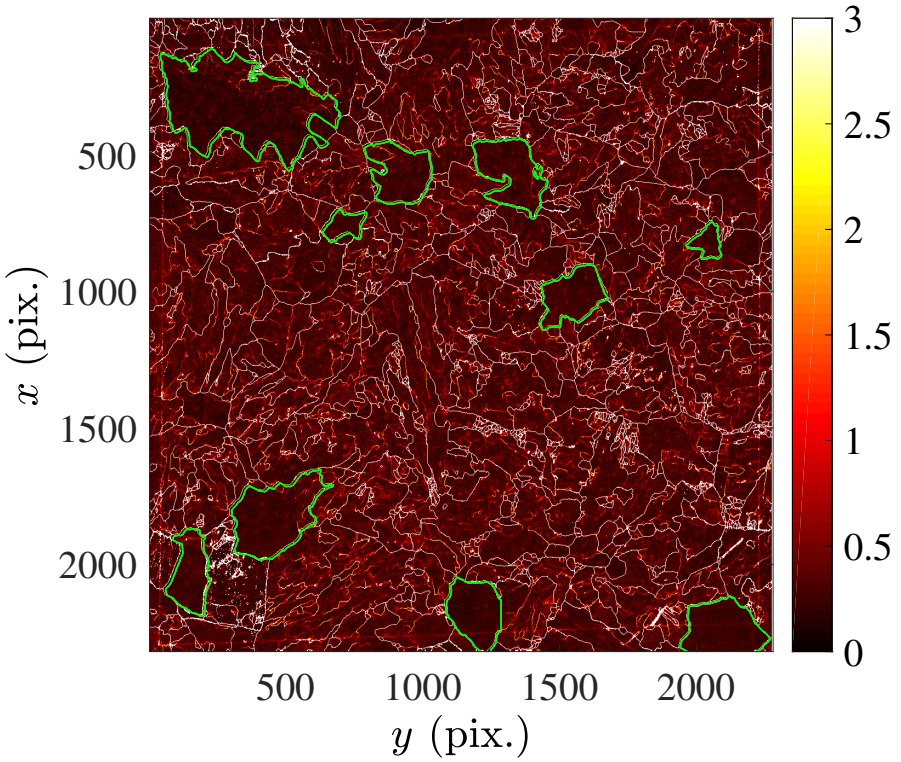

Figure 4.14: Kernel average misorientation (expressed in degrees) of the 16MND5 sample at reference state. Proeutectoid ferrites are encircled by green lines.

The difference between successive acquisitions (without any difference in loading) is not visible to the naked eye, and hence, they were analyzed using quaternion correlation. The DIC parameters for quaternion correlation and IQ field correlation are: i) an unstructured triangular mesh with element size 25 pixels; ii) the mechanical regularization length is brought down gradually from 400 to 200 and 100 pixels, each time initialized with the results of the last calculation; iii) the displacement field obtained by IQ field correlation is used as initialization for quaternion correlation, to save computation time. The results provided by quaternion correlation reveal non negligible disorientations and the displacement field provided by IQ field correlation show spatial inconsistencies, as shown in Figures 4.15 and 4.16.

It can be seen that the displacement fields in x and y directions have a range of 11 pixels and 22 pixels, respectively, for the undeformed sample, 90 pixels and 50 pixels for the deformed sample. Significant displacement gradients of are visible at the top, indicating severe instabilities in the beginning of EBSD acquisition. In addition, horizontal traces appear in both x and y directions, which means the slow scan direction drift studied in Section 4.3 is also present in EBSD acquisitions (presumably because of the long duration of the acquisition overnight). The large uncertainty in location must be taken into consideration during

the exploitation of EBSD results.

The amplitude of disorientation and the corresponding rotation vector components are shown in these figures. It is seen that a tilted thick band of low disorientation zone, *i.e.*, less than $0.5°$, exists even though no load was applied (Figure 4.15(c)). The corresponding rotation vector components ω_x, ω_y and ω_z are noisy in the band. This is in accordance with the small magnitude of rotation that renders the rotation vector ill-defined. However, outside the band the disorientation level increases very significantly, reaching about $1.8°$ in the corner. The rotation vector $\boldsymbol{\omega}$ shows a tendency, too. For example, Figure 4.15(e) shows a low level of ω_y at the top left corner and higher level at the down right corner.

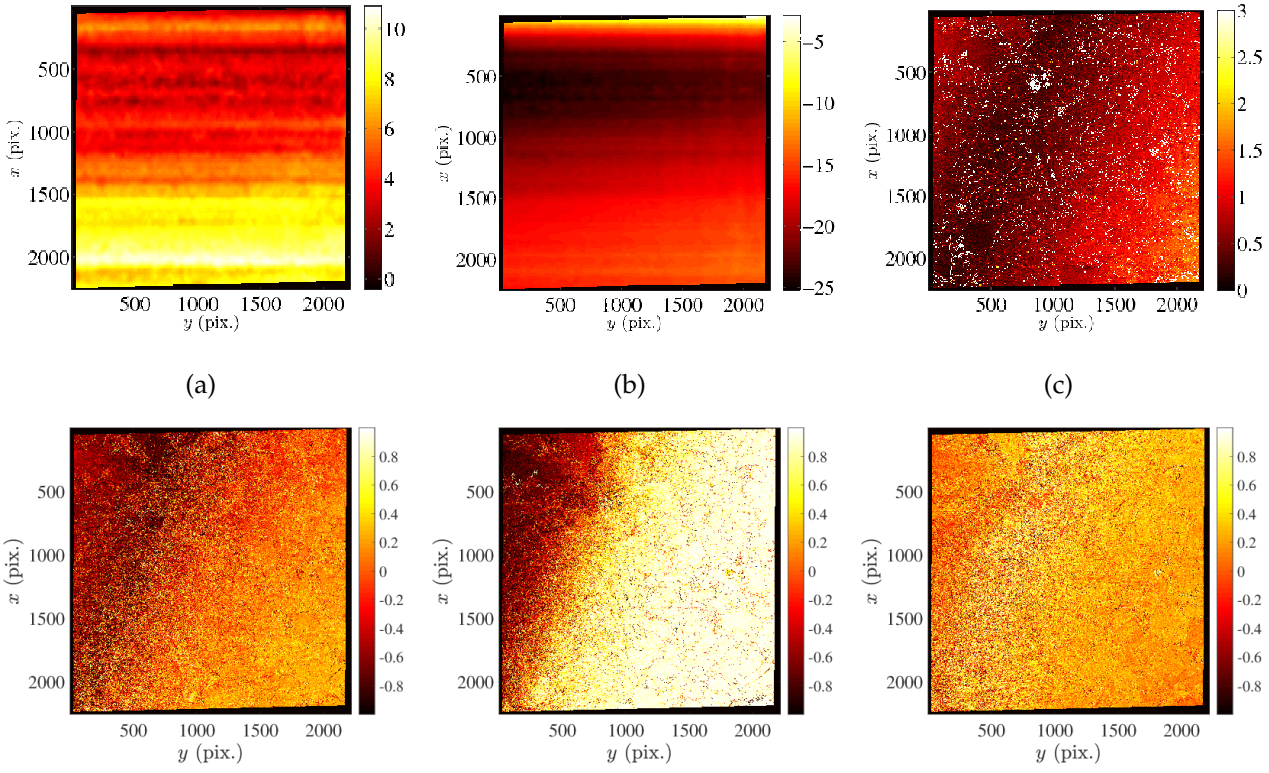

Figure 4.15: DIC results between successive EBSD acquisitions (virgin sample). (a-b) Displacement field in x and y directions respectively. (c) Disorientation angle (in °); (d-f) 3 components of disorientation vector ω_x, ω_y and ω_z, respectively. The pixel size is 50 nm

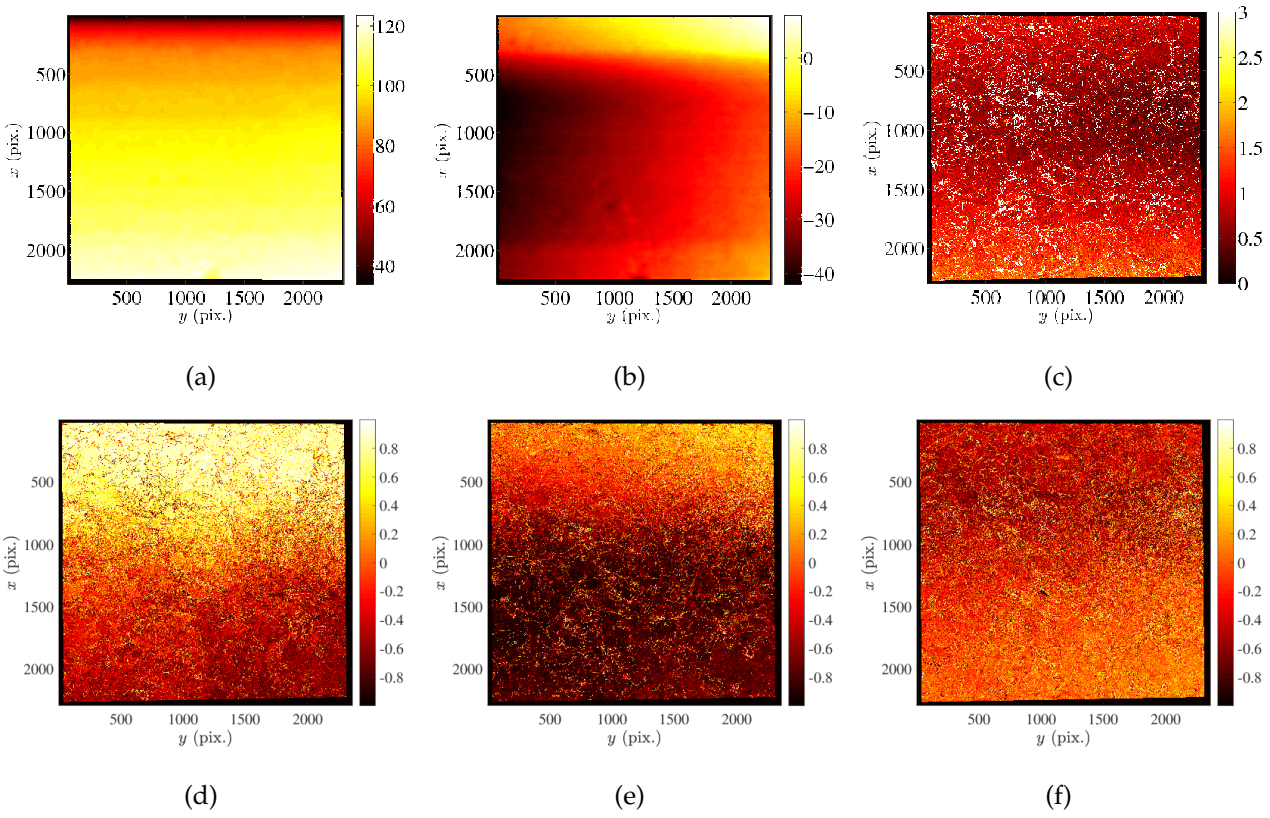

Figure 4.16: DIC results between successive EBSD acquisitions (deformed sample). (a-b) Displacement field in x and y directions respectively. (c) Disorientation angle (in °). (d-f) 3 components of disorientation vector ω_x, ω_y and ω_z, respectively. The pixel size is 50 nm

Satisfactory explanations to the indexed orientation 'drift' are not available yet. Several possible reasons may be proposed: i) the sample has a thermal distortion between two scans, either by heat induced by the electron beam, or due to the room temperature differences between the two days of the experiment. ii) Dynamic focus does not work perfectly. As during the experiment, dynamic focus is performed on the image center, the electron beam is not well focused for the upper and lower parts, as the working distance may vary. This phenomenon explains the horizontal band in Figure 4.16(c), but not the tilted band in Figure 4.15(c). iii) Physical drift of the imaging device, namely, either the sample support drifts during acquisitions, or the EBSD device is sucked firmly into the chamber by vacuum during the two-day acquisitions. As a result, the indexed orientation is to be used with caution. However, as the macroscopic tensile strain level is 6% and significant crystal rotations occur, the uncertainty associated with such smooth spatial variations with a maximum level of $1.8°$ will not be considered as a severe problem.

Quaternion correlation has been run to study crystal rotations during the tensile test.

However, as quaternion correlation is based on the hypothesis that the crystal orientation and grain boundaries do not change significantly (see Chapter 2), which is not the case herein, a precise initialization is needed. A global and regularized DIC procedure has been successfully applied to grain boundary images to obtain an initial displacement field. A regular triangular mesh with characteristic length of 30 pixels is chosen and mechanical regularization length is reduced gradually from 200 to 70 pixels [Tomičević et al. 2013]. The grain boundary images and the corresponding displacement field are shown in Figure 4.17.

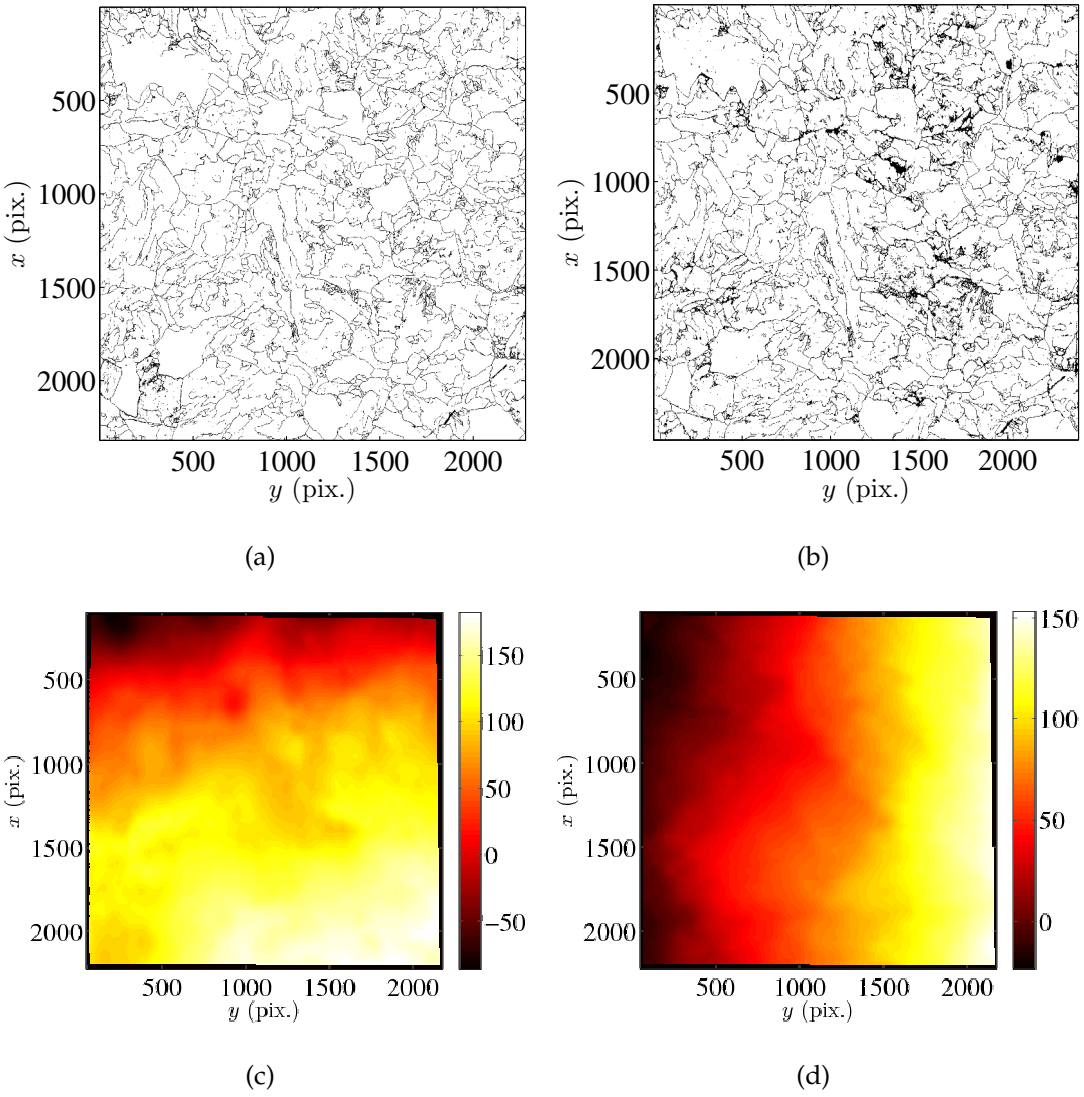

Figure 4.17: DIC results on grain boundary images. (a) Reference picture corresponding to Figure 4.13(b). (b) Deformed picture corresponding to Figure 4.13(e). (c-d) Resulting u_x and u_y displacement fields, respectively. The physical size of one pixel is equal to 50 nm

This displacement field is used to initialize quaternion correlation, which results in the rotation field shown in Figure 4.18. It is observed that rotations concentrate significantly,

with a maximum level $15°$. High gradients exist in several grains.

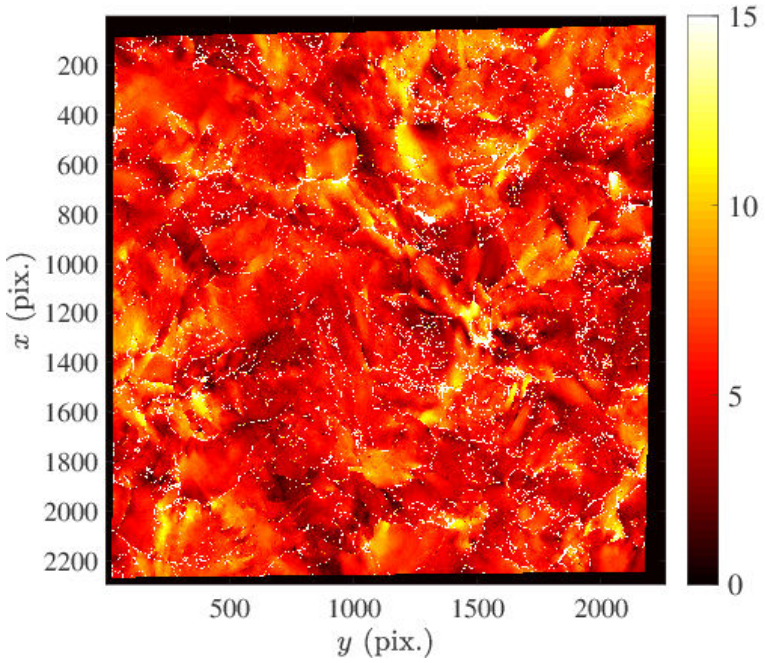

Figure 4.18: Rotation field (in ∘) between two EBSD acquisitions before and after the tensile test (Figures 4.13(b) and 4.13(e)). The pixel size is 50 nm

Until now the BSE image series has been registered by DIC, and EBSD images by quaternion correlation. However, the matching of these two modality images and its benefits have not been discussed yet and are detailed in the next section.

4.5 Registration of EBSD and BSE images

EBSD images provide the crystal orientation with a standard angular uncertainty of $0.5°$, thus accurate enough for describing the microstructure of the sample. As discussed in Section 4.3, BSE images with fast scan accuracy in both directions can be obtained, so the spatial coordinates of pixels are obtained very precisely. A natural idea is to combine EBSD and BSE images to give a description of the microstructure with the accuracy of crystal orientation of EBSD image and spatial coordinates of BSE images. Manual matching of EBSD and SEM images has been performed in previous works [Jin et al. 2011], without stating the accuracy of the registration. The matching has also been performed by associating manually chosen 'control points' on different imaging modalities through 'thin plate spline' [Zhang et al. 2014], or calculating a transformation matrix $\boldsymbol{F}$ from several markers visible in EBSD and SEM images [Héripré et al. 2007]. The corresponding error has been predicted to be about

15 pixels or 2 µm for an area of 400×400 µm^2. Precise registration can be obtained by correlating the two types of images in the present work, thanks to the image contrast introduced by a large number of speckles that are visible in both modalities.

4.5.1 Analysis of speckles in EBSD and BSE images

Figure 4.19 shows a zone in EBSD (orientation and IQ) and BSE images. It is observed that the speckles are invisible in the orientation map (Figure 4.19(a)), thus the deposited speckles do not impact the crystal orientation indexation. For the IQ image, each speckle corresponds to two roughly vertical darker spots (Figure 4.19(b)). The darkest pixels of the twin spots are separated with around 9 pixels, i.e. 450 nm (Figure 4.19(c)).

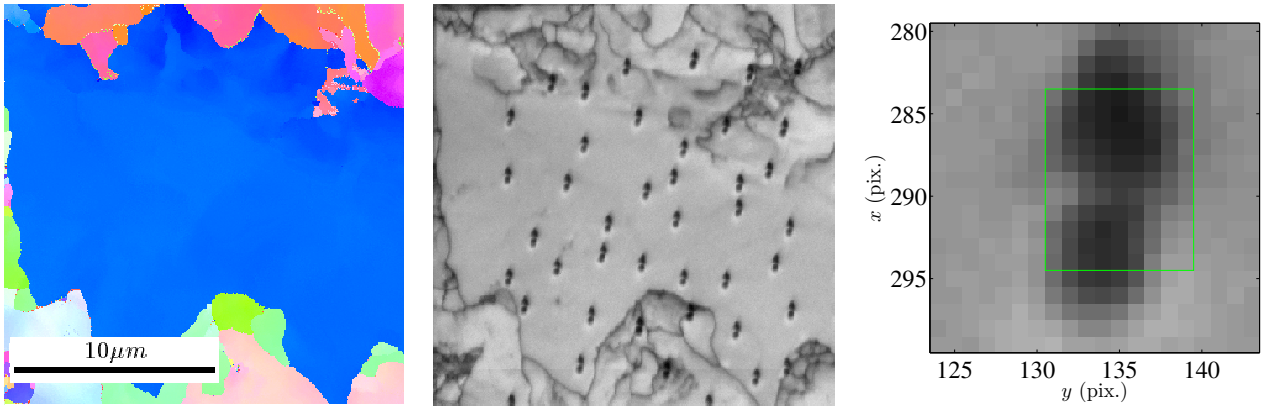

(a) (b) (c)

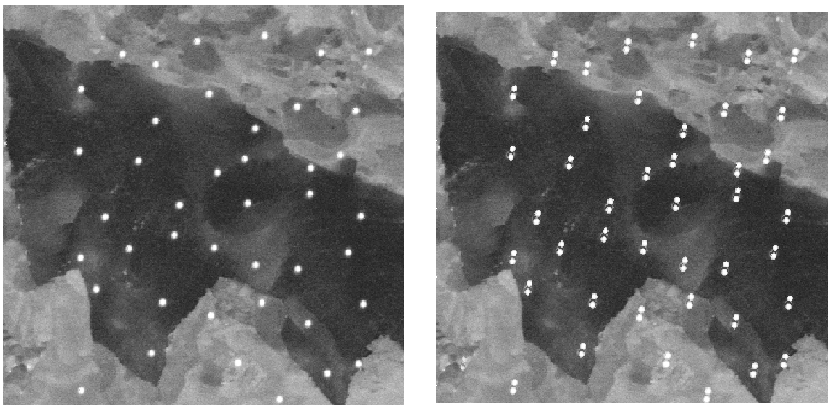

(d) (e)

Figure 4.19: Several images of the same region of interest of the sample obtained from (a) EBSD orientation map, (b) EBSD IQ image, (d) BSE image, (e) BSE image with artificial 'shadow' speckles. (c) is an enlargement of twin spots shown in sub-figure (b). The diffraction images corresponding to the marked rectangular area are shown in Figure 4.22

The red boxes contain extra information that was not published. The trajectories of back-scattered electrons simulated by Monte-Carlo calculations are reported.

In order to probe the formation of twin spots in EBSD IQ image, a Monte-Carlo simulation of electron interaction with Fe has been performed with Casino software [Drouin et al. 2007]. 20,000 electrons with an acceleration voltage of 30 KV have been projected on the sample with a 70° tilt in the simulation. The trajectories of all backscattered electrons are shown in Figure 4.20. It can be seen that the average ballistic range of backscattered electrons is about 200 nm and the maximum is near 400 nm, which is larger than the speckle diameter in the test. This phenomenon brings about the proposition of twin spots formation, which is detailed hereafter.

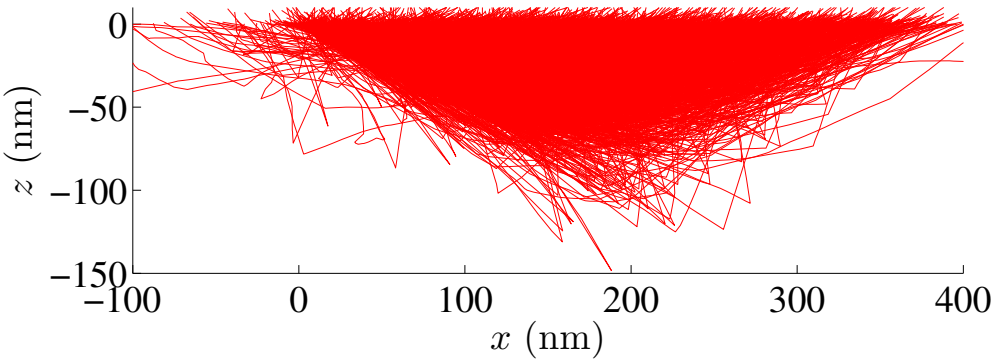

(a)

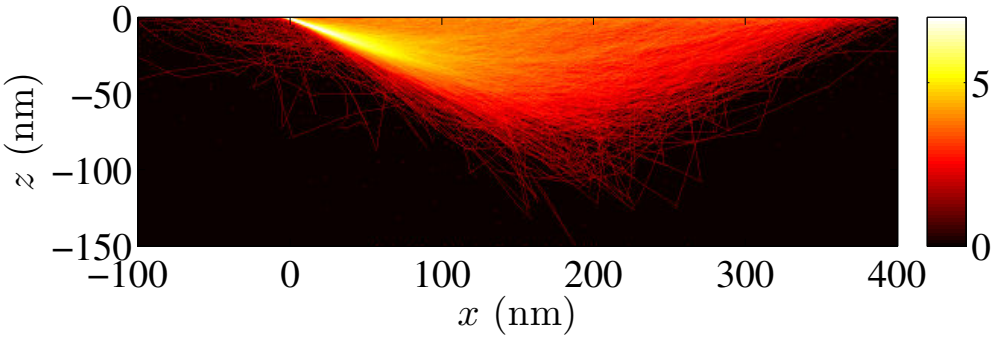

(b)

Figure 4.20: Monte-Carlo simulation of the trajectories of backscattered electrons in Fe by Casino software [Drouin et al. 2007]. (a) Trajectories of all back-scattered electrons. (b) Density (expressed in exponential term) of trajectories. The incident electron beam hits the position 0 with a 70° tilt and the energy per electron is 30KVe.

Figure 4.21 illustrates the formation of the twin spots, which is based on previous studies on the origin of diffraction patterns [Zaefferer 2007; Wisniewski et al. 2017]. One spot is

linked to the real position of the speckle, the other one is the shadow cast on the sample. When the electron beam hits the speckle (Figure 4.21(a)) its interaction with the underlying material is altered. Thus the diffraction image is deteriorated and so is the image quality of the EBSD analysis. When the electron beam hits a point near a speckle, as shown in Figure 4.21(b), and if the ballistic range of incident electron is longer than the speckle diameter, the effective back-scattering source is not obscured by the speckle. The diffraction pattern captured by the detector is of better quality than its upper and lower neighbors, thus a higher IQ score between twin spots is obtained. Otherwise if the ballistic range of the incident beam is shorter than the speckle diameter, no such region exists and the twin spots are connected with each other, as shown in Figure 4.2(b).When the electron beam hits the region above the speckle, see Figure 4.21(c), the speckle with a non negligible height will cast a shadow on the bottom of the diffraction image. The slight horizontal shift between 'real' spot and 'shadow' spot is explained by the fact that the camera is positioned with a 20° shift from the normal direction of the sample.

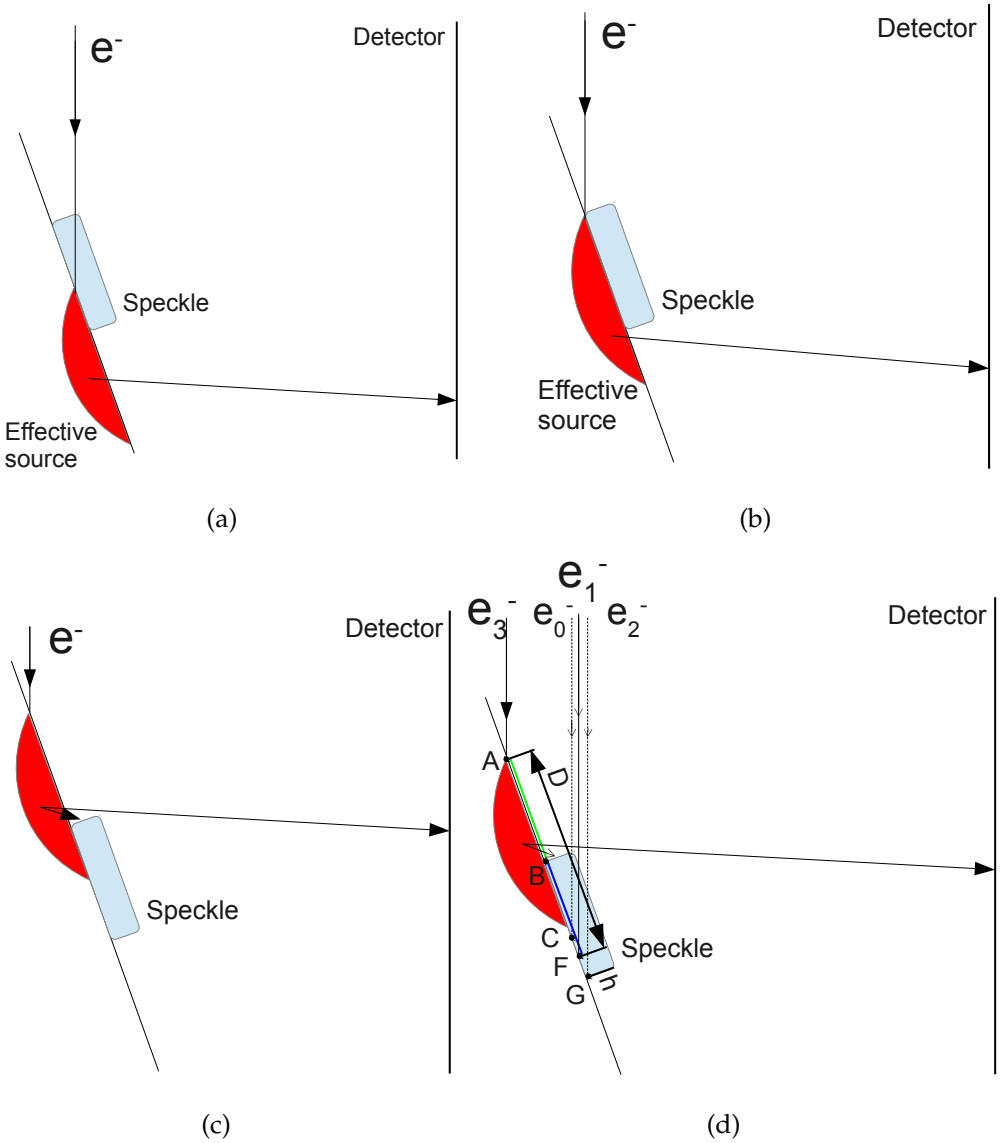

Figure 4.21: Schematic sketch providing an explanation to the formation of double spots. (a) Formation of 'real' spot. (b) Formation of 'saddle' between two spots. (c) Formation of shadow spot. (d) Schematic view explaining the distance between the shadow and real spots

As the electron beam moves away, the shadow moves even faster due to the gnomonic projection effect. This schematic explanation is confirmed by the collection of Kikuchi patterns (see Figure 4.22) recorded as the rectangle shown in Figure 4.19(c) is scanned. It can be seen that for the lower spot a shadow at the bottom of the image appears and vanishes quickly as the electron beam scans through the studied zone.

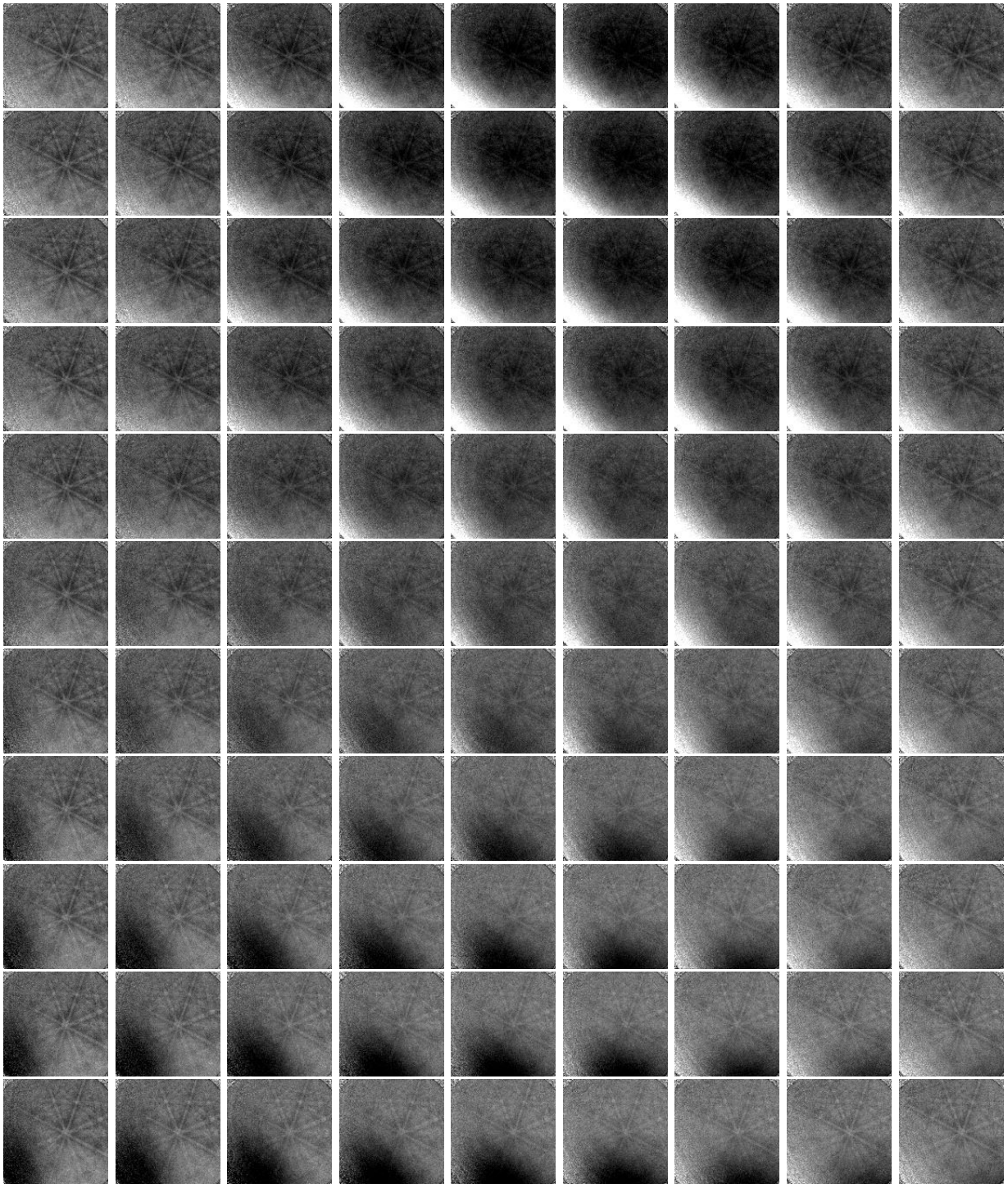

Figure 4.22: Series of diffraction images of a split speckle. The lower lines of the diffraction images correspond to the shadow spot, as the shadow is visible on the lower edge

As the speckle is a thick disk of Pt with a diameter much larger than its height, the effective obstacle area is limited. This is the reason why the shadow spot is smaller than the real one. For BSE images, a speckle generates a unique spot (Figure 4.19(d)). It can be seen from Figure 4.19(c) that the twin spots are separated by a distance D of about 9 pixels.

Figure 4.21(d) illustrates the origin of this distance. The electron beam e_0^- hits the upper edge of the speckle and reaches the sample at point $\boldsymbol{C}$, thus travels the longest distance inside the speckle. The electron beam e_2^- hits point $\boldsymbol{G}$, the lower intersection of the sample and the speckle, and also travels the longest distance. In fact, the darkest pixel corresponds to the electron beam e_1^- which hits point $\boldsymbol{F}$, the midpoint of $\boldsymbol{CG}$. As for electron beam e_3^-, the most emissive part of the back-scattering electron source is masked by the speckle, and the darkest point in the shadow spot is obtained. Consequently,

$$\begin{aligned} D &= AB + BF \\ &= AB + (BC + BG)/2 \\ &= AB + (h\tan(70°) + BG)/2 \\ &= 200 + (75 \times \tan(70°) + 300)/2 \\ &\approx 450 \text{ nm} \end{aligned} \tag{4.12}$$

where $\boldsymbol{B}$ is the intersection point of the speckle and sample surface, $\boldsymbol{A}$ is the beam hitting point of the darkest point of shadow speckle, $\boldsymbol{F}$ is the beam hitting point of the darkest point of real speckle, and h is the speckle height (*i.e.*, 75 nm). The distance between the twin spots is perfectly explained.

4.5.2 Registration results

The physics behind the 'split' speckles in EBSD IQ images being understood, one should either delete the shadow spot in EBSD IQ image, or create shadow speckles in BSE image if the two types of modalities are to be registered. The latter is chosen herein as shown in Figure 4.19(e). DIC has been run on the EBSD IQ map and BSE image with shadow speckles, and the results are shown in Figure 4.23. The coordinates given by EBSD acquisitions are distorted both in x and y directions. More importantly, the distortion is not stable in time, as it is not the same between the two successive EBSD acquisitions and the BSE image, especially in the y-direction. It is therefore not possible to characterize once-and-for-all the EBSD scan distortions and use them to correct other EBSD images. Besides, as the displacement field cannot be described by a regular/simple polynomial function, the conventional (*i.e.*, manual) registration of EBSD and SEM images based on the remarkable points in both images and global polynomial interpolation is not very accurate.

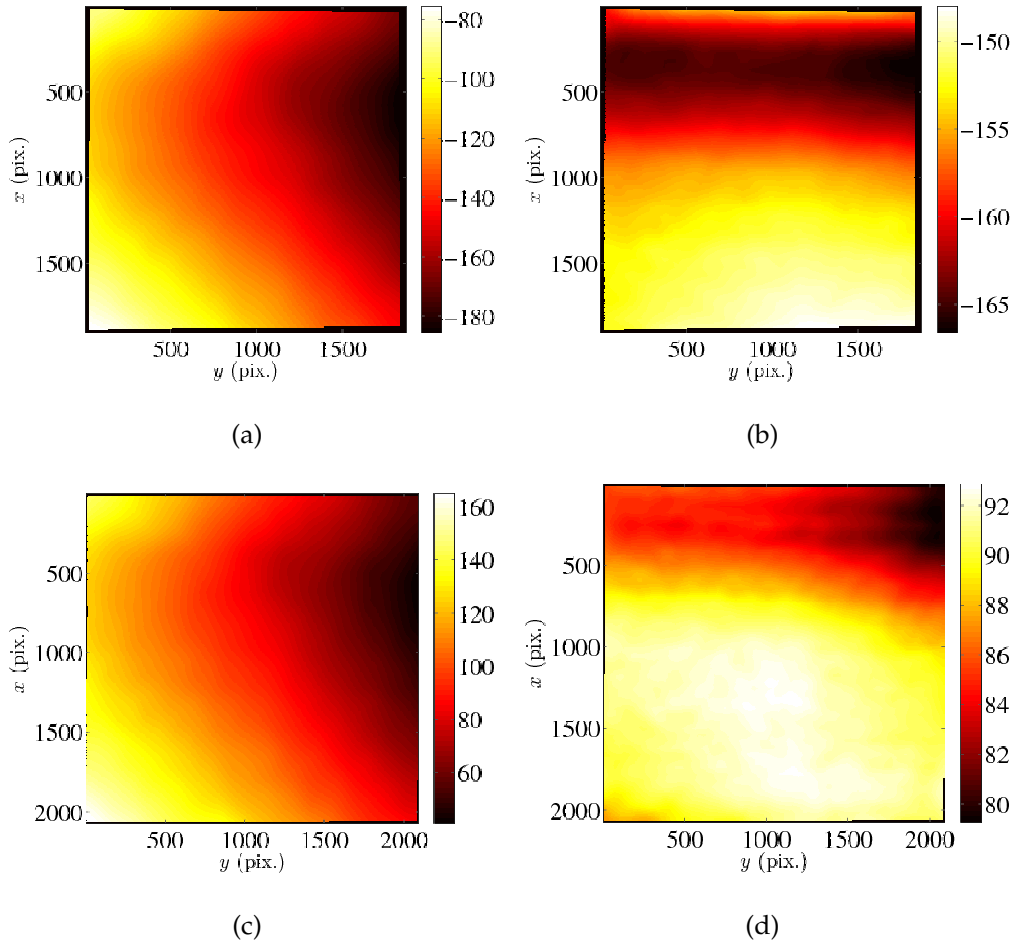

Figure 4.23: Correlation results between reference BSE image and first EBSD IQ map. (a) u_x (b) u_y expressed in pixels. Correlation results between reference BSE image and second EBSD IQ map. (c) u_x (d) u_y expressed in pixels. The physical size of one pixel is 50 nm

As mentioned in Section 4.3, the corrected BSE image is free from scan drift. Once BSE and EBSD images are registered, accurate spatial coordinates given by BSE images are combined with crystallographic orientations provided by EBSD. Figure 4.24 shows the grain boundaries extracted from the EBSD image overlaid on the reference BSE image. Those points that have a disorientation greater than 5° with neighbors are considered as grain boundaries. The magnified views (Figures 4.24(b), 4.24(c) and 4.24(d)) show that the grain boundaries extracted from EBSD pictures are always several pixels away from the grain boundaries shown in the BSE modality. This is due to the stable distance between the incident beam and the effective back-scattering electron source.

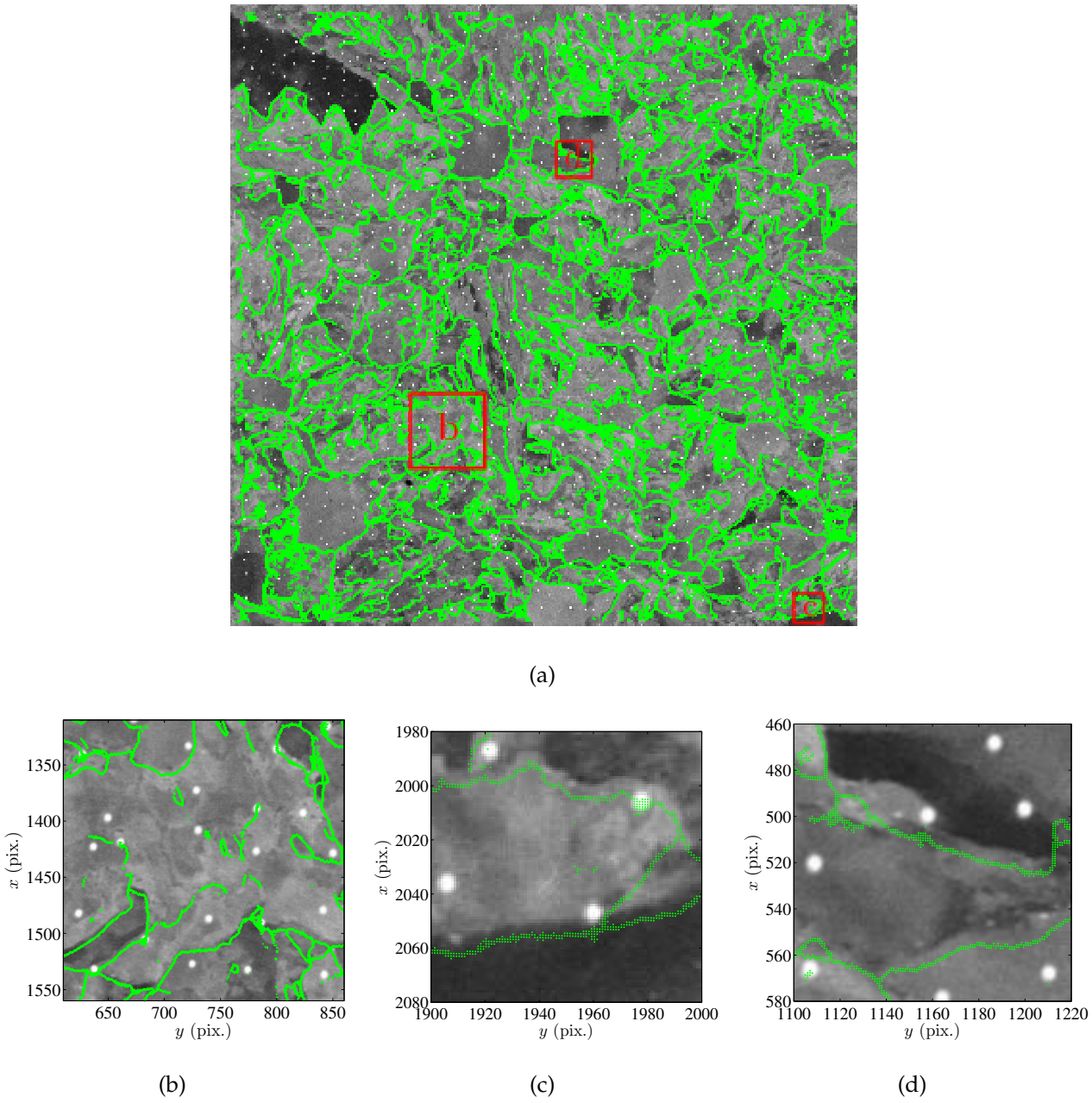

Figure 4.24: Overlay of grain boundary extracted from EBSD image on reference BSE image. Full-field (a), and three magnified views (b-d). The pixel size is 42 nm for all images

An illustration of this phenomenon is provided in Figure 4.25. The electron beam captures both grain boundary and speckle, yet they are actually separated on the sample. Thus the speckles and grain boundaries shown in the IQ field have a consistent shift. Grain boundaries, which are embedded inside the sample, are registered when encompassed by the interaction zone. As for the Pt speckle, its large atomic number/weight and position at the surface mean that it affects the incident beam directly. As a result, the consistent distance shown in Figure 4.24 can be used to quantify the distance from the incident beam hitting point and the average emission point. In fact the shift can be predicted by a sim-

ple algebra calculation: from Figure 4.21(d) and Equation (4.12) it is concluded that point $\boldsymbol{F}$, the darkest point of the speckle in IQ image, is 100 nm lower than the central point of speckle. Although the 'real' speckle is elongated vertically in IQ image, the spot is symmetrical vertically and it is thus justifiable to take the darkest point to calculate the shift. Added by 200 nm, the distance between the incident beam hitting point and the average emission point, a total distance of 300 nm is obtained. Therefore, EBSD images need to be shifted upwards by 6 pixels to be comparable to BSE/SE images.

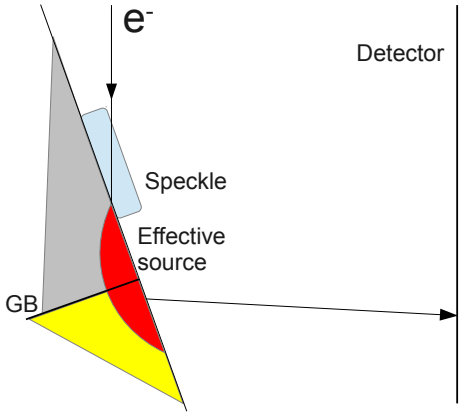

Figure 4.25: Schematic view of the distance between grain boundaries and real speckle. The electron beam captures both grain boundary and speckle, yet they are actually separated

Figure 4.26 shows the grain boundary extracted from the EBSD image overlaid on top of the reference BSE image with a constant 6-pixel shift. The magnified views (Figures 4.26(b), 4.26(c) and 4.26(d)) show that the accuracy of grain boundary positioning is about one pixel, which is deemed very satisfactory.

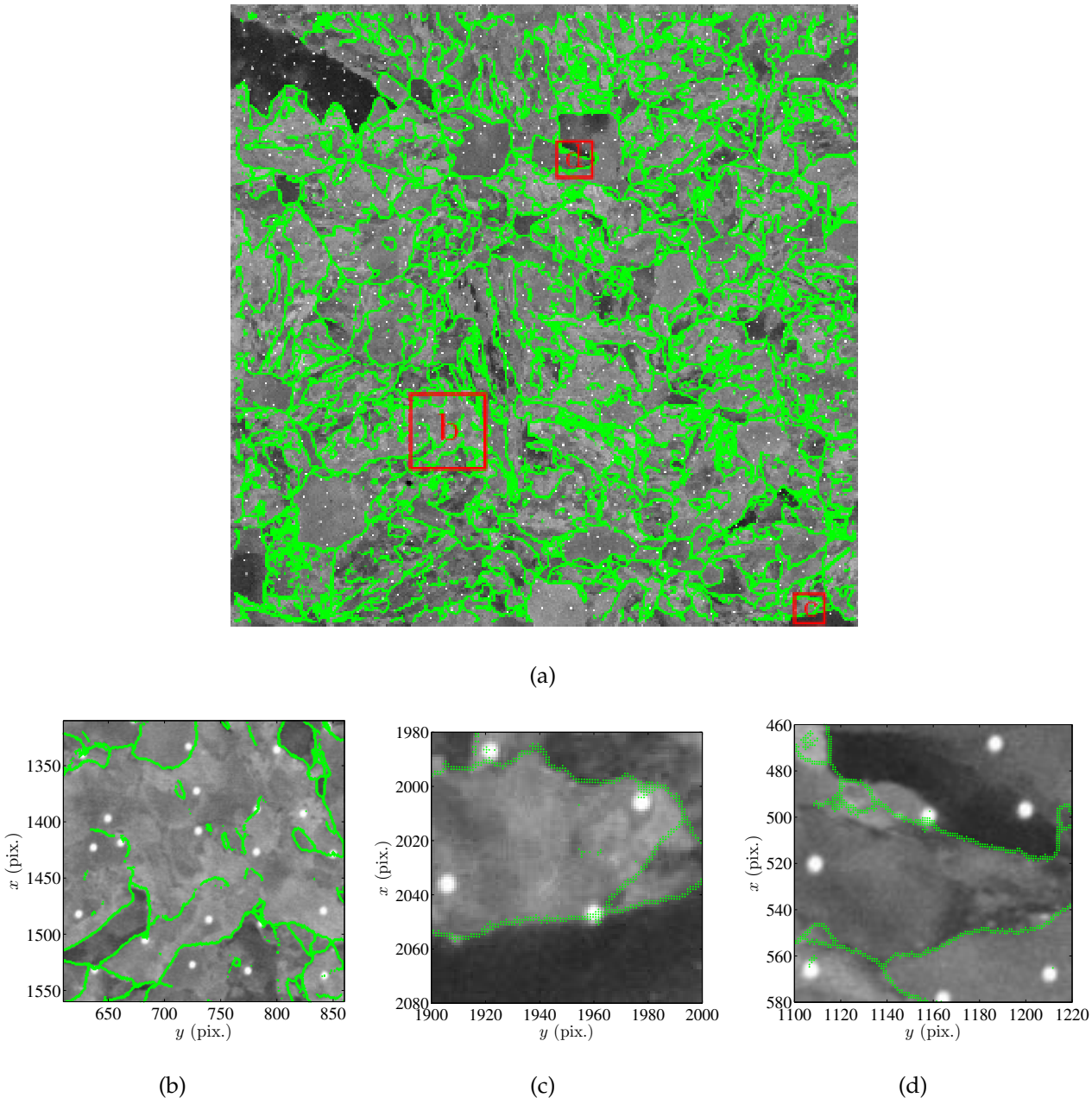

(a)

(b) (c) (d)

Figure 4.26: Overlay of grain boundary extracted from EBSD image on reference BSE image when grain boundaries are uniformly shifted by 6 pixels. Full-field (a), and three magnified views (b-d). The pixel size is 42 nm for all images

4.5.3 Correlation between crystal orientation and plastic strain

The precise registration between EBSD and BSE images opens another route, which is to study the relationship between crystal rotations and plastic strains in the same coordinate system.

The red box contains extra information that was not published. A discussion about the representation of equivalent strain is provided.

The knowledge of in-plane components of coordinates for each pixel along the tensile test allows the in-plane components of infinitesimal strain tensor to be calculated. But the computation of the Green-Lagrange strain tensor needs the components xz and yz of the deformation gradient tensor $\boldsymbol{F}$, which are unknown. The assumption to neglect these components is only satisfied if the surface of the strained sample is still plane and parallel to the initial plane, which is not the case here (see Chapter 5). Thus the local Green-Lagrange strain tensor can only be approximately calculated. An equivalent strain, ϵ_{eq}, is chosen to characterize the strain levels. Again this requires the unknown third out-of-plane principal value of the strain tensor. Allais et al. [1994] have proposed to assume the third principal value to be equal to the second in-plane principal value, even if it is only a rough approximation. Thus the equivalent strain reads

$$\epsilon_{eq} = \frac{2}{3}\left[\frac{\sqrt{2\epsilon_Y + 1}}{\sqrt{2\epsilon_X + 1}} - 1\right] \tag{4.13}$$

where ϵ_Y and ϵ_X are the principal/eigen values of the in-plane Green-Lagrange strain tensor. ϵ_{eq} is a measure of the deviatoric strain.

Figure 4.27 shows a direct comparison between crystal rotations and equivalent plastic strain for the analyzed pictures. The white pixels in Figure 4.27(a) come from the imprecise orientation indexation at grain boundaries, and hence quaternion correlation naturally provide a local estimate of the crystal rotation that is meaningless but on average much higher that the trustful crystal rotation within grains. Thus the white pixels draw very precisely the grain boundaries (see Chapter 2). In Figure 4.27(b), green curves are overlaid grain boundaries thanks to the registration of EBSD and BSE images.

In order to study the correlation between crystal rotations and equivalent plastic strains, a 2D joint histogram is shown in Figure 4.27(c) for all grains in the region of interest. Figure 4.27(d) and Figure 4.27(e) show the 2D joint histogram for ferritic and bainitic grains respectively. The classification of grain types is shown in Figure 4.14. Pixels at the grain boundaries are not counted since the measured crystal rotation is not reliable. The three histograms are based on 3.3 million, 0.6 million and 2.7 million data points respectively. By comparing Figure 4.27(d) and Figure 4.27(e), it is concluded that strains are generally higher in ferritic grains than in bainitic grains, as found in previous works [Latourte et al. 2012],

while no significant differences exist in terms of crystal rotation between the two phases. Strain and rotation are broadly distributed in the three histograms. However, they appear to be significantly correlated, thereby indicating the existence of crystal rotations and plastic strain concentrations in the same regions. To better highlight these correlations, average and median crystal rotations are calculated at fixed ϵ_{eq} (within intervals of width 0.002), and average and median ϵ_{eq} are calculated as functions of crystal rotation (within intervals of $0.1°$). In the statistically significant box, $0.03 < \epsilon_{eq} < 0.15$ and $3° < \theta < 10°$, all four trends show a marked positive correlation. This analysis does not aim at revealing a deterministic relationship between both of these quantities as they remain very broadly distributed and not only because of measurement uncertainties. A prosaic argument to support this observation is to note that in regions where the stain is small, crystal rotations are expected to remain small.

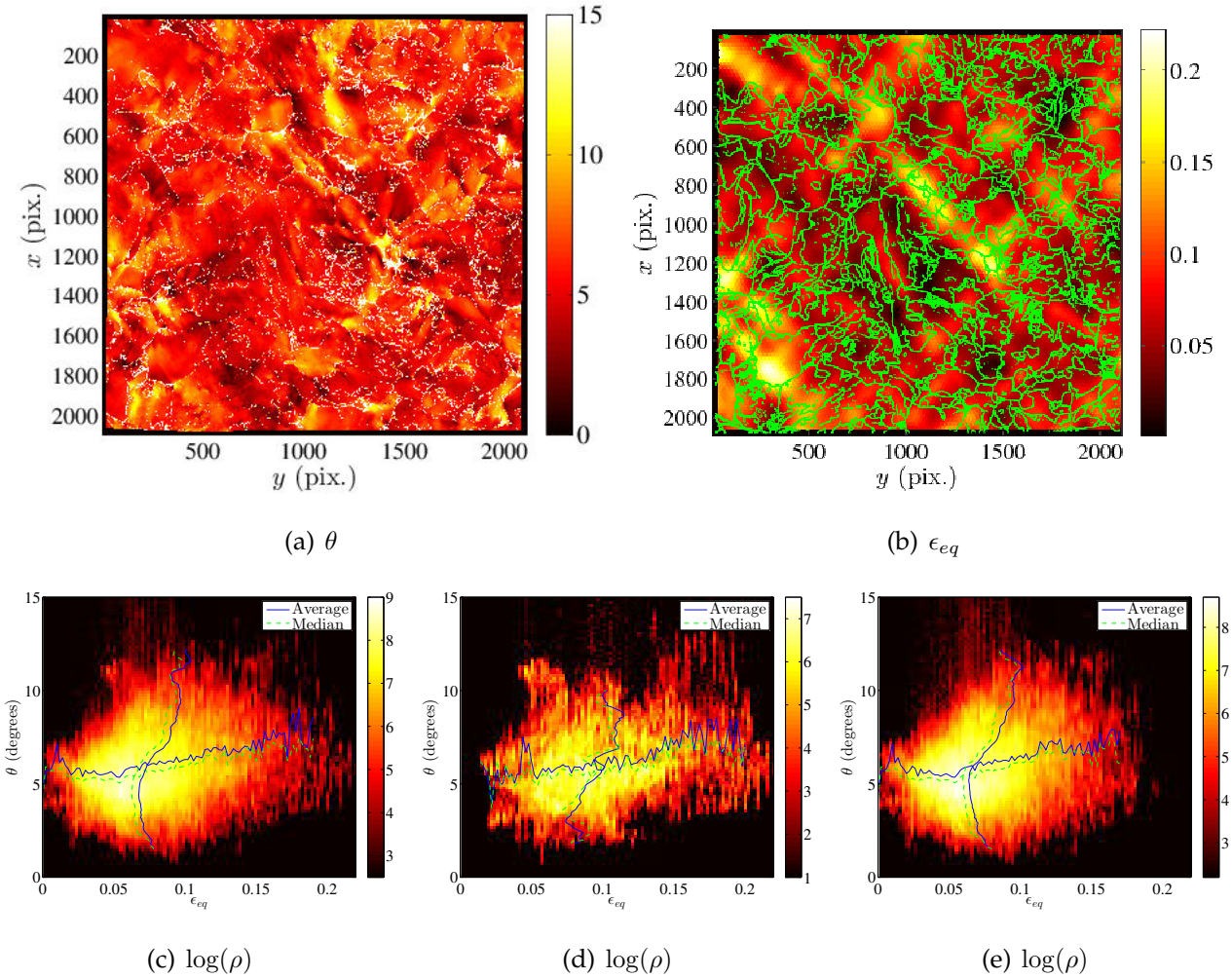

(a) θ (b) ϵ_{eq}

(c) $\log(\rho)$ (d) $\log(\rho)$ (e) $\log(\rho)$

Figure 4.27: Comparison of crystal rotations and equivalent plastic strains at the end of the tensile test. (a) Crystal rotation magnitude. (b) Equivalent plastic strain. Grain boundaries extracted from the EBSD image are overlaid. The pixel size is 50 nm for (a) and (b). 2D joint histograms of crystal rotations and equivalent plastic strains for (c) all grains, (d) ferritic grains and (e) bainitic grains. Note that the scale is in exponential terms. Average and median profiles of crystal rotation and ϵ_{eq} are overlaid in the sub-figures

4.6 Conclusion

The present chapter provides a detailed study of an *in-situ* tensile test carried out inside an SEM. Properly sized and randomly positioned platinum speckles deposited onto the sample surface facilitate the registration between different modalities including BSE and EBSD images. Regularized DIC reveals very powerful to match BSE images acquired at each increment of mechanical loading, in spite of very heterogeneous (*i.e.*, emerging shear-bands) strain fields, while quaternion correlation allows the crystal rotation field to be analyzed

between the initial and final stages. Several new findings have been reported:

1. Properly sized platinum speckles deposited onto the sample surface facilitate the registration of EBSD and BSE/SE images. When finely tuned to the suited value, the speckle thickness may not degrade the reliability of orientation detection of the underlying crystal, and yet leave clear traces in the image quality map. Such a tailoring of the Pt speckle marks reveals very instrumental for further registrations.

2. SEM images suffer from a slow-scan direction error for the SEM device tested herein. Registration of images taken for different scan directions helps to correct this artifact. However, it is worth noting that such artifacts do not impede a quantitative analysis of the surface kinematics with DIC.

3. EBSD acquisitions suffer from unstable electron beam scan, which undermines the precision of coordinates in EBSD results. Yet, DIC based on the Pt speckle seen in BSE and from the IQ map of EBSD enables this artifact to be corrected.

4. Crystallographic orientations indexed by EBSD have an uncertainty of $0.5°$. Repeated acquisitions without any change on the sample, reveal from quaternion correlation that crystal orientation and sample position could drift in time with effects as large as $2°$ spurious rotation. Quaternion correlation allows such drifts to be corrected, but it shows that an absolute measurement is not accessible.

5. In the EBSD image quality map, each speckle appears as two separate spots. One spot is created when the incident electron beam hitting the Pt disk diminishes the number of electrons interacting with the underlying sample. The other spot is due to back-scattered electrons hitting the Pt speckle, and resulting in a shadow on the Kikuchi diffraction image. Between the two spots a narrow zone may be well indexed, when both above-mentioned phenomena are avoided.

6. The registration of EBSD and BSE images based on speckles exhibits a consistent shift of grain boundaries (evaluated to 6 pixels/300 nm in the present study). This shift is interpreted as due to the penetration distance of electrons in the EBSD configuration. After the spurious shift is corrected, a pixel-level overlap of EBSD and BSE images is obtained. Thus a very precise description of the polycrystalline microstructure and its changes can be trustfully studied.

7. After registration, full surface plastic strains and crystal rotations are measured and faithfully registered onto the corresponding material points.

The ability to bring in coincidence information coming from the different modalities of SEMs is extremely precious to analyze crystal plasticity from *in-situ* tensile test. Providing proper patterns that are visible in the different SEM modalities, while not affecting others, is at the core of the success of the mechanical test analysis. Apart from deposition of Pt protrusions adopted herein, other shapes of patterns may be considered, such as dimples or chemical etching pits. An interesting scenario is to fill the pits with amorphous Pt to benefit from speckles and yet avoid its shadowing effect. Such suggestions have not been tested.

This chapter has analyzed the sample surface changes during the tensile test by BSE/SE and EBSD images. Though very rich, the information conveyed by these images is confined to the 2D surface. As can be seen from Figure 4.4(b), there are probably out-of-plane motions of the sample surface. The topography information of the sample cannot be neglected if a comprehensive characterization of the *in-situ* tensile test is sought. In chapter 5 we will focus on the topography measurement and introduce three methods to evaluate it.

Chapter 5

Measuring topographies from conventional SEM acquisitions

The present study extends the stereoscopic imaging principle for estimating the surface topography to two orientations, namely, normal to the electron beam axis and inclined at 70° as suited for EBSD analyses. In spite of the large angle difference, it is shown that topography can be accurately determined using regularized global Digital Image Correlation. The surface topography is compared to another estimate issued from a 3D FIB-SEM procedure where the sample surface is first covered by a Pt layer, and its initial topography is progressively revealed from successive FIB-milling. These two methods are successfully compared on a 6% strained steel specimen in an *in-situ* mechanical test. This analysis is supplemented by a third approach in which the change of topography is estimated from crystal rotations as measured from successive EBSD images. This last technique ignores plastic deformation, and thus holds only in an elastic regime. For the studied example, despite large plastic flow, it is shown that crystal rotation already accounts for a significant part of the deformation-induced topography.

5.1 Introduction

Surface topography is critical for many properties, especially for mechanically demanding applications. For example, fatigue failure and corrosion resistance are often controlled by surface roughness, and therefore the latter is carefully controlled in many products from dental implants [Mendonça et al. 2008] to workpiece materials [Novovic et al. 2004]. Topography measurements are also crucial for inspecting and analyzing defects in semiconductor

products [Morita et al. 2000]. They also help to study the plastic properties of materials. For example, topography changes due to crystallographic slip have been assessed quantitatively by AFM and qualitatively by SEM to characterize plastic deformations at very local levels [Kahloun et al. 2010; Franciosi et al. 2015]. The topography measurement of nanoindentation with AFM helps for the direct observation of plasticity for different crystal planes [Ramos et al. 2009]. Recent studies show that the precise measurement of the 3D material microstructure and its subsequent deformation, thus including topography, improves identification results of crystal plasticity parameters (see Chapter 6).

To characterize the surface topography and/or its changes during a mechanical test in the nano- to micrometer range, it is quite demanding to perform both mechanical test *in-situ* and at the same time utilize different techniques to measure topography. Thus using a single instrument appears quite attractive. SEMs, through their variety of modalities, offer several ways to evaluate the surface geometry. A taxonomy of 3D SEM surface reconstructions can be found in Ref. [Tafti et al. 2015]. Not all techniques offer the same reliability and measurement quality:

- FIB offers remarkable opportunities to perform nano-machining [Volkert and Minor 2007] or material deposition [Reyntjens and Puers 2000]. The successive removal of surface layers by FIB followed by EBSD analyses allows a 3D volume with crystallographic information to be reconstructed (*i.e.*, a technique called 3D-EBSD [Groeber et al. 2006]), which opened new avenues for characterizing materials in three-dimensions [Zaafarani et al. 2006; Calcagnotto et al. 2010; Guyon et al. 2016] (alas destructively). In particular, the surface topography can be measured through the very accurate estimate of successive contour lines.

- In the 1980s, photogrammetry, also known as stereomatching, provided quantitative results thanks to the advent of Digital Image Correlation (DIC) [Koenig et al. 1987]. From a pair of images of a specimen acquired at different inclination angles, the sample elevation was measured from the registration of the two images by DIC. During the last decades both DIC and pattern marking for SEM images have known significant developments. Thus measurement reliability and accuracy have improved and their application spectrum has been broadened. The uncertainty of the stereoscopic analysis of SEM images has been quantified [Lockwood and Reynolds 1999]. Various types of errors in the measurement process have been studied and partly corrected [Zhu et al.

2011], including SEM distortion, system calibration and tilt angle inaccuracy. For surfaces between the identified matching points, an interpolation is necessary to obtain an estimation of topography. Delaunay triangulation and linear interpolation have been adopted [Geiger et al. 2010], thereby resulting in a surface made of small facets of different normal directions [Yan et al. 2017]. Thus the density of matching points dictates the surface representation. One major challenge is the accurate matching of all points between images since a single error will bias the obtained topography [Koenig et al. 1987]. Neural adaptive learning or machine learning have been successfully applied to ensure matching [Binaghi et al. 2004; Tafti et al. 2016]. Yet such approaches remain fragile as long as no assessment of the registration quality is available.

- Shape-from-shading is another method that was proposed in the 1970s [Lebiedzik 1975; 1979] and revisited many times. This approach exploits the dependence of the secondary or backscattered electron intensity on the surface orientation and detector position [Horn 1977]. The use of multi-detectors has been proposed to perform topographic reconstruction in an SEM without a physical rotation of the sample. Thus only gray level differences are exploited, and not detailed registration. The difficulty is the quantitative interpretation of these gray level variations, in particular for the SE mode, in spite of their better spatial resolution [Suganuma 1985]. At present, this technique is mostly qualitative.

The more recent SEMs can operate on tilted samples thanks to their enhanced depth of focus and better control of e-beam collimation. This is in particular exploited in EBSD analyses where the sample is generally tilted to about 70°. In the present study, the stereoscopic approach is followed to evaluate the surface topography from two orientations. The latter are chosen as the ones corresponding to these standard acquisition modes (*i.e.*, normal to the beam axis and in the EBSD-tilt orientation). Although the principle of stereoscopic topography reconstruction is classical, such orientations are very unusual. To tackle this problem, regularized global DIC is used to register images after having revealed a speckle pattern consisting of Pt dots deposited onto the surface. This procedure allows the changes in gray levels due to the very large tilt angle to have no influence on the quality of registration. The sample used as a support for this study is a steel specimen with a polished surface, but subjected *in-situ* to a mechanical test up to 6 % macroscopic strain. This method and result of such topography measurements are detailed in Section 5.2.

In order to assess the quality of the surface topography measurement, 3D-EBSD is used, where only surface topography is considered herein for comparison purposes. The procedure and results are detailed in Section 5.3. Last, a third original approach is presented that aims at capturing the change in topography as resulting from crystal rotations only (Section 5.4). Crystal rotation fields are measured from a series of EBSD images acquired at different stages of deformation via so-called *"quaternion correlation,"* which was proposed to track the grain boundary kinematics in polycrystalline solids (see Chapter 2). Based on the sole crystallography, grain rotations can explain part of the out-of-plane surface displacements, and hence topography formation. However, plastic flow does not alter the crystal orientation and hence cannot be assessed with this tool. Conversely, it allows the relative part of crystal rotation vs. plastic flow in the formation of topography to be estimated. In the present case, it is shown that in spite of significant plastic flow, crystal rotations (as measured herein) capture already a significant part of topography. The relative merits and weaknesses of all these approaches is discussed in Section 5.5.

5.2 SEM tilt-imaging method

5.2.1 Mechanisms

The principle of stereoscopic topography evaluation is well-known [Howell 1975]. From images of the surface under two orientations, the topography can be reconstructed. Generally the two orientations are chosen as tilted from the electron beam axis by $\pm 10°$ [Boyde 1973; Lockwood and Reynolds 1999; Zhu et al. 2011]. Here, this technique is applied to two orientations, namely, in the first one the mean surface normal is parallel to the e-beam axis, while the second is tilted to roughly 70° in the standard EBSD configuration (Figure 5.1). This choice is made because these two orientations are often accessible when an EBSD analyzer is present. However, such a very large tilt angle is not used for stereoscopic analyses, as large distortions and shadowing effects may be feared. Moreover, the fragility of missing matching points as earlier mentioned is also expected to be increased in such a configuration. It will be shown that regularized global DIC restores the needed robustness for such a technique to be safely used.

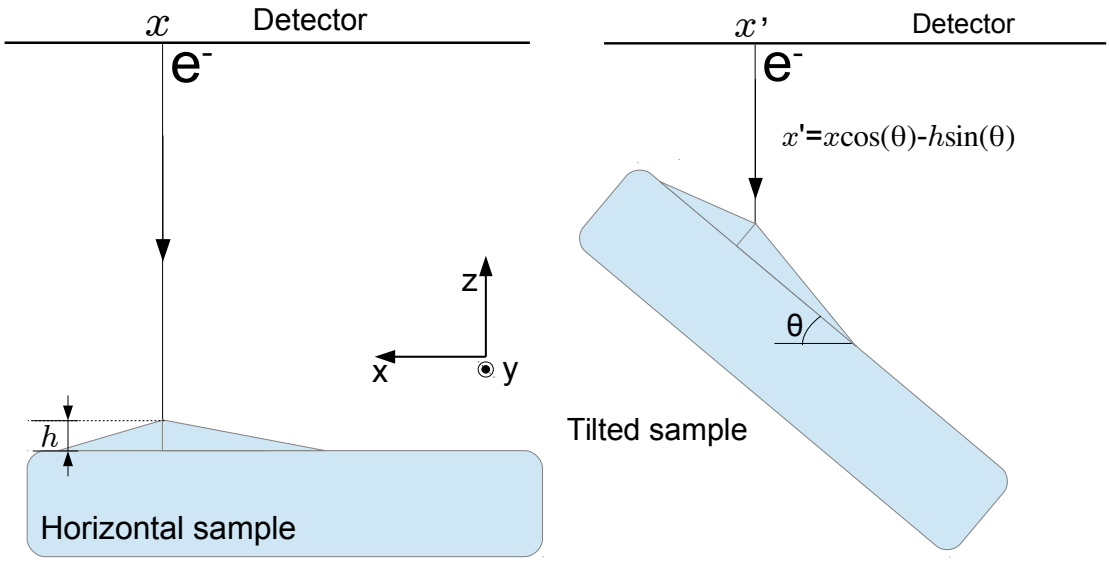

(a) (b)

Figure 5.1: Mechanism of the tilt-imaging method. SEM image of the sample on horizontal (a) and tilted (b) positions by angle θ.

Since the adopted SEM magnification is high (*i.e.*, $\times 6400$), the e-beam is considered as parallel [Koenig et al. 1987]. In the horizontal configuration, the sample surface is denoted as $z = h(x, y)$. The tilted configuration is obtained after a rotation of angle θ about the y axis, as shown in Figure 5.1.

In the tilted configuration, the point (x, y, z) is mapped horizontally at a position (x', y', z'), where

$$x' = x\cos(\theta) - h(x, y)\sin(\theta) \tag{5.1}$$

and $y' = y$. Typically, for a small roughness, $h \ll x$, the main effect of tilt is a mere affinity, by a factor $\cos(\theta)$ (*i.e.*, just as if $h = 0$ in the above equation). Compensating for this scale factor by an inverse affine transformation, $x'' = x'/\cos(\theta)$, moves the point to a position $x'' = x - h(x, y)\tan(\theta)$. Hence the topography simply translates into a displacement $u_x = h(x, y)\tan(\theta)$.

5.2.2 Uncertainty quantification

Before applying the tilt-imaging method to the real topography, an uncertainty evaluation has been performed. Pt speckles have been deposited at prescribed positions on a Ge single crystal sample with a polished surface. Each Pt speckle is a disk whose diameter is 300 nm and height 75 nm. The sample surface is assumed to be perfectly flat and the measured

topography is attributed to errors. The first image has been taken with the Ge sample in the horizontal position (see Figure 5.2(a)), and the second image when the sample has been inclined at 70° (see Figure 5.2(b)). The image definition is 2048×2048 pixels, and covers an area of 110×110 µm^2. The images have been acquired with an acceleration voltage of 30 kV and a working distance of 16 mm. To reduce the possible SEM drift distortion, each SEM image is the average result of 30 scanned frames. The scan speed is set to 3, which corresponds to a dwell time of 1 µs to lower the image acquisition duration. With these settings, it has taken 2 minutes to get an image. Global DIC with mechanical regularization has been applied on the image pair, and the resulting displacement fields in x and y directions are shown respectively in Figures 5.2(c) and 5.2(d).

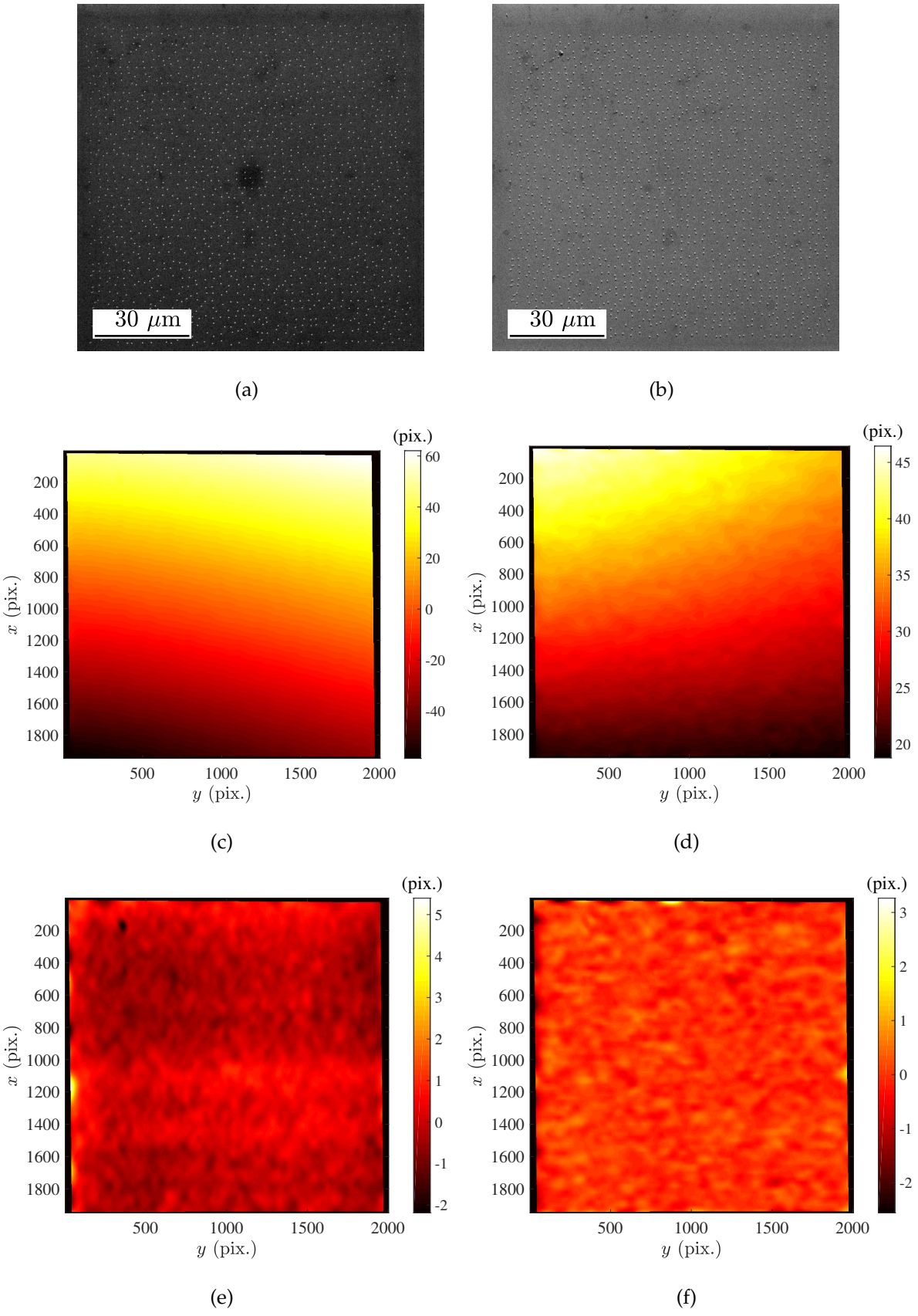

Figure 5.2: (a) SE image of horizontal Ge sample with Pt spots. (b) SE image of the Ge sample inclined at 70° after applying tilt corrections. Displacement field as measured via DIC in x (c) and y (d) directions, respectively. Displacement field after removing global quadratic trend in x (e) and y (f) directions, respectively. The displacement is expressed in pixels and the pixel size is 53.7 nm

According to Section 5.2.1, u_x contains the topography information, which is vanishing in the present case, and possibly a linear component that is related to the inclination angle θ. However, a long wavelength bias is seen in both u_x and u_y components. This is due to the scan artifacts that are not corrected. A second order polynomial regression is thus removed from the measured displacement as this bias is not considered as reliable, and being a low frequency modulation, it will lead to a minor change in the estimated topography. The resulting displacement components are shown in Figures 5.2(e) and 5.2(f). Contrary to the rather uniform u_y field, the u_x field exhibits horizontal bands. This is interpreted as a slow-scan direction error (due to the repositioning inaccuracy at the beginning of each new scanned line). An adapted global DIC procedure has been developed to correct this specific error by acquiring two images with different scanning directions [Teyssedre et al. 2011; Shi et al. 2018a], yet the algorithm cannot be applied to two images on the inclined sample by the current SEM. Without correcting the slow-scan direction error, the root mean square (RMS) average of u_x shown in Figure 5.2(e) is 0.41 pixel (or 22.3 nm). The corresponding RMS average of topography measurement uncertainty is estimated to be 8.1 nm (22.3 nm/tan(70°)). For comparison purposes, the RMS average of u_y shown in Figure 5.2(f) is 0.23 pixel (or 12.3 nm). The effect of the SEM scan drift distortion on the topography measurement is thus quantified.

It should be noted that an uncertainty level of 8.1 nm is very satisfactory, with respect to the pixel size of 53.7 nm. Although the principles of tilt-imaging are far from new, the recourse to such high tilt angle is unusual, and global DIC used herein together with a well-suited speckle patterning provide very robust and accurate topography measurements.

5.2.3 Test case

The tensile test sample described in Ref. [Shi et al. 2018a] is used to validate the tilt-imaging method. The same Pt speckles described in Section 5.2.2 have been deposited onto the sample surface. In addition, using the same technique, a Pt rectangle was drawn around the speckled region to easily locate the region of interest (ROI). The "horizontal" SE image of the sample is shown in Figure 5.3. The image definition is 3072×3072 pixels and covers an area of 130×130 µm^2. The images have been acquired with an acceleration voltage of 30 kV and a working distance of 13 mm. To reduce the possible SEM drift distortion, each SEM image is the average of 30 scanned frames. The dwell time has been set to 1 µs to increase

the image acquisition speed. With these settings, 5 minutes were needed per acquisition.

The SEM drift distortion for the aforementioned conditions have been analyzed in Ref. [Shi et al. 2018a], and amount to approximately 1 % in both x and y directions. The uniform linear SEM drift distortion will not lead to topography measurement errors, since its effect will be removed in the linear fitting step. The random SEM drift from line to line has been analyzed and quantified in Section 5.2.2. As a result, the large image resolution together with the adopted acquisition conditions provide a rich characterization of the sample surface, while the uncertainty due to SEM drift is kept to a limited level.

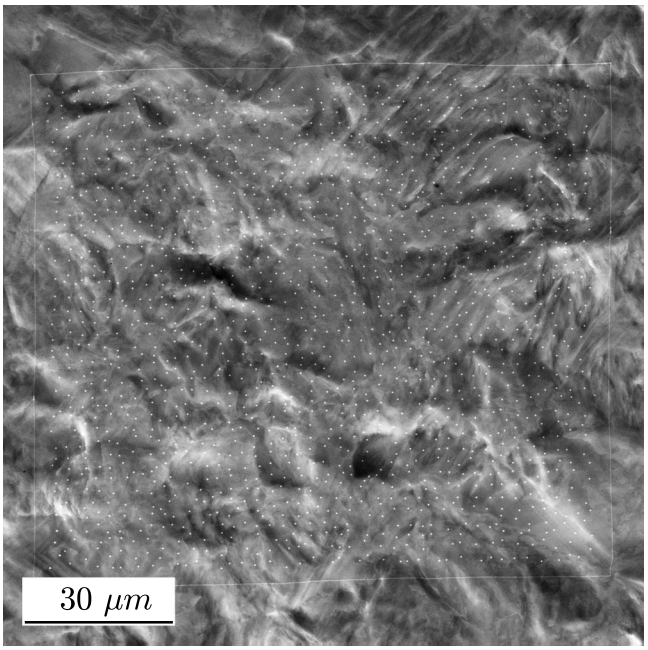

Figure 5.3: SE image of the sample in the horizontal configuration.

Then the sample is tilted by about 70° and an SE image of the same size is recorded *without activating the tilt correction function of the SEM* (Figure 5.4(a)). The stage rotation parameter of the SEM has been adjusted to make the Pt rectangle horizontal. The lateral surface of the sample is imaged in the bottom part of the image. The "valleys" and "hills" are very prominent on the sample surface because of the shadowing effect of a rather grazing incidence. The affinity due to tilt along the vertical direction is first corrected, as shown in Figure 5.4(b), by a scale factor of $1/\cos(\theta) = 2.7$, where this value is a rough estimate obtained by tracking the rectangular marking on the surface. This factor will however be accurately determined in the following and hence this first rough determination is only aimed at initializing the registration procedure.

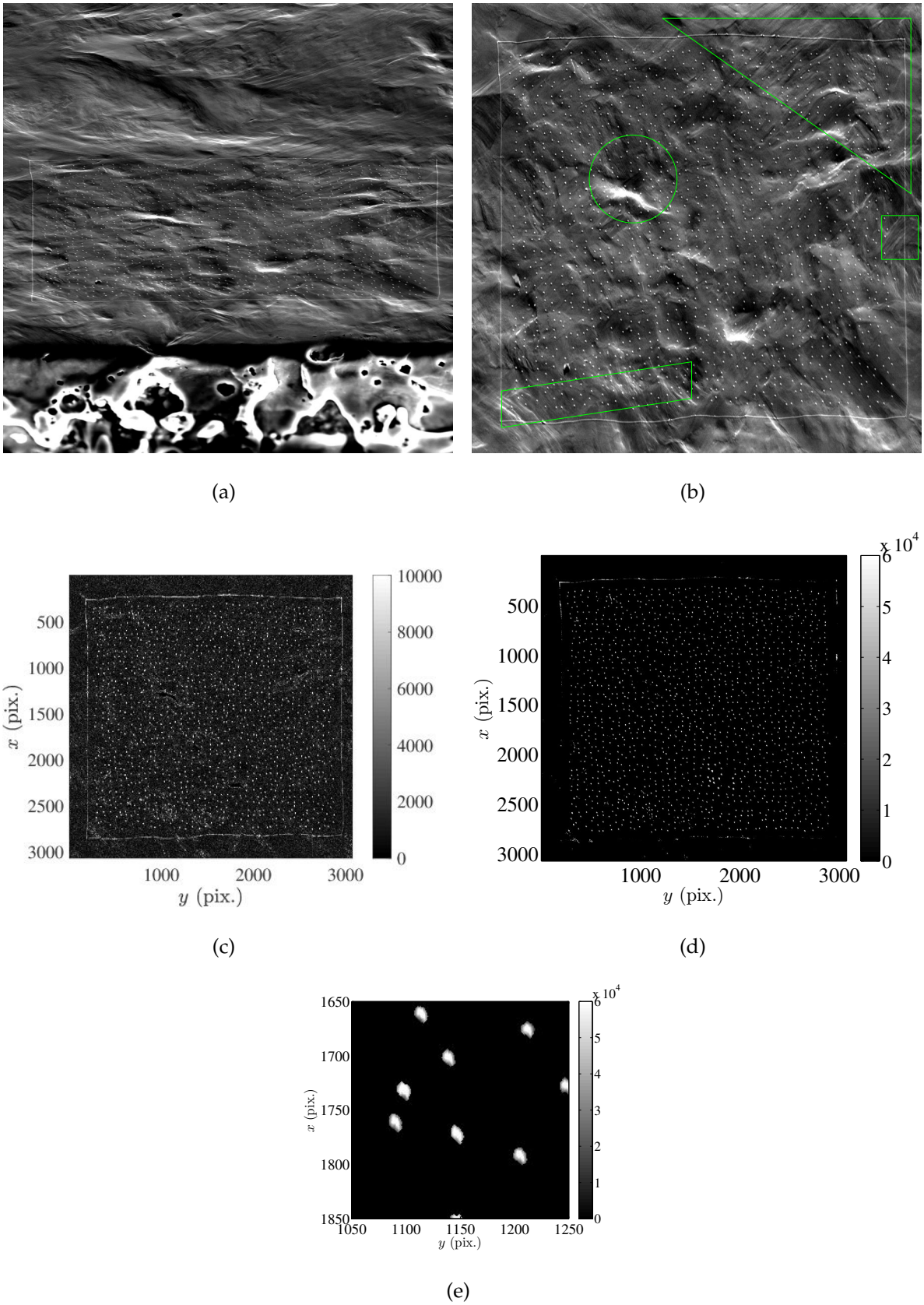

Figure 5.4: Pre-correction of the tilted image. (a) Original SE image of the tilted sample. (b) Stretched image 2.7 times along the vertical direction. Several regions with visible slip traces are indicated in green. (c) Norm of the gray level gradient. (d) Processed tilted image and (e) zoom to show the rendering of the Pt spots. The pixel size is 42 nm for all images.

In such a transformation, the brightness and contrast change very significantly, which is due to the interaction between the e-beam and the sample surface. The goal is not to explore such physics and propose a model interpreting the gray levels. Rather it is preferred to focus on the surface marking, namely, the Pt spots that were deposited as a speckle pattern. They are very clearly visible in the reference image. They become also much clearly visible in the tilted image (Figure 5.4(a) and 5.4(b)). In order to filter out the brightness information of the substrate material, the norm of the gray level gradients is calculated (Figure 5.4(c)). The Pt spots are better revealed, which is due to their steep gray level variations. A threshold has been applied to Figure 5.4(c) to get the positions of all the Pt spots, with the exception of a few locations that cannot be distinguished from the bright background. The gray level of Pt spots and their vicinity is kept, while all other pixel levels are set to 0 in the treated tilted image (Figure 5.4(d)). A zoom of the final image is shown in Figure 5.4(e) where the gray level gradient at Pt spots are visible.

The displacement field is assessed via DIC between the two images shown in Figure 5.3 and 5.4(d). A finite-element description of the kinematics is used with 3-noded elements with linear interpolation functions (*i.e.*, T3-DIC [Tomičević et al. 2013]). Only the region covered by Pt speckles is studied, as shown in Figure 5.5(a), and an unstructured mesh with characteristic length of 25 pixels is used.

Due to the concentration of contrast around Pt speckles (Figure 5.4(d)), regularization is introduced to provide a smooth interpolation at very small scales when Pt speckles are not seen or very faintly. A regularization based on an elastic kernel [Tomičević et al. 2013] is utilized in the present work to filter out high frequencies, with a cut-off frequency (*i.e.*, the inverse of the so-called regularization length) that can be tuned at will (see Section 1.2.1.3). The regularization length has been gradually reduced from 400 pixels down to 100 pixels. It can be seen in the DIC residual field (*i.e.*, the difference between reference and corrected deformed images after registration) shown in Figure 5.5(b) that all the Pt speckles are well matched between both images, with the exception of the lost speckles in bright regions shown in Figure 5.4(b). Displacement fields in x and y directions are shown in Figure 5.5(c) and 5.5(d).

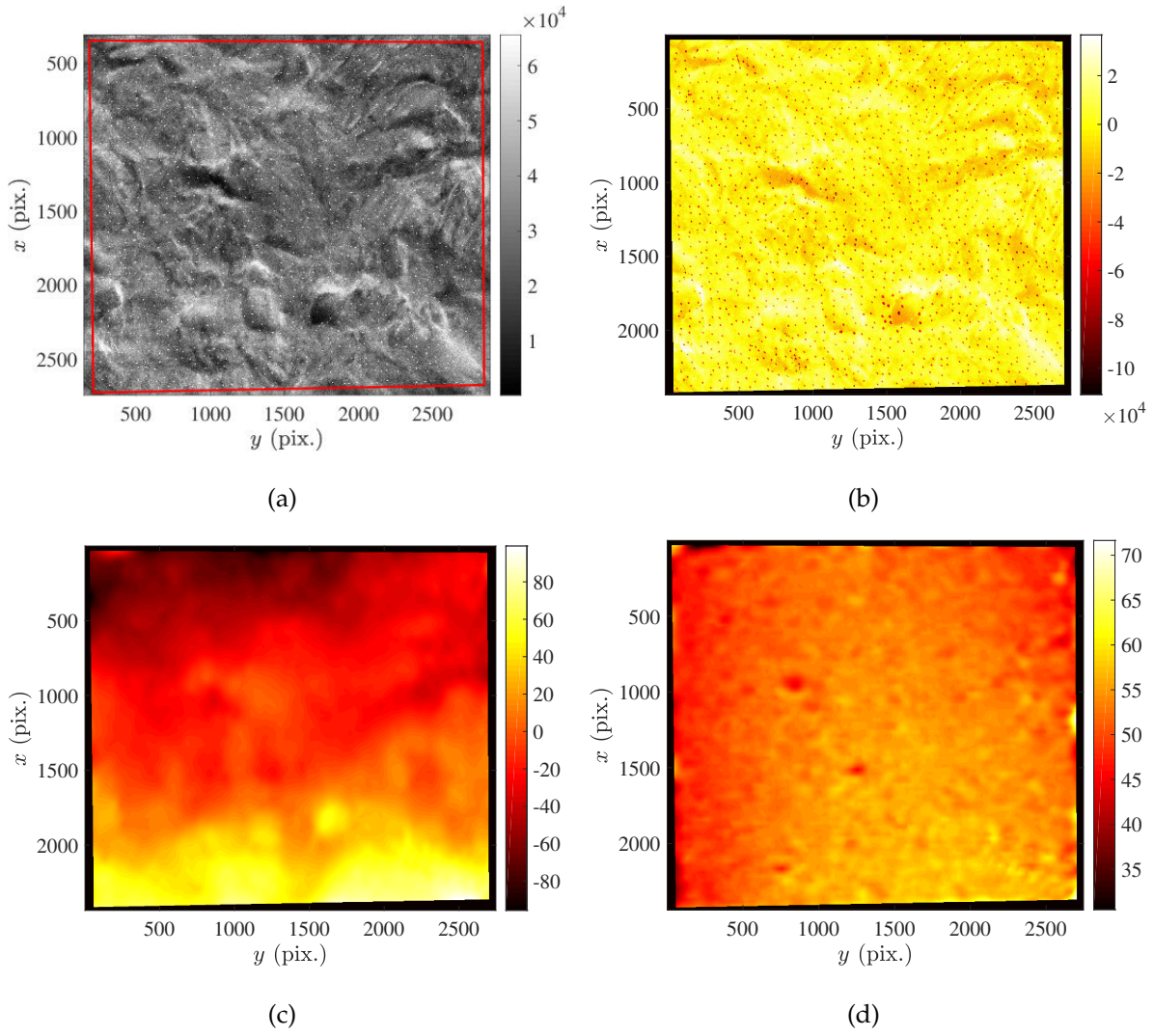

Figure 5.5: DIC calculation in the tilt-imaging method. (a) Region of interest for DIC. (b) Gray level residual field. (c,d) respectively x and y component of the resulting displacement field (expressed in pixels, 1 pixel $\leftrightarrow$ 42 nm) between the images shown in Figures 5.3 and 5.4(b).

The u_x displacement component shows a significant gradient along x, proving that the initial guess used for the pre-correction by the scale factor $1/\cos(\theta) = 2.7$ was not the best suited value. A linear regression through the data is performed to perform a better tilt compensation, leading to a much more precise estimate of the tilt angle

$$\cos(\theta) = 0.39 \tag{5.2}$$

or $\theta \approx 67.1°$. It should be noted that a precise assessment of the tilt angle in EBSD positions has a big impact on EBSD acquisitions, not only on the absolute value of the indexed crystallographic orientation, but also on the coordination of EBSD figures after the tilt correction [Nolze 2007]. It is believed that this method could become a routine process prior to

EBSD acquisition when high precision is required.

Then the topography field h is computed from $h(x, y) = u_x \cot(\theta)$ (see Figure 5.6(a)). For comparison purposes, the ferritic grains in the studied region are manually selected and highlighted in Figure 5.6(b). The selection criterion of ferritic grains is the absence of lath structure in the range 1-3 µm.

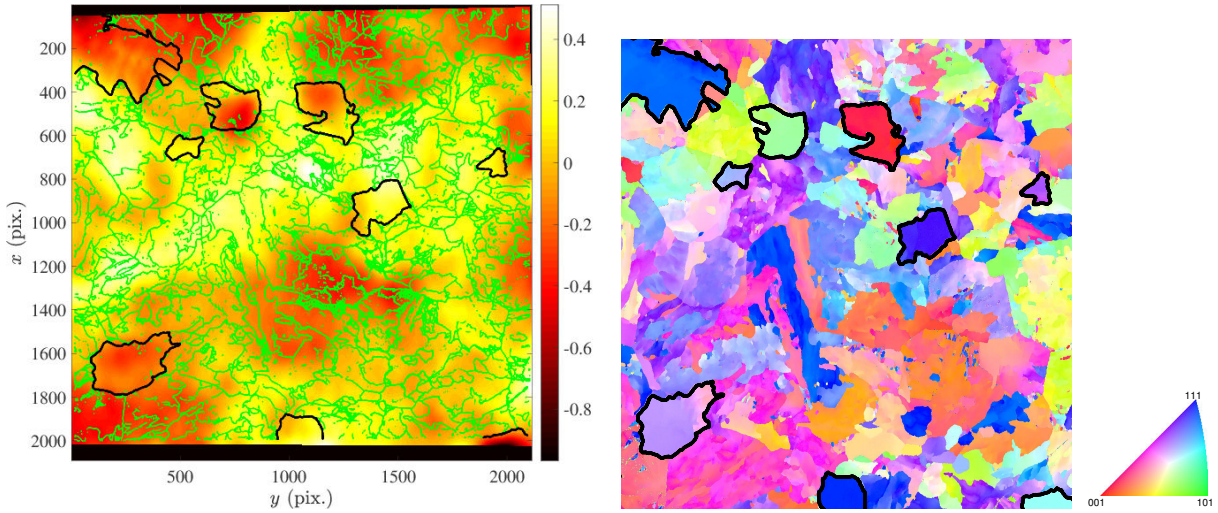

(a) (b)

Figure 5.6: (a) Estimated topography field. To better illustrate the relationship between topography and sample microstructure, the grain boundaries are shown as green lines for bainite and black lines for ferrite. (b) Ferritic grains in the studied region are highlighted for comparison purposes. The pixel size is 50 nm.

The RMS of the topography measured by tilt-imaging is 188 nm, while the maximum peak-to-value distance is 1.36 µm. It is concluded from Figure 5.6 that the height of large ferritic grains tends to be lower than average, especially at the grain center. This phenomenon is not surprising, as this softer phase tends to elongate more in a tensile test, thus due to plastic incompressibility, the surface contracts more than other grains. Note that there exist several regions rich of visible activated slip systems in Figure 5.4(b), which indicate the presence of "paddy-rice-field"-like topography. However, these structures are beyond the resolution and thus not captured in Figure 5.6(a). A higher resolution and suited marking would be required to resolve them.

The sizes of Pt speckles are adjusted for EBSD acquisitions. Consequently, relatively large and rather few spots have been deposited onto the sample surface. If topography were chosen to be the principal quantity of interest, then a finer and denser speckle marking would lead to a better spatial resolution. In the present case, the evaluation of topography

was seen as an opportunity, namely, a side-result that could be obtained at no additional cost after an EBSD analysis was chosen.

It should be emphasized that the tilt-imaging method does not differ from standard stereoscopic SEM techniques in terms of underlying principle. However the stereoscopic technique usually involves two acquisitions with a tilt difference of about 10°. Thus the displacement magnitude between the acquired images is very limited. By adopting a fixed detector, in-lens or not, and tilting the sample, the "stereo-angle" can be chosen freely, preferably larger tilt angles to increase the signal-to-noise ratio. As soon as an EBSD device is installed in an SEM, such analysis can be performed by acquiring an additional SE/BSE image (without the tilt correction functionality), provided sufficient surface markings are engineered to enable for image registration. Further, as the above result shows, regularized DIC makes use of the limited and localized contrasted areas between the two stereo-images to measure a displacement field, thereby resulting in a smooth topography for the whole area of interest. The abrupt slope change at mesh boundaries is thus avoided.

5.3 FIB method

After the *in-situ* tensile test, a region of the same sample has been chosen as potential FIB milling area. This region, roughly 1/9th of the speckled part of the sample surface, is located near the edge to make milling easier and at the boundary middle of the speckled zone to benefit from precise displacement measurements. The whole area around the region of interest is FIB-milled with high current to free the access and limit pollution during further analyses. This preparatory step can also reduce the volume to be milled during the main FIB-EBSD process, thus accelerate the experiment and reduce the potential coordinate drift. The region of interest has been covered by a 1 µm-thick layer of Pt (Figure 5.7(a)). This Pt coating acts as a sacrificial protective layer for FIB milling. Moreover, performing EBSD after successive slice removals, amorphous Pt is easy to distinguish from the steel substrate. The successive interfaces with Pt follow precisely the initial free surface of the sample. Note that a similar protective tungsten layer was deposited in the past to mainly protect the free edges against diffuse FIB cutting [Zaafarani et al. 2006]. So-called 3D-EBSD provides a much richer information than surface topography, but this technique also allows for quantitative measurements of topography, and is used herein as the ground truth.

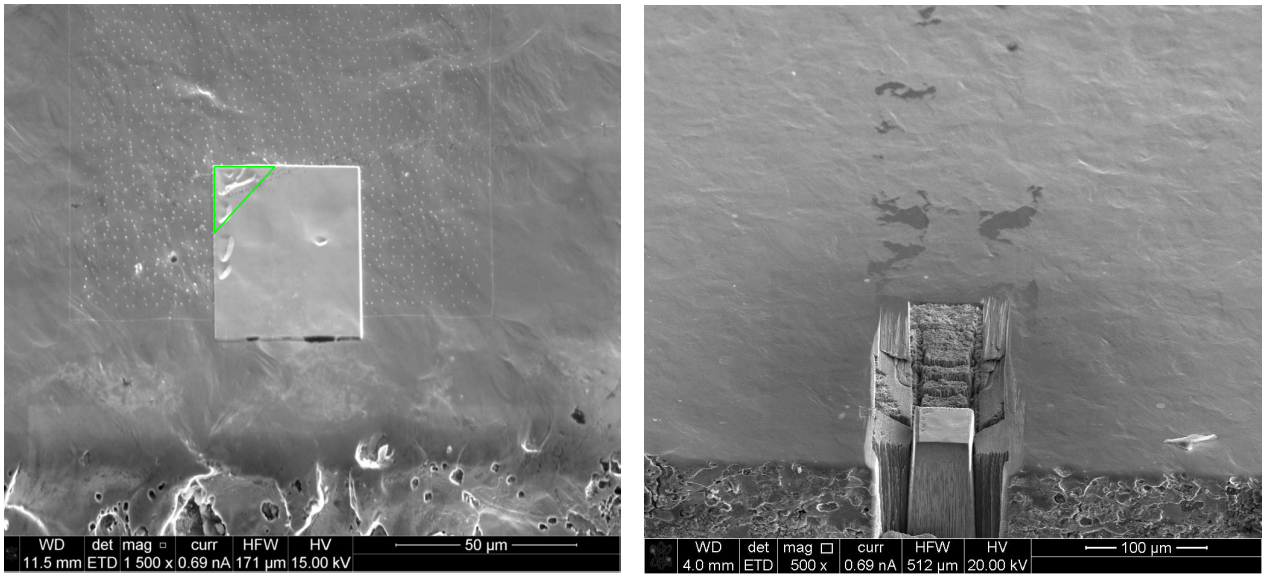

(a) (b)

Figure 5.7: Preparations of FIB-EBSD. (a) Chosen area covered by a layer of Pt. (b) Neighborhood of the area of interest is first removed to make milling easier. The volume to follow the 3D-EBSD procedure is at the top of the pillar that was carved out (bottom of sub-figure (b)).

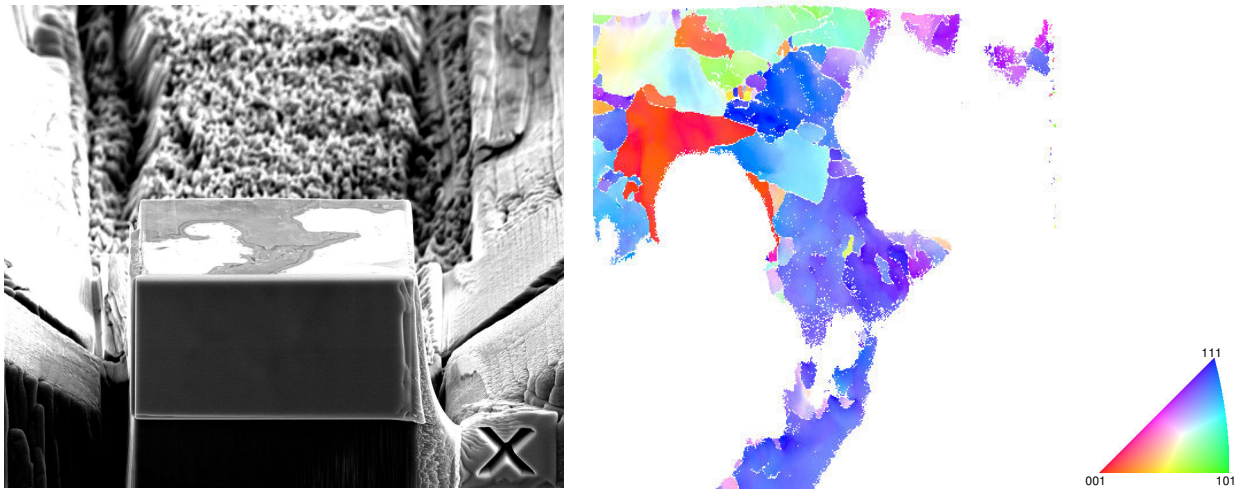

(a) (b)

Figure 5.8: (a) Sample aligned in FIB position at an intermediate stage of the 3D-EBSD procedure. The top of the pillar shows both the emergence of the most salient regions of the sample surface and the Pt covered deeper regions. (b) Indexing of crystal orientation by EBSD at the same stage.

Prior to the main FIB-EBSD process, the surface of the ROI has FIB-milled with high

current to ensure a flat surface thus prevent "theater curtaining" [Munroe 2009]. Special care is required to enable for accurate z-direction realignment after each sample motion as FIB milling and EBSD analyses require different positions of the sample in the SEM chamber. A cross-shaped mark has been milled close to the studied area for such an alignment. The software EBS3 G2 used for FIB-EBSD recognizes the mark and measures its motion by cross-correlation with sub-pixel resolution. The sample in the FIB position is shown in Figure 5.8(a) after few milling steps. The clear contrast at the sample surface reveals that the substrate material emerges at some places while the Pt coating persists at others. The crystal orientation map as indexed by EBSD (Figure 5.8(b)) accurately quantifies this analysis. The acceleration voltage has been 30 kV, and the physical size of one pixel 100 nm for every EBSD acquisition. Each EBSD indexing takes about 50 min. The pollution induced by the EBSD analysis has been eliminated by the next FIB milling step.

In total, 118 slices have been milled and indexed for a duration of one week. A volume of $42 \times 41 \times 11.8$ µm^3 is available. The orientation maps of the first eight slices of FIB-EBSD are shown in Figure 5.9. The white area indicates the not-indexed region, which is covered by the Pt layer. As a result, the first 8 inverse pole figures can be seen as a binary height image for sample surface. The Pt layer gradually recedes and completely disappears at the eighth slice. The first slice shown in Figure 5.9(a) has already a significant indexed area, especially at the upper left region. This is where the Pt deposition is thinner, as shown in the boxed region of Figure 5.7(a). Besides, the FIB-milling of the ROI surface before FIB-EBSD (in order to remove the roughness of the ROI surface) could have removed the Pt layer, even some substrate material, at peaks of the sample. This phenomenon implies that the Pt layer was not thick enough and presumably the most salient peaks of the topography were erased during the first surface preparation.

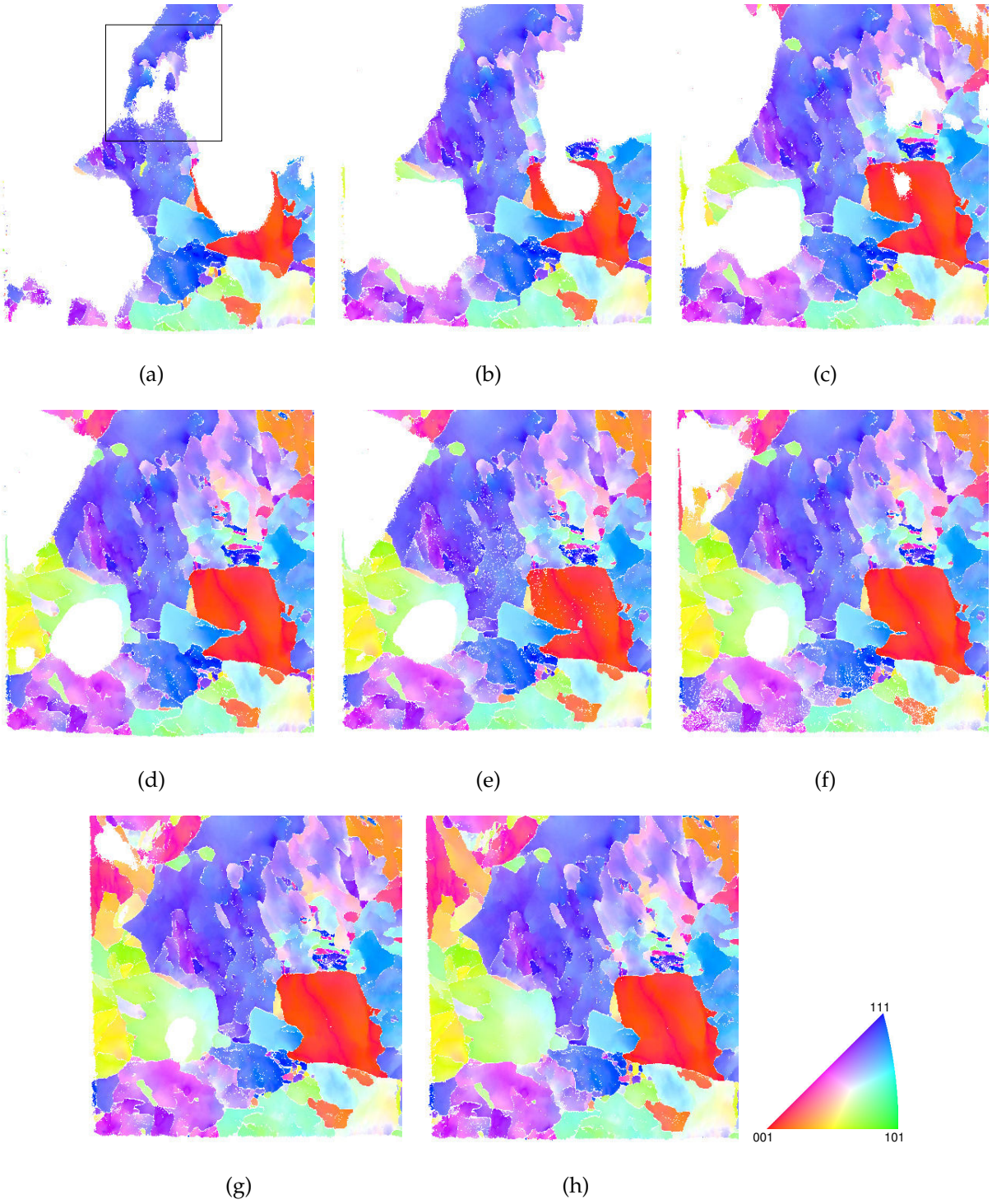

Figure 5.9: Orientation maps of the first 8 FIB-EBSD slices. The deposited Pt layer (appearing in white) is completely removed in the eighth slice.

The transition between indexed and not-indexed areas is gradual in most cases, thus the indexed grains near the remaining Pt layer seem more "transparent," as shown in the boxed area of Figure 5.9(a). A filter process is applied to provide a more clear-cut binary height image. Simple image processing operations are used, "open" and "close" steps involving

only nearest neighbor pixels so as not to alter the large scale features by artificial smoothing. The effect of the filter is shown in Figure 5.10. It is observed that not only a more precise topography image results from such procedure, but also a finer microstructure is revealed.

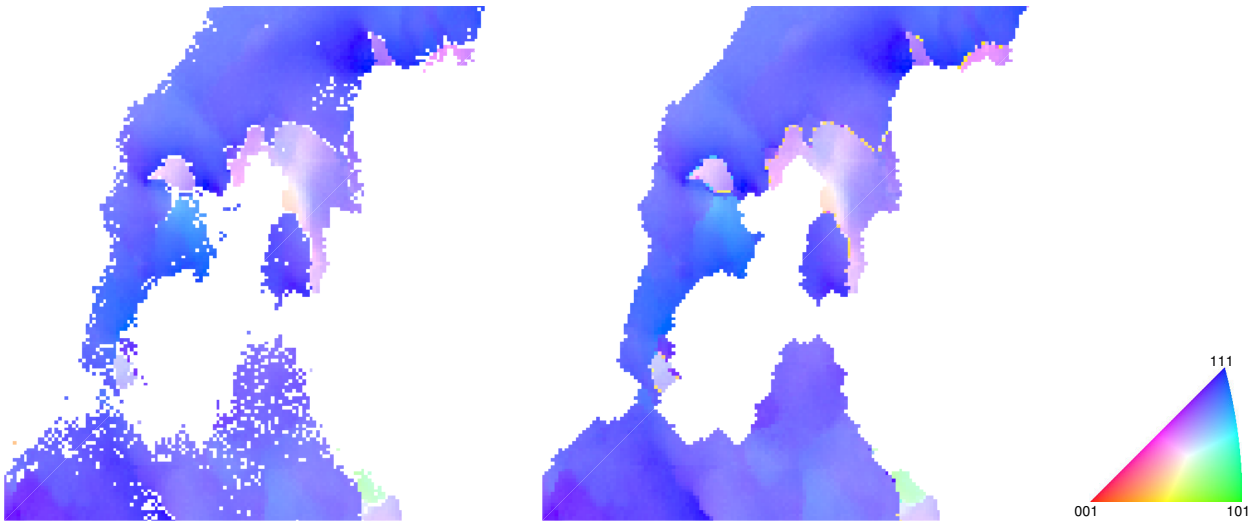

(a) (b)

Figure 5.10: Effect of filter operation on FIB-EBSD images. (a) Raw FIB-EBSD figure extracted from Figure 5.9(a). (b) Filtered image. Image "open" and "close" steps, and interpolation of the crystallographic orientation are involved.

The filtered 3D-EBSD data were collected and processed with Dream3D, an open source software dedicated to the analysis of 3D microstructures [Groeber and Jackson 2014]. For FIB-EBSD data, the code reads the indexed orientation maps, realigns each slice in the (x, y) plane and labels each grain based on a user-defined disorientation threshold. Slice realignment is necessary since shift inevitably occurs between subsequent EBSD acquisitions.

Indexing of crystal orientation at grain boundaries is difficult and imprecise, and one should pay attention to automatic corrections performed on non-indexed pixels. Here, the Pt coating phase was labelled manually as a grain on its own to prevent spurious modifications of the Pt-sample interface in the standard data "cleaning" procedure that is automatically performed. After completion, it suffices to delete the Pt grains and the topography becomes visible (Figure 5.11(a)). Besides, a full crystallographic image of the sample surface is also obtained by combining the first 8 FIB-EBSD slices (Figure 5.11(c)). The reconstructed sample surface is identical to the inverse pole figure of the sample before Pt layer deposition, which is shown in Figures 4.13(d) and 4.13(e). It should be noted that due to the discrete nature of the FIB milling process, the topography reconstructed by this procedure has terraces, each

of height 100 nm (or 1 pixel). To filter out the topography while preserving the terrace edges, successive Fourier filtering enforcing the terrace edges has been performed, and the result is shown in Figure 5.11(b).

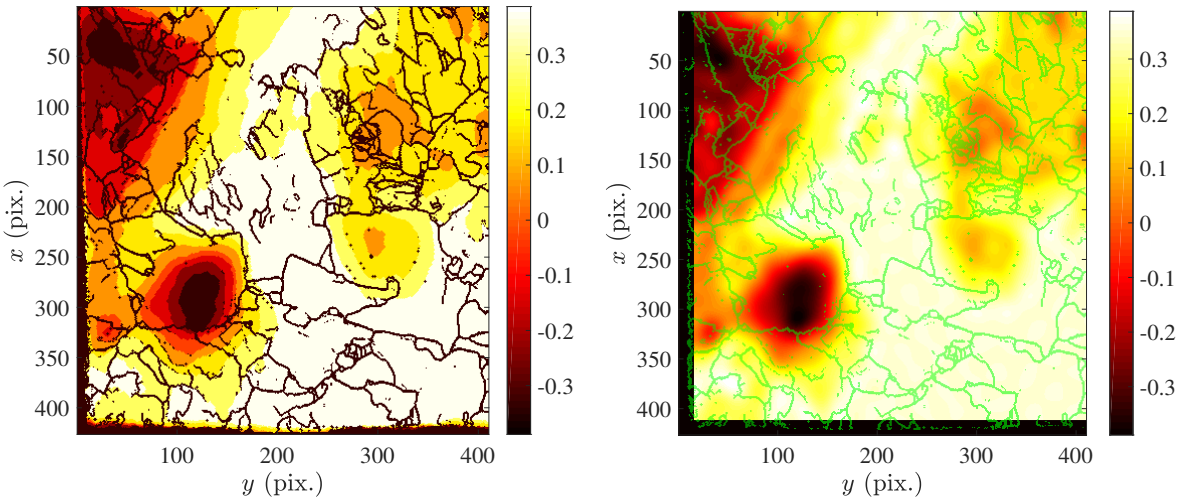

(a) (b)

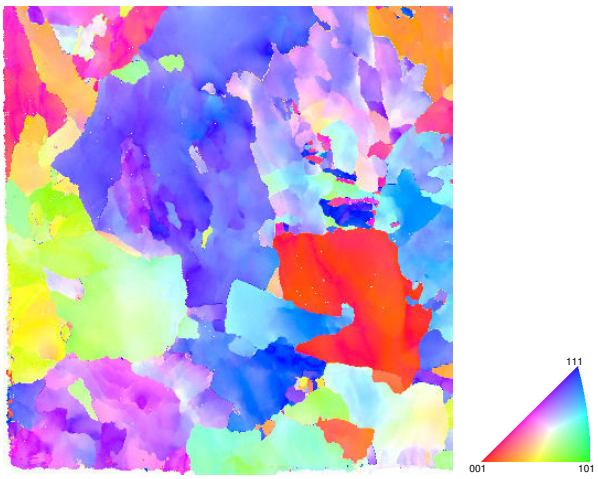

(c)

Figure 5.11: Reconstructed sample surface by FIB-ESBD. (a) Raw topography (expressed in µm). (b) Topography with a Fourier transform interpolation based on on-edge pixels. (c) Inverse pole figure of the sample surface obtained from the first 8 slices of 3D-EBSD procedure. The pixel size is 100 nm for all images.

5.4 Rotation-integration method

Quaternion correlation provides the displacement field and, more importantly, the crystal rotations (see Chapter 2). With the exception of plastic strains due to the motion of dislocations along activated slip systems, the displacements in all three directions are related to

crystal rotations. This principle can be used to extract the fraction of topographic changes due to plastic flow and due to crystal rotation.

In the following to make the discussion easier, it is first assumed that no plastic flow has occurred. The crystal rotation, which is applied to the pixel length, is then interpreted as the antisymmetric part of the displacement gradient (within the small perturbation framework). Moreover the sample surface is traction free, and hence the symmetric part of the displacement gradient (*i.e.*, the infinitesimal strain tensor $\boldsymbol{\epsilon}$) is constrained. In particular, vanishing shear stresses and strains $\varepsilon_{xz} = \varepsilon_{yz} = 0$ imply that the change in topography, u_z, which is the change in surface elevation between the two states chosen for quaternion correlation, are related to the rotation matrix $[\boldsymbol{Q}]$ based on axis-angle $(\theta, [d_1, d_2, d_3])$

$$[\boldsymbol{Q}] = \begin{bmatrix} (1-d_1^2)\cos\theta + d_1^2 & d_1 d_2\,(1-\cos\theta) + d_3\sin\theta & d_1 d_3\,(1-\cos\theta) - d_2\sin\theta \\ d_1 d_2\,(1-\cos\theta) - d_3\sin\theta & (1-d_2^2)\cos\theta + d_2^2 & d_2 d_3\,(1-\cos\theta) + d_1\sin\theta \\ d_1 d_3\,(1-\cos\theta) + d_2\sin\theta & d_2 d_3\,(1-\cos\theta) - d_1\sin\theta & (1-d_3^2)\cos\theta + d_3^2 \end{bmatrix} \tag{5.3}$$

The calculation of $(\theta, [d_1, d_2, d_3])$ from reference and deformed EBSD images is detailed in Appendix A. From this rotation field, the initially flat surface roughens and the topography gradients read

$$\begin{aligned} G_x &= \boldsymbol{e}_z \cdot \boldsymbol{Q} \cdot \boldsymbol{e}_x \\ G_y &= \boldsymbol{e}_z \cdot \boldsymbol{Q} \cdot \boldsymbol{e}_y \end{aligned} \tag{5.4}$$

where $\boldsymbol{e}_i$ is a unit vector in direction i (*i.e.*, x, y or z), and

$$\begin{aligned} G_x &= u_{z,x} \\ G_y &= u_{z,y} \end{aligned} \tag{5.5}$$

Note that the same argument would also hold for finite strains using the polar decomposition of the deformation gradient tensor.

The two fields G_x and G_y are theoretically related by the equality of cross-derivatives $G_{x,y} = G_{y,x}$. However, since they are estimated independently, numerically this relationship is violated (due to measurement noise). In order to minimize the effect of data noise, an integration using gradients in both directions via Fourier transform is well suited [Frankot and Chellappa 1988]. Denoting Fourier transforms with a ˜ symbol, and wave vectors as $\boldsymbol{k}$, the change in elevation u_z reads

$$\widetilde{u_z} = \frac{-i}{2\pi|\boldsymbol{k}|^2}(k_x\widetilde{G_x} + k_y\widetilde{G_y}) \tag{5.6}$$

which means that u_z variations are calculated from crystal rotations.

5.4.1 Uncertainty assessment

Before applying the rotation-integration method to the real topography, an uncertainty evaluation is performed. Two successive EBSD acquisitions were performed on the initial (*i.e.*, before tension) 16MND5 steel sample with a polished surface. The first image, shown in Figure 5.12(a), is arbitrarily chosen as the reference state and the second as the "deformed" configuration (Figure 5.12(b)). Quaternion correlation on these two images provides the "crystal rotation" between them, which combines the systematic and random errors in the crystallographic orientation determination of the SEM. Figure 5.12(c) shows the misorientation magnitude, ω, and Figures 5.12(d), 5.12(e) and 5.12(f) display the three components of a unit vector $\mathbf{\Omega}$ along the rotation axis. The mean value of ω is 0.69°, and its standard deviation is equal to 0.39°.

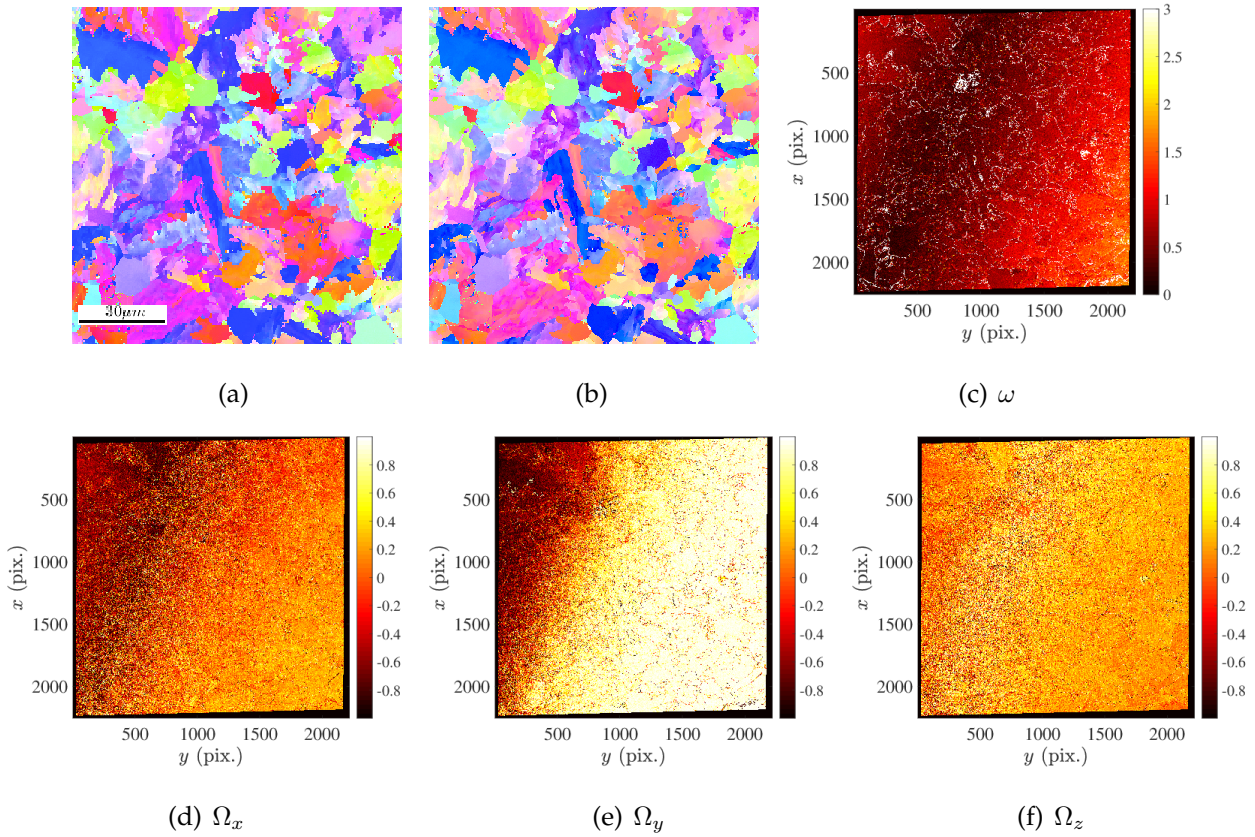

(a) (b) (c) ω

(d) Ω_x (e) Ω_y (f) Ω_z

Figure 5.12: Reference (a) and "deformed" (b) states of the polished sample surface. (c) Rotation angle ω (in degrees). (d-f) x, y and z components of the $\mathbf{\Omega}$ rotation axis. The pixel size is 50 nm for all images.

The corresponding topography gradients in x and y directions are shown in Figure 5.13(a) and 5.13(b). Combined with Figure 5.12, low frequency fields are seen especially in the G_y component. Because the initial geometry is flat, the displacement along z is equiv-

alent to the elevation. When integrated, the topography is obtained (Figure 5.13(c)). Rigid body motions of the sample between the two images can neither explain the misorientation shown in Figure 5.12(c), nor the integrated topography shown in Figure 5.13(c). This significant long wavelength misorientation could be attributed to the inadequate precision of pattern center during orientation indexing [Alkorta 2013]. A 2nd order polynomial regression through the elevation map is performed and removed in Figure 5.13(d). Compared to Figure 5.13(c), the 2nd order polynomial removes the majority of spurious topography, while the resulting elevations in Figures 5.13(d) and 5.13(e) imply that a 4th order polynomial is necessary to remove the remaining signal (Figure 5.13(f)). However, a regression by higher order polynomials may delete real signals, thus a compromise has to be made in real measurement cases. It is concluded that, after 4th order polynomial regression, the standard uncertainty of topography measurement is about 10 nm.

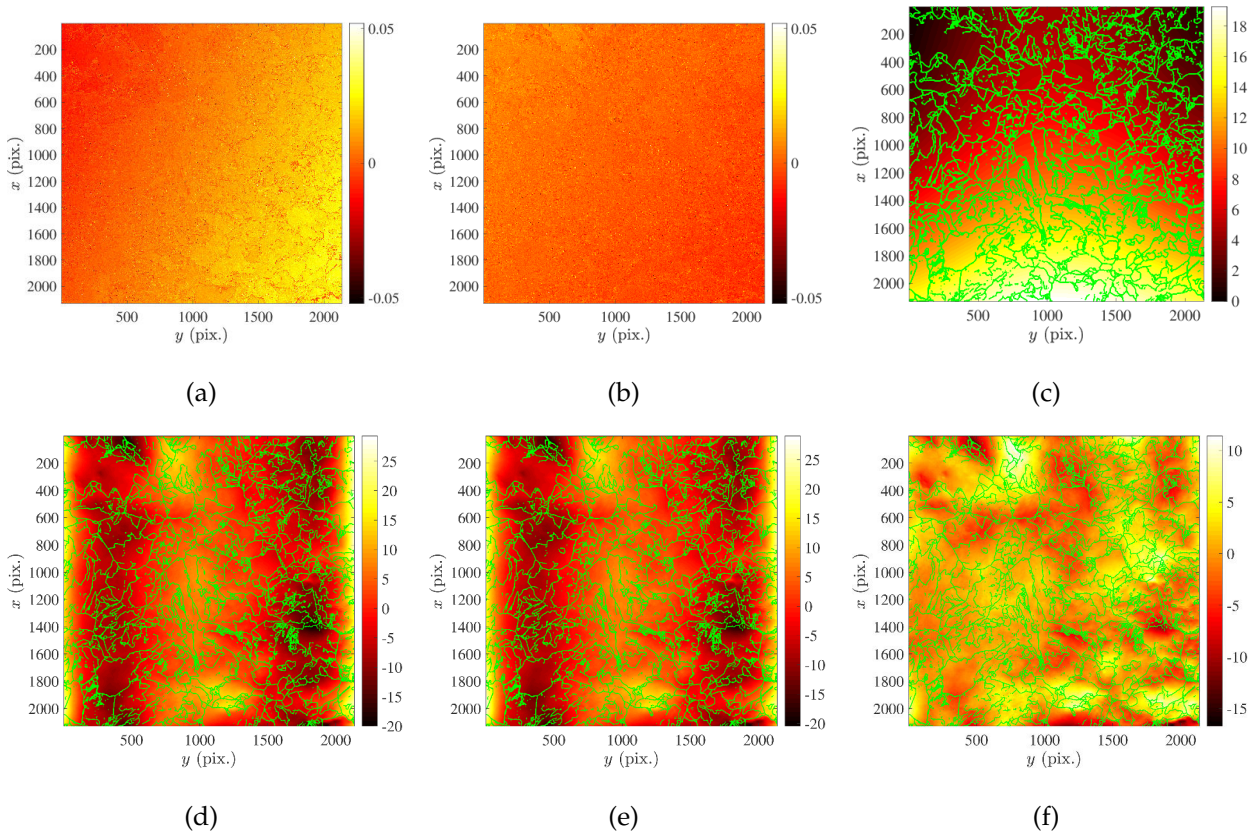

Figure 5.13: Surface elevation gradient in (a) x and (b) y directions obtained by crystal rotation. (c) Integrated elevation (expressed in µm) from the gradients. Elevation (expressed in nm) after removal of quadratic (d), 3rd-order (e), or 4th-order (f) polynomial trends. The pixel size is 50 nm for all images.

The method was also applied to two successive EBSD acquisitions on the deformed

sample surface to measure the topography reconstruction uncertainty. Again the artifactual topography due to global orientation drift is assumed to be removed with a 4th-order polynomial. The remaining topography field has a standard uncertainty of 11 nm, slightly higher than the previous test, due to the degraded EBSD image quality on strained samples. Consequently, it is observed that the SEM used in the present work has a non-negligible orientation indexing "drift," which makes the removal of fitted 4th-order polynomials from the topography necessary. As a result, only the local relative topography remains after this removal and is thus accessible for the EBSD images acquired by the tested SEM machine.

5.4.2 Analysis of the test

The EBSD acquisitions are first rectified to correct the coordinate distortions (see Section 4.5), then analyzed by the rotation-integration method. Figure 5.14(a) shows the crystal rotation magnitude and the components of the rotation axis director between the reference state where the surface is again flat (*i.e.*, initially polished surface), so that in the absence of plastic strain, the integrated displacement u_z would be equal to the elevation. Gradients G_x and G_y are shown in Figure 5.14(b) and 5.14(c) respectively. Crystal rotations at grain boundaries are omitted since they cannot be trusted. Figure 5.14(d) shows the estimated elevation obtained from integration and after a linear regression to the data has been removed to cancel out the possible global orientation drift and rigid body motion.

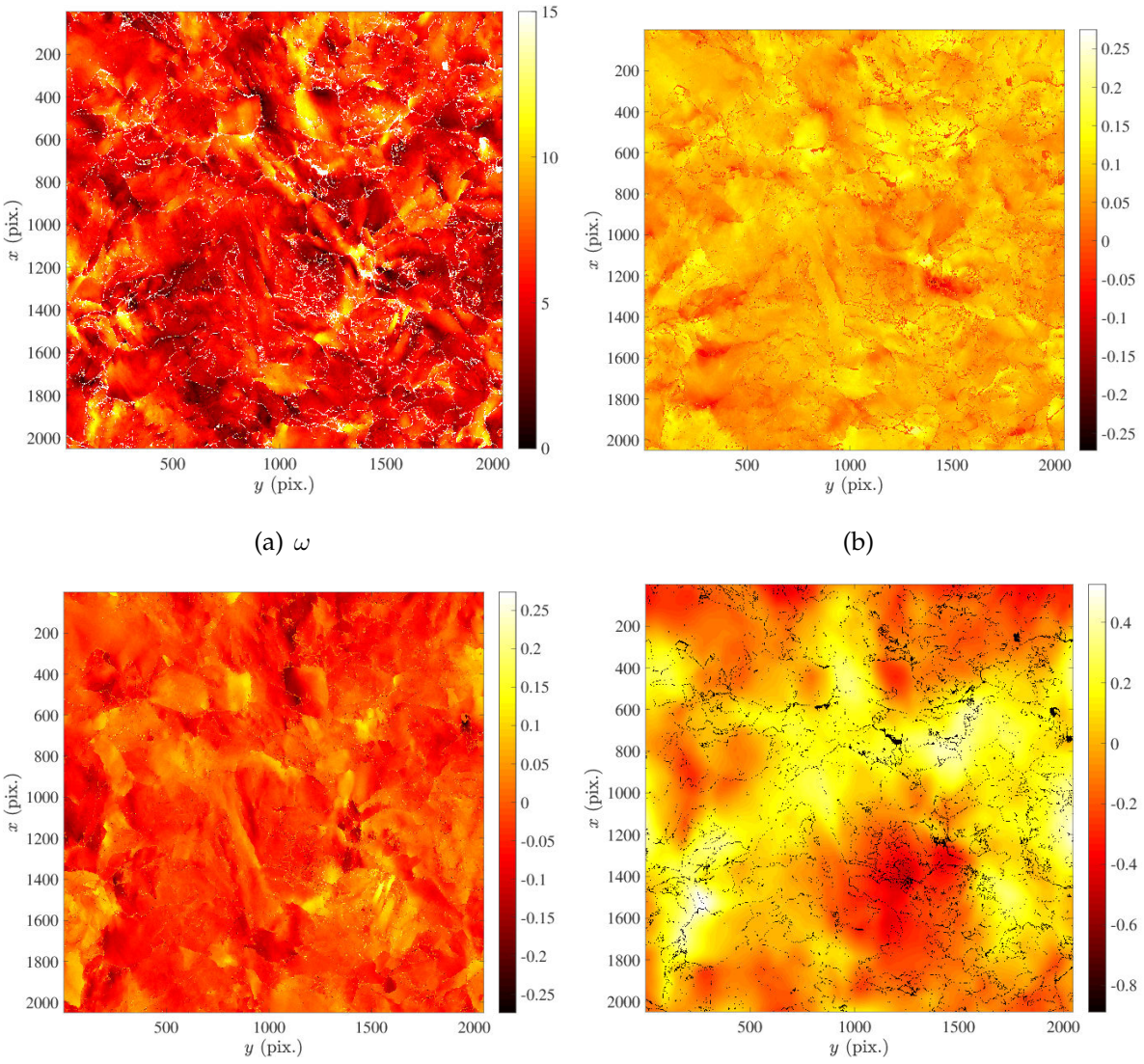

(a) ω (b)

(c) (d)

Figure 5.14: (a) Rotation magnitude (in degrees) between initial and final states of the tensile test. (b,c) Surface elevation gradient respectively in x and y directions obtained from crystal rotations. (d) Topography (expressed in µm) obtained from integration and subtraction of a linear regression through the data corresponding to orientation indexing "drifts" and rigid body motions. The pixel size is 50 nm for all images.

5.5 Comparison and discussions

The two methods introduced in the present chapter have been tested on the same sample. Thus it is interesting to perform a quantitative comparison of the topography measurement results. Due to time limitation and experimental cost, only 1/9 of the ROI surface was estimated by FIB-milling, while the entire ROI topography was measured by the stereo-

scopic method (as well as crystal rotation integration). The topography fields of the milled area measured by tilt-imaging and FIB (with FFT smoothing) are shown in Figures 5.15(a) and 5.15(b) respectively. Figure 5.15(c) shows the difference between tilting-image and FFT filtered 3D-EBSD measurements. It is observed that the first two methods give very consistent answers. The remaining differences are believed to be due to the lost peak topography information caused by insufficient Pt layer thickness. Note that since the reference plane may not be identical in the two measurements, a regression with a plane has been subtracted from the difference (this is equivalent to changing the reference plane $z = 0$ in one measurement in order to match the other one at best). Consequently, the tilt-imaging method is deemed validated, in spite of the very oblique incidence angle.

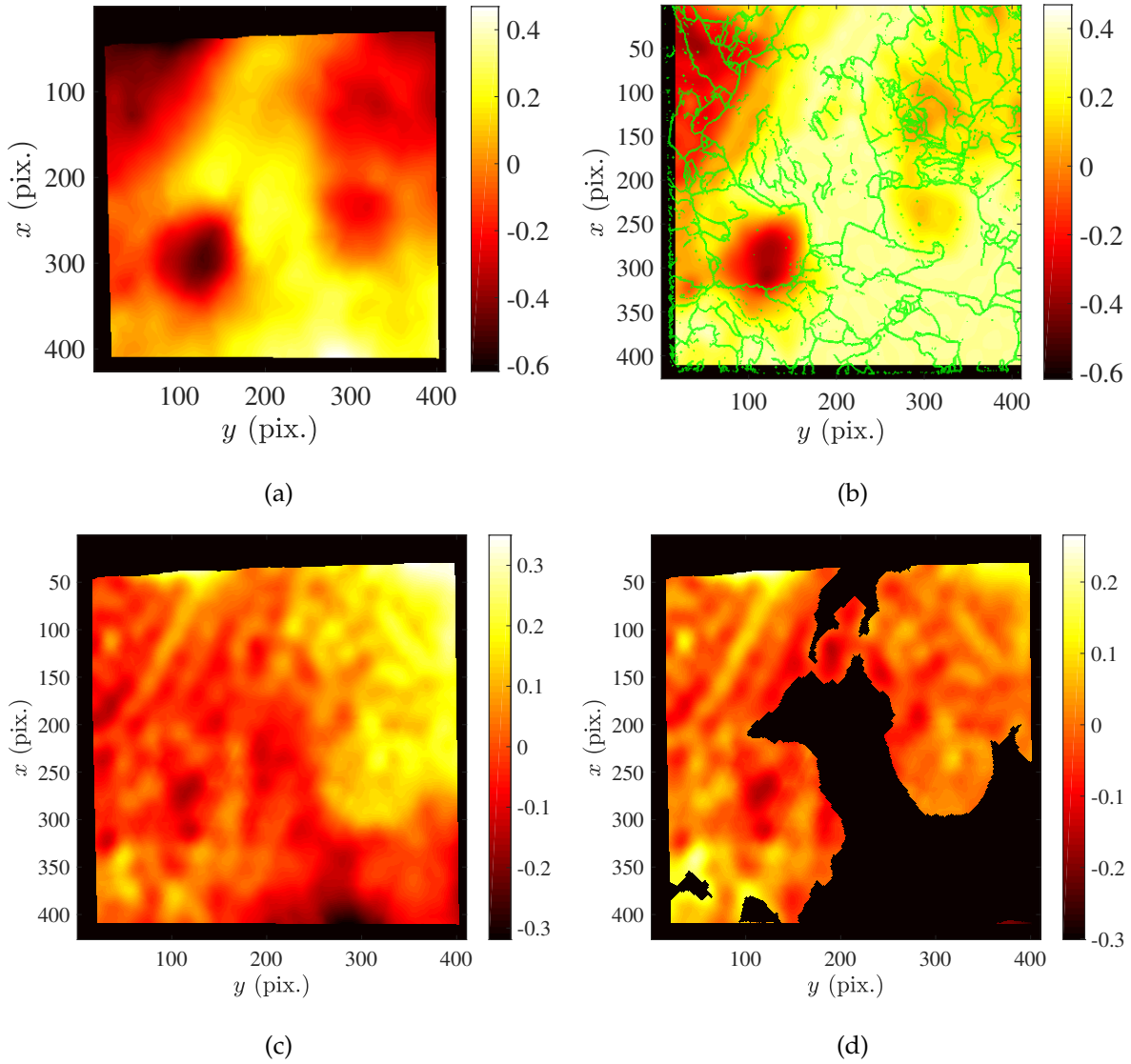

Figure 5.15: Topography field of the milled area measured by tilt-imaging (a) and FIB with FFT smoothing (b). (c) Difference between FFT smoothed FIB and tilt-imaging topography measurements. (d) Reliable part of (c) after the subtraction of a plane. The unity of topography is µm and the pixel size is 100 nm for all images.

Over the reliable part of the measurement (*i.e.*, below the initially emerged topography shown in Figure 5.15(d)), the RMS difference in topography is measured to be 46 nm. The uncertainty of the tilt-imaging method being estimated to be 8.1 nm, the topography measurement uncertainty is about 45 nm for the FIB-EBSD method, as opposed to the RMS of topography of 188 nm. Knowing that the pixel size in SEM imaging is 42 nm and the voxel size in FIB-EBSD 100 nm, the topography measurement uncertainty is below the SEM imaging resolutions. This excellent agreement opens up the field of topography measurement to all SEMs equipped with an EBSD setup. Although the principles are far from new, the

recourse to such high tilt angle is unusual, and global DIC used herein together with a well-suited speckle patterning provide very robust and accurate topography measurements.

The topographies measured by tilt-imaging and rotation-integration methods, after correction of coordinate distortions, are shown in Figure 5.16(a) and 5.16(b) respectively. Similar results are observed since the two topography fields have a Pearson correlation coefficient of 0.64. This is a proof that, even after filtering out with low order polynomials, the rotation-integration method captures part of the topography. However, the RMS of the topography measured by rotation-integration is equal to 171 nm, while that for tilt-imaging topography is equal to 188 nm. Knowing that the rotation-integration method only measures the topography due to elastic deformations, it is concluded that plasticity-induced and elasticity-induced topographies are mostly along the same direction and have comparable orders of magnitude.

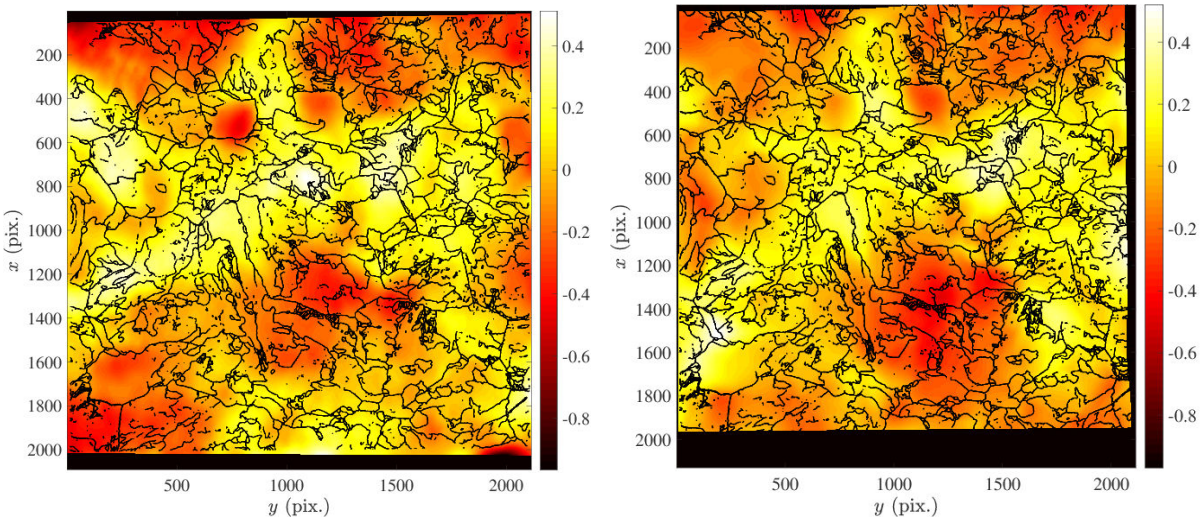

(a) (b)

Figure 5.16: Comparison of topographies (expressed in µm) calculated by (a) tilt-imaging and (b) rotation-integration methods. The pixel size is 50 nm for all images.

Last, an evaluation of each presented method is proposed:

- 3D FIB-EBSD is very simple in its principle and data processing is straightforward, thereby resulting in very reliable three-dimensional microstructures including the surface topography. However, the method is by nature destructive and can only be performed *postmortem*. Besides, the experimental setup is much more involved (*i.e.*, it requires many operations and the duration of the test is much longer than for the other two methods). Additionally, the measurement resolution is the thickness of each

FIB layer, and cannot offer the sub-pixel resolution provided by DIC. An interesting prospect of resolution improvement is to extract more topography information from a FIB slice, such as taking images probing different depths after each FIB removal.

- Stereoscopic tilt-imaging is the fastest method. Its accuracy depends on the size and density of the surface speckles as well as the positioning of the sample in horizontal and tilted configurations. The tilt angle is an essential parameter in the measurement, namely, large angles enhance the magnification of the displacement field issued from the topography during tilt, as demonstrated in previous works [Lockwood and Reynolds 1999]. However, large θ angles also yield a more severe contraction effect, leading to poorer resolution in the direction perpendicular to the tilt axis. Moreover, large angles may induce shadows that preclude topography reconstruction in these regions. Therefore, a compromise has to be made in the choice of θ. It is recommended that for very rough surfaces θ should be small, while for flatter and well-marked surfaces θ can be set between 40-70°. It should be noted that this method can also be used in other imaging equipments, such as optical cameras and microscopes. A key feature is here the possibility to reveal the surface patterning (*i.e.,* speckles) that circumvent gray level variation issues.

- Rotation-integration can only be applied for samples that have EBSD acquisitions before and after the process by which roughness has appeared (*e.g.,* mechanical test). In theory, the procedure can only give access to the roughness that is due to crystal rotations (and not plastic flow). An integration algorithm combining gradients in x and y directions helps to minimize the effect of (high frequency) Gaussian noise of the crystallographic orientations. However, a low frequency orientation error has been observed. A high-pass filter (*i.e.,* subtraction of low order polynomial fit) may cancel out or dampen this artifact. However, this is at the risk of removing a significant part of the signal so that the method should be considered with care. Nonetheless, it provides an interesting piece of information distinct from the previous methods, which allows roughness induced by plastic flow and by crystal rotation to be distinguished. This method may benefit from more stable EBSD acquisitions (*i.e.,* less orientation "drift"), or with more precise orientation data, as for example results obtained from high resolution EBSD (HR-EBSD [Wilkinson et al. 2006a], see Chapter 3).

5.6 Conclusion

Two very different methods for measuring topographies with SEM images were proposed herein exploiting different modalities. They were tested on a strained sample subjected to a tensile test, conducted *in-situ* in an SEM chamber. The surface topography features were of the order of 1 µm.

FIB-SEM and tilt-imaging methods measured the overall topography, and provided very consistent results. Their standard uncertainties were evaluated to be of the order of 30 nm. The rotation-integration method was designed to evaluate the topography changes without inelastic strains between two EBSD acquisitions. The resulting topography that differed from the previous two methods showed the effect of plastic flow in the generation of surface roughness in the mechanical test.

These approaches broaden the wealth of information that can be extracted from the different modalities offered by scanning electron microscopy. Last, one of them (based upon stereoscopic tilt-imaging) can be performed at no additional cost with standard SEMs.

A thorough characterization of the sample surface evolution along the *in-situ* tensile test has been acquired, including three-dimensional displacements of the sample surface and crystal rotations. Before exploring the 3D grain configurations by FIB process, a critical problem must be solved, namely, how to estimate the initial microstructures from the deformed ones, since the destructive FIB procedure can only be performed *postmortem*. The next chapter will focus on this problem.

Chapter 6

Backtracking depth-resolved microstructures for crystal plasticity identification

Reproduced from: Qiwei SHI, Félix LATOURTE, François HILD and Stéphane ROUX. Backtracking depth-resolved microstructures for crystal plasticity identification - Part 1: Backtracking microstructures. JOM, December 2017, 69(12):2810–2818.
and
Qiwei SHI, Félix LATOURTE, François HILD and Stéphane ROUX. Backtracking depth-resolved microstructures for crystal plasticity identification - Part 2: Identification. JOM, December 2017, 69(12):2803–2809.

In-situ mechanical tests performed on polycrystalline materials in a scanning electron microscope suffer from the lack of information on depth-resolved 3D microstructures. The latter can be accessed with focused ion beam technology only *postmortem*, because it is destructive. The present study considers the challenge of backtracking this deformed microstructure to the reference state and identifying crystal plasticity parameters. This theoretical question is tackled on a numerical (synthetic) test case. A 2D microstructure with one dimension along the depth is considered, and deformed using a crystal plasticity law. The proposed numerical strategy is shown to retrieve precisely the reference state. This reconstructed depth-resolved information reveals very beneficial for identification purposes.

6.1 Introduction

Many enrichments of multiscale plasticity constitutive models have been proposed in the past decades, motivated by better predictions of the macroscopic behavior. Many fields of application benefited from these developments, ranging from metal forming or fatigue failure [Horstemeyer 2012], to long-term behavior of materials subjected to irradiation [Leclercq et al. 2010]. In particular for sensitive industrial applications, this progress calls for experimental *validation*, at the relevant scale(s), or *identification* of unknown constitutive parameters, that become more challenging with the increased sophistication of the models.

In this context, validations of crystal plasticity models exploiting kinematic fields have been conducted, and more specifically the displacement and strain fields obtained from images acquired with a Scanning Electron Microscope (SEM) [Héripré et al. 2007; Lim et al. 2015; Guery et al. 2016b]. However, only surface measurements are accessible. For the purpose of validating the experimental identification procedure and its upscaling to macroscopic laws, specimen with columnar and coarse grains have been prepared, so that a mere extrusion of the surface microstructure is a valid description [Lim et al. 2015]. Such an approach has the merit of addressing the methodology with a good control of the microstructure. Yet, it is limited to materials that are not representative of most key applications. If a similar procedure, *e.g.*, extrusion of the observation face microstructure, is applied to materials with unknown grain geometry in the depth direction, numerical modeling is expected to lead to a poor agreement with *in-situ* observations, as documented from numerous numerical simulations (see *e.g.*, [Zeghadi et al. 2007b]). Another option is to generate in-depth microstructure synthetically based on surface grain structures, which introduces randomness into models. Nonetheless, numerous works have adopted extruded model from surface [Guery et al. 2016b] or synthetic in-depth microstructure [Lebensohn et al. 2008] in 3D simulations, due to the lack of real 3D microstructures. It is believed that any progress achieving a better determination of the microstructure will lead to much more constrained, and hence reliable, identification.

On the experimental side, a major break-through has been achieved in the past few years with techniques such as 3D-XRD and Diffraction Contrast Tomography (DCT) [Herbig et al. 2011; Ludwig et al. 2009]. These techniques allow for retrieving the full 3D grain geometry with the associated crystallography. Such a complete characterization will certainly lead to a major step forward in the context of identification and validation of crystal plasticity in

the future. Yet, using such methods, is still exceptional as they require monochromatic and coherent X-ray beams as produced by synchrotron facilities. They also suffer (today) from some limitations (such as a small (few thousand at most) number of grains with simple shapes). Although one may be confident on the future breaking of those limitations, these techniques are not yet mature enough for *in-situ* mechanical tests on materials such as fine grain steels as needed for some demanding industrial cases.

The other large avenue to access the 3D microstructure, which is compatible with a broad class of materials, is to resort to 3D-FIB SEM tomography also known as 3D-EBSD [Groeber et al. 2006; Calcagnotto et al. 2010]. This technique consists of EBSD characterization of surfaces obtained after successive FIB milling revealing progressively the material in depth. Such a technique allows for very fine spatial resolution down to 50 nm, and very accurate crystallographic orientations (about 0.5°). Microstructure models have for instance benefited from this technique, as reported in [Altendorf et al. 2014].

The limitation of the latter approach is obviously its *destructive* character, that may lead to the erroneous conclusion that it is not compatible with an *in-situ* mechanical test. In fact, such a 3D-EBSD could be performed but only at the end of the mechanical test, and hence after a potentially large plastic deformation, whereas a standard mechanical modeling necessitates the knowledge of the undeformed geometry.

The present study aims at addressing precisely the feasibility of back-tracking the 3D depth-resolved microstructure of the final state to the initial one, in order to increase the reliability of the interpretation of a surface characterization of mechanical test performed *in-situ* in a SEM. The surface deformation of sample surfaces can be measured thanks to full-field measurement techniques such as Digital Image Correlation [Allais et al. 1994; Hoc et al. 2003; Héripré et al. 2007]. More recently, it was shown that the crystal rotation fields can also be measured on surfaces by registering EBSD images via so-called quaternion correlation (see Chapter 2). The active slip systems can also be revealed since they induce surface roughness detected in SEM pictures [Abuzaid et al. 2012; Carter et al. 2014]. High angular resolution EBSD provides insight into the surfaces residual deformation at each step [Wilkinson et al. 2006b]. All this detailed information is specific from the observation surface, and as previously mentioned, without a reliable 3D microstructure, it remains uncomplete for the mechanical modeling.

It will be shown that an approximate, yet accurate, picture of the depth resolved microstructure of the *initial state* can be achieved. However, the problem remains ill-posed as

the in-depth boundary conditions remain unknown. Therefore it is essential to evaluate the added value of the inferred 3D grain geometry and crystallography on the identification of the crystal plasticity constitutive law from the kinematic characterization of the free surface during the test.

To the best of the authors' knowledge, such a problem definition has never been addressed in the past and in particular the limitations due to its ill-posed character (although reduced as compared to bare surface measurements) are difficult to assess. Hence, a 2D (one surface and one depth directions) toy problem is considered in the following, because of the high numerical cost of the direct and inverse modeling. It is believed that the issue of depth is well captured by such a simplified approach, though surface measurements are obviously much poorer in the 2D toy problem than in the real 3D cases. Thus assessing the feasibility in 2D is a very encouraging result for applying the very same methodology in an actual experiment.

The chapter is organized as follows. Section 6.2 details the proposed procedure to combine the determination of the reference configuration and the calibration of material parameters. Section 6.3 is dedicated to a virtual experiment carried out to validate the procedure.

6.2 Proposed procedure

6.2.1 Definition of the problem

Modeling *in-situ* mechanical tests at the microstructure scale, requires two types of unknowns, namely, the reference configuration Ω_{ref} of the microstructure and the constitutive equation parameters $\{\boldsymbol{p}\}$, (assuming the constitutive law itself is either known or chosen). The configuration Ω_{ref} consists here only in the crystal orientation $\boldsymbol{\Xi}$ — parameterized with *e.g.*, Euler angles or quaternions — at each material point $\boldsymbol{X}$. Additional internal parameters which could be included in this configuration are here ignored.

From 3D-EBSD, it is assumed that what is known is the deformed configuration Ω_{def}^{exp}, namely the field of crystal orientation $\boldsymbol{\xi}$ at each material point $\boldsymbol{x}$ of the deformed geometry. From surface SEM observations and digital image correlation, the Lagrangian displacement field $\boldsymbol{u}^{exp}(\boldsymbol{X}, t)$ is known for $\boldsymbol{X}$ at the observed surface, and in the course of time (or loading) t. Additional measurements may be available such as the remote load $\boldsymbol{F}^{exp}(t)$.

In classical continuum mechanics, the displacement field is the only relevant kinematic

field, and hence modeling consists in computing the transformation of the reference material points, $\boldsymbol{X}$, into a new position $\boldsymbol{x}$ at any stage t of the loading. This can be written

$$\boldsymbol{x} = \Phi(\boldsymbol{X}, t) \equiv \boldsymbol{X} + \boldsymbol{u}(\boldsymbol{X}, t) \tag{6.1}$$

where $\boldsymbol{u}(\boldsymbol{X})$ is the Lagrangian displacement field. For crystal plasticity, an enriched description is required, as each material point is endowed with a crystal orientation, and its transport in the plastic flow has to be accounted for. Hence, the generalized or enriched kinematic transformation has to be considered, where both current position *and* orientation $(\boldsymbol{x}, \boldsymbol{\xi})$ have to be related to their initial state $(\boldsymbol{X}, \boldsymbol{\Xi})$. Thus the configuration $\Omega_{ref} = \boldsymbol{\Xi}(\boldsymbol{X})$ is transformed into a deformed one $\Omega_{def} = \boldsymbol{\xi}(\boldsymbol{x})$ as described by a generalized transformation still denoted by Φ,

$$(\boldsymbol{x}, \boldsymbol{\xi}) = \Phi(\boldsymbol{X}, \boldsymbol{\Xi}, t) \tag{6.2}$$

where the dependence with respect to the reference orientation has been made explicit, although a given finite element computation only computes Φ for a given configuration since the constitutive law itself depends on the crystal orientation, and hence only the restriction $\widehat{\Phi}(\boldsymbol{X}, t) = \Phi(\boldsymbol{X}, \boldsymbol{\Xi}(\boldsymbol{X}), t)$ is directly accessible. Strain for instance can be computed from gradients of $\widehat{\Phi}(\boldsymbol{X}, t)$ along $\boldsymbol{X}$. However, sensitivity with respect to the local orientation $\partial\Phi/\partial\boldsymbol{\Xi}$ requires several finite element simulation from which finite differences can be estimated. Let us also stress that $\boldsymbol{\xi}$ cannot be estimated from the sole displacement field and thus is a needed independent output of Φ.

Identification consists in providing estimates of the unknown Ω_{ref} and $\{\boldsymbol{p}\}$. The proposed strategy aims at solving this problem iteratively, assuming one set of unknowns and estimating the other up to stationarity. Those two steps are done alternatively until convergence of both. The whole procedure is summarized in Figure 6.1 and detailed in following subsections. The left part of the chart aims at the determination of the configuration at fixed constitute parameters. The right part determines the constitutive parameters at fixed configuration. The global loop shown in Figure 6.1, is indexed by a simple superscript, m. Each left or right block also contains iterations labeled internally with an index (n) in between parenthesis. The global loop is interrupted when a stationarity condition is met, based on the relative incremental correction norm between $m+1$ and m.

It is to be emphasized that model error, *i.e.*, the fact that the actual plasticity behavior would not be described by the chosen constitutive law, is not considered here. It is a very important and often limiting point, however addressing such a problem is beyond the am-

bition of the present study. In the following, it will be assumed that the algebraic form of the law and the relevant internal parameters are correct and only *parameters* $\{\boldsymbol{p}\}$ are to be identified.

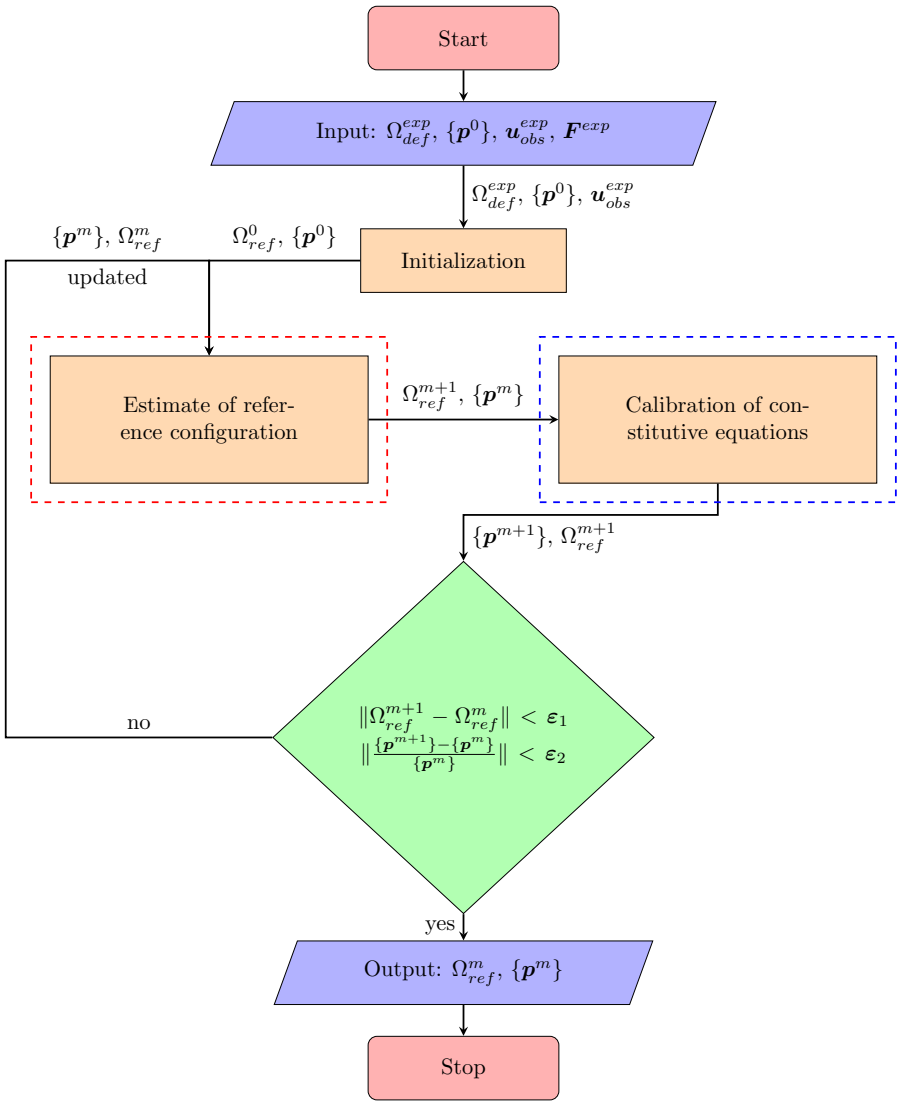

Figure 6.1: Flow chart summarizing the determination of the reference configuration of the microstructure and the parameters of the chosen constitutive equation

6.2.2 Microstructure estimate

The present procedure is designed to estimate the reference configuration from the deformed one, assuming that the constitutive law is close to the actual one. It is sketched in Figure 6.2 (accounting for the left wing of Figure 6.1).

In this procedure, the inputs are:

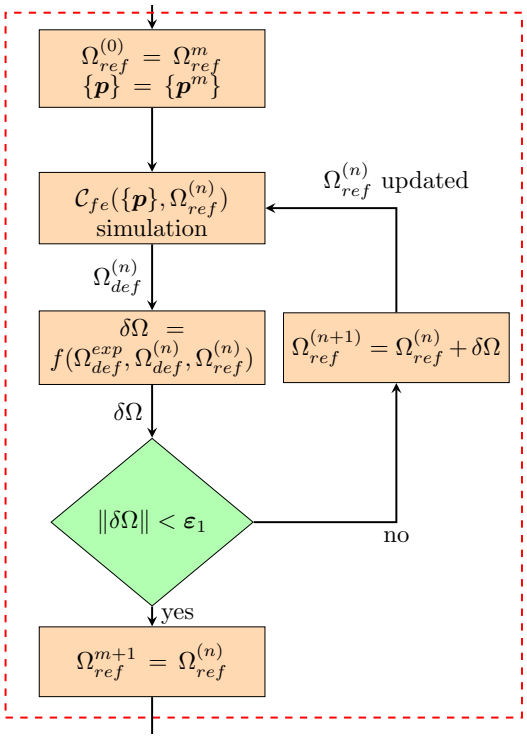

Figure 6.2: Flow chart describing the determination of the reference configuration.

- the material parameters $\{\boldsymbol{p}^m\}$ that are assumed to be known and are not updated;
- an initial estimate of the reference configuration $\Omega_{ref}^{(0)}$ that will be updated iteratively (index n);
- boundary conditions prescribed on the reference configuration during FE analyses;
- experimental deformed configuration Ω_{def}^{exp}, including in-depth texture.

The output is an updated estimate of the reference configuration, which approaches at best the exact yet unknown reference configuration Ω_{ref}^{exp}. In order to proceed with the FE computation of the deformed configuration (*i.e.*, the so-called direct problem), the boundary conditions are needed.

The observed free surface is very well documented since the surface displacement is known, and moreover, it is a free surface with zero surface traction. Hence both Dirichlet or Neumann conditions could be used. This redundancy will be used in the following. However, in depth, the information is lacking and has to be inferred somehow. Various prescriptions can be envisioned to guess a depth extrapolated displacement field, compatible with the surface displacement. None of them will be exact, but it may be expected that the errors due to the extrapolation will mostly affect the boundary of the studied domain, and that

the central part of the observed surface will only be marginally dependent on the boundary condition prescription. This question will be addressed in the following Section 6.3.

Equipped with the reference configuration, the constitutive law and boundary conditions (as defined through a given prescription), an appropriate finite element computation provides the (generalized) transformation Φ.

$$(\boldsymbol{x}(\boldsymbol{X}), \boldsymbol{\xi}(\boldsymbol{X})) = \Phi(\boldsymbol{X}, \boldsymbol{\Xi}, t) \tag{6.3}$$

The difficulty is now to solve the inverse problem. The proposed strategy is a simple correction step based on an approximation of the tangent transformation. Let us consider a small modification of the reference configuration, $\mathrm{d}\Xi(\boldsymbol{X})$, and study its effect in the deformed configuration

$$(\boldsymbol{x}(\boldsymbol{X}) + \boldsymbol{\delta x}(\boldsymbol{X}), \boldsymbol{\xi}(\boldsymbol{X}) + \boldsymbol{\delta \xi}(\boldsymbol{X})) = \Phi(\boldsymbol{X}, \boldsymbol{\Xi} + \boldsymbol{\delta \Xi}(\boldsymbol{X}), t) \tag{6.4}$$

and written generally as involving non-local but linear operators

$$\boldsymbol{\delta x}(\boldsymbol{X}) = \int \boldsymbol{G}_1(\boldsymbol{X}, \boldsymbol{X}') \boldsymbol{\delta \Xi}(\boldsymbol{X}') \, \mathrm{d}\boldsymbol{X}' \tag{6.5}$$

$$\boldsymbol{\delta \xi}(\boldsymbol{X}) = \int \boldsymbol{G}_2(\boldsymbol{X}, \boldsymbol{X}') \boldsymbol{\delta \Xi}(\boldsymbol{X}') \, \mathrm{d}\boldsymbol{X}' \tag{6.6}$$

Let us note that this explicit computation is prohibitive as it requires multiple finite element computations for any perturbation $\boldsymbol{\delta \Xi}(\boldsymbol{X})$. Therefore it is proposed to use a very simple approximant of these transformations G_1 and G_2, trivially inverted in order to update the reference configuration based on observed differences in the deformed configurations.

An additional specificity of the granular microstructure that is addressed here is that roughly, each grain i is considered to have a unique orientation, $\boldsymbol{\Xi}_i$ and hence only the boundary of the grain matters. Moreover, grains are considered to be polyhedral in 3D (resp. polygonal in 2D) and hence can be defined by a set of triplets (resp. doublet) of points, which define local facets from a connectivity table. The latter defines the granular *topology* that is believed not to be affected by the plastic deformation and thus that can be read from the deformed state. Therefore only the coordinates of these vertices A_j, $\boldsymbol{X}(A_j)$, (akin to finite element nodes) contribute to the definition of the deformed granular system. These vertices are also physical points lying at grain boundaries. The set of discrete orientations $\boldsymbol{\Xi}_i$, one per grain, and of vertices $\boldsymbol{X}(A_j)$ forming the grain boundaries, is a natural parametrization of the granular configuration. Within iteration n of the procedure, one computes the deformed state $\boldsymbol{\xi}_i^{(n)}$ and $\boldsymbol{x}(A_j)^{(n)}$.

Because the sought microstructure is piecewise constant, the considered perturbations are mainly of two types. The first corresponds to a slight variation of the orientation uniformly within a grain, at fixed shape. The second type is a slight modification of the boundary between grains at fixed orientation. Indeed, this is a convenient representation of the *residual* difference between the computed and observed configuration. Within each grain, i, the mean difference of orientation $\Delta\boldsymbol{\xi}_i^{(n)} = \boldsymbol{\xi}_i^{exp} - \boldsymbol{\xi}_i^{(n)}$ is of the first type, whereas the differences of position $\Delta\boldsymbol{x}^{(n)}(A_j) = \boldsymbol{x}^{exp}(A_j) - \boldsymbol{x}^{(n)}(A_j)$ for each face vertex, j, easily identified from topological features, make up the second type.

For the first case, the approximations $\widetilde{\boldsymbol{G}_1}(j,j') = 0$ and $\widetilde{\boldsymbol{G}_2}(i,i') = \delta_{ii'}\boldsymbol{I}$ are chosen. Hence, the observed grain mis-orientation between computed and observed configuration in the final state is simply corrected by the same amount locally, *i.e.*, per grain, without altering its shape.

For the second case, the mispositioning of a vertex is simply transported back to the reference configuration again locally, that is without affecting other vertices, and identically, i.e. with no alteration of the magnitude and orientation of the mispositioning ΔA_j. Likewise, the grain orientations are unaltered. In other words, the approximations $\widetilde{\boldsymbol{G}_1}(j,j') = \delta_{jj'}\boldsymbol{I}$ and $\widetilde{\boldsymbol{G}_2}(i,i') = 0$ are chosen. Therefore, the differences noted in the deformed state are simply directly accounted for in the reference one:

$$\begin{aligned} \boldsymbol{X}^{(n+1)}(A_j) &= \boldsymbol{X}^{(n)}(A_j) + \boldsymbol{x}^{exp}(A_j) - \boldsymbol{x}^{(n)}(A_j) \\ \boldsymbol{\Xi}_i^{(n+1)} &= \boldsymbol{\Xi}_i^{(n)} + \boldsymbol{\xi}_i^{exp} - \boldsymbol{\xi}_i^{(n)} \end{aligned} \tag{6.7}$$

More elaborate variants could be considered in particular if large rotations are involved, the first correction could benefit from the rotation matrix extracted from the deformation gradient. However, although inexact, the relative expected error is expected to be a small fraction of the displacement gradient, and hence unnecessary for the treated examples.

This defines one iteration of the microstructure correction, that is repeated until a stationary condition is observed, namely until incremental changes in $\boldsymbol{X}(A_j)$ or $\boldsymbol{\Xi}_i$ are considered as small enough, i.e. less than a given parameter ε_1. It should be emphasized that to solve the inverse problem, iterations of the direct method have been adopted to evaluate the sought answer. The inversion of the constitutive law and related possible instabilities have been avoided at the price of multiple direct calculations.

6.2.3 Calibration of material parameters

Finite Element Model Updating (FEMU), which is described in Figure 6.3, will be used to calibrate material parameters. The FEMU algorithm is based on measured and computed displacement fields $\boldsymbol{u}$, and applied load $\boldsymbol{F}$ data. Such approaches have already been used for analyses and calibration purposes of crystal plasticity models [Héripré et al. 2007; Guery et al. 2016b]. It will be referred to as FEMU-UF. In this procedure, the inputs are:

- the reference configuration Ω^m_{ref}, which is assumed to be known and is not updated;
- an initial estimate of the material parameters $\{\boldsymbol{p}^{(n)}\}$ that will be updated iteratively (index n);
- boundary conditions prescribed on the reference configuration during FE analyses;
- experimental kinematic field $\{\boldsymbol{u}^{exp}\}$, experimental loading force $\{\boldsymbol{F}^{exp}\}$.

The outputs are an updated estimate of the material parameters, which are based on the current reference configuration Ω^m_{ref}.

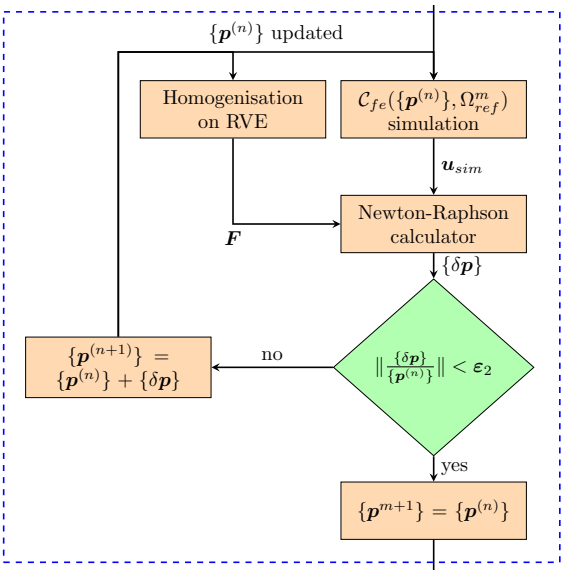

Figure 6.3: Flow chart describing FEMU-UF

FEMU-UF consists in minimizing a global cost function [Héripré et al. 2007; Guery et al. 2016b]

$$\chi(\{\boldsymbol{p}^m\}) = \frac{1}{2\eta_f^2 N_{dof} N_t} \sum_t \{\boldsymbol{\delta u}\}_t^T [\boldsymbol{M}] \{\boldsymbol{\delta u}\}_t + \frac{1}{\eta_F^2 N_t} \{\boldsymbol{\delta F}\}^T \{\boldsymbol{\delta F}\} \tag{6.8}$$

where N_{dof} the number of (scalar) degrees of freedom of the surface mesh, N_t the number of time steps, $\{\boldsymbol{\delta u}\}_t$ is the column vector of the difference evaluated at surface mesh node between 'experimental' $\{\boldsymbol{u}^{exp}\}_t$ and simulated $\{\boldsymbol{u}^{sim}(\{\boldsymbol{p}^m\})\}_t$ displacements at time step t. $[\boldsymbol{M}]$ is the DIC matrix [Mathieu et al. 2015], whose inverse characterizes the covariance matrix of the measured degrees of freedom [Hild and Roux 2012a]. When displacement and load information is taken into account, (hence the acronym UF for the FEMU algorithm used herein), $\{\boldsymbol{\delta F}\}$ is the column vector of the load differences between measured and computed values. η_f and η_F are the standard deviation of noise of the "experimental" images, and load measurement, respectively.

Boundary conditions of the FE calculation are a crucial point here again, in a similar spirit as for determining the configuration. For the buried boundaries that are not accessible a prescription is used, to extrapolate the displacement from those measured at the boundary of the observed surface (the discussion about those prescriptions is deferred to the following Section 6.3). The observed surface is left traction free (Neumann condition). This is sufficient for the computation and because the displacements are not prescribed, the differences between computed and observed values, $\{\boldsymbol{\delta u}\}_t$ can be used to drive the identification using FEMU-UF.

The minimization of χ with respect to the material parameters $\{\boldsymbol{p}\}$ is performed iteratively by a Newton-Raphson algorithm. The initial set of parameters is $\{\boldsymbol{p}^{(0)}\} = \{\boldsymbol{p}^m\}$. At iteration n, the parameter corrections $\{\delta\boldsymbol{p}\}$ are obtained by

$$\left(\left[\boldsymbol{H}_u^{(n)}\right] + \left[\boldsymbol{H}_F^{(n)}\right]\right)\{\delta\boldsymbol{p}\} = \left[\boldsymbol{N}_u^{(n)}\right] + \left[\boldsymbol{N}_F^{(n)}\right] \tag{6.9}$$

with the Hessian matrices

$$\begin{aligned}\left[\boldsymbol{H}_u^{(n)}\right] &= \tfrac{1}{2\eta_f^2 N_{dof} N_t}\textstyle\sum_t \left[\boldsymbol{S}_u^{(n)}\right]_t^T [\boldsymbol{M}] \left[\boldsymbol{S}_u^{(n)}\right]_t \\ \left[\boldsymbol{H}_F^{(n)}\right] &= \tfrac{1}{\eta_F^2 N_t}\left[\boldsymbol{S}_F^{(n)}\right]^T \left[\boldsymbol{S}_F^{(n)}\right]\end{aligned} \tag{6.10}$$

and the Jacobian vectors

$$\begin{aligned}\left[\boldsymbol{N}_u^{(n)}\right] &= \tfrac{1}{2\eta_f^2 N_{dof} N_t}\textstyle\sum_t \left[\boldsymbol{S}_u^{(n)}\right]_t^T [\boldsymbol{M}]\{\delta\boldsymbol{u}\}_t \\ \left[\boldsymbol{N}_F^{(n)}\right] &= \tfrac{1}{\eta_F^2 N_t}\left[\boldsymbol{S}_F^{(n)}\right]^T \{\boldsymbol{\delta F}\}\end{aligned} \tag{6.11}$$

where $\left[\boldsymbol{S}_u^{(n)}\right]$ and $\left[\boldsymbol{S}_F^{(n)}\right]$ are the sensitivity matrices of the displacement field at time step t and load, respectively. They are evaluated with the current parameter estimates $\{\boldsymbol{p}^{(n)}\}$. The correction vector $\{\delta\boldsymbol{p}\}$ allows to update the current determination

$$\{\boldsymbol{p}^{(n+1)}\} = \{\boldsymbol{p}^{(n)}\} + \{\delta\boldsymbol{p}\} \tag{6.12}$$

Convergence is declared to be reached when the stationarity condition

$$\max \left| \frac{\delta \boldsymbol{p}}{\boldsymbol{p}^{(n)}} \right| < \varepsilon_2 \tag{6.13}$$

is met. Then the material parameters are updated to $\{\boldsymbol{p}^{m+1}\}$:

$$\{\boldsymbol{p}^{m+1}\} = \{\boldsymbol{p}^{(n)}\} \tag{6.14}$$

6.3 Proof of concept

6.3.1 Virtual experiment

In the following a 2D synthetic test case is considered in order to study the feasibility of the proposed procedure by comparing the results Ω_{ref} and $\{\boldsymbol{p}\}$ with known values. In 2D, the top edge of the considered model corresponds to the observation surface whereas the vertical direction is along the depth. The displacement field is computed from a Finite Element simulation with Code_Aster [EDF 2017]. A two-dimensional microstructure shown in Figure 6.4 with isotropic texture is modeled. It corresponds to an experimental orientation map of a reactor pressure vessel steel sample [Latourte et al. 2014]. Two sets of isotropic crystallographic orientations are generated randomly, each being uniform inside each grain, as shown in Figure 6.4(a) and 6.4(b). This domain represents a large scale solid at the boundary of which simple boundary conditions are applied. It is meshed as shown in Figure 6.4(c) conforming to the grain shapes. The finite element calculation is performed under a plane strain assumption. The entire domain is subjected to a monotonic uniaxial tensile strain up to 6% with the following boundary condition. The left and right edges both have uniform displacements in the x (horizontal) direction. All data extracted from the simulations are considered as "experimental" data in the following.

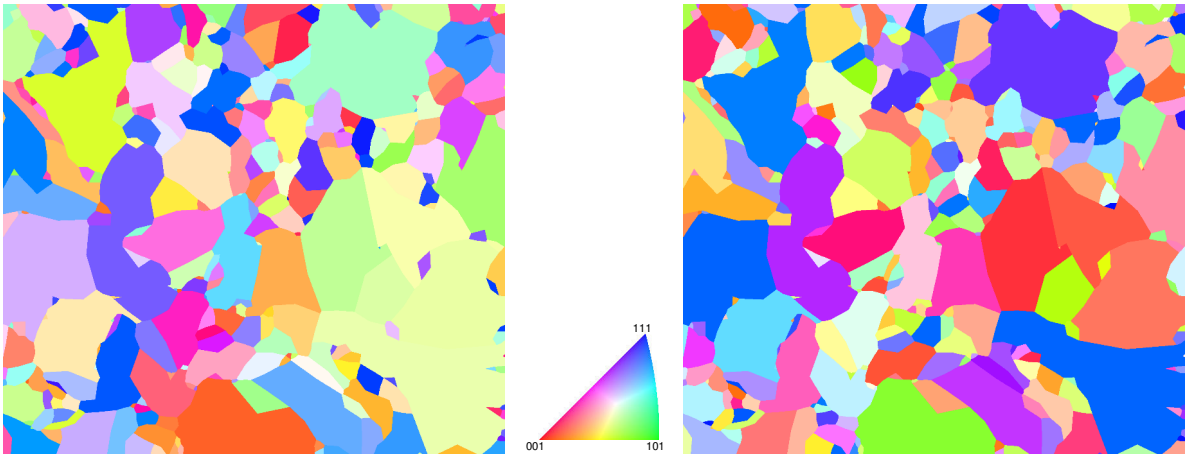

(a) (b)

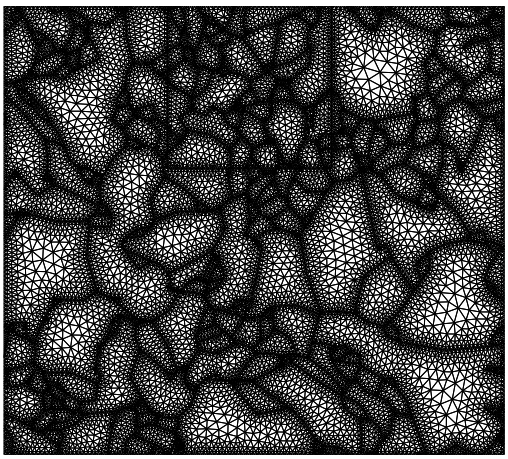

(c)

Figure 6.4: (a) Inverse pole figure of the 2D polycrystalline model, orientation set 1 (a) and set 2 (b). (c) FE mesh of the virtual experiment. The square region at the top, of size 50×50 µm^2, is the region of interest (ROI) before deformation, *i.e.*, Ω_{ref}^{exp}

A constitutive law based on dislocation dynamics for body centered cubic crystals (DD_CC [Monnet et al. 2013]) has been chosen in the FE simulations. The parameters adopted in DD_CC are summarized in Table 1.5. They correspond to a reactor pressure vessel steel, and were obtained by identification on a stress-strain curve of steel ASTM A508 cl3 (16MND5) at room temperature. A finite strain framework is used to implement the constitutive equations in order to properly account for crystal rotation during the applied load.

In order to be representative of the future experiment, a smaller square Zone Of Interest (ZOI) is defined. Its size is on third of the initial domain in each direction. It is centered in the horizontal direction, and attached to the free surface along the vertical direction. This

ZOI mimics the region that would be analyzed using 3D-EBSD. The surrounding part is introduced here as a buffer zone that mediates a uniform displacement applied at the outer boundary to a more "natural" one at the edges of the ZOI.

The grain boundaries of the global model using orientation set 1 before (black) and after (red) straining the sample are shown in Figure 6.5(a), and the grain boundaries inside the ZOI are shown in Figure 6.5(b). The red lines in Figure 6.5(b) indicate the grain boundaries of the deformed configuration Ω_{def}^{exp}, which would be available in real-life experiments by *postmortem* 3D-EBSD. Note that Ω_{def}^{exp} will be the starting point of all the following calculations.

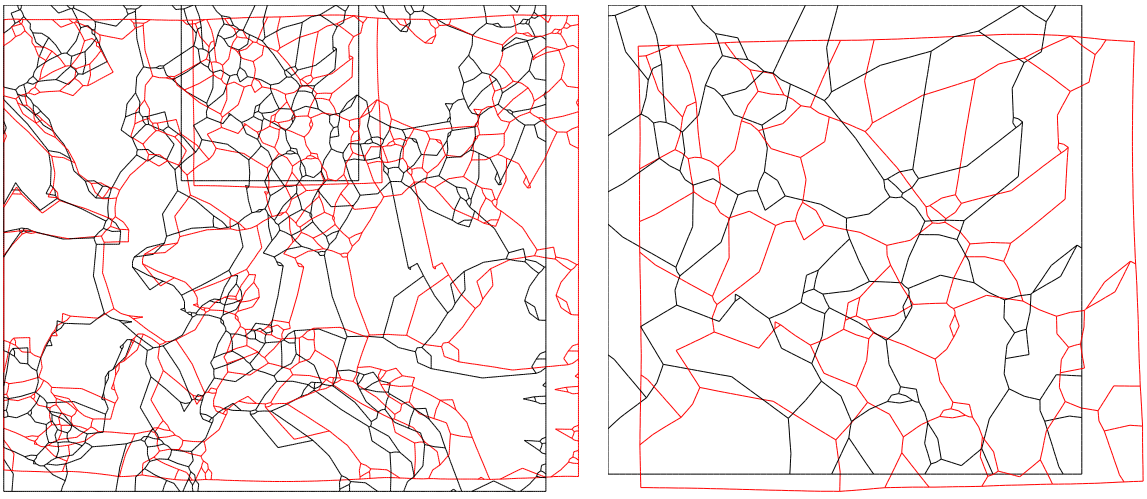

(a) (b)

Figure 6.5: Reference (in black) and deformed (in red) configurations of the the whole model (a) and the region of interest (b) of the virtual experiment

The standard deviation of image noise, η_f, is set to 2% of the gray level range of the 'experimental' image and η_F, the standard deviation of macroscopic load measurement is set to 2 Newton. The 'experimental' macroscopic load $\boldsymbol{F}^{exp}$ is estimated independently by integration on edge subjected to tension from a numerical homogenization on an RVE model [Héripré et al. 2007; Kraska et al. 2009; Guery et al. 2016b], as shown in Figure 6.6 with the reference parameters of DD_CC using the same RVE model. Boundary conditions are the same as the tensile simulation to generate the "experimental" data.

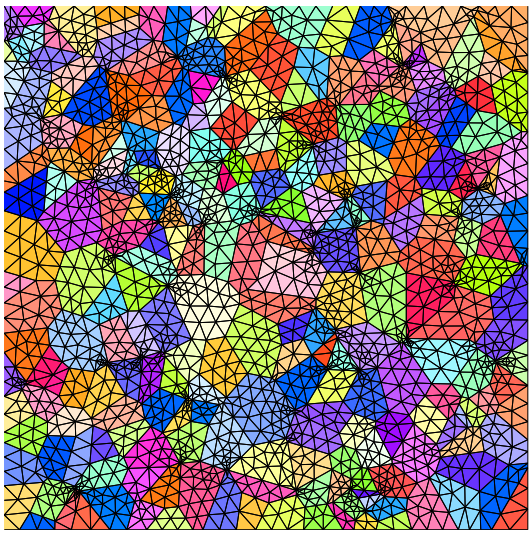

Figure 6.6: 2D RVE model for the calculation of macroscopic load. It consists of 250 Voronoi-style grains

Two parameters, τ_F and K_{self} are chosen as the sought constitutive parameters; τ_F influences principally the initial yield stress and K_{self} affects the hardening ratio. Unlike other parameters in DD_CC (*e.g.*, D_{lath}, D_{obs}, b), these two parameters cannot be determined directly by physical measurement. Their values have to be identified, and they are natural candidates for assessing the feasibility. Reference values are set to 35 MPa for τ_F and 100 for K_{self}. Convergence is obtained when neither of the two parameters changes by more than 0.5% between two successive iterations.

To provide fair comparisons with the proposed procedure, Ω_{ref}^{est} labeled "est" for estimated, two other models are adopted. First, the reference microstructure Ω_{ref}^{exp}, the "ideal" one, which is not available in real-life experiment except on the sample observation surface, corresponds to the limit case where the determination of the microstructure would be exact, and, second, a quasi 2D extruded model Ω_{ref}^{2D} based on the microstructure of the observation surface that is simply considered as invariant along the depth as shown in Figure 6.7. The latter is very commonly used [Guery et al. 2016b] for identification from *in-situ* SEM experiments.

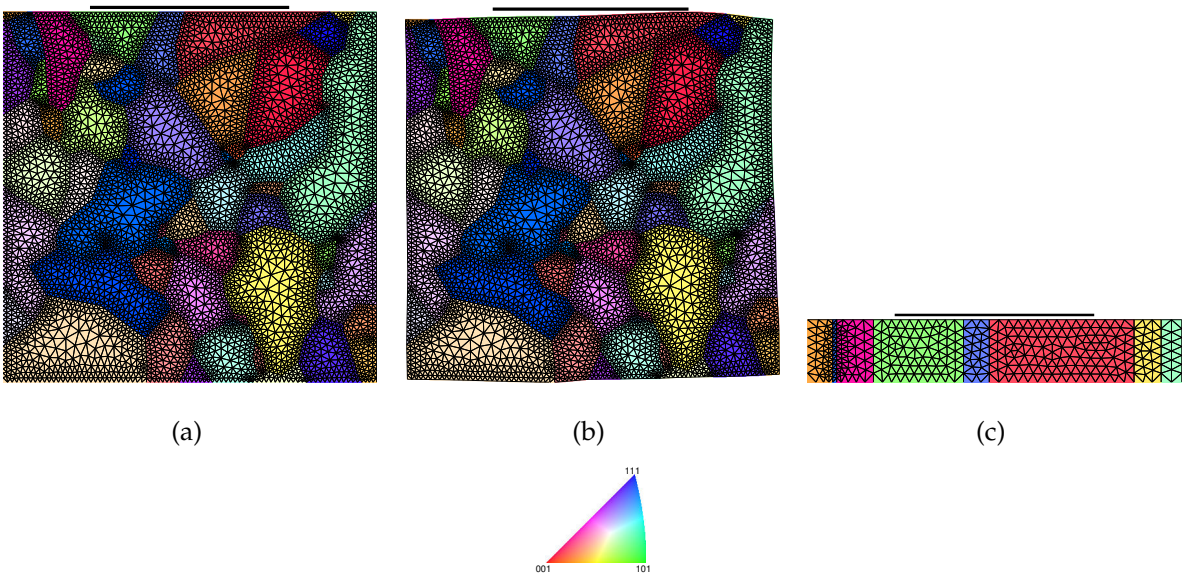

Figure 6.7: Microstructures used for identification purposes. (a) Ω_{ref}^{exp}; (b) Ω_{ref}^{est}; (c) Ω_{ref}^{2D}. The top lines indicate the observed ZOI surface used for displacement measurement, which will be discussed in Section 6.3.4.

6.3.2 Choice of boundary conditions

Boundary conditions (BCs) are essential in crystal plasticity calculations and strongly affect the mechanical response of grains in the vicinity of the boundary. As earlier mentioned, boundary conditions are to be inferred along the boundaries that are buried underneath the observed surface. Along them, boundary conditions are of Dirichlet type, *i.e.*, with prescribed displacements, whereas the observed surface is considered to be traction free (Neumann type). Boundary conditions are involved in both determination steps (configuration and constitutive parameters). Although there is no hope to achieve an exact estimate, an appropriate guess may presumably lead to slight differences with the actual boundary conditions, differences mostly confined in the immediate vicinity of edges.

Different prescriptions for the unknown boundary conditions are considered:

- (BC1) consists in moving the two surface corner points to their original position while keeping the buried boundaries fixed;
- (BC2) assumes that the left and right edges are subjected to a mere solid translation, (in both spatial directions), as set by the surface corner points;
- (BC3) assumes that only the horizontal component of the displacement along the left

and right edges are those of the surface corner points. The vertical components are such that the resulting shear forces along the vertical edges are both equal to 0;

- (BC4) is comparable with the previous (BC3) prescription, but the vertical displacement along the bottom side (opposite to the observed surface) is assumed to be uniform all along the edge.

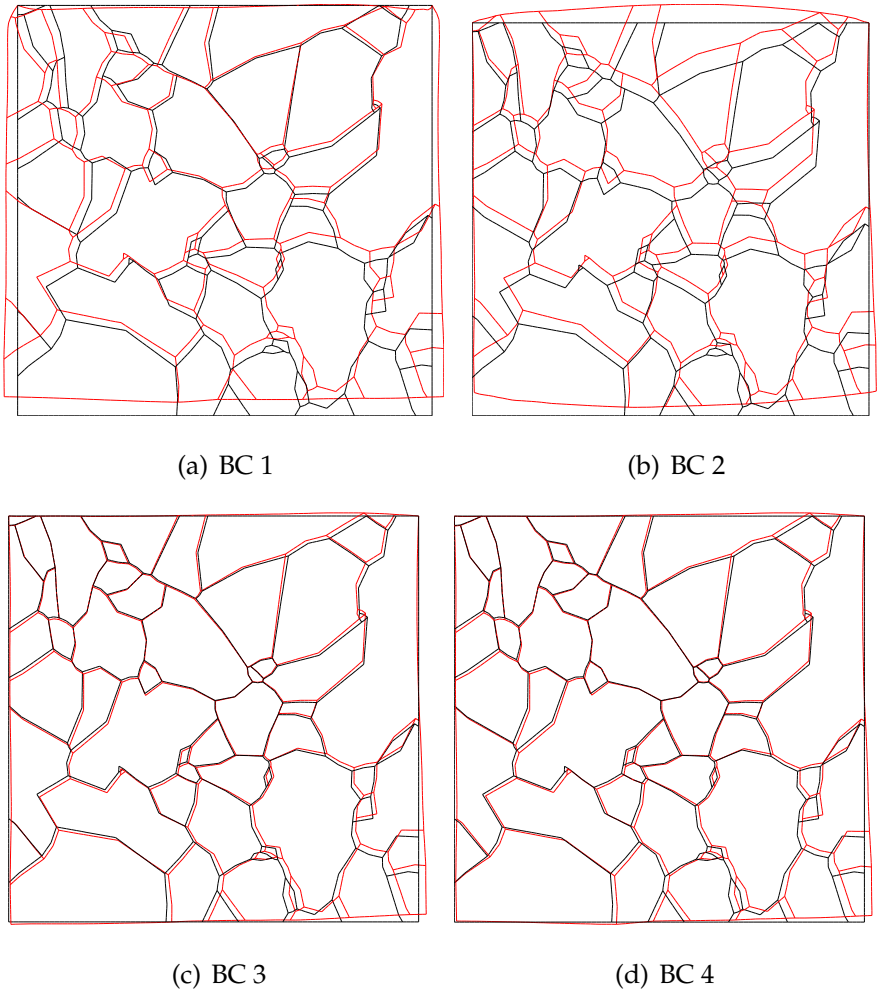

(a) BC 1 (b) BC 2

(c) BC 3 (d) BC 4

Figure 6.8: Reference microstructure (in black) and reversed microstructures (in red) based on different boundary conditions

Figure 6.8 shows the different estimated configurations, obtained from the first procedure only while keeping the constitutive parameters set to their exact values (those used to generate the data). It is observed that the (BC4) prescription gives the best estimate of the reference microstructure. Thus this prescription is kept for all the remaining studies, including initial microstructure estimation and crystal plasticity parameters' identification.

The contrast of the correct nodal displacement boundary condtions and the applied ones (BC4) is shown in Figure 6.9. Figure 6.9(a) provides an illustration of nodal displacements

obtained by a first direct calculation during which the domain Ω is surrounded by a polycristalline material providing realistic grain-to-grain interaction effects at the boundary $\partial\Omega$. During the reconstruction procedure, the estimated microstructure is loaded with the BCs depicted in Figure 6.9(b). Only the two upper corners are loaded with the exact two components of the displacement that can be measured experimentally, and drawn in blue color in Figure 6.9(a). Artifacts in boundary conditions will mostly affect the response of grains surrounding the boundary. Since errors are known to result from the discrepancy between exact BCs and assumed BCs, quantifications will be provided hereafter.

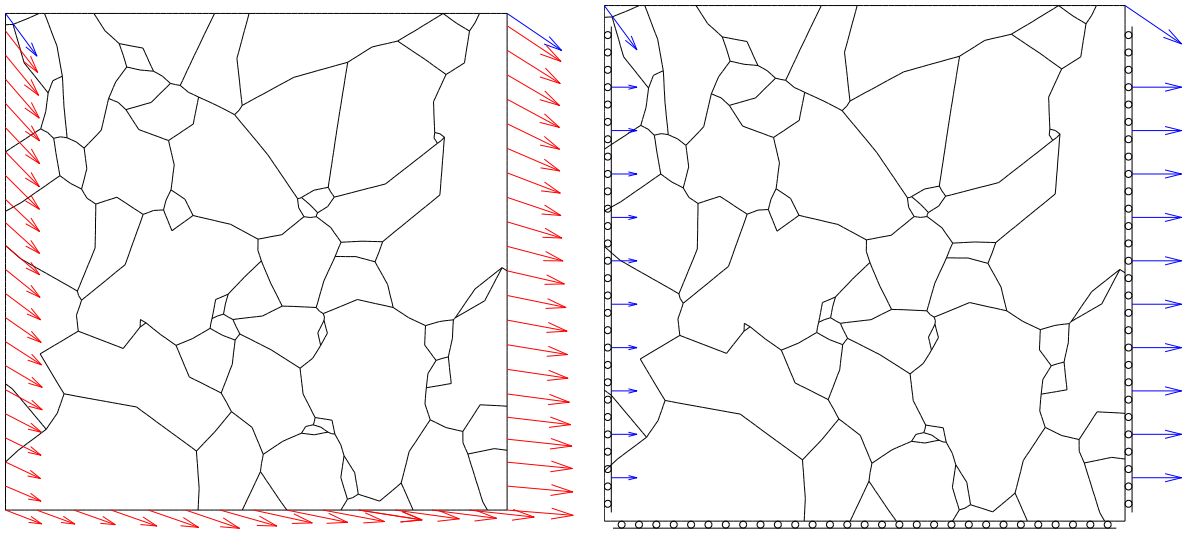

(a) (b)

Figure 6.9: Comparison of boundary conditions. (a) exact BC applied on the model, extracted from the synthetic experiment calculations; (b) adopted BC for all of the FE analyses.

6.3.3 Initialization of the configuration Ω^0_{ref}

To initialize the iterative process, one may choose Ω^{exp}_{def} as Ω^0_{ref}. However, a very simple constitutive equation, namely, macroscopic pseudo-elasticity, is adopted to provide the first estimate. The true elastic part of DD_CC constitutive law is ignored. The average hardening modulus is used as the pseudo-elastic modulus and the Poisson's ratio is set to 0.499 to describe plastic impressibility and avoid numerical issues (Figure 6.10(a)). To undertake this initialization step, the BCs shown in Figure 6.9(b) are reversed, and then applied to Ω^{exp}_{def} with the isotropic elastic law shown in Figure 6.10(a). Figure 6.10(b) indicates that the simple estimate of Ω^0_{ref} does not deviate much from the correct configuration and hence constitutes a fair (but cheap) initialization. Note that the deformed configuration shown in Figure 6.8d

was not chosen as initialization because i) the correct constitutive law used in compression is not known in real-life experiments; ii) compression by DD_CC law takes much longer computation time than an isotropic elastic law.

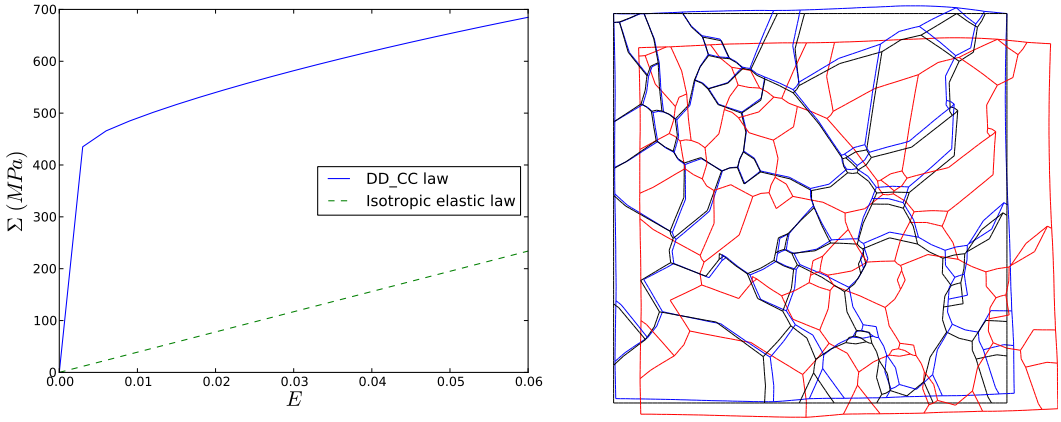

(a) (b)

Figure 6.10: Initialization of Ω^0_{ref}. (a) Stress-strain curve of DD_CC law and reference (tangent) pseudo-elastic law; (b) blue: Grain boundaries of Ω^0_{ref}. For comparison purposes, the black lines show Ω^{exp}_{ref}, the red lines show Ω^{exp}_{def}, which can be measured by 3D-EBSD

6.3.4 Choice of metric for displacement field u

The FEMU-UF method calls for a comparison between computed and observed displacement fields on the observation surface, and a L2 norm of the difference was mentioned as a standard. However, in contrast with usual application of FEMU, boundary conditions in the depth are known to be approximate at best. This implies that the displacement on the observation surface cannot be securely compared with the computed values.

To illustrate this point, Figures 6.11(a) and 6.11(c) display, respectively for the two chosen cases, displacement fields u_x as a function of the surface coordinates x. They correspond to three different inferred microstructures: exact Ω^{exp}_{ref}, estimated with the current procedure Ω^{est}_{ref}, and extruded Ω^{2D}_{ref}. For these computations, the DD_CC constitutive law is chosen with the exact parameters. The boundary condition prescription was chosen to be BC4 as earlier mentioned. Over the observed surface, all edge displacements (that is, in the present 2D case, the displacements at the two end points) coincide with the "experimental" data (shown in green), as a result of the BC4 prescription for boundary conditions. Nevertheless, when using the exact microstructure Ω^{exp}_{ref}, and exact constitutive law, the computed displacement over the observed surface (shown in blue) differs significantly from the "experimental"

data. This emphasizes the large impact of the boundary conditions in the depth. For the experimental case, the displacements along the ZOI boundaries results from the elasto-plastic behavior of the surrounding grains shown in Figure 6.5(a). In contrast, the displacement profile computed with the exact microstructure is obtained for the boundary condition prescription (BC4), and u_x for instance is uniform along the vertical boundaries. It is also to be observed on the same figures that the displacement fields from the "estimated" microstructure (shown in red) give a result that is extremely close to that of the exact microstructure. In contrast, the extruded microstructure, Ω^{2D}_{ref}, give rise to displacement profiles that are rather distinct. However, in a blind application of this method in real life, only the experimental data are available and hence the metric to be chosen for comparing different displacement profiles or fields is critical for estimating the correct constitutive parameters.

When considering only the central zone of the observation surface, the sensitivity with respect to erroneous boundary conditions is reduced, and the local microstructure imprints its signature in a more obvious way. Thus it is proposed to focus on the central half of the observation window $x_1 < x < x_2$ where $x_1 = L/4$ and $x_2 = 3L/4$, where L is the initial length of the surface. When extracting only this central part, the mean translation and mean strain over the surface are different. In order to compare these profiles, a linear rescaling is proposed so that the displacements at the end of the considered comparison window coincide. More precisely, any displacement profile $v_x(x)$ is rescaled to $w_x(x)$ as

$$w_x(x) = u_x(x_1) + (v_x(x) - v_x(x_1))\frac{(u_x(x_2) - u_x(x_1))}{(v_x(x_2) - v_x(x_1))} \tag{6.15}$$

where $u(x)$ refers to the experimental data. It is noteworthy that this rescaling is not exact, but it assumes that the local relative strains varies in proportion to the mean (just as if the localization operator were insensitive to the total amount of plastic strain) that may be considered as a decent approximation.

After such a rescaling over the comparison window the displacement profile are shown in Figures 6.11(b) and 6.11(d) for test cases 1 and 2 respectively. Apart from the extruded quasi-2D microstructure that shows a poor agreement, the experimental data is very well captured by the exact and estimated microstructures, and this for the two test cases.

Therefore, it is proposed in the following to use this comparison window after rescaling as a substitute to the L2 norm used in the FEMU-UF cost function. Let us also point out that the 2D nature of the toy model restricts the comparison to a rather narrow interval, and thus few grains, and in 1D. As a consequence, the 1D comparison window bears little

information as compared to a more realistic 2D surface case.

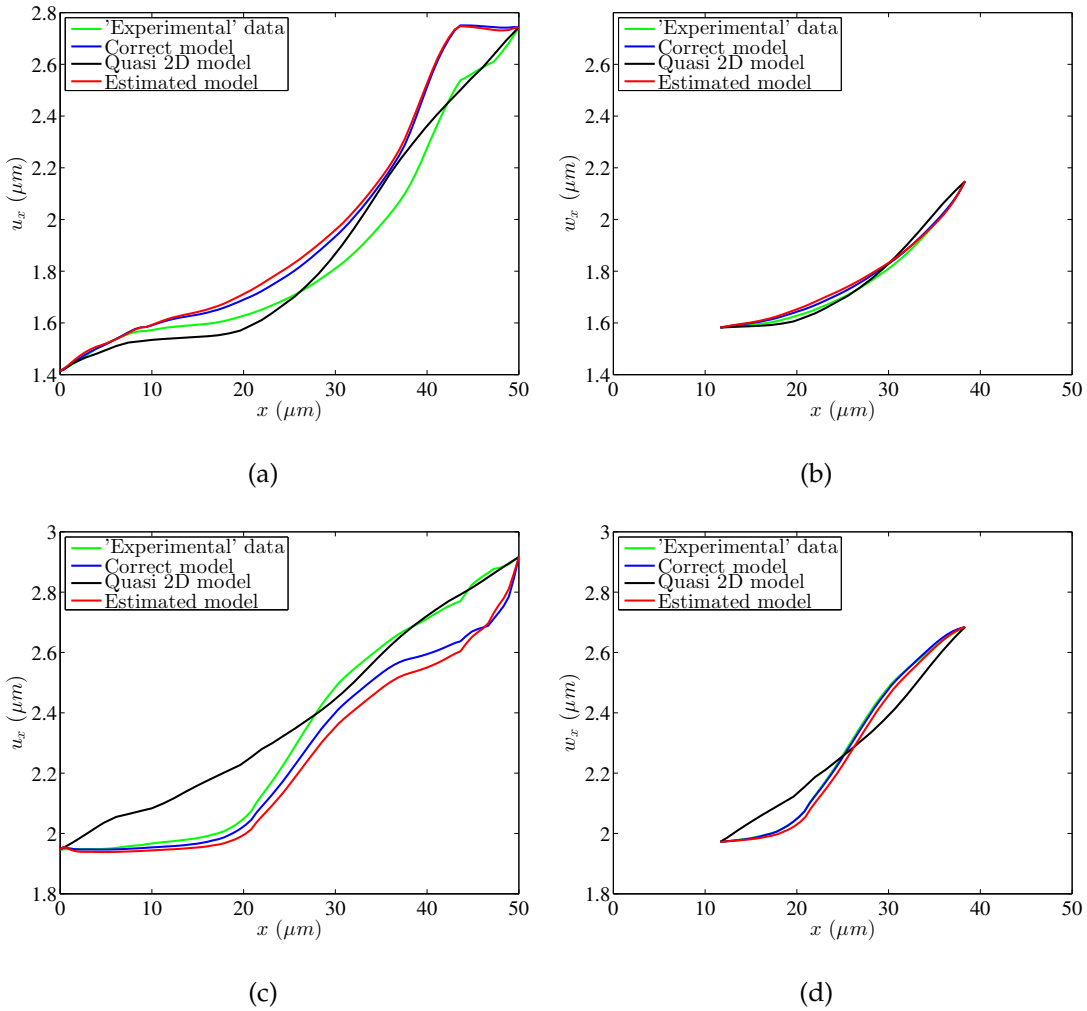

Figure 6.11: Surface displacement profiles as functions of coordinates (x) along the observation surface for all models calculated with the exact DD_CC parameters. Top row (a-b) corresponds to test case 1, and bottom row (c-d) to test case 2, with similar data. The left plots (a-c) correspond to the displacement profiles computed for all microstructures and the "experimental" data (green). The right plots (b-d) show the same profiles over a narrower comparison window and rescaled to match the experimental data at the two end points

Section 6.3.5 will now address the complete problem of estimating the configuration *and* identification of the constitutive parameters. To this aim, only test case 2 is selected as its microstructure appears to be more influential on the displacement profile and hence discriminating.

6.3.5 Results

The results of this 2D synthetic case are shown in Figure 6.12. The whole procedure converges after only $m = 3$ iterations of the global algorithm, as the difference between $\Omega_{def}^{(3)}$ and Ω_{def}^{exp} is less than the convergence criterion, as shown in Figure 6.12(b). However, the estimated initial configuration, $\Omega_{ref}^{(3)}$, is different from the exact solution, as shown in Figure 6.12(a). A slight yet visible difference also exists in the inverse pole figures, as shown in Figure 6.12(c) and Figure 6.12(d). In terms of the quality of the estimate for the reference configuration, one may resort to a "distance" measurement which is the root mean square distance between corresponding vertices defining the grain structure between the exact configuration and the estimate in the reference state. To make this indicator dimensionless, it is normalized by the same distance computed for the known deformed configuration. Therefore, a normalized distance error of 100% is obtained when comparing the reference microstructure with the deformed microstructure obtained after a macroscopic strain of 6%. As a consequence, small changes between microstructures are emphasized with high error values resulting from the normalization choice. The initial estimate obtained by isotropic elastic compression reduces this relative coordinate error down to 56%, and the iterative determination lowers it down to 43% of the coordinates error. Similarly, one can define an orientation error, normalized by the deformed state. At convergence, the orientation error also decreases as shown in Table 6.1, but in a lesser degree. In other words, the error of reference configuration estimate drops and stabilizes in the iterations, but does not vanish completely.

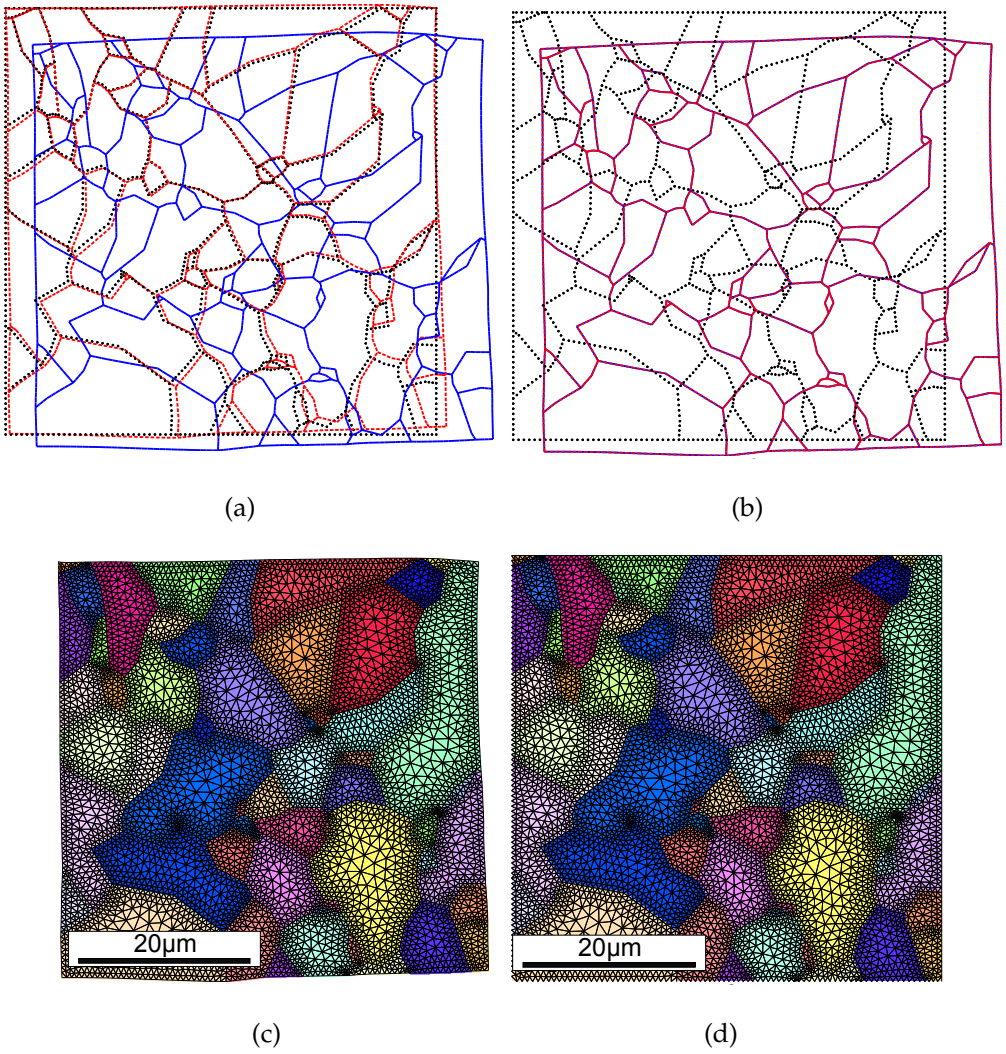

Figure 6.12: Backtracked reference configuration. (a) Grain boundaries of $\Omega_{ref}^{(3)}$ is shown in red lines. (b) Grain boundaries of $\Omega_{def}^{(3)}$ is shown in cyan lines. For comparison purposes, Ω_{ref}^{exp} is shown in black lines and Ω_{def}^{exp} is shown in blue lines in both figures. Note that $\Omega_{def}^{(3)}$ coincides with Ω_{def}^{exp} in (b). (c) $\Omega_{ref}^{(3)}$ is shown as an orientation map. (d) Ω_{ref}^{exp} is shown as an orientation map for comparison purposes

Table 6.1: Distances of several configurations to Ω_{ref}^{exp}

Configuration	Ω_{def}^{exp}	Ω_{ref}^{0}	$\Omega_{ref}^{(1)}$	$\Omega_{ref}^{(2)}$	$\Omega_{ref}^{(3)}$
RMS distance to Ω_{ref}^{exp} (µm)	1.17	0.65	0.51	0.50	0.50
Normalized distance error	100%	55.7%	43.7%	42.9%	42.9%
RMS misorientation to Ω_{ref}^{exp} (°)	2.61	2.61	1.69	1.68	1.68
Normalized orientation error	100%	100%	64.8%	64.4%	64.4%

The estimated reference configuration at convergence, Ω^3_{ref} is shown in Figure 6.12. In terms of deviation from the correct reference configuration Ω^{exp}_{ref}, Ω^3_{ref} is 23% lower than Ω^0_{ref} and 57% lower than Ω^{exp}_{def}. This remaining error results from boundary conditions that cannot be determined exactly. The crystal plasticity analyses are sensitive to boundary conditions, which are unknown except at the measurement surface. The only differences between the two cases are the initial configuration and the BCs. Because the direct problem is treated without approximation, if the boundary conditions were exact so would be the computed initial microstructure. Hence the resulting discrepancy in the estimated and reference microstructure configuration does only result from differences in boundary conditions.

The appreciation of how good or bad the above errors are, is highly subjective. However, since the initial motivation is to incorporate the depth resolved microstructure in order to better identify a plasticity law, it is important to evaluate the consequence of this additional piece of information on identification.

The identification results are shown in Figure 6.13. It can be seen that convergence is reached after $n \approx 4-5$ iterations for all the models, which is relatively fast. Three outer iterations are needed, $m = 3$, for the estimated model to reach convergence. The correct and estimated models lead to very good identification results, whereas model Ω^{2D}_{ref} gives much poorer results. The efforts for having a more faithful picture of the in-depth microstructure are rewarded by the accuracy of the identification results for constitutive parameters.

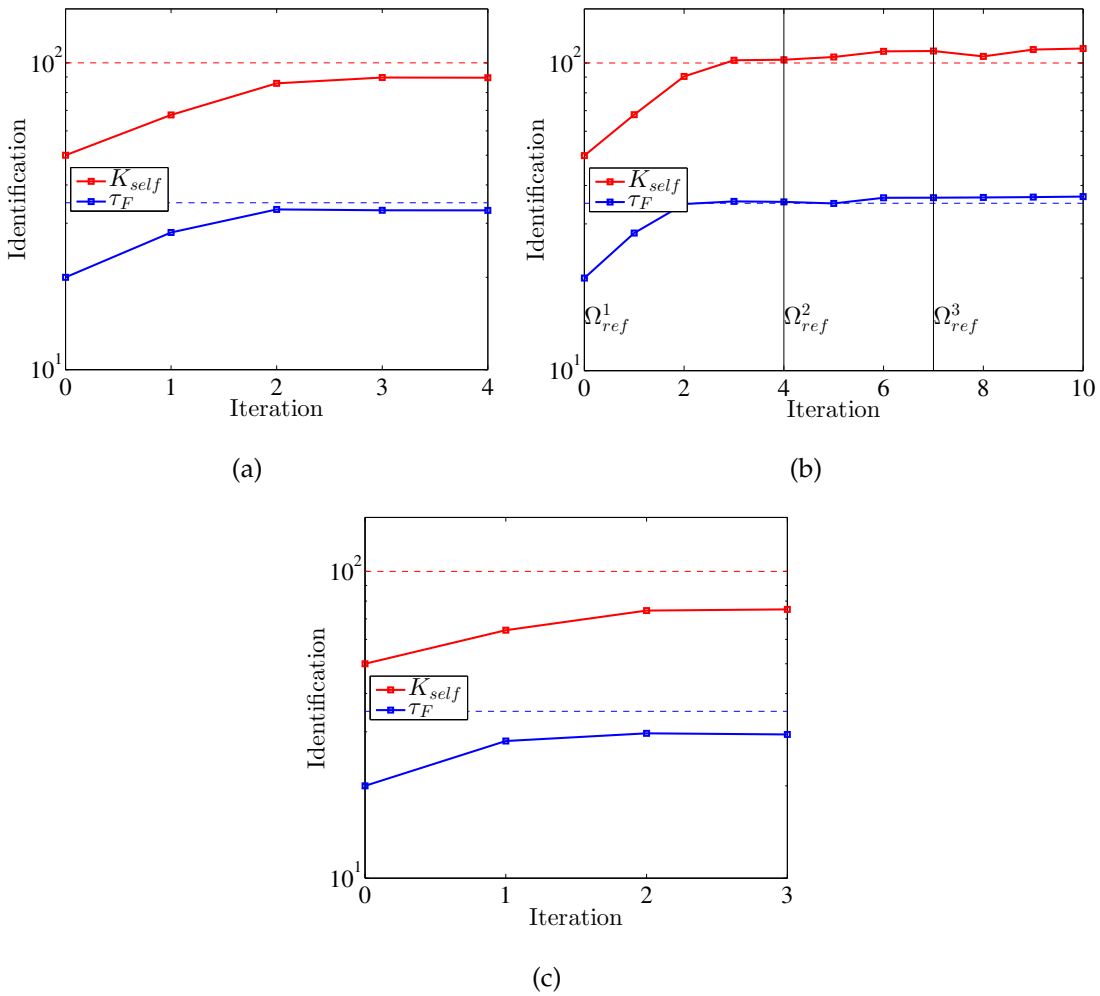

Figure 6.13: Calibration results for τ_F and K_{self} for different microstructures: (a) exact; (b) estimated; (c) Quasi 2D configurations. The reference values are shown as dashed lines

The change of the cost function during the identification iterations are shown in Figure 6.14. As shown in Figure 6.14(b), as the calculation model changes from the initialization to the first estimated model, Φ_u drops significantly, although using the same parameters of DD_CC law. This phenomenon illustrates the beneficial effect of estimated configuration updating. The drop is much smaller in the transition from Ω^1_{ref} to Ω^2_{ref}. At convergence the estimated model leads to comparable displacement residual Φ_u to the correct model, both much lower than Ω^{2D}_{ref} (*i.e.*, quasi 2D model). This is another proof that having a better knowledge of the in-depth microstructure brings better synergy between experiments and simulations.

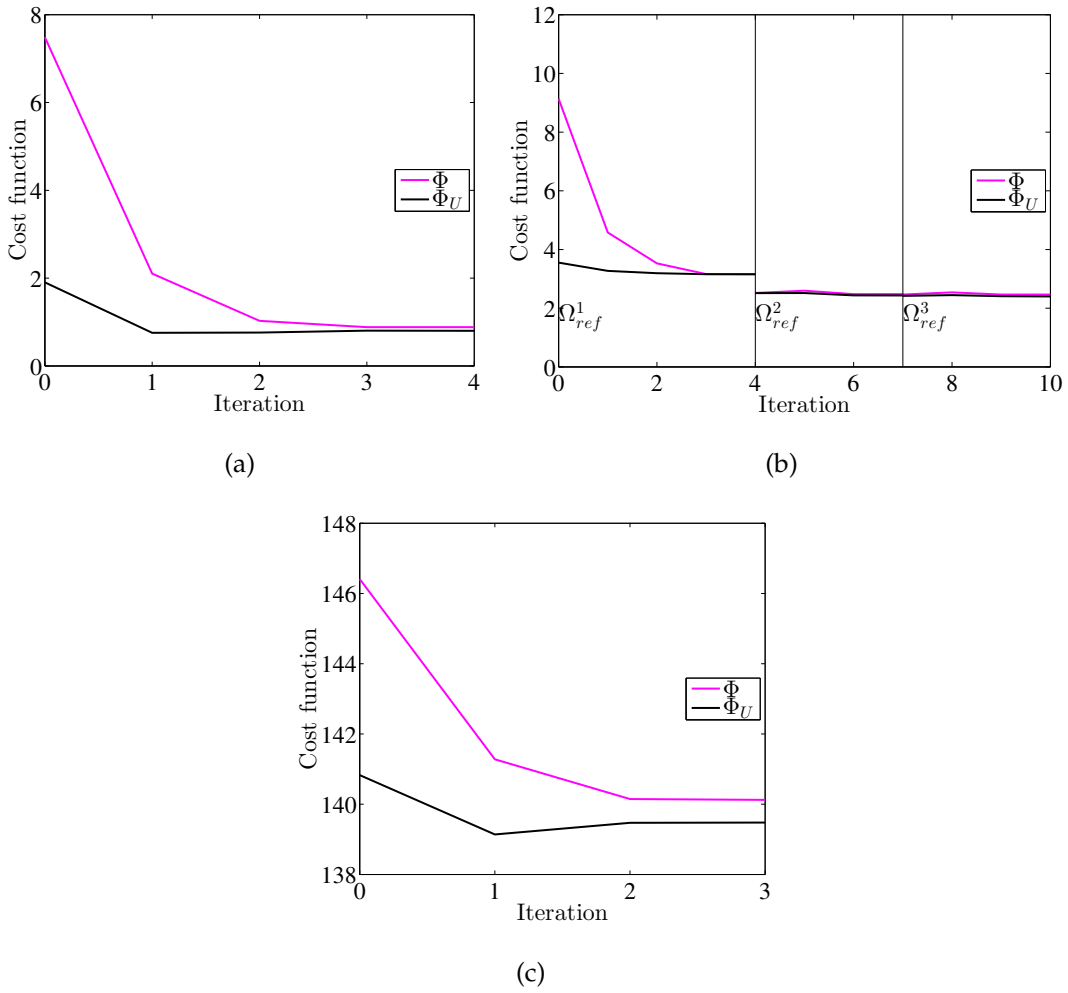

Figure 6.14: Cost function changes during the identification for each model: (a) exact; (b) estimated; (c) Quasi 2D configurations

In other words, the procedure that combines the determination of the reference configuration and the calibration of material parameters gives satisfactory results in this virtual experiment.

6.4 Conclusion

This chapter discussed the feasibility for the determination of undeformed microstructures from *postmortem* microstructures and calibration of material parameters. A backtracking approach has been proposed to solve the inverse problem by iteratively updating the reference configuration via direct calculations. It is proposed to run FE analyses on the estimated reference configuration Ω^{est}_{ref} and get an estimated deformed configuration Ω^{est}_{def}, then modify Ω^{est}_{ref} based on the difference between Ω^{exp}_{def} and Ω^{est}_{def}. Due to lack of in-depth information,

displacements at surface are extruded to provide approximate boundary conditions for the FE simulations.

A virtual experiment on a 2D model serves as proof of concept. A sophisticated constitutive law, DD_CC, has been adopted to generate "experimental" data. Only the data at the top line (*i.e.,* the measurable surface) are considered to be known. Besides, the deformed model, including the in-depth microstructure, is considered known, as FIB-EBSD reveals the microstructure in experiments. It has been found that for relatively small plastic strains, simple constitutive laws such as isochoric elasticity restore much of the reference configuration.

An iterative process of corrections based on more sophisticated constitutive equations is then proposed to improve the microstructure estimate. This process results in an estimated model that is closer to the exact one, with errors reduced by 57%. More accurate boundary conditions need be adopted if the error is to be reduced further. As approximate boundary conditions are guessed an exact undeformed configuration cannot be obtained. Nonetheless, this algorithm is a step forward compared to the commonly used extruded microstructure from surface and the artificially generated Voronoi-style microstructure. From the better reconstructed model and with all information available at the surface, crystal plasticity can be studied more precisely. For example, identification based on the backtracked reference configuration results in more precise parameters than those based on extruded model from surface.

More efforts should be devoted to provide better descriptions of boundary conditions in the depth of the material, as they are the current limitation to further lower the discrepancy with the exact reference configuration. One option would be to treat the in-depth boundary conditions as unknowns to be calibrated [Bertin et al. 2016]. Another problem to address is the heavy calculation cost, as the procedure proposed herein contains nested loops of FE calculations. An important approach to reduce this time cost would be to reduce the dimension along the depth, paying special attention to avoiding compromise of the whole model.

It should be noted that this chapter is devoted to a feasibility check of the proposed algorithm, and hence a synthetic two-dimensional example is considered. The efficiency and correctness of the process for three-dimensional models should be validated in simulations and, all the more importantly, with experimental data. It is not expected that the obvious additional complexity of the 3D topology as compared with 2D situations will cause extra

difficulties in either the backtracking procedure or calibration step. The next chapter will apply the strategy on experimental data.

Chapter 7

Comparison of experimental and simulated surface 3D kinematic fields and its exploitation in plasticity parameter calibration

This chapter assembles all the experimental observations and numerical methods presented previously. The comparison between experimental and numerical kinematic fields on a fine-grained sample with a realistic 3D microstructure is provided. A novel FIB slice realignment method based on DIC is proposed and tested. A realistic 3D mesh has been generated from the strained experimental microstructure. The extraction of boundary conditions and their propagation along the depth are revisited. The surface 3D kinematic fields obtained by FE simulation with two crystal plasticity laws are compared with experimental observations, and their differences are quantified. Two pairs of plasticity parameters are calibrated for the two phases in 16MND5 steel via finite element model updating.

7.1 Introduction

Many enrichments of multiscale plasticity constitutive models have been proposed in the past decades, which are motivated by better predictions of the macroscopic behavior (see Chapter 1). In this context, validations of crystal plasticity models exploiting kinematic fields have been conducted, and more specifically the displacement and strain fields obtained from images acquired via SEM [Héripré et al. 2007; Lim et al. 2015; Guery et al. 2016b].

However, only surface information is accessible by SEM analysis, while tensile test samples live in a three-dimensional world. Hence the 2D characterization performed during the experiment is incomplete for studying 3D crystal plasticity for both tensile experiment and numerical simulation.

For the purpose of validating the identification procedure and its upscaling to macroscopic laws, samples with columnar and coarse grains have been prepared so that mere extrusion of the surface microstructure is a valid description [Grennerat et al. 2012; Lim et al. 2015]. Such an approach has the merit of addressing the methodology with a good control of the microstructure. Yet, it is limited to materials that are not representative of most key applications. If a similar procedure, *e.g.*, extrusion of the observed surface microstructure, is applied to materials with unknown grain geometry in the depth direction, numerical modeling is expected to lead to poor agreement with *in-situ* observations, as documented from numerous numerical simulations (see *e.g.,* [Zeghadi et al. 2007b]).

Another option is to synthetically generate in-depth microstructure based on surface grain structures, which introduces randomness into models. The effect of the synthetically generated in-volume data on the mechanical responses at microscale has been studied by [Zeghadi et al. 2007b; Guery 2014]. It has been found that two artificially generated 3D simulation models, even based on the same surface grains, will result in distinct simulated mechanical responses on the surface. Nonetheless, numerous works have adopted extruded model from surface data [Héripré et al. 2007; Lim et al. 2014; Guery et al. 2016b] or synthetic in-depth microstructure [Lebensohn et al. 2008] in 3D simulations, due to the lack of information on real 3D microstructures. Any better determination of the actual microstructure is expected to lead to a much more constrained, and hence reliable, identification (Chapter 6).

On the experimental side, a major breakthrough has been achieved in the past few years with techniques such as 3D-XRD and Diffraction Contrast Tomography (DCT) [Ludwig et al. 2009; Herbig et al. 2011]. These techniques allow the full 3D grain geometry with the associated crystallography to be retrieved. Such a complete characterization constitutes a major step forward in the context of identification and validation of crystal plasticity models. Yet, using such methods is still exceptional as they require (up to now) monochromatic and coherent X-ray beams as produced by synchrotron facilities. They also suffer (today) from some limitations, such as a small (few thousands at the most) number of grains with simple shapes and uniform orientations. Although one may be confident on the future breaking of those limitations, these techniques are not yet mature enough for *in-situ* mechanical tests on

materials such as fine-grained steels as needed for some demanding industrial cases (*e.g.*, 16MND5 steel).

During the last decades one approach to access 3D microstructure, which is compatible with a broad class of materials, has been proposed and adopted. It is 3D-FIB SEM tomography also known as 3D-EBSD [Groeber et al. 2006; Calcagnotto et al. 2010]. This technique consists of EBSD characterization of surfaces obtained after successive FIB milling, which progressively reveals the material in depth. A detailed description of the technique is available [Zaefferer and Wright 2009]. 3D-EBSD and 3D crystal plasticity FE simulations have been coupled to bridge experiments and simulations. The 3D texture and microstructure below a nanoindent in a Cu single crystal have been studied using 3D-EBSD and crystal plasticity calculations [Zaafarani et al. 2006]. Statistically-equivalent virtual microstructure has also been proposed for crystal plasticity finite element (CPFE) simulations [Groeber et al. 2008a;b]. Although the microstructure properties are statistically respected, the statistically-equivalent model still involves random tessellation and thus cannot be used for direct comparison between experiment and simulation at local scales. A realistic polycrystal model of Mo-TiC30% metal-ceramic composite has been generated based on FIB-EBSD experimental data, and yields better prediction of the stress-strain curve than the columnar-grain crystal aggregates [Cédat et al. 2009; 2012]. The improvement has been attributed to the more accurate 3D microstructure of the initial state. To the best knowledge of the author, no previous work comparing simulated and measured experimental kinematic fields of realistic 3D model for fine-grained steels have been reported.

In-plane kinematic fields are often utilized for validating crystal plasticity laws and calibrating their parameters [Héripré et al. 2007; Lim et al. 2015; Guery et al. 2016b]. However, very few works are reported on the comparison of experimental and simulated out-of-plane kinematic fields. An Al sample with a single quasi-2D layer of coarse grains (average size $\approx$3.5 mm) has been deformed plastically and its kinematic fields have been observed [Zhao et al. 2008]. Quite similarly, a Ta sample with a single quasi-2D layer of coarse grains (average size $\approx$2 mm) has been deformed plastically and its surface kinematic fields have also been observed [Lim et al. 2014]. Their surface topographies were measured using a white-light confocal microscope, then compared to CPFE simulation values [Zhao et al. 2008; Lim et al. 2014], where similitudes and discrepancies have been found, as shown in Figures 1.30 and 1.31. To the best of the author's knowledge, no comparison between experimental and CPFE simulation out-of-plane motions has been made for fine-grain materials at the mi-

croscale.

In this chapter these problems will be tackled as follows: Section 7.2 introduces the FIB-EBSD data and generates a 3D-tetrahedral mesh, including a novel slice alignment method based on global DIC. Section 7.3 is dedicated to the validation of two crystal plasticity laws by using the 3D mesh. Several identification processes have also been performed on the experimental 3D mesh.

7.2 FIB-EBSD settings and data

After the tensile test detailed in Chapter 4, a region of the same sample has been chosen as the targeted milling area (see Chapter 5). The region, roughly 1/9 of the patterned part of the sample, is located near the sample edge to facilitate the milling and at the edge center to benefit from precise displacement measurement (see Figures 4.9 and 4.10). The steps of FIB-EBSD process have been detailed in Section 5.3.

In total 118 slices have been milled and indexed (by HKL CHANNEL 5 [HKL 2007]) for a duration of two weeks. An area of 42×41×11.8 µm^3 has been studied in 3D. The Ga^+ gun overheated after the 89^{th} slice and had to be rebooted. Thus it is likely that the 89^{th} and 90^{th} slices have a step size larger than 0.1µm. As a result, only the first 89 slices are used to reconstruct the volume. The orientation maps of the first eight slices of FIB-EBSD are shown in Figure 5.9, and the topography of the eroded area has been reconstructed (Chapter 5). Figure 7.1 shows the inverse pole figures of the 9th, 29th, 49th, 69th, 89th and 109th FIB-EBSD slices, where a gradual yet significant grain morphology change is observed. These slices need to be compiled to reconstruct the 3D microstructure of the region.

Dream3D is an OpenSource software dedicated to the analysis of microstructures in 3D [Groeber and Jackson 2014]. For FIB-EBSD experimental data, it reads the indexed orientation data, realigns each slice and labels each grain based on user-set disorientation threshold. The slice realignment is necessary since there is inevitably a shift between adjacent EBSD acquisitions, even with the built-in sample realignment by cross-correlation in the FIB-EBSD process. Figure 7.2(a) shows the lateral view of the compiled FIB-EBSD data without realignment. Unphysically rugged grain boundaries are visible at the bottom left and top right regions. During the Dream3D realignment process, the disorientation between adjacent slices is calculated. Then the slice is shifted rigidly along the x and y directions to achieve a minimal disorientation. The shift is uniformly performed on the entire slice, and

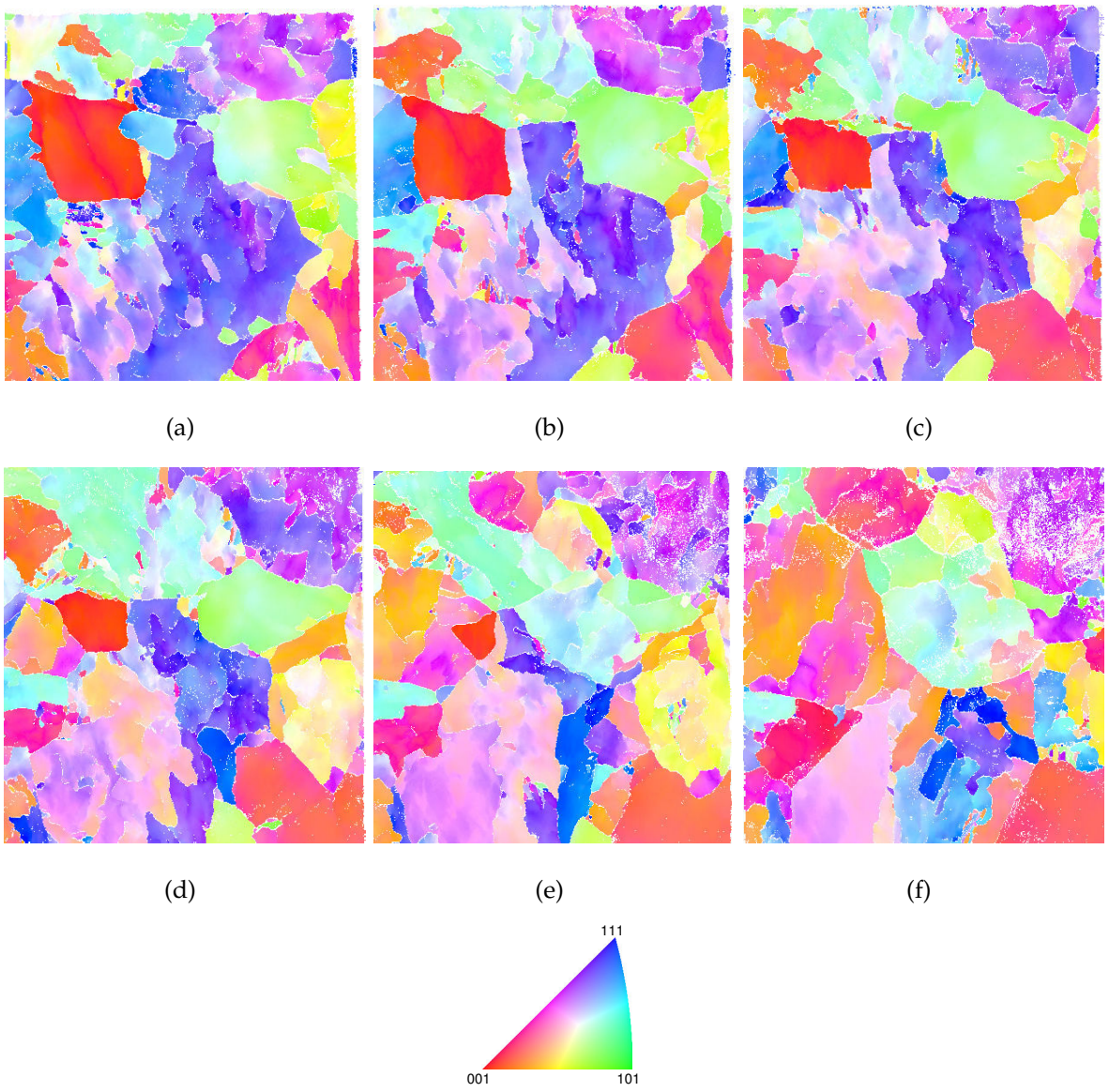

Figure 7.1: Orientation maps of the 9th (a), 29th (b), 49th (c), 69th (d), 89th (e) and 109th (f) FIB-EBSD slices.

only by integer number of pixels without interpolation. However, as revealed in Chapter 4, the coordinates in EBSD images are not stable, especially at the beginning of acquisition. This effect will limit the realignment performance, and spurious rugged grain boundaries cannot be fully removed, as shown in Figure 7.2(b). A global-DIC-based realignment process is proposed in the following.

7.2.1 FIB slice realignment by DIC

DIC applied to neighboring FIB sections can be based on different physical quantities, such as crystallographic orientation (by *quaternion correlation* detailed in Chapter 2), or Kikuchi

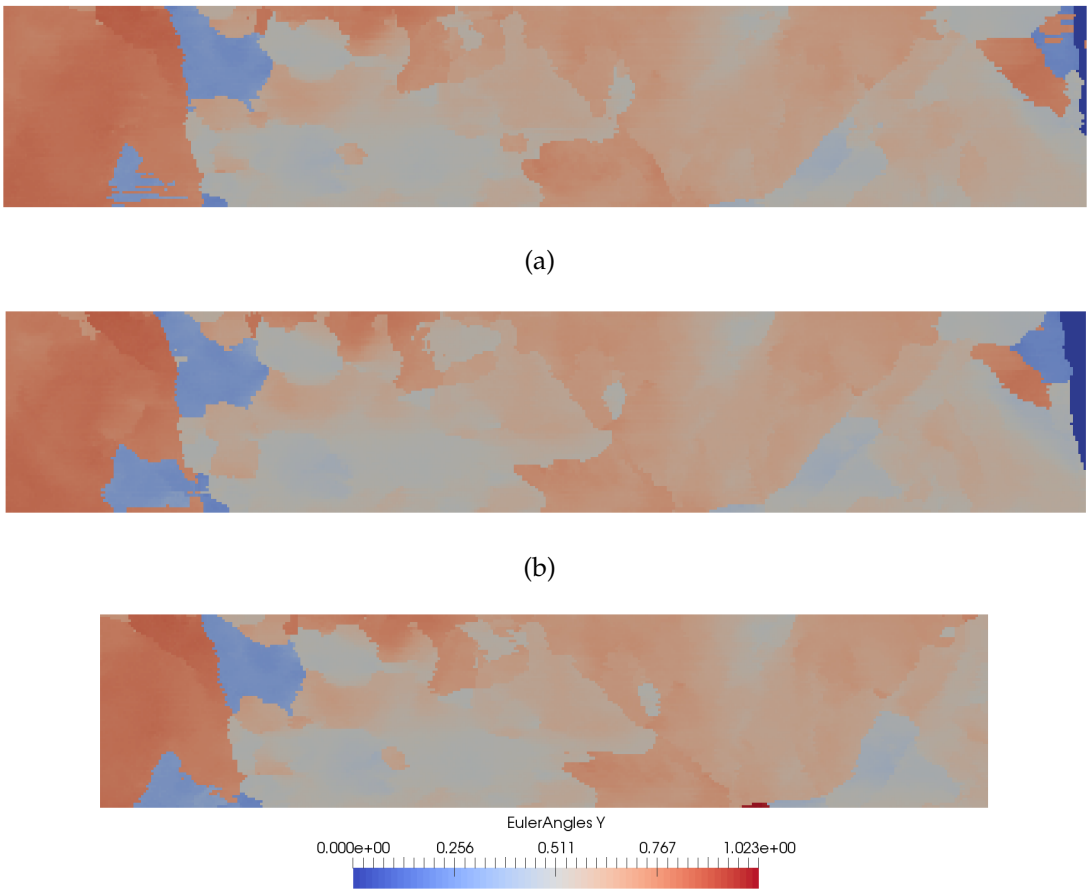

(a)

(b)

(c)

Figure 7.2: Lateral view of the second Euler angle of compiled FIB-EBSD data. (a) Compilation without re-alignment. (b) Compilation with uniform shift provided by Dream3D. (c) Compilation with the herein proposed DIC method. This figure is shorter than the two previous ones, since the ROI covers only the central part of image.

image quality (IQ field or band contrast field according to different indexing software). Band contrast is a scalar indicator of the average intensity of the Kikuchi bands with respect to the overall intensity within the electron back-scattered pattern [HKL 2007]. For computation cost reasons, the following discussion is based on the band contrast information of different FIB slices.

DIC on a series of FIB-EBSD images faces several particular challenges. Generally little image contrast is available, mostly concentrated on grain boundaries. The commonly used speckle deposition for low contrast surface is no longer possible, namely, the deposited speckle will simply be removed by the FIB milling process. Besides, there is potentially significant grain morphology difference between neighboring FIB slices, especially for thick slices. Moreover, the image registration for FIB slices of a specimen with a texture will lead

to skewed results. For example, if the grains are mostly elongated along a specific direction, DIC (together with the uniform shift proposed by Dream3D) will tend to rectify the inclined grains. In this case, the precise registration of FIB slices will bias the reconstruction. A possible remedy for the problem of specimen with a texture is to take images of both ends of the sample, then launch the FIB-EBSD process that runs through the sample entirely. Another solution is to do coarse 3D microstructure measurement by non-destructive methods, and use it as reference for finer FIB-EBSD measurements.

Although the 16MND5 sample used herein does not exhibit particular texture, poor information contrast and potential significant difference mean that the high resolution of displacement fields cannot be obtained. However, a few degrees of freedom can be allowed to account for possible shifts and imaging distortions between slices, thus making the alignment more precise than uniform shifts. A poorer global DIC calculation has been performed in this context. An example of the Band Contrast (BC) chosen for FIB slice registrations is shown in Figure 7.3(a). According to previous correlation results on EBSD images, displacement field show traces along the scanning direction, especially for the beginning part (see Figures 4.15(a), 4.15(b), 4.16(a) and 4.16(b)). A tailored mesh with only 6 horizontally elongated triangles is proposed for DIC analyses, as shown in Figure 7.3(b). All the equations for global DIC introduced in Section 1.2.1.2 still hold true. No mechanical regularization has been implemented in the DIC procedure, as only a few degrees of freedom are sought here and grain boundary information between slices is sufficient to evaluate the nodal displacements. Besides, the line specific displacement of EBSD acquisition, as revealed by Figures 4.15(a) and 4.15(b), could not be well treated by regular elastic regularization.

The measured displacement fields in x and y directions are shown in Figures 7.3(c) and 7.3(d). Though less rich than the majority of displacement fields obtained in DIC calculations, they already provide a much richer information than the commonly used uniform shift of slices, and will lead to more precise alignment between FIB slices. Figure 7.3(e) shows the residual between two neighboring FIB slices after a uniform shift, while Figure 7.3(f) shows the residual after the herein proposed DIC calculation. The RMS of the gray level residuals has been evaluated to be 8.4 for the uniform shift alignment and 7.2 for the FIB-DIC calculation. The latter leads to a better registration between the two slices. The first slice with full orientation indexing, *i.e.*, the 8th slice, is used as the initial reference image, and the 9th slice is registered. Then the corrected 9th slice is used as reference image to register the 10th slice, and so on. Consequently, all the slices are transported to the coordinate

system of the 8th slice. The measured displacement fields have been applied on the crystallographic orientation fields by quaternion interpolation, in which the 'nearest' interpolation method has been used (see Chapter 2). The interpolated crystal orientation at a query pixel is the value at the nearest sample grid point, in order to avoid creating spurious orientations at grain boundaries. Then the DIC-aligned crystal rotation field is fed to Dream3D without activating its realignment function. A better alignment is obtained in this way, as shown in Figure 7.2(c). Compared to the uniform shift realignment adopted by Dream3D shown in Figure 7.2(b), the FIB-DIC method results in smoother grain boundaries.

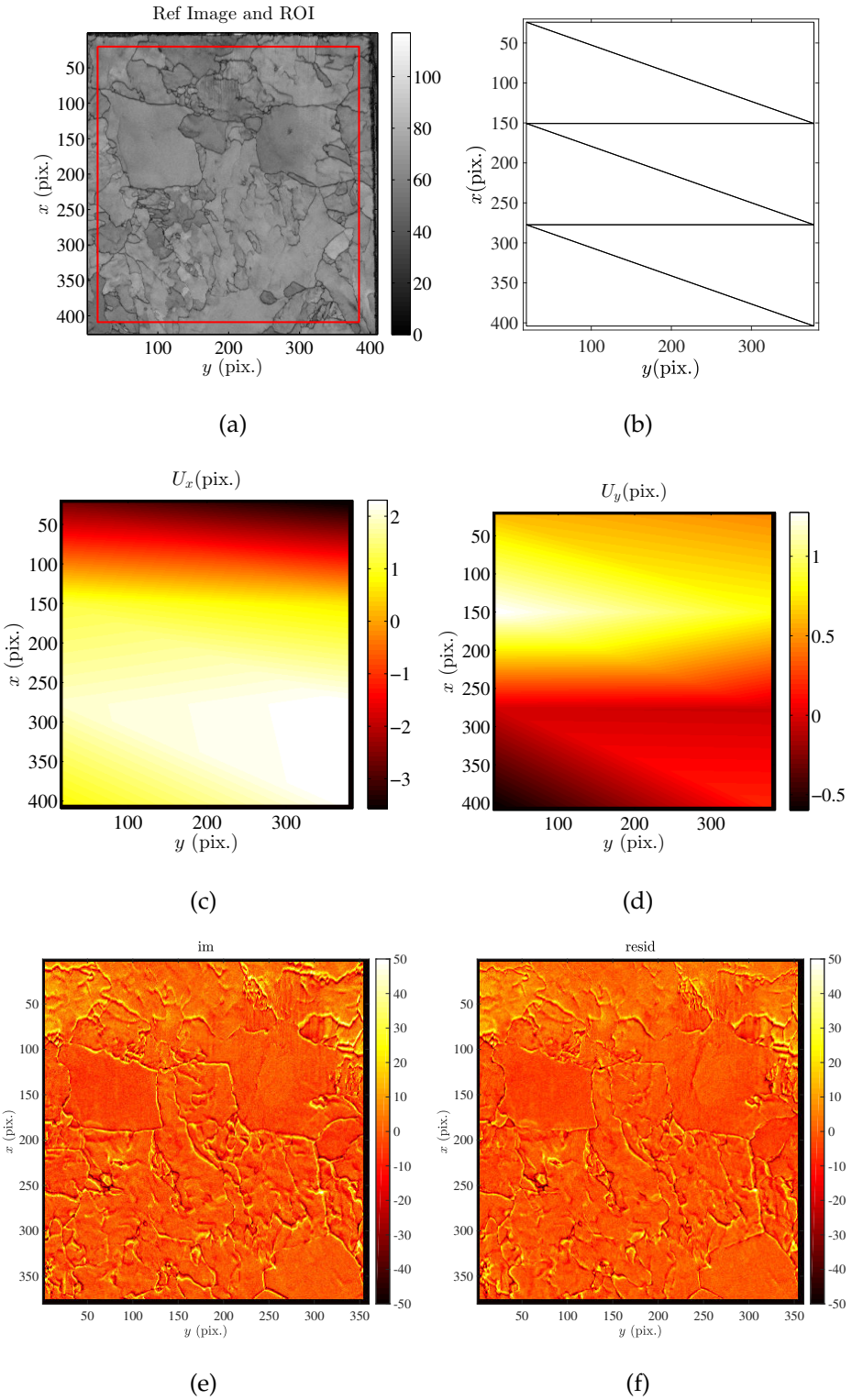

Figure 7.3: Registration of FIB slices by global DIC with a few degrees of freedom. (a) The Band Contrast image of a slice, used as reference image. The boxed area is the ROI. (b) Triangular mesh used for the registration. Measured displacement (expressed in pixel, 1 pixel $\leftrightarrow$ 100 nm) fields between neighboring FIB slices in x and y directions are shown in (c) and (d) respectively. (e) Gray level residual between 2 neighboring slices after applying a uniform shift. (f) Gray level residual after the DIC calculation.

To provide a statistical comparison for the recompilation quality, the misorientation between neighboring voxel pairs has been calculated for the three reconstructions. For a cube of 9,842,000 voxels, 280,387 voxel pairs exhibit a misorientation greater than 5° for the reconstruction without shift, 260,661 pairs for the reconstruction by uniform shift, and 259,171 pairs for the reconstruction by FIB-DIC. It is concluded that the realignment by FIB-DIC leads to a better reconstruction than the other two reconstructions.

It should be noted that the FIB-EBSD test is performed on a relatively small region with a limited number of indexed points and a short acquisition time. The instability of scanning, *i.e.,* distortions of electron beams and inconsistent step distances in x and y directions, are thus limited. For example, as shown in Figure 7.3(c) and 7.3(d), the DIC-realigned displacement field is of the order of 1-2 pixels from uniform shift. If tested on a FIB-EBSD acquisition with larger regions of interest, FIB-DIC will exhibit more significant advantages than the re-alignment by uniform shift. The reconstructed volume is shown in Figure 7.4 and its topography is visible. The volume is ready for mesh generation.

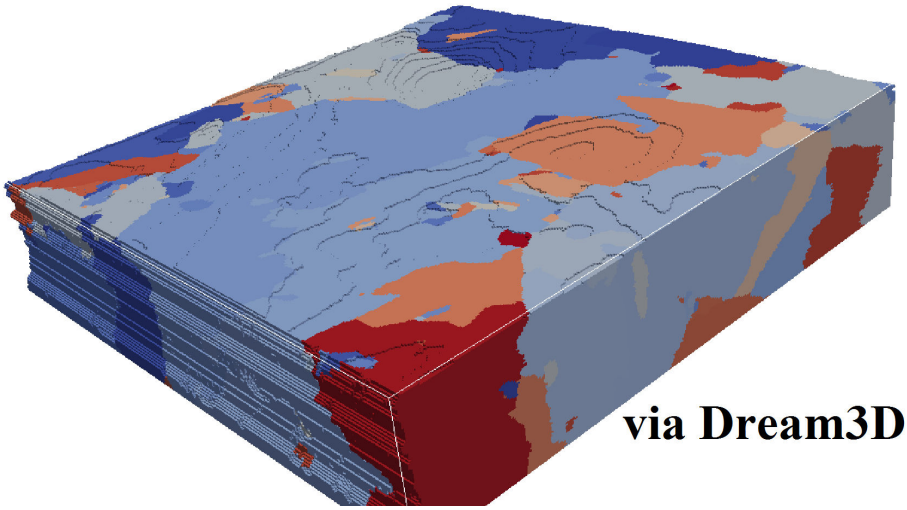

Figure 7.4: Result of slice reconstruction by Dream3D, where topography is visible.

7.2.2 Mesh generation

2D meshing is provided in Dream3D, where outer-surface and grain boundaries will be meshed with triangle elements, as shown in Figure 7.5. The process meshes along the voxel surfaces along the grain boundaries. As a result the raw triangular mesh is of unit size (the voxel size) and always parallel or perpendicular to the principal axes of the cubic voxel array.

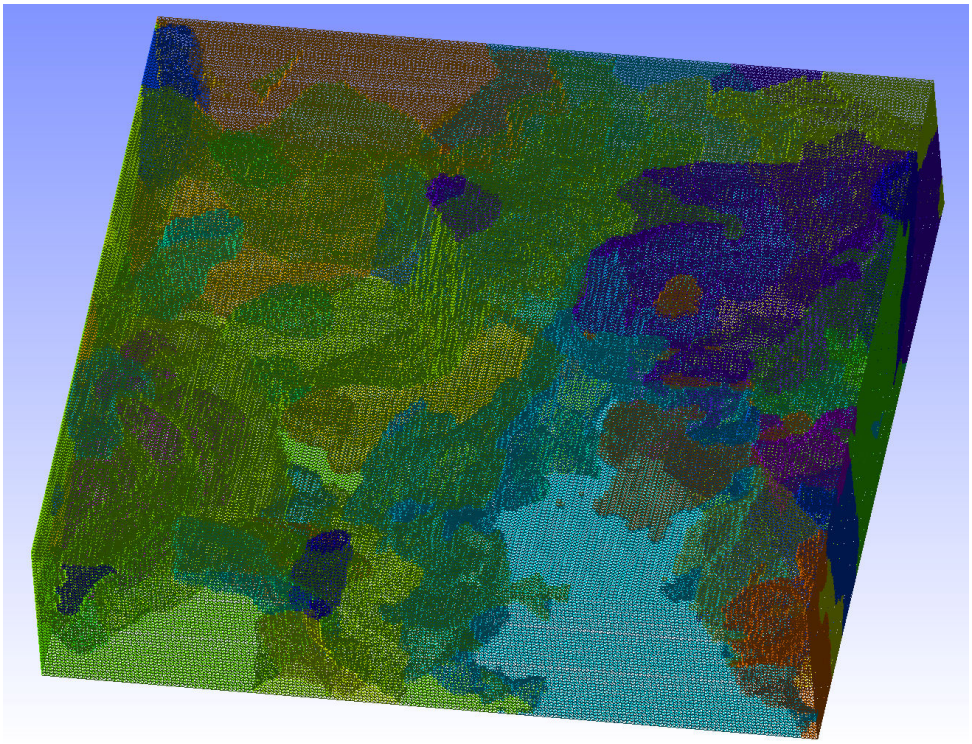

Figure 7.5: Raw 2D triangular mesh provided by Dream3D.

The 2D raw mesh requires a simplifying process to represent the experimental microstructure with fidelity while keeping the numerical cost low. A Laplacian smoothing algorithm [Field 1988] is provided in Dream3D and its effect is shown in Figure 7.6. Laplacian filtering results in smooth grain boundaries. However, some elements may be degenerated and hinder future 3D meshing. For example, several singular points are visible in Figure 7.6. Besides, grain sizes tend to be modified by Laplacian smoothing, where an additional volume control for each grain is necessary. As a result, Laplacian smoothing has been abandoned in the mesh generation.

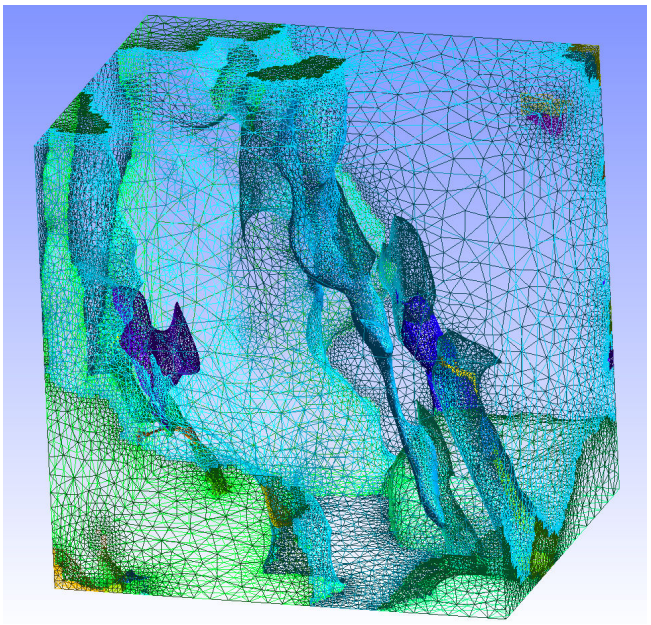

Figure 7.6: Result of Laplacian smoothing on a local part of the model.

To reduce the microstructure complexity and the corresponding computation cost, a binning operation is adopted to reduce every 7×7×7 voxels to 1 super voxel. The resulting raw 2D mesh is shown in Figure 7.7(a). Though many microstructure details are lost in this process, the voxel size of 0.7 µm allows the model to keep the major features of the studied region. Compared to the full definition image shown in Figure 7.5, Figure 7.7(a) shows a much simpler mesh yet keeps the major features of grain morphologies. It should be noted that the gain in rectification precision by the proposed DIC procedure has been mostly lost in the binning process. However, it is believed that with the ever growing computing power, FE simulations could be performed with more complex models in the future. Hence the binning process will no longer be necessary, and the more precise realignment between FIB slices by DIC will lead to more accurate simulation results.

Another tool for processing an existing mesh is MeshGems (www.meshgems.com), a commercial software developed by Distene. Three products of MeshGems have been adopted in the present work: *Cleaner*, *SurfOpt* and *Tetra*. The first one cleans up a 2D mesh, for example merges very close nodes, while the second optimizes a 2D mesh, for example increasing the element size whenever possible. Figure 7.7(b) shows the effect of *SurfOpt*, where a 25% reduction of element number is achieved compared to the mesh shown in Figure 7.7(a).

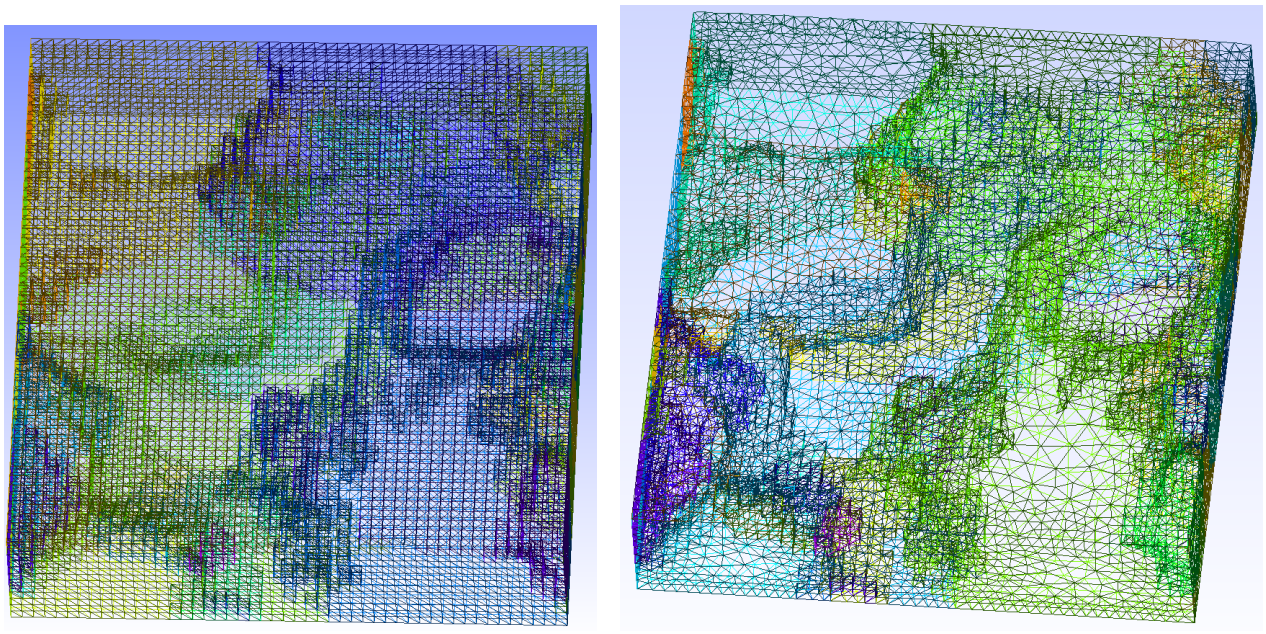

(a) (b)

Figure 7.7: (a) Raw surface mesh after the 7×7×7 binning as obtained from Dream3D. (b) Result of surface mesh optimization by MeshGems of (a).

It should be noted that the *SurfOpt* function modifies the position of nodes and not every node motion is as expected. For example moving nodes at the mesh surface is generally undesired. Fortunately, the surface microstructure is known precisely, as shown in Chapter 5, and the undesired node positioning can be corrected. The surface mesh correction is shown in Figure 7.8(b). After the optimization of 2D surface meshes, the function *Tetra* of MeshGems is utilized to generate tetrahedral elements based on the 2D surface meshes. In total, there are 180,081 tetrahedral elements in the generated mesh. Once the mesh is created, linear tetrahedral or reduced integration quadratic tetrahedral elements can be used. The 3D tetrahedral mesh is shown in Figure 7.8(a), where different colors correspond to different grains.

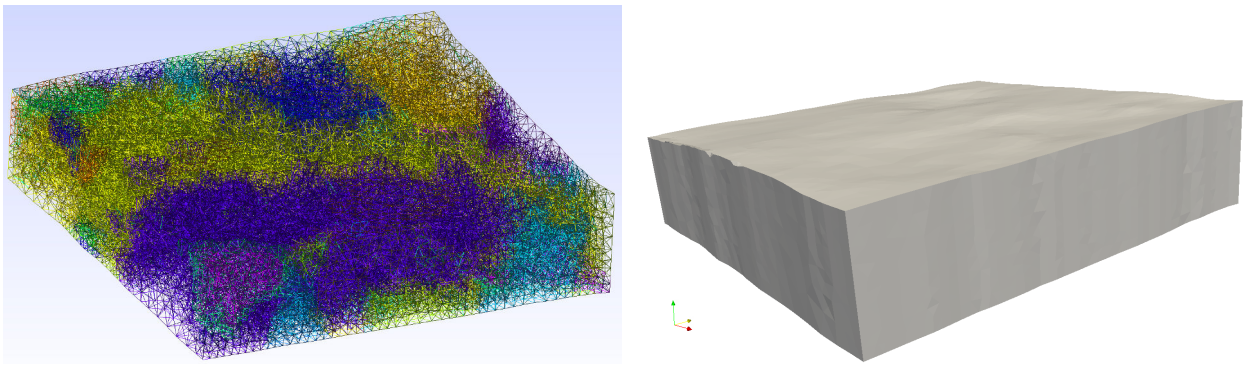

(a) (b)

Figure 7.8: Generated FE mesh based on the FIB-EBSD data. (a) Tetrahedral mesh (different colors correspond to different grains). (b) The topography of the mesh is visible.

The different steps of the procedure are highlighted on a big proeutectoid ferritic grain (grain A in Figure 7.13(b)) Figures 7.9-7.11. The 3D shape of the grain, viewed in three different positions, in full resolution of the FIB-EBSD data is shown in Figure 7.9. The complexity of the grain morphology makes the initial microstructure prohibitive for numerical calculations. The grain shape after a $7\times7\times7$ binning is shown in Figure 7.10, where the shape complexity is drastically reduced. The topography of the grain is also visible in Figures 7.9(a) and 7.10(a). After the 3D mesh generation process, the shape of the grain is shown in Figure 7.11. It can be seen that the major features of the grain morphology are kept in the final mesh, while the number of elements is limited, and the spurious oscillations at the grain boundary surfaces are avoided. Besides, the element sizes are rather homogeneous.

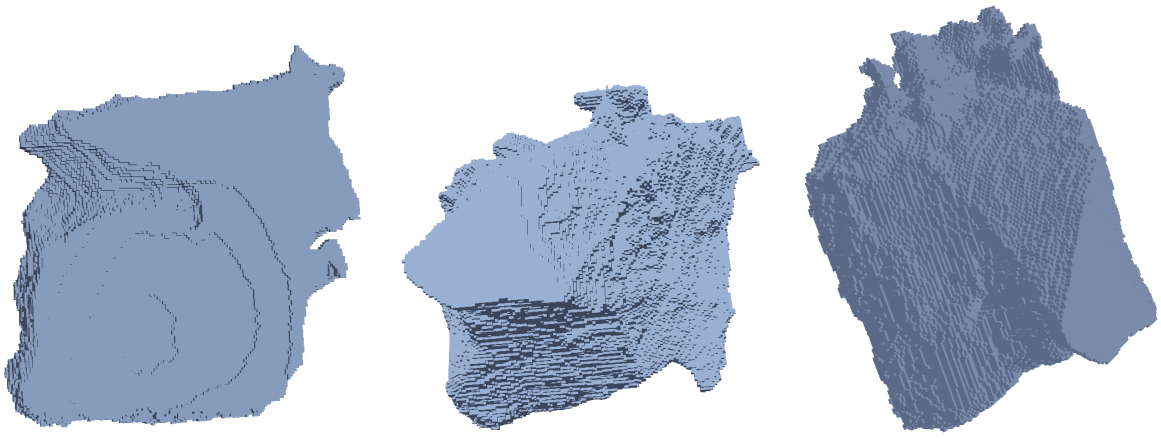

(a)

Figure 7.9: 3D shape of a big proeutectoid ferritic grain as measured by FIB-EBSD

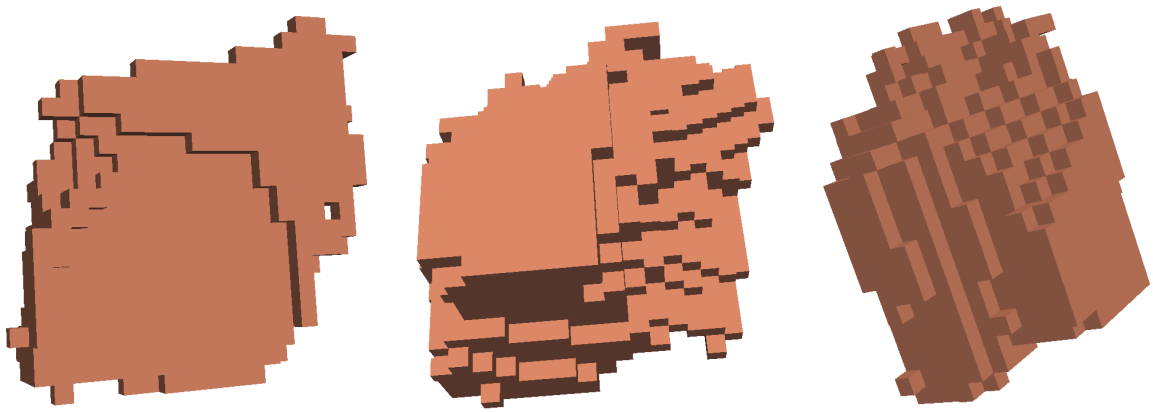

(a)

Figure 7.10: 3D shape of the same grain (Figure 7.9) after 7×7×7 binning of the raw data

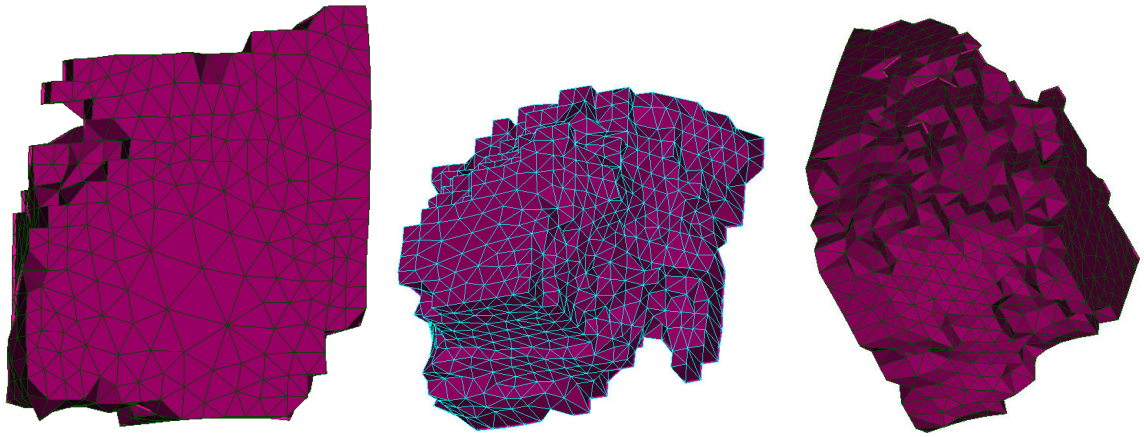

Figure 7.11: Generated tetrahedral elements of grain of Figure 7.10. Note that a part of the grain is not included in the meshed area.

A crystallographic orientation is prescribed to each tetrahedral element, which is determined as the median orientation of the voxels in the element area. Figure 7.12(a) shows the crystal orientation at the model surface, while the experimental orientation for the model area is shown in Figure 7.12(b). It can be concluded that the discretization of the microstructure simplifies the experimental observations, yet the majority of the microstructure information is kept. The mesh together with the crystal orientations, generated from 3D experimental data, will be used in the following FE simulations.

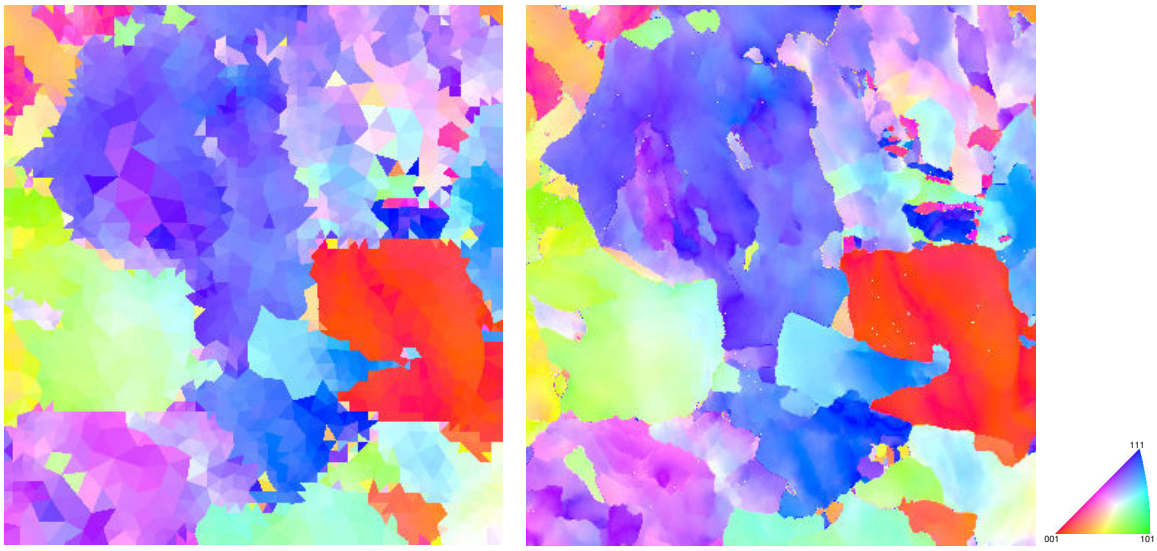

(a) (b)

Figure 7.12: (a) Prescribed crystal orientation for the model surface. (b) Experimental crystal orientation for the meshed area.

7.3 Validation and identification of crystal plasticity laws on 3D model

7.3.1 Determination of boundary conditions

Surface boundary conditions can be obtained by registering the SEM images acquired during the tensile test. However, as shown in Section 4.4, coordinates of EBSD acquisitions are subjected to spurious displacements. FIB-EBSD images are no exception. Their coordinates need to be corrected should precise extraction of boundary conditions be aimed at. The following strategy has been chosen:

i) Build a full surface EBSD image by combining the 8 slices shown in Figure 5.9. In the process if a pixel is not indexed in slice 1, then the orientation of the same pixel of slice 2 is kept. A shift between neighboring slices is applied when necessary. (For any 2D position (x, y) inside the cube model, the orientation of the highest indexed pixel at that position is assigned to the pixel (x, y) of the resulting surface EBSD image.) The result is shown in Figure 7.13(a). The kernel average misorientation (KAM) of the region is shown in Figure 7.13(b), where isolated points correspond to initial Pt speckles. The bright curvy lines indicate the grain boundaries, and darker lines highlight the lath boundaries. Two major grains are short of lath boundaries, and they correspond to proeutectoid ferrite designated

as grains A and B.

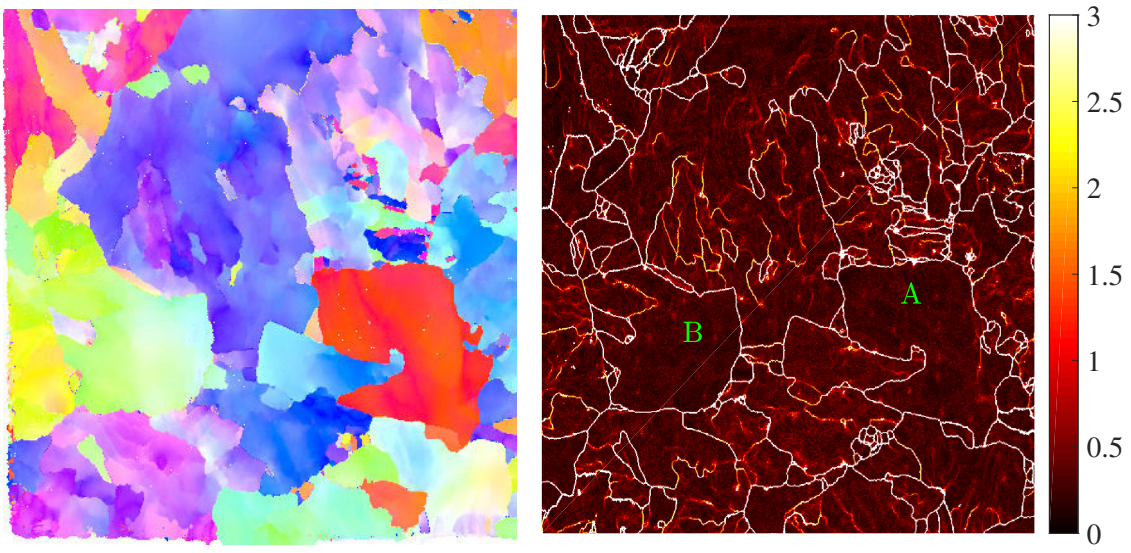

(a) (b)

Figure 7.13: (a) Reconstructed surface EBSD image obtained by combining the images of Figure 5.9. (b) Kernel average misorientation of the milled surface.

ii) The meshed region of the FIB-EBSD data is shown in Figure 7.14(a). The reconstructed EBSD image has been registered by quaternion correlation with the EBSD image after tensile loading (Figures 4.13(d) and 4.13(e)). Then the meshed area is mapped onto the full EBSD figure after tensile test (Figure 7.14(b)). It can be seen that the overlaid mesh edge is straight on the left and right sides, but curvy on the top and bottom sides. This is the evidence that the SEM machines used for *in-situ* tensile tests and for FIB-EBSD have different scanning drifts in the x direction. As a consequence, the constructed EBSD image can be registered with BSE images all along the tensile loading and its coordinates are corrected, as shown in Figures 7.14(c) and 7.14(d). Their difference in coordinates is the sought surface boundary conditions, which are illustrated on the surface triangular meshes in Figure 7.15. The out-of-plane displacement, which is measured as topography in Chapter 5, on the model boundary is also prescribed. Note that contrary to the displacements in the x and y directions, the displacement in z direction is only available for the final state, as shown in Figure 7.16. To prescribe u_z on model boundary for the intermediary steps, the displacement u_z is assigned proportionally to the mean applied strain $\langle \epsilon_{yy} \rangle$. In this way, the omni-present shift in EBSD acquisition has been avoided and correct boundary conditions can be extracted.

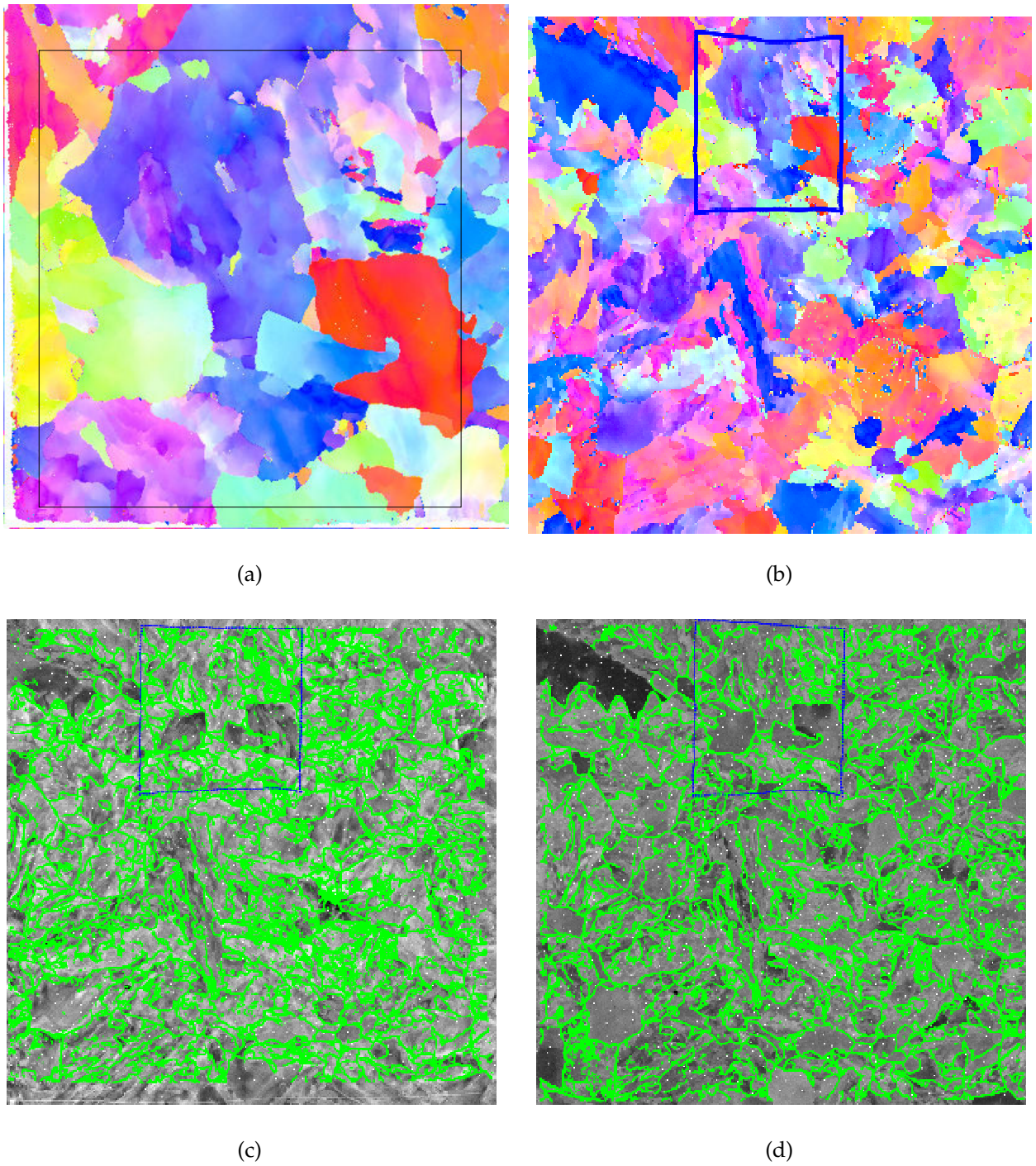

(a) (b)

(c) (d)

Figure 7.14: Steps of extraction of boundary conditions for the meshed area for FE calculation. (a) Reconstructed sample surface computed from the first 8 slices of FIB-EBSD. (b) Post-test EBSD image. (c) Post-test BSE image. (d) Reference BSE image.

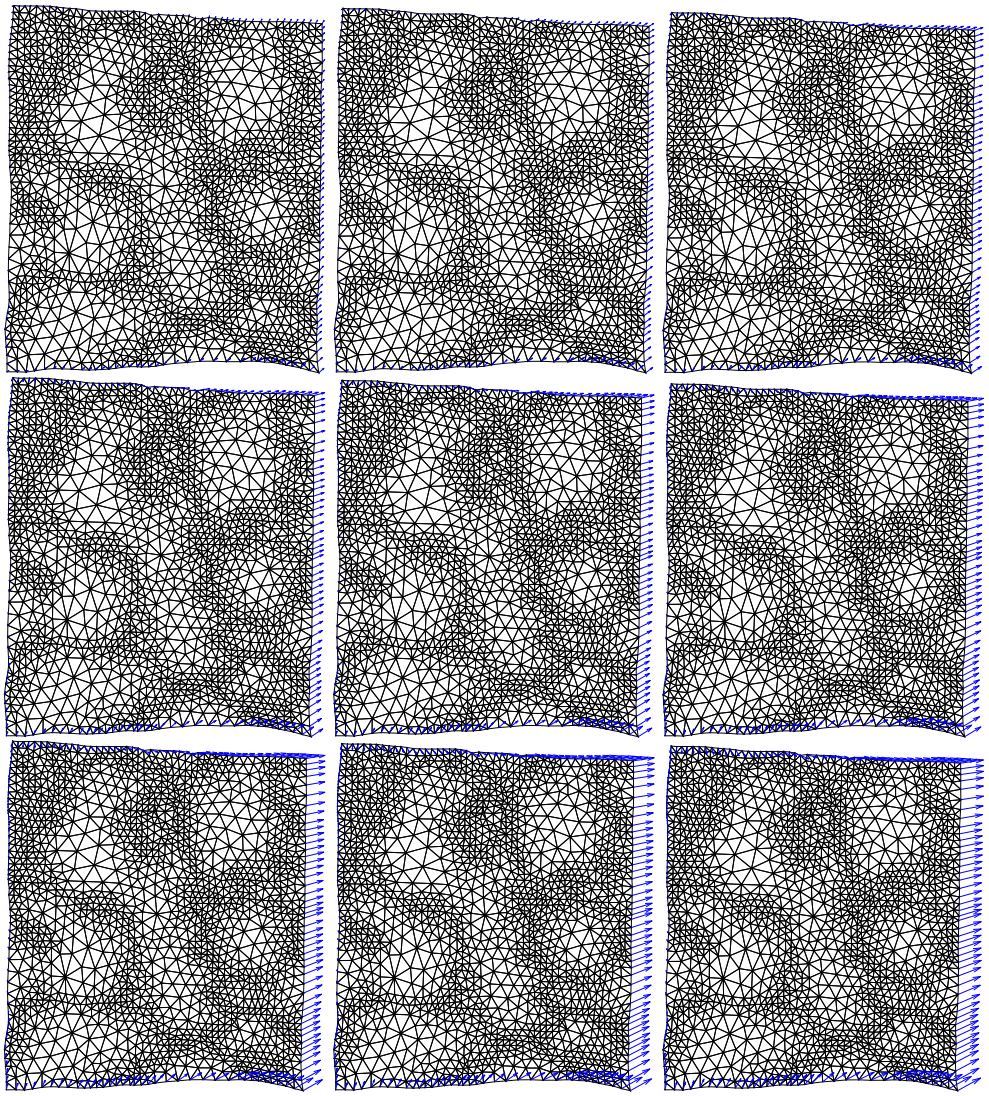

Figure 7.15: Measured 2D surface boundary conditions for all the loading steps.

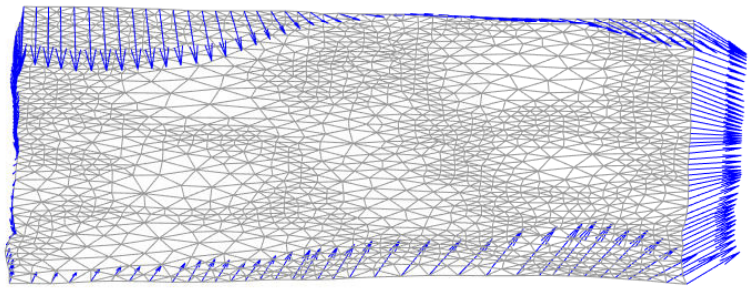

Figure 7.16: 3D kinematic boundary conditions on model surface for the tensile simulation. The out-of-plane component is magnified 5 times to make it more visible.

The next step is to estimate the in-depth boundary conditions, not accessible by SEM observations, from the surface measurements. It has been found that concentrated strain

bands form lines tilted nearly 45° with respect to the tensile direction, as shown in Figures 4.11 and 4.12. The inter-grain strain bands hint that the fine-grained steel sample can be simplified as an isotropic ideally plastic material in the SEM observation scale. Consequently, according to the slip theory [Schmid and Boas 1935], the activated slip systems should possess: i) slip direction at 45° with respect to the tensile direction, ii) plane normal direction also 45° with respect to the tensile direction. These two conditions constrain the slip planes to be vertical on the sample surface, which suggests that the observed surface boundary conditions can be reasonably extruded along the sample depth and form the 3D boundary conditions for the FEM model.

Based on the discussion of effects of BC on the FE simulations in Section 6.3.2, two following BCs are proposed and tested hereafter:

- BC1: extrude the displacements in x and y directions on the surface edges of the model into the depth, while the z components are such that the resulting shear forces along the vertical faces are equal to 0. The observed exterior surface and the parallel embedded surface are left traction free (*i.e.,* Neumann condition).

- BC2: extrude the displacements in x, y and z directions on the surface edges of the model into the depth. The observed exterior surface and the parallel embedded surface are left traction free (*i.e.,* Neumann condition).

It is important to mention that, even with the justification of BC extrusion discussed above, the obtained BCs are approximate. As mentioned in Section 6.4, one option would be to treat the in-depth boundary conditions as unknowns to be calibrated [Bertin et al. 2016].

7.3.2 Backtracking the initial microstructure of the 3D experimental model

The generated mesh shown in Figure 7.8 corresponds to the deformed microstructure. According to Chapter 6 , a compression by an effective plasticity with a constant hardening ratio recovers most of the deformation during the tensile test, and already leads to rather precise crystal plasticity parameters. A similar compression has been applied on the mesh. The true elastic part of the stress-strain curve shown in Figure 7.18 is ignored. The average hardening modulus is used as the pseudo-elastic modulus and the Poisson's ratio is set to 0.499 to describe plastic impressibility and avoid numerical issues (see Figure 6.10(a)). The

boundary conditions used for this compression composed of the reversed boundary conditions proposed in Section 7.3.1 for the model edges, and the reversed 3D displacements of all the surface nodes. During this compression, all the surface nodes have thus been restored to their original positions before tension, including the elevation (out-of-plane coordinates). After the compression procedure, the mesh is transported to its original configuration and the topography is flat, as seen in Figure 7.17(a). The 3D meshes for the two big ferritic grains are shown in Figure 7.17(b). All the following CPFE simulations are based on the mesh shown in Figure 7.17(a).

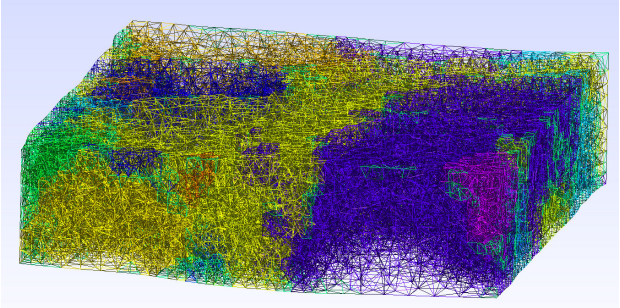

(a)

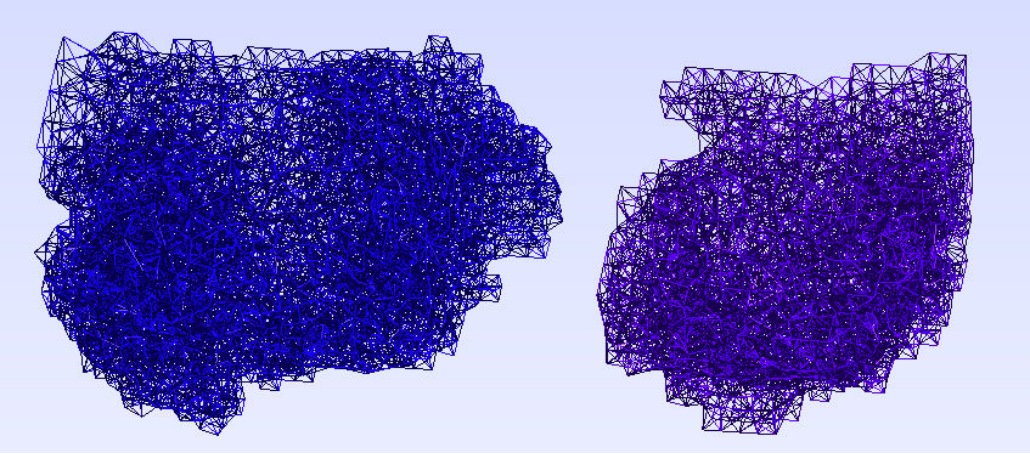

(b)

Figure 7.17: (a) The 3D mesh restored to its initial configuration, where the mesh surface is flat. (b) Tetrahedral mesh of the two big ferritic grains.

At first glance, it seems odd to assume the material as perfectly plastic in Section 7.3.1 and as plastic with a constant (non zero) hardening ratio in the present section. However, this is not contradictory, as plastic deformation constitutes the majority of the strain of a macroscopic 7% level. As aforementioned, the measured strain bands hint that the steel sample exhibits some perfect plasticity behavior. Thus the extrusion of boundary conditions based on the perfect plasticity assumption is partly justified. The synthetic constant-hardening

plastic behavior used in the present section aims to provide a good enough initialization of the initial configuration for the double loop process introduced in Chapter 6. The synthetic 2D calibration case presented in Chapter 6 shows that this prescription already leads to precise calibration results, even without the following microstructure updates.

7.3.3 Identification strategies for crystal plasticity laws

Two constitutive laws are adopted to simulate the tensile test on the above meshes: the simplified Méric-Cailletaud (SMC) and the Dislocation Dynamics for BCC materials (DD_CC). A finite strain frame has been used in the simulation with both laws. The constitutive equations are detailed in Section 1.3.3. Before identifying the plasticity parameters, the reference parameters should be tested along with the boundary conditions. The reference crystal plasticity parameters of SMC are listed in Table 1.3, and the parameters for DD_CC are given in Table 1.5.

The two extruded boundary conditions BC1 and BC2 are first tested, and the differences between the simulation results and the experimental values are shown in Table 7.1. BC1 and BC2 lead to similar kinematic fields in x and y directions. However, while BC1 gives access to comparable u_z with the experimental observations, BC2 results in overwhelmingly lower u_z. This phenomenon indicates that in a tensile test, the displacements in z direction in the bulk are mainly higher than those at the free surface. Consequently, the observed surface u_z should not be extruded in the volume, thus BC1 are the appropriate boundary conditions. All the following results are based on BC1.

Table 7.1: Comparison of difference (expressed in μm) between experimental and simulated surface kinematic fields with BC1 and BC2.

	BC1	BC2
Δu_x	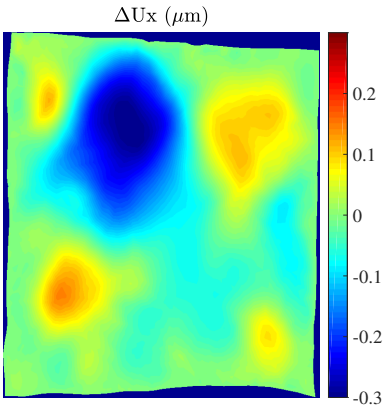	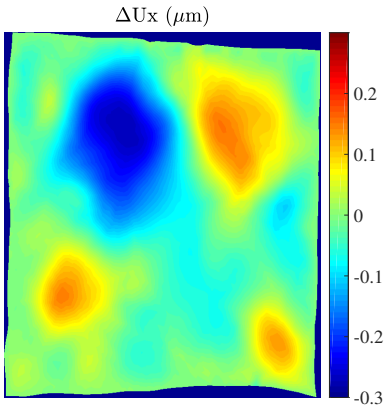
Δu_y	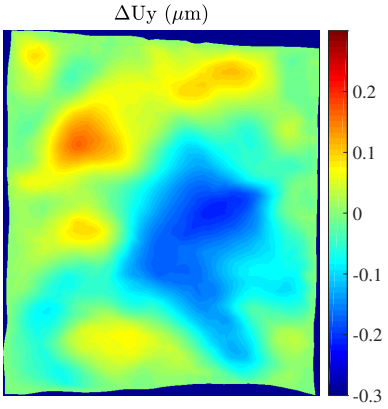	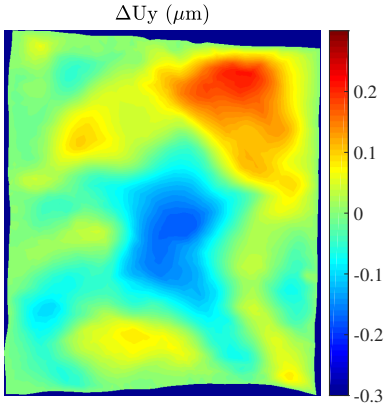
Δu_z	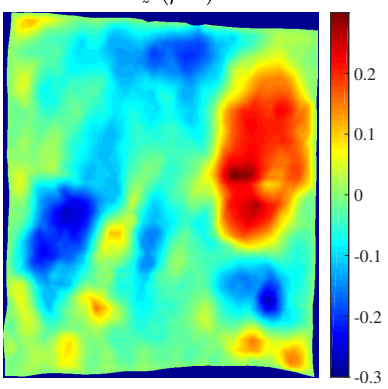	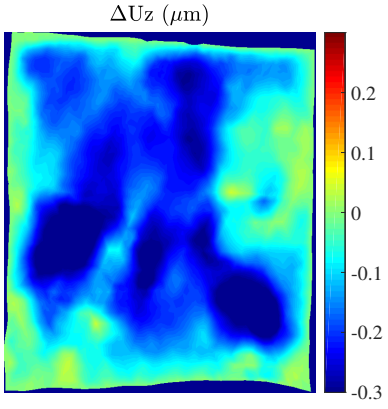

The computation times for different element types and plasticity laws are listed in Table 7.2. It is found that the SMC law is 30 times faster than DD_CC, and reduced integration on quadratic elements is around 20 times slower than that with linear elements. Using both SMC and DD_CC constitutive equations, the simulated and experimental displacements of the model surface are reported in Table 7.3, and the difference between experimental and simulated kinematic fields is shown in Table 7.4. The standard variances of the experimen-

tal displacement fields in three dimensions are listed in Table 7.5. The standard variances of the distances of simulated kinematic fields to the experimental displacement fields are summarized in Table 7.6, together with their ratio to the experimental ones. The simulated displacement fields in all three directions look alike the experimental ones, especially for the model boundaries. By taking the reference parameters, without distinguishing the bainitic and ferritic grains, the FE simulation already represents the experimental in-plane kinematic fields with an accuracy between 80-90%. The prediction of the out-of-plane kinematic fields is less remarkable, *i.e.*, 40-50% accurate, but it is already a good result. It is also visible that although FE simulation on linear tetrahedral elements cannot treat correctly the plastic incompressibility, due to a phenomenon called 'volumetric locking' [Chiumenti et al. 2004], it results in closer synergies with the experimental values than the FE simulation on quadratic elements. The reason for this phenomenon is not yet clear.

Table 7.2: Computation time for different element types and constitutive equations with Code-Aster, version 13.4 parallelized on 32 CPUs.

SMC with quadratic elements	SMC with linear elements	DD_CC with linear elements
70h	3.5h	110h

This result is quite satisfactory, especially given the fine microstructure and the simplifications adopted in CPFE (intense voxel binning, approximate backtracking of the initial microstructure, approximate boundary conditions and unique set of crystal plasticity for bainite and ferrite). It can be concluded from Tables 7.3 and 7.4 that different crystal plasticity laws (SMC and DD_CC) and different element types result in similar kinematic fields. Contrary to the displacement fields, the similarity of crystal rotations between experimental and numerical values is less remarkable (see last row of Table 7.3), in agreement with previous works that found that the rotation is more difficult to predict numerically [Zaafarani et al. 2006]. Note that the FE simulation with quadratic elements results in a rotation field spatially denser to that with linear elements, since there exist more integration points in quadratic elements (here 4 for the reduced-integration). In order to provide a fair comparison between the simulations, the rotation angles of the 4 integration points are averaged then assigned to the element uniformly. Though different from the experimental values, the three FE simulations result in similar rotation fields. Consequently, the crystal rotations are

not analyzed in the following.

Table 7.3: Comparison of experimental and three simulated surface kinematic fields. The displacements in three dimensions are expressed in µm, and the crystal rotation fields in °.

	SMC on quadratic elements	SMC on linear elements	Experimental data	DD_CC on linear elements
u_x	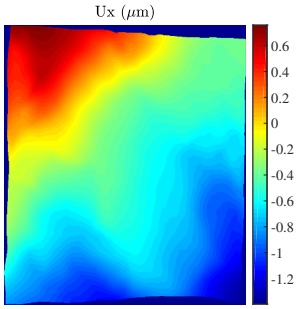	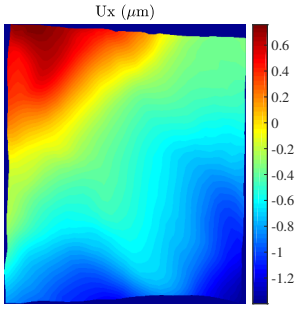	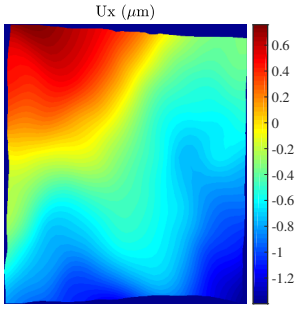	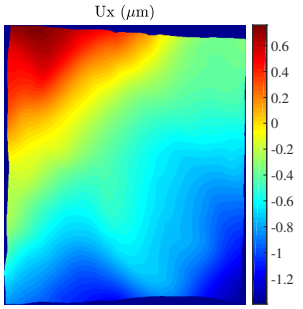
u_y	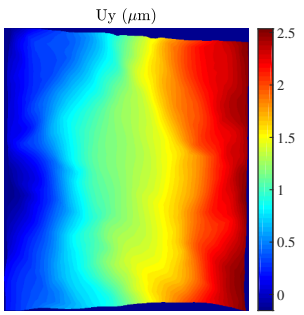	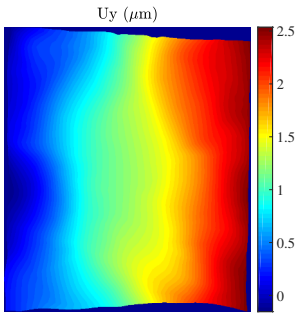	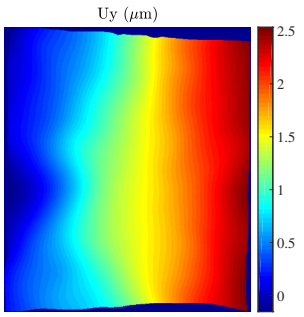	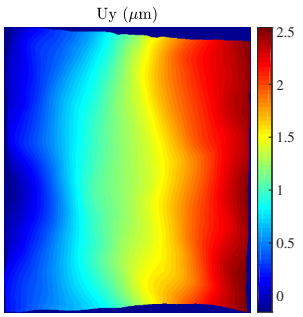
u_z	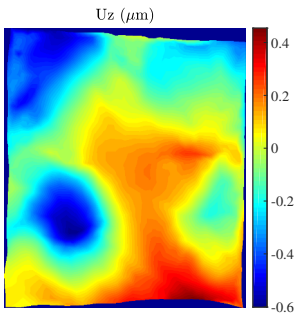	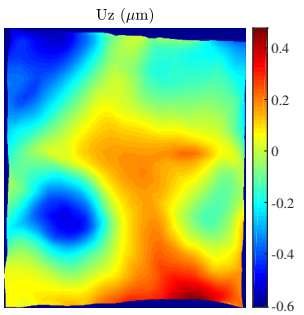	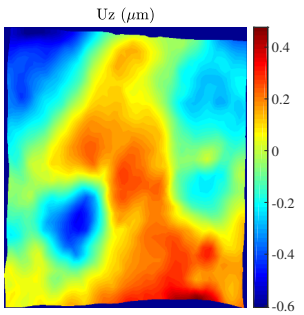	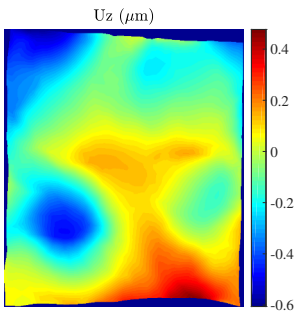
θ	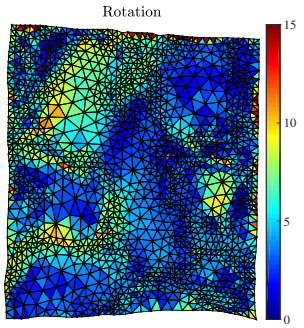	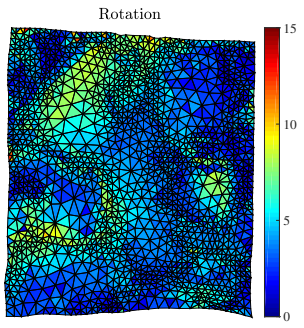	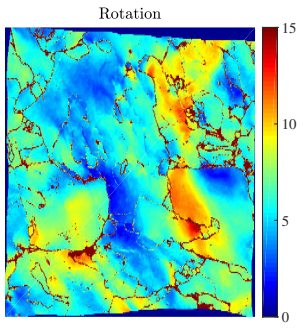	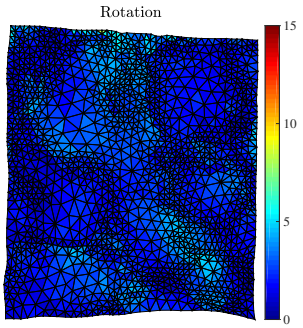

Table 7.4: Comparison of experimental and three simulated surface kinematic fields. The displacements in three dimensions are expressed in µm, and the crystal rotation fields in °.

	SMC on quadratic elements	SMC on linear elements	DD_CC on linear elements
Δu_x	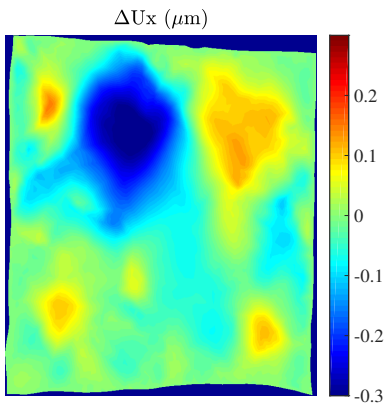	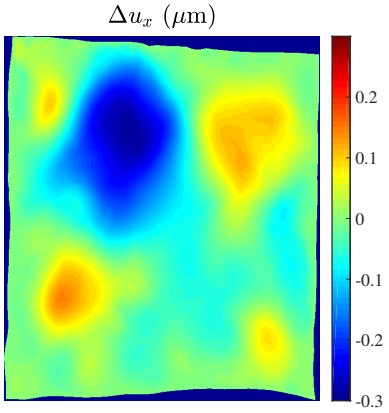	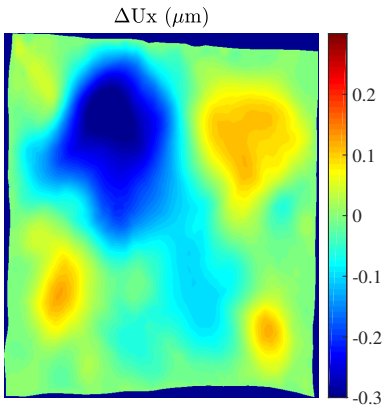
Δu_y	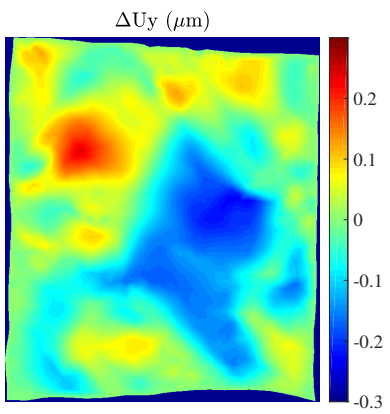	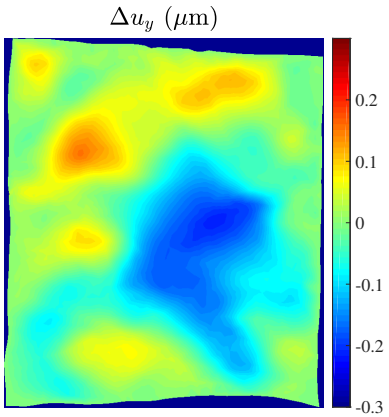	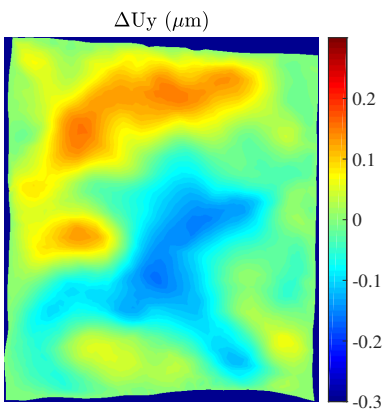
Δu_z	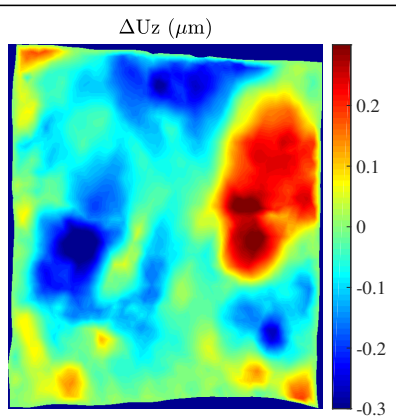	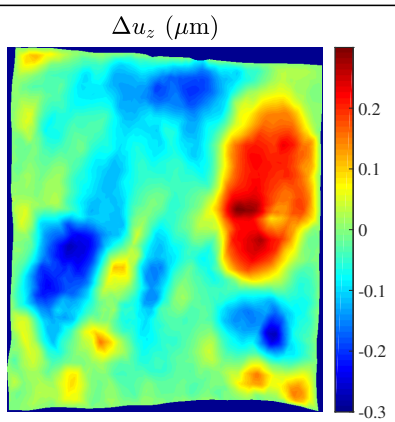	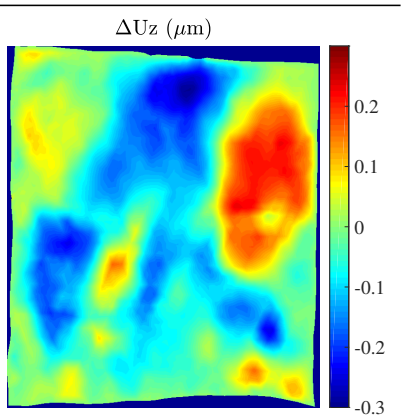

Table 7.5: Standard variance of experimental displacement fields (expressed in nm).

$\sigma_{u_x^{exp}}$	$\sigma_{u_y^{exp}}$	$\sigma_{u_z^{exp}}$
461.5	740.1	200.2

Table 7.6: Standard variance of difference between experimental and simulation displacement fields

	$\sigma_{\Delta u_x}$ (nm)	$\frac{\sigma_{\Delta u_x}}{\sigma_{u_x^{exp}}}$	$\sigma_{\Delta u_y}$ (nm)	$\frac{\sigma_{\Delta u_y}}{\sigma_{u_y^{exp}}}$	$\sigma_{\Delta u_z}$ (nm)	$\frac{\sigma_{\Delta u_z}}{\sigma_{u_z^{exp}}}$
SMC on quadratic elements	84.1	18.2%	82.5	11.1%	116.3	58.1%
SMC on linear elements	83.3	18.0%	73.1	9.9%	96.9	48.5%
DD_CC on linear elements	93.4	20.2%	70.1	9.5%	100.5	50.2%

It is concluded that the two constitutive laws give almost the same kinematic response of the 3D model. For time considerations, the identification of SMC parameters has been performed with linear tetrahedral elements via FEMU-UF.

7.3.4 Identification of SMC parameters

FEMU-UF consists in minimizing a global cost function Φ, which is the sum of squared displacement difference Φ_U and the macroscopic equilibrium gap Φ_F [Hériphé et al. 2007; Guery et al. 2016b]. This formulation assumes no model error, which is mainly composed of the constitutive equation formulation errors, finite element mesh geometry errors, local crystal orientation errors and in particular boundary condition errors. The global cost function writes as

$$\begin{aligned} \Phi(\{\boldsymbol{p}\}) &= \Phi_U + \Phi_F \\ &= \frac{1}{2\eta_f^2 N_{dof} N_t^u} \sum_t \{\boldsymbol{\delta u}\}_t^T [\boldsymbol{M}] \{\boldsymbol{\delta u}\}_t + \frac{1}{\eta_F^2 N_t^F} \{\boldsymbol{\delta F}\}^T \{\boldsymbol{\delta F}\} \end{aligned} \tag{7.1}$$

where N_{dof} the number of (scalar) degrees of freedom of the surface mesh, N_t^u the number of time steps in displacement field measurement, N_t^F the number of time steps in macroscopic loading force measurement (note that N_t^u and N_t^F are not same since they are acquired in different tests), $\{\boldsymbol{\delta u}\}_t$ is the column vector of the difference evaluated at surface mesh node between 'experimental' $\{\boldsymbol{u}_{exp}\}_t$ and simulated $\{\boldsymbol{u}_{sim}(\{\boldsymbol{p}\})\}_t$ displacements at time step t. Note that the displacements in three dimensions are used here, *i.e.*, $\{\boldsymbol{\delta u}\} = \{\boldsymbol{\delta u}_x,\ \boldsymbol{\delta u}_y,\ \boldsymbol{\delta u}_z\}$. $[\boldsymbol{M}]$ is the DIC matrix [Mathieu et al. 2015], whose inverse characterizes the covariance matrix of the measured degrees of freedom [Hild and Roux 2012a]. When displacement and load information is taken into account (hence the acronym UF for the FEMU algorithm used herein), $\{\boldsymbol{\delta F}\}$ is the column vector of the load differences between measured values $\{\boldsymbol{F}_{exp}\}$

and computed ones $\{\boldsymbol{F}_{sim}\}$. η_f and η_F are the standard deviation of noise of the experimental images and load measurement, respectively. In the present case, η_f is set to 4000 gray levels, and η_F to 3 N.

As discussed in Section 7.3.1, the observed surface is left free of prescribed displacements (Neumann condition). This is sufficient for the computation and because the displacements are not prescribed, the differences between computed and observed values, $\{\boldsymbol{\delta u}\}_t$ can be used to drive the identification using FEMU-UF.

The minimization of Φ with respect to the material parameters $\{\boldsymbol{p}\}$ is performed iteratively by a Newton-Raphson algorithm [Bonnet 2012]. The initial set of parameters is $\{\boldsymbol{p}^{(0)}\}$. At iteration n, the parameter corrections $\{\delta\boldsymbol{p}\}$ are obtained by

$$\left(\left[\boldsymbol{H}_u^{(n)}\right]+\left[\boldsymbol{H}_F^{(n)}\right]\right)\{\delta\boldsymbol{p}\}=\left[\boldsymbol{N}_u^{(n)}\right]+\left[\boldsymbol{N}_F^{(n)}\right] \tag{7.2}$$

with the Hessian matrices

$$\begin{aligned}\left[\boldsymbol{H}_u^{(n)}\right]&=\tfrac{1}{2\eta_f^2 N_{dof} N_t^u}\textstyle\sum_t\left[\boldsymbol{S}_u^{(n)}\right]_t^T[\boldsymbol{M}]\left[\boldsymbol{S}_u^{(n)}\right]_t\\ \left[\boldsymbol{H}_F^{(n)}\right]&=\tfrac{1}{\eta_F^2 N_t^F}\left[\boldsymbol{S}_F^{(n)}\right]^T\left[\boldsymbol{S}_F^{(n)}\right]\end{aligned} \tag{7.3}$$

and the gradient vectors

$$\begin{aligned}\left[\boldsymbol{N}_u^{(n)}\right]&=\tfrac{1}{2\eta_f^2 N_{dof} N_t^u}\textstyle\sum_t\left[\boldsymbol{S}_u^{(n)}\right]_t^T[\boldsymbol{M}]\{\delta\boldsymbol{u}\}_t\\ \left[\boldsymbol{N}_F^{(n)}\right]&=\tfrac{1}{\eta_F^2 N_t^F}\left[\boldsymbol{S}_F^{(n)}\right]^T\{\boldsymbol{\delta F}\}\end{aligned} \tag{7.4}$$

where $\left[\boldsymbol{S}_u^{(n)}\right]$ and $\left[\boldsymbol{S}_F^{(n)}\right]$ are the sensitivity matrices of the displacement field at time step t and load, respectively. They are evaluated with the current parameter estimates $\{\boldsymbol{p}^{(n)}\}$

$$\begin{aligned}\left[\boldsymbol{S}_u^{(n)}\right]&=\left[\frac{\{\boldsymbol{\delta u}_{sim}^{(n)}\}}{\{\boldsymbol{\delta p}\}}\right]_t\\ \left[\boldsymbol{S}_F^{(n)}\right]&=\left[\frac{\{\boldsymbol{\delta F}_{sim}^{(n)}\}}{\{\boldsymbol{\delta p}\}}\right]_t\end{aligned} \tag{7.5}$$

where $\boldsymbol{\delta p}=\varepsilon_1\{\boldsymbol{p}^{(n)}\}$, ε_1 is set to 2% in the present study.

The correction vector $\{\delta\boldsymbol{p}\}$ allows the current determination to be updated

$$\{\boldsymbol{p}^{(n+1)}\}=\{\boldsymbol{p}^{(n)}\}+\{\delta\boldsymbol{p}\} \tag{7.6}$$

Convergence is declared to be reached when the condition

$$\max\left|\frac{\delta\boldsymbol{p}}{\boldsymbol{p}^{(n)}}\right|<\varepsilon_2 \tag{7.7}$$

is met. In the present chapter ε_2 is set to 1%.

A macroscopic strain curve of 16MND5 steel at 0 °C issued from [Renevey 1997] has been used for the calibration (since only the curves between -150 °C - 0 °C were measured by Renevey [1997]), as shown in Figure 7.18. Note that the present *in-situ* tensile test is performed at room temperature, thus the strain-stress curve in Figure 7.18 overestimates the real stress value by around 20 MPa [Renevey 1997]. The simulated strain-stress curve is predicted by an RVE model of 200 grains with random orientation using Berveiller-Zaoui homogenization method, which is detailed in Section 1.3.6.1. Among the 200 grains, 150 grains are assigned to be bainitic and 50 ferritic. The ferritic percentage of 25% is based on previous experimental observations [Diawara 2011].

A convenient tool is available to write tailored constitutive equations and compile them for further calculations, namely *MFront* developed at the French Atomic Energy Commission (CEA) [Helfer et al. 2015; 2017]. A handy tool called *MTest* is also proposed in the framework of *MFront*. *MTest* probes the local behavior of a material by imposing independent constraints on each component of the strain or stress. Calculation by *MTest* is much faster (from ten to several hundred times depending on the test case) than using a full-fledged finite element solver [Helfer et al. 2015]. An *MFront* source code for the dual-phase 16MND5 steel via BZ homogenization with SMC has been implemented in the present work, and *MTest* has been adopted to run the homogenization. With *MTest*, a single computation of the strain-stress curve for an average strain level of 7.5% takes about 2 minutes. The strain-stress curve predicted by *MTest* with the reference parameters of SMC is shown in Figure 7.18.

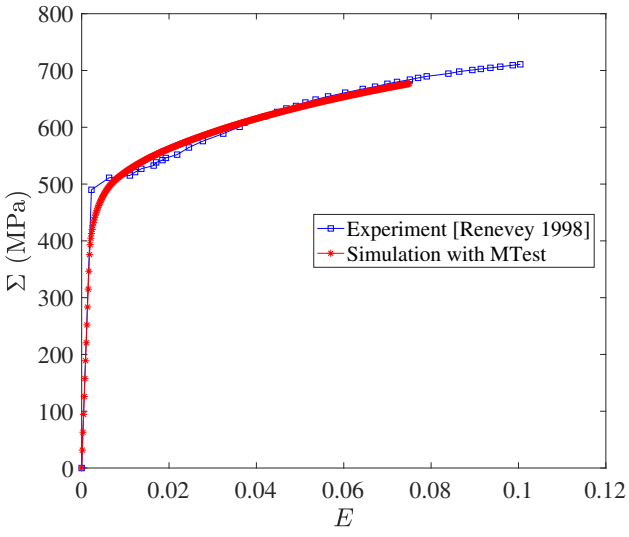

Figure 7.18: Comparison of experimental macroscopic stress-strain curve of 16MND5 steel at 0 °C [Renevey 1997] and simulated curve with reference SMC parameters.

For time reasons, the updating of the reference microstructure proposed in Section 6.2.2 is not performed hereafter. Thus the obtained microstructure after the isotropic constant-hardening plastic compression is chosen as the initial configuration.

The present PhD sets an aim to identify the parameters R_0, influencing the yield stress, and Q and b, impacting the hardening ratio, for the two phases. They are denoted as R_0^f, Q^f, b^f, R_0^b, Q^b and b^b for the ferritic and bainitic phases. The identifiability of the parameters is investigated with a sensitivity analysis where the Hessian of the FEMU ($[\boldsymbol{H}_u]$) is analyzed [Bertin et al. 2017]. Figure 7.19(a) shows the global Hessian of the FEMU process obtained with the reference parameters. b^f is the parameter with the largest influence. The corresponding correlation matrix of the Hessian is shown in Figure 7.19(b), where a high correlation exists between R_0^f, Q^f and b^f. As a result, R_0^f, Q^f and b^f cannot be identified at the same time. Similarly, Q^b and b^b cannot be identified simultaneously neither. R_0^f is kept for the calibration, while both Q^f and Q^b are prescribed equal to Q. Both b^f and b^b are prescribed with the reference value. This choice is based on the experimental observation that ferrite and bainite have very similar hardening ratios, as shown in Figure 1.10. As a result, this calibration, denoted as RQR afterward, seeks two independent R_0 parameters for bainitic and ferritic phases and a single hardening modulus Q for the two phases. To provide a comparison for the RQR calibration, another calibration is launched where the 16MND5 steel is considered as a unique phase metal, and one set of parameters R_0 and Q is sought. The latter calibration is denoted as RQ hereafter.

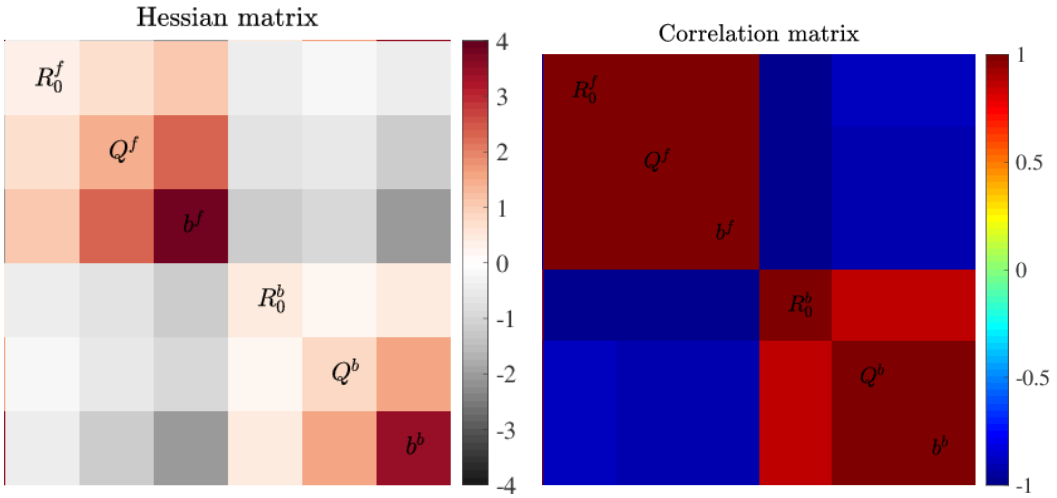

(a) (b)

Figure 7.19: Global Hessian (a) and its corresponding correlation matrix (b) for the investigated model (*i.e.*, $\{\boldsymbol{p}\} = \{R_0^f,\ Q^f,\ b^f,\ R_0^b,\ Q^b,\ b^b\}^t$).

Figure 7.20 illustrates the change of the cost functions for the RQ and RQR identifications: Φ_U is shown in Figure 7.20(a), Φ_F in Figure 7.20(b) and Φ in Figure 7.20(c). It can be seen that the RQ identification only reduces Φ_U by 1%, while the RQR identification reduces Φ_U by 7%. This phenomenon means that taking the same set of crystal plasticity parameters for ferrite and bainite cannot reproduce the microscale heterogeneity of the experiment, while two different sets of parameters help to simulate the heterogeneity (though to a limited extent). During the calibration Φ_F does not vary too much, as the reference parameters already account well for the macroscopic strain-stress responses. As a result, the whole cost function Φ is reduced more in the RQR identification than in the RQ identification. Both Φ_F and Φ_U are not reduced to 1, indicating that there exists non-negligible model errors. However Φ has been reduced by 2% with RQ and by 7% with RQR in comparison with the reference parameters.

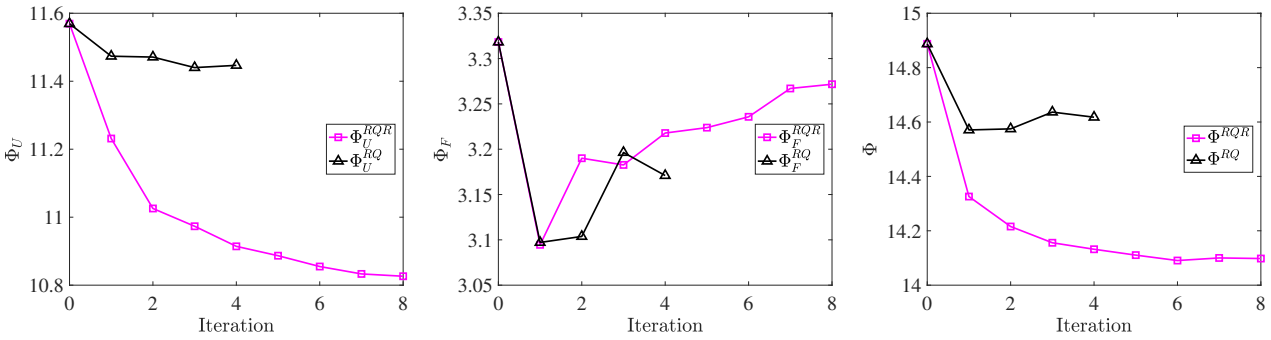

(a) (b) (c)

Figure 7.20: Change of cost functions (a) Φ_U (b) Φ_F and (c) Φ_T for the RQR and RQ identifications with the iteration number.

Figure 7.21(a) shows the change of R_0 values in the two identifications, and Figure 7.21(b) those of Q. It is found that starting from the same initial value, R_b^{RQR} and R_f^{RQR} diverges quickly and stabilizes at distinct values, 190 MPa and 100 MPa respectively. This trend is anticipated, since bainite is a harder phase with more dispersed carbides and finer structures (see Section 1.1.2). Previous X-ray diffraction studies have already shown that, in the same sample, the bainite grains exhibit higher stress levels than ferrite grains [Mathieu 2006]. The value of R_0 in the RQ identification does not vary much and stabilizes around 164 MPa, between R_b^{RQR} and R_f^{RQR} values. The values of Q vary by a few MPa for the two calibrations.

Figure 7.22(a) and 7.22(b) show the difference of simulated and experimental u_x fields before and after the RQR identification, and Figure 7.22(c) and Figure 7.22(d) show the corresponding u_y fields, Figure 7.22(e) and Figure 7.22(f) show the corresponding u_z fields. The

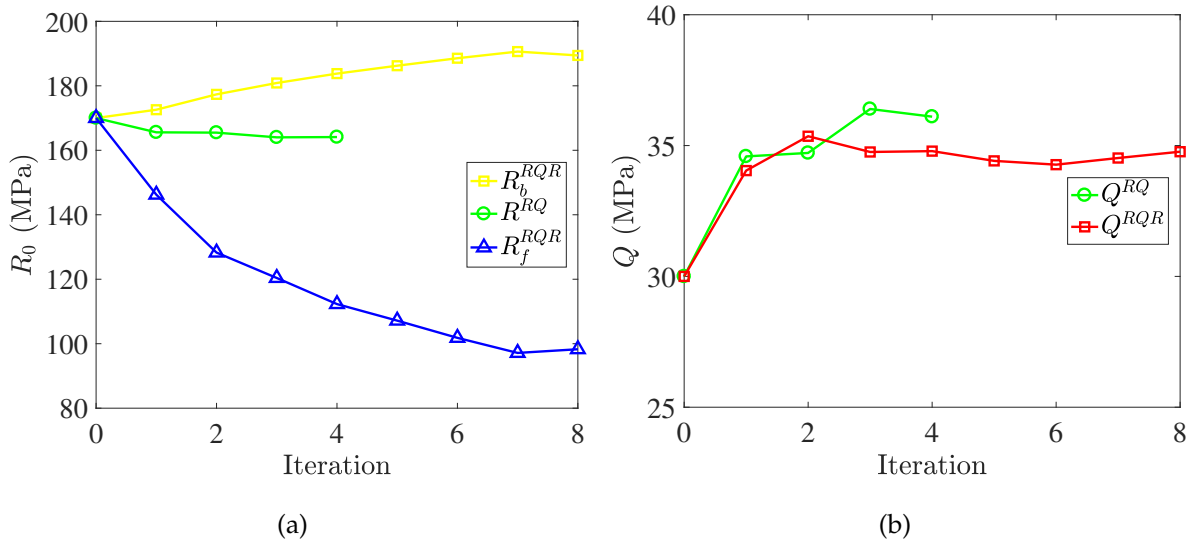

(a) (b)

Figure 7.21: Evolution of parameters R_0 (a) and Q (b) in RQ and RQR identifications.

RMS of the difference between experimental and simulated kinematic fields before and after the calibration is listed in Table 7.7. The standard measurement uncertainties in x and y directions are of the order of 1.3 nm (0.026 pixel), which is evaluated by DIC on an experimental image and an artificial one that adds the image noise to the experimental image [Hild and Roux 2006]. The standard measurement uncertainty for u_z is 30 nm, as demonstrated in Section 5.5. It can be seen that:

- The difference of simulated and experimental displacement fields mainly occurs near the center of the model. The displacements on the edges, and especially at the corners, are prescribed with measured values (Saint Venant effect).

- The difference of displacement fields reduces in x and y directions during the identification, but only by 3.5% compared to the differences with reference parameters of SMC. On the contrary, the difference in u_z increases along the calibration, but it does not impede the FEMU-UF process since the out-of-plane motion measurement comes with a much higher uncertainty level. Significant signals still exist in the residual field, indicating that the FE simulation adopted in the present study, even with identified parameters, still cannot capture all the kinematic details. Better boundary conditions, finer meshes, closer similitude of the model microstructure to the experimental one, more precise classifications of grains could further reduce the difference.

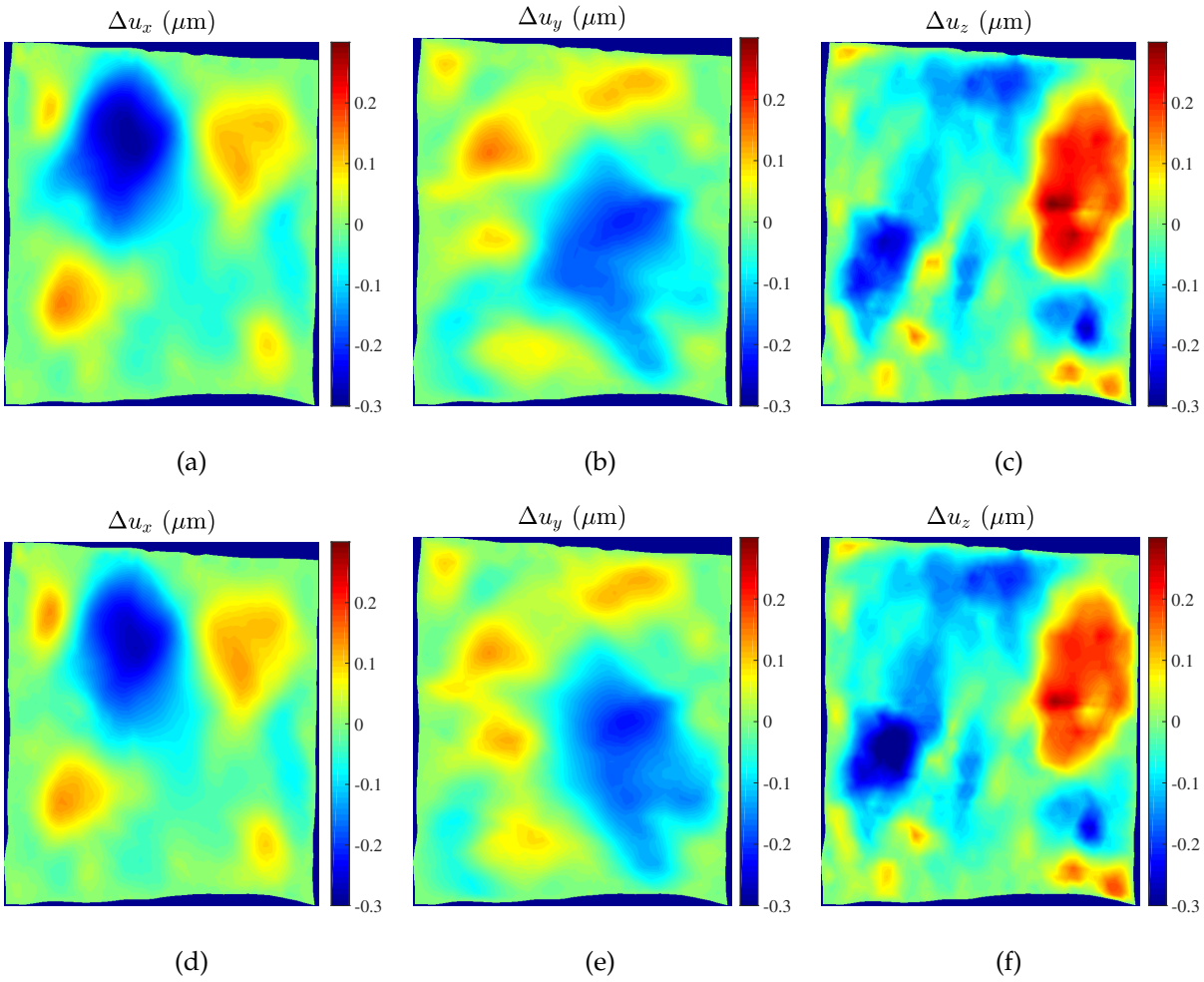

Figure 7.22: Difference (expressed in µm) of simulated and experimental kinetic fields. Displacement difference in x direction between experimental values and (a) simulated values with reference SMC parameters (b) simulated values with RQR calibrated SMC parameters. Displacement difference in y direction between experimental values and (c) simulated values with reference SMC parameters (d) simulated values with RQR calibrated SMC parameters. Displacement difference in z direction between experimental values and (e) simulated values with reference SMC parameters (f) simulated values with RQR calibrated SMC parameters.

Table 7.7: Standard variance of difference between experimental and simulation displacement fields

	$\sigma_{\Delta u_x}$ (nm)	$\frac{\sigma_{\Delta u_x}}{\sigma_{u_x^{exp}}}$	$\sigma_{\Delta u_y}$ (nm)	$\frac{\sigma_{\Delta u_y}}{\sigma_{u_y^{exp}}}$	$\sigma_{\Delta u_z}$ (nm)	$\frac{\sigma_{\Delta u_z}}{\sigma_{u_z^{exp}}}$
Before calibration	83.3	18.0%	73.1	9.9%	96.9	48.5%
After calibration	77.6	16.8%	72.4	9.8%	99.4	49.6%

The average equivalent stress profiles during the tensile simulation for the two phases are drawn in Figure 7.23(a), while the curve calculated with the RQ calibration results is shown in Figure 7.23(b). Compared to the experimental strain-stress curve (see Figure 7.18), the simulated curves exhibit higher hardening ratios for both calibration results. This is typically the volumetric locking phenomenon with inappropriate FE models. The calculations based on reduced-integration with quadratic elements will presumably lead to local stress levels closer to the experimental ones. The difference between stress levels in ferritic and bainitic grains has been evaluated experimentally by X-ray diffraction to be about 110 MPa at low temperature [Mathieu 2006], while the difference between proeutectoid ferritic and bainitic grains is predicted to be around 200 MPa by the present identification. A possible explanation to the contrast is that the X-ray diffraction has a spatial resolution of a few micrometers, which leads to an averaging effect that decreases the observed stress difference.

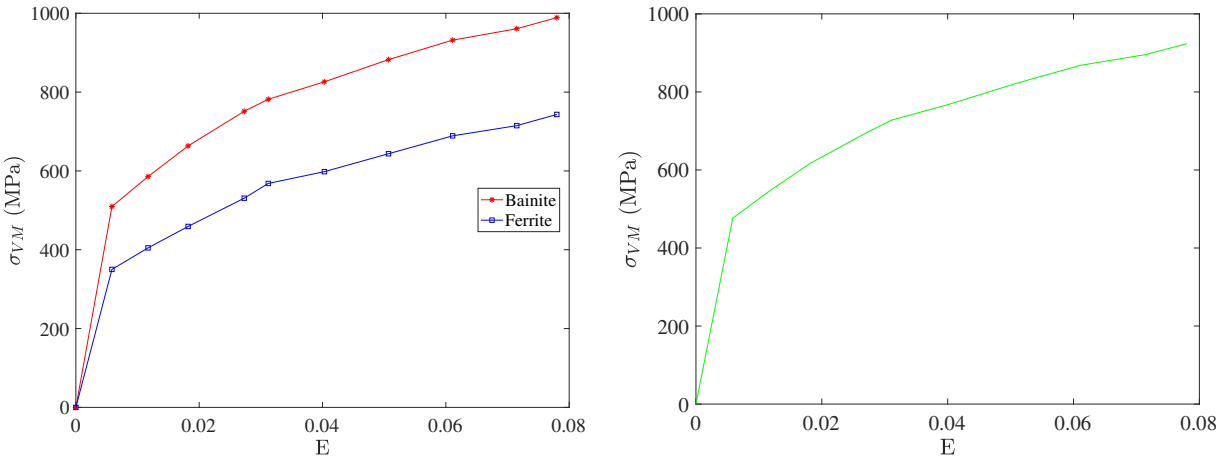

Figure 7.23: (a) Average equivalent stress profiles along the tensile simulation for ferrite and bainite with the RQR identification results. (b) Average σ_{VM} profile calculated with the RQ calibration results.

Note that due to the volumetric locking phenomenon, the stress levels are overestimated in the present work. A comparison of simulated stress levels with RQR and RQ calibrations is provided in Figure 7.24. The simulated Von Mises stress σ_{VM} at the model surface for the final state with the two calibrations is shown in Figures 7.24(a) and 7.24(b), and their histograms are overlaid in Figure 7.24(c). It is concluded that the parameters obtained in RQ calibration underestimate the stress levels at the higher end in bainite. A similar conclusion can be drawn with the predicted first principal stress levels, which are shown in

Figure 7.24(d), 7.24(e) and 7.24(f). From the simulated stress tensors a cleavage stress can be calculated, which is defined as the maximum (tensile) normal stress level applied on the cleavage planes. Then the possibility of brittle fracture of 16MND5 steel can be evaluated by a local approach [Hausild 2002; Mathieu 2006]. Considering the steel as a unique phase will presumably underestimate the failure possibility.

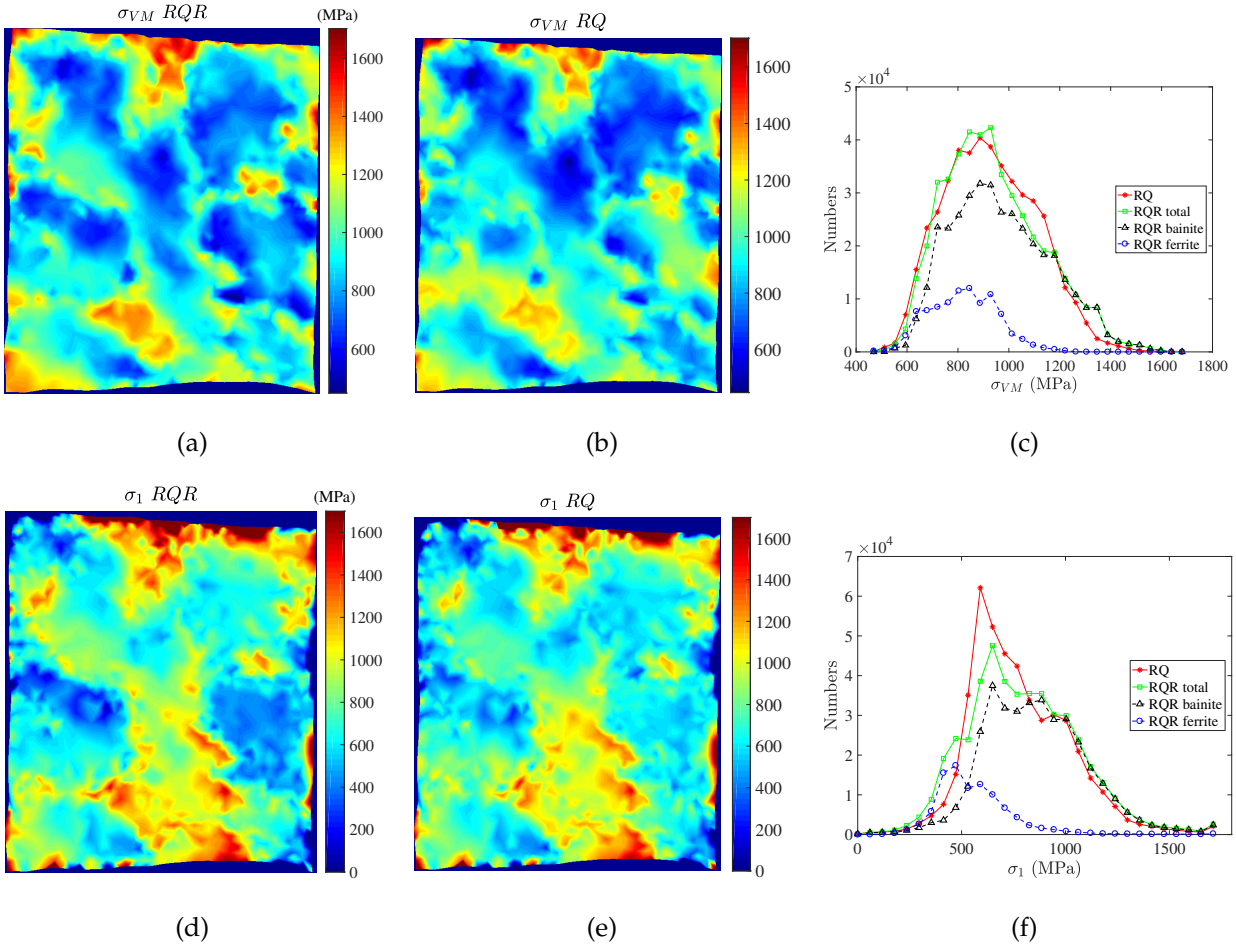

Figure 7.24: Comparison of predicted stress levels by RQR and RQ calibrations. Von Mises equivalent stress levels (expressed in MPa) at the model surface predicted by RQR (a) and RQ (b) calibrations. (c) Histograms of Von Mises stress at the model surface predicted by the two calibrations. The first principal stress level (expressed in MPa) at the model surface predicted by RQR (d) and RQ (e) calibrations. (f) Histograms of the first principal stress at the model surface predicted by the two calibrations.

7.4 Conclusions and prospects

The lack of in-depth microstructure information is a major challenge in polycrystal simulations at the microscale. Thanks to a FIB-EBSD procedure after an *in-situ* tensile test, a three-

dimensional mechanical simulation with experimental in-depth grain morphology has been performed in the present work. The only missing piece of information is the in-depth kinematic boundary conditions for carrying out a simulation of the experiment. Here a simple procedure has been chosen, but ideally, the boundary conditions should be identified in the same way as the constitutive law.

The FIB-EBSD procedure has been performed *postmortem* on a bainitic-ferritic steel sample to get its in-depth microstructure. A DIC calculation between neighboring FIB slices has been proposed to account for the scanning beam artifacts of EBSD acquisition. Due to the poor image contrast and possible structural changes between FIB slices, the degrees of freedom for the DIC have been limited by adopting a very coarse FEM mesh. It has been found that the DIC procedure reduces further the spurious grain boundary roughness of the reconstructed 3D volume. After a binning operation, a 3D tetrahedral FE mesh has been generated with a compromise between computation cost and microstructure detail.

The reconstructed 3D microstructure, which is deformed artificially to its initial configuration via a synthetic isotropic constant-hardening plastic constitutive law, has been used to conduct 3D CPFE simulations with DD_CC and simplified Méric-Cailletaud crystal plasticity laws. By adopting the extruded surface boundary conditions, the 3D CPFE simulations give similar kinematic responses (for in-plane and out-of-plane motions) in comparison to experimental ones. A FEMU-UF identification step has been applied to the 3D microstructure model. It has been found that a unique set of parameters for the two phases reduces very mildly the kinematic distance to the experimental displacement field, while two sets of parameters for bainite and ferrite respectively reduce the distance to a larger degree. The two sets of obtained material parameters, softer for ferrite and harder for bainite, are consistent with previous experimental observations [Mathieu 2006], and allow for future multi-phase simulations for the considered material. This first attempt for performing a full 3D identification has shown the feasibility of the global procedure. Repeating those steps including a better determination of the boundary conditions, and suited constitutive laws, should allow for a much enhanced reliability of the determination of the material parameters for such a strategic part in the nuclear industry.

The proposed material simulation (including constitutive parameter calibration) based on real 3D microstructure and surface kinematic fields overcomes the major limitation of including the actual 3D microstructure for the comparison between experiments and simulations of polycrystals. It is expected to have a broad application in materials science and en-

gineering, including investigating plasticity mechanisms, proposing new constitutive equations and identifying their parameters.

Chapter 8

Conclusions and Perspectives

The PhD project developed experimental and simulation approaches to study the plastic behavior of 16MND5 steel. This steel has fine microstructures and is composed principally of proeutectoid ferrite and bainite. The experiment consists in conducting an *in-situ* uniaxial tensile test inside an SEM chamber employing different imaging modalities, and *postmortem* FIB-EBSD milling to study the in-depth microstructure of the sample. Although uniaxial tension test is the most fundamental and conventional mechanical test, special efforts have been dedicated to improve its practices in various aspects. The main development/improvement are as follows:

1. Different speckle sizes (diameter and thickness) have been tested to find a proper size for multi-modality SEM observations (BSE, EBSD). Platinum speckles of diameter 300 nm and thickness 75 nm fulfill the demand: very good contrast in SE/BSE images, recognizable traces in EBSD IQ images and good crystal orientation indexing for underlying material surfaces. Those speckles made strain and rotation measurements significantly easier;

2. Position of the sample during *in-situ* test. Both 70° tilted, which is optimal for EBSD acquisition, and horizontal positions, for SE/BSE full-resolution imaging, have been tested and analyzed. Surprisingly, the image processing of the tilted test reveals some artifacts of SEM imaging techniques that are difficult to account for. Since the coordinate precision of BSE images is of great importance for quantitative analyses, the horizontal positioning is kept for the study;

3. Slow-scan direction drift has been detected and corrected in BSE/SE images. Inspired by previous works on AFM imaging drifts, SE/BSE images have been acquired at Scan-

Rotation 0° and 90°. Specific correlative algorithms have been proposed to correct the drift and improve SEM imaging quality;

4. An algorithm has been proposed to correlate EBSD images. Crystallographic orientation has been considered as image contrast, and an algebra based on quaternion has been found convenient to treat 3D orientations, including misorientation calculation, orientation interpolation and crystal symmetry application. By registering EBSD images, quaternion correlation leads to displacement and crystal rotation fields, both with satisfactory uncertainty.

5. Development of elastic strain measurement by an integrated DIC version processing HR-EBSD data. Cross-correlation between high-resolution Kikuchi images has been at the heart of HR-EBSD, a technique developed since 2006 to measure elastic strains of crystals. Global DIC and especially integrated DIC has been tested on HR-EBSD, resulting in significant improvements: 3-10 times speed acceleration, 40% improvement of data scatter, together with other byproducts. Though not applied in the present study of 16MND5 steel, the proposed algorithm for HR-EBSD has a significant industrial potential. A pending patent about the procedure is deposed in France.

6. Precise registration of EBSD and SE/BSE images. A phenomenon of speckle 'split' has been identified and explained in EBSD IQ images. Speckles in BSE images are artificially doubled, making it is possible to correlate the two types of images. After adjusting a consistent 7-pixel vertical shift, a pixel-level registration of EBSD and SE/BSE images has been obtained. Therefore, each and every EBSD, SE and BSE images taken during the test can be correlated and an unbiased sample microstructure and its motions can be tracked at surfaces. Imaging errors including the standard deviation of gray level of BSE and crystal orientation indexing uncertainty have been quantified. The constant shift also provides insights into the information depth of EBSD acquisitions.

7. Three distinct methods of topography measurements by conventional SEM techniques have been proposed. They are tested on the strained 16MND5 sample, whose surface features topography of the order of 1 µm. FIB-SEM and tilt-imaging methods measure the overall topography, while rotation-integration method is designed to measure the topography changes due to elastic deformation between two BESD acquisitions. The

topography results of the first two methods exhibit a standard uncertainty of 50 nm, which cross-validates the two methods. The similitude of the rotation-integration result with the former ones shows that crystal rotation already accounts for a significant part of the deformation-induced topography. The advantages and disadvantages of all three methods are analyzed.

8. Observation of 3D deformed microstructure by FIB milling. FIB-EBSD has been carried out on the sample, focusing on a region of the tested sample, to study its 3D structure. A tailored global DIC with elongated triangular elements has been proposed, which registers the FIB slices more precisely than the commonly used uniform shift. The registration of FIB-EBSD slices with surface BSE images allows un-distorted kinematic fields to be extracted. A comprehensive characterization of the *in-situ* tensile test has then been performed.

For the numerical side of research on the mechanics at the microscale, a major challenge is the lack of high-resolution information of in-depth experimental grain microstructures. It has been addressed in the present work by *postmortem* FIB-EBSD acquisitions of the deformed state. A specific difficulty arises, which is to backtrack the initial microstructure, which is the starting point of the 'direct problem'. Three unknowns intertwined in the procedure: the initial microstructure configuration, in-depth boundary conditions, and the material constitutive parameters. After prescribing in-depth boundary conditions estimated from measured ones, an algorithm has been developed to iteratively seek the other two unknowns one by one. Upon convergence, the unknowns will altogether be obtained given the assumption that the constitutive equation is correct. The algorithm has been tested on a synthetic 2D case and satisfactory results were achieved.

A physical crystal plasticity law DD_CC and a phenomenological model, namely a simplified version of Méric-Cailletaud (SMC) law, have been tested on the 3D experimental FE model. Both linear and quadratic tetrahedral elements have been considered for the simulation. It has been found that, although the computation time varies substantially (ratio of 20), different crystal plasticity laws and element types result in similar kinematic fields for the tested plasticity parameters. A satisfactory synergy has been found between the experimental 3D kinematic fields and the simulated values with reference plasticity parameters. Several identification calculations have been performed via FEMU-UF with the SMC law, where the 3D model has been considered for a unique-phase and dual-phase setting. It has

been found that calibration by imposing a unique set of plasticity parameters for the steel reduces very little (0.5%) the difference between simulated and experimental kinematic fields. In contrast, the kinematic field difference reduces by 3.5% when calibrating different plasticity parameters for the proeutectoid ferrite and bainite respectively. Besides, the two sets of obtained material parameters, softer for ferrite and harder for bainite, are consistent with previous experimental observations, and allow for future multi-phase simulations for the considered material.

In terms of perspectives, the following points are to consider if someone is to continue the adventure in crystal plasticity by synergy between experiments and simulations:

1. The elastic strain measurement by HR-EBSD has not been carried out in the principal test. For future tests, it is suggested to take a few HR-EBSD acquisitions along the test, especially at lower strain levels. Although absolute strain and stress levels are difficult to get, relative elastic strains and misorientations are yet accessible by HR-EBSD, which, together with other properties such as GND density, will further enrich the experiment and simulation.

2. The generation of 3D FEM meshes has always been a challenge for comparing experimental and simulation results. A software named MeshGems has been used in the thesis to generate a viable tetrahedral mesh from FIB-EBSD data. However, the quality of the mesh is not as good as the showcase in the brochure of MeshGems. For example, at grain boundaries the mesh tends to be step-like. Future research is suggested to continue exploring the potential of the software, or develop post-processing to improve the mesh. Quadratic tetrahedral elements should be directly generated from the experimental data, instead of creating quadratic tetrahedral elements from linear ones.

3. The in-depth boundary conditions cannot be accessed by SEM, thus it has to be estimated from the available information on surface. For the present thesis the surface boundary condition is simply extruded to the volume, with a certain degree of justification. More adapted boundary conditions could be considered, and it will fulfill the last uncertainty of analogy between simulation and experiments. Several initial works have started in the present dissertation to consider the material as perfectly plastic, and calculate the slip planes and slip directions. More precise boundary conditions can thus be generated.

4. The crystal rotation obtained by quaternion correlation is a rich kinematic information for crystal plasticity. However, the rotation fields from simulation and experiment show a considerable difference. The rotation was not included in the crystal plasticity parameter identification. Future work is needed to seek the reason for the underestimation of crystal rotations by FE simulation, to correct it and to add it to the cost function. With more information taken into consideration, the calibrated parameters are believed to be more trustworthy. It may also give a hint to further developments of constitutive laws.

Appendix A: Basic properties of quaternions

Multiplication rules for elementary quaternions reads

$$\begin{array}{rclrclrcl} \boldsymbol{i}\times\boldsymbol{i} &=& -1, & \boldsymbol{j}\times\boldsymbol{j} &=& -1, & \boldsymbol{k}\times\boldsymbol{k} &=& -1 \\ \boldsymbol{i}\times\boldsymbol{j} &=& \boldsymbol{k}, & \boldsymbol{j}\times\boldsymbol{k} &=& \boldsymbol{i}, & \boldsymbol{k}\times\boldsymbol{i} &=& \boldsymbol{j} \\ \boldsymbol{j}\times\boldsymbol{i} &=& -\boldsymbol{k}, & \boldsymbol{k}\times\boldsymbol{j} &=& -\boldsymbol{i}, & \boldsymbol{i}\times\boldsymbol{k} &=& -\boldsymbol{j} \end{array} \tag{8.1}$$

The multiplicative sign $\times$ was shown explicitly in order to avoid possible confusions. In particular, the third line shows that the product is not commutative, and thus special care is to be exercised. In the following, to simplify notations, the product sign will be omitted and $\boldsymbol{q}_1 \times \boldsymbol{q}_2$ will be denoted $\boldsymbol{q}_1\boldsymbol{q}_2$. The conjugate of a quaternion $\boldsymbol{q} = a + b\boldsymbol{i} + c\boldsymbol{j} + d\boldsymbol{k}$ is defined as

$$\boldsymbol{q}^* = a - b\boldsymbol{i} - c\boldsymbol{j} - d\boldsymbol{k} \tag{8.2}$$

and its quadratic norm is

$$\|\boldsymbol{q}\|^2 = \boldsymbol{q}\boldsymbol{q}^* = a^2 + b^2 + c^2 + d^2 \tag{8.3}$$

A unit quaternion $\boldsymbol{U}_q$ is such that its norm is unity, and hence its inverse is its conjugate

$$\boldsymbol{U}_q^{-1} \;=\; \boldsymbol{U}_q^* \tag{8.4}$$

The multiplication of two unit quaternions produces a new unit quaternion, its corresponding rotation is the combination of the two original quaternions. The "division" of two unit quaternions $\boldsymbol{p}$ and $\boldsymbol{q}$, $\boldsymbol{q}\boldsymbol{p}^{-1}$, indicates the rotation between them, with the following relationship between rotation angle θ and $(\boldsymbol{q}\boldsymbol{p}^{-1})_1$

$$(\boldsymbol{q}\boldsymbol{p}^{-1})_1 = \cos\frac{\theta}{2} \approx 1 - \frac{\theta^2}{8}, \text{ with small } \theta \tag{8.5}$$

Linear quaternion interpolation (Lerp) reads

$$L(\boldsymbol{p}, \boldsymbol{q}, h) = \boldsymbol{p}(1-h) + \boldsymbol{q}h \tag{8.6}$$

Linear quaternion interpolation needs to be projected onto the unit sphere in 4D to obtain unitary quaternions

$$U_{L(\boldsymbol{p},\boldsymbol{q},h)} = \frac{\boldsymbol{p}(1-h) + \boldsymbol{q}h}{\|\boldsymbol{p}(1-h) + \boldsymbol{q}h\|} \tag{8.7}$$

Figure 8.1 illustrates the Lerp of quaternions in 2 dimension. The secant `pq` is equally split by Lerp, while the angle between $\boldsymbol{p}$ and $\boldsymbol{q}$ is not. Lerp is easy to implement, namely, componentwise linear interpolation and renormalization.

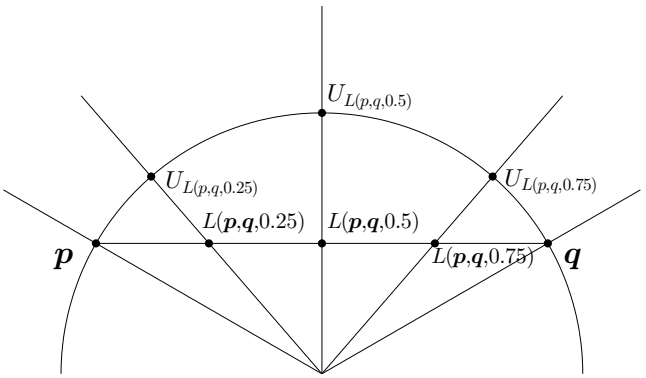

Figure 8.1: Lerp illustrated in the orientation space. Quaternions $\boldsymbol{p}$ and $\boldsymbol{q}$ are shown in the orientation space with their linear interpolations

All representations of rotation, namely, Euler angle notation, axis-angle notation and quaternion are interchangeable. Their transformation can be performed by comparison of the rotation matrices. The rotation matrix based on Euler angles $(\varphi_1, \Phi, \varphi_2)$ reads in Bunge notations

$$\begin{bmatrix} \cos\varphi_1\cos\varphi_2 - \sin\varphi_1\sin\varphi_2\cos\Phi & \sin\varphi_1\cos\varphi_2 + \cos\varphi_1\sin\varphi_2\cos\Phi & \sin\varphi_2\sin\Phi \\ -\cos\varphi_1\sin\varphi_2 - \sin\varphi_1\cos\varphi_2\cos\Phi & -\sin\varphi_1\sin\varphi_2 + \cos\varphi_1\cos\varphi_2\cos\Phi & \cos\varphi_2\sin\Phi \\ \sin\varphi_1\sin\Phi & -\cos\varphi_1\sin\Phi & \cos\Phi \end{bmatrix} \tag{8.8}$$

The rotation matrix based on axis-angle $(\theta, [d_1, d_2, d_3])$ is written as

$$\begin{bmatrix} (1-d_1^2)\cos\theta + d_1^2 & d_1d_2\,(1-\cos\theta) + d_3\sin\theta & d_1d_3\,(1-\cos\theta) - d_2\sin\theta \\ d_1d_2\,(1-\cos\theta) - d_3\sin\theta & (1-d_2^2)\cos\theta + d_2^2 & d_2d_3\,(1-\cos\theta) + d_1\sin\theta \\ d_1d_3\,(1-\cos\theta) + d_2\sin\theta & d_2d_3\,(1-\cos\theta) - d_1\sin\theta & (1-d_3^2)\cos\theta + d_3^2 \end{bmatrix} \tag{8.9}$$

The quaternion (q_1, q_2, q_3, q_4) and axis-angle notation $(\theta, [d_1, d_2, d_3])$ are related by

$$q_1 = \cos\frac{\theta}{2},\ q_2 = \sin\frac{\theta}{2}d_1,\ q_3 = \sin\frac{\theta}{2}d_2,\ q_4 = \sin\frac{\theta}{2}d_3 \tag{8.10}$$

Appendix B: 48 unitary quaternions corresponding to cubic crystal symmetry

There are 24 crystal symmetry systems in a cubic crystal:

- 3-fold rotation symmetry in cubic diagonal direction {111}
- 4-fold rotation symmetry in orthogonal direction {100}
- 2-fold rotation symmetry in facial diagonal direction {110}

Crystal symmetry can be represented by unit quaternions. For example, a rotation of $\theta = 2\pi/3$ about $\boldsymbol{d} = (1/\sqrt{3})(1,1,1)$ can be represented as

$$\boldsymbol{p} = (\cos(\pi/3), d_1 \sin(\pi/3), d_2 \sin(\pi/3), d_3 \sin(\pi/3)) = (1/2)(1,1,1,1) \tag{8.11}$$

All of the 48 cubic symmetry quaternions $\boldsymbol{p}_i^{cub}$ are listed in Table 8.1.

Table 8.1: List of the 48 quaternions image of $\boldsymbol{q}_0 = 1$ in a cubic symmetry. For the sake of simplicity a constant scale factor is factorized in the first column

Scale factor	p_1	p_2	p_3	p_4	Scale factor	p_1	p_2	p_3	p_4
1	+1	0	0	0	1	-1	0	0	0
1	0	+1	0	0	1	0	-1	0	0
1	0	0	+1	0	1	0	0	-1	0
1	0	0	0	+1	1	0	0	0	-1
1/2	+1	+1	+1	+1	1/2	-1	-1	-1	-1
1/2	+1	-1	-1	-1	1/2	-1	+1	+1	+1
1/2	+1	+1	-1	+1	1/2	-1	-1	+1	-1
1/2	+1	-1	+1	-1	1/2	-1	+1	-1	+1
1/2	+1	-1	+1	+1	1/2	-1	+1	-1	-1
1/2	+1	+1	-1	-1	1/2	-1	-1	+1	+1
1/2	+1	-1	-1	+1	1/2	-1	+1	+1	-1
1/2	+1	+1	+1	-1	1/2	-1	-1	-1	+1
$\sqrt{2}/2$	+1	+1	0	0	$\sqrt{2}/2$	-1	-1	0	0
$\sqrt{2}/2$	+1	0	+1	0	$\sqrt{2}/2$	-1	0	-1	0
$\sqrt{2}/2$	+1	0	0	+1	$\sqrt{2}/2$	-1	0	0	-1
$\sqrt{2}/2$	+1	-1	0	0	$\sqrt{2}/2$	-1	+1	0	0
$\sqrt{2}/2$	+1	0	-1	0	$\sqrt{2}/2$	-1	0	+1	0
$\sqrt{2}/2$	+1	0	0	-1	$\sqrt{2}/2$	-1	0	0	+1
$\sqrt{2}/2$	0	+1	+1	0	$\sqrt{2}/2$	0	-1	-1	0
$\sqrt{2}/2$	0	-1	+1	0	$\sqrt{2}/2$	0	+1	-1	0
$\sqrt{2}/2$	0	0	+1	+1	$\sqrt{2}/2$	0	0	-1	-1
$\sqrt{2}/2$	0	0	-1	+1	$\sqrt{2}/2$	0	0	+1	-1
$\sqrt{2}/2$	0	+1	0	+1	$\sqrt{2}/2$	0	-1	0	-1
$\sqrt{2}/2$	0	-1	0	+1	$\sqrt{2}/2$	0	+1	0	-1

Bibliography

Abdolvand, H., Majkut, M., Oddershede, J., Wright, J., and Daymond, M. (2015). Study of 3D stress development in parent and twin pairs of a hexagonal close-packed polycrystal: Part I in-situ three-dimensional synchrotron X-ray diffraction measurement. *Acta Materialia*, 93:246 – 255.

Abuzaid, W., Sangid, M., Carroll, J., Sehitoglu, H., and Lambros, J. (2012). Slip transfer and plastic strain accumulation across grain boundaries in Hastelloy X. *Journal of the Mechanics and Physics of Solids*, 60(6):1201–1220.

Acharya, A., Bassani, J. L., and Beaudoin, A. (2003). Geometrically necessary dislocations, hardening, and a simple gradient theory of crystal plasticity. *Scripta Materialia*, 48(2):167–172.

Adjanor, G., Bugat, S., Domain, C., and Barbu, A. (2010). Overview of the RPV-2 and INTERN-1 packages: From primary damage to microplasticity. *Journal of Nuclear Materials*, 406(1):175–186.

Alkorta, J. (2013). Limits of simulation based high resolution EBSD. *Ultramicroscopy*, 131:33 – 38.

Allais, A., Bornert, M., Bretheau, T., and Caldemaison, D. (1994). Experimental characterization of the local strain field in an heterogeneous elastoplastic material. *Acta Metallurgica Materialia*, 42(11):3865–3880.

Altendorf, H., Latourte, F., Jeulin, D., Faessel, M., and Saintoyant, L. (2014). 3D reconstruction of a multiscale microstructure by anisotropic tessellation models. *Image Analysis and Stereology*, 33:121–130.

Amiot, F., Périé, J. N., and Roux, S. (2012). Equilibrium gap method. In *Full-Field Measurements and Identification in Solid Mechanics*, pages 331–362. John Wiley & Sons, Inc.

Askeland, D. and Wright, W. (2013). *Essentials of materials science and engineering*. Cengage Learning.

Badulescu, C., Grédiac, M., Haddadi, H., Mathias, J.-D., Balandraud, X., and Tran, H.-S. (2011). Applying the grid method and infrared thermography to investigate plastic deformation in aluminium multicrystal. *Mechanics of Materials*, 43(1):36–53.

Barbe, F., Decker, L., Jeulin, D., and Cailletaud, G. (2001). Intergranular and intragranular behavior of polycrystalline aggregates. Part 1: F.E. model. *International Journal of Plasticity*, 17(4):513–536.

Barbe, F. and Quey, R. (2011). A numerical modelling of 3D polycrystal-to-polycrystal diffusive phase transformations involving crystal plasticity. *International Journal of Plasticity*, 27(6):823 – 840.

Batsale, J., Chrysochoos, A., Pron, H., and Wattrisse, B. (2012). Thermographic analysis of material behavior. In *Full-Field Measurements and Identification in Solid Mechanics*, pages 439–468. John Wiley & Sons, Inc.

Bay, B., Smith, T., Fyhrie, D., and Saad, M. (1999). Digital volume correlation: three-dimensional strain mapping using X-ray tomography. *Experimental Mechanics*, 39:217–226.

Belgacem, M. and Bretheau, T. (1985). A local study of the mechanical interaction between a rigid inclusion and the surrounding plasticized matrix. *Scripta Metallurgica*, 19(3):285–288.

Berfield, T., Patel, J., Shimmin, R., Braun, P., Lambros, J., and Sottos, N. (2007). Micro- and nanoscale deformation measurement of surface and internal planes via digital image correlation. *Experimental Mechanics*, 47:51–62.

Bertin, M., Du, C., Hoefnagels, J. P., and Hild, F. (2016). Crystal plasticity parameter identification with 3D measurements and Integrated Digital Image Correlation. *Acta Materialia*, 116:321 – 331.

Bertin, M., Hild, F., and Roux, S. (2017). On the identifiability of the hill-1948 model with one uniaxial tensile test. *Comptes Rendus Mécanique*, 345(6):363 – 369.

Berveiller, M. and Zaoui, A. (1978). An extension of the self-consistent scheme to plastically-flowing polycrystals. *Journal of the Mechanics and Physics of Solids*, 26(5):325 – 344.

Besnard, G., Hild, F., and Roux, S. (2006). "Finite-Element" displacement fields analysis from digital images: application to Portevin-Le Châtelier bands. *Experimental Mechanics*, 46:789–803.

Bhandari, Y., Sarkar, S., Groeber, M., Uchic, M., Dimiduk, D., and Ghosh, S. (2007). 3d polycrystalline microstructure reconstruction from FIB generated serial sections for FE analysis. *Computational Materials Science*, 41(2):222 – 235.

Binaghi, E., Gallo, I., Marino, G., and Raspanti, M. (2004). Neural adaptive stereo matching. *Pattern Recognition Letters*, 25(15):1743 – 1758.

Bonnet, M. (2012). Introduction to identification methods. In *Full-Field Measurements and Identification in Solid Mechanics*, pages 223–246. John Wiley & Sons, Inc.

Bornert, M., Brémand, F., Doumalin, P., Dupré, J.-C., Fazzini, M., Grédiac, M., Hild, F., Mistou, S., Molimard, J., Orteu, J.-J., Robert, L., Surrel, Y., Vacher, P., and Wattrisse, B. (2009). Assessment of digital image correlation measurement errors: Methodology and results. *Experimental Mechanics*, 49(3):353–370.

Bornert, M., Chaix, J., Doumalin, P., Dupré, J., Fournel, T., Jeulin, D., Maire, E., Moreaud, M., and Moulinec, H. (2004). Mesure tridimensionnelle de champs cinématiques par imagerie volumique pour l'analyse des matériaux et des structures. *Instrumentation, Mesure, Métrologie*, 4:43–88.

Bouchet, C. (2007). *Extension de l'approche locale de la rupture dans le domaine de la transition fragile-ductile. Application au cas du programme de surveillance des aciers de cuves des centrales nucléaires françaises.* PhD thesis, Mines ParisTech.

Bouchet, C., Tanguy, B., Besson, J., and Bugat, S. (2005). Prediction of the effects of neutron irradiation on the charpy ductile to brittle transition curve of an a508 pressure vessel steel. *Computational Materials Science*, 32(3):294 – 300.

Boyde, A. (1973). Quantitative photogrammetric analysis and qualitative stereoscopic analysis of SEM images. *Journal of Microscopy*, 98(3):452–471.

Brauser, S., Kromm, A., Kannengiesser, T., and Rethmeier, M. (2010). In-situ synchrotron diffraction and digital image correlation technique for characterizations of retained austenite stability in low-alloyed transformation induced plasticity steel. *Scripta Materialia*, 63(12):1149–1152.

Brenner, R. and Suquet, P. (2013). Overall response of viscoelastic composites and polycrystals: exact asymptotic relations and approximate estimates. *International Journal of Solids and Structures*, 50:1824–1838.

Britton, T., Jiang, J., Clough, R., Tarleton, E., Kirkland, A., and Wilkinson, A. (2013). Assessing the precision of strain measurements using electron backscatter diffraction - part 1: Detector assessment. *Ultramicroscopy*, 135:126 – 135.

Britton, T. and Wilkinson, A. (2011). Measurement of residual elastic strain and lattice rotations with high resolution electron backscatter diffraction. *Ultramicroscopy*, 111(8):1395–1404.

Britton, T. and Wilkinson, A. (2012). High resolution electron backscatter diffraction measurements of elastic strain variations in the presence of larger lattice rotations. *Ultramicroscopy*, 114:82 – 95.

Broggiato, G. (2004). Adaptive image correlation technique for full-field strain measurement. In *Proceedings 12th International Conference on Experimental Mechanics*, pages 635–643, Bari, Italy.

Caillard, D. (1996). Dislocation-obstacle interactions and mechanical properties of intermetallics. *Journal de Physique IV Colloque*, 06:199–210.

Cailletaud, G. and Sai, K. (2008). A polycrystalline model for the description of ratchetting: Effect of intergranular and intragranular hardening. *Materials Science and Engineering: A*, 480(1):24 – 39.

Calcagnotto, M., Ponge, D., Demir, E., and Raabe, D. (2010). Orientation gradients and geometrically necessary dislocations in ultrafine grained dual-phase steels studied by 2D and 3D EBSD. *Materials Science and Engineering: A*, 527(10-11):2738 – 2746.

Carpenter, D., Pugh, J., Richardson, G., and Mooney, L. (2007). Determination of pattern centre in EBSD using the moving-screen technique. *Journal of Microscopy*, 227(3):246–247.

Carroll, J., Efstathiou, C., Lambros, J., Sehitoglu, H., Hauber, B., Spottswood, S., and Chona, R. (2009). Investigation of fatigue crack closure using multiscale image correlation experiments. *Engineering Fracture Mechanics*, 76(15):2384 – 2398.

Carroll, J. D., Abuzaid, W., Lambros, J., and Sehitoglu, H. (2013). High resolution digital image correlation measurements of strain accumulation in fatigue crack growth. *International Journal of Fatigue*, 57:140–150.

Carter, J., Kuper, M., Uchic, M., and Mills, M. (2014). Characterization of localized deformation near grain boundaries of superalloy René-104 at elevated temperature. *Materials Science and Engineering: A*, 605(0):127–136.

Charbal, A., Dufour, J., Guery, A., Hild, F., Roux, S., Vincent, L., and Poncelet, M. (2016). Integrated digital image correlation considering gray level and blur variations: Application to distortion measurements of IR camera. *Optics and Lasers in Engineering*, 78:75 – 85.

Cheng, J. and Ghosh, S. (2015). A crystal plasticity FE model for deformation with twin nucleation in magnesium alloys. *International Journal of Plasticity*, 67(Supplement C):148 – 170.

Chiumenti, M., Valverde, Q., de Saracibar, C. A., and Cervera, M. (2004). A stabilized formulation for incompressible plasticity using linear triangles and tetrahedra. *International Journal of Plasticity*, 20(8):1487 – 1504.

Cho, J., Rollett, A., and Oh, K. (2005). Determination of a mean orientation in electron backscatter diffraction measurements. *Metallurgical and Materials Transactions A*, 36(12):3427–3438.

Claire, D., Hild, F., and Roux, S. (2004). A finite element formulation to identify damage fields: the equilibrium gap method. *International Journal for Numerical Methods in Engineering*, 61(2):189–208.

Cogswell, D. J. (2010). *Statistical Modelling of the Transition Toughness Properties of Low Alloy Pressure Vessel Steels Volume 1: Main Body*. PhD thesis, University of Birmingham.

Cordero, N., Forest, S., Busso, E., Berbenni, S., and Cherkaoui, M. (2012). Grain size effects on plastic strain and dislocation density tensor fields in metal polycrystals. *Computational Materials Science*, 52(1):7–13.

Couvant, T., Legras, L., Ghys, T., Gambier, P., Huin, N., and Ilevbare, G. (2012). Strain path effect on IGSCC initiation and oxidation of alloy 182 exposed to PWR primary water. In *15th International Conference on Environmental Degradation of Materials in Nuclear Power Systems-Water Reactors*, pages 1631–1643. John Wiley & Sons, Inc.

CrossCourt3 (2012). www.blgproductions.co.uk. BLG Productions Ltd, Bristol, UK.

Crépin, J., Bretheau, T., and Caldemaison, D. (1995). Plastic deformation mechanisms of β treated zirconium. *Acta Metallurgica et Materialia*, 43(10):3709–3719.

Cédat, D., Fandeur, O., Rey, C., and Raabe, D. (2012). Polycrystal model of the mechanical behavior of a mo-tic30 vol.metal-ceramic composite using a three-dimensional microstructure map obtained by dual beam focused ion beam scanning electron microscopy. *Acta Materialia*, 60(4):1623 – 1632.

Cédat, D., Libert, M., Leflem, M., Fandeur, O., Rey, C., Clavel, M., and Schmitt, J.-H. (2009). Experimental characterization and mechanical behaviour modelling of molybdenum-titanium carbide composite for high temperature applications. *International Journal of Refractory Metals and Hard Materials*, 27(2):267 – 273.

Delaire, F., Raphanel, J., and Rey, C. (2000). Plastic heterogeneities of a copper multicrystal deformed in uniaxial tension: experimental study and finite element simulations. *Acta Materialia*, 48(5):1075–1087.

Dexet, M. (2006). *Méthode de couplage entre expérimentations et simulations numériques en vue de l'identification de lois de comportement intracristallin. Application aux alliages de zirconium*. PhD thesis, Ecole Polytechnique.

Diard, O., Leclercq, S., Rousselier, G., and Cailletaud, G. (2005). Evaluation of finite element based analysis of 3D multicrystalline aggregates plasticity: Application to crystal plasticity model identification and the study of stress and strain fields near grain boundaries. *International Journal of Plasticity*, 21:691–722.

Diawara, B. (2011). *Caractérisation quantitative de la microstructure de l'acier 16MND5 des cuves de réacteurs nucléaires à eau pressurisée*. PhD thesis. Université Grenoble.

Dingley, D., Wright, S., and Nowell, M. (2005). Dynamic background correction of electron backscatter diffraction patterns. *Microscopy and Microanalysis*, 11(S02):528.

Doumalin, P. and Bornert, M. (2000). Micromechanical applications of digital image correlation techniques. In Jacquot, P. and Fournier, J.-M., editors, *Interferometry in Speckle Light*, pages 67–74. Springer Berlin Heidelberg.

Drouin, D., Couture, A. R., Joly, D., Tastet, X., Aimez, V., and Gauvin, R. (2007). CASINO v2. 42–a fast and easy-to-use modeling tool for scanning electron microscopy and microanalysis users. *Scanning*, 29(3):92–101.

Du, C., Maresca, F., Geers, M., and Hoefnagels, J. (2018). Ferrite slip system activation investigated by uniaxial micro-tensile tests. *Acta Materialia*. in press.

Duda, R. and Hart, P. (1972). Use of the Hough transformation to detect lines and curves in pictures. *Communications of the ACM*, 15(1):11–15.

Dufour, J., Leclercq, S., Schneider, J., Roux, S., and Hild, F. (2016). 3D surface measurements with isogeometric stereocorrelation-application to complex shapes. *Optics and Lasers in Engineering*, 87:146 – 155.

Dutta, R., Huizenga, R., Amirthalingam, M., King, A., Gao, H., Hermans, M., and Richardson, I. (2013). In situ synchrotron diffraction studies on the temperature-dependent plane-specific elastic constants in a high-strength quenched and tempered structural steel. *Scripta Materialia*, 69(2):187–190.

Dève, H., Harren, S., McCullough, C., and Asaro, R. (1988). Micro and macroscopic aspects of shear band formation in internally nitrided single crystals of Fe-Ti-Mn alloys. *Acta Metallurgica*, 36(2):341 – 365.

EDF (2017). Finite element code-aster, analysis of structures and thermomechanics for studies and research. Open source on www.code-aster.org.

Espinosa, H., Bernal, R., and Minary-Jolandan, M. (2012). In situ TEM electromechanical testing of nanowires and nanotubes. *Small*, 8:3233–3252.

Falco, S., Jiang, J., Cola, F. D., and Petrinic, N. (2017). Generation of 3D polycrystalline microstructures with a conditioned Laguerre-Voronoi tessellation technique. *Computational Materials Science*, 136(Supplement C):20 – 28.

Field, D. A. (1988). Laplacian smoothing and delaunay triangulations. *Communications in Applied Numerical Methods*, 4(6):709–712.

Forquin, P., Rota, L., Charles, Y., and Hild, F. (2004). A method to determine the macroscopic toughness scatter of brittle materials. *International Journal of Fracture*, 125(1):171–187.

Franciosi, P. (1985). The concepts of latent hardening and strain hardening in metallic single crystals. *Acta Metallurgica*, 33:1601–1612.

Franciosi, P., Le, L., Monnet, G., Kahloun, C., and Chavanne, M.-H. (2015). Investigation of slip system activity in iron at room temperature by SEM and AFM in-situ tensile and compression tests of iron single crystals. *International Journal of Plasticity*, 65:226 – 249.

Frankot, R. T. and Chellappa, R. (1988). A method for enforcing integrability in shape from shading algorithms. *IEEE Transactions on Pattern Analysis and Machine Intelligence*, 10(4):439–451.

Garnaes, J., Nielsen, L., Dirscherl, K., Jørgensen, J., Rasmussen, J., Lindelof, P., and Sørensen, C. (1998). Two-dimensional nanometer-scale calibration based on one-dimensional gratings. *Applied Physics A*, 66(1):S831–S835.

Geiger, A., Roser, M., and Urtasun, R. (2010). Efficient large-scale stereo matching. In *Asian conference on computer vision*, pages 25–38. Springer.

Gioacchino, F. D. and da Fonseca, J. Q. (2015). An experimental study of the polycrystalline plasticity of austenitic stainless steel. *International Journal of Plasticity*, 74:92–109.

Grennerat, F., Montagnat, M., Castelnau, O., Vacher, P., Moulinec, H., Suquet, P., and Duval, P. (2012). Experimental characterization of the intragranular strain field in columnar ice during transient creep. *Acta Materialia*, 60(8):3655–3666.

Groeber, M., Ghosh, S., Uchic, M. D., and Dimiduk, D. M. (2008a). A framework for automated analysis and simulation of 3D polycrystalline microstructures. Part 1: Statistical characterization. *Acta Materialia*, 56(6):1257 – 1273.

Groeber, M., Ghosh, S., Uchic, M. D., and Dimiduk, D. M. (2008b). A framework for automated analysis and simulation of 3D polycrystalline microstructures. Part 2: Synthetic structure generation. *Acta Materialia*, 56(6):1274 – 1287.

Groeber, M., Haley, B., Uchic, M., Dimiduk, D., and Ghosh, S. (2006). 3D reconstruction and characterization of polycrystalline microstructures using a FIB-SEM system. *Materials Characterization*, 57(4-5):259 – 273.

Groeber, M. A. and Jackson, M. A. (2014). DREAM.3D: A digital representation environment for the analysis of microstructure in 3D. *Integrating Materials and Manufacturing Innovation*, 3(1):5.

Guery, A. (2014). *Développement d'une méthode de corrélation d'images numériques adaptée aux mesures cinématiques dans les polycristaux: application à l'identification de paramètres de lois de plasticité cristalline*. PhD thesis, Ecole normale supérieure de Cachan.

Guery, A., Hild, F., Latourte, F., and Roux, S. (2016a). Slip activities in polycrystals determined by coupling DIC measurements with crystal plasticity calculations. *International Journal of Plasticity*, 81:249 – 266.

Guery, A., Hild, F., Latourte, F., and Roux, S. (2016b). Identification of crystal plasticity parameters using DIC measurements and weighted FEMU. *Mechanics of Materials*, 100:55 – 71.

Guery, A., Latourte, F., Hild, F., and Roux, S. (2014). Characterization of SEM speckle pattern marking and imaging distortion by digital image correlation. *Measurement Science and Technology*, 25(1):015401.

Guilhem, Y., Basseville, S., Curtit, F., Stéphan, J.-M., and Cailletaud, G. (2010). Investigation of the effect of grain clusters on fatigue crack initiation in polycrystals. *International Journal of Fatigue*, 32(11):1748–1763.

Guilhem, Y., Basseville, S., Curtit, F., Stéphan, J.-M., and Cailletaud, G. (2013). Numerical investigations of the free surface effect in three-dimensional polycrystalline aggregates. *Computational Materials Science*, 70(0):150–162.

Gurtin, M., Anand, L., and Lele, S. (2007). Gradient single-crystal plasticity with free energy dependent on dislocation densities. *Journal of the Mechanics and Physics of Solids*, 55(9):1853 – 1878.

Guyon, J., Gey, N., Goran, D., Chalal, S., and Pérez-Willard, F. (2016). Advancing FIB assisted 3D EBSD using a static sample setup. *Ultramicroscopy*, 161:161 – 167.

Gérard, C., N'Guyen, F., Osipov, N., Cailletaud, G., Bornert, M., and Caldemaison, D. (2009). Comparison of experimental results and finite element simulation of strain localization scheme under cyclic loading. *Computational Materials Science*, 46:755–760.

Hamilton, W. (1853). *Lectures on Quaternions*. Dublin : Hodges and Smith.

Hamilton, W. (1866). *Elements of Quaternions*. London, Longmans, Green, & co.

Han, J., Jee, K., and Oh, K. (2003). Orientation rotation behavior during in situ tensile deformation of polycrystalline 1050 aluminum alloy. *International Journal of Mechanical Sciences*, 45(10):1613 – 1623.

Han, X. (2013). *Modélisation de la fragilisation due au gonflement dans les aciers inoxydables austénitiques irradiés*. PhD thesis, Mines ParisTech.

Harland, C., Akhter, P., and Venables, J. (1981). Accurate microcrystallography at high spatial resolution using electron back-scattering patterns in a field emission gun scanning electron microscope. *Journal of Physics E: Scientific Instruments*, 14(2):175.

Hausild, P. (2002). *Transition ductile-fragile dans un acier faiblement allié*. PhD thesis. Ecole centrale de Paris.

Helfer, T., Fandeur, O., Haboussa, D., Deloison, D., Jamond, O., Munier, R., Berthon, L., Étienne Castelier, and Ramière, I. (2017). New functionalities of the 3.0 version of TFEL, MFront and MTest. In *13ème Colloque National en Calcul des Structures*.

Helfer, T., Michel, B., Proix, J.-M., Salvo, M., Sercombe, J., and Casella, M. (2015). Introducing the open-source MFront code generator: Application to mechanical behaviours and material knowledge management within the PLEIADES fuel element modelling platform. *Computers & Mathematics with Applications*, 70(5):994 – 1023.

Herbig, M., King, A., Reischig, P., Proudhon, H., Lauridsen, E., Marrow, J., Buffière, J., and Ludwig, W. (2011). 3D growth of a short fatigue crack within a polycrystalline microstructure studied using combined diffraction and phase-contrast X-ray tomography. *Acta Materialia*, 59(2):590 – 601.

Hild, F. and Roux, S. (2006). Digital image correlation: from displacement measurement to identification of elastic properties - a review. *Strain*, 42(2):69–80.

Hild, F. and Roux, S. (2012a). Comparison of local and global approaches to digital image correlation. *Experimental Mechanics*, 52:1503–1519.

Hild, F. and Roux, S. (2012b). Digital image correlation. In Rastogi, P. and Hack, E., editors, *Optical Methods for Solid Mechanics. A Full-Field Approach*, pages 183–228. Wiley-VCH, Weinheim (Germany).

Hirth, J. (1960). On the dislocation interactions in the FCC lattice. *Journal of Applied Mechanics*, 32:700–706.

HKL (2007). *Oxford Instruments HKL CHANNEL 5 user Manual*.

Hoc, T., Crépin, J., Gélébart, L., and Zaoui, A. (2003). A procedure for identifying the plastic behavior of single crystals from the local response of polycrystals. *Acta Materialia*, 51(18):5477–5488.

Horn, B. K. (1977). Understanding image intensities. *Artificial intelligence*, 8(2):201–231.

Horstemeyer, M. (2012). *Integrated Computational Materials Engineering (ICME) for Metals: Using Multiscale Modeling to Invigorate Engineering Design with Science*. Wiley-TMS.

Howell, P. (1975). Taking, presenting and treating stereo data from the SEM. *Scanning electron microscopy*, 1975:697–706.

Héripré, E. (2006). *Méthode de couplage multi-échelles entre simulations numériques polycristallines et mesures de champs pour l'identification des paramètres de lois de comportement et de fissuration des matériaux métalliques. Application à l'étude des alliages TiAl*. PhD thesis, Ecole Polytechnique.

Héripré, E., Dexet, M., Crépin, J., Gélébart, L., Roos, A., Bornert, M., and Caldemaison, D. (2007). Coupling between experimental measurements and polycrystal finite element calculations for micromechanical study of metallic materials. *International Journal of Plasticity*, 23(9):1512–1539.

Jaoul, B. (1965). *Etude de la plasticité et application aux métaux*. Presses des Mines, Paris.

Jin, H., Lu, W., Haldar, S., and Bruck, H. (2011). Microscale characterization of granular deformation near a crack tip. *Journal of Materials Science*, 46(20):6596–6602.

Joo, H., Kim, J., Kim, K., Tamura, N., and Koo, Y. (2004). In situ synchrotron X-ray microdiffraction study of deformation behavior in polycrystalline coppers during uniaxial deformations. *Scripta Materialia*, 51(12):1183 – 1186.

Jumel, S. and Van-Duysen, J. C. (2005). Rpv-1: A virtual test reactor to simulate irradiation effects in light water reactor pressure vessel steels. *Journal of Nuclear Materials*, 340(2):125 – 148.

Kacher, J., Basinger, J., Adams, B. L., and Fullwood, D. T. (2010). Reply to comment by Maurice et al. in response to "Bragg's law diffraction simulations for electron backscatter diffraction analysis". *Ultramicroscopy*, 110(7):760 – 762.

Kacher, J., Landon, C., Adams, B., and Fullwood, D. (2009). Bragg's law diffraction simulations for electron backscatter diffraction analysis. *Ultramicroscopy*, 109(9):1148 – 1156.

Kahloun, C., Badji, R., Bacroix, B., and Bouabdallah, M. (2010). Contribution to crystallographic slip assessment by means of topographic measurements achieved with atomic force microscopy. *Materials Characterization*, 61(9):835 – 844.

Kajberg, J., Sundin, K., Melin, L., and Ståhle, P. (2004). High strain rate tensile testing and viscoplastic parameter identification using microscopic high-speed photography. *International Journal of Plasticity*, 20:561–575.

Kamaya, M. and Itakura, M. (2009). Simulation for intergranular stress corrosion cracking based on a three-dimensional polycrystalline model. *Engineering Fracture Mechanics*, 76:386–401.

Kanjarla, A., Lebensohn, R., Balogh, L., and Tomé, C. (2012). Study of internal lattice strain distributions in stainless steel using a full-field elasto-viscoplastic formulation based on fast Fourier transforms. *Acta Materialia*, 60:3094–3106.

Kapur, J. and Casasent, D. (2000). Geometric correction of sem images. *Proceedings of SPIE*, 4044:165–176.

Khan-Jetter, Z. and Chu, T. (1990). Three-dimensional displacement measurements using digital image correlation and photogrammic analysis. *Experimental Mechanics*, 30(1):10–16.

Koenig, G., Nickel, W., Storl, J., Meyer, D., and Stange, J. (1987). Digital stereophotogrammetry for processing SEM data. *Scanning*, 9(5):185–193.

Konrad, J., Zaefferer, S., and Raabe, D. (2006). Investigation of orientation gradients around a hard laves particle in a warm-rolled Fe3Al-based alloy using a 3D EBSD-FIB technique. *Acta Materialia*, 54(5):1369 – 1380.

Kraska, M., Doig, M., Tikhomirov, D., Raabe, D., and Roters, F. (2009). Virtual material testing for stamping simulations based on polycrystal plasticity. *Computational Materials Science*, 46(2):383 – 392.

Kröner, E. (1961). Zur plastischen Verformung des Vielkristalls. *Acta Metallurgica*, 9:155–161.

Lahellec, N. and Suquet, P. (2013). Effective response and field statistics in elasto-plastic and elasto-viscoplastic composites under radial and non-radial loadings. *International Journal of Plasticity*, 42:1–30.

Latourte, F., Rupin, N., He, M., Parrot, A., and Leclercq, S. (2012). Full field measurements used for assessing industrial issues - Two examples. *Procedia IUTAM*, 4(0):92–105.

Latourte, F., Salez, T., Guery, A., Rupin, N., and Mahé, M. (2014). Deformation studies from in-situ SEM experiments of a reactor pressure vessel steel at room and low temperatures. *Journal of Nuclear Materials*, 454(1-3):373–380.

Lebensohn, R. A., Brenner, R., Castelnau, O., and Rollett, A. D. (2008). Orientation image-based micromechanical modelling of subgrain texture evolution in polycrystalline copper. *Acta Materialia*, 56(15):3914–3926.

Lebiedzik, J. (1975). Multiple detecter method for quantitative determination of microtopography in the SEM. *Scanning Electron Microscopy*, pages 181–188.

Lebiedzik, J. (1979). An automatic topographical surface reconstruction in the SEM. *Scanning*, 2(4):230–237.

Leclerc, H., Périé, J.-N., Roux, S., and Hild, F. (2009). Integrated digital image correlation for the identification of mechanical properties. *MIRAGE 2009, LNCS*, 5496:161–171.

Leclercq, S., Lidbury, D., Dyck, S., Moinereau, D., Alamo, A., and Mazouzi, A. (2010). PERFORM 60 – prediction of the effects of radiation for reactor pressure vessel and in-core materials using multi-scale modelling – 60 years foreseen plant lifetime. *Journal of Nuclear Materials*, 406(1):193–203.

Lecompte, D., Smits, A., Sol, H., Vantomme, J., and Hemelrijck, D. V. (2007). Mixed numerical–experimental technique for orthotropic parameter identification using biaxial tensile tests on cruciform specimens. *International Journal of Solids and Structures*, 44(5):1643–1656.

Ledbetter, H. (1981). Predicted single-crystal elastic constants of stainless-steel 316. *British Journal of Non-Destructive Testing*, 23:286–287.

Ledbetter, H. M. and Reed, R. P. (1973). Elastic properties of metals and alloys, i. iron, nickel, and iron-nickel alloys. *Journal of Physical and Chemical Reference Data*, 2(3):531–618.

Li, C., Liu, Z., and Xie, H. (2013). A measurement method for micro 3D shape based on grids-processing and stereovision technology. *Measurement Science and Technology*, 24(4):045401.

Libert, M. (2007). *Etudes expérimentale et numérique de l'effet des mécanismes de plasticité sur la rupture fragile par clivage dans les aciers faiblement alliés*. PhD thesis. Ecole centrale de Paris.

Lim, H., Carroll, J., Battaile, C., Boyce, B., and Weinberger, C. (2015). Quantitative comparison between experimental measurements and CP-FEM predictions of plastic deformation in a tantalum oligocrystal. *International Journal of Mechanical Sciences*, 92(0):98 – 108.

Lim, H., Carroll, J., Battaile, C., Buchheit, T., Boyce, B., and Weinberger, C. (2014). Grain-scale experimental validation of crystal plasticity finite element simulations of tantalum oligocrystals. *International Journal of Plasticity*, 60:1 – 18.

Lin, F. X., Ubhi, H. S., Petrenec, M., Zhang, Y. B., and Jensen, D. J. (2015). Local strain distributions in partially recrystallized copper determined by in situ tensile investigation. *IOP Conference Series: Materials Science and Engineering*, 82(1):012103.

Ling, C. (2017). *Modeling the intragranular ductile fracture of irradiated steels. Effects of crystal anisotropy and strain gradient*. PhD thesis, Mines ParisTech.

Liu, Y. and Castañeda, P. P. (2004). Second-order theory for the effective behavior and field fluctuations in viscoplastic polycrystals. *Journal of the Mechanics and Physics of Solids*, 52(2):467–495.

Liu, Y. and Fischer, G. (1997). In situ measurement of local strain in a metal matrix composite by the object grating technique. *Scripta Materialia*, 36(10):1187–1194.

Lockwood, W. and Reynolds, A. (1999). Use and verification of digital image correlation for automated 3D surface characterization in the scanning electron microscope. *Materials Characterization*, 42(2):123 – 134.

LTD, B. P. (2012). Methods, apparatuses and computer programs for crystallography.

Lucas, B. and Kanade, T. (1981). An iterative registration technique with an application to stereo vision. pages 121–130.

Ludwig, W., King, A., Herbig, M., Reischig, P., Marrow, J., Babout, L., Lauridsen, E. M., Proudhon, H., and Buffière, J. Y. (2010). Characterization of polycrystalline materials using synchrotron X-ray imaging and diffraction techniques. *JOM*, 62(12):22–28.

Ludwig, W., King, A., Reischig, P., Herbig, M., Lauridsen, E., Schmidt, S., Proudhon, H., Forest, S., Cloetens, P., du Roscoat, S. R., Buffière, J., Marrow, T., and Poulsen, H. (2009). New opportunities for 3D materials science of polycrystalline materials at the micrometre lengthscale by combined use of X-ray diffraction and X-ray imaging. *Materials Science and Engineering: A*, 524(1-2):69 – 76. Special Topic Section: Probing strains and Dislocation Gradients with diffraction.

Ma, A., Roters, F., and Raabe, D. (2006a). On the consideration of interactions between dislocations and grain boundaries in crystal plasticity finite element modeling – Theory, experiments, and simulations. *Acta Materialia*, 54(8):2181–2194.

Ma, A., Roters, F., and Raabe, D. (2006b). Studying the effect of grain boundaries in dislocation density based crystal-plasticity finite element simulations. *International Journal of Solids and Structures*, 43(24):7287–7303.

Mandel, J. (1973). Equations constitutives et directeurs dans les milieux plastiques et viscoplastiques. *International Journal of Solids and Structures*, 9(6):725 – 740.

Martin, F., Bataillon, C., and Cousty, J. (2008). In situ AFM detection of pit onset location on a 304L stainless steel. *Corrosion Science*, 50(1):84–92.

Mathieu, F., Leclerc, H., Hild, F., and Roux, S. (2015). Estimation of elastoplastic parameters via weighted FEMU and integrated-DIC. *Experimental Mechanics*, 55(1):105–119.

Mathieu, J.-P. (2006). *Analyse et modélisation micromécanique du comportement et de la rupture fragile de l'acier 16MND5 : prise en compte des hétérogénéités microstructurales*. PhD thesis, ENSAM.

Maurice, C., Driver, J., and Fortunier, R. (2012). On solving the orientation gradient dependency of high angular resolution EBSD. *Ultramicroscopy*, 113:171–181.

Maurice, C., Dzieciol, K., and Fortunier, R. (2011). A method for accurate localisation of EBSD pattern centres. *Ultramicroscopy*, 111(2):140 – 148.

Maurice, C., Quey, R., Fortunier, R., and Driver, J. (2013). High angular resolution EBSD and its materials applications. In *Microstructural Design of Advanced Engineering Materials*, pages 339–365. Wiley-VCH Verlag GmbH & Co. KGaA.

Maynadier, A., Poncelet, M., Lavernhe-Taillard, K., and Roux, S. (2012). One-shot measurement of thermal and kinematic fields: Infrared image correlation (IRIC). *Experimental Mechanics*, 52(3):241–255.

Mazouzi, A. A., Alamo, A., Lidbury, D., Moinereau, D., and Dyck, S. V. (2011). PERFORM 60: Prediction of the effects of radiation for reactor pressure vessel and in-core materials using multi-scale modelling - 60 years foreseen plant lifetime. *Nuclear Engineering and Design*, 241(9):3403 – 3415.

McHugh, P., Asaro, R., and Shih, C. (1993). Computational modeling of metal matrix composite materials - isothermal deformation patterns in ideal microstructures. *Acta Metallurgica et Materialia*, 41(5):1461 – 1476.

Mendonça, G., Mendonça, D., Aragão, F., and Cooper, L. (2008). Advancing dental implant surface technology – from micron- to nanotopography. *Biomaterials*, 29(28):3822 – 3835.

Meuwissen, M., Oomens, C., Baaijens, F., Petterson, R., and Janssen, J. (1998). Determination of the elasto-plastic properties of aluminium using a mixed numerical–experimental method. *Journal of Materials Processing Technology*, 75:204–211.

Miller, M. and Burke, M. (1992). An atom probe field ion microscopy study of neutron-irradiated pressure vessel steels. *Journal of Nuclear Materials*, 195(1):68 – 82.

Mingard, K., Day, A., Maurice, C., and Quested, P. (2011). Towards high accuracy calibration of electron backscatter diffraction systems. *Ultramicroscopy*, 111(5):320 – 329.

Mishin, O., Bowen, J., and Godfrey, A. (2012). EBSD analysis of deformed and partially recrystallized microstructures in ECAE-processed copper. *Materials Science Forum*, 715-716:825–830.

Miyamoto, G., Shibata, A., Maki, T., and Furuhara, T. (2009). Precise measurement of strain accommodation in austenite matrix surrounding martensite in ferrous alloys by electron backscatter diffraction analysis. *Acta Materialia*, 57(4):1120 – 1131.

Monnet, G. and Vincent, L. (2011). Loi de comportement en plasticité cristalline pour acier à basse température. *Mécanique & Industries*, 12(3):193–198.

Monnet, G., Vincent, L., and Devincre, B. (2013). Dislocation-dynamics based crystal plasticity law for the low- and high-temperature deformation regimes of BCC crystal. *Acta Materialia*, 61(16):6178–6190.

Montagnat, M., Blackford, J. R., Piazolo, S., Arnaud, L., and Lebensohn, R. A. (2011). Measurements and full-field predictions of deformation heterogeneities in ice. *Earth and Planetary Science Letters*, 305(1–2):153–160.

Morita, S., Abe, M., Yokoyama, K., and Sugawara, Y. (2000). Defects and their charge imaging on semiconductor surfaces by noncontact atomic force microscopy and spectroscopy. *Journal of Crystal Growth*, 210(1):408 – 415.

Munroe, P. (2009). The application of focused ion beam microscopy in the material sciences. *Materials Characterization*, 60(1):2 – 13.

Méric, L., Poubanne, P., and Cailletaud, G. (1991). Single crystal modeling for structural calculations : Part 1 – Model presentation. *Journal of Engineering Materials and Technology*, 113:162–170.

Naamane, S. (2008). *Etude de la déformation plastique de la ferrite à basse température : simulations de dynamique des dislocations*. PhD thesis. Université Paris 6.

Naamane, S., Monnet, G., and Devincre, B. (2010). Low temperature deformation in iron studied with dislocation dynamics simulations. *International Journal of Plasticity*, 26(1):84 – 92.

Nolze, G. (2006). Geometrically caused image distortion effects and their influence on interpretation of ebsd measurements. *Materials Science and Technology*, 22(11):1343–1351.

Nolze, G. (2007). Image distortions in SEM and their influences on EBSD measurements. *Ultramicroscopy*, 107(2-3):172 – 183.

Novovic, D., Dewes, R., Aspinwall, D., Voice, W., and Bowen, P. (2004). The effect of machined topography and integrity on fatigue life. *International Journal of Machine Tools and Manufacture*, 44(2):125 – 134.

Nye, J. (1953). Some geometrical relations in dislocated crystals. *Acta Metallurgica*, 1:153–162.

Petit, J., Castelnau, O., Bornert, M., Zhang, F. G., Hofmann, F., Korsunsky, A. M., Faurie, D., Le Bourlot, C., Micha, J. S., Robach, O., and Ulrich, O. (2015). Laue-DIC: a new method for improved stress field measurements at the micrometer scale. *Journal of Synchrotron Radiation*, 22(4):980–994.

Plancher, E. (2015). *Full-field measurements of elastic and total strains for the determination of the local behaviour in polycrystals*. PhD thesis, Ecole nationale supérieure d'arts et métiers - ENSAM.

Plancher, E., Petit, J., Maurice, C., Favier, V., Saintoyant, L., Loisnard, D., Rupin, N., Marijon, J.-B., Ulrich, O., Bornert, M., Micha, J.-S., Robach, O., and Castelnau, O. (2016). On the accuracy of elastic strain field measurements by Laue microdiffraction and high-resolution EBSD: a cross-validation experiment. *Experimental Mechanics*, 56(3):483–492.

Podesta, L. (2016). *Etude expérimentale de la fissuration en fluage de l'acier 316H vieilli sous environnement CO_2*. PhD thesis, Université de Montpellier.

Pouillier, E., Gourgues, A.-F., Tanguy, D., and Busso, E. (2012). A study of intergranular fracture in an aluminium alloy due to hydrogen embrittlement. *International Journal of Plasticity*, 34(0):139–153.

Quey, R., Dawson, P., and Barbe, F. (2011). Large-scale 3D random polycrystals for the finite element method: Generation, meshing and remeshing. *Computer Methods in Applied Mechanics and Engineering*, 200(17):1729 – 1745.

Queyreau, S. (2008). *Etude des mécanismes d'écrouissage sous irradiation de la ferrite par simulations de dynamique de dislocations*. PhD thesis. Université Paris 6.

Queyreau, S., Monnet, G., and Devincre, B. (2009). Slip systems interactions in α-iron determined by dislocation dynamics simulations. *International Journal of Plasticity*, 25(2):361–377.

Raabe, D., Sachtleber, M., Zhao, Z., Roters, F., and Zaefferer, S. (2001). Micromechanical and macromechanical effects in grain scale polycrystal plasticity experimentation and simulation. *Acta Materialia*, 49(17):3433–3441.

Ram, F., Zaefferer, S., Jäpel, T., and Raabe, D. (2015). Error analysis of the crystal orientations and disorientations obtained by the classical electron backscatter diffraction technique. *Journal of Applied Crystallography*, 48(3):797–813.

Ramos, K. J., Hooks, D. E., and Bahr, D. F. (2009). Direct observation of plasticity and quantitative hardness measurements in single crystal cyclotrimethylene trinitramine by nanoindentation. *Philosophical Magazine*, 89(27):2381–2402.

Rannou, J., Limodin, N., Réthoré, J., Gravouil, A., Ludwig, W., Baïetto-Dubourg, M.-C., Buffière, J.-Y., Combescure, A., Hild, F., and Roux, S. (2010). Three dimensional experimental and numerical multiscale analysis of a fatigue crack. *Computer Methods in Applied Mechanics and Engineering*, 199(21):1307 – 1325.

Reichelt, R. (2007). Scanning electron microscopy. In Hawkes, P. W. and Spence, J. C., editors, *Science of Microscopy*, pages 133–272. Springer New York, New York, NY.

Renevey, S. (1997). *Approches globale et locale de la rupture dans le domaine de transition fragile-ductile d'un acier faiblement allie*. PhD thesis, Université Paris 11.

Reyntjens, S. and Puers, R. (2000). Focused ion beam induced deposition: fabrication of three-dimensional microstructures and Young's modulus of the deposited material. *Journal of Micromechanics and Microengineering*, 10(2):181.

Roters, F., Eisenlohr, P., Hantcherli, L., Tjahjanto, D., Bieler, T., and Raabe, D. (2010). Overview of constitutive laws, kinematics, homogenization and multiscale methods in crystal plasticity finite-element modeling: Theory, experiments, applications. *Acta Materialia*, 58(4):1152–1211.

Roux, S. and Hild, F. (2006). Stress intensity factor measurements from digital image correlation: post-processing and integrated approaches. *International Journal of Fracture*, 140(1):141–157.

Roux, S., Hild, F., and Leclerc, H. (2012). Mechanical assistance to DIC. *Procedia IUTAM*, 4:159–168.

Roux, S., Hild, F., Viot, P., and Bernard, D. (2008). Three-dimensional image correlation from X-ray computed tomography of solid foam. *Composites Part A: Applied Science and Manufacturing*, 39(8):1253–1265.

Ru, C., Zhang, Y., Sun, Y., Zhong, Y., Sun, X., Hoyle, D., and Cotton, I. (2011). Automated four-point probe measurement of nanowires inside a scanning electron microscope. *IEEE Transactions on Nanotechnology*, 10:674–681.

Réthoré, J., Roux, S., and Hild, F. (2009). An extended and integrated digital image correlation technique applied to the analysis of fractured samples. *European Journal of Computational Mechanics*, 18:285–306.

Saai, A., Louche, H., Tabourot, L., and Chang, H. (2010). Experimental and numerical study of the thermo-mechanical behavior of Al bi-crystal in tension using full field measurements and micromechanical modeling. *Mechanics of Materials*, 42(3):275–292.

Schmid, E. and Boas, W. (1935). *Kristalplastizität*. Springer Verlag.

Schroeter, B. M. and McDowell, D. L. (2003). Measurement of deformation fields in polycrystalline OFHC copper. *International Journal of Plasticity*, 19(9):1355–1376.

Schwartz, J. (2011). *Approche non locale en plasticité cristalline : application à l'étude du comportement mécanique de l'acier AISI 316LN en fatigue oligocyclique.* PhD thesis, Ecole Centrale Paris.

Schwartz, J., Fandeur, O., and Rey, C. (2010). Fatigue crack initiation modeling of 316LN steel based on non local plasticity theory. *Procedia Engineering*, 2:1353–1362.

Scrivens, W., Luo, Y., Sutton, M., Collette, S., Myrick, M., Miney, P., Colavita, P., Reynolds, A., and Li, X. (2007). Development of patterns for digital image correlation measurements at reduced length scales. *Experimental Mechanics*, 47:63–77.

Sekfali, S. (2004). *Influence de la microstructure sur le comportement local dans les aciers 16MND5*. PhD thesis, Ecole Centrale Paris.

Sevillano, G. J. (1993). Flow stress and work hardening. In Mughrabi, H., editor, *Plastic deformation and fracture of materials*, volume 6, pages 19–88. WILEY-VCH Verlag GmbH.

Seward, G., Celotto, S., Prior, D., Wheeler, J., and Pond, R. (2004). In situ SEM-EBSD observations of the HCP to BCC phase transformation in commercially pure titanium. *Acta Materialia*, 52(4):821–832.

Shi, Q. (2014). Validation of a dual-phase crystal plasticity model of a pressure vessel steel and its application in a micro-mechanical brittle failure approach. Master's thesis, Mines ParisTech.

Shi, Q., Latourte, F., and Cailletaud, G. (2015). Micro-mechanical failure model of a ferritic-bainitic steel : consequence and interests of a dual-phase polycrystalline model. In *22ème congrès français de mécanique, Aug 2015, Lyon, France*, page 25.

Shi, Q., Latourte, F., Hild, F., and Roux, S. (2016). Quaternion correlation for tracking crystal motions. *Measurement Science and Technology*, 27(9):095006.

Shi, Q., Latourte, F., Hild, F., and Roux, S. (2017a). Backtracking depth-resolved microstructures for crystal plasticity identification - Part 1: Backtracking microstructures. *JOM*, 69(12):2810–2818.

Shi, Q., Latourte, F., Hild, F., and Roux, S. (2017b). Backtracking depth-resolved microstructures for crystal plasticity identification - Part 2: Identification. *JOM*, 69(12):2803–2809.

Shi, Q., Latourte, F., Roux, S., and Hild, F. (2017c). Procédé, dispositif et programme de traitement d'images de diffraction d'un matériau cristallin. French patent filed in December 2017, number: 1761926.

Shi, Q., Roux, S., Latourte, F., Hild, F., Loisnard, D., and Brynaert, N. (2018a). On the use of SEM correlative tools for in situ mechanical tests. *Ultramicroscopy*, 184(Part A):71 – 87.

Shi, Q., Roux, S., Latourte, F., Hild, F., Loisnard, D., and Brynaert, N. (2018b). Measuring topographies from conventional SEM acquisitions. *Ultramicroscopy*. , accepted.

Simo, J. and Miehe, C. (1992). Associative coupled thermoplasticity at finite strains: Formulation, numerical analysis and implementation. *Computer Methods in Applied Mechanics and Engineering*, 98(1):41 – 104.

Simonovski, I. and Cizelj, L. (2013). Cohesive element approach to grain level modelling of intergranular cracking. *Engineering Fracture Mechanics*, 110(0):364–377.

Stockbarger, D. (1936). The production of large single crystals of lithium fluoride. *Review of Scientific Instruments*, 7(3):133–136.

Suganuma, T. (1985). Measurement of surface topography using SEM with two secondary electron detectors. *Journal of Electron Microscopy*, 34(4):328–337.

Sun, Y. and Pang, J. H. (2006). AFM image reconstruction for deformation measurements by digital image correlation. *Nanotechnology*, 17(4):933.

Sutton, M. (2013). Computer vision-based, noncontacting deformation measurements in mechanics: a generational transformation. *Applied Mechanics Reviews*, 65(5):050802.

Sutton, M., Li, N., Garcia, D., Cornille, N., Orteu, J., McNeill, S., Schreier, H., and Li, X. (2006). Metrology in a scanning electron microscope: theoretical developments and experimental validation. *Measurement Science and Technology*, 17:2613–2622.

Sutton, M., Li, N., Garcia, D., Cornille, N., Orteu, J.-J., McNeill, S., Schreier, H., Li, X., and Reynolds, A. (2007a). Scanning electron microscopy for quantitative small and large deformation measurements Part II: Experimental validation for magnifications from 200 to 10.000. *Experimental Mechanics*, 47(6):789–804.

Sutton, M., Li, N., Joy, D., Reynolds, A., and Li, X. (2007b). Scanning electron microscopy for quantitative small and large deformation measurements Part I: SEM imaging at magnifications from 200 to 10.000. *Experimental Mechanics*, 47(6):775–787.

Sutton, M., Orteu, J.-J., and Schreier, H. (2009). *Image Correlation for Shape, Motion and Deformation Measurements: Basic Concepts, Theory and Applications*. Springer US, New York.

Sutton, M., Wolters, W., Peters, W., Ranson, W., and McNeill, S. (1983). Determination of displacements using an improved digital correlation method. *Image and Vision Computing*, 1(3):133 – 139.

Swinburne, T., Dudarev, S., Fitzgerald, S., Gilbert, M., and Sutton, A. (2013). Theory and simulation of the diffusion of kinks on dislocations in BCC metals. *Physical Review B*, 87(6):064108.

Tafti, A. P., Holz, J. D., Baghaie, A., Owen, H. A., He, M. M., and Yu, Z. (2016). 3DSEM++: Adaptive and intelligent 3D SEM surface reconstruction. *Micron*, 87(Supplement C):33 – 45.

Tafti, A. P., Kirkpatrick, A. B., Alavi, Z., Owen, H. A., and Yu, Z. (2015). Recent advances in 3D SEM surface reconstruction. *Micron*, 78(Supplement C):54 – 66.

Taillandier-Thomas, T., Roux, S., Morgeneyer, T. F., and Hild, F. (2014). Localized strain field measurement on laminography data with mechanical regularization. *Nuclear Instruments and Methods in Physics Research Section B: Beam Interactions with Materials and Atoms*, 324(0):70–79.

Tang, M., Kubin, L., and Canova, G. (1998). Dislocation mobility and the mechanical response of BCC single crystals: A mesoscopic approach. *Acta Materialia*, 46(9):3221 – 3235.

Tatschl, A. and Kolednik, O. (2003). On the experimental characterization of crystal plasticity in polycrystals. *Materials Science and Engineering: A*, 356(1-2):447–463.

Teyssedre, H., Roux, S., Régnier, G., and Tracz, A. (2011). Filtering out slow-scan drifts in atomic force microscopy images. *The Journal of Strain Analysis for Engineering Design*, 46(5):361–367.

Thornton, P. R., Mitchell, T. E., and Hirsch, P. B. (1962). The strain-rate dependence of the flow stress of copper single crystals. *The Philosophical Magazine: A Journal of Theoretical Experimental and Applied Physics*, 7(74):337–358.

Tikhonov, A. and Arsenin, V. (1977). *Solution of ill-posed problems*. Winston, New York (USA).

Tjahjanto, D., Eisenlohr, P., and Roters, F. (2010). A novel grain cluster-based homogenization scheme. *Modelling and Simulation in Materials Science and Engineering*, 18(1):21pp.

Tomičević, Z., Hild, F., and Roux, S. (2013). Mechanics-aided digital image correlation. *Journal of Strain Analysis for Engineering Design*, 48:330–343.

Tschopp, M., Bartha, B., Porter, W., Murray, P., and Fairchild, S. (2009). Microstructure-dependent local strain behavior in polycrystals through in-situ scanning electron microscope tensile experiments. *Metallurgical and Materials Transactions A*, 40(10):2363–2368.

Venables, J. and Bin-jaya, R. (1977). Accurate microcrystallography using electron backscattering patterns. *Philosophical Magazine*, 35(5):1317–1332.

Vereecke, B. (2004). *Une analyse probabiliste du comportement d'une famille d'aciers pour cuve de REP en cas d'accident grave*. PhD thesis, Université Paris VI.

Verhulp, E., van Rietbergen, B., and Huiskes, R. (2004). A three-dimensional digital image correlation technique for strain measurements in microstructures. *Journal of Biomechanics*, 37(9):1313–1320.

Villert, S. (2008). *Analyse des déformations élastiques locales par la technique EBSD*. PhD thesis. Ecole des Mines Saint-Etienne.

Villert, S., Maurice, C., Wyon, C., and Fortunier, R. (2009). Accuracy assessment of elastic strain measurement by ebsd. *Journal of Microscopy*, 233(2):290–301.

Volkert, C. A. and Minor, A. M. (2007). Focused ion beam microscopy and micromachining. *MRS bulletin*, 32(5):389–399.

Wagne, B., Roux, S., and Hild, F. (2002). Spectral approach to displacement evaluation from image analysis. *European Physical Journal: Applied Physics*, 17:247–252.

Wang, Y., Zang, S., Sun, L., and Ma, J. (2017). Constructing micro-mechanical representative volume element of medium Mn steel from EBSD data. *Materials & Design*, 129(Supplement C):34 – 43.

Watanabe, O., Zbib, H. M., and Takenouchi, E. (1998). Crystal plasticity: micro-shear banding in polycrystals using voronoi tessellation. *International Journal of Plasticity*, 14(8):771–788.

Wilkinson, A., Meaden, G., and Dingley, D. (2006a). High-resolution elastic strain measurement from electron backscatter diffraction patterns: New levels of sensitivity. *Ultramicroscopy*, 106(4-5):307 – 313.

Wilkinson, A., Meaden, G., and Dingley, D. (2006b). High resolution mapping of strains and rotations using electron backscatter diffraction. *Materials Science and Technology*, 22(11):1271–1278.

Wilkinson, A. J. and Britton, T. B. (2012). Strains, planes, and EBSD in materials science. *Materials Today*, 15:366–376.

Williams, D. B. and Carter, C. B. (1996). The transmission electron microscope. In *Transmission Electron Microscopy: A Textbook for Materials Science*, pages 3–17. Springer US, Boston, MA.

Wisniewski, W., Saager, S., Böbenroth, A., and Rüssel, C. (2017). Experimental evidence concerning the significant information depth of electron backscatter diffraction (EBSD). *Ultramicroscopy*, 173:1 – 9.

Wright, S. (2000). Fundamentals of automated EBSD. In Schwartz, A. J., Kumar, M., and Adams, B. L., editors, *Electron Backscatter Diffraction in Materials Science*, pages 51–64. Springer US, Boston, MA.

Wu, C., Adams, B., Bauer, C., Casasent, D., Morawiec, A., Ozdemir, S., and Talukder, A. (2002). Mapping the mesoscale interface structure in polycrystalline materials. *Ultramicroscopy*, 93(2):99 – 109.

Wulfinghoff, S., Forest, S., and Böhlke, T. (2015). Strain gradient plasticity modeling of the cyclic behavior of laminate microstructures. *Journal of the Mechanics and Physics of Solids*, 79:1–20.

Xu, Z.-H., Li, X.-D., Sutton, M. A., and Li, N. (2008). Drift and spatial distortion elimination in atomic force microscopy images by the digital image correlation technique. *The Journal of Strain Analysis for Engineering Design*, 43(8):729–743.

Yan, S., Adegbule, A., and Kibbey, T. C. (2017). A hybrid 3D SEM reconstruction method optimized for complex geologic material surfaces. *Micron*, 99(Supplement C):26 – 31.

Zaafarani, N., Raabe, D., Singh, R., Roters, F., and Zaefferer, S. (2006). Three-dimensional investigation of the texture and microstructure below a nanoindent in a Cu single crystal using 3D EBSD and crystal plasticity finite element simulations. *Acta Materialia*, 54(7):1863 – 1876.

Zaefferer, S. (2007). On the formation mechanisms, spatial resolution and intensity of backscatter Kikuchi patterns. *Ultramicroscopy*, 107(2-3):254 – 266.

Zaefferer, S. and Wright, S. I. (2009). Three-dimensional orientation microscopy by serial sectioning and EBSD-based orientation mapping in a FIB-SEM. In Schwartz, A. J., Kumar, M., Adams, B. L., and Field, D. P., editors, *Electron Backscatter Diffraction in Materials Science*, pages 109–122. Springer US, Boston, MA.

Zeghadi, A., N'Guyen, F., Forest, S., Gourgues, A.-F., and Bouaziz, O. (2007a). Ensemble averaging stress-strain fields in polycrystalline aggregates with a constrained surface mi-

crostructure - Part 1: Anisotropic elastic behaviour. *Philosophical Magazine*, 87(8):1401–1424.

Zeghadi, A., N'Guyen, F., Forest, S., Gourgues, A.-F., and Bouaziz, O. (2007b). Ensemble averaging stress-strain fields in polycrystalline aggregates with a constrained surface microstructure - Part 2: Crystal plasticity. *Philosophical Magazine*, 87(8):1425–1446.

Zhang, F., Castelnau, O., Bornert, M., Petit, J., Marijon, J., and Plancher, E. (2015). Determination of deviatoric elastic strain and lattice orientation by applying digital image correlation to Laue microdiffraction images: the enhanced Laue-DIC method. *Journal of Applied Crystallography*, 48(6):1805–1817.

Zhang, Y., Elbrønd, A., and Lin, F. (2014). A method to correct coordinate distortion in EBSD maps. *Materials Characterization*, 96:158–165.

Zhang, Z.-F., Kang, Y.-L., Wang, H.-W., Qin, Q.-H., Qiu, Y., and Li, X.-Q. (2006). A novel coarse-fine search scheme for digital image correlation method. *Measurement*, 39(8):710 – 718.

Zhao, Z., Ramesh, M., Raabe, D., Cuitino, A., and Radovitzky, R. (2008). Investigation of three-dimensional aspects of grain-scale plastic surface deformation of an aluminum oligocrystal. *International Journal of Plasticity*, 24(12):2278–2297.

Zhu, T., Sutton, M. A., Li, N., Orteu, J.-J., Cornille, N., Li, X., and Reynolds, A. P. (2011). Quantitative stereovision in a scanning electron microscope. *Experimental Mechanics*, 51:97–109.

Zhu, Y., Corigliano, A., and Espinosa, H. (2006). A thermal actuator for nanoscale in situ microscopy testing: design and characterization. *Journal of Micromechanics and Microengineering*, 16:242–253.

université PARIS-SACLAY
ÉCOLE DOCTORALE
Sciences mécaniques et énergétiques, matériaux et géosciences (SMEMAG)

Titre : Etudes expérimentales et numériques de plasticité cristalline d'un acier de cuve

Mots clés : Plasticité cristalline, Rotation cristalline, microscopie électronique, Corrélation d'images numériques, Recalage de modèles éléments finis, Acier bainitique-ferritique.

Résumé : Cette thèse vise à étudier le comportement mécanique de l'acier de cuve 16MND5 (ou A508cl3 pour la norme anglaise) à l'échelle de la microstructure en croisant des approches expérimentale et numérique. Plusieurs contributions au développement de l'essai de traction in-situ à l'intérieur de MEB ont été apportées. En premier, les biais de mesure de différentes modalités (BSE, EBSD et SE) d'acquisition d'images sous MEB ont été caractérisés et corrigés. Les images MEB de différentes modalités ont été corrélées de façon précise afin de décrire la topographie de l'éprouvette. Les images d'orientation cristallographique (EBSD) ont été corrélées afin de révéler la rotation cristalline et les champs de déplacement de surface au long de la traction. La déformation élastique de l'éprouvette a été mesurée par corrélation intégrée des images de diffraction électronique à haute-résolution. Les microstructures fines de l'éprouvette à trois dimensions après déformation ont été mesurées par FIB-EBSD.

L'essai a également été simulé par calcul de plasticité cristalline sur un maillage 3D, basé sur les microstructures mesurées dans la configuration déformée. Un algorithme a été proposé pour estimer la configuration initiale de l'éprouvette et identifier les paramètres de loi de plasticité en procédant par itérations. Un cas test synthétique 2D a été employé pour valider la faisabilité de l'algorithme. Deux lois de plasticité cristalline ont été testées sur le maillage 3D: dynamique des dislocations des cristaux cubiques centrés, et une version modifiée de la loi Méric-Cailletaud. Pour cette dernière loi, deux jeux de paramètres ont été identifiés pour les ferrites et bainites par recalage des éléments finis.

Title : Experimental and numerical studies on the micromechanical crystal plasticity behavior of an RPV steel

Keywords: Crystal plasticity, Crystal rotation, Scanning electron microscopy, Digital image correlation, Finite element model updating, Bainitic-ferritic steel.

Abstract: The PhD project studies the mechanical response of the reactor pressure vessel steel A508cl3 (or 16MND5 in French nomenclature) at the microscopic scale by experimental analyses and numerical simulations. Different aspects of in-situ tests inside an SEM chamber have been considered. First, the characterization and corrections of bias and uncertainties of different SEM imaging modalities (SE, BSE, and EBSD) have been performed. Precise registrations of SEM images in different modalities have been developed in order to give a comprehensive description of the sample surface topographies. Crystallographic orientation maps (from EBSD analyses) are registered to measure the crystal rotation and displacement fields along the tensile test. The elastic deformations of the surface are assessed by integrated correlation of high-resolution electron diffraction images. The 3D microstructure of the analyzed sample is revealed a posteriori by combining FIB milling and EBSD images.

The experimental test is also simulated by crystal plasticity calculations on a 3D mesh created according to the 3D microstructure observed in the deformed configuration. An algorithm has been proposed to estimate its initial configuration and to identify the plastic parameters iteratively. A synthetic 2D model has been used to prove its feasibility. Two crystal plasticity laws have been validated on the 3D mesh, namely dislocation dynamics for body-centered cubic crystals and a modified version of Méric-Cailletaud model. In the present work finite element model updating was used to provide two sets of parameters (for ferrite and bainite) for the latter law.

Université Paris-Saclay
Espace Technologique / Immeuble Discovery
Route de l'Orme aux Merisiers RD 128 / 91190 Saint-Aubin, France